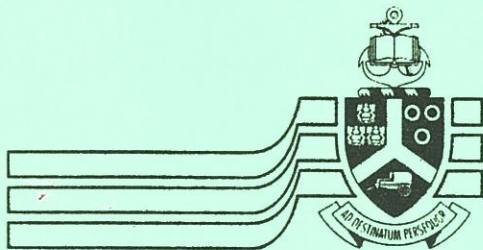


# **SAUPEC - 95 SAUKIK - 95**

## **SOUTHERN AFRICAN UNIVERSITIES POWER ENGINEERING CONFERENCE**



University of Pretoria



Pretoria Technikon

CONVENED BY

*THE UNIVERSITY OF PRETORIA*

AND

*PRETORIA TECHNIKON*

## **Proceedings of the Fifth Conference**

PRETORIA

19 - 20 JANUARY 1995

*Fifth Conference of*

# **Southern African Universities Power Engineering**

19 & 20 January 1995

*Organised by*

The University of Pretoria

and

Pretoria Technikon

*Venue*

University of Pretoria



## **ORGANISING AND TECHNICAL PROGRAMME COMMITTEE**

Prof. IE Lane	University of Pretoria
Mr T Bornman	Pretoria Technikon
Mrs A Lane	University of Pretoria
Prof. HR Van Niekerk	University of Pretoria
Prof. ED Smith	University of Pretoria
Prof. JC Van Alphen	University of Pretoria
Mr J Bouwer	Pretoria Technikon
Mr GJ Delport	University of Pretoria
Mr GMJ Parsley	University of Pretoria
Mr JG Roos	University of Pretoria
Mr JLM Pretorius	University of Pretoria
Mr G Donev	University of Pretoria
Ms R Hewitt	FRD

Responsibility for the contents of papers bound in this Proceedings, rests with the authors and not with the organising committee.

Published by the Department of Electrical and Electronic Engineering,  
University of Pretoria, Pretoria, South Africa  
December 1994



# TABLE OF CONTENTS : INHOUDSOPGAWE

**THURSDAY 19 JANUARY 1995 : DONDERDAG 19 JANUARIE 1995**

**Plenary Session : Volsitting** **Chairman/Voorsitter : IE Lane**  
**08:30 - 10:15**  
**Van Der Bijl Lecture Theatre, Kanseliers Building**

Postgraduate Competency Based Training of Power System Engineers in Australia  
*E Palmer, D Birtwhistle and L McKinnon - Queensland University of Technology, Australia* . . . . . 1

**Parallel Session A-1.1 : Parallel Sessie A-1.1** **Chairman/Voorsitter : D van Wyk**  
**10:45 - 12:00**  
**Hall 1-1 Engineering Tower Block : Lokaal 1-1 Ingenieurstoringblok**  
**Power Transmission and Distribution : Kragtransmissie en -Verspreiding**

Introductory Analysis of the Thermal Effects on Aerial Bundled Conductors  
Feeding Stochastic Domestic Loads  
*DR Theron, R Herman - University of Stellenbosch* . . . . . 5

A Single-Phase Active Distortion Cancellation  
*S Purmanund, M Malengret - University of Cape Town* . . . . . Supl

Active Three-Phase Load Balancing  
*I Terblanche, M Malengret - University of Cape Town* . . . . . Supl

Optimal Capacitor Placement on Radial Distribution Systems to Minimise Harmonic  
Distortion  
*HV Hitzeroth, A Petroianu - University of Cape Town* . . . . . 9

**Parallel Session A-1.2 : Parallel Sessie A-1.2** **Chairman/Voorsitter : JLM Pretorius**  
**14:00 - 15:00**  
**Hall 1-1 Engineering Tower Block : Lokaal 1-1 Ingenieurstoringblok**  
**Power Transmission and Distribution : Kragtransmissie en -Verspreiding**

A Financial Comparison of Three-Phase Versus Single-Phase Rural Electricity  
Distribution  
*G Wyatt, CE Dingley - University of Cape Town* . . . . . 13

An Investigation into the Use of Intermediate Voltage for Rural Electrification  
*C Badenhorst, CE Dingley and I Ferguson - University of Cape Town & Eskom* . . . . . 17

Low Cost Three-Phase Rural Electrification  
*G Naldrett, M Malengret - University of Cape Town* . . . . . Supl

The Life-Cycle Costing of Urban Electrical Distribution Transformers  
*SD Michie, CE Dingley - University of Cape Town* . . . . . 21

## TABLE OF CONTENTS

Parallel Session A-1.3 : Parallel Sessie A-1.3	Chairman/Voorsitter : T Bornman
15:15 - 16:30	
Hall 1-1 Engineering Tower Block : Lokaal 1-1 Ingenieurstoringblok	
Power Transmission and Distribution : Kragtransmissie en -Verspreiding	

Measurement of Capacitive Voltage Transformer Earth Return Current Harmonics <i>H J Vermeulen, J van Rooijen, GH Muller and SR Stadler - University of Stellenbosch</i> . . . . .	25
The Economics and Application of Single Pole Protection Schemes on Radial 132 kV Feeders <i>O Von Abo - Eskom, Pretoria Technikon</i> . . . . .	29
An Investigation of Characteristics for Tripping Protection Used for Detecting Out- Of-Step Conditions. An Eskom Case Study <i>J van Eyssen, A Petroianu - Eskom &amp; University of Cape Town</i> . . . . .	34
Experimental Investigation and Modelling of Thermal Transients of Underground High Voltage Cables <i>F Smith, JP Holtzhausen - University of Stellenbosch</i> . . . . .	38
Method of Using Data from Computer Simulation to Test Protection Relays <i>R Zivanovic, PA Weyers and DC Barry - Pretoria Technikon</i> . . . . .	42

Parallel Session B-1.1 : Parallel Sessie B-1.1	Chairman/Voorsitter : J Bouwer
10:45 - 12:00	
Hall 1-4 Engineering Tower Block : Lokaal 1-4 Ingenieurstoringblok	
Power Electronics and Electrical Machines : Drywingselektronika en Elektriese Masjiene	

Measurement of Laminated Steel Properties at High Flux Densities and Non- Sinusoidal Operation <i>C Slabbert, FS van der Merwe and H J Vermeulen - University of Stellenbosch</i> . . . . .	45
Fault Diagnosis in Induction Motors Using Acoustic Techniques <i>A Gaylard, AS Meyer and CF Landy - University of the Witwatersrand</i> . . .	49
Controlling the Speed of an Induction Motor by Supplying the Stator with a Variable Frequency and Operating the Rotor Close to Resonance <i>RM da P Adanjo, GMJ Parsley - University of Pretoria</i> . . . . .	53
Electrical Motor for Low Cost Reticulation Scheme <i>M Hippner, AR Perkin - University of Natal</i> . . . . .	57
Robust Excitation Control of Power Systems Using Fixed Structure Controllers <i>L Chen, S Ahmed and A Petroianu - University of Cape Town</i> . . . . .	61

## TABLE OF CONTENTS

**Parallel Session B-1.2 : Parallel Sessie B-1.2**      **Chairman/Voorsitter : GMJ Parsley**  
**14:00 - 15:00**

**Hall 1-4 Engineering Tower Block : Lokaal 1-4 Ingenieurstoringblok**  
**Power Electronics and Electrical Machines : Drywingselektronika en Elektriese**  
**Masjiene**

The Mathematics Governing the Rotor Torque Relationship of Wound Rotor Induction Motors through Synchronous switching of Rotor Resistance  
*DJ Bouwer - Pretoria Technikon* . . . . . 65

The Practical Development of a Neural Network Induction Motor Drive  
*B Burton, RG Harley, JL Rodgerson and D Levy - University of Natal & Sydney University, Australia* . . . . . 69

Die Spoorkanon as Elektromagnetiese Lanseerder  
*SD Roos, JA Ferreira - Rand Afrikaans University* . . . . . 73

A Drive Development Platform for Direct Portation of Control Algorithm Code Between Simulation and Hardware Environment  
*CE Kleinhans, RG Harley, G Diana, MD McCulloch and MC Randelhoff - University of Natal & Oxford University, UK* . . . . . 77

**Parallel Session B-1.3 : Parallel Sessie B-1.3**      **Chairman/Voorsitter : ED Smith**  
**15:15 - 16:00**

**Hall 1-4 Engineering Tower Block : Lokaal 1-4 Ingenieurstoringblok**  
**Power Electronics and Electrical Machines : Drywingselektronika en Elektriese**  
**Masjiene**

Linear Induction Motors in Automated Manufacturing Systems  
*JF Gieras - University of Cape Town* . . . . . 81

Transient Analysis and Performance of a Solid State Series Reactance Compensator  
*BS Rigby, RG Harley - University of Natal* . . . . . 85

A Development System for Automated Generation of Hard Real-Time Control Code for Motion Control Systems  
*MC Randelhoff, CE Kleinhans, RG Harley and DC Levy - University of Natal & University of Sydney, Australia* . . . . . 89

## TABLE OF CONTENTS

<b>Parallel Session C-1.1 : Parallel Sessie C-1.1</b> <b>10:45 - 12:00</b> <b>Hall 1-2 Engineering Tower Block : Lokaal 1-2 Ingenieurstoringblok</b> <b>Power System Control and Demand Management : Kragstelselbeheer en</b> <b>Aanvraagbestuur</b>	<b>Chairman/Voorsitter : AB Johnston</b>
--	--

Load Curtailment Cost Modelling of Electrical Arc Furnaces in an Integrated Steel Plant <i>FGT Radloff, IE Lane - University of Pretoria</i>	93
The Role that Load Analysis of Electrical Arc Furnaces has to play in a Steel Plant <i>MM Ferreira, IE Lane - Potchefstroom University for CHE &amp; University of Pretoria</i>	97
Load Management Scenario and Constraint Modelling based on Steel Plant Product Scheduling and Feedstock Switching <i>W Mulder, IE Lane - University of Pretoria</i>	101
Innovative Electricity Pricing and Energy Management in Industry <i>JG Roos, IE Lane and EC Botha - University of Pretoria</i>	105
Integrated Electricity End-Use Planning in Deep Level Mines <i>GJ Delpont, IE Lane - University of Pretoria</i>	109

<b>Parallel Session C-1.2 : Parallel Sessie C-1.2</b> <b>14:00 - 15:00</b> <b>Hall 1-2 Engineering Tower Block : Lokaal 1-2 Ingenieurstoringblok</b> <b>Power System Control and Demand Management : Kragstelselbeheer en</b> <b>Aanvraagbestuur</b>	<b>Chairman/Voorsitter : GJ Delpont</b>
--	---

Residential Load Modelling Using Cooking Appliance Proclivity, Availability and Usage Functions <i>JPG Engelbrecht, IE Lane - University of Pretoria</i>	113
System Analysis and Design of an Intelligent Decentralised Domestic Load Controller <i>GL van Harmelen, IE Lane - University of Pretoria</i>	117
Improvement of Quality of Electricity Supply <i>A van Zyl, JHR Enslin, R Koch and R Spée - University of Stellenbosch, Eskom TRI &amp; Oregon State University, USA</i>	121
Neural Networks for Non-Intrusive Appliance Load Monitoring <i>J Vermaak, IE Lane - University of Pretoria</i>	125

## TABLE OF CONTENTS

---

Parallel Session C-1.3 : Parallel Sessie C-1.3 15:15 - 16:00 Hall 1-2 Engineering Tower Block : Lokaal 1-2 Ingenieurstoringblok Power System Control and Demand Management : Kragstelselbeheer en Aanvraagbestuur	Chairman/Voorsitter : CE Dingley
---	----------------------------------

Device Level Modelling of the Risk of Unserved Energy for the Domestic Hot Water Heater <i>B Rautenbach, IE Lane - University of Pretoria</i> . . . . .	129
The Development of a Low Cost Refrigerator for Low Income Households <i>T Baker, CE Dingley - University of Cape Town</i> . . . . .	134
Calculation of the Risk of Unserved Energy <i>JJ Smit, IE Lane - University of Pretoria</i> . . . . .	138

# TABLE OF CONTENTS

## FRIDAY 20 JANUARY 1995 : VRYDAG 20 JANUARIE 1995

Parallel Session A-2.1 : Parallel Sessie A-2.1      Chairman/Voorsitter : JC Van Alphen  
08:00 - 10:00  
Hall 1-1 Engineering Tower Block : Lokaal 1-1 Ingenieurstoringblok  
Power Transmission and Distribution : Kragtransmissie en -Verspreiding

Insulator Pollution Monitor : Calibration Results <i>P Davel, JP Holtzhausen and WL Vosloo - University of Stellenbosch</i> . . .	143
Rod-to-Plane Gap: A Simple Technique to Quasi-Equalize the Breakdown Voltages for Positive and Negative Impulses <i>A Hoch, DA Swift - University of Natal</i> . . . . .	Supl
Corona Power Loss from Sharply-Pointed Components of Transmission Plant <i>DA Swift, JL Rodgerson and AC Britten - University of Natal &amp; TRI Eskom</i> . . . . .	Supl
Design and Realisation of an Automated Impulse Test Facility <i>G Kwasnik - Technikon Witwatersrand</i> . . . . .	147
Formation of Dry Bands on Polluted High Voltage Insulators: Influence of Air Density <i>A Hoch, DA Swift - University of Natal</i> . . . . .	Supl
An assessment of VFT V-t curves generated in mixtures of SF <sub>6</sub> and N <sub>2</sub> gas in a 180/110 mm coaxial test gap <i>D Reynders, R Traynor, SD Nielsen, IR Jandrell and JP Reynders - University of the Witwatersrand</i> . . . . .	151
A Life Management Program for the Stator Winding Insulation of Eskom's Power Generators <i>H van der Merwe, P Rasekhi - Eskom TRI &amp; WITS Technikon</i> . . . . .	155

Parallel Session A-2.2 : Parallel Sessie A-2.2      Chairman/Voorsitter : O von Abo  
10:30 - 12:00  
Hall 1-1 Engineering Tower Block : Lokaal 1-1 Ingenieurstoringblok  
Power Transmission and Distribution : Kragtransmissie en -Verspreiding

Bad Data Rejection in a Linear Programming Based Power System State Estimation <i>R Zivanovic, A Petroianu - Pretoria Technikon &amp; University of Cape Town</i> . . . . .	159
Object Orientated Software Package for Fault Analysis <i>L Mzamo, S Darie - University of CapeTown</i> . . . . .	163

## TABLE OF CONTENTS

Unit Connected Back-to-Back Pumped-Storage Schemes <i>TA Rae, RG Harley, GD Jennings and MT Wishart - University of Natal &amp; Eskom TRI</i> . . . . .	167
Consideration of the use of LPATS for Optimisation of Transmission Lines <i>M G Redelinghuys, W C van der Merwe and IR Jandrell - Eskom &amp; University of the Witwatersrand</i> . . . . .	171
Exploratory Design of a Southern African Grid for the year 2025 <i>R Ahlschlager, CE Dingley - University of Cape Town</i> . . . . .	175
Writing an Object-oriented Graphical User Interface for ATP as a Pre-processor to the Program <i>T Orbach, IR Jandrell and B Dwolatzky - University of the Witwatersrand</i>	179
<b>Parallel Session A-2.3 : Parallel Sessie A-2.3 Chairman/Voorsitter :  14:00 - 15:00  Hall 1-1 Engineering Tower Block : Lokaal 1-1 Ingenieurstoringblok  Power Transmission and Distribution : Kragtransmissie en -Verspreiding</b>	
The Development of an Integrated set of Software Tools for Use in the Design of an Electrical Reticulation Network <i>B Dwolatzky, AS Meyer - University of the Witwatersrand</i> . . . . .	183
The Use of Perchloroethylene to Enhance the Thermal and Insulating Properties of Mineral Oil <i>MSA Minhas, DA Hoch and JP Reynders - University of the Witwatersrand</i> . . . . .	186
The Effect of Corona Activity on the Hydrophobic Surface Properties of Silicon Rubber Insulators <i>AE Dickson, JP Reynders - University of the Witwatersrand</i> . . . . .	190
The Use of Neural Networks to Recognise Electrical Symbols on a Township Map <i>JC Shapiro, B Dwolatzky and AS Meyer - University of the Witwatersrand</i>	194

## TABLE OF CONTENTS

<b>Parallel Session B-2.1 : Parallel Sessie B-2.1</b> <b>08:00 - 10:00</b> <b>Hall 1-4 Engineering Tower Block : Lokaal 1-4 Ingenieurstoringblok</b> <b>Power Electronics and Electrical Machines : Drywingselektronika en Elektriese Masjiene</b>	<b>Chairman/Voorsitter : HR Van Niekerk</b>
---	---

Assessment of the Failure of Equalisers in a Lap Wound DC Generator <i>A Pagel, AS Meyer and CF Landy - University of the Witwatersrand . . .</i>	198
Flexible Three Phase Converter for Microprocessor Power Control <i>JA duToit, HJ Beukes, P Petzer, JHR Enslin and R Spée - University of Stellenbosch &amp; Oregon State University, USA . . . . .</i>	202
Nine Phase Permanent Magnet Synchronous Motor and Drive for an Electric Vehicle <i>MA Khan, M Malengret - University of Cape Town . . . . .</i>	Supl
Evaluation of Converter Topologies in High Power Utility Devices <i>HJ Beukes, JHR Enslin - University of Stellenbosch . . . . .</i>	Supl
The Use of Finite Element Analysis to Design a Low Cost Synchronous Reluctance Motor for the South African Market <i>MA Rohde, AS Meyer and CF Landy - University of the Witwatersrand .</i>	206
Simulation and Implementation of Sensorless Speed Control applied to a CSI-FED Field Oriented Controlled Induction Motor <i>KJ Talbot, CE Kleinhans, RG Harley and G Diana - University of Natal . .</i>	210
A New Rotating UPS <i>ED Smith, J Yang - University of Pretoria . . . . .</i>	214
An Inverting DC Traction Substation, Incorporating Active Power Filtering <i>PJ Randewijk, JHR Enslin - University of Stellenbosch . . . . .</i>	Supl

<b>Parallel Session B-2.2 : Parallel Sessie B-2.2</b> <b>10:30 - 12:00</b> <b>Hall 1-4 Engineering Tower Block : Lokaal 1-4 Ingenieurstoringblok</b> <b>Power Electronics and Electrical Machines : Drywingselektronika en Elektriese Masjiene</b>	<b>Chairman/Voorsitter : CF Landy</b>
---	---------------------------------------

A Formal Link between the Power, Mass, Speed and Efficiency of Electrical Machines <i>HR van Niekerk - University of Pretoria . . . . .</i>	218
Position Control of a Linear Induction Motor for Conveyance Applications <i>RJ Cruise, JF Pritchard and CF Landy - University of the Witwatersrand</i>	222

## TABLE OF CONTENTS

Solid State Torque Control of Slip-Ring Induction Machines <i>W Deyzel - Pretoria Technikon &amp; Anglo American Research Laboratories</i>	226
A PLC Based Control System for a Rotating UPS <i>J Yang, ED Smith - University of Pretoria</i>	230
Finite Element Assessment of Eddy Current Starters <i>R Melaia, AS Meyer and CF Landy - University of the Witwatersrand</i>	234
2 kW Photo-Voltaic Water Pump for the Kalahari Desert <i>M Baret, M Malengret - University of Cape Town</i>	Supl
<div style="border: 1px solid black; padding: 5px;"> <b>Parallel Session C-2.1 : Parallel Sessie C-2.1</b>      <b>Chairman/Voorsitter : A Calitz</b>  <b>08:00 - 10:00</b>  <b>Hall 1-2 Engineering Tower Block : Lokaal 1-2 Ingenieurstoringblok</b>  <b>Power System Control and Demand Management : Kragstelselbeheer en</b>  <b>Aanvraagbestuur</b> </div>	
Modelling the Efficiency of Domestic Water Heating Systems to Assess the Potential of DSM Options <i>JC van Tonder, IE Lane and LJ Grobler - University of Pretoria</i>	239
Domestic Stochastic Process Evaluation for Networks of Decentralised Load Controllers <i>GL van Harmelen, IE Lane - University of Pretoria</i>	244
Domestic Ligthing Load Shape Modelling Based on Survey Data <i>JF Peyper, IE Lane - University of Pretoria</i>	249
Spectrum Analysis Technology as Applied to Power Systems <i>GW Louw, MJ Case - Rand Afrikaans University</i>	254
Comfort-Cost Analysis for the Optimization of Domestic Load Controllers <i>GL van Harmelen, IE Lane - University of Pretoria</i>	258
FACTS front end for EMTP <i>NH Ramage, JM van Coller and R Koch - University of the Witwatersrand &amp; Eskom TRI</i>	264
Development of Cost-Effective Energy Management Strategies <i>NM Ijumba - University of Nairobi</i>	268

## TABLE OF CONTENTS

<b>Parallel Session C-2.2 : Parallel Sessie C-2.2</b> <b>10:30 - 12:00</b>	<b>Chairman/Voorsitter : R Herman</b>
---	---------------------------------------

<b>Hall 1-2 Engineering Tower Block : Lokaal 1-2 Ingenieurstoringblok</b> <b>Power System Control and Demand Management : Kragstelselbeheer en</b> <b>Aanvraagbestuur</b>
---

The Modelling of Arc Furnace Flicker and Synchronous Condenser Compensation <i>H Peterson, RG Koch, R van Heerden and PH Swart - Rand Afrikaans University &amp; Eskom TRI</i> . . . . .	272
Bofrekwensie Drywingsmeter en Bofrekwensie Drywing Tariefstelsel <i>WJ van der Merwe, PH Swart en MJ Case - Randse Afrikaanse Universiteit</i> . . . . .	277
Elektro-osmotiese Droging van Steenkool <i>W Mulder, ED Smith - University of Pretoria</i> . . . . .	281

# POSTGRADUATE COMPETENCY BASED TRAINING OF POWER SYSTEM ENGINEERS IN AUSTRALIA

E. Palmer

D. Birtwhistle

L. McKinnon

School of Electrical and Electronic Systems Engineering  
Queensland University of Technology  
Brisbane, Australia

**Abstract:** *This paper describes the design and implementation of a competency based postgraduate training scheme for electrical power engineers. The training course consists of 24 modules each of which were designed based on competency standards developed jointly by the Queensland University of Technology (QUT) and local power authorities. The method by which the competency standards for power engineers were developed is described as is the various modes of delivery of the various modules. The place of competency based training in higher education is discussed as are plans to market the courses overseas and in remote localities by means of distance education.*

## 1. Introduction

The Australian government in recent years has taken positive steps to bring about award restructuring throughout Australian industry which in turn has meant training courses at all levels have needed to focus on the development of recognised skills or competencies. In other words as a consequence of this award restructuring career paths have been created based on the attainment of competencies rather than simply knowledge or experience which may not necessarily translate into increased skills.

Until recently competency based training has had little impact on the professions, with the exception of the medical profession. In recent years there has been a dramatic reduction in staffing levels across the electrical supply industry in Australia and this has meant that there have been less experienced engineers left to help train newly employed graduate engineers. Furthermore, those that are left have had less time to devote to such training. With the development of a greater commercial focus within Australian power authorities and the consequent increased focus on efficient use of assets there is a notion that the postgraduate training of power engineers working in industry should be more industry focussed rather than research oriented like traditional engineering postgraduate courses.

With this in mind the Queensland Electricity Commission (QEC), the local generation/transmission authority and the South East Queensland Electricity Board (SEQEB), the local distribution authority contracted with QUT in 1992 to develop a training program for their professional engineering staff. Prior

to beginning development of these courses an Australia-wide survey was carried out by QUT seeking the opinion of the Australian power industry regarding a competency based postgraduate training program.

There were five survey questions asked, namely

A - Do you feel that there is a need for postgraduate training in power system engineering?

B - Do you believe there is a need for industry-specific postgraduate courses in electricity supply engineering?

C - Do you feel that such postgraduate courses should lead to formal qualifications?

D - Do you believe that such a postgraduate course is necessary to improve performance and productivity in the workplace?

E - Would you recommend that selected electrical engineers from your organisation participate in the proposed postgraduate program?

**Table 1 Response to Australia-Wide Survey**

Quest.	SA	A	U	D	SD
A	30	64	6	0	0
B	32	68	0	0	0
C	29	52	15	4	0
D	15	63	14	8	0
E	11	52	35	2	0

SA=Strongly Agree, A=Agree, U=Undecided, D=Disagree, SD=Strongly Disagree.

The response to the survey was 35% and the results are summarised in Table 1. The results of the survey as illustrated by Table 1 are overwhelmingly positive and according to many of the power authorities contacted the response to question E would have been even more positive had the courses been offered by distance education.

## 2. Development of Competency Standards

The competency approach to training had already drawn a lot of attention at the time the QUT/QEC/SEQEB training agreement was signed, [1]. While the Institution of Engineers, Australia, (IEAust.) had produced a set of generic competency standards for engineers in general, [2], there were no competency standards in existence for professional engineers working in the electrical supply industry.

Therefore the first major task confronting the designers of these courses was to draw up a set of competency standards for professional electrical

engineers working in the electricity supply industry. Workshops were arranged involving professional engineering staff from the Queensland electricity supply industry and lecturing staff from QUT. These workshops used the functional analysis method, [1], to break the jobs of professional power system engineers into a set of *key purpose statements* each of which in turn was broken down into several *units of competency*. There were 27 key purpose statements formulated each of which involved up to 9 units of competency.

As an example the key purpose statement "Design Distribution Systems" had as one unit of competency "Develop Generation Options". The units of competency were then in turn broken down into several *elements of competency*. Examples of elements of competency include:

- Assess Quality of Supply - Harmonic Distortion
- Establish Environmental Policy - For Transmission Lines
- Select Protection Schemes
- Assess Future Demand Side Management Options

Associated with each element of competency in the competency standards, [3], is a *Performance Criteria* statement which defines the standard required of each element of competency. As well associated with each element and unit of competency is a *Range of Variables* statement and a *Knowledge and Skills* statement. The range of variables statement defines the range of conditions over which the tasks must be performed, while the knowledge and skills statement defines the knowledge and skills required to perform the task.

Once completed the draft of the competency standards was about 400 pages in length and showed that engineers must show competence in managerial and commercial activities as well as technical activities. The standards differ from competency standards which have hitherto been developed for tradespeople by requiring a high level of innovation and application of latest technologies as well as managerial expertise.

While these standards were originally developed with the Queensland electricity supply industry in mind, they have attracted attention nationally and even internationally. It is therefore hoped that they may in time evolve into national standards of competency.

### 3. Design of Training Programs

In order to identify training needs from the competency standards a list was made of fields of knowledge. A total of 170 fields of knowledge were identified, each of which had a number of secondary fields associated with it. For example, "Testing" was

identified as a primary field of knowledge with "acceptance", "commissioning" and "workshop" being associated secondary fields of knowledge.

The fields of knowledge enabled senior power industry staff to identify training needs and a steering committees made up of representatives of the three parties to the training agreement drew up a list of 24 modules, see Appendix I. Detailed module syllabi were drawn up by the academic partner in consultation with industry with the objectives of each module being framed in terms of required competencies as listed in the competency standards. Being thus based on standards of competency it was deemed important that assessment be directed at testing whether or not a student had mastered various skills or the application of certain knowledge.

So far it has been the intention to present the various modules in five week blocks with a class of three hours duration per week. Alternatively the modules have been presented in "short course mode" whereby the fifteen hours of class contact per module have been run over two and a half days. The short course mode has been particularly successful for attracting students from remote areas.

Generally most of the subject material has been easily taught inside fifteen hours of class contact, however difficulty has been experienced in covering adequately all the material in some modules, most notably the stability module.

As an added inducement for power engineers to participate in the course it was suggested and agreed by all three parties to the training agreement that some kind of formal qualification would be desirable.

The award courses developed were qualifications in electricity supply engineering at the graduate certificate, graduate diploma, and masters degree levels. The requirements of the various award courses being as follows.

#### **Graduate Certificate in Electricity Supply Engineering**

Students must complete 12 modules.

#### **Graduate Diploma in Electricity Supply Engineering**

Students must complete 24 modules.

#### **Master of Engineering Science in Electricity Supply Engineering**

Students must complete 18 modules and prepare a practitioner's thesis based on 100 days of supervised professional practice.

These courses commenced operation on January 1994 with some pilot short courses being run in late 1993.

As the courses were designed to support industry competencies, a matrix was developed that shows

which units of competency and elements of competency are supported by QUT units. This matrix is generally sparse in nature. Indeed, it would not be expected that all the training requirements of the Queensland Electricity Supply Industry, (QESI), can be supported by this training program, and some competencies refer to material which could not or should not be taught in universities. In some parts of the matrix a large number of the units and elements of competency are supported by the training program. In the future the matrix will be used to show how effective new courses are in supporting value-added activities in the industry.

#### 4. Operation of the Training Programs

At the time of writing the various modules have been offered as short two-to-three day short courses and as 5 week modules as part of the award course program. Students completing short courses may claim credit towards one of the award courses. The enrolment statistics for 1993-1994 are detailed in table 2.

**Table 2 Unit Enrolment 1993-1994**

Course Mode	Enrolment
Short Course 1993	64 <sup>2</sup> /3 *
Day/Evening 1994, Semester 1	94
Day/Evening 1994, Semester 2	80
Short Course 1994, Semester 1	40
TOTAL	278 <sup>2</sup> /3

\* The two thirds results from a student enrolling in only two days of one module of the short course.

The level of enrolment is approximately double expectations, [4].

It should be noted that the emphasis of these courses is in the imparting of skills and knowledge accepted as being essential in the performance of tasks in industry. This is done by ensuring that students have a good grasp of the principles of the topic and then quickly moving to applications rather than emphasising detailed mathematical proofs or computational techniques.

For example in the case of the load flow module students spend the first three hours of the module covering the principles of the various types of load flow. Students are then introduced to a modern software and then use it to examine the dynamics of a realistic power system. In this way students gain an understanding of the behaviour of a power system over a range of operating conditions. Also they become adept at using modern analysis tools, and gain insight into the factors that limit the accuracy and reliability of the software.

As about 75% of course hours are taught by industry staff it is considered essential to give staff some guidance on teaching techniques before classroom

exposure. All teaching staff were therefore required to attend a half day course on teaching that was mainly presented by staff of the QUT central teaching development unit. At these courses simple techniques of class presentation, the philosophy behind the course, and assessment techniques were reviewed. Analysis of the student evaluation sheets completed at the end of each module showed that industry staff generally scored better than their QUT counterparts in terms of module presentation, thus demonstrating the quality of the industry staff employed.

At the end of each semester a review meeting of teaching staff was held with a view to gaining suggestions for improvements in course organisation, presentation, assessment, and facilities.

As mentioned earlier, at the end of each unit students are given the opportunity to provide feedback regarding the course undertaken. To this end students are requested to complete a course evaluation sheet. The questions asked deal with lecturer performance, and the effectiveness of the course undertaken in improving on-the-job skills. The questions asked were:

1. *Rate the extent to which the subject matter will help you carry out your job more effectively?*
2. *How realistic were the practical components of the course and how well did they reflect workplace practices?*
3. *How well did the theory lessons assist your understanding of work procedures?*
4. *Sum up your enjoyment of the course*

The results of the student evaluation were used to ascertain how the course presentation and facilities might be improved. It was shown that a general improvement had occurred on most items over time.

From experiences with the courses run to date it is concluded that the 5 week mode of presentation is far superior in imparting skills and knowledge than short courses. In the 5 week course students have time to assimilate material and to practise their skills, whereas in short courses they do not. This is further illustrated by the fact that for the first group of short courses conducted in 1993 only a small number of students completed all assessment items.

Since it is an objective of the QUT award courses and a high industry priority to ensure that engineers remote from population centres have access to educational opportunities. Some of these modules are currently being developed for presentation in a distance education mode. Thirteen modules are currently in production for presentation by distance education. Hopefully six will be ready by the start of 1995, with others being phased in during the first semester of 1995.

In order to ensure that students undertaking the modules through distance education have equal access to the software used by their short course and 5 week module counterparts time-locked copies of the power system analysis are being prepared for use by distance education students. This will enable students to receive a disc containing a copy of the power systems analysis package and example power systems and will have use of this material for two months. After this time the program will become disabled. In the two months however the students be able to gain experience in analysing power systems and will be able to complete assignment work.

At this stage no student has completed the thesis requirement of the Master of Engineering Science (MEngSc) course, although one student has been placed on a short term contract enabling him to complete the 100 day engineering practice requirement. During this time he will be working on the redesign of a transmission line being upgraded in voltage. In his thesis he will have to review all factors affecting line design including newer technologies that may permit a line uprating as well as giving descriptions of the technical and economic aspects of the design.

## 5. Future Developments

Additional units are planned for introduction in 1995 in order to cover a wider range of industry training needs and to offer students a wider choice of study areas. The 1995 courses will run in the short course mode, the 5 week mode and, for the first time, the distance education mode.

Furthermore, starting in November 1994 it is planned to run short courses in regional centres throughout the state of Queensland in order to enable students in remote locations to attend the courses. This is, of course, dependent on the industry demand for such courses. Already there has been a large demand for the first such regional short courses to be offered in Rockhampton in central Queensland. Engineers working in the mining industry have been included in this demand for the first time. Such students are particularly interested in the fault calculations module, the maintenance and reliability modules, and the protection modules.

Some modules, for example the stability module, have been found to be in need of revision. The topic of power system stability is one which is very complex and specialised with an extremely restricted student demand. Options for the future presentation of this unit include the splitting of the unit up into two modules.

Over the next few years the effectiveness of the courses in enhancing the job skills of power engineers will be

evaluated. If it is found that there has been an improvement in the time required for engineers to achieve competence then the training scheme will be deemed to have been a success.

## 6. Conclusions

An innovative solution to the requirements of the Australian power industry for on-going assessed training of its professional engineers has been developed by a close partnership between industry and a university. While the scheme is still in its early stages the high demand for the course together with the lower rates of graduation of electrical engineers with a specialisation in power, appears to indicate that the training scheme is quite viable.

## 7. References

1. Gonczi, A., Hager, P., and Oliver, L., "Establishing Competency-Based Standards in the Professions", National Office of Overseas Skills Recognition, Research Paper No. 1, December 1990
2. "The National Competency Standards for Professional Engineers (Stage 1 and 2)", The Institution of Engineers, Australia, March 1993
3. Draft Competency Standards in Electrical Engineering (unpublished), QEC/SEQEB/QUT, October 1993
4. Course Submission - Graduate Certificate, Graduate Diploma, and Master of Engineering Science (Electricity Supply), QUT, November 1993

## 8. Address of Authors

School of Electrical and Electronic Systems, QUT,  
GPO Box 2434, Brisbane, Qld 4001, Australia.

# INTRODUCTORY ANALYSIS OF THE THERMAL EFFECTS ON AERIAL BUNDLED CONDUCTORS FEEDING STOCHASTIC DOMESTIC LOADS

D R Theron      R Herman

Department of Electrical Engineering University of Stellenbosch  
South Africa

**ABSTRACT** - The drive to provide economic, properly installed electricity for low-cost housing schemes has opened the way for ABC's. There are however still some uncertainties in the thermal sizing of these cables. The aim of this paper is to address these uncertainties. Two published calculation methods, [1] and [2], are compared. The latter is used in a PC-based method for calculating the transient temperature rise of an ABC supplying a time-dependent load. The thermal behaviour of ABC's feeding stochastic domestic loads have been investigated by applying data from a load study on a local, low-cost housing scheme to the proposed analytical method.

## 1 INTRODUCTION

An aerial bundled conductor (ABC) consists of insulated conductors, bundled together to form one cable that is suspended in air.

Low-voltage, underground cabling is costly and time-consuming. ABC's on the other hand are more expensive than open wire uninsulated conductors, but installation and maintenance costs are much cheaper.

In the reconstruction and development program the South African government has allocated R1 350 million for low-cost housing. Cost-effective methods have to be used to electrify these houses, leaving the way open for ABC's.

In the following pages the thermal effects on ABC's are investigated to optimize the size selection of these cables. This will reduce the costs even more.

## 2 EXTERNAL THERMAL RESISTANCE

In the IEC publication 286 [1] a method for calculating the maximum continuous current,  $I$ , of cables is described. For a cable in free air exposed to solar radiation, without a metallic sheath or armouring and neglecting dielectric heating:

$$I = \left[ \frac{\Delta\theta - \sigma D_e^* H T_4^*}{R(T_1 + nT_4^*)} \right]^{1/2} \quad (1)$$

where:  $\Delta\theta$  = permissible temperature rise of the conductor above ambient [K]

$\sigma$  = absorption coefficient of solar radiation

$D_e^*$  = external diameter of the cable [m]

$H$  = intensity of solar radiation [ $W/m^2$ ]

$R$  = AC resistance per unit length of conductor [ $\Omega/m$ ]

$n$  = number of conductors per cable

$T_1$  = Thermal resistance of conductor and sheath [ $K.m/W$ ]

$T_4^*$  = Thermal resistance of the surrounding medium [ $K.m/W$ ]

The external thermal resistance  $T_4^*$  can be obtained as follows:

$$T_4^* = \frac{1}{\pi D_e^* h (\Delta\theta_s)^{1/4}} \quad (2)$$

$$h = \frac{Z}{(D_e^*)^g} + E \quad (3)$$

where:  $\Delta\theta_s$  = surface temperature rise of the cable above ambient [K]

$h$  = heat dissipation coefficient [ $W/m^2(K)^{1/4}$ ]

$Z$ ,  $E$  and  $g$  are constants given in table V, page 81 of [1]

Calculating the external thermal resistance as stated above has the disadvantage that it can only be used for a few specific cable arrangements, those for which  $Z$ ,  $E$  and  $g$  are available. A low-voltage, three phase ABC system normally has a quatrofoil arrangement, which is not available in Table V [1].

V.T. Morgan [2] has developed a method to calculate  $T_4^*$  for arbitrary cable arrangements by making use of an effective characteristic diameter,  $D_g$ . The effective diameter is that of the circle that circumscribes the bundle. Morgan's [2] formula for calculating  $T_4^*$  is the same as equation (2), except replacing  $h$  with  $h_N$ . Since the use of  $D_g$  introduced a general calculation method, the calculation of the heat dissipation coefficient,  $h$  has to be generalized as well, see equation (4).

$$h_N = \frac{1}{\Delta\theta_s^{1/4}} \left[ \frac{1.23 \Delta\theta_s^{1/4}}{D_g^{1/4}} + \frac{B\epsilon_o}{\Delta\theta_s} [(\Delta\theta_s + \theta_a + 273)^4 - (\theta_a + 273)^4] \right] \quad (4)$$

where: B = Stephen-Boltzmann constant  
 $\epsilon_s$  = emissivity of the cable surface  
 $\theta_a$  = ambient temperature [ $^{\circ}\text{C}$ ]

The first term within braces is the convective coefficient, and the second term is the radiative coefficient.




Equation (5) is now derived from Morgan's paper [2] to obtain a single formula to calculate the surface temperature rise for a cable suspended in air and exposed to solar radiation.

$$\Delta\theta_s = \Delta\theta + \left[ \frac{\sigma D_g H T_1}{n} \right] - \left[ \frac{\pi D_g T_1 h_N \Delta\theta_s^{4/5}}{n} \right] \quad (5)$$

An iterative approach is required to solve this equation.

The external thermal resistance and the maximum continuous current have been calculated according to the two mentioned methods for comparison. The results are shown in table 1. Calculations were done for a 35mm<sup>2</sup>, low-voltage aerial bundled conductor exposed to solar radiation, with a maximum permissible conductor temperature of 90 $^{\circ}\text{C}$ .

**Table 1:** Comparison between IEC [1] and Morgan [2].

Arrangement	IEC [1]		Morgan [2]	
	$T_4^*$ [K.m/W]	I [A]	$nT_4^*$ [K.m/W]	I [A]
	1.569	163.9	1.667	158.6
	3.159	111.6	2.513	131.2
	—	—	2.765	125.1

Note that  $T_4^*$  (according to IEC [1]) has to be compared to  $nT_4^*$  for the Morgan [2] case, because for this case  $T_4^*$  resembles the external resistance per conductor and there are n conductors in the effective diameter. For the single arrangement the two methods correlates well, within 3.5%. The difference for the trefoil arrangement is larger, about, 17%.

The method proposed by Morgan [2] is recommended for ABC-systems, because:

- \* it makes provision for ABC cable arrangements.
- \* it allows for the effects of heat dissipation by radiation and convection.
- \* the circumscribing circle method compensates for twisting of ABC's.

### 3 RESIDENTIAL LOADS

The current rating of power cables is determined by the permissible temperature rise of the insulation. The heat in the cable is generated from the conductor losses  $I^2 R_{AC}$ , in other words, the load current is directly responsible for the temperature rise.

The methods mentioned, [1] and [2], calculate the maximum permissible continuous current. A load study conducted at a local, low-cost housing scheme showed that such a residential load has a very distinct stochastic nature. A single current value cannot be used to model a residential load. The factor called after diversity maximum demand (ADMD) is often used to make provision for variable loads. The result is, however, also a single value of current. A much clearer picture of the transient temperature rise will be obtained if all the fluctuations of the load are accounted for.

### 4 TRANSIENT TEMPERATURE RISE WITH VARIABLE LOADS

In the IEC-publication 853 [3], part 2, section 2 a method is presented to calculate the transient temperature response to a step function of current. This work evidently originated from a paper by J.H. Neher [4]. The method is based on the lumped thermal network representation of a cable system. The lumped thermal network consists of a combination of thermal capacitances and resistances. Generally, the accuracy obtained depends upon the extent of this lumped network, but the complexity of solution increases rapidly with the number of sections used. It is possible to reduce the network to two sections in most cases and for this a relatively simple mathematical solution is available:

$$R_t(t) = [T_a(1 - e^{-at}) + T_b(1 - e^{-bt})] \quad (6)$$

$R_t$ , is the transient thermal resistance in ohm per metre. Electrical analogies are often used in heat flow problems. Equation (7) is known as Ohm's thermal law.

$$\Delta T = PR_t \quad (7)$$

**Table 2:** Thermal/Electrical analogies.

Thermal	Electrical
$\Delta T$ (Temperature)	$\Delta V$ (Potential difference)
$R_t$ (Thermal resistance)	$R_e$ (Electrical resistance)
P (Heat in watts)	I (Current)

The transient temperature rise, above ambient is thus

the following:

$$\Theta_c = (I^2 R_{AC}) [T_a(1 - e^{-at}) + T_b(1 - e^{-bt})] \quad (8)$$

The factors  $T_a$ ,  $T_b$ ,  $a$  and  $b$  are calculated according to section 4.2.2 of reference [3]. Among other elements, the external thermal resistance ( $T_a$ ) is needed for these factors. It is recommended that Morgan's method [2] be used for calculating  $T_a$ .

The transient temperature rise of figure 1 is obtained when a current step of 125 ampere is applied to a 35mm<sup>2</sup> gautofoil ABC. The cable temperature stabilizes at 90°C. This agrees with the values of table 1, which predict a maximum permissible current of 125 ampere at a conductor temperature of 90°C.

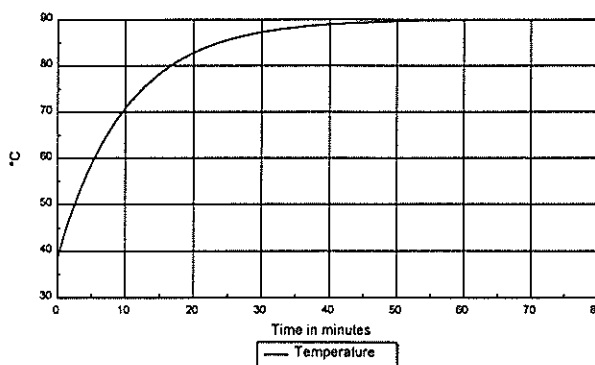


**Figure 1:** Transient temperature rise for a single current step function.

It is thus possible to calculate the temperature rise of the conductor as time passes for a single current step function. The aim is, however, to calculate the temperature rise for a variable load.

Neher, describes briefly in appendix III of his paper [4] a method to calculate the temperature rise for a variable load. A variant of this procedure that gives the same results is described in detail in a paper by R.J. Wiseman [5].

The following is a sequential summary of Neher's method [4]:

1. Calculate the transient thermal resistance  $R(t)$  with equation (6).
2. Calculate the load curve in watts per metre,  $P = I^2 R_{AC}$ .
3. Divide the load curve into a sufficient number of time intervals, during any of which the loading may be assumed substantially constant.
4. Calculate all the additional temperature rises occurring at every time interval established in step. 3. These additional rise curves are calculated by multiplying  $R(t)$  with the difference in the load for two consecutive time intervals.
5. Summate all the additional rise curves to give the

total temperature rise curve. Note that when there is a decrease in the load that the additional rise curve is subtracted.

The availability of computers nowadays, makes it possible to get an even better transient response with this method suggested by Neher [4] in 1964. It is relatively easy, with a computer program, to handle each variation of the load current as a different current step.

The proposed analytical method has been applied to the acquired load data. These data have been collected by means of data loggers. The loggers sample the load current every 0.5 seconds and 5 minute averages are then stored in memory. Each current step is thus five minutes long.

## 5 THERMAL ANALYSIS

The load study showed that the weekly maximum demand occurs normally on Sundays round noon. The load current and transient temperature rise for a typical Sunday is shown in figure 2.

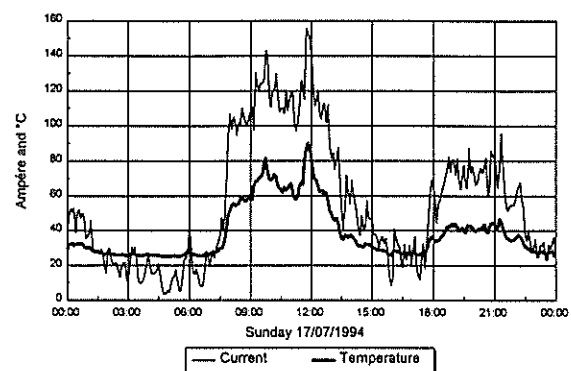


**Figure 2:** Load current and temperature rise for a typical Sunday.

The thermal behaviour of a power cable resembles the charging of a RC-circuit. It is well known that when a cyclic voltage, eg. a square wave, is applied to a capacitor, the average capacitor voltage will gradually increase and stabilize after a certain time.

The load patterns for the five weekdays are very similar. Saturdays and Sundays, on the other hand, have two very distinct load patterns. This weekly load cycle causes the cable temperature to have the same behaviour as that of the mentioned RC-circuit. The transient temperature rise for 20 days has been calculated, see figure 3.

It is thus important that thermal analysis of power cables should be carried out over long periods.

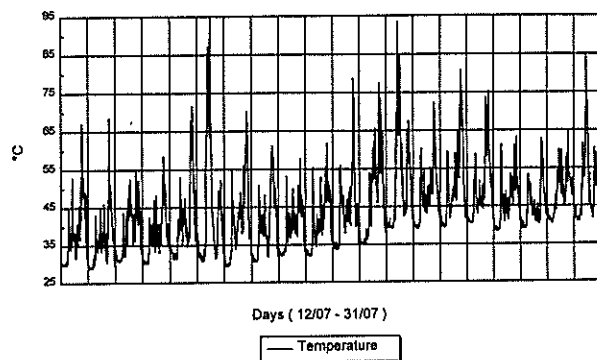


**Figure 3:** Temperature rise over 20 days.

## 6 TRANSIENT TEMPERATURE RISE VS ADMD

The after diversity maximum demand factor is calculated by adding the coincident load data of the users in the group together. The maximum peak of the added data is then used to calculate the maximum temperature. Figure 4 compares the temperature rise according to the ADMD factor with that calculated for the variable load.

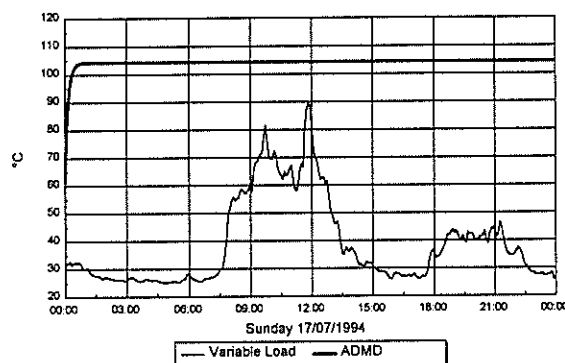


**Figure 4:** ADMD vs Variable Load.

The percentage overestimate for of the ADMD method for this example is 16%. A lower temperature value means a smaller cable could be used for a specific installation.

## 7 OPTIMAL SAMPLE PERIOD

Less disk space and down loading is needed if a longer sample period (averaging interval) is used. The accuracy of the calculation tends however to decrease with a longer sample interval. In figure 5 the transient temperature rise for different sample periods are shown.

The temperature with a fifteen minute load averaging interval correlates fairly well with the five minute case, especially at the maximum temperature. The difference is too large for a twenty minute sample period. A fifteen minute sample period is therefore recommended.

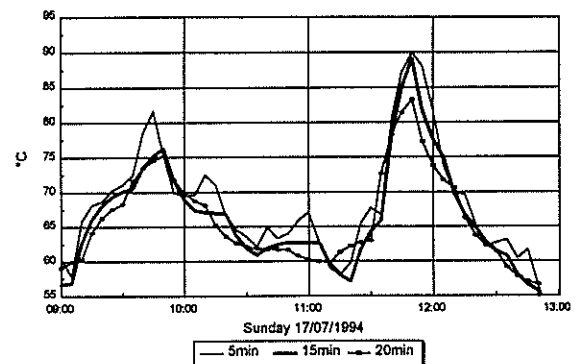


**Figure 5:** Temperature rise for different sample periods.

## 8 CONCLUSION

It is necessary to eliminate over estimates in design procedures to cut costs. This is possible with good knowledge of the load that a cable will supply. Extensive data logging for various user groups is thus needed. With these data available and with accurate calculation methods, cost effective thermal sizing of aerial bundled conductors is possible.

## 9 FUTURE WORK

Even with extensive data logging it will not be possible to forecast the exact loads for future installations. The only way of making a scientific acceptable forecast of such a load, is with a statistical load model.

The future goal is to make use of the Beta density function, as proposed by R. Herman and J.J. Kritzing [6], in the thermal sizing of ABC's

## 10 REFERENCES

- [1] "Calculation of the continuous current ratings of cables (100% load factor)" IEC, Publication 287-2, 1982.
- [2] Morgan, V.T.: "External thermal resistance of aerial bundled cables" IEE Proceedings-C, Vol. 140, No. 2, pp. 65-72, March 1993.
- [3] "Calculation of cyclic and emergency current rating of cables" IEC, Publication 853-2, 1989.
- [4] Neher, J.H.: "The transient temperature rise of buried cable systems" IEEE Transactions, PAS-83, pp.102-112, February 1964.
- [5] Wiseman, R.J.: "An empirical method for determining transient temperatures of buried cable systems" Power Apparatus and Systems, pt. III, Vol. 72, pp. 545-551, August 1953.
- [6] Herman, R., Kritzing, J.J.: "The statistical description of grouped domestic electrical load currents" Electric Power System Research, Vol. 27, pp.43-48, 1993.

# OPTIMAL CAPACITOR PLACEMENT ON RADIAL DISTRIBUTION SYSTEMS TO MINIMISE HARMONIC DISTORTION

H V Hitzeroth  
University of Cape Town

A Petroianu  
University of Cape Town

## Abstract

This paper describes a new method to determine the optimal locations of shunt compensation capacitors for radial distribution systems with harmonic distortion. The state space equations for a network are derived and the network poles and zeros are obtained. The solution to the harmonic resonance problem is formulated as a discrete optimisation problem in terms of pole and zero locations. Optimal capacitor locations are determined by means of a neighbourhood search algorithm. The procedure is demonstrated on an 18 bus radial distribution network. Furthermore, it is shown that the algorithm does provide optimal harmonic attenuation.

## 1. Introduction

Harmonic distortion in the power system is becoming an increasingly important issue in distribution system planning, design and operation. Not only are harmonic levels increasing in distribution systems but consumer loads are also becoming more sensitive to harmonic distortion [1].

Harmonics are generated by a variety of sources, ranging from arc furnaces, drives, transformers to lighting and computers. Most of these sources inject harmonic currents into the power system. These currents in turn result in harmonic voltage drops across various network elements. In this way harmonics can propagate throughout the power system to buses remote from the harmonic source [2].

If these harmonics are ignored, they can cause harmonic problems such as resonant conditions, telephone interference, capacitor bank failures, overheating of motors, vibrations as well as false tripping of equipment [1].

One way of solving the harmonic distortion problem (HDP) is by making use of sensitivity analysis methods [3, 4]. However, this requires much computational effort since all the system eigenvalues and eigenvectors need to be calculated. In addition, the sensitivity methods rely on a step by step method of analysis, whereby the sensitivity factors have to be analysed for each proposed system configuration.

Recently, the HDP was formulated as an optimisation problem [5]. However, the proposed method requires the solution of a three phase load flow at each iteration. This makes the computation cumbersome.

In this paper the HDP is formulated as a discrete optimisation problem. The objective function and its constraint are formulated in terms of distances from poles and zeros to the harmonic frequencies. A simple neighbourhood search is used to obtain the optimal solution. The method is tested on an 18 bus radial distribution network and the results are presented.

## 2. Mathematical Formulation of the HDP

### 2.1. State Space Model

In this study two types of radial distribution systems are considered, namely systems that have a capacitor at the end of each feeder and systems ending with a line on each feeder. The second case can be modelled in the same way as the first case, by modelling the line as part of the load.

In order to derive the state space model for such distribution systems, the independent state variables need to be chosen. These are taken as all the capacitor voltages, as well as all the nodal current injections at buses with capacitors attached to them. The loop and node equations can then be determined and expressed in the familiar state space form:

$$s\mathbf{x} = \mathbf{A}\mathbf{x} + \mathbf{B}\mathbf{u} \quad (1)$$

$$\mathbf{y} = \mathbf{C}\mathbf{x} \quad (2)$$

$$\mathbf{x}' = [I_1 \ I_2 \dots I_n \ V_1 \ V_2 \dots V_n] \quad (3)$$

where:  $s$  is the Laplace operator

$\mathbf{x}$  is the  $2n \times 1$  state space vector containing the  $n$  independent line currents as well as the  $n$  independent capacitor voltages

$\mathbf{A}$  is the  $2n \times 2n$  state coefficient matrix

$\mathbf{B}$  is the  $2n \times m$  input coefficient matrix

$m$  is the number of harmonic current sources

$\mathbf{u}$  is the  $m \times 1$  input vector of harmonic source currents

$\mathbf{y}$  is the  $p \times 1$  voltage output vector

$p$  is the number of nodal output voltages

$\mathbf{C}$  is the  $p \times 2n$  constant matrix relating the states to the output

$I_n$  is the current injected into node  $n$

$V_n$  is the voltage at node  $n$

Once the state space model has been determined, the parallel resonant frequencies (poles) are obtained by calculating the eigenvalues of the matrix  $\mathbf{A}$ .

It is well known, that the system transfer function is given by the following [6]:

$$Z(s) = \frac{y}{u} = C \frac{\text{adj}(sI - A)}{\det(sI - A)} B \quad (4)$$

where:  $Z(s)$  is the transfer function in the Laplace domain

In the case of a single input, single output system (SISO), where the input is applied at a capacitor node, the system impedance can be rewritten as follows [3]:

$$Z = \frac{1}{C_n} \frac{\det(sI - A_n)}{\det(sI - A)} \quad (5)$$

where:  $C_n$  is the capacitance of the capacitor bank at node  $n$

$A_n$  is obtained by eliminating the row and column of  $A$ , corresponding to the output node

Thus the series resonant frequencies (zeros) are determined by calculating the eigenvalues of the matrix  $A_n$ , which is of dimension  $(2n-1) \times (2n-1)$ .

## 2.2. Formulation of the HDP as an Optimisation Problem

In order to minimise the effect of the HDP, specifications can be placed on the poles and zeros of the system. The zeros should be close to harmonic frequencies and poles should be far from harmonic frequencies unless there is a zero between that pole and the harmonic frequency in question. Furthermore, poles and zeros should be close to each other.

These requirements are formulated as an objective function as follows:

$$\text{maximise}_{CS} (J = \min_i (\min_j |H_i - P_j|)) \quad (6)$$

subject to the constraint:

$$C = \min_i (\min_j |H_i - Z_j|) < \gamma \quad (7)$$

where:  $H_i$  is the  $i$ th harmonic frequency injected by the harmonic source

$P_j$  is the  $j$ th system pole

$Z_j$  is the  $j$ th system zero

$CS$  is the configuration space or feasibility set [4]

$J$  is the value of the objective function

$C$  is the value of the constraint for the zeros

$\gamma$  is the limit of the constraint

The configuration space is given by all the possible combinations of capacitor locations. A neighbourhood search results when only one capacitor at a time is switched on to another bus, thereby changing two bits in the configuration space.

The formulation of (6) and (7) was chosen, since it is desirable to have the poles far away from a harmonic frequency in order to avoid resonance effects. Furthermore, by choosing  $\gamma=1$  it is ensured, that there is a zero in the vicinity of a harmonic frequency. This is desirable, as it mitigates the dominance of the harmonic frequency.

## 2.3. Method of Solution

Figure 1 shows a flowchart of the procedure that was used to obtain a solution to the optimisation problem as posed in (6) and (7).

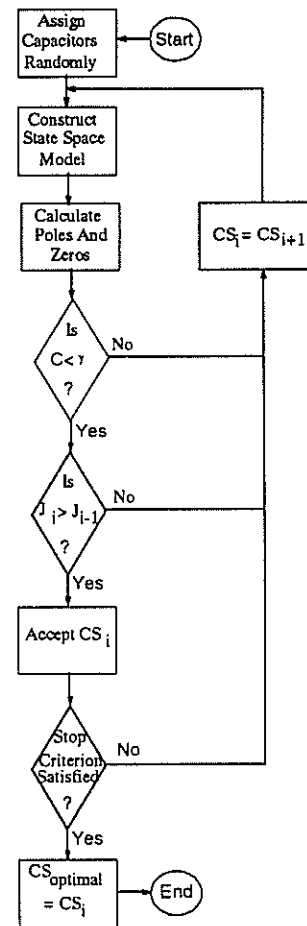


Figure 1: Flowchart of the optimisation algorithm.

After a random initial assignment of capacitors the state space model is generated and the system poles and zeros are calculated. The constraint for the zeros is then checked. If it is not satisfied, a new configuration space element is chosen by changing the position of one capacitor, resulting in a neighbourhood search. If the constraint is satisfied,

the value of the objective function is calculated and compared to the previous one.

If  $J_i < J_{(i-1)}$ , a new configuration space element is chosen as explained above. The objective function is once again evaluated and compared to the original value. If  $J_i < J_{(i-1)}$ , then  $CS_i$  is taken as the feasible capacitor assignment.

If  $J_i > J_{(i-1)}$ , the feasible configuration space element is updated. The process repeats itself until the stop criterion is met. The stop criterion states that if two iterations have not produced an improved  $J$  value, the algorithm terminates.

### 3. Case Study

The distribution system shown in Figure 2 was studied [3]. The system consists of three feeders connected to a transformer.

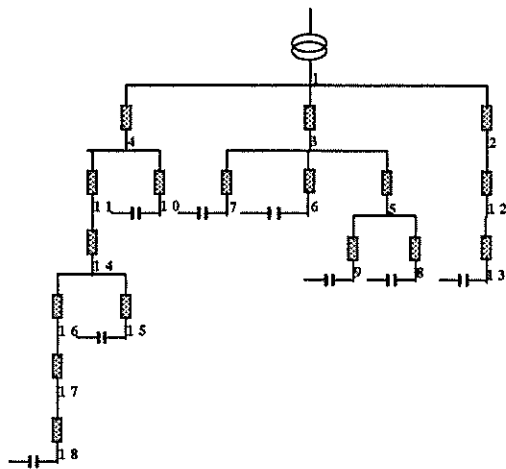


Figure 2: Positive sequence representation of the example network.

The system bases are 1 MVA, 13.2 kV and 377 rad/s. The line data as well as the transformer data is given in Table 1. The capacitor values are all 0.5 per unit. The line resistance and the loads were neglected in the study, as they only have minimal effects on the system poles and zeros thus resulting in a more conservative design. The shunt line capacitance was ignored, as it is negligible compared to the capacitor banks connected to the system.

A 1 MVA 6 pulse converter is connected to bus 18. Only the 5th and 7th harmonic are injected.

The poles and zeros, listed in Table 2, were calculated by using Matlab®. Furthermore, the system response shown in Figure 3, was obtained by using V-Harm®, which was developed by Cooper Industries specifically for harmonic analysis of power systems [8]. The V-

Harm® simulation was done by injecting a 0.3 per unit current over all frequencies up to the 10th harmonic.

Line	L	Line	L
Transformer	0.532	5-9	0.127
1-2	0.174	1-4	0.278
2-12	0.246	4-10	0.096
12-13	0.107	4-11	0.171
1-3	1.209	11-14	0.045
3-5	2.968	14-15	0.164
3-6	0.160	14-16	0.251
3-7	2.282	16-17	0.354
5-8	0.055	17-18	0.134

Table 1: Line and transformer data in percent of per unit values.

Poles	Zeros
$\pm j15.3027$	$\pm j35.2219$
$\pm j9.18034$	$\pm j33.3099$
$\pm j7.47741$	$\pm j30.0978$
$\pm j4.11069$	0

Table 2: Lower system poles and zeros in per unit before the optimisation.

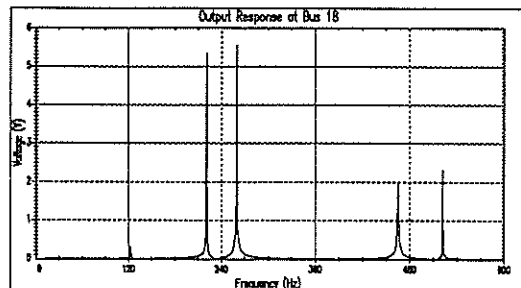


Figure 3: V-Harm® output response before the optimisation.

From Table 2 it can be seen that all the zeros are far from the 5th and 7th harmonic. Furthermore, the poles are very close to these frequencies. This indicates that there will be a harmonic distortion problem in the network if no countermeasures are applied. This is confirmed by Figure 3 which shows that there are very high resonant peaks in the vicinity of the 5th and 7th harmonic. The magnitudes for the 5th and 7th harmonic are 0.0344074 per unit and 0.0127801 per unit respectively.

In order to minimise the voltage distortion that is produced by the converter, four additional capacitors of 0.5 per unit each are at first randomly placed at the network buses. The  $A$  matrix and the poles and zeros for the output response at bus 18 are calculated. The optimisation algorithm as described in section 2.3. is applied, resulting in a neighbourhood search over the configuration space.

Figure 4 shows the value of the objective function for each iteration. It can be seen that  $J$  increases with each iteration. The optimal capacitor assignment is obtained after five iterations. The maximum value of  $J$  is 0.96337 per unit. For this example the optimal response at bus 18 is obtained when additional capacitors are connected to the following buses: 2, 12, 16 and 17.

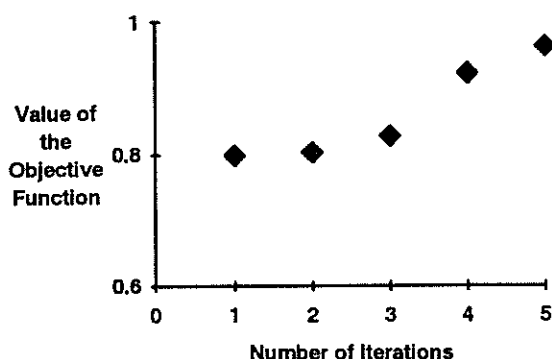


Figure 4: Value of the objective function for each iteration.

The poles and zeros for the optimal configuration are shown in Table 3. The output response is shown in Figure 5.

Poles	Zeroes
$\pm j16.6779$	$\pm j16.8447$
$\pm j11.2373$	$\pm j16.4566$
$\pm j7.98704$	$\pm j7.99356$
$\pm j5.96337$	$\pm j4.59542$
$\pm j3.96613$	0

Table 3: Lower system poles and zeros in per unit with the optimal capacitor assignment.

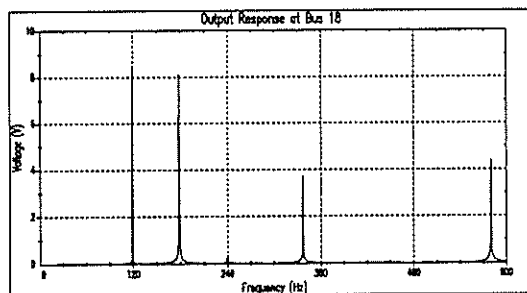


Figure 5: V-Harm<sup>®</sup> output response with the optimal capacitor assignment.

From Table 3 it can be seen that the nearest poles to the 5th and 7th harmonic are at 5.96337 and 7.98704 respectively. The frequency response of the simulation performed in V-Harm<sup>®</sup> also confirms the significant improvement over the original system. The magnitudes of the 5th and 7th harmonic are 0.0022821 per unit and 0.00708988 per unit

respectively. This is an improvement by a factor of about 15 and 2 respectively.

The new network configuration is therefore better than the original distribution system in terms of harmonic distortion.

#### 4. Conclusion

It has been shown in this paper, that the HDP can be formulated in terms of an optimisation problem. The objective function and its constraint can be expressed in terms of differences between poles, zeros and harmonic current injections. The optimisation algorithm was successfully applied to an 18 bus example network and the validity of the method was confirmed by V-Harm<sup>®</sup> simulations.

#### 5. References

- [1] Arrillaga, J., Bradley, D. and Bodger, D.: *Power System Harmonics*, John Wiley & Sons, New York 1985.
- [2] IEEE Tutorial Course: "Power System Harmonics" Course Text, 84 EH0221-2-PWR, 1984.
- [3] Ortmeyer, T.H. and Zehar, K.: "Distribution System Harmonic Design" *IEEE Transactions on Power Delivery*, Vol. 6, No. 1, pp. 289-294, January 1991.
- [4] Wickramasekara, M.G. and Lubekeman, D.: "Application of Sensitivity Factors for the Harmonic Analysis of Distribution System Reconfiguration and Capacitor Problems" *Proceedings of the Third International Conference on Harmonics in Power Systems*, pp. 141-148, Purdue, September 1988.
- [5] Grady, W.M., Samotyj, M.J. and Noyola, A.H.: "The Application of Network Objective Functions for Actively Minimising the Impact of Voltage Harmonics in Power Systems" *IEEE Transactions on Power Delivery*, Vol. 7, No. 3, pp. 1379-1386, July 1992.
- [6] Friedland, B.: *Control System Design*, McGraw-Hill, New York, 1987.
- [7] Fletcher, R.: *Practical Methods of Optimisation*, John Wiley & Sons, Chichester, 1987.
- [8] V-Harm Users Manual: Power System Harmonics Simulation and Analysis Program, McGraw-Edison, Cooper Industries, May 1988.

#### 6. Acknowledgements

We would like to thank Mr. S.S. Ahmed for his constructive contributions to this project.

# A FINANCIAL COMPARISON OF THREE-PHASE VERSUS SINGLE-PHASE RURAL ELECTRICITY DISTRIBUTION

Gary Wyatt and Charles Dingley  
University Of Cape Town

## ABSTRACT

There are presently 13.7 million people living in the rural areas of South Africa's former homelands. Of these only some 600 000 have access to electricity. A significant proportion of the costs of supplying electricity to these people will be attributed to the construction of medium voltage distribution systems. This paper examines how the cost of MV systems may be reduced by the adoption of single phase distribution techniques.

## 1. INTRODUCTION

Of the approximately 2.1 million households in the rural areas of South Africa's former Self Governing and TBVC states, by far the majority (93 %) do not have access to electricity. These areas will thus play an important part in the implementation of Eskom's *Electricity for All* campaign.

The problems of electrifying the rural homeland areas are twofold. Firstly, the per connection and operation costs are significantly greater than those of urban areas because large, sparsely populated areas have to be covered. Secondly, the consumption, and thus return on investment, is lower than that of urban areas because the majority of domestic consumers are extremely poor and there is generally little or no prospect for industrial or commercial growth. The successful implementation of an Rural Electrification (RE) program will thus depend on our ability to reduce the costs involved. One way of reducing the costs of RE may be by adopting alternative medium voltage distribution (normally 22 kV) systems.

The costs of MV lines may be reduced by the use of single-phase instead of three-phase lines. Single-phase lines may be either phase-to-phase, phase-to-neutral or single wire earth return (SWER).

The phase-to-neutral system has been successfully used in the USA to achieve almost full rural electrification. One of the authors (G Wyatt) gained experience with this system by spending 4 months with Intermountain Rural Electric Association in Colorado, USA. A number of months were also spent with Eskom's regional office in East London to gain insight into the conventional methods of rural electricity distribution used in South Africa.

## 2. INFLUENCE OF MV SYSTEM ON THE COST OF RE

The costs associated with the construction of MV lines will have a major impact on the overall costs of RE in South Africa. This is because:

- (a) The MV systems in many of the former homelands are not extensive. RE programs in these areas are necessarily going to have to extend these systems so that remote and isolated areas can be reached.
- (b) The lower customer densities in the rural areas requires longer Low Voltage (LV) runs than those used in urban areas to feed the same number of customers. This leads to voltage drop problems along these, which must be overcome by increasing the LV cable size and thus cost. It is therefore likely that in rural areas a approach whereby fewer customers are fed from a larger number of smaller distribution transformers will be justified. This shifts the emphasis, in rural areas, from the construction of LV runs to the construction of MV lines.

## 3. MV DISTRIBUTION SYSTEMS CONSIDERED

### 3.1 ALL THREE-PHASE

This is the system that has traditionally been used in South Africa; it is a delta connected, source only earthed system. Source earthing is achieved by a zig-zag transformer at the distribution (132 or 66 to 22 kV) substation. All of the distribution lines and distribution transformers are three-phase. The LV lines are also three-phase, and customers are supplied with either three-phase or single-phase supply depending on their preference. The advantages of this system are that it takes three-phase supply to all customers who require it (for example to run a large motor), the load is usually well balanced amongst the phases of the MV line thus avoiding negative phase sequence (NPS) voltage distortion, and it supports sensitive earth-fault (SEF) protection. The only disadvantage of this system is its high cost.

### 3.2 THREE-PHASE SYSTEM WITH SINGLE-PHASE, PHASE-TO-PHASE LINES

This type of system is similar to that above except here single-phase lines, taken between two phases of

the three-phase lines, are used where ever possible. This is done to reduce the line construction costs but, as with all single-phase systems, means that three-phase supply is not available to all customers and unbalanced loading may occur amongst the phases of three-phase lines being tapped, causing NPS voltage distortion.

### 3.3 THREE-PHASE FOUR-WIRE SYSTEM

This system is used throughout the rural areas of the USA. The distribution system is Y-connected and employs a distributed, multiple-earthed neutral. The system backbone consists of three-phase lines which carry 3 phase conductors and a neutral conductor. Single-phase, phase-to-neutral lines are tapped directly from the backbone and are used wherever possible. The advantage of this system is its low cost because single-phase lines only require protection equipment to be provided for the single phase conductor, and the use of the neutral conductor reduces the earthing costs. Of concern is the fact that this distribution system does not support SEF protection and must rely solely on Earth-Fault (E/F) and Over-Current (O/C) protection.

### 3.4 SINGLE WIRE EARTH RETURN DISTRIBUTION

As its name implies this form of distribution is based on the use of a single phase conductor with the earth acting as the return conductor for load currents. SWER lines would not make up an entire distribution system but are used in conjunction with any of the above systems, the SWER lines being used only where they offer cost advantages.

SWER lines are normally supplied from an isolating transformer to restrict the extent of the earth return currents and allow freedom in the choice of SWER line voltage. The earthing of the isolating transformer is of particular importance as it must carry the full load current while ensuring step potentials remain within safe limits (13 V/m). The only protection available on SWER lines is O/C protection, which must be set sufficiently low to detect all faults. Because of this and in a effort to limit step potentials at the earth electrodes the maximum current of SWER lines is usually limited. Eskom uses a maximum current of 8 A [1].

## 4. COSTS SYSTEM ELEMENTS

In order to determine the total costs of the various systems it is necessarily to first derive the costs of their various system elements.

The system elements considered here are the distribution lines themselves and the earthing and protection of distribution transformers. The latter are included because their cost is directly a function

of the type of distribution to which they are connected.

The costs of distribution transformers are also dependent (to a lesser extent) on the type of system from which they are fed. However these costs are not included in the analysis because their prices could not be accurately established due to the fact that certain of the transformers are not commonly available in South Africa (e.g. 12.7 kV, phase-to-earth transformers) and the present prices of others (e.g. single and three-phase transformers) are distorted by present economies of scale.

### 4.1 DISTRIBUTION LINES

The costs of distribution lines are a function of two main components, the line conductors and the supporting structures.

Two types of conductors were considered, namely 6/1 ACSR and 'extra-strong' 3/4 ACSR. The standard sizes used in the analysis are: Mink, Fox and Squirrel for 6/1 ACSR and Magpie and Bantam for 3/4 ACSR. Bantam was included in the study (although it is not commonly available in South Africa) because it is a small high-strength conductor, making it ideal for RE.

The supporting structure designs used for all of the lines but SWER were based on the staggered vertical design as specified by Eskom [2]. The SWER design simply consists of an insulator located on top of an 'L'-bracket at the very top of the pole.

The maximum span lengths, limited by conductor sag and the wind moment on the pole, were calculated for each line type, conductor and for both 11 and 12 m poles. These span lengths ranged from 137 m for the three-phase, four-wire lines to 297m for the SWER lines.

From the calculated maximum span lengths, the structure cost per km were determined and added to the conductor cost to give the total line cost per km. These costs include material, labour and transport charges. As an example of the costs obtained Figure 1 shows the costs of the various types of lines using Mink conductors on 12 m poles.

### 4.2 DISTRIBUTION TRANSFORMER PROTECTION

The cost of lightning and over current protection of distribution transformers is directly dependent on the number of phases to which the transformer is connected. Based on standard distribution practices it is assumed that each transformer is protected by a set of MOV lightning arrestors and a set of drop-out fuses. A single MOV lightning arrestor costs R257 to purchase, transport and install while a drop-out fuse costs R236.

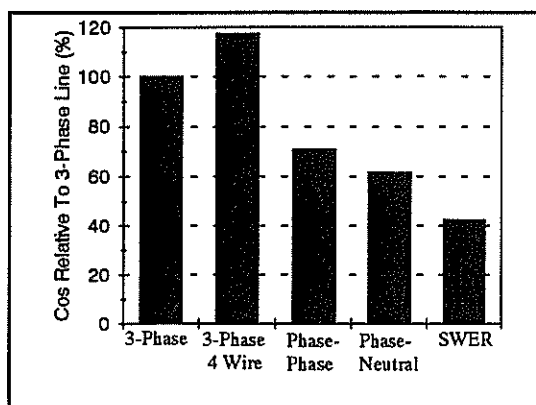


**Figure 1:** Costs Of Mink Conductor Lines On 12 m Poles (100 % = R16 145).

### 4.3 DISTRIBUTION TRANSFORMER EARTHING

For source-only earthed systems, the earthing of the MV side of distribution transformers must be such that a fault from a phase to the transformer tank generates enough current to be cleared rapidly. To achieve this Eskom requires that the earth electrode resistance at distribution transformers be less than  $30 \Omega$  [2]. On distributed neutral systems this is not a concern as a conductor path (the neutral) exists for any fault-current. The earthing of SWER distribution transformers is governed by the fact that full-load current must be continuously carried by the earth electrode, whilst limiting the voltage across the electrode to less than 20 V. The cost of earthing distribution transformers range from R77 for distributed neutral systems to R2124 for transformers supplied from SWER lines.

### 4.4 ISOLATING TRANSFORMERS

SWER lines require isolating transformers, as discussed previously. These represent a fixed cost which ranges from R8 540 for 50 kVA transformers to R 18 300 for 200 kVA transformers. The earthing of the SWER side of these transformers is achieved by the use of 4 deep drilled electrodes, at an approximate cost of R 9 100.

## 5. THEORETICAL CASE STUDY

The theoretical distribution system layout shown by **Figure 2** was used to compare the three-phase, three-phase with single-phase and the three-phase, four-wire systems. Because SWER is used in conjunction with other systems the comparison involving SWER was rather done on an individual line basis.

The theoretical system layout is based on 1 of 6 distribution lines leaving a substation, serving a  $60^\circ$  area. The distribution transformers are evenly dispersed throughout the area being served and a voltage drop of 7 % is allocated to the distribution

lines. Other basic assumptions made, were a maximum radial line length of 20 km and an ADMD growing to 1.5 kVA after 25 years.

The distribution line voltage was taken as 22 kV (line-to-line) except for the single-phase, phase-to-neutral lines which necessarily operate at the corresponding voltage of 12.7 kV (line-to-earth) and the SWER lines which were chosen to have a voltage of 22 kV (line-to-earth), based on Eskom's [1] recommended practice.

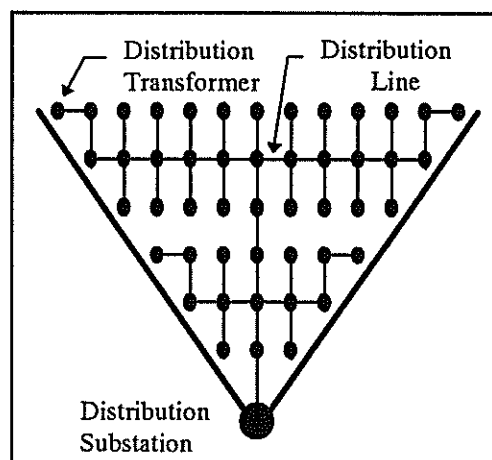


**Figure 2:** Physical Layout Of Distribution System For Case Study

The two major load determinants that influence the per connection cost of RE are the number of customers within a specific area (density) and how these customers are dispersed in relation to one another. The first factor determines the over-all load while the second determines the number of customers that can be supplied from each distribution transformer. The cost of the various distribution systems were determined for the theoretical layout as these two parameters were varied.

### 5.1 VARIATION OF NUMBER OF CUSTOMERS PER TRANSFORMER

The area covered by the line model is  $244 \text{ km}^2$ , assuming a density of 9.2 households per  $\text{km}^2$  (a typical value) there exist a total of 2232 households. The distribution system costs were calculated as the number of households supplied per distribution transformer was varied from 1 to 70. These costs are shown in relative terms by **Figure 3**.

### 5.2 VARIATION OF CUSTOMER DENSITY

**Figure 4** shows the relative costs for each of the systems as the density of households within the area being served is varied. This is done by assuming a constant number of 4 households per distribution transformer, and varying the number of transformers being served.

### 5.3. VIABILITY OF SWER

The viability of a SWER line over any other type of line, in a given situation, is dependent on the number of distribution transformers to be supplied and the total line length required. This is because SWER lines have a high fixed cost but a low cost per km with the result that the total per km costs of SWER lines decrease as the line length is increased. Thus beyond a specific line length SWER lines become less costly than their alternatives

The distances at which SWER lines supplied by a 150 kVA isolating transformer have the same cost as their alternatives are shown by Figure 5. The shorter the break-even distance the more widely the SWER lines will be used.

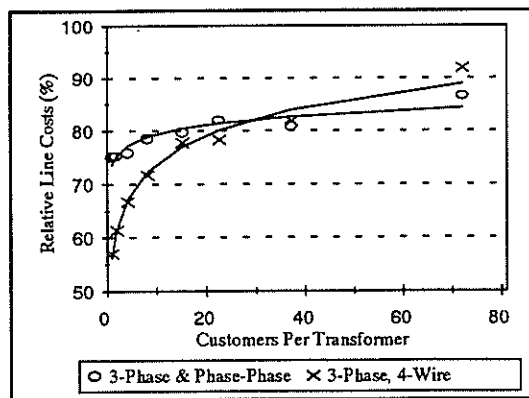


**Figure 3:** Effect Of Household Distribution On The Costs Of Single-Phase Systems Relative To Three-Phase.

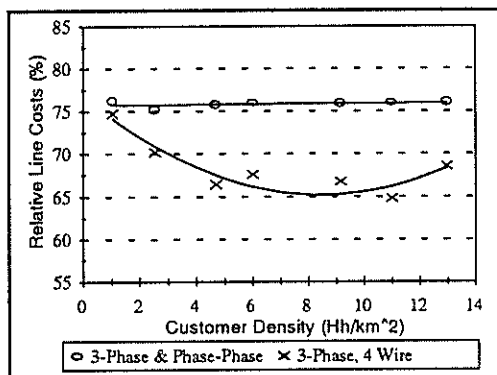


**Figure 4:** Effect Of Customer Density On The Cost Of Single-Phase Systems Relative To Three-Phase.

## 6. CONCLUSIONS

A successful RE program in South Africa will depend to a large extent on our ability to reduce connection costs. The costs of MV systems will make up a large proportion of the total costs of an RE program and is thus worth examining.

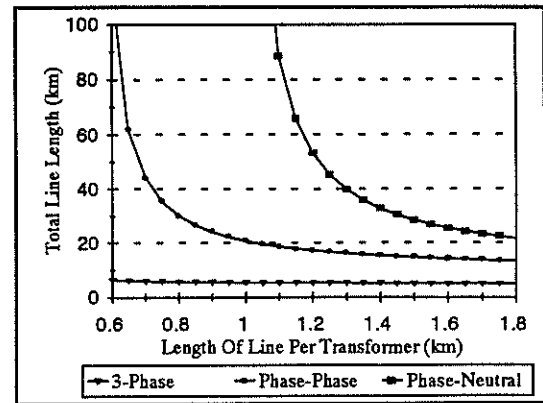


**Figure 5:** Break-Even Distance Of SWER Versus Other Line Types.

The savings obtainable on the MV system by adopting single-phase distribution systems are shown by the theoretical study to vary from 10 to 45 %. The level of saving and the choice between single-phase, phase-to-phase or phase-to-neutral technology is dependent on the number of customers that may be supplied per transformer, but is largely independent of the total number of customers supplied.

The application of SWER lines is very dependent on the system against which they are competing, as indicated by the varying break-even distances. For example, if a three-phase, four-wire system were adopted the need for SWER would be very limited; however it would be more widely used if the alternative were phase-to-phase lines.

Although the theoretical model indicates large savings are possible by the adoption of single-phase distribution systems (especially the three-phase, four-wire systems where only a few households could be served per transformer) a practical study is required, and is presently under way, to confirm these results.

## 6. REFERENCES

- [1] Eskom: "Single Wire Earth Return (SWER) Guidelines For Application" Distribution Technology, November 1992.
- [2] Eskom: "Eskom Electrification Standard" Distribution Technology, Revision 2, 1993.
- [3] NRS 034-1:1992: "Guidelines For The Provision Of Electrical Distribution Networks In Residential Areas - Part 1" Pretoria, 1994.
- [4] REA: "Mechanical Line Design Manual For Overhead Distribution Lines" US Department Of Agriculture, Bulletin 160-2, Washington D.C., USA, 1982.
- [5] Scott R.: "Comparison and Evaluation Of Pole Top Designs" MSc Thesis, Department Of Electrical Engineering, University Of Cape Town, 1990.

# AN INVESTIGATION INTO THE USE OF INTERMEDIATE VOLTAGE FOR RURAL ELECTRIFICATION

C Badenhorst

University of Cape Town, SA

C E Dingley

University of Cape Town, SA

I Ferguson

Eskom, New Germany

## ABSTRACT

A common problem that exists in the electrification of many rural areas in South Africa, using conventional low (LV) voltage techniques, is that the houses in these areas are often far apart. This requires the use of long LV cable runs which, in turn, causes voltage drop problems.

One solution to the problem is to increase the length of the medium voltage (MV) backbone, and decrease the length of LV. This, however, means a significant increase in cost.

This paper investigates the use of an intermediate voltage (IV) approach as a possible solution to this problem.

## 1. INTRODUCTION

Rural electrification has fast become a primary issue in South Africa. With the drive to provide access to electricity for all South Africans comes the need for research into the most effective method of achieving this. Due to the vast differences between the rural and urban area characteristics, particularly the density of the houses, the conventional method of urban reticulation would not necessarily be the most effective rural reticulation system. Thus, in order to optimize rural reticulation practices, various alternative reticulation methods should be investigated.

This study investigates one approach to rural area reticulation, namely, the use of intermediate voltage (IV). The paper is the result of a final year thesis project at the University of Cape Town.

This paper is structured as follows: the three types of rural areas investigated are first defined, and relevant characteristics are given. The general model used to represent the reticulation system is then described. Thereafter, the various electrification methods (systems) that were investigated are described. The method of costing is then given. Finally, the results are provided in diagram form and discussed.

## 2. RURAL AREA CHARACTERISTICS

The layout of the dwellings in the rural areas can be classified into three categories, namely, i) normal rural household loads, ii) clustered household loads, and iii) single bulk loads.

### 2.1 NORMAL HOUSEHOLD LOADS

This type of layout represents the majority of the rural area communities in South Africa. Generally, there is no specific pattern to which the houses are built. This is due to the lack of planning in the development of the area.

The density of the houses in this layout differs from one area to another, but in general for the rural areas this is less than 50 houses/km<sup>2</sup> [1].

### 2.2 CLUSTERED HOUSEHOLD LOADS

This type of household layout occurs mainly in the KwaZulu/Natal rural areas. Typically, one family (father, sons, close relatives, etc.) would build their houses very close to each other ( $\pm 10$ m apart). This cluster normally contains between three and six houses. These individual clusters are then fairly widely separated from other such clusters and, once again, do not have a specific development pattern.

The density of the clusters is similar to that of the normal single loads as described above.

### 2.3 SINGLE BULK LOAD

It is sometimes necessary to provide electricity to a single isolated rural load. This type of layout requires a considerable length of cable to supply the load. A typical example is a farm or a small community. The size of this type of load is normally larger than that of the previously described loads.

The single load could also be a single isolated cluster of houses.

### 3. GENERAL MODEL USED

A model was developed to generalise an area to be electrified. This was done so that mathematical calculations could be performed on the model, and various systems compared. The model was to be fairly representative of the rural areas, and had to have a specific conductor layout. The general model decided upon is shown in figure 1.

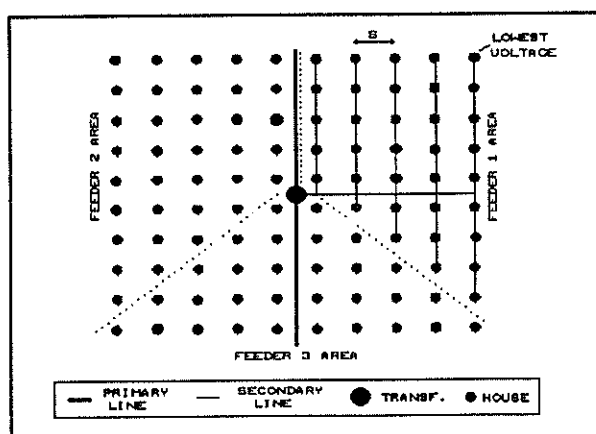


Figure 1 BASIC MODEL

The model has the following characteristics:

- i) Houses are equally spaced. As was explained in a previous section, there is no particular pattern associated with the construction of houses in the rural areas. This is mainly due to the fact that there is often no pre-planning involved, and sometimes no features that force a certain pattern of development such as roads, rivers, hills, etc. It can therefore be appreciated that a model can not be obtained that will represent exactly every rural area housing layout. The best approximation to represent this type of area in general, is to have equally spaced houses.
- ii) MV transformer is situated in the load centre. This is common practice throughout the electrification industry. The advantage of such a position is that a similar load will be placed on each of the outgoing feeders, thus a similar voltage drop as well as line current, thereby maximising the area that can be electrified from one transformer.
- iii) Reticulation is by means of three radial feeders. This means that one feeder supplies approximately a third of the load (see diagram). The method of using three feeders optimises the amount of conductor used, and is convenient for the layout using a three phase transformer with one feeder per phase.

### 4. SYSTEMS INVESTIGATED

This section provides a brief description of the various electrification systems investigated.

#### 4.1 CURRENTLY USED SYSTEMS

In order to assess the IV systems, they were compared, costwise, with currently used systems, namely:

CONVENTIONAL - consisting of a 3 $\phi$  MV backbone stepped down to LV reticulation,  
 MAYPOLE - two phase MV system stepped down to LV (only using service connections),  
 1000V - 3 $\phi$  MV backbone stepped down to 1000V, and then to LV at each house.

#### 4.2 IV SYSTEMS

The IV systems investigated were as follows:

##### LAYOUT 1

This layout consists of a MV backbone which is stepped down to 1900/3300V. The 3 $\phi$  1900/3300V conductor used was ABERDARE's Interdac 3 (for underground) or Inter ABC (for overhead).

The supply is then tapped off a single phase to neutral of the 3 $\phi$  IV and stepped down to LV at each house. The normal Airdac service conductor then takes the LV to the house.

##### LAYOUT 2

This layout is as above, but, here one IV/LV transformer supplies five houses, and the LV network consists of both single phase 35mm<sup>2</sup> ABC and service conductors.

##### LAYOUT 3

As before, but this time the ABC is three phase 35mm<sup>2</sup>, and one IV/LV transformer supplies 5 to 30 houses.

### 5. METHOD OF COSTING

The costing of a reticulation system is a complex process which involves the costs of both i) the initial outlay, as well as ii) the lifetime costs of the system.

- i) The initial cost is that amount which is needed to install the system, and includes such costs as materials, labour, and equipment usage/hire. In this investigation, two types of materials are used, namely "standard" materials and "non-standard"

materials.

Standard materials are those materials that are kept as stock, or readily available, within ESKOM. The cost of these materials were obtained using ESKOM's computer network database called BMS (Business Management Support). As the 3.3kV reticulation layouts investigated are not currently used by ESKOM, some of the materials were non-standard items. The cost of these items was obtained from the actual manufacturers, on the assumption of a bulk order.

- ii) The lifetime costs include losses and maintenance costs. The lifetime period of a reticulation system is generally taken to be between 10 and 25 years.

There is very little difference between the maintenance costs of the various alternative systems investigated. The maintenance cost was therefore not taken into account when comparing the different systems.

The energy loss that occurs in the conductors of a reticulation network performs no useful function. It must however be generated. Various systems incur different losses; the cost of these losses was therefore taken into account in the comparison.

The various systems investigated were compared on the basis of their costs. It was very important, therefore, that each system was costed in the same manner. Although some costing information was available for currently used systems, unfortunately this information was not very substantial, and did not express the cost in terms of the various types of areas. It was decided, therefore, to cost each system in the same manner, in order to achieve the best results.

## 6. RESULTS AND DISCUSSION

The purpose of this section is to provide an analysis of the cost results. This is achieved by means of a series of system selection diagrams. These diagrams indicate which system is the cheapest, for certain given parameters (eg. density, ADMD, etc.).

### 6.1 RESULTS

#### NORMAL LOAD LAYOUT

The system selection diagram for this layout, according to cost, is shown in figure 2.

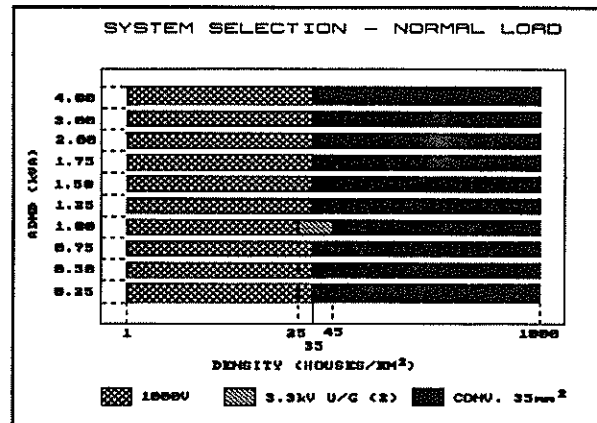


Figure 2 NORMAL LOAD SELECTION DIAGRAM

#### CLUSTERED LOAD RETICULATION

Figure 3 shows the system selection for the clustered load layout.

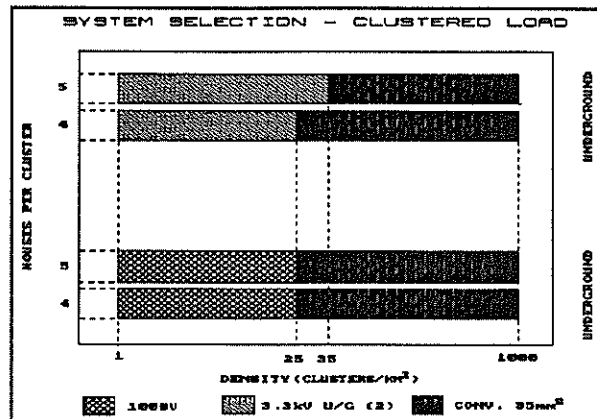


Figure 3 CLUSTERED LOAD SELECTION DIAGRAM

#### SINGLE LOAD LAYOUT

The results obtained are illustrated in figure 4.

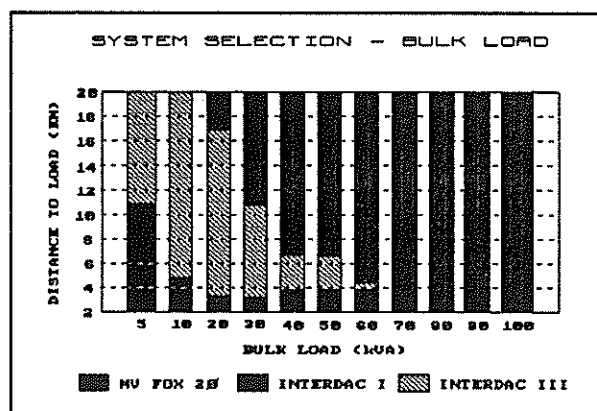


Figure 4 SINGLE LOAD SELECTION DIAGRAM

## 6.2 DISCUSSION

This investigation has shown that the use of a 1900/3300V intermediate voltage network is cheaper in the following circumstances:

- \* In normal rural load areas for densities between 25 and 45 houses/km<sup>2</sup>, and an ADMD of 1 kVA - with a cost saving up to 2% on the next cheapest (1000V system).
- \* In clustered load areas for densities between 1 and 25 clusters/km<sup>2</sup> (4 houses/cluster) or between 1 and 35 clusters/km<sup>2</sup> (5 houses/cluster) - with a cost saving up to 32% on the conventional system and 2% on the 1000V system.
- \* For the single load case for the combinations of loads and distances to the load, as shown in figure 4, with a cost saving up to 50% for the single phase INTERDAC 1, and 8% for the three phase INTERDAC 3.

Note that the above only applies to areas suitable for using underground conductors. None of the IV systems using the INTER ABC conductor came up as the cheapest option.

It would not be wise to accept that the IV system is the most feasible for the circumstances given above, without considering the following question:

DOES THE COST SAVING OF THE IV SYSTEM JUSTIFY THE DEVELOPMENT OF A NEW ELECTRIFICATION SYSTEM ?

In order to attempt to answer the question, the following issues should be examined.

### \* NON STANDARD MATERIALS

Because the system is relatively new to both ESKOM and electrical materials suppliers, some of the materials are not standard items, in particular the transformers and switch isolators. It is therefore important to test and approve all materials for a new electrification system before purchasing in bulk.

### \* USE OF AN UNTESTED SYSTEM

Most new electrification systems have teething problems. It is therefore important to iron these out before standardising the system. A good way of achieving this is by the use of a pilot project, i.e. building an IV system in one area, and then assessing its operation over a period of time.

### \* EXISTING SYSTEMS

The 1000V system mentioned in the text already has a pilot project, and its problems appear to be sorted out. A bill of materials, and method of building the system has also been determined. The fact that the cost saving of the IV system over the 1000V system in the normal and clustered areas is very little; combined with the fact that the 1000V system is cheaper over a larger range of densities than the IV system, indicates that it might not be worth spending too much effort on the development of the IV system for those areas.

Based on the above implications, it is my opinion that the IV system should not be used in the normal and clustered load areas, but instead, the 1000V system should be developed further.

For the single load layout, however, a considerable cost saving is achieved, especially with the use of the underground INTERDAC 1 conductor.

This method of single load electrification is already widely used by AGRELEK, a division of ESKOM. It should, however be noted that this system can only be used for certain combinations of loads and distances to the loads. It is also only useful in areas suitable for underground cabling.

Due to the simplicity of this type of layout, the installation of such a network can be achieved with reasonable ease.

I therefore recommend that for the single load layout, the intermediate voltage network should be used according to the selection diagram in figure 4.

## REFERENCES

- [1] ESKOM Electrification Standard, ESKOM publication, revision 2, February 1993.

## ADDRESS OF AUTHORS

Dept of Electrical Engineering, University of Cape Town, Rondebosch, 7700.

TEL: (021) 650 - 2793

FAX: (021) 650 - 3465

# THE LIFE-CYCLE COSTING OF URBAN ELECTRICAL DISTRIBUTION TRANSFORMERS

S D Michie

University of Cape Town

C E Dingley

University of Cape Town

## ABSTRACT

This paper examines the life-cycle costing of small urban electrical distribution transformers.

The paper begins by looking at the creation of a model to calculate transformer manufacturing costs. It then goes on to cover the calculation of cost of losses over the life-cycle. Adding this to the manufacturing cost gives the life-cycle cost of the transformer which allows different options to be compared.

This costing process is done for a range of load and no-load loss values and for a number of transformer configurations and sizes. The results obtained are discussed and conclusions are drawn.

## 1. INTRODUCTION

At present in South Africa, distribution transformer tenders are adjudicated solely on the manufacturing cost of the transformer. Other costs, such as the cost of losses and maintenance, are often not considered. These costs can make up a considerable part of the life-cycle cost. The only reference to transformer losses in tenders is that the transformer should conform to the SABS 780 levels.

The total life-cycle cost of a transformer consists of the initial purchase cost and the running costs such as the cost of losses and maintenance. The aim of this paper is to investigate the effect of the cost of losses on the life-cycle cost of a distribution transformer and to test whether the current SABS specification leads to a minimum cost. Other costs such as maintenance costs have not been considered as they are difficult to quantify and are likely to remain unchanged for the variations in parameters considered here.

The types of transformers investigated in this paper are distribution transformers with a primary voltage of 11 or 22 kV and a secondary voltage of 400 V. The range of sizes is 100 kVA to 500 kVA.

The process for calculation of the life-cycle cost can be split into two parts. The first part is the calculation of the manufacturing cost of a transformer. The second part is to calculate the cost of losses for that transformer and to add it to the manufacturing cost to get the life-cycle cost.

## 2. A MODEL FOR TRANSFORMER MANUFACTURING COSTS.

The first step towards calculating the life-cycle cost of a transformer is to determine the manufacturing cost of that transformer. A model is needed to give the manufacturing cost of a transformer using the following input parameters:

- transformer size
- no-load loss
- load loss
- primary and secondary voltages
- connection types
- winding metal

It is important that the range of load and no-load loss levels can be varied in small steps over a wide range so that the life-cycle cost for a range of transformers for a given size can be calculated. In this way it is possible to find the loss levels that give the minimum cost.

Based on discussions with the designers at some local transformer manufacturers and on some book research [1, 2], an algorithm was developed to design transformers to the input parameters given above.

Transformer design is a complicated procedure in that the relationships between the different parameters are complex and tightly interwoven. For example, decreasing the no-load loss causes the core to become bigger which increases the conductor length of the windings which causes the load loss to increase. Decreasing this load loss requires larger conductor sizes which need more space and cause the core size to decrease increasing no-load losses again. These interactions force the solution method to be an iterative one.

The outputs produced by the algorithm are:

- volts per turn
- magnetic flux density
- impedance
- winding dimensions and masses
- core dimensions and mass
- the cost of the materials

The outputs other than the cost are used to check the validity of the design.

This algorithm was coded in the form of a Turbo Pascal program. This program takes as its inputs the parameters described as well as the range of load and no-load losses

required. The main output of the program is a file containing the material costs of the transformer for the different loss levels.

The material costs are converted to manufacturing costs by the addition of a fixed amount for the size of transformer for labour and fittings. Based on information from a transformer manufacturer, the labour amount is taken as 72% of the cost of materials of a standard specification transformer. In the case of the 100 kVA transformer, the SABS standard specification is a load loss of 1700 W and no-load loss of 360 W. The fittings costs are taken at a fixed amount of R500.

### 3. THE LIFE-CYCLE COST OF LOSSES

The second step in the calculation of transformer life-cycle costs is the calculation of the cost of losses. This cost can be divided into the cost of no-load losses and the cost of load losses.

The factors that go into the costing of losses are:

- the cost of electricity
- transformer loading patterns
- the method used for equating losses costs to investment costs

#### 3.1 The Cost of Electricity

The cost of electricity depends on the viewpoint from which it is valued. An electricity utility such as Eskom would value losses in terms of the costs of generation and transmission incurred in supplying the losses, be that marginal costs or long term average costs.

Municipalities or other electricity distributors would value losses in terms of the tariffs paid to the supplier which, in the case of South Africa, is Eskom.

For this investigation, three prices for electricity have been investigated. These are Eskom's Tariff A, Tariff T1 and marginal costs.

#### 3.2 Transformer Loading Patterns

An important factor in the calculation of the load loss costs is the expected loading on the transformer over its life-cycle. However this is hard to predict, especially given the scarcity of suitable information in South Africa.

There are two pieces of information needed. The first is the expected load growth over the life of the transformer. The second is the loss load factor of the transformer, used to related the maximum load loss to the average load loss.

For this investigation use has been made of typical loss load factors derived from some load data obtained from Eskom. A load growth curve developed to give a profile for developing communities was used to provide the load growth information.

#### 3.3 The Capitalization of Losses

The method used to capitalize the losses costs is the net present worth method. This method is the one that is recommended for use in NRS 034 [3].

The present worth of an expense  $C$  deferred to year  $n$  is

$$PV_n = \frac{C}{r^n} \quad (1)$$

The value  $r$  is the net discount factor, which is used to account for both inflation and the cost of money over the years. For projects in South Africa it is advised that a net discount factor of 8% to 10% be used for evaluation of projects [3]. If there are severe constraints on the availability of capital it is recommended that 15% be used.

The net present worth method allows direct comparison of different options as it relates the future cost of losses to the initial transformer purchase cost. Provided that the input factors have been chosen correctly, the transformer with the lowest net present value will be the cheapest over the life-cycle.

#### 3.4 The Cost of No-Load Losses

No-load losses in transformers are simple to cost since these losses occur continuously and are constant in value.

The cost,  $C_{NL}$ , of a year's worth of a kilowatt of no-load loss is

$$C_{NL} = C_D + 8760 C_E \quad (2)$$

Where:  $C_D$  is the demand cost  
 $C_E$  is the energy cost

#### 3.5 The Cost of Load Losses

Load losses are require that the loss load factor and load growth be taken into account. The cost of a year's worth of load losses per kilowatt is

$$C_{LL} = C_D LG^2 + 8760 C_E LLF LG^2 \quad (3)$$

Where:  $LLF$  is the annual loss load factor, %  
 $LG$  is the load growth factor, %

#### 3.6 The Total Cost of Losses

The total life-cycle cost of losses is simply the summation of the cost of no-load and load losses over the years in the life-cycle.

$$C_L = \sum_{i=1}^n \frac{P_{NL} C_{NL} + P_{LL} C_{LL}}{r^i} \quad (4)$$

Where:  $P_{NL}$  is the no-load loss in kilowatts  
 $P_{LL}$  is the load loss in kilowatts

The life-cycle cost of a transformer is the sum of its investment cost and the capitalized cost of losses over its life-cycle.

$$C_T = C_I + C_L \quad (5)$$

## 4. PRESENTATION AND DISCUSSION OF RESULTS

### 4.1 Manufacturing Costs

Figure 1 shows the manufacturing costs of a 100 kVA, 22 kV transformer for a range of load and no-load losses.

As would be expected, the manufacturing cost is lowest at high load and no-load loss levels and increases with decreasing loss values. There is a sharp increase in the region of very low losses. At high losses the slope flattens out. The small irregularities in the surface are due to the step changes that occur such as the insertion of cooling ducts and changes in the number of winding layers.

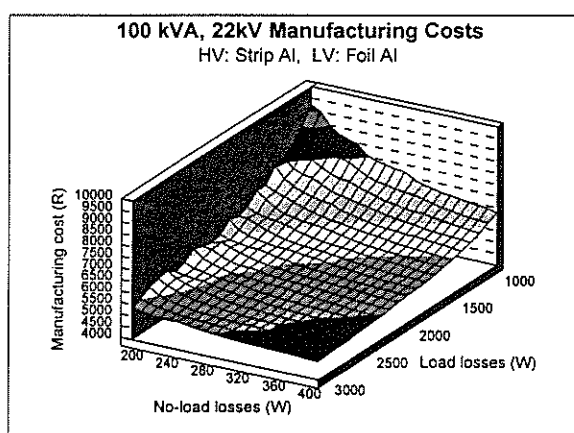


Figure 1: Manufacturing Costs for 100 kVA Transformer

### 4.2 Life-Cycle Costs

In this section, the effect of the variation of the parameters involved in the calculation of life-cycle costs are observed. The parameters looked at are

- load growth
- loss load factor
- valuation of losses
- length of life-cycle
- winding material
- transformer size
- primary voltage level

Owing to the large number of possible permutations, a base case has been chosen and each of the parameters varied to observe its effect on the optimum loss levels.

The parameters for the base case are

- size = 100 kVA
- loss load factor = 15%
- a middle of the road load growth

- the Tariff T1 cost of losses
- life-cycle = 25 years
- primary voltage = 22 kV

Figure 2 shows the life-cycle costs for this base case. The minimum life-cycle cost occurs at a no-load loss of 240 W and a load loss of 2300 W. The no-load loss minimum is well below the SABS standard of 360 W, while the load loss is higher than the SABS standard of 1700 W.

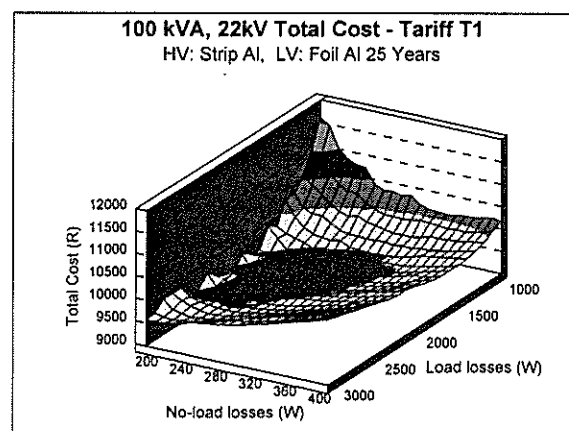


Figure 2: Life-Cycle Cost for the Base Case Transformer

However the slope of the surface around the minimum is relatively flat. Taking the range of costs that fall within 2% of the minimum cost gives a no-load loss range of 220 W to 300 W and a load loss range of 1500 W to 2400 W. The range of loss specifications that give rise to costs close to the minimum cost is therefore quite wide.

The rest of this section discusses the effects of the variations of some of the parameters of the base case on the optimum loss values.

### 4.3 Electricity Cost

The use of Tariff A for the electricity cost has a marked difference on the outcome when compared to Tariff T1. The range for no-load loss is increased to fall between 220 W and 350 W. The range for load loss is reduced to between 1300 W and 1900 W. This can be attributed to the greater emphasis on the demand charge over the energy charge when compared to Tariff T1.

Using marginal costs for the electricity pricing gives similar results to those of Tariff A.

### 4.4 Transformer Size

The transformer sizes looked at in addition to the base case were 200, 315, 400 and 500 kVA. The effect for all the sizes is the same as for the base case. The minimum cost load loss level is higher than the SABS value by 7% to 27%, while the no-load loss value is lower by 37% to 44%. The size of the percentage differences increased as the size increased.

#### 4.5 Load Growth

Load growth has the greatest effect on the load loss values. Lower load growths, i.e. where the average loading over the lifetime is high, cause the load loss range to narrow and to fall between 1500 W and 2100 W. The no-load loss range remains unaltered.

For the case of high load growth, i.e. where the load starts off small and takes longer to reach the final value, the load loss range expands to cover 1800 W to 2900 W. Again the no-load range remained unaltered.

#### 4.6 Loss Load Factor

The variation of loss load factor has the effect of varying the balance between the load losses demand and energy costs. However, the overall effect on the optimum loss levels however is similar to that of the variation of the load growth with a low loss load factor having the same effect as the high growth case.

#### 4.7 Length of the Life-Cycle

Varying the life-cycle has a similar effect to the variation of the loss load factor. A longer life-cycle has a similar effect to a higher loss load factor and vice versa.

A shorter life-cycle economic evaluation therefore gives the distribution system designer more freedom in the choice of transformer.

#### 4.8 Net Discount Factor

The choice of the net discount factor can have a large effect on the ranges of the optimum loss values. For a reduction in discount factor from the base case of 10% to 8%, the no-load loss range shifts by 10 W to 210 W to 300 W. The load loss range shrinks and moves to 1500 W to 2100 W.

An increase in discount rate to 15% causes the biggest changes to occur. The no-load loss range increases to 220 W to 330 W. The load loss range broadens to 1800 W to over 3000 W, which is well above the SABS specification of 1700 W.

Therefore for the case where there is not much emphasis on future costs, the designer can be more liberal with the choice of transformer specifications.

#### 4.9 Maximum Loading on the Transformer

Increasing the maximum load on the transformer from its rated load to 150% of its rated load has the effect of reducing the optimum load loss level. The range is now 1000 W to 1700 W, with the minimum at 1400 W. The no-load loss range shifts to 230 W to 380 W with a minimum at 300 W.

The tariff A evaluation for this loading case has its optimum load loss at 1000 W and no-load loss at 340 W.

These parameters are all lower than the SABS standard values.

### 5. CONCLUSIONS

In all the cases considered, the optimum no-load loss levels were significantly lower than the SABS recommended value. This suggests that South African built transformers need to be redesigned to lower no-load loss levels.

The optimum load loss levels depend heavily on the parameters that are chosen. Load losses are not critical in situations where the expected loading will be light. However if the loading will be heavy or the transformer significantly overloaded then the load loss level of the transformer becomes significant and must have careful attention paid to it.

A comparative example is the Irish ESB which specifies lower load loss levels, but similar load loss levels to the SABS [4]. The no-load levels are similar to those found in this study.

There are two ways of achieving the reduction of no-load losses. One is to simply use more core steel to reduce the magnetic flux and the other is to use a better grade of core steel. Since the South African manufacturers use the lowest grade of steel available, it could well be time that the use of better materials is investigated. Using better core steels would reduce the core size for the same load loss and therefore also have the spin-off of making it easier to reduce load losses.

The cost of losses in a distribution transformer is significant and cannot be continued to ignored. It is hoped that with the increasing electrification and pressure on Eskom's resources that more attention will be paid to this aspect of distribution design in the future.

### 6. REFERENCES

1. Franklin A C and Franklin D P: "The J & P Transformer Book" 11th Ed. Butterworths, London, 1983
2. Say M G: "Alternating Current Machines" Pitman, London, 1976.
3. NRS 034-1:1992: "Guidelines for the provision of electrical distribution networks in residential areas - Part 1: Planning and design of distribution systems" Addendum A. SABS, Pretoria., February 1994.
4. Irish ESB: "Distribution System Loss Reduction Guidelines" Irish Electricity Supply Board, Nov. 1991.

# MEASUREMENT OF CAPACITIVE VOLTAGE TRANSFORMER EARTH RETURN CURRENT HARMONICS.

H.J. Vermeulen

J. van Rooijen

G.H. Muller

S.R. Stadler

University of Stellenbosch

**Abstract** — The earth return current of the capacitive divider associated with capacitive voltage transformers (cvt's) can in principle be used for the assessment of harmonic voltage distortion levels on high voltage systems. Due to safety considerations, it is undesirable for such a current measuring arrangement to interfere with the earthing arrangement of an installed cvt. It follows that a measurement system is required which senses and measures the harmonic components of the current in the earth strap by means of a non-intrusive method. This paper investigates a method employing a Hall effect sensor in combination with an iron core for the above application. Design details of the electronic hardware and measured results are given and evaluated, and the data acquisition and signal processing software required for the assessment of harmonic distortion levels are discussed. The overall performance of the system is evaluated with reference to criteria such as linearity, frequency response and noise rejection. It is shown that the system performs satisfactory under real operating conditions.

## 1. Introduction

Supply utilities typically use capacitive voltage transformers (CVT's) for measuring and protection purposes on transmission systems for system voltages of 275 kV and above. Figure 1 shows a block diagram for a typical CVT. Under steady state conditions, the primary voltage  $V_1(t)$  can be expressed as a sum of the harmonic components, i.e.

$$V_1(t) = \sum_{i=1}^N A_i \cos(\omega_i t + \Phi_i) \quad (1)$$

where

$$\begin{aligned} \omega_i &= 2\pi f_i \\ &= 2\pi i f_1 \end{aligned}$$

with  $f_1$  denoting the frequency of the 1<sup>st</sup> harmonic or fundamental component.

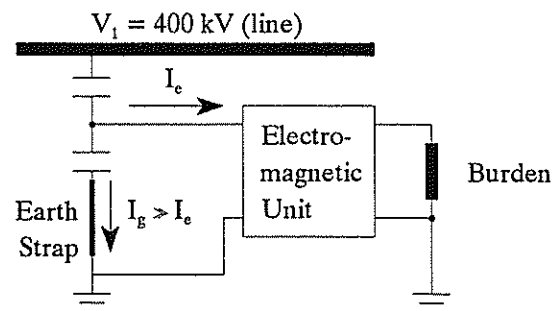


Figure 1: Capacitive voltage transformer

The current flowing into the electromagnetic unit is small compared to the current through the earth return strap, i.e.  $i_e(t) \ll i_g(t)$ . Therefore  $i_g(t)$  is the derivative of  $V_1(t)$ , and is given by:

$$\begin{aligned} i_g(t) &= C_d dV_1(t)/dt \\ &= C_d \sum_{i=1}^N \omega_i A_i \sin(\omega_i t + \Phi_i) \end{aligned} \quad (2)$$

where  $C_d$  denotes the capacitance of the divider. This equals 3 nF for the test specimen used in this investigation. Equation 2 shows that the magnitude of the current harmonics is frequency dependent, with the  $i^{th}$  harmonic having a magnitude of  $C_d 2\pi i f_1 A_i$ . The maximum allowable total harmonic distortion (THD) on high voltage systems is typically of the order of 1.5% [1]. If a fixed magnitude of voltage harmonics is assumed, then there will be a linear relationship between the harmonic number and the current harmonic component in the earth return strap.

Figure 2 shows the voltage waveform for a 100% fundamental and uneven harmonic components up to the thirteenth order with amplitudes of 2% each. Figure 3 shows the current in the earth return strap of the CVT due to the primary voltage shown in figure 2.

It is unlikely for the higher order voltage harmonics to be of any significant magnitude on high voltage distribution systems, thus minimizing the possibility of excessive high order current harmonics in the ground strap. The overall bandwidth for the measuring system has however been specified as 2.5 kHz to allow for frequencies up to the 50<sup>th</sup> harmonic. Only the relative magnitudes of the harmonic components with respect to the fundamental component are of importance for harmonic distortion measurements. This is because harmonic distortion figures

are typically expressed as a percentage value based on the amplitude of the fundamental component. This implies that it is not necessary to measure the earth return current on an absolute basis, but that the relative magnitudes of the fundamental and harmonic components must be determined.

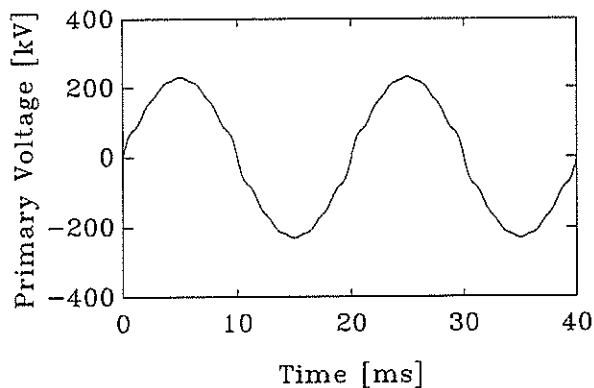


Figure 2: Primary voltage waveform with 2% uneven harmonics up to the thirteenth harmonic.

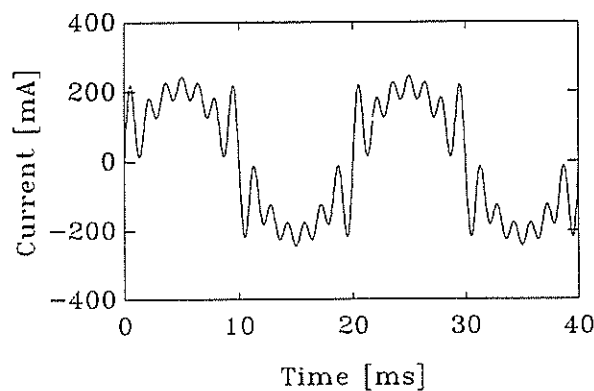


Figure 3: CVT earth strap current.

## 2. Analog circuitry

Two non-intrusive current sensing techniques were investigated, namely

1. An induction coil sensor based on the Rogowski coil principle.
2. An iron core with a Lohett II Hall element sensor.

### 2.1 Rogowski coil sensor

The first sensor was realized using two induction coils in series (one on either side of the earth strap) as can be seen in figure 4. Figure 5 shows the block diagram of the analog circuitry used with the induction coils. The voltage induced in the coil ( $V_{RC}$ ) is proportional to the rate of change of  $I_g$ . The coil voltage is integrated to regain the current waveform  $I_g$  [2, 3, 4]. A 100 x gain is used to amplify the current signal.

The frequency response of these coils were measured for a sinusoidal strap current of 200 mA, allowing for variable frequency excitation up to 40 kHz. Figure 6 shows  $V_{RC}/I_g$  as a normalized function of frequency, with the 50 Hz value taken as 0 dB.

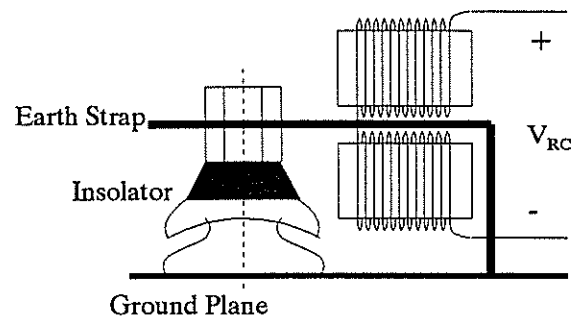


Figure 4: Physical Rogowski coil setup.

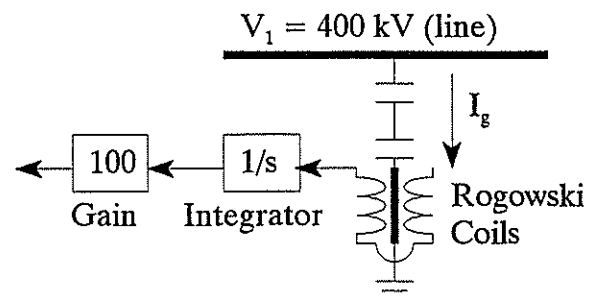


Figure 5: Block diagram of Rogowski coil analog circuitry.

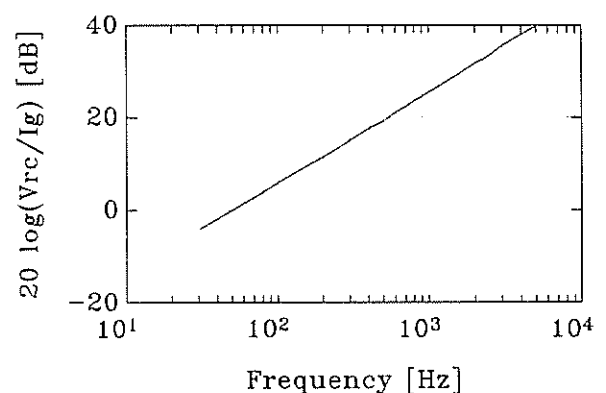


Figure 6: Frequency response of Rogowski coils.

The response of the coils are linear up to 10 kHz, which is well above the 50<sup>th</sup> harmonic at 2.5 kHz.

Despite shielding by means of a foil casing, the coils were still prone to interference from magnetic fluxes from the surrounding 50 Hz equipment, making the output signal quite noisy. A coil wound on a torus produced better results, but had to be wound by hand since no equipment was available to do it. A high degree of accuracy is needed for the integrator, which tends to inject a degree of DC drift to the system. These constraints reduces the overall suitability of the Rogowski coil principle.

## 2.2 Hall effect sensor

The second sensor developed makes use of an iron core with a Lohett II Hall element. The Lohett II element has a response time of  $20\mu\text{s}$  or  $50\text{ kHz}$  [5], which is much higher than the  $50^{\text{th}}$  harmonic at  $2.5\text{ kHz}$ . This Hall element also exhibits a noise output, but measurements done using two Lohett sensors in a differential setup has shown the noise to be of an internal rather than external origin. This noise can be filtered out by the signal processing software.

The frequency response of the Hall element were measured by keeping the strap current at  $200\text{ mA}$ , while the frequency of the current was varied. Figure 7 shows  $V_{\text{hall}}/I_g$  as a normalized function of frequency, with the  $50\text{ Hz}$  value taken as  $0\text{ dB}$ . The response of the Hall element is flat up to  $3\text{ kHz}$ .

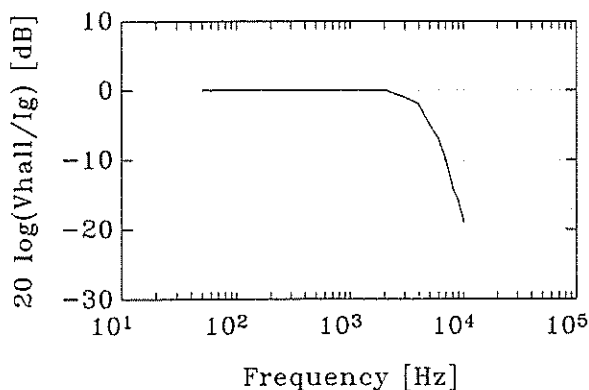


Figure 7: Frequency response of Hall element.

The output of the Hall sensor is amplified and then filtered with a  $3^{\text{rd}}$  order low pass butterworth filter with a  $5\text{ kHz}$  cutoff frequency. The signal is then transmitted to the data acquisition circuitry by the driving circuit.

Since the Hall effect sensor and the associated circuitry is less prone to noise and DC drift, it is more suitable for this application than the Rogowski coil sensor.

## 2.3 4 - 20 mA driving circuit

The distance over which the signal has to be transferred can be up to  $100\text{ m}$ . A voltage signal is subject to distortion because of noise interference and voltage drops across the communications cable. The standard  $4 - 20\text{ mA}$  current loop method is therefore used, with the zero reference at  $12\text{ mA}$ .

The driving circuit consists of a voltage follower, an adder and a voltage to current converter. The voltage follower acts as a buffer to supply the adder with sufficient current without distorting the sensor waveform. The adder adds a DC offset to the signal to shift the zero level up to  $6\text{ V}$ . This corresponds to  $12\text{ mA}$  output from the voltage to current converter. The total current swing is then between  $6$  and  $18\text{ mA}$ , which corresponds to a current swing of  $I_g = 175\text{ mA}$  to  $I_g = 275\text{ mA}$  in the earth strap, which is the  $100\% \pm 20\%$  points.

The connection with the data acquisition equipment is via a  $100\text{ m}$  double twisted pair wire. One twisted pair is used to supply DC power to the sensor circuitry, while the other pair carries the current signal. The current signal terminates in a resistor with the data acquisition circuitry monitoring the voltage over this resistor.

## 3. Signal Processing Software

The digital signal processing was accomplished using a MATLAB program. The procedure involves the following:

The waveform data is digitized and recorded using a Yokogawa model 3656 analyzing recorder. The sampled data sequences are subsequently downloaded to a personal computer via a IEEE GP-IB connection. The data is stored in the form of a binary file which is then converted to an ASCII format for use by the Matlab program.

The waveform is filtered using a digital bandpass filter to obtain the fundamental component, which is always of the order of  $50\text{ Hz}$ . The pass band of the filter is  $40$  to  $60\text{ Hz}$  and it is realized with a second order butterworth filter. The period of the fundamental waveform subsequently estimated.

The original waveform data is subjected to a comb filter and averaging is performed over a number of cycles to minimize the random noise component. The frequency spectrum is then obtained by means of a discrete Fourier transform and the harmonic components are normalized with respect to the magnitude of the fundamental component.

## 4. Experimental Results

A test setup was used in the laboratory to simulate the normal operating conditions of the test system in the field. Figure 8 shows a block diagram of the experimental setup as used with the Hall effect sensor.

The required waveform data is generated by a Pascal software program on a personal host computer. The data is then downloaded to the transputer based  $5\text{ MHz}$  12-bit digital to analog (D/A) converter. A  $150\text{ W}$  LM12 linear operational amplifier circuit is used as a current source capable of supplying  $500\text{ mA}$  through a test strap of the same shape as a earth strap on a CVT. The measuring core with the Hall sensor measures the current in the test strap and the output of the sensor is amplified and transmitted via the  $100\text{ m}$  twisted pair current loop to the Yokogawa analyzing recorder. From there the recorded waveforms is downloaded to the computer for processing as described in section 3 above.

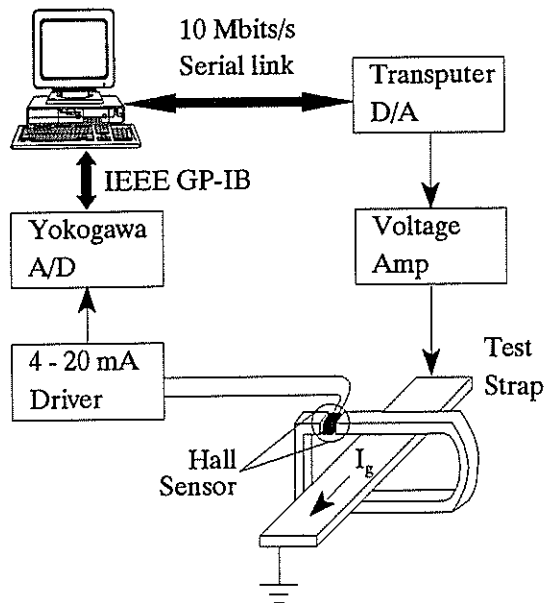


Figure 8: Experimental setup.

Figure 3 shows a representative test waveform used for evaluation of the circuit. Figure 9 shows the output of the sensing circuit.

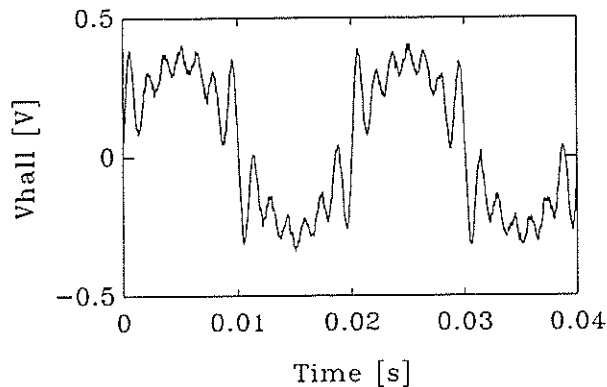


Figure 9: Output of Hall sensor.

Figure 10 shows the frequency spectra of the simulated and measured harmonics, with the harmonic amplitudes expressed as percentage values of the fundamental component.

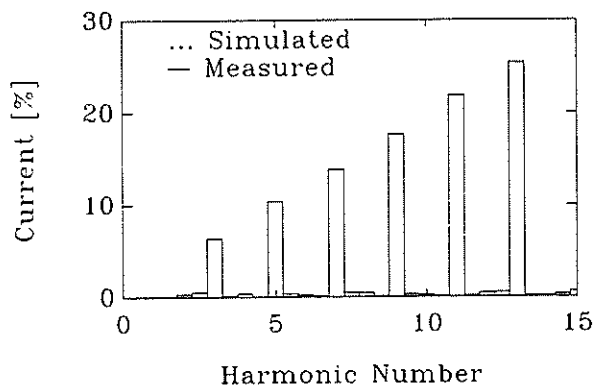


Figure 10: Frequency spectra of simulated and measured signals.

Table 1 compares the frequency spectra of the measured and simulated results. The measured and theoretical results show excellent correlation.

Table 1: Frequency spectrum comparison.

n	$V_1$	$I_g$	$V_{hall}$	%err
1	100 %	100 %	100 %	0 %
3	2 %	6 %	6.39 %	+6.50 %
5	2 %	10 %	10.39 %	+3.90 %
7	2 %	14 %	13.84 %	-1.14 %
9	2 %	18 %	17.66 %	-1.88 %
11	2 %	22 %	21.82 %	-0.82 %
13	2 %	26 %	25.36 %	-2.46 %

## 5. Conclusion

The Rogowski coil principle has been found unsuitable for this application due to noise interference and dc drift. The Hall element sensor and the associated circuit performs well with respect to noise and accuracy. The results given in table 1 indicate that error levels of less than 6.5% of the harmonic current value can be obtained. In practice the errors are most severe for the lower harmonic orders due to the amplification of high frequencies by the voltage/current relationship of the capacitive divider.

## Acknowledgment

The authors appreciate the support and sponsorship of the project by the local electricity supply utility ESKOM.

## References

- [1] N. Mohan, T.M. Underland, W.P. Robbins, *Power electronics: Converters, Applications and Design*, John Wiley & Sons, Singapore, 1989.
- [2] H.A. Haus, J.R. Melcher, *Electromagnetic fields and energy*, Prentice-Hall, New Jersey, 1989.
- [3] P. Lorrain, D.R. Corson, *Electromagnetic fields and waves*, Freeman Press, California, 1970.
- [4] A.J. Schwab, *High voltage measurement techniques*, MIT Press, Cambridge, 1972.
- [5] Siemens, *Galvanomagnetic Devices*, Data Book.

## Address of Author

Mr J.H. Vermeulen, Dept of Electrical and Electronic Eng., Faculty of Engineering, Banhoek Road, STELLENBOSCH, 7600, South Africa.

E-mail: vermeuln@firga.sun.ac.za

# THE ECONOMICS AND APPLICATION OF SINGLE POLE PROTECTION SCHEMES ON RADIAL 132kV FEEDERS

by

Olaf von Abo

Eskom, Pretoria Technicon, South Africa

## 1. ABSTRACT

Large industrial power users require a firm electrical supply to ensure the continuity of sensitive processes. A loss of power causes loss of production and revenue. The most secure supply is obtained by duplicated overhead lines to the load point. This arrangement will save the power user money by reduced outages, but requires a very high initial capital investment which may never be recovered. This study investigates the viability of two single line options - equipped with three or with single pole tripping facilities respectively.

## 2. INTRODUCTION

Power can be made available to power users by means of underground power cables or overhead lines. Due to long distances and very high costs involved, cables are not normally used to supply large power users and will not be considered in this study.

Large power users require firm power supplies to limit power outages and the resultant outage costs. The best way to ensure a firm supply to large power users is the provision of two overhead lines. These lines should preferably be supplied from two independent power supply points. This arrangement ensures that the loss of supply at one supply point, or the loss of one of the overhead lines does not result in a loss of supply at the load point.

This ideal supply has two constraints. The first is a practical limitation caused by the general lack of reliable supply points close to the load point, making it impossible to supply the load from two independent supplies. The second limitation is the cost involved in duplicating supply points and overhead lines.

A second option, and a more practical one, is to supply the load on two overhead lines from a single supply point with dual redundancy. This supply point is typically a substation with at least two transformers and double busbars.

This approach to firm power supplies was very common in the past, but due to increasing economic pressure, large power users and power supply utilities have sought alternatives. Ideally this alternative should be cheaper than the double overhead line configuration, but still provide an acceptable quality of supply. Simply changing the configuration to a single overhead line would satisfy the first criteria, but not the quality of supply requirements.

One option available to the design engineer is single pole protection operating on a single overhead line. The greatest advantage of such a scheme is that it saves the cost of a second overhead line, which is a considerable saving when long distances have to be covered.

It was necessary to quantify the expected success rate of single pole auto reclosing on 132kV lines. The factors influencing the ratio of single to three phase faults are lightning intensity in the area, tower footing resistance and earth resistivity, tower construction (horizontal or delta configuration), double or single circuit lines and the basic insulation level per phase. In addition, the single pole dead time and line construction will influence the percentage of single phase faults successfully cleared by single pole tripping.

From the information available, an assumption was made that a success rate of 80% is not only obtainable, but also realistic. This assumption was used as a basis throughout the study, but practical limitations were recognised.

## 3. TRANSFER CAPABILITIES OF STAR-DELTA TRANSFORMERS

An investigation was undertaken to determine the exact power transfer capability of star-delta transformers after one primary phase had been disconnected. This data was required to prove the advantage of single pole reclosing and it was also necessary to determine the effect on customers.

The effect on power users would play a crucial role in determining the outage costs due to different types of faults and the resultant loss of supply.

The power transfer capabilities were determined using three methods: a mathematical calculation, a computer simulation study and an experiment.

### 3.1 Mathematical Study

To begin with, sequence components were used to solve a healthy three phase network. The purpose of this calculation was to determine the load voltages and currents under normal load conditions.

Secondly, one phase was disconnected on the high voltage side of the star-delta transformer and the load voltages and currents were re-calculated. A comparison between these two sets of results was an indication of the power transfer capabilities of star-delta transformers.

### 3.2 Computer Study

The preceding study was followed by a computer study along similar lines. Simulated tap change operations were undertaken by the computer to correct the voltage at the load point.

The results could not be the same as those of the previous study, but would serve the purpose of confirming the excellent power transfer capabilities of star-delta transformers.

### 3.3 Experiment

As a final step in this part of the study a practical experiment was performed to determine if any practical implications had possibly been overlooked in the theoretical analysis.

### 3.4 Percentage effect on parameters

Parameter	Calculated	Computer	Experiment
Va	-8.4%	-10.9%	-1.7%
Vb	-22.8%	-21.6%	-4.3%
Vc	-0.7%	-7.3%	+0.1%
Ia	-4.1%	-1.3%	-4.0%
Ib	-19.4%	-13.1%	-6.2%
Ic	+3.6%	+2.7%	+3.2%

### 3.5 Conclusion

The excellent power transfer capabilities of star-delta transformers make the application of single pole tripping protection on radial 132kV lines a very attractive option.

The advantage of this application is a greatly improved quality of supply to large power users and a potential saving of millions of Rand per annum.

## 4. THE ECONOMICS OF SINGLE POLE AUTO-RECLOSE SCHEMES

An economic study is a process whereby the economic viability or return on capital investment is investigated and expenditure and income are the basic components of any economic study. This study differs in that the economic viability of a power supply to a power user is not under consideration here. Instead, this is a comparative study to determine the most economical means of providing electrical supply. The income component of this study is therefore more difficult to define.

Due to added equipment and manpower requirements for duplicated overhead lines, this option will obviously require the highest initial capital investment. It will also be the most reliable option in terms of continuity of supply. A better continuity of supply will save the power user money owing to the reduction of outage costs, which are the costs incurred by a power user as a direct result of power losses. This saving can be considered an extra income to the power user and will be a return on his higher initial capital investment.

Following from the above, an economic study was carried out with the extra initial capital investment forming the expenditure criteria of the study. The outage costs that the user would have incurred, had another option been selected, formed the income criteria.

### 4.1 Outage Costs

Although some information regarding outage costs has been available for many years, no flexibility was allowed for in these readily obtainable statistics. In order to obtain first-hand information, six large industrial power users in Eskom were visited and questionnaires were completed. These questionnaires allowed for variables such as outage duration, differences in processes, restart duration, spoilage of goods etc.

For the purpose of this study, outages of four durations were considered. These are listed below:

- Single phase outage for 1.1sec.
- Three phase outage for 3.0sec.
- Three phase outage for 5.0min.
- Three phase outage for 30min.

The average outage cost per outage duration is usually not very useful in an economic study and therefore had to be adapted to expected average outage costs per annum. For the purpose of this study it was assumed that the average line length for bulk supply points was 35km. This average was obtained from previous projects.

The 1990 fault statistics were used to determine the average faults/km/annum on the 132kV network.

Faults of different durations have different effects on power users. To account for this difference, a distinction was made between permanent and transient faults in the calculation of outage costs. From the statistics the expected outages per annum for a 35km 132kV overhead line was calculated with the following results:

Permanent faults:	0,728 per annum
Transient faults:	3,738 per annum

The expected outage costs per annum were calculated for the three single overhead line options.

#### 4.2 Project Cost

The budget cost of a 35km 132kV overhead line (with Wolf conductor) and its associated feeder bay was used to fill the project cost criteria.

#### 4.3 The Economic Model

To ensure that the economic model was based on sound economic principles, a computer program was used to determine the most viable option. The program took into account the life expectancy of the user's plant, inflation, maintenance costs and discount rate to calculate internal rate of return (IRR) and the net present value (NPV) at the end of the plant lifetime. The result is an indication of the viability of the second line.

#### 4.4 Results

- If the single overhead line with three pole reclosing option is compared to the double overhead line option:

IRR	= 19.56%
NPV	= R664 000 after 20 years
Payback period	= 18 years

- If the single overhead line with single pole tripping and with communication channels option is compared to the double overhead line option:

IRR	= 14.89%
NPV	= -R1 299 000 after 20 yrs
Payback period	= > 20 years

- If the single overhead line with single pole tripping and without communication channels option is compared to the double overhead line option:

IRR	= 14.36%
NPV	= -R1 560 000 after 20 yrs
Payback period	= > 20 years

#### 4.5 Conclusion

From the results it is obvious that the double overhead line is a better option economically than the single overhead line equipped with three pole tripping facilities. Furthermore the double overhead line option is not a better option economically than either of the single overhead lines with single pole tripping facilities.

### 5. APPLICATION AND PROTECTION SETTINGS

Chapter 4 concludes that the most economical option is the single line option with single pole protection and no communication channels. Single pole tripping complicates the protection application and philosophy.

Fault studies were performed to determine the fault current distribution for faults at various points along the overhead line. The results of these studies are used to recommend protection setting philosophies and the most effective mode of operation.

#### 5.1 Multi-phase faults

A three phase fault on the line is cleared by the three pole tripping of the circuit breaker at the supply substation. This guarantees the removal of all electrical energy at the fault point. The relay at the load substation is not required to operate for this type of fault.

#### 5.2 Earth faults

The only way to clear an earth fault on the overhead line is to trip the breaker poles of that phase at both the supply and the load substations. Tripping of a different phase at the load substation will not guarantee fault clearance and results in the transformer being energised on one phase only with a resultant loss of power transfer capabilities. Opening of all three phases results in a total loss of supply and all the advantages of the single pole protection application are lost.

### 5.3 Earth fault compensation

The first step was to confirm that the way in which fault information was presented to the load end relay for measurement was correct. This step was deemed necessary due to the difference in fault current distribution at the load and source ends. The earth fault compensation was checked for accuracy for the case where the current in all three phases was equal in magnitude and in phase.

Under earth fault conditions, a compensation factor is used to modify the reach of the relay to ensure correct measurement even under earth fault conditions. Various symbols are used for this factor, but for the purpose of this study it is denoted KO. The purpose of this factor is to change the earth fault impedance measured, to the line impedance setting of the relay.

$$I_{\text{relay}} = I_{\text{fault}} (KO \times I_{\text{residual}})$$

$$\text{With } I_{\text{residual}} = I_a + I_b + I_c$$

$$KO = \frac{1}{3} \times \frac{Z_0}{(Z_1 - 1)}$$

From fault studies performed, it was evident that the KO factor is also applicable to remote or load end relays.

### 5.4 Starter settings

The fault infeed from the remote end relay for an earth fault close to the supply end is very small. The impedance relay generally used is equipped with two starters operating in parallel. The one is an over-current starter, while the other is a combined over-current and under-voltage starter. In the latter, both conditions must be satisfied before the starter will operate. Both these starters perform phase selection but the combination starter is the more reliable unit in this regard.

A typical fault current calculated (206A) was less than the full load current of a 60MVA load (262A). This means that the over-current starter cannot be used for load end earth fault detection. The under-impedance starter will serve as the only earth fault sensitive starter, as the output will be blocked by the under-voltage unit despite the operation of the over-current unit. An under-voltage condition will only result from a fault and this arrangement is considered acceptable, even though it is far from ideal. A better solution would be to make use of relays with under-impedance starters for these applications, but where this is not possible care should be taken with the settings of the starters.

Load current and earth fault detection are not the only application problems of the relay with the two starters as described. It has been stated that phase selection is an essential part of the single pole protection application. This is one of the functions of the starter unit and is performed by both the over-current and the combination starter. From a typical current distribution diagram it can be seen that the fault current at the load end will be equal in all three phases for earth faults anywhere on the line. These currents will be of significant magnitude for faults close to the load substation. If this current is higher than the over-current starter setting, it will lead to a three phase fault measurement for a single phase fault.

Considerable fault studies will be required before the protection settings of the load end relay starter units can be calculated and the results will be different for each network.

### 5.5 Effect on other bays

A high zero sequence current component is present in the high voltage network when one phase is opened. This zero sequence current flows from the load end transformer earthed star-point to the earth point of the supply. In a complicated interconnected power system this source earth point will not be a single generator with an earthed neutral, but rather a source network with multiple earth points.

A complete study will be required for each application to determine the magnitude of fault current flowing in each earthed neutral point of the network.

## 6. CONCLUSION

In general it can be concluded that a single overhead line, equipped with single pole tripping facilities and not equipped with communication channels, is an economical, reliable alternative to double overhead lines.

Power utilities have an obligation to their customers to provide electrical power that will satisfy the needs of the customer. It is much easier to provide the customer with double overhead lines because the double redundancy can serve to conceal application, setting, maintenance and human errors, all at the expense of the user.

More care is required in all of these areas so that only power outages outside the control of the power utility occur.

If the single overhead line with single pole tripping option is selected for economical reasons, then the power user must accept that he will have to pay a price for the huge initial saving in the form of outages over the lifetime of his plant.

Power users should be involved in the decision of an option so that accurate estimates on outage costs can be obtained and so that they can be made aware of all the implications of the most economical option. Care must be taken by the power utility not to make decisions for the user and to keep records of all agreements for future reference.

## REFERENCES

- (1) Levy, H. & Sarnat, M. "Capital Investment and Financial Decisions". Prentice Hall International (UK) Ltd., Hertfordshire, Fourth Edition, 1990.
- (2) GEC Measurements. "Protective Relays Application Guide". Balding & Mansell Ltd., Stafford, Second Edition, 1975.
- (3) Westinghouse Electric Corporation. "Applied Protection Relaying". Silent Sentinels, Florida, 1982.
- (4) Slatem R.R. "Single-phase Auto-reclosing - Philosophy and Experience in Southern Africa". IFAC Symposium, Pretoria, Republic of South Africa, pp. 141-153, September 1980.

## ADDRESS OF AUTHOR

Mr O von Abo, Eskom, PO Box 36099, MENLO PARK, 0102.

# AN INVESTIGATION OF CHARACTERISTICS FOR TRIPPING PROTECTION USED FOR DETECTING OUT-OF-STEP CONDITIONS. AN ESKOM CASE STUDY.

J van Eyssen

Eskom (South Africa)

Prof A Petroianu

University of Cape Town (South Africa)

**Abstract:** During an out-of-step condition, power system distance protection may detect an out-of-step condition and consequently operate to trip unfaulted lines. The tripping of lines interrupts supply to load and exacerbates and already existing problem. Out-of-step blocking protection is primarily used to detect an out-of-step condition and block distance protection.

Research shows that if all distance protection is blocked during out-of-step conditions, separation in a system cannot take place. One solution is to use out-of-step tripping protection. This protection detects the condition and trips local and/or remote lines thereby allowing system separation.

This paper investigates different characteristics for out-of-step tripping protection.

## 1. INTRODUCTION

When two generators or various groups of generators are out of step with one another, they must be separated into islands. These islands must be stable, with a sufficient generation-load balance.

Based on the fact that the performance of power system distance protection is affected by out-of-step conditions in that system, these relays may detect an out-of-step condition and consequently operate to trip unfaulted lines. The tripping of these lines interrupts supply to load and exacerbates an already existing stability problem. Out-of-step blocking protection is primarily used to detect an out-of-step condition and block distance protection.

Research shows that if all distance protection is blocked during out-of-step conditions, system separation in a system cannot take place [1].

There are two possible solutions:

- 1) Distance protection relays can intentionally not be blocked by out-of-step blocking protection. This will allow tripping at selected locations during out-of-step conditions.
- 2) In power systems where all distance protection operation is blocked during out-of-step conditions, a type protection called out-of-step tripping protection detects out-of-step conditions and trip some local and/or remote lines. These elected lines allow system separation to take place during out-of-step conditions.

At present out-of-step tripping relays are installed on Eskom's Cape system at various locations. During an out-of-step condition that occurred in 1990 none of the tripping relays detected the incident. As a consequence, a further cascade tripping of unfaulted lines due to distance protection operation (with no out-of-step blocking protection) occurred and eventually the Cape system experienced a system blackout.

Modelling of protection in a stability study provides an indication of protection performance during an out-of-step condition [1]. An investigation of the performance of the protection, using the above approach, indicated amongst others, a problem as to which type of characteristics to use for out-of-step detection.

This paper investigates different characteristics for out-of-step tripping protection. The respective characteristics of the protection were mathematically modelled. These models were included in the protection model. Stability studies were done and the behaviour of the protection was investigated.

## 2. THE POWER SYSTEM MODEL

The structure of the Eskom power system is shown in Figure 1.

The power system is characterised by a major capacity of coal-fired power stations in the north. A nuclear power station and a pumped storage scheme are situated in the south. The power generated in the south is not sufficient to supply the local load, however, and power has to be imported from the north, over a distance of  $\pm 1400$  km.

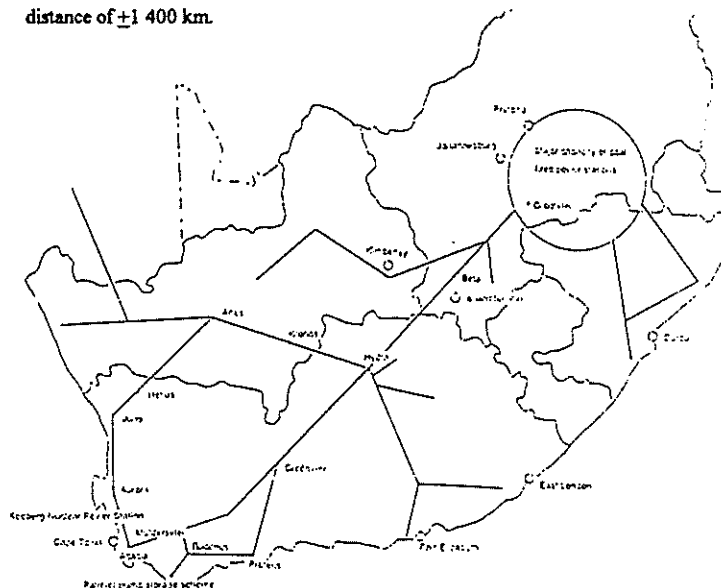


Figure 1: The Eskom power system

The Eskom power system was represented by mathematical models describing the following:

- 1) each generator;
- 2) generator excitation controls;
- 3) the transmission network<sup>1</sup>; and
- 4) loads at transmission substations.

In addition to the Eskom power system model, different characteristics for out-of-step tripping protection were mathematically modelled. These characteristics were modelled in such a way as to simulate out-of-step detection for selected locations in Eskom's Cape system.

Three types of characteristics for out-of-step tripping protection were modelled, namely:

- 1) segment-circle type characteristic;
- 2) double-blinder type characteristic; and
- 3) rectangular-type characteristic.

### Segment-circle type characteristic

The segment-circle type characteristic can be seen in Figure 2. There are two philosophies for out-of-step detection, namely:

- 1) detection on the way in; and
- 2) detection on the way out.

<sup>1</sup> Transformers, lines, compensation equipment, etc.

Detection on the way in occurs when a passage time greater than  $T1$  through zone 1 and a passage time greater than  $T2$  through zone 2 occur consecutively before the apparent impedance enters zone 3.

Detection on the way out occurs when, in addition to the passage times for detection on the way in, the apparent impedance stays in zone 3 for  $T3$  cycles and exits through zones 2 and 1 for a period greater than  $T4$  in a direction opposite to which it originally entered.

A rapid passage through any zone signifies that no out-of-step condition has occurred. The measured impedance must leave all zones and re-enter to restart the timers.

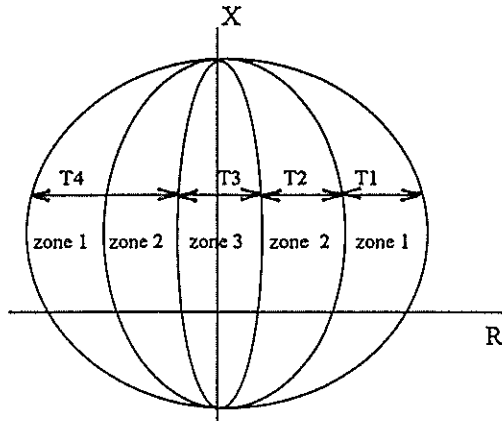


Figure 2: Segment-circle type characteristic

#### Double-blinder type characteristic

The double-blinder type characteristic can be seen in Figure 3. An out-of-step condition is detected by measuring the time taken by the measured impedance to pass through defined zones. As in the case of segment-circle type characteristic, there are two philosophies for out-of-step detection:

- 1) detection on the way in; and
- 2) detection on the way out.

Detection on the way in occurs when the impedance enters zone 2 and the impedance took a minimum predetermined time (interzone travel time) to travel from the outer zones (4 or 5) through the inner zones (3 and 4 respectively).

In addition to the passage times for detection on the way in, detection on the way out occurs either

- 1) when the measured impedance goes through zone 5, after spending a definite time in zone 1, if it originally started in zone 4; or
- 2) when the apparent impedance goes through zone 4, after spending a definite time in zone 3, if it originally started in zone 5.

A rapid passage through any zone signifies that no out-of-step condition has occurred. The measured impedance must leave all zones and re-enter to restart the timers.

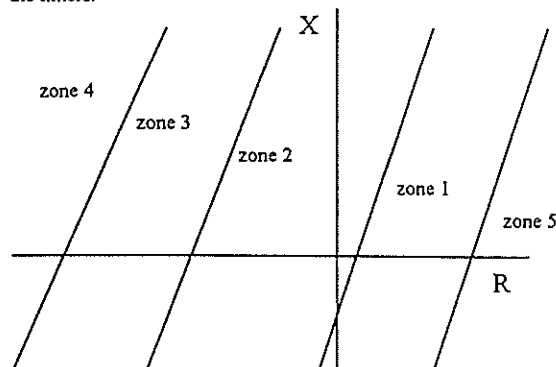


Figure 3: Double blinder type characteristic

#### Rectangular-type characteristic

The rectangular-type characteristic can be seen in Figure 4. As in the case of the segment-circle type and the double-blinder type characteristics, there are two philosophies for out-of-step detection:

- 1) detection on the way in; and
- 2) detection on the way out.

As the measured impedance enters zone 1, timer  $T1$  starts. When the time allowed by timer  $T1$  expires, an out-of-step condition will be detected on the way in, when the impedance enters zone 2. On the way out detection will occur when the impedance exits from zone 1 and zone 2 in a direction opposite to which it originally entered.

A rapid passage through any zone signifies that no out-of-step condition has occurred. The measured impedance must leave all zones and re-enter to restart the timers.

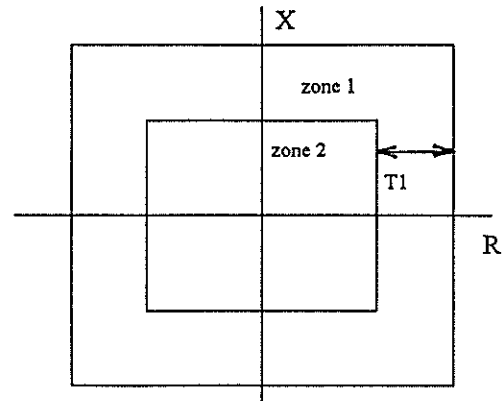


Figure 4: Rectangular-type characteristic

### 3. CASE STUDIES AND RESULTS

Four stability studies were done to obtain electrical centres in Eskom's Cape system. The results indicated that electrical centres are either in the northern part of the Cape system or in the Western part of the Cape system, or in both. Three locations for out-of-step tripping protection were identified from these electrical centres, namely:

- 1) on the Muldersvlei-Bacchus line at Muldersvlei Substation;
- 2) on the Muldersvlei-Droërvier line at Muldersvlei Substation; and
- 3) on the Aurora-Juno line at Aurora Substation.

To investigate the three types of characteristics for out-of-step tripping protection, the four stability studies were repeated.

#### Stability study 1:

A permanent three-phase fault was simulated on the busbar at Grootvlei Substation and cleared within 460 milliseconds by tripping all the breakers at the substation. As a result, small angular oscillations (with a swing bus in the north as reference) occurred at Koeberg Power Station in the south. An increase in angle separation between the north and the south eventually developed.

The respective characteristics for the out-of-step tripping protection located on the Muldersvlei-Bacchus line at Muldersvlei Substation, as well as the measured impedance at this location, are shown in Figure 5.

#### Conclusion

The segment-circle type characteristic and the double-blinder type characteristic overlaying the measured impedance show that out-of-step tripping protection using one of these types will not detect the out-of-step condition. The measured

impedance enters both these characteristic types in such a way that the sequence of operation required by the relay for out-of-step detection will not occur.

The rectangular-type characteristic overlaying the measured impedance shows that out-of-step tripping protection using this type of characteristic will detect the out-of-step condition.

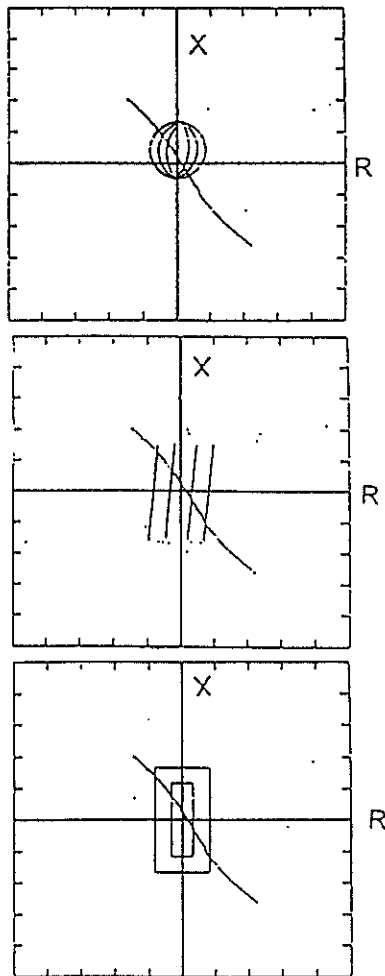


Figure 5: Out-of-step relay characteristics

#### Stability study 2:

As a prefault condition, an outage of the series capacitor on the Perseus-Hydra 400 kV line was assumed. A permanent three-phase fault was simulated on the busbar at Beta Substation and cleared within 460 milliseconds by tripping all the breakers at the substation. As a result, small angular oscillations (with a swing bus in the north as reference) occurred at Koeberg Power Station in the south. An increase in angle separation between the north and the south eventually developed.

The respective characteristics for the out-of-step tripping protection located on the Aurora-Juno line at Aurora Substation, as well as the measured impedance at this location, are shown in Figure 6.

#### Conclusion

As in stability study 1, the segment-circle type characteristic and the double-blinder type characteristic overlaying the measured impedance show that out-of-step tripping protection using one of these types will not detect the out-of-step condition. The measured impedance enters both these types of characteristics in such a way that the sequence of operation required by the relay for out-of-step detection will not occur.

The rectangular-type characteristic overlaying the measured impedance shows that out-of-step tripping protection using this type of characteristic will detect the out-of-step condition.

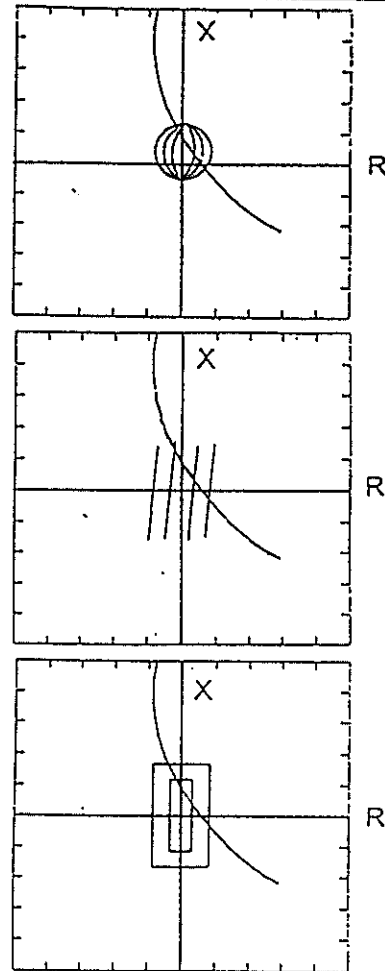


Figure 6: Out-of-step relay characteristics

#### Stability study 3:

A permanent three phase fault was simulated on the busbar at Hydra and cleared within 460 milliseconds by tripping all the line breakers at Hydra for the series-compensated lines. The line breaker for the Hydra-Kronos series-compensated line was not opened. Small angular oscillations (with a swing bus in the north as reference) occurred at Koeberg Power Station in the south. An increase in angle separation between the north and the south eventually developed.

The electrical centre for this study was located in the northern part of Eskom's Cape system due to the tripping of all the lines linking the north with the western part of Eskom's Cape system. Out-of-step tripping relays located in the western part will therefore not detect the out-of-step condition. The various characteristics for out-of-step tripping protection located in the northern part of Eskom's Cape system, as well as the measured impedance, are shown in Figure 7.

#### Conclusion

In this study, the segment-circle type, the double-blinder type and the rectangular-type characteristics overlaying the measured impedance show that out-of-step tripping protection using any one of these characteristic types will detect the out-of-step condition.

#### Stability Study 4:

Stability study 3 was repeated, except that for this study (stability study 4) the series-compensated Hydra-Kronos line breaker was opened and the line breaker

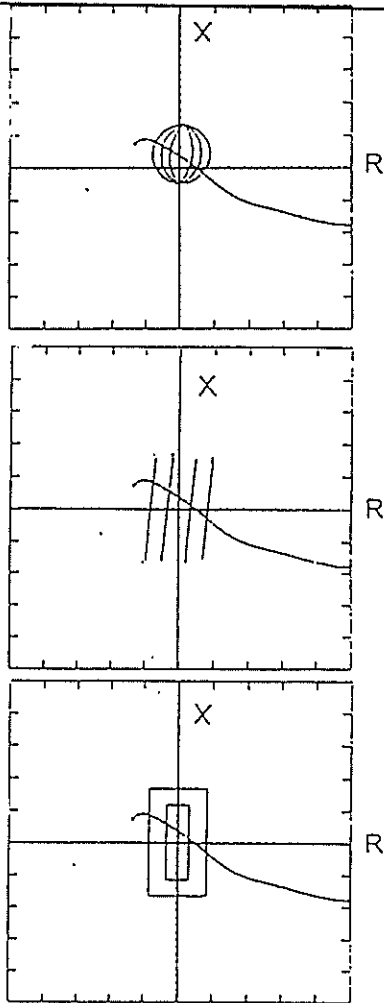


Figure 7: Out-of-step relay characteristics

Koeberg Power Station in the south and an increase in angle separation between the north and the south eventually developed.

The electrical centre for this study was located in the western part of Eskom's Cape system due to the tripping of the line linking the north with the northern part of Eskom's Cape system. An out-of-step tripping relay located in the northern part will therefore not detect the out-of-step condition. The various characteristics for out-of-step tripping protection located in the western part of Eskom's Cape system, as well as the measured impedance, are shown in Figure 8.

#### Conclusion

In this study out-of-step tripping protection using the segment-circle type characteristic will not detect the out-of-step condition. If out-of-step tripping protection located on the Muldersvlei-Droërivier line were to use a double-blinder type characteristic, the out-of-step may be detected, but out-of-step protection located on the Muldersvlei-Bacchus line using the double-blinder type characteristic will not detect the out-of-step condition. As in studies 1 and 2, the measured impedance enters both these types of characteristics in such a way that the sequence of operation required by the relay for out-of-step detection will not occur.

The rectangular-type characteristic overlaying the measured impedance shows that out-of-step tripping protection using this type of characteristic will detect the out-of-step condition.

#### 4. CONCLUSIONS

The modelling of various characteristics for out-of-step tripping protection provided an indication of out-of-step protection performance during out-of-step

conditions. The results also indicated that out-of-step tripping protection using characteristic types such as the segment-circle type or double-blinder type may not detect an out-of-step condition. This is mainly due to the measured impedance entering both these types of characteristics in such a way that the sequence of operation required by the relay for out-of-step detection will not occur.

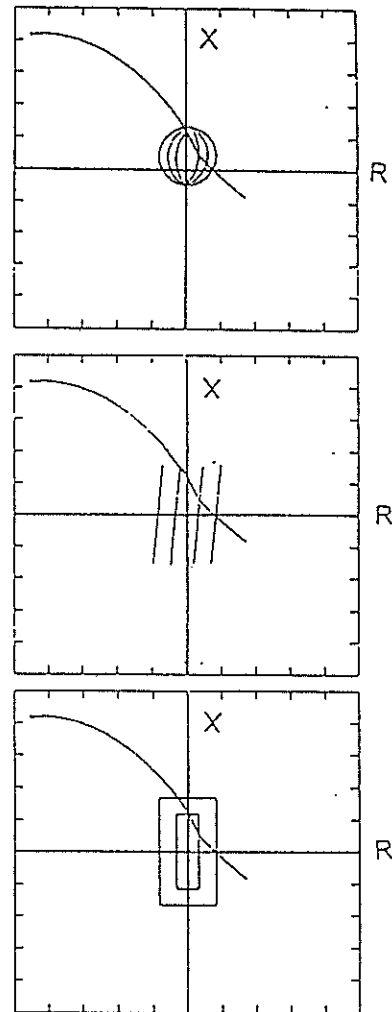


Figure 8: Out-of-step relay characteristics

In all four studies the results indicated that out-of-step tripping protection using rectangular-type protection will detect an out-of-step condition.

This investigation also shows the importance of considering mathematical models of protection when performing stability studies. The modelling of protection - in this case out-of-step tripping protection - in a stability study provides an indication of the protection performance of the system during an out-of-step condition.

#### 5. REFERENCES

- [1] J van Eyssen 'An investigation into the importance of considering protection performance during power system out-of-step conditions', Thesis submitted to Engineering Faculty, UCT, January 1994
- [2] John Berdy, 'Application of Out-of-Step Blocking and Tripping Relays General Electric.
- [3] 'Applied Protective Relaying' Westinghouse Electric Corporation pp 19-1 to 19-14

# EXPERIMENTAL INVESTIGATION AND MODELLING OF THERMAL TRANSIENTS OF UNDERGROUND HIGH VOLTAGE CABLES

F Smith, J P Holtzhausen

University of Stellenbosch, South Africa

## ABSTRACT

This paper describes a laboratory investigation into the transient heating of buried XLPE cables and a computer simulation of the laboratory set-up. The transient heat flow was represented by a ladder network of thermal resistances and capacitances. The circuit was analyzed using a transient circuit analysis program. Due allowance was made for the drying out of the soil layer next to the cable. The results of the simulation achieves a good correspondence with the measured temperatures.

## 1 INTRODUCTION

A considerable amount of work has been done in the area of thermal modelling of underground cables during the first half of this century. Almost all of this was done on cables with paper insulation, but since then a considerable amount of new technology emerged. Nowadays poly-ethylene and XLPE are used extensively for insulation in HV cables. The thermal transient response of cross linked poly-ethylene differ considerably from that of paper. The maximum operating current for XLPE cables should be kept below 90°C. If the temperature exceeds this value, the insulation will start to soften and eventually melt. This will cause the conductor to sink down into the insulation and thus deforming the electric field in the cable. This will decrease the stress handling capability of the cable and degrade its voltage capacity.

A convenient way of dealing with conduction heat flow problems, is to make use of electrical analogies. Heat flow through a thermal resistance can be calculated using the following equation:

$$P = \frac{\Delta T}{R_t} \quad (1)$$

In this equation P is the heat generated in watts,  $\Delta T$  the temperature rise with respect to the ambient (in °C) and  $R_t$  is the thermal resistance (K.m/W). Eq. 1 is also known as Ohm's thermal law and the following analogies with respect to electrical quantities are identified:

$\Delta T$ (temp. difference)	$\rightarrow \Delta V$ (volts)
$R_t$ (thermal resistance)	$\rightarrow R_e$ (electrical ohms)
P (heat in Watts)	$\rightarrow I$ (ampere)

Likewise, the thermal counterpart for capacitance is thermal capacitance. The thermal capacitance of an object

is defined as the amount of heat (in Joule) absorbed per centigrade temperature rise. The product of the thermal resistance and the thermal capacitance is the thermal time constant of the object.

When considering the heat dissipation from an underground cable, the thermal resistance and thermal capacitance should be represented as distributed parameters radially away from the cable. One approach is to divide the cable and the surrounding soil into discrete cylindrical layers, thus obtaining an equivalent lumped parameter network, similar to Figure 1.

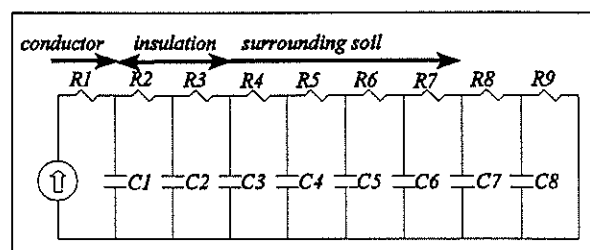


Figure 1: Equivalent electrical ladder network.

In the figure, a typical electrical equivalent circuit is shown, with the thermal resistances ( $R_1$  to  $R_9$ ) and the thermal capacitances ( $C_1$  to  $C_8$ ) representing the radial conduction and the heat capacity, respectively, of the cylindrical subdivisions.

The transient heat flow problem is solved with the electromagnetic transient simulation program, EMTP, using the equivalent circuit above.

## 2 THE EXPERIMENTAL SET-UP

In order to evaluate the accuracy of the simulation, it was decided to perform a laboratory investigation under controlled conditions and to compare the model to the experimental data.

To obtain the data, a wooden box of 1.5 m x 1.5 m x 3 m was built wherein the cable (11kV 150mm<sup>2</sup> XLPE) was buried. The dimensions of the box were chosen after a preliminary mathematical investigation and are adequate to eliminate boundary effects. The box was housed inside a laboratory in order to control the atmospheric conditions.

As is shown in Figure 2, current is injected into the cable using four reversely connected current transformers (CT's).

The cable forms the shorted primary winding of the CT's. The secondary windings are connected in series so that the applied voltage is shared among them while the total current in the test cable can be increased to the desired level without saturating the CT's.

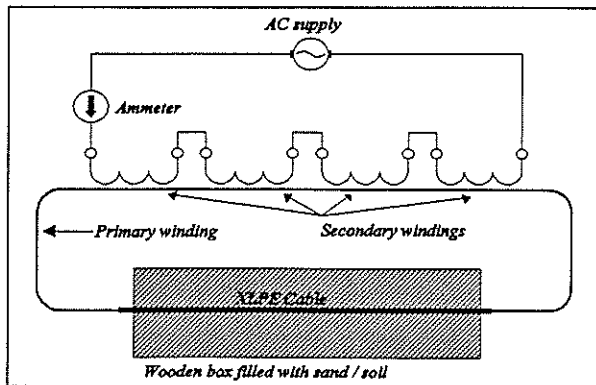


Figure 2: The electrical circuit for the experiment.

The continuous current capacity of the cable, buried at a depth of 0.8 m, is 360 ampere rms. To ensure a sufficient temperature increase in the soil surrounding the cable, the cable was loaded to 120 % of its capacity, a continuous current of 430 ampere. As dielectric losses are not important compared to  $I^2R$  in XLPE cables, the experiment was performed at low voltage.

A computer-based data logging system was designed, built and tested to measure the temperature distribution in the soil surrounding the cable. The system makes provision for forty eight simultaneous temperature measurements from the various sensors. It was assumed that, for the case of homogeneous soil, symmetry can be expected and therefore the sensors were concentrated in one quadrant. Several sensors were placed at locations in other quadrants to confirm the assumption of symmetry. A detailed description of the positioning of the sensors and the instrumentation is given in [3].

### 3 EXPERIMENTAL RESULTS

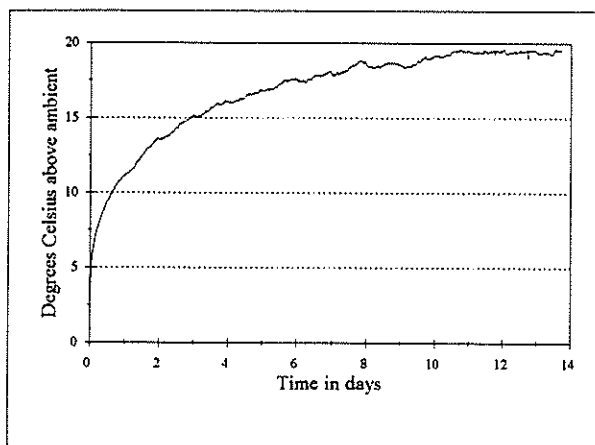


Figure 3: Temperature rise on the surface of the cable.

The graph in Figure 3 represents the rise in temperature on the surface of the buried cable while being subjected to a continuous AC current of 430 ampere. From the figure it

can be seen that the temperature reached a steady state after 11 days. From the curve an increase of 20°C above the ambient temperature of the soil can be noted on the surface of the cable.

Figure 4 contains graphs of the temperature rise at 5 cm intervals along the vertical axes from the surface of the cable to the surface of the soil.

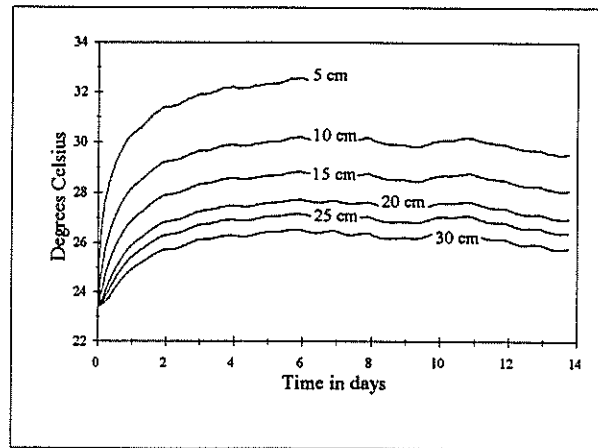


Figure 4: Temperature transients along the vertical axis, measured from the cable surface.

### 4 DEVELOPMENT OF THE MODEL

The power dissipated in the cable, is:

$$P = I^2 \cdot R_e = I^2 \cdot \left( \frac{\rho_e}{\pi r^2} \right)$$

$$P = \frac{430^2 \times 1.7241e^{-8}}{\pi \times (7.4e^{-3})^2} = 18.53 \text{ W} \cdot \text{m}^{-1} \quad (2)$$

$r = \text{outside radius of conductor [m]}$

Since current is the electrical analogue of heat (thermal power in watts), a source in the form of a current step with a magnitude of  $P = I^2 \times R_e$  (current<sup>2</sup> × electrical resistance) is used as an equivalent power supply to the thermal network. The power generated is 18.53 W.m<sup>-1</sup> (Eq. 2) and is the magnitude of the applied current step.

Since the analogy between the thermal and the electrical equations has already been established, the equations for the thermal resistance and capacitance are derived using the same methods.

In the work published on the subject of thermal capacitance, there are several methods of calculating and placing the lumped thermal capacitances. Some authors prefer to use an equivalent  $\Pi$ -network, assigning half of the layer's capacitance to each node while others suggest an equivalent T-topology, locating the entire capacitance on the mid-layer radius. Van Wormer [4] suggested a method of dividing the capacitance with a factor which is a function of the inner and outer radius of the insulation. Since the aim of this paper is to arrive at a acceptable solution without involved calculations, the entire capacitance of each layer is placed at the end node of that

layer as a first approach.

### Equations

The thermal resistance ( $R_t$ ) as a function of the radii, can be derived as follows:

$$\frac{d R_t}{d r} = \frac{\rho}{2 \pi r} \quad K \cdot W^{-1}$$

$$R_t = \frac{\rho}{2 \pi} \int_{r_1}^{r_2} \frac{1}{r} dr \quad (3)$$

$$R_t = \frac{\rho}{2 \pi} \ln \frac{r_2}{r_1} \quad K \cdot m \cdot W^{-1}$$

In Eq. 3,  $\rho$  is the thermal resistivity ( $K \cdot m/W$ ) of the medium and  $r$  is the radial distance from the centre of the cable in meters. The thermal capacitance ( $C_t$ ) as a function of the radius is similarly derived from the relevant differential equation:

$$\frac{d C_t}{d r} = \frac{2 \pi r}{\alpha \rho} \quad W \cdot h \cdot K^{-1} \cdot m^{-2}$$

$$C_t = \frac{2 \pi}{\alpha \rho} \int_{r_1}^{r_2} r dr \quad (4)$$

$$C_t = \pi \kappa (r_2^2 - r_1^2) \quad W \cdot s \cdot K^{-1} \cdot m^{-1}$$

In these equations  $\kappa$  is the heat capacity ( $J/K \cdot m^3$ ) and  $\alpha$  is the thermal diffusivity ( $m^2/s$ ) of the medium. The relationship between  $\alpha$ ,  $\kappa$  and  $\rho$  is

$$\alpha = \frac{1}{\rho \cdot \kappa} \quad (5)$$

### Equivalent thermal network

As a first step, the cable and its surroundings were divided into four different media through which the heat is conducted. Table 1 contains the parameters that were used to characterise the different media as well as the number of layers into which each section was divided. The radii has the centre of the conductor as origin.

**Table 1:** Constants characterising the soil and the cable.

	Copper	XLPE	PVC	Soil
Layers	1	5	2	15
rad <sub>(min)</sub>	0	7.4e-3	1.175e-2	1.275e-2
rad <sub>(max)</sub>	7.4e-3	1.175e-2	1.275e-2	0.75
$\rho$	2.597e-3	3.5	5	1.5 - 2.2
$\kappa$ (e-7)	3.45e6	2.4e6	1.7e6	3.8 - 2.7

The thermal resistivity and the specific heat of XLPE and PVC and the specific heat of copper were obtained from the relevant IEC document [2]. The thermal resistivity of copper was taken as the reciprocal of its thermal conductance which is  $385 W \cdot K^{-1} \cdot m^{-1}$ . The soil resistivity

was based on the moisture content of the soil before and after the experiment. With  $\rho_{t(\text{soil})}$  known, the specific heat of the soil ( $\kappa$ ) was calculated from Eq. 5 using diffusivity values given in [2].

Eqs. 3 and 4 together with the constants given in Table 1, can now be used to calculate the values of the equivalent thermal components for the various layers.

### 5 SIMULATING THE MEASURED RESPONSE

Figure 5 contains the result of a simulation that was done with the preliminary model.

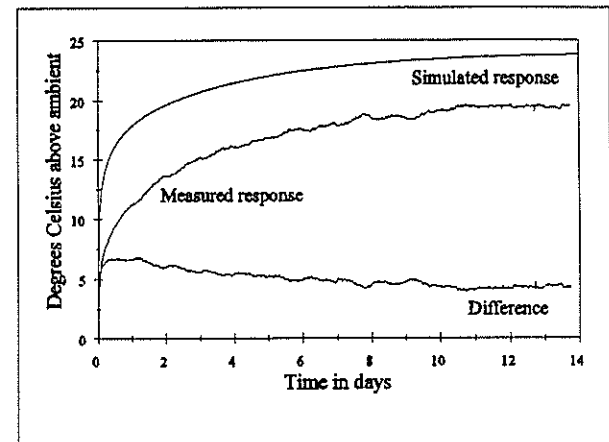


**Figure 5:** A comparison between the first simulation and the measured response.

From Figure 5 it is clear that the simulation done with an average thermal resistivity of  $2.0 K \cdot m/W$  (derived from the initial and the final thermal resistivity of the soil) is not acceptable. According to Cox and Coates [1], the temperature increase of the soil in the immediate vicinity of the cable causes the moisture in that area to migrate to "colder" areas away from the cable. This decrease in moisture content of the soil close the cable, causes the soil thermal resistance to increase. They suggested the existence of a boundary isotherm which implies that soil above a certain critical temperature is dried out and should have a higher  $\rho_t$  than soil excluded by the isotherm.

In the model,  $\rho_t$  of the soil within the boundary isotherm increases gradually from the initial value to its final value.

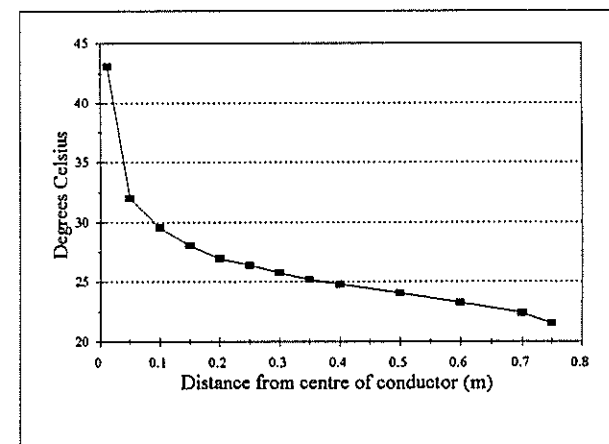


**Figure 6:** Measured soil steady state temperature.

The graph in Figure 6, shows the temperature gradient in the soil as measured towards the end of the experiment. According to the value of the critical temperature (35°C) as defined by [1], the area within 4 cm of the surface of the cable is the area of interest. The boundary isotherm would then be at a distance of 4 cm from the surface of the cable in the vertical above the cable.

Since the minimum and the maximum  $\rho_t$  was known, the rate of increase could be obtained through experimenting with the results of several simulations. The function that was developed, is shown in Figure 7.

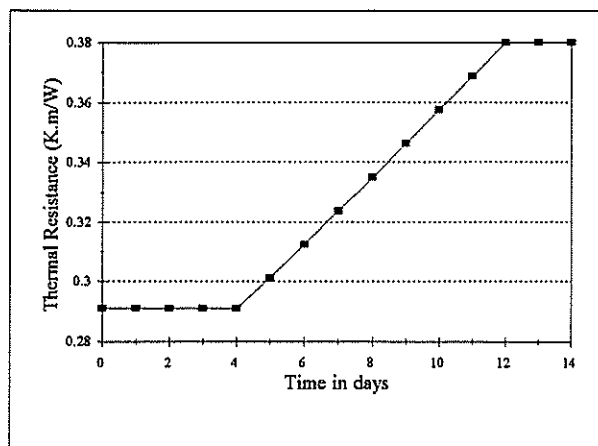


Figure 7: A piecewise-linear  $R_t$  function.

The initial time delay of 4 days is to allow the temperature to reach the critical value of 35°C (refer to Figure 4). Figure 8 shows the new simulation results.

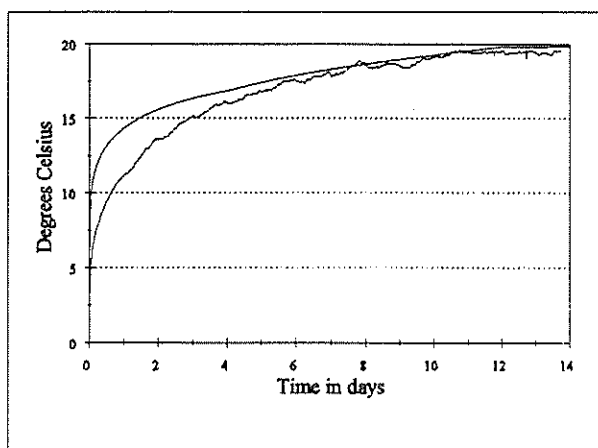


Figure 8: Results obtained with the new model.

The improvement is clear to see, especially in the steady state, but the simulation is still not satisfactory during the initial 5 days. Since the equivalent network represents a systems of distributed parameters with lumped equivalents, an improvement in the distribution of the parameters should improve the simulation of the transient. F.C. van Wormer [4] developed a technique which improves the distribution of the equivalent thermal capacitances. He derives a fraction,  $P$ , which is based on the inner ( $r_1$ ) and the outer ( $r_2$ ) radii of the individual layers. He then calculates the total thermal capacitance of the layer and divides it in the following manner:

$$\begin{aligned} P \times C_{Total} \text{ at } r_1 \\ (1 - P) \times C_{Total} \text{ at } r_2 \end{aligned} \quad (6)$$

Figure 9 shows the results that was obtained with this improvement in the thermal capacitance distribution.

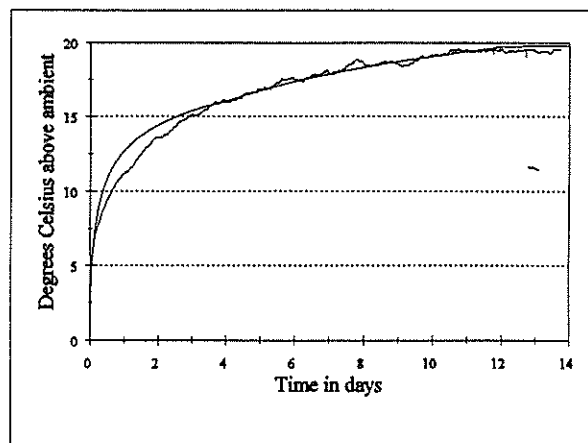


Figure 9: Results obtained with an improved thermal capacitance distribution.

## 6 CONCLUSIONS

A laboratory set-up has been established to record the temperatures in the surrounding soil during the transient heating of a XLPE cable. A model was developed to predict the temperature rise of the cable in the soil using the electric current / heat flow analogy. It was found that the measured temperatures could be matched with the model by allowing for the increase in the thermal resistivity of the soil close to the cable due to moisture migration. The structure of the ladder network also allows the user to obtain temperature profiles at various distances from the surface of the cable without the need to recalculate involved analytical equations. The measurements also proved the concept of a critical temperature as suggested by [1] as valid.

Further work will include the modelling of non-homogeneous soils and cyclic loads on cables.

## 7 REFERENCES

- 1 Cox H.N. and Coates R., "Thermal analysis of power cables in soils of temperature responsive thermal resistivity", Proc. IEE, Vol 12, No 12, Dec 1965
- 2 IEC Document 853-2, "Calculation of the cyclic and emergency rating of cables - Part 2"
- 3 Smith F. and Holtzhausen J.P., "Experimental investigation and modelling of transients on underground HV cables", Proc. UPEC '94
- 4 Van Wormer, F.C. "An improved approximate technique for calculating cable temperature transients", AIEE Transactions, Volume 74, Part 3, 1955

# METHOD OF USING DATA FROM COMPUTER SIMULATION TO TEST PROTECTION RELAYS

R Zivanovic

P A Weyers

D C Barry

Technikon Pretoria

**This paper describes a method for testing relays by using data from computer simulation. The testing method provides a relay under evaluation with current and voltage inputs similar to those that would be encountered under fault conditions in a real power system. The application of the method is illustrated by testing of an overcurrent relay for possible transient overreach.**

## 1. Introduction

The most common equipment for testing protection relays is portable test-set, capable of producing steady-state voltage and current signals. Another method of testing is based on simulation of full transient behaviour of a power system. This type of testing produces voltage and current signals that correspond to events in a real power system. These signals are obtained at the required relay location for the period during which the response of the relay is to be evaluated.

Testing equipment capable to generate transients can be classified in three groups, depending on the applied technology:

- a) small physical models,
- b) analog computers,
- c) digital simulators.

The equipment specified in groups a) and b) are very reliable for relay testing, but however are very costly. In the last decade, due to very extensive development in microprocessor technology, a number of digital simulators became available.

There are two kinds of testing methods which use digital simulation: open-loop and real-time. The open-loop approach is based on an off-line digital simulation program, such as Electromagnetic Transient Program (EMTP) [1]. The program produces an accurate simulation of power system behaviour under fault and switching conditions. Data generated using EMTP is transferred to a relay under evaluation. Alternatively in the real-time approach EMTP computation and configuration changes are performed on the relay within a closed-loop system. The latter method needs fast computer hardware, such as digital signal processors.

This paper provides the implementation details of the method for relay testing based on a digital simulator. The method has been developed for research and training in protection relaying. The relays under test are adapted in a special way, so that expensive amplifiers are not used. The method used is open-loop procedure, i.e. data produced in off-line computer simulation is injected directly without any feedback from the relay. The method is applied in testing an overcurrent relay under transient conditions.

## 2. Description of the Method

### 2.1 Hardware System

The testing method is based on a standard micro-computer (80386) with co-processor (80387). This type of low-cost computer provides access to a wide selection of third party interface cards and software. The specialised interface D/A card is mounted in the micro-computer. The D/A converter has the following characteristics [2]:

- a) The number of channels : 12 (8 bipolar, 4 monopolar).
- b) Resolution : 12 bit.
- c) Maximum output voltage :  $\pm 5V$  to  $\pm 10V$  (adjustable).
- d) Maximum output current :  $\pm 10mA$  at  $\pm 10V$ .

The overcurrent relay used for our experiment is the Siemens 7SJ50 [3]. The method allows testing without aid of an amplifier. Therefore the following adaptations to the relay are necessary:

- a) The internal current transformers are removed.
- b) The output signal from D/A converter is voltage instead of current. To configure the relay, with regard to D/A output, the internal current divider circuit has been changed to a voltage divider circuit so that the plug setting function of the relay stays the same.
- c) The rectification and summation circuits are also removed. Data preparation program (explained in the next section) mathematically perform rectification and summation of the three-phase current signals.

## 2.2 Software System

The testing method is based on a few computer programmes. Some of them are available free-of-charge (EMTP/ATP version [1]), and the others are developed specifically for our method. All these programmes are running on the same computer, in a sequence, as explained below.

The first step is simulation of the transient behaviour of a power system, under fault and switching conditions, by using EMTP [1]. The results from EMTP simulation are current and voltage signals at the specific relay location. These results are obtained by using certain numerical integration time interval (sample rate). That interval should be small enough to prevent numerical instabilities and maintain accuracy in EMTP. The results from EMTP simulation will form the basis of the actual testing on a protection relay.

The second step of the method is data preparation. The data obtained from simulation needs to be converted in a suitable format, required by the real-time program which controls the D/A card. The data preparation program has the following functions:

- Reducing the sampling rate and the number of samples if it is necessary.
- Scaling the signals using current transformer and voltage transformer ratios. Linear transducers are assumed.
- Mathematical transformation of the signals, due to certain adaptations of the relay, as explained in section 2.1.
- The minimum and maximum instantaneous values of the signals are checked against the dynamical range of the D/A converter to ensure that signal clipping problems are avoided.
- Converting the data into binary format which can be directly loaded into the computer's memory before running the test.

In the last step the D/A card generates the voltage output signals which represent the current waveforms. The D/A control program uses the information in the data blocks located at specific locations in the computer's memory. These waveforms are directly injected to the relay under test. The program operates in real-time under the control of the internal computer's clock. The program mathematically manipulates the internal clock, thereby outputting the samples for time periods determined by the sampling frequency selected for each individual test. The frequency can be set to match the used sampling period in the EMTP simulation. The control program must complete its data transfers and control functions before the next pulse from the clock, otherwise it produces distortions in the output waveforms.

## 3. An Application of the Method

An application of the method in testing the transmission line overcurrent relaying is illustrated by using the 22kV radial feeder divided in two sections, as shown in Figure 1. The length of the sections are the same (20km). The r/x ratio of both sections is equal to 1. A load taking 100A is connected to the end of the second section. The overcurrent protection relays are located at points A and B, as shown in Figure 1.

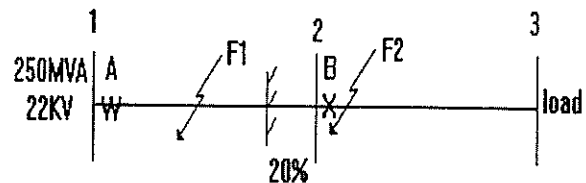


Figure 1: Single line diagram of power system under analysis.

In our experiment Siemens microprocessor overcurrent relay (7SJ50) has been tested [3]. The relay can be used for overcurrent and earth fault main and back-up protection of radial feeders. The relay has five selectable characteristics [3]: normal inverse, very inverse, extremely inverse, definite time and thermal overload. In each of the inverse time characteristics and in the definite time characteristic we can set different values for three different overcurrent elements: phase-fault, high-set and earth-fault. As specified in the manual [3] the high-set overcurrent element is transient-insensitive, i.e. DC components do not affect the performance. In order to test that feature, the method of using data from computer simulation is applied.

The overcurrent relay 7SJ50 is located at point A (Figure 1). We choose the normal inverse characteristic for relay A. The high-set element should protect 80% of the first section. The phase-fault element should protect the rest of the first section, and it operates as a back-up protection for relay B. The fault current at relay A is equal to 255A in the case of three-phase short circuit at 80% length of the first section. The current settings for high-set element is 2.25 and for phase-fault element is 1.13 (the nominal current of the relay is 1A and the CT ratio is 100/1). Time setting for high-set element is lower than time setting for phase-fault element (we choose 0.1s and 0.2s respectively).

The goal of the experiment is to test the high-set element for possible transient overreach. Two faults were simulated. The first one in the protection zone of the high-set element (fault F1, 5km from the relay A), and the second one just in front of relay B. The EMTP was used to simulate current waveforms at

relay A, during the selected faults. Two conditions were simulated for both faults: pre-fault steady-state condition, lasting from 0s to 0.05s, and transient condition during the fault, lasting from 0.05s to 0.1s. Figures 2 and 3 show the simulated current waveforms for all three phases before, and during the faults F1 and F2, at location of relay A. The high frequency transients are quickly attenuated. The exponentially decaying DC components, however, persist for a longer period, as shown in Figures 2 and 3. The DC component can induce the overreach of the high-set element.

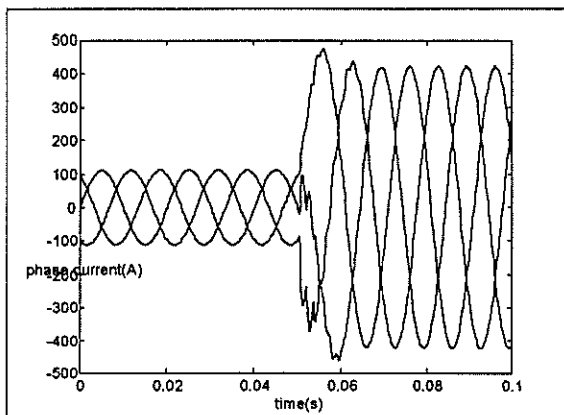


Figure 2: Phase currents at location of relay A with fault condition F1, EMTP output.

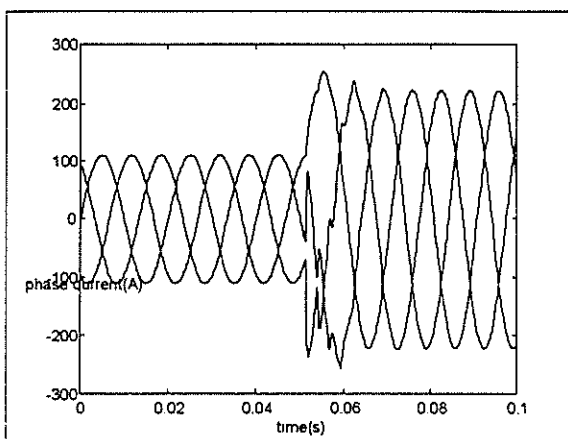


Figure 3: Phase currents at the location of relay A with fault condition F2, EMTP output.

Testing was performed using the data preparation and real-time control programmes, as explained in section 2. Testing has shown that the high-set element of the relay trips for the fault F1. Transients caused by the fault F2 have no effect on the high-set element, and the relay trips only in phase-fault element of the normal inverse characteristic.

#### 4. Conclusions

The method for computer testing of protection relays has been developed. The method has been demonstrated by testing the overcurrent relay for possible transient overreach. The following conclusions can be drawn:

- The method provides a powerful laboratory for evaluating a wide range of protection relays.
- The method has ability to test relays for a large variety of power system configurations and phenomena using off-line simulations.
- The method is low cost and easy to implement.

#### 5. References

- [1] Leuven EMTP Centre, "Alternative Transients Program Rule Book", LEC Belgium, July 1987
- [2] "PC-66 12 Channel D/A card" User Manual. 2nd Ed, December 1989.
- [3] "Overcurrent and Thermal Overload Relay, 7SJ50 - Instruction Manual", Siemens AG, 1986

# MEASUREMENT OF LAMINATED STEEL PROPERTIES AT HIGH FLUX DENSITIES AND NON-SINUSOIDAL OPERATION

C Slabbert    F S van der Merwe    H J Vermeulen

University of Stellenbosch

## ABSTRACT :

An iron loss tester for high flux density and non-sinusoidal operation is described. The system comprises a modified Epstein frame, a bridge MOSFET power amplifier and a computer-based control circuit. The system is capable of performing tests at flux densities up to 2,2 T at frequencies from 50 Hz to 150 Hz, alternatively at frequencies up to 4 kHz, but then at lower values of flux density. The system also allows for flux harmonics to be superimposed on a fundamental frequency. Experimental results are given to verify the correct operation of the system.

## 1. INTRODUCTION

Recently the trend has been to increase the flux density in the electrical machine cores to obtain a higher torque/volume ratio. This, and the increasing use of solid-state switching devices in motor drive applications, lead to higher losses in the magnetic core of the machine. This is mainly due to the additional harmonic loading of the machine, which is a result of the very high values of flux density that occur, especially in the tooth tip areas of the stator and rotor. The harmonic content in the supply voltage and current from solid state motor drives also contributes significantly to these additional losses. This prompted the need for a better knowledge of the behaviour of magnetic materials at high values of flux density.

One question that arises is whether there exists an exact relationship between flux harmonics and core losses. Fuchs et al. [1] did extensive research on the effect that a non-sinusoidal voltage supply has on the magnetizing current, iron losses and forces of three-phase induction machines. Their results showed that the increase in iron losses due to the presence of harmonics in the flux waveform can only be predicted approximately.

Furthermore, it is also still unknown what the effect of very high values of flux density is on the increase in iron losses in core materials. Standardized

references of iron losses are only given to maximum flux density values of 1,5 T on non-orientated electrical steels and 1,8 T on grain-orientated electrical steels [2]. It is however known that the values of flux density that occur in the tooth tip areas of electrical machines can be as high as 2,3 T.

The above-stated questions give rise to the need for a new measuring system to investigate the relationship between high values of flux density, flux harmonics and iron losses. The new system is capable of performing tests at fundamental frequencies from 50 Hz to 150 Hz at flux densities up to 2,2 T, and at frequencies up to 4 kHz, but then at lower flux densities. Tests are possible with both sinusoidal and non-sinusoidal flux waveforms, thus allowing for flux harmonics.

A block diagram of the complete measuring system is shown in Figure 1.

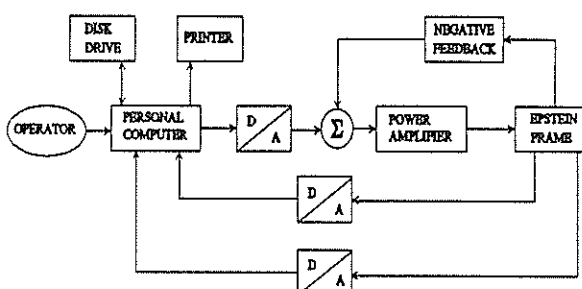


Figure 1. Block diagram of measuring system

The measuring system consists of a personal computer, power amplifier, 25-cm Epstein frame and D/A and A/D facilities. The personal computer is used for the control of the complete measuring process. The power amplifier supplies the necessary magnetizing power to generate the specified flux waveform in the test samples in the Epstein frame. Negative feedback control of the induced secondary voltage of the Epstein frame ensures that the desired flux waveform is maintained in the test samples. Sampled data is processed by the computer and can be stored on disc.

## 2. THE MODIFIED EPSTEIN FRAME

The standard 25-cm Epstein frame specifications and test procedures [2] only allow testing at magnetizing forces up to about 12 000 At/m. To accommodate for tests at the values of flux densities and harmonic frequencies associated with core and tooth tip saturation in electrical machines required that some modifications had to be made to the electrical parameters of the standard Epstein frame.

After examining the BH-characteristics of several different steel samples, it was decided that a peak magnetizing force of 100 000 At/m would be adequate to enable a peak flux density of 2,2 T to be generated in most materials. For a conventional Epstein frame it is calculated that a peak magnetizing current of 134,3 A is needed to generate a magnetizing force of 100 000 At/m. The problem that arises is that the gauge of the wires that have to be used for such a high current is too large to construct the coils of the frame within standard size limits. The solution was to use thinner wires, and by increasing the number of turns on the coils, the maximum current required is reduced.

The frame used in this system was designed and built by Smit [3]. In order to use the standard 305 mm long test samples, the dimensions of the new frame are according to the ASTM standards. The frame consists of four multi-layer coils and an air-flux compensating inductor. The four coils, each constructed with a primary and secondary winding, are connected in series. The primary winding of each coil comprises 215 turns evenly wound in five layers, using two parallel 2 mm diameter wires. A single layer of 210 turns, 0,8 mm diameter wire, forms the secondary winding of each coil. The construction of the air-flux compensating inductor allows that the position of its secondary coil can be shifted with respect to its primary coil, thus allowing for easy adjustment of the amount of compensation to be applied.

## 3. THE POWER AMPLIFIER

The power amplifier has to be capable of supplying the required voltage and current to the Epstein frame in order to generate the desired flux waveform in the test samples. It is calculated that a peak magnetizing current of 109,3 A is required for a maximum magnetizing force of 100 000 At/m. In order to generate 2,2 T at 150 Hz, a maximum primary voltage of 100,6 V is required. A frequency bandwidth of 50 Hz to 4 kHz is required to accommodate the flux harmonics present.

Figure 2 shows the simulated waveforms of magnetizing current, applied voltage and flux of a

saturated coil at 50 Hz. The applied voltage and magnetizing current is nearly 90° out of phase. This leads to a high power dissipation in the output stage devices, which has to be considered in the design of the amplifier.

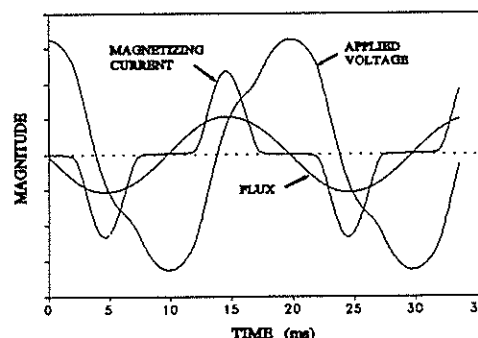


Figure 2 Simulated exciting waveforms

The power amplifier used in this circuit is a linear MOSFET bridge amplifier [5]. By using a bridge topology it is possible to deliver the same output power with only half the supply rail voltage that would be needed in the case of a single push-pull amplifier. MOSFETs are chosen instead of bipolar transistors as output stage devices. Due to the relatively high supply rail voltages and output currents required, a bipolar transistor output stage, as was used by Vermeulen [4], is subject to second breakdown problems. It is also known that, due to their negative temperature coefficient, MOSFETs are more suitable to be paralleled.

The bridge power amplifier consists of two class AB push-pull amplifiers operating 180° out of phase. Each amplifier is formed by a driver stage and output stage. The driver stage consists of an input and feedback signal buffer, an input stage and a voltage amplifier stage with a biasing network. Protection circuitry for the output stage devices are also included in the driver stage. The output stage of each amplifier is formed by complementary N- and P-channel MOSFET pairs. In order to be capable of supplying the full load current, 24 MOSFETs are connected in parallel in each leg of the output stage, thus giving a total number of 96 MOSFETs used in the bridge amplifier. Current sharing resistors with a value of 0,5 Ω are included to ensure equal sharing between the devices at low currents.

Due to the fact that the load voltage and current is almost 90° out of phase, it is possible to reduce the power dissipation in the output stages by placing a resistor in series with the load. This not only reduces the voltage across the devices when peak current is flowing, thus reducing the power dissipated in the devices, but it also improves the overall amplifier stability. A circuit diagram of the complete output stage for the bridge amplifier is shown in Figure 3.

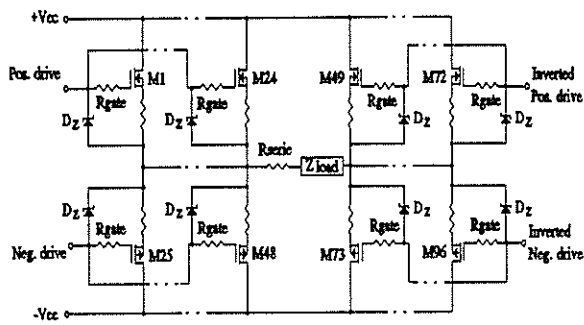


Figure 3. Circuit diagram of bridge amplifier output stage

#### 4. THE CONTROL STRATEGY

The control strategy is based on the control of the flux waveform by negative feedback of the induced secondary voltage of the Epstein frame. This voltage  $e(t)$  is given by

$$e(t) = N_s \frac{d\phi}{dt} \quad (1)$$

with  $N_s$  the number of secondary turns, and  $d\phi/dt$  the flux wave. By controlling the waveform of  $e(t)$ , the waveform of the flux  $\phi(t)$  in the test samples is controlled. A block diagram of the complete feedback circuit is shown in Figure 6.

A Turbo Pascal program was developed to manage the complete measuring process. The program provides for the operator to define the test sample and the desired flux waveform. The program then generates 500 data points, representing one cycle of the voltage that has to be induced in the secondary winding of the frame to ensure that the desired flux waveform is generated in the test samples. These data points are downloaded to a transputer-based D/A converter, where it is converted at a rate of 250 kHz, to an analog signal of 200 cycles. This signal is fed through a bandpass filter, firstly to ensure that there is no dc component present in the signal, and secondly to eliminate any high frequency noise that might be present on the signal. From there the signal is fed to the power amplifier. Negative feedback is utilized to ensure that the desired secondary voltage waveform is maintained.

Three cycles of magnetizing current and secondary voltage waveforms is sampled simultaneously by a 4 channel, 12-bit A/D converter. The sampled data is stored on disc under a filename specified by the operator. Graphs of the flux waveform, magnetizing current and induced voltage can be viewed on the screen directly. Graphs of the BH-characteristic and core-loss vs flux density can also be determined from the sampled data.

To ensure accurate measurements it is essential

that the dc component in the primary current has to be sufficiently small. The dotted sections in the circuit of Figure 6 show feedback loops to eliminate any dc component in the current. These feedback loops have however been omitted in the final circuit for stability reasons. It has however been found that the dc component in the primary current can be limited to less than 0,1 % of the maximum current through proper adjustment of the biasing voltage.

#### 5. EXPERIMENTAL RESULTS

Extensive testing of the circuit proved that the design specification have been met. Measurements of the primary voltage and magnetizing current are shown in Figure 4 and Figure 5. A maximum primary voltage of 104 V was measured, while a peak magnetizing current of 112 A was measured.

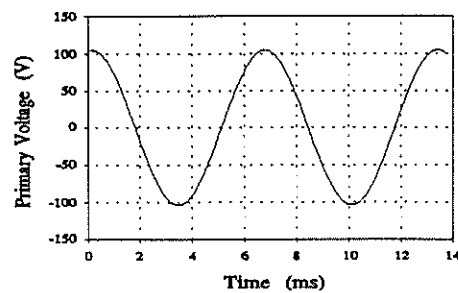


Figure 4 Maximum primary voltage

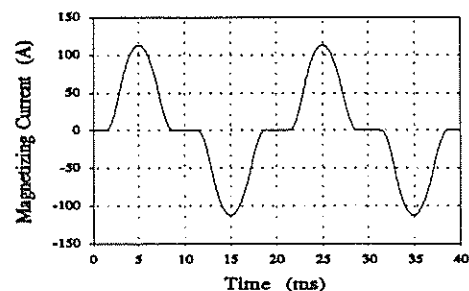


Figure 5 Maximum magnetizing current

Figure 7 shows a comparison between the signal from the D/A converter and the induced voltage for a 400 Hz fundamental frequency with a 10 %, 4 kHz harmonic superimposed on it. The phase shift between the two signals is introduced by the bandpass filter in the control circuit, and does not influence the correct operation of the system in any way. PSPICE simulations, as well as experimental results, showed that the system has a closed loop frequency bandwidth of 48,2 kHz, which is above the maximum operating frequency of 4 kHz.

The accuracy of the voltage and current measurements is within 0,3 %, while the accuracy of the flux density calculations was found to be in the order of 2 %. This can be improved by using a more accurate method of numerical integration.

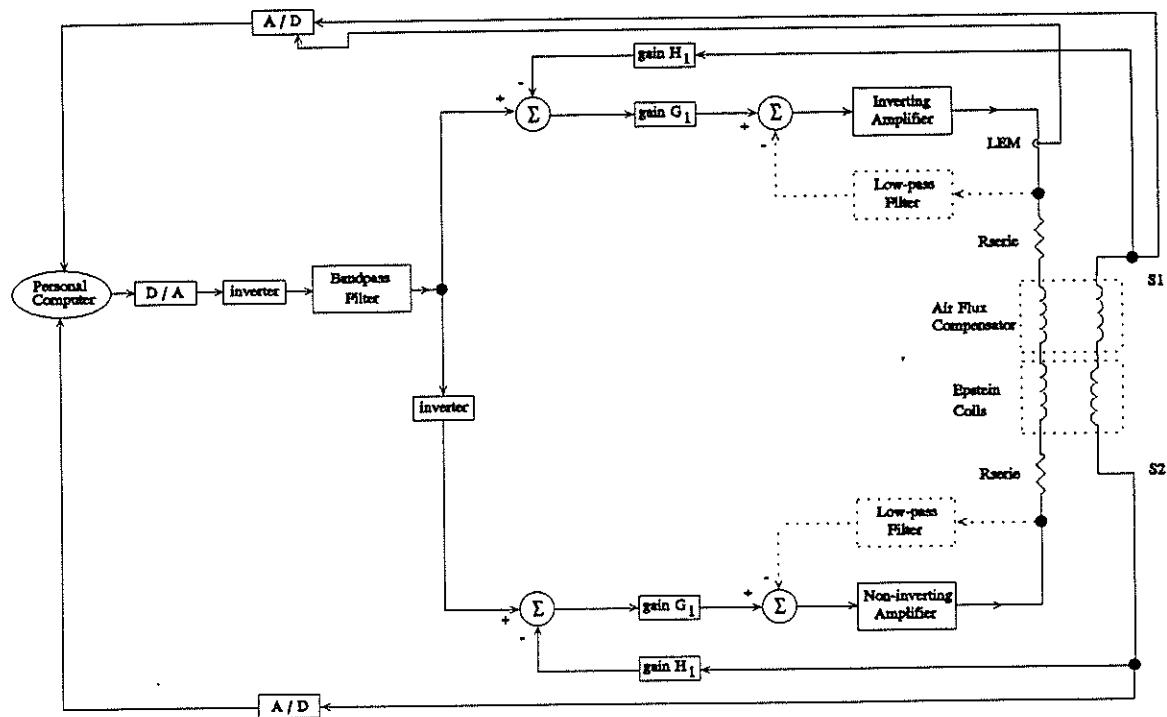


Figure 6 The complete control circuit

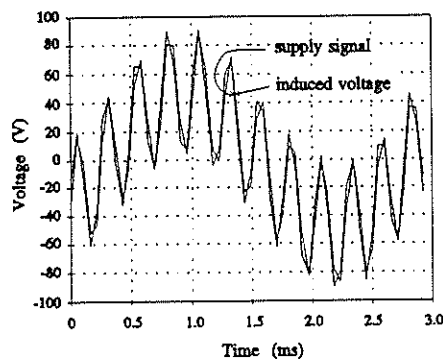


Figure 7 Comparison between supply and induced voltages

## 6. CONCLUSIONS

Results showed that the new measuring system is capable of performing tests at flux densities up to 2.2 T under sinusoidal and non-sinusoidal operating conditions. The power amplifier is able to supply a peak magnetizing current of 110 A and peak voltage of 104 V. The control strategy employed works well to control the flux waveform in the tests samples. The overall accuracy of iron loss measurements was found to be within the specifications of the ASTM standards.

## 7. REFERENCES

- [1] E.F. Fuchs, L.H. Chang, J. Appelbaum,

"Magnetizing Current, Iron Losses and Forces of Three-phase Induction Machines at Sinusoidal and Non-sinusoidal Terminal Voltages: Analysis and Results", *IEEE Transactions on Power Apparatus and Systems*, Vol. PAS-103, No. 11, pp. 3303-3325, November 1984.

- [2] "1985 Annual Book of ASTM Standards, Metals Test Methods and Analytical Procedures", Section 3, Volume 03.04, American Society for Testing and Materials 1985, pp. 47-65.
- [3] P.M. Smit, "The Measurement of the Properties of Laminated Sheet Steel", M-thesis, University of Stellenbosch, 1989.
- [4] H.J. Vermeulen, P.M. Smit, F.S. van der Merwe, "Computer-aided Measurement of the Properties of Laminated Steel at High Flux Densities", *South African Universities Power Engineering Conference*, Stellenbosch, November 1989.
- [5] C. Slabbert, F.S. van der Merwe, H.J. Vermeulen, "Measurement of Laminated Steel Properties at High Flux Densities and Non-sinusoidal Operation", *Proceedings of the fourth South African Universities Power Engineering Conference*, Cape Town, pp. 291-294, January 1994.

# Fault diagnosis in induction motors using acoustic techniques

A. Gaylard, A. Meyer, and C. Landy  
University of the Witwatersrand, South Africa

**Abstract** Condition monitoring of induction motors traditionally involves current measurements to detect electrical faults, and accelerometer measurements to determine mechanical faults. This work focusses on the use of acoustic measurements for condition monitoring, and proceeds from preliminary work done by Reynders, Landy, Meyer, and Wolmarans [1]. The feasibility of identifying loose coils by acoustic measurements is shown, as is the identification and verification of a suitable neural network to perform this task automatically.

## 1 Overview

To diagnose a fault in a machine before it becomes critical is the main challenge in condition monitoring. This allows for contingency plans to be made, plant downtime to be planned, and replacement parts or an entire new motor to be obtained. Thus the earlier a fault is detected, the better.

Traditionally, condition monitoring of induction motors makes use of current measurements to detect incipient electrical faults, and vibration measurements using accelerometers to detect developing mechanical faults. [2] More recently, motor windings have been subjected to tan-delta tests to evaluate the state of the winding insulation. As this requires disconnection of the motor from the supply, this is strictly speaking more a testing procedure than a monitoring procedure. Typical electrical faults which can occur are broken rotor bars and winding insulation failure; typical mechanical faults are bearing failure, rotor imbalance, and airgap distortion.

This paper proposes a new approach to condition monitoring: the use of acoustic signals to detect developing faults. This requires an understanding of the possible causes of noise in an induction machine. These are: slot harmonics, supply harmonics, winding asymmetry, rotor eccentricity, bearings, fan, and loose structural elements

such as loose coils.

Some of these causes are inherent in the design of the machine and hence are constant over its lifetime (slot harmonics, winding asymmetry, fan noise), some develop over time (bearing noise, loose structural elements), and others are due to external circumstances (supply harmonics). All of these add to the noise emitted by the machine, to a greater or lesser extent. Often, a fault becomes more severe the longer it is present. An example is a worn bearing: as wear proceeds, so the rotor vibrates more. This serves to exacerbate the wear on the bearing, causing faster deterioration.

To detect a fault in a machine, a common approach is to compare a present measurement with a measurement taken at a stage where the machine was known to be in good condition. This comparison may be done in the time domain, or in the frequency domain. Signals which are "significantly" different are cause for alarm. Thus, a system needs to be in place to take measurements at regular intervals, to allow for variations to be tracked; these measurements need to be carefully categorised and archived.

## 2 Measurements

For this work, 31 identical large (6600V, 4060kW) motors were tested. The noise emanating from a motor was measured using a sound level meter with a precision microphone, and the signal digitally stored. In addition, tan-delta tests were performed on the windings of these motors; the results produced were: tan-delta, tan-delta tip-up, and capacitance change over voltage increase. [1]

Each measurement consisted of 1600 time samples, taken at a sampling frequency of 6000Hz; four averages of this signal were taken. For each motor, four measurements

were taken: the ambient noise, the noise during start-up beginning at 2 seconds after switch-on, the noise during steady-state running conditions, and the noise immediately after switch-off while the rotor was still spinning. These measurements were all windowed with the Hanning window before the spectra were obtained using the Fast Fourier Transform (FFT) [3]. The quantisation noise of the signals was calculated; all signals were 40dB above the noise floor and were thus valid. The measurements for starting conditions had the highest average dynamic range (55dB), and were the measurements of choice for subsequent analysis.

The tan-delta results were used to grade the condition of the motors' windings by assigning a "merit figure" derived from the tan-delta results. The weightings attached to the tan-delta, tan-delta tip-up, and capacitance change were 2, 3, and 3 respectively. A large population of motors will have a Gaussian distribution of merit figures with the curve peaking at a figure of 0.0. Those motors with merit figures greater than this are described as having insulation systems above the average, while motors having figures lower than this have insulation that is degraded and below average.

### 3 Neural networks

Given that a motor's insulation may be evaluated using the tan-delta tests, and hence a decision made on whether or not it is necessary to open the machine for further winding examination, the question arises whether some correlation can be shown between the acoustic tests, which do not interrupt the service of the motor, and the tan-delta tests, which do require interruption of operation.

This is a typical neural network application [4]; such problems are characterised by two measured data sets which appear unrelated. It is possible to train a neural network on the data sets to generalise the properties present to other data sets which may be presented later. If there is no relationship between the two data sets, the network will not exhibit accurate behaviour when presented with unknown data; only the data which is known will result in accurate prediction. If there is a relationship between the data sets, new data will result in accurate prediction.

In this work, 30 possible neural networks of various configuration, training and parameter values were tested. The majority of these showed extremely poor performance. The network which exhibited acceptable accuracy is shown in figure 1.

The network has as its inputs all the frequency points in the spectrum 0 to 2996.25Hz at a spacing of 3.75Hz ( $n = 800$ ); there are  $m = 6$  tan-sigmoid neurons in the first layer, and a single linear neuron in the second (output) layer. The output is one of the three parameters: tan-delta, tan-delta tip-up, or capacitance change. The training procedure used was backpropagation with momentum, and the selection of weights and biases was performed using the method of Nguyen and Widrow [5].

Each network was trained on 8 data sets (26% of the total data), randomly chosen from the complete collection of data sets. After training, the network was presented with the complete data collection and the output used as predicted values. The procedure of training and evaluation was repeated 100 times, each time on a different batch of 8 data sets, to ensure that any accurate results were not a statistical anomaly. The average sum-squared error (SSE) was used as a measure of the effectiveness of each network at generalising the characteristics of the audio signal. For all networks tested, the SSE was unacceptably large ( $> 10\,000$ ), except for the final one, where it was acceptably small (around 26).

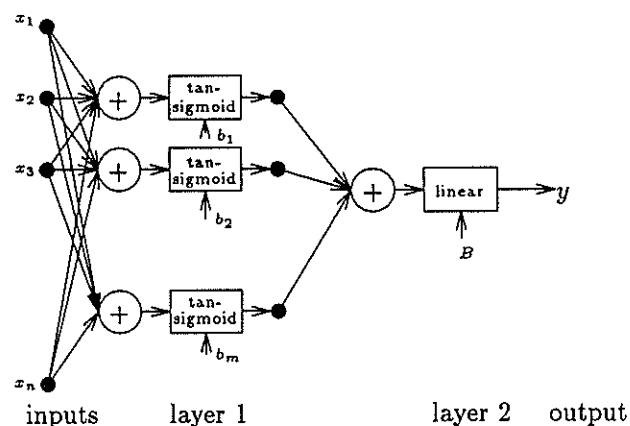


Figure 1: Neural network model

## 4 Results

Visual inspection of the audio spectra of the motors tested indicates that this method has the potential for predicting faults. An example is presented in figure 2. The spectra of two motors are compared: motor 36L has an above-average merit figure of +0.3, while motor 34L has a sub-standard merit rating of -0.3.

The machine with loose coils is seen to have considerably more energy in the region around 1kHz, when compared to an identical machine with fixed coils. This analysis is far easier when measurements have been recorded over a prolonged period; trends are more readily identified.

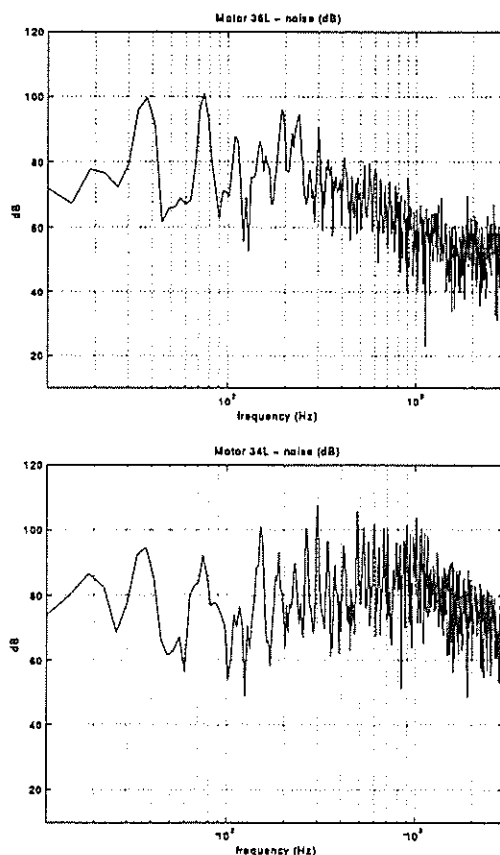


Figure 2: Comparison of audio measurements for a healthy machine (top) with a machine having loose coils (bottom)

The tan-delta tip-up showed clearly that it is closely correlated to the audio signal. A plot of actual vs. predicted results is shown in figure 3; the predicted tan-delta tip-up figures are seen to match the measured ones closely. Thus it is clear that by subjecting the audio signal to analysis by the neural network, an accurate estimate of the tan-

delta tip-up may be obtained. This result may be improved in two ways: the network may be given more audio signals and corresponding tan-delta tip-up results for training, and results taken over prolonged periods may be examined for developing trends.

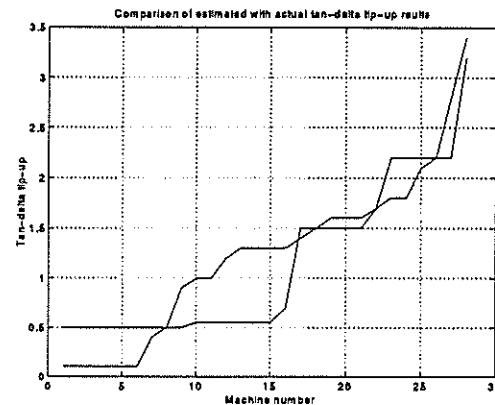


Figure 3: An indication of the effectiveness of the neural network in predicting the tan-delta tip-up values for a range of motors

## 5 Conclusion

Inspection of the noise spectra showed no discernable difference between the signals under running and those under stopping conditions. It had been hoped that an indication of the nature of the fault would be shown: a mechanical problem would contribute vibration modes to the spectrum measured while running *and* the spectrum measured while rotating after power shut-down, while a fault due to electrical causes would affect only the spectrum taken under running conditions where the electrical forces are present. The feasibility of distinguishing between a mechanical fault and an electrical fault using this method has not been excluded, however.

Examination of the noise spectra under starting conditions showed that a motor with loose coils had considerably more midrange noise energy (around the 1kHz region) than a motor with healthy coils. This is attributed to the fact that under starting conditions the current is several times greater than the current drawn while running. It was not possible to quantify accurately the condition of a machine's windings with a single measurement; long-term trending would improve this considerably but is not always possible. In addition, the noise

from one motor is different from that of a motor of different size and geometry; care is required to avoid making meaningless comparisons.

The tan-delta tip-up measurements exhibited a close correlation with the audio measurements taken during motor start-up. This was shown by the fact that the neural network could be trained on a small fraction of the total data available, and be seen to closely approximate the characteristics of subsequently presented data sets. It is thus possible to make a decision on whether to remove a motor from service for examination based entirely on non-invasive, non-interruptive acoustic measurements.

## References

1. Reynders, J.P., Landy, C.F., Meyer, A.S., Wolmarans, A.D.W.: "Experience in the use of electrical and acoustic diagnostic procedures on a significant population of similar large high voltage induction motors", *Conference Proceedings of CIGRÉ*, August-September 1992, Paris
2. Tavner, P.J., Penman, J.: "Condition Monitoring of Electrical Machines", Letchworth Research Studies Press, 1987
3. Shiavi, R.: "Introduction to Applied Statistical Signal Analysis", Asken Associates, 1991, pp 82-100
4. Kosko, B.: "Neural networks for signal processing", Prentice Hall, 1992, pp 9-14
5. Nguyen, D., and Widrow, B.: "Improving the learning speed of 2-layer neural networks by choosing initial values of the adaptive weights", *International Joint Conference of Neural Networks*, vol 3, pp. 21-26, July 1990

## Address of author

Andrew Gaylard,  
Dept. of Electrical Engineering,  
University of the Witwatersrand,  
P.O. WITS 2050, South Africa  
Fax: +27-11-4031929  
e-mail: landy@odie.ee.wits.ac.za

# CONTROLLING THE SPEED OF AN INDUCTION MOTOR BY SUPPLYING THE STATOR WITH A VARIABLE FREQUENCY AND OPERATING THE ROTOR CLOSE TO RESONANCE.

R.M.da P.Adanjo    G.M.J.Parsley

Department of Electrical and Electronic Engineering University of Pretoria

**Abstract** - This paper will illustrate the effects of varying the speed of an induction motor by varying the supply frequency while having reactive components in the rotor circuit. It will be shown that high torques can be achieved at a variety of speeds in this manner by operating the rotor close to a fixed resonance frequency.

## 1 INTRODUCTION

A number of different methods have been applied to obtain variable-speed operation of a wound-rotor induction motor. In applications where reliability and simplicity are dominant factors, a method of controlling the speed of a wound rotor induction motor is by external variable rotor resistance.

This paper proposes a different approach by adopting the reasoning that to obtain maximum torque at standstill (slip = 1), the rotor resistance  $R_r$  must be increased via the slip rings such that  $R_r$  is equal to  $X_r$ , the rotor reactance. Alternatively, another way is to reduce  $X_r$  at stand still to the same value as  $R_r$ . The only way  $X_r$  can be reduced via the slip rings is to cancel it out by capacitive reactance.

By introducing capacitance to the rotor circuit it is noted that the characteristic torque speed curve of an induction motor alters considerably, and by being able to supply the rotor with a variable frequency, linear speed control can be acquired.

## 2 THEORETICAL ANALYSIS

The induction motor produces maximum torque ( $T_{max}$ ) when the rotor resistance is approximately equal to the slip times the rotor reactance.

$$R_r = s \cdot X_r \quad (1)$$

$X_r$  is usually much greater than  $R_r$ , so at standstill to reach maximum torque (slip = 1), the rotor reactance can be decreased by adding capacitive reactance to the rotor circuit, so that  $R_r = X_r$  in order to obtain maximum torque.

To obtain characteristic torque speed curves one must consider the simplified rotor equivalent circuit for one

phase with the capacitance inserted via the slip rings, as shown in Fig 1.

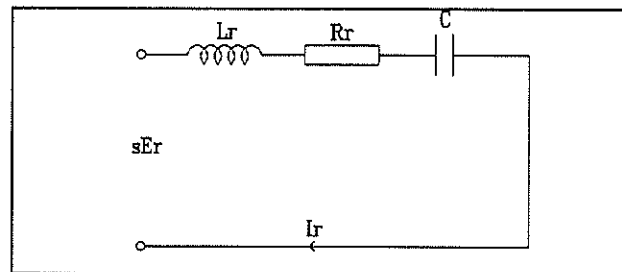


Figure 1 Per phase equivalent circuit

Firstly, by applying simple circuit theory the rotor current  $I_r$  can be expressed as follows (see Nomenclature for symbols not defined in the text)

$$s \cdot E_r = I_r \cdot [R_r + j(s \cdot \omega \cdot L_r - \frac{1}{s \cdot \omega \cdot C})]$$

$$I_r = \frac{E_r}{\sqrt{(\frac{R_r}{s})^2 + (\omega \cdot L_r - \frac{1}{s^2 \cdot \omega \cdot C})^2}} \quad (2)$$

The torque can now be derived from the power transferred across the air gap ( $P_{ag}$ ):

$$P_{ag} = \omega \cdot T = \frac{I_r^2 \cdot R_r}{s}$$

$$T = \frac{I_r^2 \cdot R_r}{\omega \cdot s} \quad (3)$$

Substituting  $I_r$  from (2) into (3)

$$T = \frac{E_r^2 \cdot R_r}{\omega \cdot s \cdot [(\frac{R_r}{s})^2 + (\omega \cdot L_r - \frac{1}{s^2 \cdot \omega \cdot C})^2]}$$

with,

$$\omega = \frac{2 \cdot \pi}{60} \cdot N_s$$

$$s = \frac{N_s - N}{N_s}$$

$$\omega \cdot s = \frac{2 \cdot \pi}{60} \cdot (N_s - N) = K(N_s - N)$$

The equation for torque now becomes:

$$T = \frac{Er^2 Rr (Ns - N)}{K Ns^2 \left[ (Rr)^2 + \left( K (Ns - N) Lr - \frac{1}{K (Ns - N) C} \right)^2 \right]} \quad (4)$$

with,

$$Ns = \frac{120 \cdot f}{p}$$

thus, the torque equation now becomes:

$$T = \frac{Er^2 Rr \left( \frac{120f}{p} - N \right)}{K \left( \frac{120f}{p} \right)^2 \left[ (Rr)^2 + \left( K \left( \frac{120f}{p} - N \right) Lr - \frac{1}{K \left( \frac{120f}{p} - N \right) C} \right)^2 \right]} \quad (5)$$

An induction machine that will be considered in this paper is a 3-phase, 2-pole wound rotor induction motor, with rotor resistance and inductance found to be 0.287  $\Omega$  and 1.544 mH per phase respectively. It has a synchronous speed of 3000 rpm when connected as a 2-pole machine and a rated torque of 7.6 Nm. As an illustration, if the air gap voltage is to be taken as 100 V at standstill and the supply frequency is kept constant at 50 Hz. Then, the various characteristic torque speed curves are shown in Fig 2.

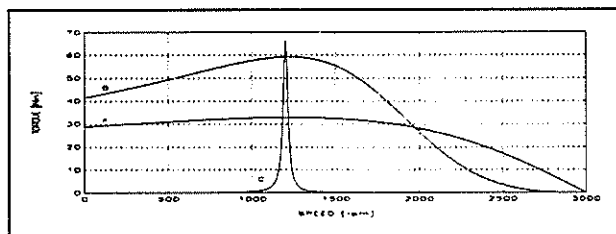


Figure 2 Torque-Speed curves with (A) no external reactance, (B) external capacitance only and (C) with external capacitance and inductance.

Curve A is the normal torque-speed curve when the slip rings are short circuited. Curve B, is the theoretical resonant rotor condition that achieves maximum torque at the same speed as curve A. The value of the capacitance that would be needed to achieve this was found to be 28 000  $\mu$ F. Note that  $T_{max}$  has increased from 33 Nm in curve A to 60 Nm in curve B, however the quantity of capacitance needed is extremely large.

Instead of just adding exceptionally large values of capacitance to the rotor circuit, one can increase the rotor inductance to bring about a decrease in the rotor capacitance needed. Curve C, illustrates this. By increasing the rotor inductance by 80 mH, the rotor capacitance can be decreased to a more appropriate value of 345  $\mu$ F. It can be seen that the curve C is "sharper", or has a higher "Q", than the other curves.

Thus by increasing the inductance in the rotor circuit, the required capacitance becomes smaller and the Q's will become higher. This can be seen in Fig 3 curve A and B. Curve A has an inductance of 90 mH and a capacitance of 700  $\mu$ F, curve B has an inductance of 180

mH and a capacitance of 350  $\mu$ F.

Keeping the rotor circuit reactance constant with the same values as used in curve A figure 3 and decreasing the supply frequency so that the resonant peak is at half synchronous speed,  $T_{max}$  increased as illustrated in Curve C, figure 3. Also curve D shows a decrease in  $T_{max}$  and a smaller Q if the rotor resistance is increased to 0,95  $\Omega$  per phase.

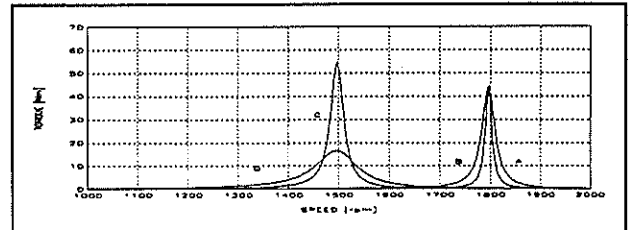


Figure 3 The influence of different amounts of (A) and (B) capacitance and inductance and (C) and (D) resistance.

The theoretical speed control of the machine from standstill is now considered and attention is drawn to Fig 4 in this regard. For the purpose of this illustration, the induction machine shown in Fig 3, curve A is used, with a rated full load torque of 7.6 Nm. The rotor circuit is kept constant with an added inductance of 40 mH and capacitance of 950  $\mu$ F. Fig 4 indicates those parts of the resonant torque-speed curves close to standstill. One must note that only the down-side of the torque-speed curves is of importance, because that is where the machine settles. Suppose a torque of 7.6 Nm is necessary at standstill as well as for the rest of the speeds (up to 3000 rpm). By supplying a frequency of 22.44 Hz at standstill the torque is 7.6 Nm, thus the machine will not move, as the frequency is increased by 0.2 Hz to 22.64 Hz, the machine will start to move with a net accelerating torque of 1 Nm, until it reaches a constant speed of 10.88 rpm, as is illustrated in Fig. 4.

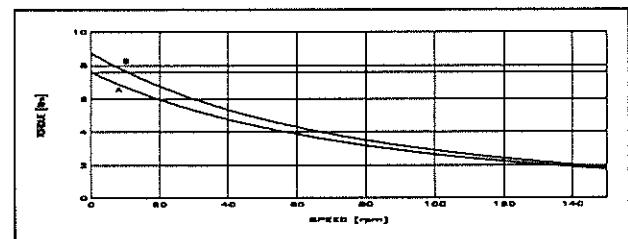


Figure 4 Curves (A) and (B) show an increase in frequency of 0.2 Hz.

Thus as the supply frequency is increased so is the speed. In Fig. 5, a continuous increase of frequencies is supplied to the induction motor. A few resonant peak curves are shown at different speeds, for purpose of illustration.

It can be seen that the peak of the resonant curves decreases as the speed increases, thus one great advantage of this is the high starting torques at stand still. From Fig 5 one can infer that for every change of 1 Hz in the supply frequency there is a change of 60 rpm in speed. If the load torque is low, the machine

operates close to the foot of the resonant curves and this linearity is lost, this is due to each resonant curve differing from each other at different frequencies. If the motor has a rated speed of 3000 rpm, a frequency range slightly more than 50 Hz is necessary to achieve this range of speeds up to 3000 rpm.

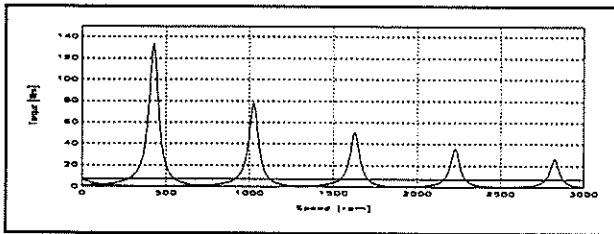


Figure 5 A number of resonant peak curves at different speeds.

### 3 PRACTICAL VERIFICATION

The above theory was verified on a Mawdsley Generalised machine. A variable frequency was generated and supplied to the induction motor. Tests were done by connecting different reactive components to the rotor and then supplying different frequencies to the motor in order to determine at what frequency the motor would start to turn, noticing whether the speed increased with increased supply frequency.

Fig. 6 illustrates the relation between the supplied frequency and the motor speed, with the rotor having 80 mH and 924  $\mu$ F external inductive and capacitive reactance respectively. The rotor circuit has the following values:

$$R_2 = 0.287 \Omega/\text{phase}$$

$$L_2 = 1.544 \text{ mH}/\text{phase}$$

$$E_2 = 20 \text{ Volts (Air gap Voltage)}$$

The starting torque was assumed to be 0.015 Nm. Curve A indicates the theoretical relationship by using equation (5). Curve B, the practical, and, curve C the linear relationship, if for every hertz changed there is a 60 rpm change. As can be seen from Fig. 6 the theoretical value does not deviate much from the practical one and there is a small deviation from linearity. There is room for error though, because the torque required to start the motor turning is not the same as when the motor is turning at a certain speed. At a certain speed the rotor has to overcome windage and friction, thus the load torque does not remain constant.

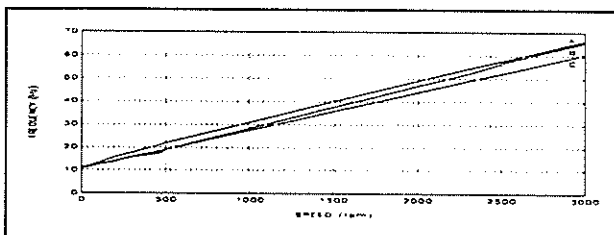


Figure 6 Frequency-Speed relationship, curve (A) indicates the theoretical, curve (B) the practical and curve (C) the linear.

By changing the reactive components on the rotor slip

rings basically changes the starting frequency, the relationship between theoretical and practical cases remain much the same as mentioned above.

In the other tests done, no measurements were taken due to the fact that it was virtually impossible to take accurate readings and that a visual description would suffice for the purpose of this illustration. One of the tests carried out was to lock the rotor and apply an increasing frequency to the stator. From the ammeter one could see the current increasing, thus signifying a torque increase, as the frequency was increased. This indicates that the machine has high starting torques.

The other test carried out was keeping the frequency constant and braking the rotor. The current increased and the speed lowered, thus indicating that the machine will settle on the down side of the torque speed characteristic curve. The machine limitations prevented the absolute verification of the large resonant torques predicted by the theory.

The experimental work revealed the problem of synchronous torques. These were found to exist in the characteristics of the machine at certain speeds. This phenomena could be overcome by increasing the external rotor resistance, thereby lowering the Q.

### 4 APPLYING IT IN THE PRACTICAL WORLD

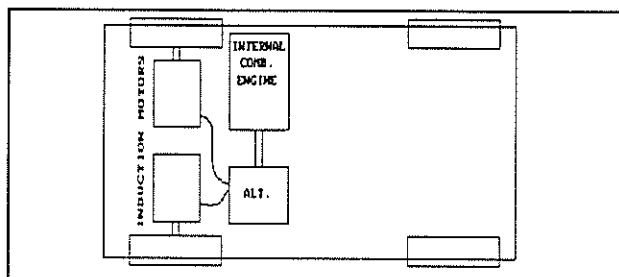


Figure 7 A motor vehicle using the variable frequency speed control of induction motors with reactive components.

This concept can be utilized in the practical world by applying it to motor vehicle traction. Fig. 7 shows a vehicle with an internal combustion engine mechanically coupled to an alternator, this alternator will rotate at the differing engine speeds, giving an output of variable frequency. This output can be applied to two induction motors with external reactive components on the rotor. The induction motors are connected mechanically to the two front wheels.

For this system to operate properly, the following criteria has to be applied. When the engine is idling the vehicle must not move, as soon as the engine output is increased, by increasing its speed, the vehicle must start moving. Lets say when the engine turns at an idling speed of 800 rpm. At 800 rpm the alternator supplies a frequency of 13.33 Hz to the induction motors. At this frequency the induction motors can be made to just start

rotating if the correct external reactive components are chosen according to this frequency as well as the starting torque.

For an example let's look at a vehicle with the following parameters, the mass of the vehicle is 1000 kg, the tyres have a radius of 0.25 m and the rubber to tar friction coefficient is 0.015, the torque necessary for each induction motor to start the vehicle moving on a horizontal plane is determined as follows:

$$T = \frac{1}{2} * \mu * F * s$$

$$T = 18.4 \text{ Nm}$$

For purpose of illustration one maintains that this is the required torque at any speed. The induction motors has a rotor resistance of  $0.287 \Omega$ , a rotor inductance of  $1.544 \text{ mH}$  and a constant rotor voltage of  $100 \text{ V}$ . A  $60 \text{ mH}$  inductor is added externally to the rotor via the slip rings, the value of capacitance needed to deliver a torque of  $18.39 \text{ Nm}$  at standstill with a frequency of  $13.33 \text{ Hz}$ , from equation (5), is thus  $1840 \mu\text{F}$ .

Speed-control is achieved by increasing the speed of the internal combustion engine, thus in turn the alternator's speed is increased and so is the frequency. If the induction motor is a 2-pole, then the motor is able to turn up to  $3000 \text{ rpm}$ , the vehicle can thus reach a speed of,

$$v = \frac{2 * \pi}{60} * N * s * \frac{60 * 60}{1000}$$

$$v = 282.74 \text{ km/h}$$

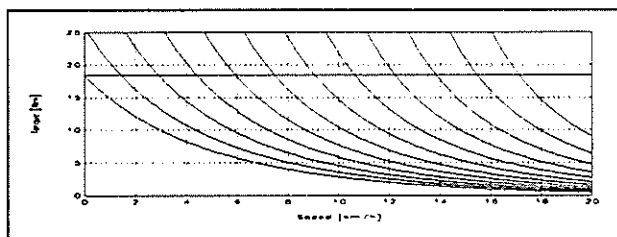


Figure 8 The speed-control of the vehicle, the 'X' marks where the induction motors settle at each resonant curve.

Fig. 8 illustrates the speed-control available in this particular vehicle. As the vehicle moves faster the load torque should increase, due to air drag and possibly moving up a gradient, as can be seen from fig. 8 this torque is available.

## 5 CONCLUSION

Speed control of an induction motor by supplying the stator with a variable frequency and operating the rotor close to resonance is a distinct possibility. The disadvantages of operating a induction machine as stated are the high cost involved. A wound rotor machine is more costly than a squirrel cage machine and reactive components capable of conducting large currents and

withstanding high voltages are relatively expensive.

The advantage of speed control using the above mentioned technique is the large torques available, particularly at standstill and low speeds. These torques lend a great "stiffness" to the machine and could be an advantage in traction applications with a particular use in mine winders.

What is of particular interest is that the torque of the motor can be made to be zero from zero supply frequency up to a particular supply frequency which can be determined by the value of the reactive components in the rotor circuit. This has an advantage if the supply frequency is a function of the speed of an alternator driven by an internal combustion engine. Such an engine cannot be operated with significant torques at low speeds ( $0$  to  $500 \text{ rpm}$ ). It is therefore possible to drive a motor indirectly from an internal combustion engine, starting at a point where such an engine is capable of delivering a significant torque, and continuing to do so for a considerable range of speeds.

If the proposed technique is to be applied in a vehicle, the induction motors would replace the gearbox, which is heavy and bulky.

## 6 NOMENCLATURE

C	= Capacitance/phase	[F]
Er	= Air gap voltage	[V]
Ir	= Rotor current	[A]
K	= Constant	
Lr	= Rotor inductance/phase	[H]
N	= Rotor speed	[rpm]
Ns	= Synchronous speed	[rpm]
Pag	= Power transferred across the air gap	[W]
Rr	= Rotor resistance/phase	[Ω]
s	= Slip	
T	= Torque/phase	[Nm]
Xr	= Rotor reactance/phase	[Ω]
w	= angular velocity	[rad/s]
p	= number of poles	

## REFERENCES

- [1] G.M.J. Parsley, "Controlling the Speed of an Induction Motor by Resonating the Rotor", *Electron*, vol. 7, no.5, pp. 22-25, May 1990.
- [2] J. Reinert and G.M.J. Parsley, "Controlling the Speed of an Induction Motor by Resonating the Rotor".
- [3] P.C. Sen, "Principles of Electric Machines and Power Electronics", John Wiley & Sons, 1989.

# ELECTRICAL MOTOR FOR LOW COST RETICULATION SCHEME

M Hippner, A R Perkin

University of Natal, Durban, South Africa

## ABSTRACT

The paper tries to identify an electrical motor or drive capable of operating from single-phase, 230 V mains and rated at least 30 kW. Three options are discussed in detail. They are: single-phase induction motors, a three-phase induction motor driven by a single-phase to three-phase converter, and "Written Pole" synchronous motor. The main features as well as advantages and disadvantages of all the options are described. Finally, conclusions are drawn, regarding suitability of the presented solutions for low cost reticulation scheme.

## 1. INTRODUCTION

There is growing interest in South Africa in developing a low cost reticulation scheme for rural and informal settlement areas. Since the cost of bringing three-phase power to remote locations is always high, this system would probably consist of single-phase overhead lines utilising the earth as a return path. Electrification of those areas will lead to light industrialisation, which would require electrical motors. Possible applications of these motors include water pumps, small manufacturing machines and variety of farming equipment. Such applications would require single-phase motors of rating up to at least 30 kW.

## 2. POSSIBLE OPTIONS

### 2.1. Single-phase induction motors

There are many types of single-phase induction motors. The most popular ones for industrial and commercial applications are [1]:

- capacitor-start capacitor-run motor
- capacitor-start motor
- permanent split capacitor motor

A capacitor-start capacitor-run motor, which schematic diagram is shown in Fig. 1, has two different values of capacitance, a high for starting and a lower for running. The starting capacitor is usually

an electrolytic type, which provides high capacitance per unit volume. The running capacitor is usually a metallised polypropylene capacitor rated for continuous operation. The type of starting switch most commonly used is centrifugally actuated switch built into the motor. However, other types of devices such as current-sensitive and voltage-sensitive relays are also used as starting switches. More recently, solid-state switches have been developed and used to a limited extent.

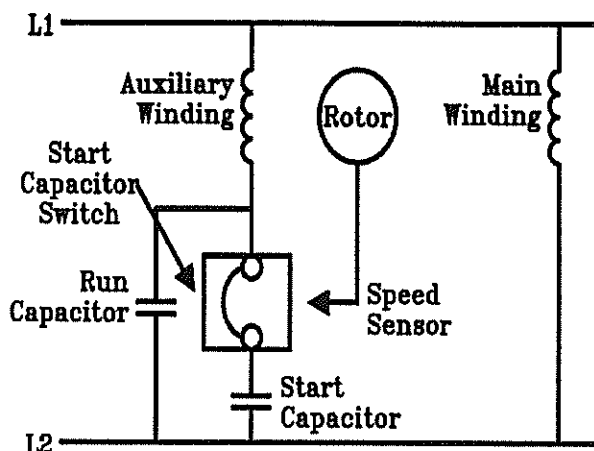


Fig. 1: Capacitor-start capacitor-run induction motor

Capacitor-start capacitor-run motor outperforms other types of the motors mentioned in this section, especially in terms of efficiency, power factor and starting torque. Capacitor-start and permanent split capacitor motors are just economical versions of capacitor-start capacitor-run motor. Generally, performance of single-phase motors is always lower than comparable three-phase motors. However, the running performance of a capacitor-start capacitor-run can approach the performance of a three-phase motor.

Another important aspect, which should be discussed is what is the maximum power rating available for this kind of motor and what limitations should be taken into account. Looking at manufacturers' data one can find that the maximum rating of a single-phase 230 V motors is 7.5 to 10 kW. Only motors up to 5 kW can

be direct-on-line started, higher ratings call for special starting equipment. According to one of the manufacturers [2], higher ratings are not possible because: (1) starting current becomes unacceptable for the electricity supplier, (2) starting capacitor and starting switch reach uneconomical sizes.

To summarise, use of single-phase induction motors in rural areas would be restricted by the following factors:

- limited maximum rating (presently up to 10 kW)
- high starting current
- low reliability
- relatively high price

## 2.2. Single-phase to three-phase converters

Single-phase to three-phase converters are one of the choices in the situation when a three-phase power is not available. The main advantage of such a solution is the use of a three-phase induction motor that is more reliable, cheaper, more efficient and easier available than its single-phase version.

Single-phase to three-phase converters can be classified into four categories [3]:

- rotary type
- autotransformer with switched capacitors
- reactive phase converters
- static converters

The last category seems to be the most attractive due to advances in power semiconductor devices and their control logic. Two kinds of static converters should be in particular mentioned here because of their relative simplicity and cost effectiveness. They are: an economical version of dc link converter and single-phase to three-phase cycloconverter.

Various versions of economical dc link converters are described in detail in [3]. Fig. 2 shows a half-bridge converter that converts the available single-phase supply into a balanced three-phase output of fixed frequency and fixed voltage. Only four semiconductor devices, two active switches  $T_1$  and  $T_2$  and two diodes  $D_1$  and  $D_2$ , are employed. This is fewer than in a typical dc link converter. This makes the converter cost effective. Another advantage is that due to advanced PWM schemes several lower order harmonics are eliminated, which results in high quality output waveforms. Unfortunately, switches  $T_1$  and  $T_2$  are subjected to twice the peak voltage of the single-phase mains, and high VA rating capacitors are required.

More advanced version, which provides active input current shaping feature, is shown in Fig. 3. This

feature offers improved power factor and low distortion of the current drawn from the single phase mains. Furthermore, it also permits bidirectional power flow between the single-phase source and three-phase load, which makes regenerative braking of an induction motor possible.

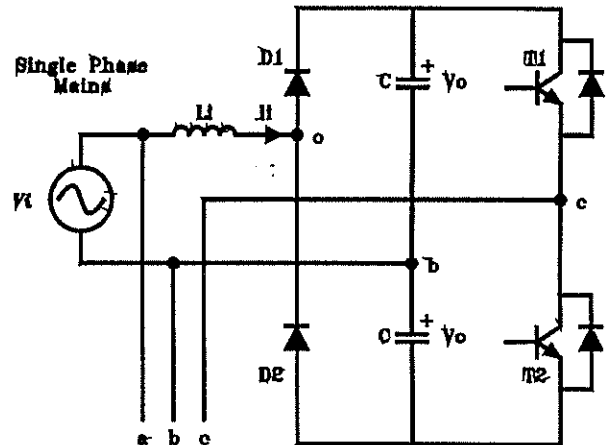


Fig. 2: Half-bridge 1-phase to 3-phase converter

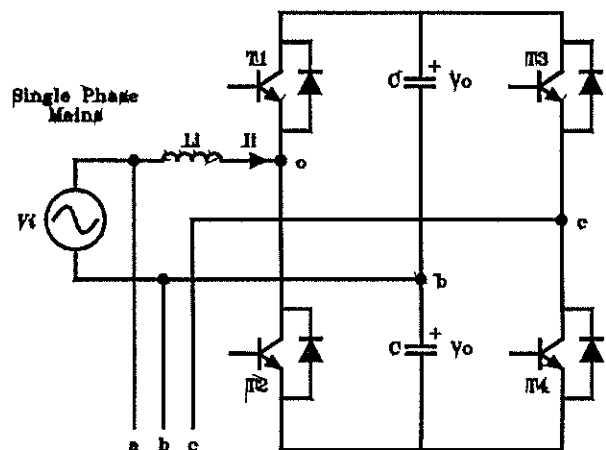


Fig. 3: Half-bridge 1-phase to 3-phase converter with active input current shaping

There are three main disadvantages of the converters presented in Fig. 2 and Fig. 3. Low output voltage (230 V) which calls for special versions of induction motors (usually manufactured as 380 V), limited power rating (probably up to a few kVA), and lack of build-in soft-start feature that could limit starting current.

Another promising option is a single-phase to three-phase cycloconverter presented in [4]. The cycloconverter employs (see Fig. 4) a six-triac full-

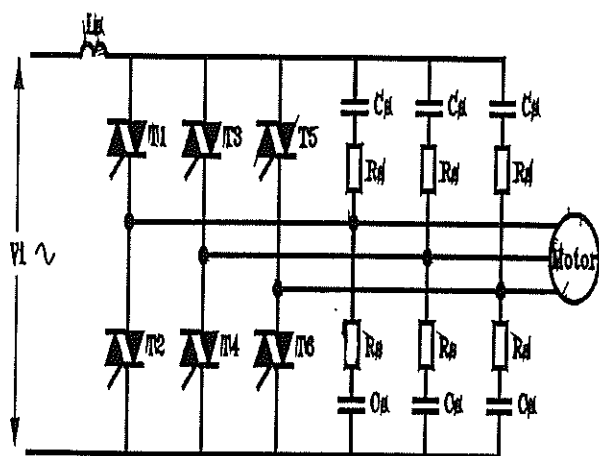


Fig. 4: 1-phase to 3-phase cycloconverter

bridge circuit and a three-phase motor. A microprocessor is used to implement the double integral control algorithm. It is an all digital method that requires only voltage feedback, resulting in a simple control circuit. This method allows the drive to operate up to 25 Hz from 50 Hz supply, giving a maximum synchronous speed of 1500 rpm for a 2-pole motor.

This inexpensive topology allows for soft-start and regenerative operation. The three-phase currents are symmetrical, and the motor speed ripple is low.

Unfortunately, there are some disadvantages. The three-phase currents contain significant amount of harmonics, especially the third. The result is increased winding loss and lower efficiency. The power factor is also lower than for a three phase sinusoidal supply. The cycloconverter can supply a standard voltage star-connected induction motor provided it can be reconnected into delta. However, much better performance can be achieved if the motor is redesigned to reduce the extra winding losses caused by harmonic currents.

### 2.3. "Written Pole" motor

The "Written Pole" motor [5] is a unique synchronous motor that overcomes many of the limitations of conventional synchronous machines.

Conventional synchronous machines have a fixed, even number of poles which defines the relationship between supply frequency and shaft speed. In the new class of machine described here, the rotor is covered by a layer of hard magnetic material as shown in Fig. 5. The main windings of the stator are similar to those of conventional machines, but with an additional concentrated winding forming an exciter pole. The continuous magnetic layer can be magnetised (or

"written") by the exciter pole, into any desired pole pattern, while the machine is running.

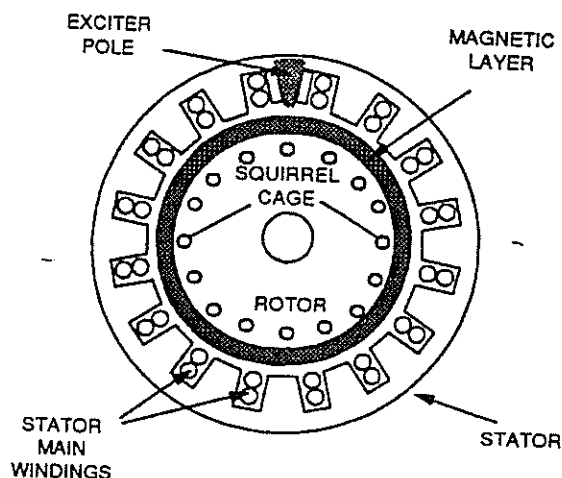


Fig. 5: Construction of "Written Pole" synchronous motor

As other synchronous motors, this type of motor cannot develop significant starting torque without help. Starting torque is provided by designing the motor magnetic circuit to allow the stator starting current to magnetise the rotor's high coercive magnetic layer to provide hysteresis torque. Additional starting torque is provided by a high resistance squirrel cage rotor winding. The starting process is illustrated in Fig. 6.

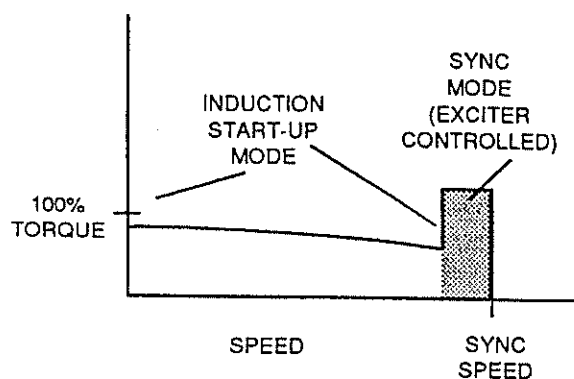


Fig. 6: Starting of "Written Pole" motor

The high resistance (to limit starting current) rotor cage produces torque which together with hysteresis torque brings the motor to approximately 80% of mechanical synchronous speed. At that moment the exciter coil is energised (at supply frequency) and a pole pattern is continuously "written" in the rotor surface which is magnetically synchronous with the stator rotating field. With the proper phase relationship between the exciter current and the stator magnetic

field, the rotor will accelerate with maximum synchronous torque to a predetermined mechanical synchronous speed. After reaching the synchronous speed the exciter can be turned off and the motor will continue to operate as a permanent magnet synchronous motor.

"Written Pole" motors can be constructed as a three-phase or as a single-phase version. The single-phase version is shown in Fig. 7.

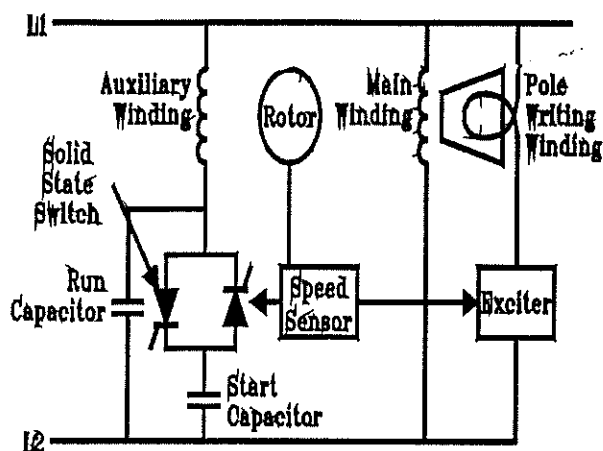


Fig. 7: Capacitor-start capacitor-run "Written Pole" motor

The main features of single-phase "Written Pole" motors are: low starting current, synchronous operation with unity or leading power factor, and high efficiency. The motors can also ride through momentary power interruptions and may be restarted instantly and as often as required. Those features are very attractive from quality of supply point of view.

### 3. CONCLUSIONS

The paper tried to identify an electrical motor or drive capable of operating from single-phase, 230 V mains and rated at least 30 kW. Three different options were discussed in detail. None of these options is undisputable the best. Two of them: "Written Pole" motor and single-phase to three-phase converter driven induction motor seem to be the most promising. However, extensive investigation is still required to identify all features of the two options and to find out which solution is the most suitable for low cost reticulation scheme.

### REFERENCES

1. Andreas J C: "Energy-Efficient Electric Motors". Marcel Dekker, New York, 1992
2. Personal communication, Elmac, Benoni
3. P N Enjeti, A Rahman, R Jakkli: "Economic Single Phase Converter Topologies for Fixed and Variable Frequency Output". IEEE Trans. on Power Electronics, vol.8, no. 3, 1993, pp. 329-335
4. Zhang, G P Hunter, V S Ramsden: "Optimum Design of an Induction Motor for a 1-phase to 3-phase Cycloconverter". International Conference on Electrical Machines, Paris, September, 1994, vol. 3, pp. 230-23
5. R T Morash, J F Roesel, R J Barber: "Rotating Uninterruptible Power Supply Uses No Batteries". International Conference on Power Electronics, Motion Control and Associated Applications, Warsaw, September, 1994, pp. 742-747

### Address of authors:

Department of Electrical Engineering  
University of Natal  
Private Bag X10  
Dalbridge 4014  
South Africa

# Robust Excitation Control of Power System using Fixed Structure Controllers

L. Chen S. Ahmed and A. Petroianu

Keywords: Robust Control,  $H_\infty$ , Fixed Order PSS.

**Abstract** — This paper presents a numerical optimization method, using the  $H_\infty$  norm as an objective function, to design robust, fixed order excitation controllers. The optimization method is based on a constrained Sequential Quadratic Programming algorithm. The main constraint is the required damping of the mechanical mode oscillation. The method presented allows for the selection of the order of the controller. It is shown that the controllers designed using this method are more robust than conventional power system stabilizers.

## I INTRODUCTION

Conventional generator excitation control systems consist of Automatic Voltage Regulators (AVR) for transient voltage regulation and Conventional Power System Stabilizers (CPSS). The CPSS introduces positive damping to damp the low-frequency mechanical mode oscillations. The classical design techniques used to design the lead-lag CPSS are only valid for a small region about the operating point, and therefore are not robust. This implies that a change in operating conditions can cause a well tuned CPSS to become ineffective.

There is therefore a need to design controllers which are insensitive to the changes in the parameters of the power system. Robust controllers based on  $H_\infty$  control theory are particularly suited for this purpose. Although  $H_\infty$  controllers achieve robustness, the controllers have a number of shortcomings. Optimal  $H_\infty$  controllers are of the same order as the plant which is typically too high for practical implementation. These controllers achieve their objectives by means of inverting the stable part of the open loop plant, while inverting the reflected unstable part of the open loop plant.  $H_\infty$  therefore achieves its goal by affecting the observability of the open loop poles, and does not affect the damping factor of these poles. In excitation control this is an undesirable characteristic. [1]

In order to overcome these difficulties we will formulate the controller design problem in terms of a numerical optimization formulation. This method allows for the selection of the order of the controller. A low order controller is achieved by augmenting the controller with the open loop plant. The resulting closed loop system contains the unknown parameters of the low order controller. The parameters of the controller is obtained by using an optimization search method. The optimization formulation uses the  $H_\infty$  norm of the closed loop as the

objective function, while using damping as one of the optimization constraints. We will show that the controller designed using this method is more robust than a controller designed using classical techniques.

## II MATHEMATICAL FORMULATION

Consider an n-dimensional MIMO power system, which can be expressed in a state-space formulation as follows:

$$\dot{x} = Ax + Be \quad (1)$$

$$y = Cx + De \quad (2)$$

and a controller of the form

$$\dot{z} = Ez + Fy \quad (3)$$

$$r = Gz + Hy \quad (4)$$

Combining equations 1 through 4, the closed loop state-space can be written as,

$$\begin{bmatrix} \dot{x} \\ \dot{z} \end{bmatrix} = \begin{bmatrix} A - BLHC & -BLG \\ FC - FDLHC & E - FDLG \end{bmatrix} \begin{bmatrix} x \\ z \end{bmatrix} + \begin{bmatrix} BL \\ FDL \end{bmatrix} u \quad (5)$$

$$y = [C - DLHC \quad -DLG] \begin{bmatrix} x \\ z \end{bmatrix} + \begin{bmatrix} DL \\ 0 \end{bmatrix} u \quad (6)$$

where:

$$L = (I + HD)^{-1}$$

$I$  is the identity matrix.

This paper addresses the problem of maximising the robustness of the closed loop system to changes in the plant parameters. In order to achieve this we need to minimize the maximum singular value of the closed loop system. The  $H_\infty$  optimization problem addressed in this paper can therefore be formulated as the following optimization problem. (see [4] for definition of  $H_\infty$  norm.)

minimize:

$$J \triangleq \|CL(s)\|_\infty = \sup_w [\bar{\sigma}(CL(s))] \quad (7)$$

subject to the following constraints:

$$\lambda_i(\text{CL}(s)) < 0 \text{ for } i = 1 \dots n$$

$$\bar{U}(\text{CL}(s)) \geq \xi$$

$$T_i < \gamma_i$$

where:  $\bar{\sigma}$  is the maximum singular value.

$\lambda_i$  are the closed loop eigenvalues.

$\bar{U}$  denotes damping.

$\xi$  is the minimum required damping value.

$T_i$  is the  $i$ th unknown parameter.

$\gamma_i$  is the constraint for parameter  $i$  obtained from the limits on the tuning devices.

$\text{CL}(s)$  is the closed loop transfer function matrix.

### III NUMERICAL OPTIMIZATION

To solve for the unknown parameters we make use of a constrained optimization method, based on Sequential Quadratic Programming (SQP). The SQP allows one to mimic Newton's method for constrained optimization. At each major iteration a positive definite approximation is made of the Hessian matrix of the Lagrangian function using quasi-Newton updating method. This is used to generate a Quadratic Programming sub-problem whose solution is used to find a search direction for a line search procedure. [2][3]

### IV SYSTEM UNDER INVESTIGATION

To prove the effectiveness of the method in the design of PSS, we apply the optimization method to a single machine, infinity bus (SMIB) power system (see figure 1). A sixth order generator model, with a second order Automatic Voltage Regulator (AVR) was used. An algebraic approximation was used to represent the network. PSS/E was used to generate the state-space representation of the power system.

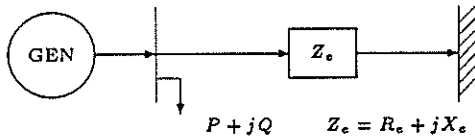


Figure 1: SMIB Power System

The power system is a two-input-two-output MIMO system and can be represented as shown in figure 2.

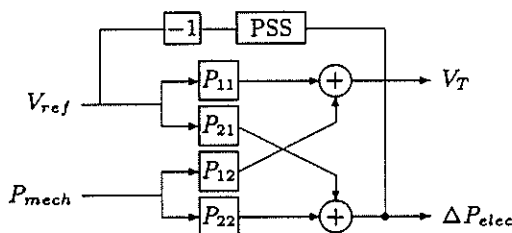


Figure 2: MIMO Control Configuration of SMIB System

We are interested in damping the mechanical mode of the generator. The input to the PSS is  $\Delta P_{elec}$  and the output is feed into  $V_{ref}$ . This implies that for the optimization problem we are interested in  $P_{21}$ .

The classical PSS controller used is of the form:

$$Q_{clas}(s) = K' \frac{(1 + sT_1)^2}{(1 + sT_2)^2} \quad (8)$$

However in the case of the optimization procedure, a more generalized second order controller, as defined by equation 9, was selected.

$$Q(s) = K \frac{s^2 + as + b}{s^2 + cs + d} \quad (9)$$

where:

$K, a, b, c, d$  are the unknown parameters.

### V RESULTS

To show that the design method presented in this paper gives a more robust solution than the classical method, a brief design of a classical PSS will be given. The controllers designed will be evaluated based on the  $H_\infty$  norm criterion for robustness.

#### A Conventional PSS Design

To design a conventional PSS, the phase margin at the mechanical mode frequency is required. In the case of the system under investigation, it was found that the phase was  $-30$  degrees at a frequency of  $5.8$  rad/s. It was decided to design two first order controllers to give  $15$  degrees of phase-lead each. The design method used is described in [5]. A value for  $T_2 = 0.1$  and a damping factor of  $0.3$  was selected, and the required equations were solved. The following values were obtained:

$$K' = 1$$

$$T_1 = 0.17$$

For the evaluation of the controllers, we rewrite the PSS transfer function, as

$$Q_{clas}(s) = 2.89 \frac{(s + 5.8824)^2}{(s + 10)^2} \quad (10)$$

#### B Robust Controller Design

To design robust PSS with the form of equation 9, the values of  $K, a, b, c$  and  $d$  were constrained within a certain range. We also included a damping constraint on the closed loop response, using the same damping factor used in the design of the classical PSS. Two controllers were designed. For the first controller,  $K$  was constrained between  $0$  and  $2$ , while for the second controller,  $K$  was constrained between  $0$  and  $10$ .

From Table 1 it should be noted that the first robust controller ( $H_\infty^1$ ) designed resulted in a complex controller, while the second controller ( $H_\infty^2$ ) is clearly a phase-lead controller. Although PSS are usually only real, it will be shown that the complex controller still performs better than the classical controller.

PSS	K	Zeros	Poles
Classical	2.89	-5.8824 -5.8824	-10 -10
$H_{\infty}^1$	2.00	-13.9647 -0.0007	$-6.0126 \pm j1.9619$
$H_{\infty}^2$	10.00	-8.1090 -0.0012	-20.2795 -0.6890

Table 1: Parameters of PSS

### C Discussion of Results

Table 2 shows a comparison of the results of the  $H_{\infty}$  norms of the three controllers, under nominal conditions and a change in load. It can be seen that the optimization method using  $H_{\infty}$  as an objective function provides a significantly improved robustness as compared to the classical PSS. In the case of the two robust controllers,  $H_{\infty}^2$  is more robust.

PSS Used	Nominal	+20 %	-20 %
Classical (K=2.89)	0.5462	0.5273	0.5352
$H_{\infty}^1$ (K=2.00)	0.3797	0.3762	0.3781
$H_{\infty}^2$ (K=10.00)	0.2008	0.2007	0.2010

Table 2:  $H_{\infty}$  norms of Classical and Robust PSS

Figure 3 shows the open loop step responses, given a unit step input into  $V_{ref}$ , of  $V_t$  and  $\Delta P_e$  of the SMIB system under study. Examining the response of  $\Delta P_e$ , it is clear that the system has an under-damped oscillation. In the case of the classical controller, as shown in figure 4 the overall damping is improved. The effect of the  $H_{\infty}^1$  controller is shown in figure 5. The mechanical mode oscillation is well damped and the response time is dramatically improved.

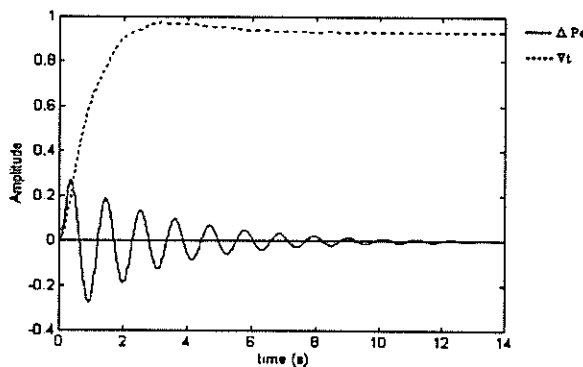


Figure 3: Step response of Open Loop system

Examining figure 6 (nominal system) it is clear that both the classical and robust controllers had little effect on the overall damping of  $V_t$ , except slightly increasing the settling time. Figure 7 and 8 show the response of  $V_t$  for a 20% increase and decrease in the load respectively. The change in load conditions had little effect.

Figure 9 shows the responses for  $\Delta P_e$  (nominal system). From the graph it is clear that both the classical and robust controllers have improved the damping and settling

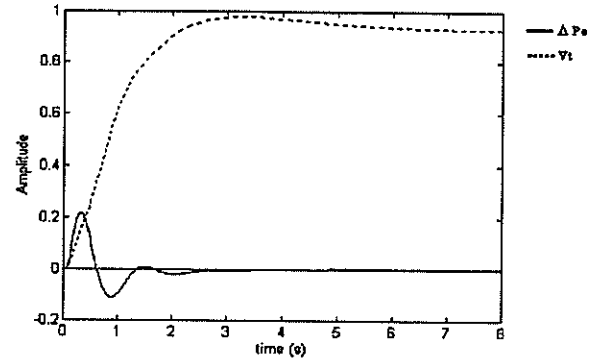


Figure 4: Step response of Closed Loop system using Classical PSS controller

time dramatically. The robust PSS performs better than the classical PSS.

For a 20% increase and a 20% decrease in load conditions, both the classical and robust controllers performed well. The results are shown in figures 10 and 11 respectively.

## VI CONCLUSION

A numerical optimization method using an  $H_{\infty}$  norm as the objective function was presented to design fixed, low order robust PSS. A damping constraint was included to achieve the required damping, since optimal  $H_{\infty}$  control does not improve damping. The PSS were chosen to be of second order. These PSS were shown to be more robust than conventional PSS under changing load conditions.

*Acknowledgement:* We would to thank J. van de Groenendaal for his valuable input.

## REFERENCES

- [1] S. Ahmed and A. Petroianu. Design of decentralised excitation controllers based on  $H_{\infty}$  control theory. *IEEE ICPST '94 China (Paper 0006)*, October 1994.
- [2] Andrew Grace. *Optimization Toolbox For use with MATLAB*. The Math Works Inc., January 1992.
- [3] L.S. Lasdon. *Optimization Theory for Large Systems*. MacMillan Series in Operations Research, January 1972.
- [4] C.H. Barret S.P. Boyd. *Linear Controller Design: Limits of Performance*. Prentice Hall, January 1991.
- [5] Yao-Nan Yu. *Electric Power System Dynamics*. Academic Press.

*Address:* Department of Electrical Engineering, University of Cape Town, Rondebosch, 7700 South Africa.

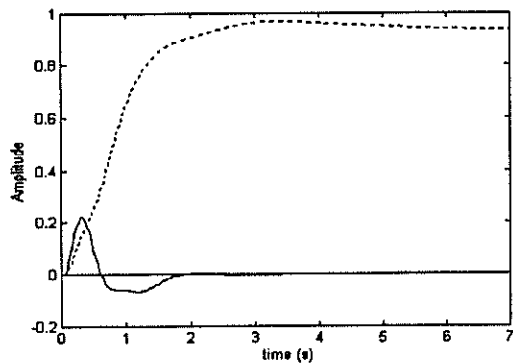


Figure 5: Step response of Closed Loop system using Robust PSS

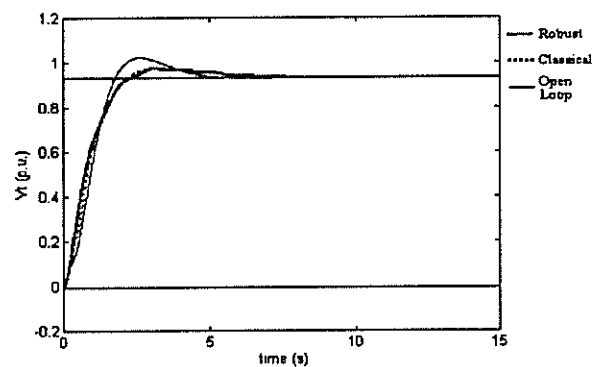


Figure 6:  $V_t$  of Nominal System

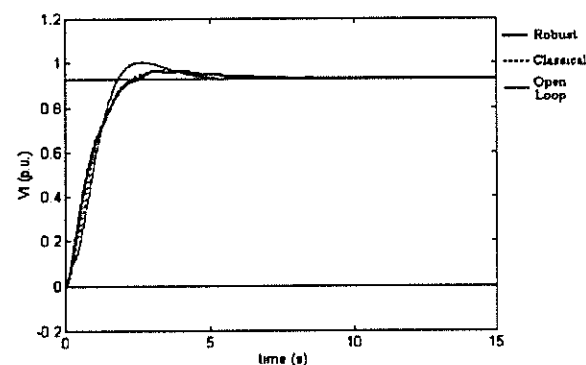


Figure 7:  $V_t$  of system with a 20 % increase in load

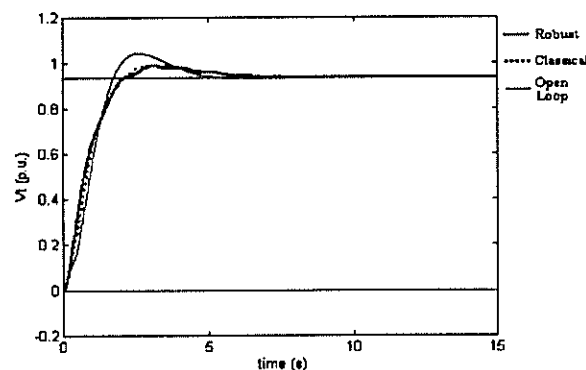


Figure 8:  $V_t$  of system with a 20 % decrease in load

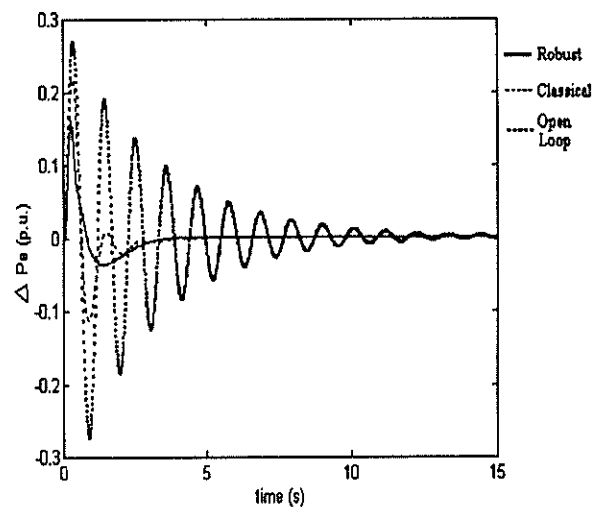


Figure 9:  $\Delta P_e$  of Nominal System

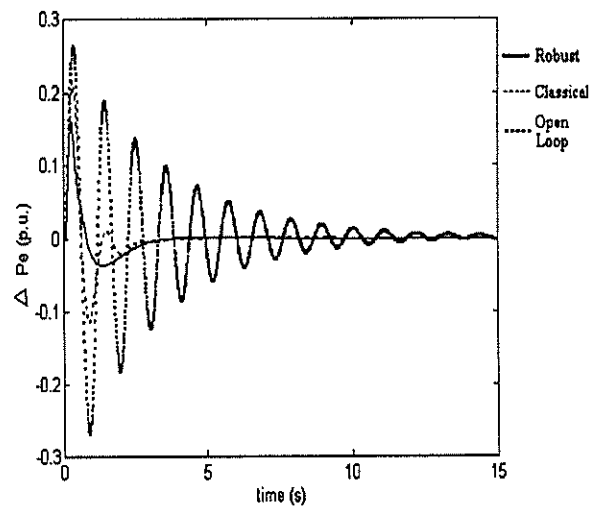


Figure 10:  $\Delta P_e$  of system with a 20 % increase in load

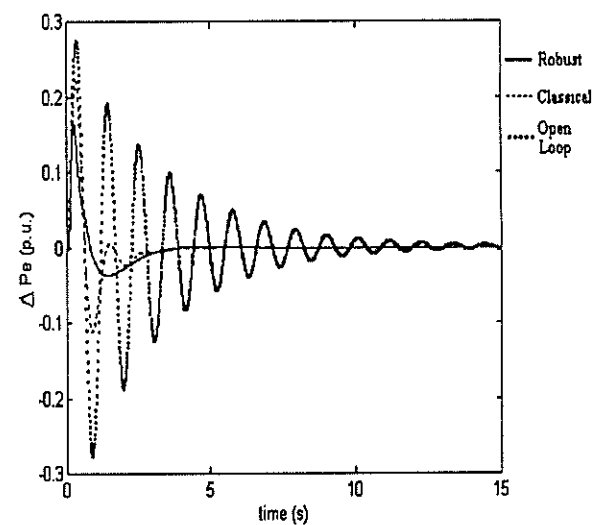


Figure 11:  $\Delta P_e$  of system with a 20 % decrease in load

# THE MATHEMATICS GOVERNING THE ROTOR TORQUE RELATIONSHIP OF WOUND ROTOR INDUCTION MOTORS THROUGH SYNCHRONOUS SWITCHING OF ROTOR RESISTANCE

Author : D Johan Bouwer BSc Eng (Elec) (Pret) MSc Eng (Birm) Pr Eng MSPE MSAIEE  
Technicon Pretoria

**ABSTRACT:** The rotor torque developed by an induction motor is governed by the rotor current that flows at any particular speed or slip. That in turn is governed by the rotor impedance at any slip. At the same time the slip at which maximum torque is developed is determined by the ratio between rotor resistance and rotor reactance at that particular slip.

These phenomena are often used to control the induction motor torque speed characteristics of wound rotor induction motors. A variable external resistor is added to each phase of the rotor circuit and these resistors are then adjusted to obtain the required torque speed characteristics.

In practice it is often bothersome to control high power resistors accurately and fast enough to achieve desired torque speed characteristics. However with the advent of modern power electronics a new technique has been developed where fixed resistors are added to the rotor circuits and these resistors are then short-circuited part of the time with the aid of the power electronics. This is done under the control of a micro-processor and synchronized with the voltage induced in the rotor circuit of the motor.

Although the technique has been applied in practice the mathematics governing the performance of such a motor has to the knowledge of the author not been developed before.

This paper is an attempt to analitically develop these relationships in order that the control algorithms for micro-processor control can be properly developed.

## 1.0 Introduction

The torque slip relationship of an induction motor is described by the equation:-

Equation 1.1

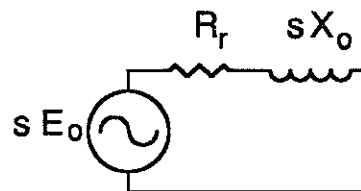
$$T = \frac{1}{\omega_s} \frac{qsE_o^2 R_r}{R_r^2 + s^2 X_o^2}$$

where the symbols used have the following meaning:-

- $\omega_s$  = synchronous angular speed;
- $q$  = number of phases;
- $E_o$  = open-circuit rotor phase voltage;
- $R_r$  = rotor resistance per phase;
- $X_o$  = rotor reactance per phase;
- $s$  = slip per unit.

and relate to the rotor equivalent circuit per phase of an induction motor as set out in Figure 1.1.

Figure 1.1



The slip for maximum torque  $S_{Tmax}$  will be:-

Equation 1.2

$$S_{Tmax} = \frac{R_r}{X_o}$$

and the maximum torque will equate to:-

2

## Equation 1.3

$$T_{\max} = \frac{1}{\omega_s} \frac{qE_o^2}{X_o}$$

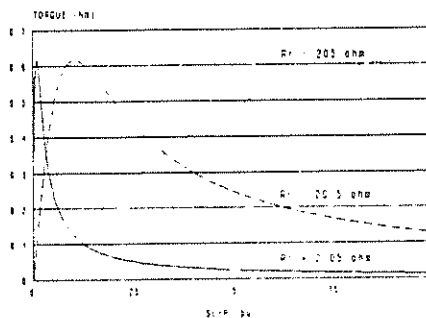
or:-

## Equation 1.4

$$T_{\max} = \frac{3}{\omega_s} \frac{E_o^2}{X_o}$$

for a three phase motor resulting in the well-known Torque Slip relationship for different values of  $R_r$  for an induction motor as seen in Figure 1.2.

Figure 1.2



For the purposes of obtaining the graphs in Figure 1.2 the values relating to a small wound-rotor induction motor available in the laboratory were used for convenience. For all further graphs in this paper they will be used.

## 2.0 Rotor Resistance in terms of Torque and Slip

If the equation for torque in terms of rotor resistance and slip ie Equation 1.1 is rewritten for rotor resistance in terms of torque and slip the following relationship emerges:-

## Equation 2.1

$$R_r^2 - 3 \frac{sE_o^2}{T \omega_s} R_r + s^2 X_o^2 = 0$$

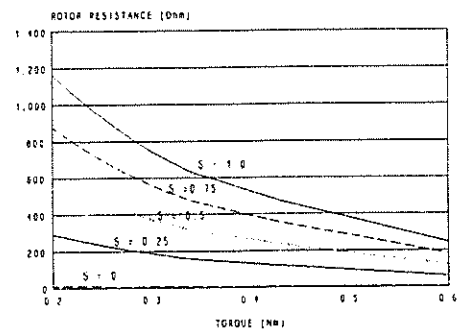
and solving for rotor resistance one of the solutions that satisfy the Equation 2.1 is:-

## Equation 2.2

$$R_r = 3 \frac{E_o^2}{2 \omega_s T} s + \sqrt{\frac{9 E_o^4 s^2}{4 \omega_s^2 T^2} - s^2 X_o^2}$$

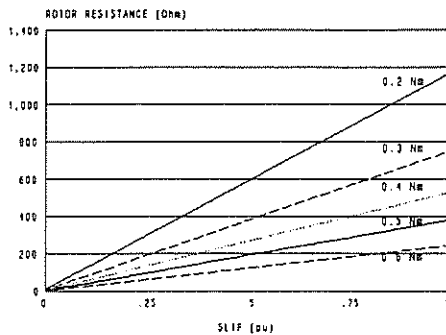
Using the values for the abovementioned motor the graphic relationship of rotor resistance as a function of torque for different values of slip is shown in Figure 2.1

Figure 2.1



and that of rotor resistance as a function of slip for different values of torque is shown in Figure 2.2.

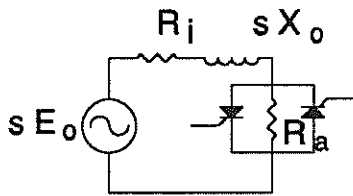
Figure 2.2



### 3.0 Switched Rotor Resistance

The above equations give the relationship between torque, maximum torque and slip related to rotor resistance  $R_r$ . A fixed or variable resistor can be used depending on the application. In the case of switched rotor resistance a fixed resistor is added to the circuit of each phase of the rotor and these resistances are made to appear to be variable by short-circuiting them by means of thyristors for part of the rotor cycle as is shown in Figure 3.1.

Figure 3.1



By varying the instant at which the thyristors are fired within the rotor cycle the average value of this resistance over half a rotor cycle can be made to vary. This is done in synchronism with the rotor current at a particular phase shift  $\theta_1$  from the rotor current having crossed zero. The average value of the resistance can then be evaluated from the following equation:-

Equation 3.1

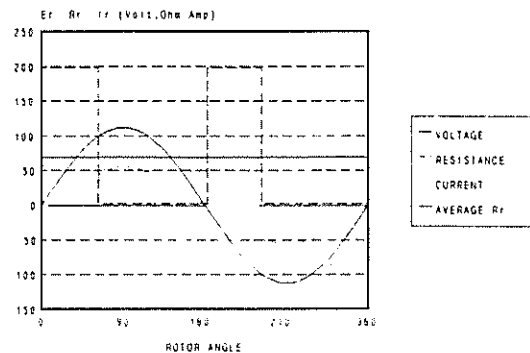
$$R_{AVE} = t_1 R_a s \frac{\omega_s}{\pi} + R_i$$

where:-

- $R_{AVE}$  = the average value of the rotor resistance over half a rotor cycle in ohms;
- $R_i$  = the internal resistance of the rotor in ohms;
- $R_a$  = the added external resistance to the rotor in ohms;
- $t_1$  = the lapsed time between zero crossings of the rotor voltage in seconds
- $s$  = per unit slip;
- $\omega_s$  = synchronous angular velocity in radians/second

and graphically it appears as in Figure 3.2.

Figure 3.2



Alternatively it can be written as:-

Equation 3.2

$$t_1 = [R_{AVE} - R_i] \frac{\pi}{s \omega_s R_a}$$

4

This can also be written in terms of rotor firing angle where the angle is:-

**Equation 3.3**

$$\theta_1 = t_1 s \omega_s = [R_{AVE} - R_1] \frac{\pi}{R_a}$$

radians.

#### 4.0 Rotor Firing Angle in Terms of Torque and Slip

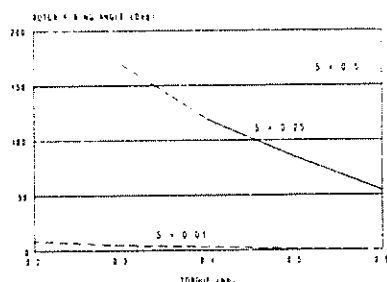
If the rotor resistance derived in Equation 2.2 is now substituted for the average rotor resistance in Equation 3.3 the relationship between rotor firing angle torque and slip is as in Equation 4.1:-

**Equation 4.1**

$$\theta_1 = \frac{\pi}{R_a} \left[ \frac{3E_o^2 s}{2\omega_s T} - R_i + \sqrt{\frac{9E_o^4 s^2}{4\omega_s^2 T^2} - s^2 X_o^2} \right]$$

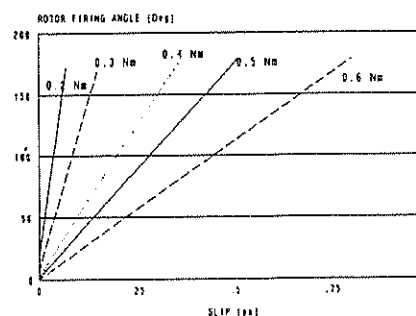
As before using the parameters of the available laboratory motor and using a value of  $R_a$  to obtain maximum starting torque (ie  $R_a = X_o - R_i$ ) the following graphic relationship for rotor firing angle in terms of slip for various values of torque emerges:-

**Figure 4.1**



Similarly the relationship between rotor firing angle and torque for different values of slip is represented in Figure 4.2.

**Figure 4.2**



#### 5.0 Conclusions and Future Research

The graphs in Figure 4.1 indicate that for this particular case of a rotor resistance which will give maximum starting torque, due to the limitation on the rotor firing angle of 180 degrees the range over which torque can be varied is limited for higher values of slip and torque can only significantly be varied at low values of slip.

Similarly Figure 4.2 indicates due to the limitation on the rotor firing angle constant low torque can only be maintained at very low slip and over a limited range. It is however significant that maximum torque can be maintained over a significant range of slip.

This is a first cut at mathematically calculating the area over which torque and slip can be controlled through rotor resistance switching for a specific set of circumstances and which can be used in the compilation of algorithms for micro-processor control of induction motors.

Future work will amount to experimentally verify theoretically calculated results. It is expected that switching phenomena not taken into account in the calculations as well as the fact that in the forward direction a silicon controlled rectifier maintains a constant voltage which will reflect a varying resistance in practice, may also affect theoretical results.

A Fourier analysis has not been done on the rotor wave forms and it is expected that through the process of switching, harmonics may be introduced, the effect of which still has to be determined. No theoretical analysis has yet been done on unsymmetrical switching during the two half cycles of the rotor cycle, this may still be of some interest.

# THE PRACTICAL DEVELOPMENT OF A NEURAL NETWORK INDUCTION MOTOR DRIVE

B Burton, R G Harley, J L Rodgerson and D C Levy\*

Department of Electrical Engineering, University of Natal, King George V Ave, Durban, 4001, South Africa

\*Department of Electrical and Computer Engineering, Sydney University, NSW, 2006, Australia

## ABSTRACT

This paper presents some of the latest results and ongoing work on a prototype implementation of a continually online trained neural network induction motor control method. The success of the current loop of the new method is demonstrated by comparison of measured and simulated current responses and the bandwidth limitations of the present transputer prototype implementation are explained. The nature and extent of the computational burden of the online training neural network algorithms are described and contrasted with the present capabilities of VLSI implementations and new methods of adapting the algorithms for parallel high speed DSP hardware.

## 1. INTRODUCTION

The basic method of applying continually online trained artificial neural networks (ANNS) for adaptive identification and control of induction motor stator currents and shaft speed was first introduced in [1]. Simulation results demonstrated the potential self commissioning and adaptive performance of the ANN method and its advantages over conventional field oriented control (FOC) of the induction motor. A subsequent paper [2] reported on the first, investigative, stages of the practical implementation of the method. In particular [2] considered different ANN topologies and learning algorithms and found the originally proposed backpropagation trained sigmoidal type, with one hidden layer, to be most suitable for practical implementation. It was argued that backpropagation shows adequate convergence in the simulations while other topologies and training algorithms offer only a slight improvement, if any, in performance at the expense of greater computational burden.

This paper summarises work subsequent to [1] and [2] on the practical implementation of the method. To date, the rapid self commissioning and tight adaptive tracking seen in simulations of the ANN current loop have been verified in practise, within the bandwidth limitations of a prototype implementation on a single embedded transputer drive controller [3]. Present efforts are immediately focused on increasing the bandwidth of the prototype current loop, shown in fig. 1. Once this has been achieved, implementation of the comparatively low bandwidth speed loop will be relatively easy. The basic

theory and operation of the current loop are briefly presented. While agreement between simulated and measured low frequency current responses demonstrate its practical viability, there is a lack of suitable high speed continually online trainable VLSI ASICs to carry the computational burden of the ANN algorithms and parallel high speed DSP hardware appears to be the only viable means of achieving very high speed ANN implementation at present. The highly parallel structure of neural networks, however, cannot be efficiently mapped directly onto multiple processors. The nature and extent of the computational burden and shortcomings of present VLSI ANNS and conventional implementations on parallel hardware are explained. Two methods of modifying the ANN structure have been developed to improve the efficiency of parallel implementation [4] and these are also briefly described.

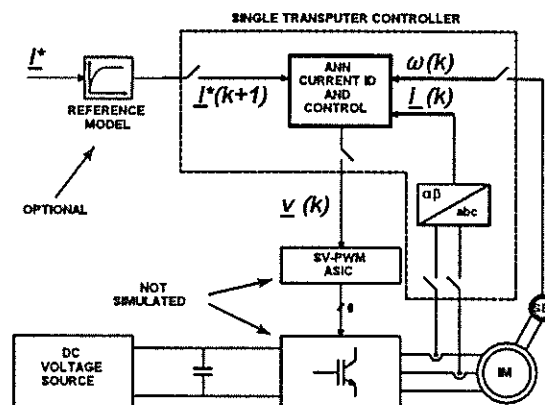


Fig. 1. Block diagram of ANN current loop prototype

## 2. ANN CURRENT LOOP PROTOTYPE

This section summarises the basic theory and operation of the current loop. The single transputer prototype implementation of fig.1 is briefly described. The main practical real time issues are explained and measured current responses are compared with simulated results.

### (a) ANN Current Identification and Control Theory

The NARMAX (Nonlinear AutoRegressive Moving Average with eXogenous inputs) discrete time model of the electrodynamics of the induction motor was introduced in [1]. It gives the one step ahead stator current vector in the stationary  $\alpha\beta$  reference frame as a function of the present and delayed current vector values  $i(k)$  and  $i(k-1)$ , the present and delayed shaft speed

values  $\omega(k)$  and  $\omega(k-1)$  and the present and delayed voltage vector values  $\underline{v}(k)$  and  $\underline{v}(k-1)$ , as

$$\hat{i}(k+1) = f(\cdot) + c_v \underline{v}(k) \quad (1)$$

where  $f(\cdot)$  is some continuous nonlinear function. The linearity of  $\hat{i}(k+1)$  with respect to the controlled variable, the present voltage vector value  $\underline{v}(k)$ , is the key to the ANN current control method. An ANN is used to identify  $f(\cdot)$  and  $c_v$  by feeding it with the values of the arguments of equation (1) captured from the motor, as shown in fig. 1. The ANN then estimates the one step ahead current vector as

$$\hat{i}(k+1) = g(\cdot) + \hat{c}_v \underline{v}(k) \quad (2)$$

and the accuracy of the estimate is determined by the closeness of  $g(\cdot)$  and  $\hat{c}_v$  to  $f(\cdot)$  and  $c_v$ . The one step ahead current vector estimate is delayed by one sampling period and compared with the actual current vector at that time to obtain the error for backpropagation training of the ANN and update of its weights. This online training takes place continuously to ensure that the ANN identifies changes in the motor as they occur. An exact control law is derived from equation (2) by substituting the desired value of the one step ahead current vector  $\hat{i}^*(k+1)$  for the estimated value and solving for  $\underline{v}(k)$  to get

$$\underline{v}(k) = \frac{\hat{i}^*(k+1) - g(\cdot)}{\hat{c}_v} \quad (3)$$

This means that the desired current vector may be made to flow in the machine by applying the voltage calculated by equation (3). The accuracy with which the actual current vector tracks the desired value simply depends on how accurately the ANN has identified equation (1), as equation (2), and adaptive control is ensured by continuous online training.

### (b) Practical Implementation

Control equation (3) assumes that the feedforward or output calculation of the ANN is instantaneous. In other words, it assumes that the function is evaluated as the ANN inputs are sampled and that  $\underline{v}(k)$  is output at the same instant. This is not practically realisable due to the time required for the many, floating point precision, multiply-accumulate operations and sigmoid functions of the ANN output calculation. The control voltage is delayed by one whole sampling period, however, to ensure predictable and synchronous operation and the backpropagation training cycle and weight updates (comprising approximately the same number and type of computations as the output calculation) are executed in the remainder of the sampling period. The online identification of parameter  $c_v$  is also omitted and the nominal value is used to achieve a 500Hz sampling rate.

### (c) Measured vs Simulated Results

Fig. 3(a) shows simulated waveforms of desired current  $i^*$  and actual current  $i^a$  response with simulated waveforms of controller output voltage  $v^a$ . Fig. 2(b)

shows the same variables as Fig. 2(a) that were captured from the prototype hardware implementation. The  $\beta$  axis component waveforms of current and voltage are not shown here, but are similar to the alpha axis waveforms in each case. The desired  $\alpha$  current waveforms comprise three instantaneous steps in magnitude, phase and frequency  $\omega_r^*$ , commencing from initial values of zero at  $t = 1$  s. The current responses show that the excellent simulated tracking ability of the controller is realised in practise. The ANN is switched into the current loop at  $t = 1$  s with random initial weights and very quickly identifies the currents and begins to track their desired values. The initial overshoot in the simulated response is diminished when a small amount of measurement noise (which is present in the practical system) is added into the simulation, since the noise excites the system and provides the ANN with more identification information. Work in progress is investigating whether a new identification model or more hidden neurons (than the 12 used) and/or a higher sampling rate (than 500 Hz achieved) are required in order for the ANN to identify and learn to compensate more completely for the sixth harmonic current distortions evident in the captured results. These current distortions are as a result of PWM voltage distortion that occurs on the 3 phase voltages. There are two source of voltage distortion. The first source of distortion is a second harmonic, pure zero crossing, distortion due to the inverter conditioning on the PWM output, which inhibits (drops) PWM pulses which are narrower than the combined turn on time and minimum on time of its power switching devices. Such narrow pulses occur near the zero crossing point of the PWM reference (and inverter output fundamental) sinusoid due to the high frequency triangular modulation and are more pronounced for low output voltages (small PWM duty cycle) since pulses become narrower and more pulses are dropped. The second source of distortion is a sixth harmonic due to a coupling of the zero crossing distortion of each of the phases through to the other two. The ANN seems to compensate well for the second harmonic distortions but for a desired  $\omega_r^* > 9$  rad/sec, the sixth harmonic distortions cause a severe degradation in the current response and the controller hunts wildly about the desired current waveform in trying to compensate for them. The inverter used for in this paper produces unacceptably high levels of voltage distortion due to very slow power switch drivers but the voltage waveforms show the extent to which the hardware ANN identified the PWM voltage distortions and compensated for them. The simulation results (obtained without modelling the PWM) show that the ANN outputs sinusoidal voltages to obtain the desired sinusoidal currents, whereas on the hardware the ANN attempts to precompensate for the PWM voltage distortion in order to obtain the desired sinusoidal currents.

### 3. High Speed ANN Implementation

The bandwidth of the ANN current loop can be increased by using either high speed continually trainable VLSI ASICS or parallel DSP hardware for implementation of

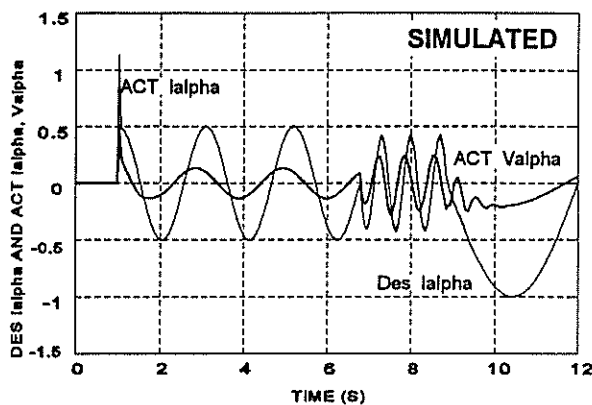


Fig. 2(a). Simulated current response and control voltage

the ANN algorithms. This section describes the shortcomings of present VLSI implementations and the low efficiency of multiple processor implementations of the standard ANN algorithms. Two methods of increasing the parallelism of the ANN structure to increase the speed of multiple processor implementations are also briefly described.

#### (a) Shortcomings of Present VLSI ASICS

ASICS which implement the ANN forward or output calculation at very high speed, based on a fixed, pre-programmed set of weights, have been available for some time. These ASICS are primarily used in applications where offline training of the ANN can be done by means of simulation. Online training has been achieved with these ASICS [5] by externally implementing the backpropagation training algorithm on DSP hardware. The bottleneck encountered in downloading new weights to the ASIC online, however, places severe limitations on the overall achievable speed. Only recently have ANN ASICS been produced with on chip implementation of the training algorithm [6],[7]. Unfortunately, the backpropagation algorithm is very sensitive to the unavoidable offsets and limited accuracy of the analogue components of the hybrid VLSI circuitry and manufacturers have had to resort to probabilistic training algorithms. These algorithms are extremely fast in terms of the execution time of one random training trial and thus the overall time taken for the number of successful trials required for convergence on each data point is fairly small *on average*. The shortcoming of these ASICS in adaptive control applications is that no guarantee of successful training within a specified sampling period can be given. This compromises the tracking performance and may even lead to instability.

#### (b) Efficiency of Standard Parallel Implementation

The Transputer Applications Research Group at the University of Natal have developed a software tool to automatically search for an optimal mapping and scheduling of tasks onto a network of transputers [8]. This tool also provides a detailed analyses of the schedule and code execution times which were used to investigate the gain in speed that could be achieved by

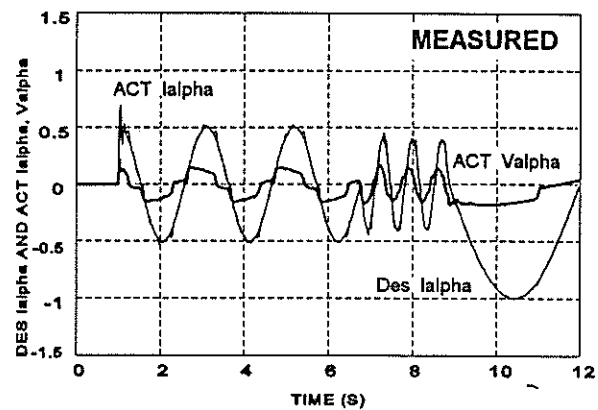


Fig. 2(b). Measured current response and control voltage

implementing the standard ANN structure on multiple processors. Fig. 3(a) depicts a typical mapping of the standard ANN structure on multiprocessor hardware. It can be seen that many connections are cut due to the highly connected ANN structure and it was found that the many communication transactions placed an upper limit on the gain in speed at 1.7 times for 5 or more processors. Ways were thus sought to increase the parallelism of the ANN structure.

#### (c) Increasing ANN Parallelism

Figs. 3(b) and (c) depict two methods of increasing ANN parallelism that did not significantly degrade the simulated performance of the ANN current loop. The first method is called *output separation* since a single multiple output ANN is replaced with *separate* smaller ANNs which each calculate one output. Each of these ANNs are then implemented on separate processors which need not communicate with any of the others. In the case of the ANN current loop, the vector valued input/output mapping function  $g(\cdot)$  of equation (2) has two components  $g_1(\cdot)$  and  $g_2(\cdot)$ . The speed of execution was *doubled* by replacing the single ANN with 12 hidden neurons used to simultaneously identify both functions with two separate ANNs with 6 hidden neurons each, as shown in fig. 3(b). The second method exploits the fact that the feedforward or output calculation and backpropagation training parts of the ANN operation take approximately equal lengths of

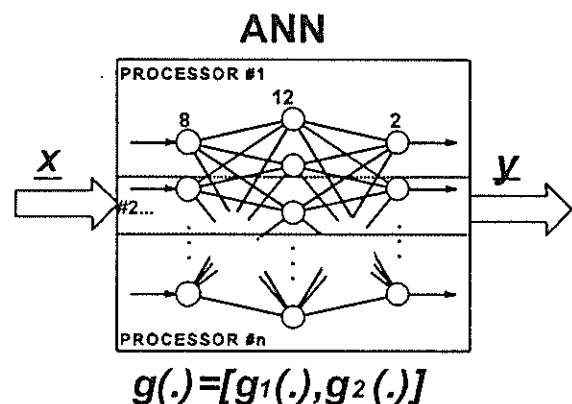


Fig. 3(a). Conventional ANN multiprocessor implementation

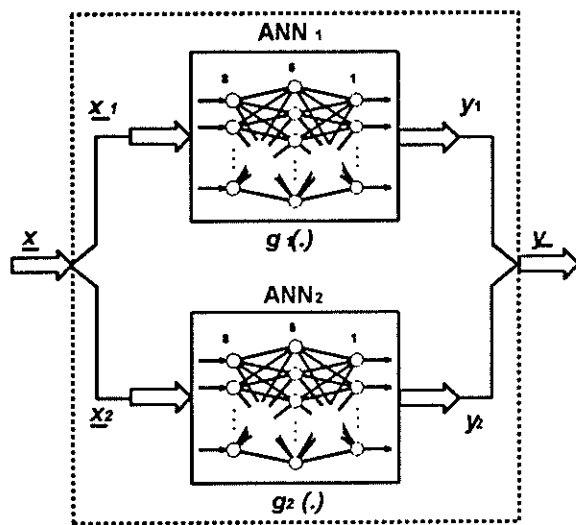


Fig. 3(b). Output separation parallelisation method

time when implemented in software on DSP hardware. It was also found that control performance did not degrade significantly if only one training cycle was done for every two forward or output calculation cycles. Fig. 3(c) shows how the standard (original) speed of execution can be *doubled* by exploiting this fact. Here two identical ANNs are implemented on separate processors, called a *tandem pair* since they operate in tandem. One ANN does the forward or output calculation while the other trains and visa versa. Once again, each ANN operates independently of the other and there is no need for communication between them. Each executes its forward or output calculation based on training information from every second cycle to effectively achieve the desired ratio of one training cycle for every two forward or output calculations.

The *output separation* and *tandem pair* methods of figs. 3(b) and (c) can be combined to further increase the parallelism of the ANN structure to *quadruple* the speed of multiple processor implementation of the ANN current loop.

#### 4. CONCLUSION

This paper has described the present state of the practical development of a neural network induction motor drive. The simulated self commissioning and adaptive tracking performance of the ANN current loop have been verified in practise, within the bandwidth limitations of the single transputer prototype implementation. The shortcomings of present VLSI ANN ASICs have been explained and two methods of increasing ANN structural parallelism for high speed multiple processor DSP hardware implementations have been described. Future work is aimed at implementation of these methods on suitable hardware, such as high speed parallel DSP or possibly new VLSI ASICs, to achieve high bandwidth current control. This will be followed by implementation of the ANN speed loop on the same hardware since the base performance of the T800 transputer (used for the prototype) is not high enough to yield the desired rate when they are paralleled.

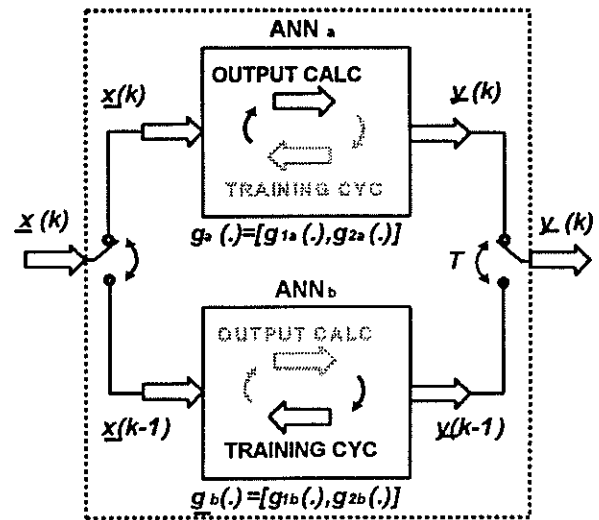


Fig. 3(c). Tandem pair two processor implementation

#### ACKNOWLEDGEMENT

The authors gratefully acknowledge the financial support of the University of Natal and the Foundation for Research and Development (FRD) in South Africa.

#### REFERENCES

- [1] Wishart MT and Harley RG, "Identification and Control of Induction machines Using Artificial Neural Networks", *Conf. Rec. of SAUPEC'94*, Cape Town, South Africa, Jan. 1994, pp 200 - 206.
- [2] Burton B, Harley RG *et al*, "Implementation of a Neural Network Induction Machine Control Strategy", *Conf. Rec. of SAUPEC'94*, Cape Town, South Africa, Jan. 1994, pp 195 - 199.
- [3] Burton B, Harley RG *et al*, "Implementation of a Neural Network to Adaptively Identify and Control VSI Fed Induction Motor Stator Currents", *Conf. Rec. of IEEE IAS Annual Meeting*, Denver, USA, Oct. 1994, ISBN 0-7803-1993-1, pp 1733-1740.
- [4] Burton B, Harley RG, "Reducing the Computational Demands of Continually Online Trained Artificial Neural Networks for Identification and Control of Fast Processes", *Conf. Rec. of IEEE IAS Annual Meeting*, Denver, USA, Oct. 1994, ISBN 0-7803-1993-1, pp 1836 -1843.
- [5] Canelo G, Hansen S, "Analog Neural Network Development System With Fast Online Training Capabilities", *Conf. Rec. of IEEE IECON*, Bologna, Italy, Oct. 1994, ISBN 0-7803-1328-3, pp 1396-40.
- [6] Hirotsu K, Brooke MA, "An Analog Neural Network Chip With Random Weight Change Learning Algorithm", *Conf. Rec. of IJCNN*, Nagoya, Japan, Oct. 1993.
- [7] Flower B, "An Analogue On-Chip Learning Implementation of an Artificial Neural Network", Paper in preparation - SEDAL, Sydney University.
- [8] van der Westhuizen M J, Harley RG *et al*, "Optimising Multirate Motion Control Algorithms on Parallel Processors by Static Scheduling", *Conf. Rec. of IEEE IAS Annual Meeting*, Denver, USA, Oct. 1994, ISBN 0-7803-1993-1, pp 1872 -1879.

# DIE SPOORKANON AS ELEKTROMAGNETIESELANSEERDER.

S.D. Roos., J.A. Ferreira.  
Energie laboratorium, Randse Afrikaanse Universiteit  
Posbus 524  
Auclandpark, 2006  
Johannesburg, Suid-Afrika.

## 1. Sinopsis.

In die soeke na 'n meer effektiewe metode as die gebruik van chemiese energie om massa te versnel, is elektromagnetiese lanseerders ondersoek.

Die bestaande kanonne en misiele kan snelhede van 650 - 1000 meter per sekonde bereik. ( Mag 2 ) Hierdie snelhede is egter amper net so vinnig as die snelhede wat deur vliegtuie behaal word. Dit raak daarom al hoe moeiliker om die vliegtuie raak te skiet, want die vlieënier het meer tyd om die misiel te ontduik.

Elektromagnetiese lanseerders het die potensiaal om hoër snelhede te bereik, wat die verdedigingsnetwerke meer effektief sal maak.

## 2. INLEIDING.

'n Elektromagnetiese lanseerder is 'n elektriese ingenieur se antwoord op 'n kanon. Waar kanonne van plofstof gebruik maak vir versnelling, maak 'n elektromagnetiese lanseerder gebruik van elektrisiteit vir versnelling.

Elektromagnetiese lanseerders kan vir verskeie toepassings gebruik word. Van die moontlike toepassings is:

- In verdedigingsnetwerke.
- In navorsing
- Ruimtevaart.

'n Spoorkanon is vir die V.S.A weermag gebou. Die Spoorkanon het 'n projektiël met 'n massa van 1 tot 2.2 kilogram teen snelhede van 2000 tot 3500 meter per sekonde gevuur. [6] Die snelhede wat deur hierdie spoorkanon behaal is sal meer geskik wees as die misiele wat tans bestaan. Dit behoort die verdedigingsnetwerk meer effektief te maak.

'n Model van die Shumacker-Levy botsing met Jupiter kon gebou word, om sodoende vooraf te voorspel wat die invloed van die botsing op die aarde sou wees.

In die ruimtevaart tegnologie kan elektromagnetiese lanseerders gebruik word om satelliete in wentelbane te plaas sonder die gebruik van brandstowwe.

Die doelwitte van hierdie studie is om eerstens die elektromagnetiese lanseerder te analiseer. Hierin is daar gelet op die verskillende elektromagnetiese lanseerders wat bestaan.

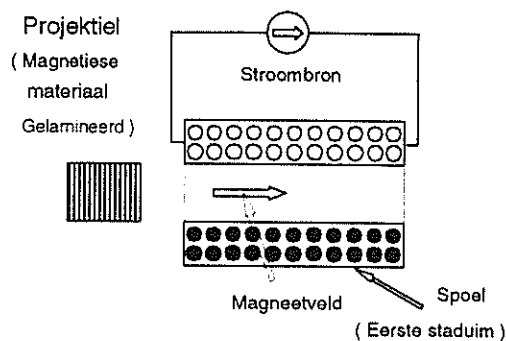
Tweedens is die teorie toegepas en 'n model van 'n spoorkanon is ontwerp.

Laastens is die model van die spoorkanon geëvalueer en moontlike verbeterings aangedui.

Die eindresultaat van hierdie projek is 'n spoorkanon wat 'n koolstof projektiël met 'n massa van 3 gram teen 'n snelheid van ongeveer 100 meter per sekonde vuur.

## 3. DIE Tipes ELEKTROMAGNETIESELANSEERDERS

### 3.1 Reluktansielanseerder.



**Figuur 1** 'n Diagramatiese voorstelling van 'n reluktansielanseerder

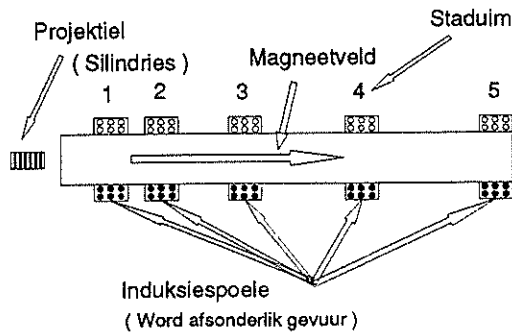
Die werking van die reluktansielanseerder berus daarop indien 'n magnetiese materiaal in 'n magneetveld geplaas word, sal die materiaal so beweeg dat die maksimum aantal vloedlyne gesny word.[1] As die loop uit 'n aantal spoel bestaan, sal die magnetiese projektiël in die loop ingetrek word. Die spoel wat die projektiël aantrek moet egter afgeskakel word wanneer die projektiël die middelpunt bereik, aangesien die magneetveld die projektiël weer sal terugtrek indien dit deur die spoel beweeg het. 'n Tweede spoel word gebruik om die snelheid wat verkry is deur die eerste spoel te verhoog. Die eindsnelheid van fase een is die beginsnelheid van fase twee waar die proses weer herhaal word.

Hierdie proses kan 'n sekere aantal kere herhaal

word om 'n bepaalde snelheid te behaal.

Die grootste ontwerpprobleem met hierdie stelsel is die sinkronisasie van die spoele, want as die magnete nie gesinkroniseer word nie sal maksimum energie oordrag nie plaasvind nie, en sodoende sal die maksimum snelheid nie bereik word nie.

### 3.2 Induksielanseerder.



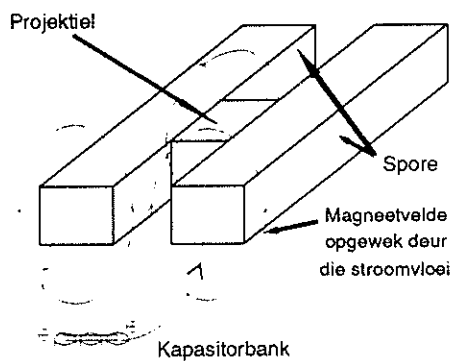
**Figuur 2** 'n Diagramatiese voorstelling van die induksielanseerder.

Verskeie konfigurasies is moontlik vir die induksielanseerder [1], maar die mees algemene hiervan bestaan uit 'n reeks induksiespoele wat afsonderlik bekragtig word. Die magneetveld wat deur die spoele opgewek word induseer werwelstrome in die silindriese projektiel. Die werwelstrome veroorsaak dat daar 'n magneetveld om die projektiel ontstaan en die versnelling word verkry deur die interaksie van hierdie twee magneetvelde.

'n Tweede metode om die magneetveld op te wek is deur van 'n hoëfrekwensie stroombron gebruik te maak. Die stroombron wek 'n loopgolf op en dien dieselfde doel as die afsonderlik opgewekte spoele.

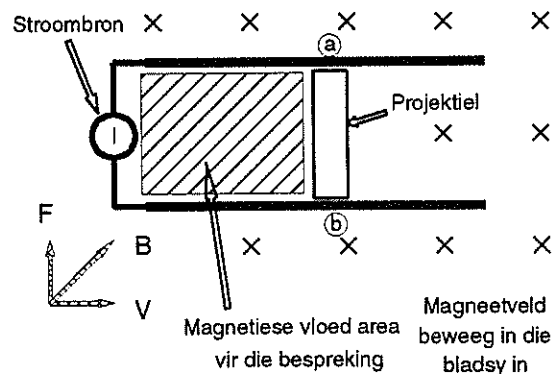
'n Voordeel van die reluktansie- en induksielanseerders is dat daar geen elektriese kontak tussen die projektiel en die stator is nie.

### 3.3 Die spoorkanon.



**Figuur 3** 'n Diagramatiese voorstelling van die spoorkanon

Soos in figuur 3 voorgestel word, bestaan die spoorkanon uit twee spore wat aan 'n stroombron gekoppel word. Die projektiel beweeg tussen die twee spore en die magneetvelde word deur die stroom opgewek. Indien die bron 'n stroom lewer sal die projektiel versnel in 'n rigting parallel aan die spore. Die stroom word op die spore van die spoorkanon aangelê. Dit veroorsaak dat daar 'n magneetveld om die spore opgewek word, sodra die stroom begin vloei. Die stroom word deur 'n kapasitorbank gelewer en moet in die rigting van b na a wees sodat die projektiel kan versnel.



**Figuur 4.** Die magnetiese vloedarea soos toegepas op die spoorkanon

Volgens Parker [2] kan die versnelling van die spoorkanon deur magnetiese vloed verklaar word (figuur 4). Die magnetiese vloed wat in die gearseerde area in vloei, wil verklein en graag 'n maksimum oppervlakte beslaan om die laagste energietoestand te bereik. Die enigste manier wat die magnetiese vloed 'sien' om die gearseerde oppervlakte te kan vergroot, is om die projektiel tussen die spore te laat af beweeg wat dan effektief die oppervlakte vergroot. Die vergroting van die vloedoppervlakte veroorsaak dan die versnelling van die projektiel. Dit kom daarop neer dat daar 'n druk op die kante van die spore en die projektiel uitgeoefen word. Die druk wat die projektiel ondervind is:

$$P = \frac{B_s^2}{2 \mu_0} \quad (1)$$

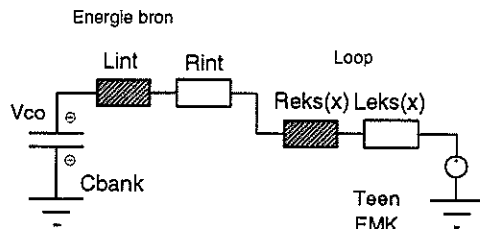
waar  $B_s$  die magnetiese vloed in die gearseerde area is.

Aangesien etlike kiloampère strome gebruik word, is die slytasie en die smelting van die projektiel 'n gedeelte van die ontwerp wat aandag moet geniet. Die strome plaas druk op die ontwerp aangesien daar verskeie komplikasies is waarna gekyk moet word.

## 4. ELEKTRIESE ANALISE

Die energiebron moet sodanig wees dat die piekstroom vir die langste tyd gelewer kan word volgens Putley [3]. Die stroom moet 'n trapesiumvorm aanneem om aan hierdie vereiste te voldoen. Die energie bron wat gebruik is, is 'n kapasitorbank van 37 mF 300 V.

'n Simulasie program is vir die spoorkanon geskryf waar van 'n vereenvoudigte stroombaan gebruik gemaak is.



Figuur 5. Die vereenvoudigte baan

Die teen elektromotoriese krag is buite rekening gelaat aangesien dit 'n weglaatbare invloed op die analise het. (Die invloed van die teen EMK is eers by 6 km/s 'n faktor).

'n Differensiaalvergelyking van die vereenvoudigte baan is opgestel. (2)

$$V_{co} - L_{int} \frac{di(t)}{dt} - R_{int} i(t) - \frac{1}{C} \int i(t) dt = 0$$

Deur van Laplace transformasies gebruik te maak kan die differensiaalvergelyking na die S vlak getransformeer word. (3)

$$I(s) = \frac{V_{co}(C \cdot 1)}{L_{int} C s^2 + R_{int} C s + 1}$$

Neem die Inverse Laplace transformasie om die tydafhanklike stroom van die baan te verkry. (4)

$$i(t) = 2 V_{co} \exp\left(-\frac{R_{int}}{2 L_{int}} t\right) \sinh\left(\frac{1}{2} \sqrt{\frac{R_{int}^2}{L_{int}^2} - \frac{4}{C}} t\right) \frac{C \cdot 1}{C \sqrt{R_{int}^2 - 4 L_{int} C}}$$

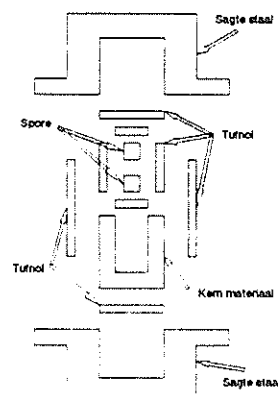
Die weerstand van die loop en die inductansie is egter van die posisie van die projektiel afhanklik. Aangesien die posisie van die projektiel nie bekend is voordat die stroom bekend is nie moet van 'n iteratiewe proses gebruik gemaak word. Dit behels dat die baan opgelos word in 'n aantal stappe. Vir die eerste stap word slegs die interne weerstand en inductansie van die energiebron gebruik.

Die stroomwaarde word bepaal waaruit die afstand en

die snelheid van die projektiel na 'n sekere tydverloop bereken word. Hierdie afstand word gebruik om die weerstand en die inductansie van die loop te bereken. Die proses word herhaal met die verandering dat die weerstand en die inductansie die som van die interne en eksterne weerstand en inductansie is. Indien hierdie proses herhaal word kan die oplossing van die spoorkanon verkry word.

## 5. MEGANIESE KONSTRUKSIE

Die loopontwerp is gedoen met die inagneming van die bevindings van Bauer en Newman [4]. Die konstruksie van die loop word in figuur 6 getoon. Dit bestaan uit 'n sagte staal omhulsel. Die omhulsel word met 'n isolasie materiaal uitgevoer (Tufnol). Binne hierdie isolasie word die gelamineerde kern materiaal geplaas. Die kernmateriaal word weer met 'n isolasie materiaal uitgevoer. Die spore word dan binne die isolasie geplaas. Die doel van die isolasie is om te verseker dat daar nie 'n kortsluiting tussen die twee spore plaasvind nie. Die omhulsel is dan ook veilig en sal nie 'n stroom dra nie. Die kern materiaal versterk die magnetiese vloed tussen die twee spore. Dit moet gelamineer wees aangesien daar 'n werwelstroom in die kernmateriaal geïnduseer word. Indien dit gelamineer is sal die werwelstroom verminder word sodat 'n beter effektiwiteit verkry word.

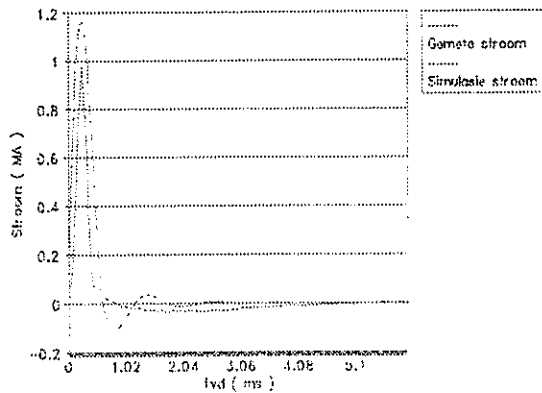


Figuur 6 Voorstelling van die loop

Die projektiel is uit koolstof vervaardig. Koolstof het 'n negatiewe temperatuur koëfisient, die weerstand van die koolstofprojektiel word al kleiner hoe warmer die projektiel word. Die smeltpunt van koolstof is ongeveer 3000 °C en kon daarom die hitte wat deur die stroomvloeï veroorsaak is hanteer. Koper is ook getoets maar die koper het gesmelt aangesien 'n 3 gram massa gebruik is en die koper kon nie in so 'n klein volume die hitte dissipeer nie.

## 6. RESULTATE

Die spoorkanon is gebou om te sien of die simulase ooreenstem met die waardes in die praktyk. Die gemete en die simulase stroomvorm word in figuur 7 getoon.



**Figuur 7.** Die simulase en die gemete stroomvorms.

Deur middel van die simulase kon die snelheid van die spoorkanon bepaal word. Die snelheid vir die simulase is 104 m/s en die van die gemete waarde is 109 m/s. Die verskil kan toegeskryf word dat daar in die simulase meer damping is as wat in die werklike geval is. ( Die simulase stroom gaan meer negatief ).

## 7. GEVOLGTREKKING.

Die optimale snelheid wat met die bestaande spoorkanon bereik kan word, is nog nie behaal nie. Deur middel van die simulasiëprogram en die gemetewaardes is vasgestel dat die energie nie vir 'n lang genoeg tyd gelewer word nie. Dit veroorsaak dat die projektiel nie vir die totale tyd wat dit in die loop is 'n versnelling ondervind nie. Die wrywing tussen die projektiel en die spore is van so 'n aard dat dit die projektiel vinnig vertraag. Die kapasitansie van die kapasitorbank kan vergroot word om die probleem te oorbrug. Dit sal die piekstroom vir 'n langer tyd handhaaf met die gevolg dat die projektiel 'n vinniger snelheid kan behaal. Hierdie vergroting van die kapasitorbank behoort die effektiwiteit van die spoorkanon ( 6.8 % ) heelwat te verhoog.

## BIBLIOGRAFIE.

- 1 Boucher, J. 1991: Die ontwerp van 'n elektromagnetiese lanserder : R.A.U.
- 2 Parker, J. A personal view of plasma armature railguns; their prospects and problems, Los Palamos National Laboratory, 1989.
- 3 Bauer, D.P. en Newman, D.C. 1993: High performance railgun barrels for laboratory

use. IEEE Transactions on magnetics, Vol 29 no 1 Jan 1993:362-367.

- 4 Sears, F.W. ; Zemansky, M.W. en Young, H.D. 1987: University physics; Seventh edition. United States of America: Addison Wesley Publishing 1987:743-745.
- 5 Hayt, H.H, 1989: Engineering electromagnetics; McGraw Hill, 1989
- 6 Holland, M.M. ; Eggers, P.D. ; Guinto, S en Stevenson, R.D. 1993: Advanced railgun experimental test results and implications for the future, IEEE Transaction on magnetics, Vol 29 no 1 Jan 1993: 431-433.

# A DRIVE DEVELOPMENT PLATFORM FOR DIRECT PORTATION OF CONTROL ALGORITHM CODE BETWEEN SIMULATION AND HARDWARE ENVIRONMENT

C E Kleinhans, R G Harley, G Diana, M D McCulloch\*, M C Randelhoff

Department of Electrical Engineering, University of Natal, King George V Ave, Durban, 4001, South Africa

\*Department of Engineering Science, Oxford University, UK

## ABSTRACT

In motion control R&D the integration of simulation environment and implementation environment is desirable to reduce system development time. As a first step to such integration this paper discusses a drive system development platform which uses *CASED* for the simulation environment and a transputer based Embedded Programmable High Speed Controller (EPHSC) for the practical implementation environment. The development platform was applied to the investigation of FOC on the CSI-fed induction machine. The simulation model developed in *CASED* is discussed briefly. Practical issues of implementation are discussed. Simulation and measured results validate the *CASED* model and hardware operation.

## 1. INTRODUCTION

Effective motion control R&D relies on the availability of a drive system development platform which integrates the simulation environment and practical implementation environment. The ultimate is to achieve automatic implementation from design to experiment when investigating a new control strategy. Certain commercial systems are available such as the dSPACE real-time interface which extends the Mathworks' SIMULINK C code generator for automatic implementation of SIMULINK models on dSPACE high speed DSP systems [1]. The dSPACE DS1003 parallel DSP board makes use of the Texas instruments TMS320C40 processor with a 50MHz clock rate and 40/32-bit floating point/integer multiplier and ALU. A similar commercial product called UNAC is available from CICS (Centre for Industrial Control Science) [2]. SAAC is the hardware implementation model used by UNAC which uses the intel 80960CA processor and 40/32-bit floating point/integer multiplier and ALU. Such commercial systems although very versatile are extremely expensive. The hardware/software interfaces are suited to motion control algorithm implementation but the software toolboxes are more generic and not aimed specifically at simulating drive systems. The switching devices of converter circuits require specific time event schedulers and state dependent change routines to accurately

simulate the full dynamic operation of the converter system. As part of ongoing work at the University of Natal the motion control group and transputer group have invested resources into developing an in-house motion control development platform which was (i) considerably cheaper than commercial systems (ii) aimed specifically at motion control R&D and (iii) integrated the simulation and practical implementation environment. This paper summarises the progress to date on this motion control development platform. A brief description is given of the transputer based Embedded Programmable High Speed Controller (EPHSC) [3] which was developed to implement controller algorithm code and provide the high speed I/O structures typically required for motion control applications. The software toolbox chosen as the complimentary simulation and analysis platform is described briefly. This software toolbox, namely *CASED*, was developed by WITS University and aimed specifically at the simulation of variable speed drives in general [4]. As a first step to towards generating the integrated simulation and implementation environment it was the objective to analyse the CSI-fed squirrel cage induction machine (SCIM) under FOC. A full dynamic model of the drive system was developed in *CASED* which for the purpose of this paper is presented only conceptually [5]. The implementation of the simulated controller code on the EPHSC is described. The EPHSC was used to break into the conventional analogue volts/hertz control strategy of an industrial CSI-fed SCIM drive system and replace it with FOC. Simulated and measured results are presented to validate the operation of the drive development platform as it stands to date. Finally a discussion is made on future work to be done on this motion control development platform.

## 2. THE EMBEDDED PROGRAMMABLE HIGH SPEED CONTROLLER (EPHSC)

The structure of the EPHSC is shown in Fig. 1. The workhorse of this digital controller platform is the 25 MHz INMOS T800 transputer. The T800 provides in a single package (i) RISC (Reduced Instruction Set Computing) which incorporates a 32 bit integer central processor unit (CPU) in parallel with a 64 bit FPU (Floating Point Unit), (ii) 4 kbytes of fast internal SRAM

configurable for high speed code and/or data access and (iii) a built in hardware based task scheduler with low-context-switch and interrupt response times to manage the execution of multiple tasks.

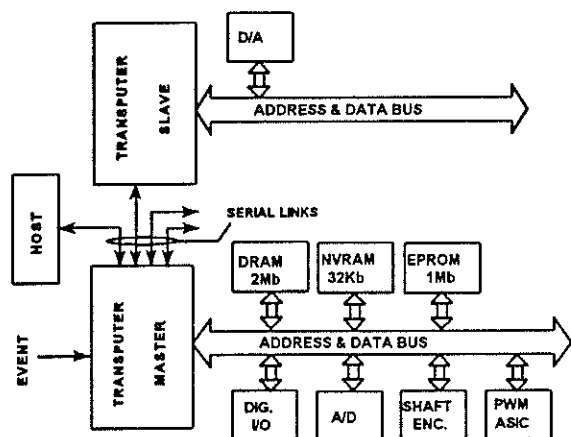


Fig.1 Block diagram structure of EPHSC

The FPU enables high speed controller algorithm code execution in floating point arithmetic. The EPHSC uses the high speed external memory interface of the transputer to couple autonomous I/O interfaces to the transputer processor by means of a dual port memory/finite state machine structure [3]. This shifts away from the transputer the processing burden of handling low level I/O tasks associated with using the serial communications links to provide I/O facilities. The I/O interfaces, based on ASIC devices, include (i) a shaft encoder card decoding rotor position, (ii) high speed simultaneous sampling of up to 16 analogue channels with 12 bit A/D resolution and  $\pm 10$  volt range, (iii) 16 bit digital I/O port, and (iv) PWM space vector modulation ASIC with associated protocol drivers. Using a simple resistor network unit the 16 bit output port can be used to provide a high speed analogue output.

The serial communication links of the transputer processor allow the connection of an IBM PC host which enables the programming of the T800 using the INMOS ANSI C TOOLSET [6]. The remaining three serial links allow slave transputers to be connected to the root transputer of the EPHSC. An additional D/A card can be connected to a slave processor to provide 16 high speed analogue output channels with  $\pm 10$  volt range.

### 3. CASED : A SOFTWARE TOOLBOX FOR ANALYSIS OF MOTION CONTROL SYSTEMS

**CASED** (Computer Analysis and Simulation of Electrical Drives) is a C based software toolbox aimed specifically at providing a simulation environment which is suitable to the design and analysis of a wide variety of complete drive systems [4]. Features of the software toolbox which are tailored specifically to motion control system simulation include:

(i) **Modularity:** Any drive system can be broken up into a group of sub-systems or *modules* each of which may be identified as an independent entity by virtue of its operation. The mains supply may be identified as one *module* similarly the converter circuit, the electrical machine, mechanical load and controller algorithm. **CASED** allows the models for each *module* to be developed independently and then linked up to form the complete drive system model. Standard library model *modules* are available or user defined model *modules* can be generated to model any diverse drive system.

(ii) **A Piecewise linear state space model of a general converter:** The converter topology is generated through a graphical interface which then configures the differential equations describing that topology automatically. It is not necessary to predetermine all the possible normal and abnormal conduction modes of the switching circuits associated with the converter topology.

(iii) **A powerful simulator "brain" and module linker:** Special *module linker* routines accommodate the linking up of the sub-model *modules* of the system and a central *simulator* or "*intelligent workhorse*" coordinates the continuous time simulation with discrete time events typically associated with changing converter switch states and discrete controllers.

(iv) **Analysis tools:** A graph routine allows viewing and manipulation of simulation data and a linearisation option within the simulator automatically generates the A-matrix for the converter and machine system. Such information is valuable for control loop design.

### 4. SIMULATION MODEL FOR THE CSI-FED SCIM UNDER FOC USING CASED

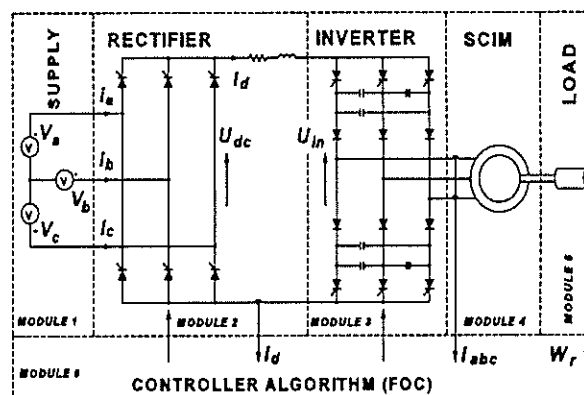


Fig. 2 Modular breakdown of CSI-fed SCIM in **CASED**.

The CSI-fed IM under FOC may be broken up into those *modules* identified in Fig.2. Models have been developed for each of these *modules* using **CASED** specific notation and then linked up to form the complete drive system simulation model [5]. This model was used to refine and optimise the FOC algorithm used for the CSI-fed IM drive system into the form of Fig.3. To achieve the necessary integration accuracy the rotor flux linkage model was to run at 5KHz and the remainder of the algorithm at 1KHz.

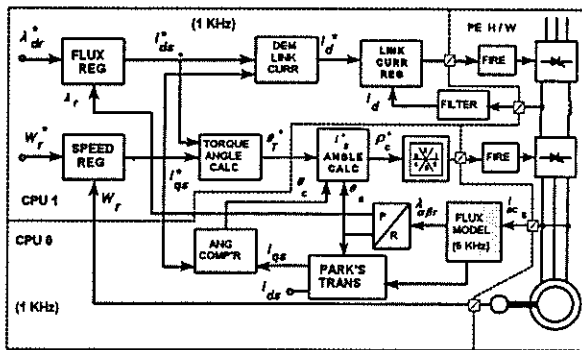


Fig.3 FOC algorithm for the CSI-fed SCIM.

The supply sub-model or *module*, rectifier *module*, inverter *module*, SCIM *module*, and mechanical load *module* together form a model describing what may be identified as the power electronics hardware *module* of the drive. Add to the power electronics hardware *module* the digital controller algorithm *module* and the result is the complete drive system model. This power electronics hardware/controller algorithm interface "boundary" plays an important role in describing the first stage of integration of the simulation and implementation environment.

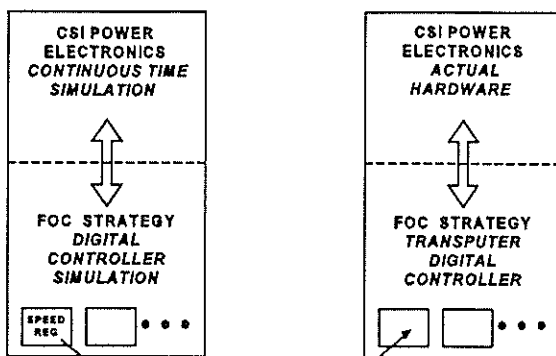


Fig.4 Integrated simulation and real-time code generation.

## 5. INTEGRATED SIMULATION AND REAL TIME CODE GENERATION

The digital controller algorithm *module* code in *CASED* was written as a number of C sub-routines. Since the ANSI C TOOLSET accommodated full parallel programming of the transputer processor using C, the controller sub-routines from simulated digital controller algorithm *module* code could be directly ported to the EPHSC. This is shown conceptually in Fig.4. This ability to use simulated controller algorithm code directly on the EPHSC describes the first stage of what is considered as an integration of the simulation and practical implementation environment: (i) the code generated for the controller algorithm in simulation is directly portable to hardware as real time code and (ii) the power electronics device drivers and sensors form an interface

to the discrete controller which becomes transparent when looking at the simulated and actual system hardware.

## 6. CONTROL ALGORITHM CODE/HARDWARE IMPLEMENTATION ISSUES

Distinct stages of development were identified in the process of controller algorithm implementation on the EPHSC:

- (i) Development of the controller algorithm structure and generation of the associated real time code (section 5)
- (ii) Development of a base implementation platform on the EPHSC. This involved the generation of C routines specific to tasks such as interrupt handling, overrun detection, fault handling and interfacing to the actual power electronics hardware protection, calculation of rotor speed from the shaft encoder card signal and routines to accommodate the reading/writing from/to allocated memory addresses of inputs/outputs.
- (iii) The configuration of the EPHSC which involved the decision as to how many processors were required and the definition of the configuration file used when downloading the compiled executable code.
- (iv) Scheduling of the real time controller code.

Since this was the first C code controller algorithm implementation on the EPHSC most of the elements in (ii) had to be generated from scratch. Future work can now use these libraries immediately. Stages (iii) and (iv) were less distinct from one another. It was necessary to establish the execution times of the different controller algorithm routines in real time. Since such execution times are strongly data dependent, special auxiliary routines had to be written to provide random data as inputs to the arguments of the real time code routines. The data had to be representative of typical operating conditions so that data range limits were incorporated into the random data generation routine. The measured execution times then allowed decisions to be made as to the scheduling of the real time code and number of processors required to achieve the necessary sampling rates. For the purposes of implementing the final FOC algorithm on the CSI-fed SCIM two processors were found necessary. The rotor flux linkage model used the stationary reference frame which is inherently more computationally intensive than the synchronous reference frame model [5]; hence the need for two processors. The bonus was that the extra D/A outputs on the slave processor allowed online monitoring of controller variables. Fig. 3 shows the final distribution (see broken line) of the controller algorithm code based on measurements of sub-routine execution times.

## 7. SIMULATED AND MEASURED RESULTS

In order to confirm the correct operation of the drive development platform, simulated and measured results are shown in Fig.5 for a step speed response. The simulated and measured results show close correlation

and minor discrepancies are due to parameter inaccuracies. Note how *CASED* manages to simulate the full dynamics of the drive system so that at the design stage, issues such as filtering of switching noise can be addressed.

### 8. CONCLUSION

A drive system development platform aimed at integrating the simulation environment and practical implementation environment has been presented. The present state of the platform has proved to be an effective tool already providing accelerated implementation of new control concepts. Future work intends to address such issues as automatic scheduling and configuration of control algorithm real time code. It is hoped ultimately to produce a windows environment where standard icons representing certain control algorithm routine functions can be retrieved, linked up on the screen, simulated in *CASED* and then automatically scheduled, configured and downloaded to the EPHSC for practical implementation.

### 9. ACKNOWLEDGMENT

The authors gratefully acknowledge the financial support of the Foundation for Research Development (FRD) and the University of Natal in South Africa.

### 10. REFERENCES

- [1] dSPACE Product Brochures, dSPACE Inc., 26677 W. Twelve Mile Road, Southfield, MI 48034, USA.
- [2] UNAC A Real-Time System for analysis, design and implementation of advanced control, Product brochure, CICS Automation, PO Box 1, Callaghan NSW 2308, Australia.
- [3] G Diana, R G Harley, D R Woodward, D C Levy, "Implementing Field Oriented Control of a Voltage fed Current Regulated Induction Motor on a Single Transputer", *Conf. Rec. of IEEE IAS Annual Meeting*, Denver, Oct. 1994, pp 1771-1776.
- [4] M D McCulloch, C F Landy, W Levy, I MacLeod, "CASED: A simulation package designed for variable speed drives", *Technical article, Simulation* 57:4, Oct. 1991, Simulation Councils, Inc., ISSN 0037-5497/91, Printed in the USA, pp 216-226.
- [5] C E Kleinhans, G Diana, R G Harley, M McCulloch, M. Randelhoff, D.R. Woodward, "Analysing a CSI-Fed Field Oriented Controlled Induction Motor Using a New Simulation Package CASED", *Conference Proceedings of the IEEE Industrial Electronics Society, IECON*, 1994, Bologna, Italy, pp 192-197, paper ref. no. EP237P102.
- [6] "The INMOS ANSI C TOOLSET USER & REFERENCE MANUAL", *INMOS Ltd.*, 1990.

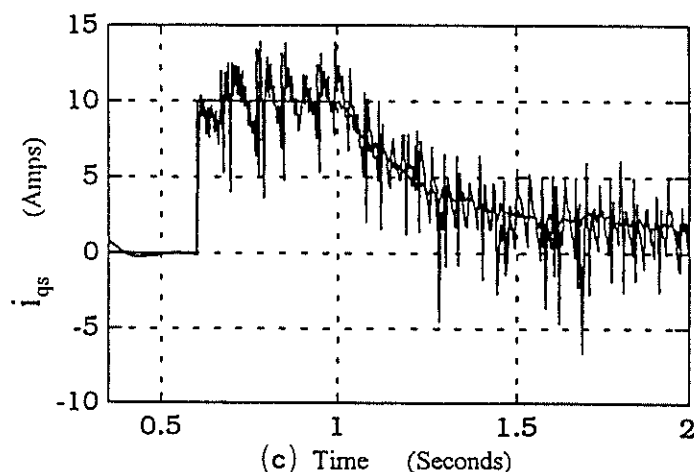
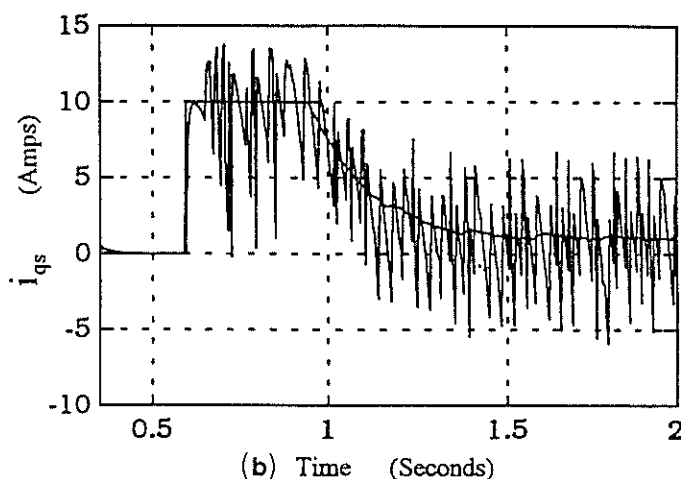
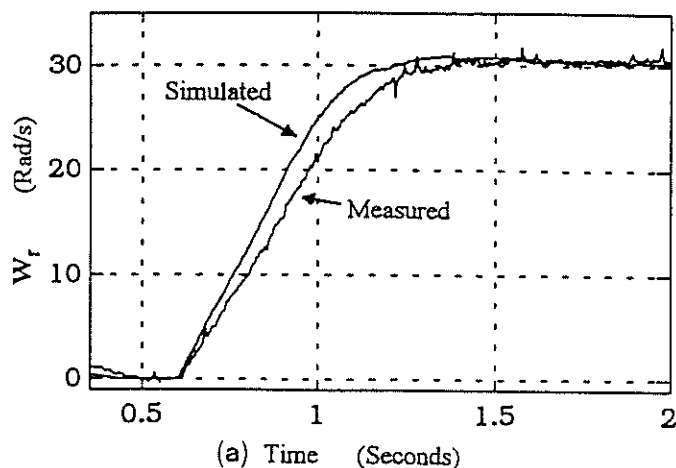


Fig.5 Simulated and measured speed step response  
 (a) Simulated/measured speed response  
 (b) Simulated q-axis current  $i_{qs}$   
 (c) Measured q-axis current  $i_{qs}$

# LINEAR INDUCTION MOTORS IN AUTOMATED MANUFACTURING SYSTEMS

J.F. Gieras  
University of Cape Town

## Abstract

The linear induction motor (LIM) can simplify many modern manufacturing processes. Typical applications include internal transport systems, transfer systems, impact machines (hammers, presses), piston pumps, linear tables, textile machinery, vibrators, rammers, saws, separators and many others. LIMs can be utilized for transfer systems in a wide variety of industries. Materials can be moved along horizontal planes, as well as rotated with LIMs. LIMs are suitable for use in linear tables and  $x - y$  tables for machine tools such as surface and cylindrical grinding machines, laser, flame and water-jet cutters, electron-beam, plasma-jet and laser welding machines. There is a lot of projects on the application of single-sided and double-sided LIMs to the textile industry. Single-sided LIMs can be used in separators of aluminum or other conductive metal pieces and separators of ferromagnetic particles. Other applications include strip tensioning of aluminium, hoisting machines, linear starters for large rotary motors and turboalternators, coal samplers, casting machines and many others. LIMs can operate as linear servo-motors in automatic control systems.

## 1 Introduction

A rotary induction motor can theoretically be replaced by a linear induction motor (LIM) in any translatory motion drives and in some cases in rotating wheels, discs and drums where small torques are transmitted and small friction forces take place. In practice, however, the range of applications of LIMs is limited by the increased temperature rise of the primary winding, increased energy consumption, reduced efficiency and reduced *output power-to-mass* and *output power-to-volume of active materials* ratio as compared with rotary induction motors. The causes of these disadvantages are the large airgap and

the open magnetic circuit producing parasitical effects.

*When designing a linear induction drive, it is always necessary to consider its benefits in comparison with traditional drives with rotary motors and mechanical gearboxes transferring rotary motion into translatory motion.* The wrong decision can lead to the wrong construction and, in effect, serious financial losses.

In this paper, the application of LIMs in factory automation systems is discussed (transportation and material handling systems, industrial drives, control systems, robotics, industrial and laboratory tests). The majority of the drives with LIMs that are described here are in practice competitive to electrical drives with rotary motors. Linear motors of all types can be available with controllers.

## 2 Factory transportation systems

In factory transportation systems, LIMs are used in material supply, mineral haulage, wagon booster-retarders, dry pipelines for the transportation of coal, ore, building materials, and agricultural products, in belt conveyors, hoists, and gantry cranes, in bakery and wafer transportation systems, in the transportation of bulk or granular materials, and heavy steel bars or blocks [4, 7].

High-speed gantry systems, which run at speeds of more than 0.25 m/s and need high rates of acceleration are well suited for linear motors.

Toshiba Corporation has developed a new electromagnetic suspension system with LIMs for transportation of materials in an environment which must be kept free from even microscopic dust particles or trifling noise [1]. The guideway, which is suspended from a ceiling or crossbeam of the building, is composed of ferromagnetic guide rails facing the hybrid

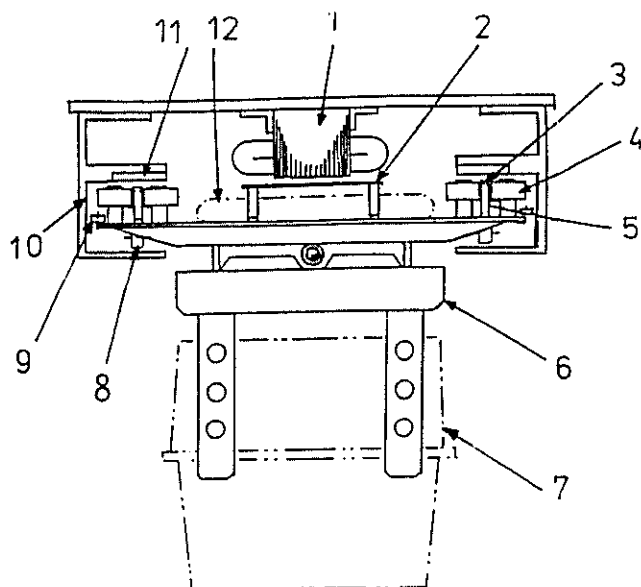


Figure 1: Magnetically levitated carrier system with a LIM: 1 — LIM primary, 2 — LIM reaction rail, 3 — gap sensor, 4 — electromagnet, 5 — permanent magnet, 6 — control circuit, 7 — load, 8 — auxiliary guide rail, 9 — auxiliary wheel, 10 — guide rail, 11 — ferromagnetic rail, 12 — battery (Courtesy of Toshiba Corporation, Japan).

magnets mounted on the vehicle and auxiliary emergency guide rails (Fig. 1). LIM primary cores facing the reaction plate attached to the top of the vehicle, inverters and controllers with optical sensors detecting the vehicle position and its cruising velocity are also installed in the guideway. The vehicle is equipped with four hybrid magnets, gap sensors, auxiliary wheels to support the vehicle in the case of unexpected troubles, and hooks for hanging the loads to be carried. The vehicle is also equipped with control circuits for calculating reference values for electromagnet coil currents, power amplifiers for exciting the electromagnets, Ni-Cd batteries used as the power supply, and copper reaction rails for a LIM.

### 3 Material handling

In certain material-handling applications using LIMs, the material itself is the secondary. In a stacker shown in Fig. 2 four rows of LIMs pick up metal blanks from the shear-discharge conveyor and move them to the piling zone [3]. The blanks are suspended in air by the balance of electromagnetic force pulling upward and the downward force of an air cushion between the blank and the LIM active surface. Holes in the

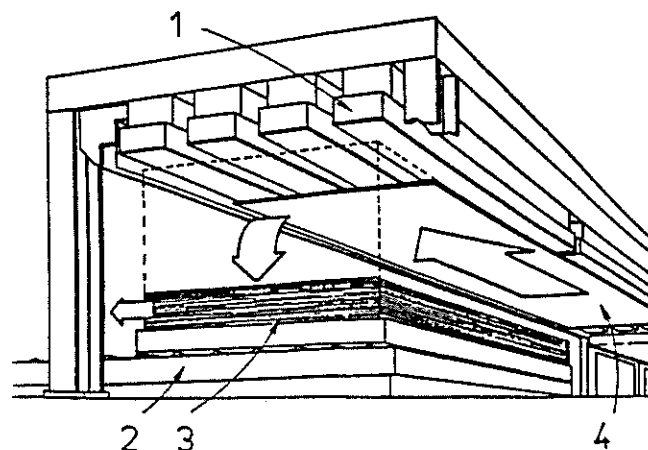


Figure 2: A novel stacker with LIMs: 1 — row of LIMs, 2 — roller conveyor, 3 — sheet-metal stack piling zone, 4 — sheet-metal blank.

bottom of a LIM segment produce an air cushion between the motor and the sheet metal. In an auto assembly plant, car body panels can be moved in a similar way. Metal panels are totally defect-free.

LIMs can be used in a wide variety of industries to design material handling systems. Materials can be moved along horizontal planes, as well as being rotated by the LIMs. For example, in an automatic stamping plant, a LIM system positions blanks accurately, then moves the blanks into and out of a stamping press.

### 4 Industrial drives

Typical applications of LIMs in factories and plants include transfer systems, machine tools, impact machines (hammers, rammers, presses, piston pumps), linear tables, textile machinery, vibrators, saws, separators, and many others.

LIMs are suitable for use in linear tables (Fig. 3) and in  $x-y$  tables for machine tools such as surface and cylindrical grinding machines, laser, flames and water-jet cutters, and electron-beam, plasma-jet, and laser welding machines. They offer long traverse ranges (up to 30 m), high travelling speeds (up to 3 m/s), high acceleration, and accurate positioning ( $\pm 0.005$  mm) using a vector control concept. In a laser machine tool LIMs drive the cutterblock in the  $x$ ,  $y$ , and  $z$  directions. The maximum velocity is 0.5 m/s, the maximum acceleration is  $30 \text{ m/s}^2$ , and the measuring system resolution is  $0.1 \mu\text{m}$ .

There are many projects on the application of single-sided and double-sided LIMs in the textile in-

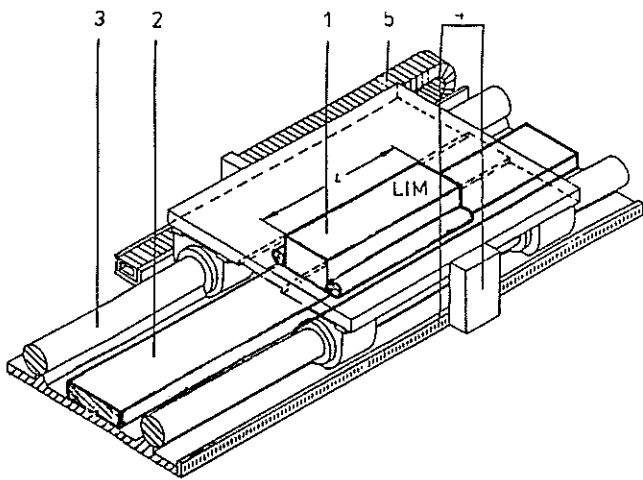


Figure 3: Linear table driven by a LIM: 1 — primary, 2 — reaction rail, 3 — guidance system, 4 — linear measuring system, 5 — cable. (Photo courtesy of Krauss-Maffei Automationstechnik GmbH, Germany.)

dustry, in particular to textile shuttle propulsion [2]. The advantages include (a) far less noise is produced than in mechanical 'picking', (b) higher shuttle velocity (more than 15 m/s), (c) more precise and stable flight of the shuttle, (d) better weaving quality. The gripper shuttle tows a thread from either side of the loom, with a single-sided LIM acting on the underside of the shuttle. The shuttle is accelerated over half the width of the loom and is braked either electromagnetically or mechanically when the shuttle enters the second LIM. Since the pole pitch is small, the shuttle velocity (about 20 m/s) requires an increased input frequency (a few hundred Hz). A shuttle of low mass is required. The overall efficiency of the drive is generally low, i.e. below 20%. Another disadvantage is the high temperature of the shuttle due to eddy current losses. LIM propulsion is recommended for large shuttles and large textile weaving widths.

Similarly to LIM-driven textile shuttles, disc saws for wood also operate at increased input frequency (400 Hz). A disc saw is propelled by a double-sided LIM.

Other industrial applications include separators, strip tensioning of aluminium, hoisting machines, coil winders, automatic reel systems, linear starters for large rotary motors and turboalternators, coal samplers, casting machines, flying cutters (for paper, glass, plastic, cloth, metal sheets, etc.), and many others [7].

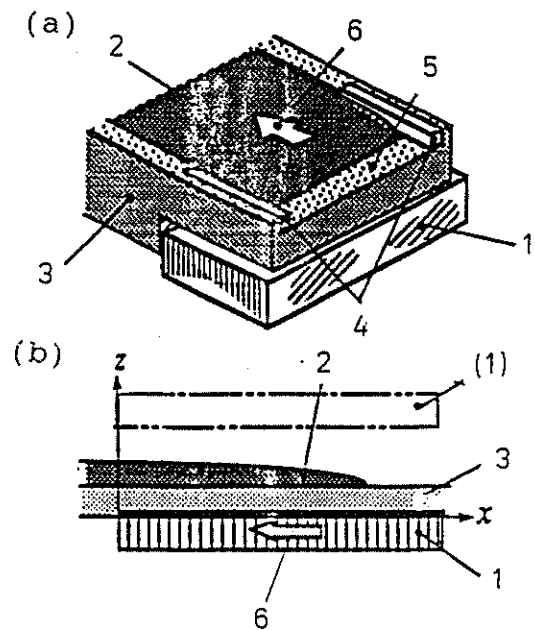


Figure 4: Molten tin controlled by a single-sided LIM: (a) configuration, (b) principle of operation. 1 — single-sided LIM, 2 — molten tin, 3 — heat insulator, 4 — side busbars, 5 — outlet fence, 6 — force produced by the LIM. (Courtesy of Prof. H. Yamada, Shinshu University, Japan).

## 5 Automotive control and robotics

Single-sided LIMs can be used for controlling the surface shape of molten metals in order to improve the float process of forming sheet glass [6] (Fig. 4). It is required to have the nonferromagnetic gap as large as possible to isolate heat flux between the LIM and molten metal. The LIM located under molten metal is superior to the upper one. As wide as 6-m primary stacks can be designed to control the surface shape of molten tin in a real float bath [6].

Flat and tubular LIMs can operate as linear servomotors in automotive control systems. Such LIMs require a special design and a controller to meet certain requirements. Because of the small thrust per mass and volume, LIMs are, in general, not satisfactory as servo-motors for industrial robots. Much smaller dimensions and higher thrust can be obtained using permanent magnet linear stepping motors.

An automatic sliding door with remote control can be easily designed using tubular LIMs [4]. This concept can also be implemented in the case of gates, shutters, valves, etc.

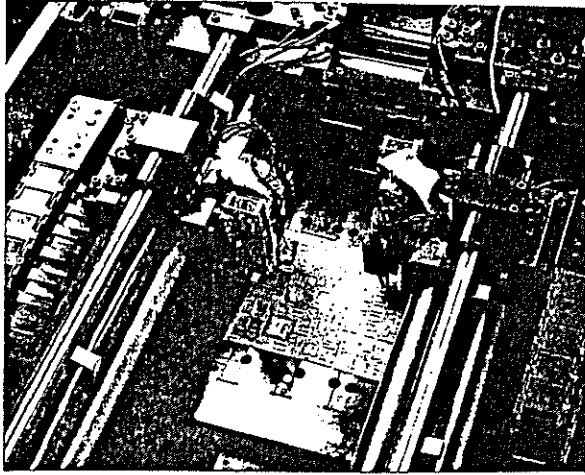


Figure 5: Linear probe with LIMs clear at each side. (Photo courtesy of Bath Scientific Ltd, Melksham, UK).

## 6 Industrial testing

To overcome the low speed drawback of using moving probes to test high density, double-sided substrates and printed circuit boards, tubular LIMs can be used to move probes between test nodes and a measurement system (Fig. 5).

Devices are required in car factories for high acceleration of car prototypes at short distances or for improved car designs. The accelerated car hits a wall in order to simulate traffic collisions. The best propulsion motor for such devices is a LIM [7].

Prior to construction of a ship, a small-scale model is built which can be tested in special pools. LIMs can be used to accelerate a model ship. A similar laboratory equipment can be built for measuring hydrodynamic forces.

LIMs can also be used in mixers, mills, in positioning control systems, in focusing optical instruments, and in the remote control of various mechanisms.

## Conclusion

The full capability of LIMs has only been recognized through recent advances in power electronics, microprocessors, programable logic controllers, digital signal processors, and electromagnetic field analysis software. In many industrial applications LIMs are competitive to rotary induction motors. *LIMs convert electrical energy directly into mechanical energy of translatory motion.* In factories and plants LIMs can be used in transportation systems, materials han-

dling, industrial drives, automatic control systems, robotics, and industrial testing. The application of LIMs is limited by the large airgap and parasitical end effects which deteriorate their performance. *When replacing rotary induction motors by LIMs, it is always necessary to consider the economical aspects.*

## Acknowledgements

This work was supported by the Foundation for Research Development (FRD), Eskom, and the UCT Research Committee, all of South Africa.

## References

- [1] Azukizawa, T., Morishita, M., Kanda, S., Tamura, N, and Yokoyama, T.: *A linear induction motor control system for magnetically levitated carrier system.* IEEE Trans. on Vehicular Technology, 38, (1989), No. 2, 102-108.
- [2] Bailey, A.R., and Edgar, J.P.: *The use of linear motor in textile shuttle propulsion.* IEE Conf. Publ. 120, 1974, 101-105.
- [3] Blease, I., Bhatia, R., and Pai, R.M.: *Applying linear motors in material handling.* Machine Design, 1989, January 26, 91-96.
- [4] Gieras, J.F.: *Linear induction drives.* Clarendon Press, Oxford, 1994.
- [5] Probes go when fixtures fear to tread. *Electronic Engineering*, 1991, November, pp. 61-62.
- [6] Sato, Y., Iga, M., and Yamada, H.: *Single-sided linear induction motor controlling the surface shape of molten tin.* IEEE Trans. on Magnetics, 28 (1992), No. 5. 3333-3335.
- [7] Yamada, H.: *Handbook of linear motor applications* (in Japanese). Kogyo Chosakai Publ. Co. Ltd., Tokyo, 1986.

# TRANSIENT ANALYSIS AND PERFORMANCE OF A SOLID STATE SERIES REACTANCE COMPENSATOR

B. S. Rigby and R. G. Harley

Department of Electrical Engineering, University of Natal, Durban, South Africa.

## ABSTRACT

This paper presents an analysis into the performance of a series capacitive compensator based on a voltage source inverter. Small signal analysis is used to illustrate how the controller gains affect the transient behaviour of the system. The results indicate that the converter based compensator could produce unstable resonances in a similar manner to conventional series capacitors

## INTRODUCTION

One of the traditional methods of increasing the steady state flow of power in a long transmission line has been to compensate for the inductance of the line by series installation of capacitor banks. However the extent to which a line can be compensated in this manner is often severely limited by concern for Subsynchronous Resonance (SSR), a dynamic instability which can arise in neighbouring generation plant due to L-C resonances in the line [4]. Furthermore, in order to ensure dynamic stability of the power system, the steady state flow of power, even with series compensation must often be far less than its theoretical maximum.

Studies have shown that if the magnitude of the series compensation can be continuously controlled (Controlled Series Capacitors or CSC) during transients, both of the aforementioned limitations may be overcome to some degree, allowing for operation of the power system closer to its theoretical limits [1]. With conventional capacitors, such fast continuous control of the degree of series compensation is not possible since it relies on the operation of circuit breakers. However with recent advances in high power semiconductors and new circuit topologies, power electronic solutions to these power system problems are becoming increasingly realizable.

Gyugi [2] first proposed the idea (shown in Fig. 1) that with suitable control, a voltage source inverter may inject an ac voltage into a transmission line in order to emulate the behaviour of a series capacitive reactance. The inverter is used to insert an rms phasor voltage  $V_c$  at its ac terminals in series with the transmission line in such a way that this voltage phasor lags the line current phasor  $I$  by 90 degrees. The amplitude of the voltage phasor  $V_c$  is controlled in order to be proportional to the amplitude of the line current phasor. Mathematically this can be represented by the phasor equation

$$V_c = k I e^{-j\frac{\pi}{2}} \quad (1)$$

such that the voltage injected by the inverter appears to the transmission line to be the volt drop across a capacitive reactance. Furthermore, by changing the constant of proportionality  $k$ , the degree of compensation can be continuously controlled. The solid state series compensator not only emulates a capacitor, but also has the potential to

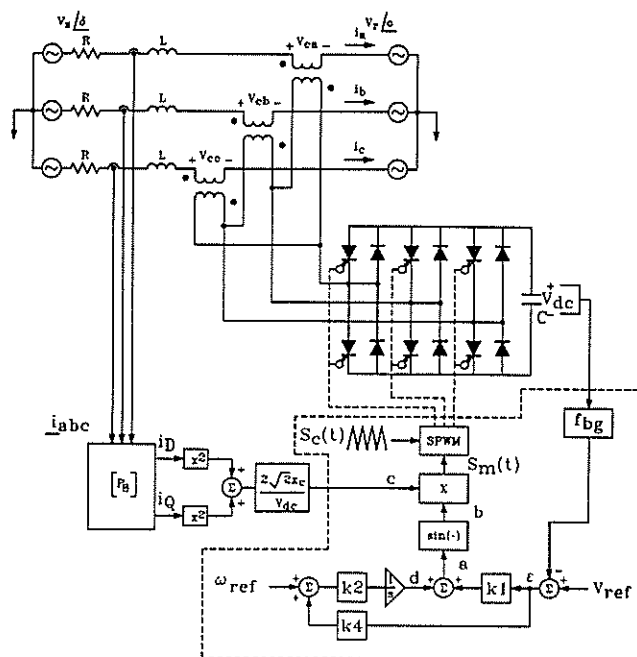


Fig. 1. Transmission line with Controlled Series Capacitance (CSC) based on Voltage Source PWM Inverter

avoid SSR, since with the correct control action the inverter injects only a voltage at the fundamental frequency and presents zero impedance at all other frequencies. The success of any practical scheme however depends upon the control strategy adopted to achieve the desired behaviour.

To date it has been successfully demonstrated that the desired series reactance property can indeed be realised, at least under steady state conditions, by suitable control of the voltage source inverter [7,8]. This paper presents the results of an analysis into the performance of a series capacitive compensator based on a voltage source inverter. The control scheme in Fig. 1 is a simple extension of the method proposed in [7]. The proposed scheme is analysed to determine firstly the effect of the controller gains on the transient behaviour of the system, and secondly to assess whether the control action has the potential to interact unfavourably with other power system elements.

## INVERTER CONTROL SCHEME

The neutral points of the sending and receiving ends of the three phase transmission line in Fig. 1 are grounded and the voltages  $V_s$  and  $V_r$  are separated by some transmission angle  $\delta$ . The transmission line currents  $i_a$ ,  $i_b$ ,  $i_c$  flow through the primaries of the series injection transformers and the secondaries of these transformers are connected in delta and supplied from the ac terminals of a six switch voltage source PWM inverter. The transformers inject in

series with the three phases of the transmission line, ac voltages  $v_{ca}$ ,  $v_{cb}$ ,  $v_{cc}$  to reproduce the effect of a capacitive reactance. The magnitude of these ac injected voltages produced by the inverter is directly proportional, at the fundamental frequency, to the magnitude of the modulating waveform  $S_m(t)$  and the voltage  $V_{dc}$  on the dc storage capacitor  $C$ . The switching intervals of the inverter are determined by the intersection of this modulating wave  $S_m(t)$  with the 1 kHz triangular carrier wave  $S_c(t)$ .

The part of the control scheme which ensures the reactive nature of the injected voltages (enclosed by the dotted box in Fig. 1) was proposed by Ooi et al [7,8]. The real power admitted to the inverter via the injection transformers charges the dc storage capacitor to some voltage  $V_{dc}$ . This dc voltage is fed back and subtracted from the reference voltage  $V_{ref}$  to form the error  $\epsilon$  which drives the voltage regulator loop. This error  $\epsilon$  is fed through proportional and integral gains, the output of which determines the angle fed to the  $\sin()$  function at point a in Fig. 1. The output of this  $\sin()$  block (point b in Fig. 1) forms the *template waveform* for the SPWM and can be described mathematically as

$$\sin [K_2 (\omega_{ref} + K_4 \epsilon) t + K_1 \epsilon] \quad (2)$$

where  $\epsilon = V_{ref} - f_{bg} V_{dc}$ . The error  $\epsilon$  then, directly controls the phase of the ac voltages injected by the inverter. If the inverter absorbs real power (from the line) at its ac terminals the voltage  $V_{dc}$  increases, thereby producing a negative error  $\epsilon$ ; on the other hand, if the inverter puts out real power at its ac terminals then the voltage  $V_{dc}$  decreases, which results in a positive error  $\epsilon$ . Thus when the error  $\epsilon$  is nulled, the inverter neither puts out nor absorbs real power, and thus the sinusoidal template waveform is of the required frequency and phase to yield the required reactive property of the injected voltage.

The template waveform at b is multiplied by a signal from c in Fig. 1. The magnitude of the signal at c determines the magnitude of the reactive voltage injected, and the polarity of the signal at c determines whether this reactive voltage is inductive or capacitive.

The transmission line currents  $i_a$ ,  $i_b$ ,  $i_c$  are sampled and passed through signal processing blocks in order to calculate the required signal at point c to provide a specified series capacitive reactance  $X_c$ ; the line currents are transformed into a synchronously rotating reference frame via the Park transform such that they become time invariant quantities  $i_D$  and  $i_Q$  at steady state, and this allows the rms value of line current and hence the required peak amplitude of the injected voltage to be determined directly.

### SYSTEM MODELLING

In order to model the system of Fig. 1 in detail, it is necessary to describe the discrete switching behaviour of the inverter. However such a detailed discrete time model of the system is not convenient for analysis of the closed loop stability properties of the controller and is not suitable for inclusion in the large order continuous time models typically used in power system stability studies. For such studies it has been shown that the system of Fig. 1 may be accurately represented by a continuous time equivalent model [5] of the form:

$$\dot{\underline{x}} = \underline{f}(\underline{x}, \underline{u})$$

$$\underline{y} = \underline{g}(\underline{x}, \underline{u}) \quad (3)$$

where  $\underline{f}$  and  $\underline{g}$  are non linear vector valued functions of the inputs  $\underline{u}$  and state variables  $\underline{x}$  [9]. Computer solution of equation (3) using numerical integration techniques then enables the transient behaviour of the system of Fig. 1 to be determined. In order to subject the system to classical dynamic analysis it is necessary to linearise the differential equations of equation (3) around the steady state operating point of the system to yield a state space model of the form:

$$\Delta \dot{\underline{x}} = [A] \Delta \underline{x} + [B] \Delta \underline{u}$$

$$\Delta \underline{y} = [C] \Delta \underline{x} + [D] \Delta \underline{u} \quad (4)$$

where  $\Delta \underline{x}$  and  $\Delta \underline{y}$  are small changes in the state vector  $\underline{x}$  and input vector  $\underline{u}$  from their steady state values  $\underline{x}_0$  and  $\underline{u}_0$  respectively. The location of the system's poles can be determined by calculation of the eigenvalues of the  $[A]$  matrix of equation (4), yielding insight into the effect of the controller gains on the system dynamics.

### IDENTIFYING SYSTEM DYNAMICS

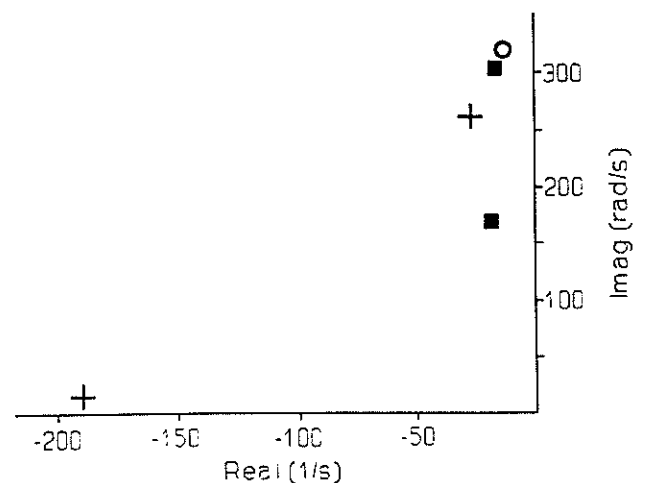


Fig. 2. The effect of controller gains on the location of the system poles

Fig. 2 shows the location of the poles of the system in Fig. 1 for different combinations of control gains. The circle in Fig. 2 shows the location of the *single pole* of the transmission system when the control is inactive ( $X_c = 0$ ). The position of this pole corresponds to that of the first order R-L transmission line with a frequency translation of 50 Hz. This frequency translation arises from the fact that the differential equations of the mathematical model are written in a synchronously rotating reference frame. The squares in Fig. 2 show the location of the system's poles once the control is set to provide a certain capacitive reactance ( $X_c = 8.59 \Omega$ ) for the combination of gains  $K_1 = 1.0$ ,  $K_4 = 50.0$ ,  $f_{bg} = 0.01$ .

With the introduction of the control action, the system has *two complex poles*: the pole associated with the transmission line at a damped natural frequency of approximately 310 rad/s and the pole associated with the controller dynamics at a damped natural frequency of

approximately 170 rad/s. The introduction of the controller thus has the effect of introducing higher order oscillatory dynamics into the first order transmission line: the response of the transmission line currents following a disturbance is now made up of a weighted sum of the responses due to these two complex poles. The effect of altering the controller gains is to shift the relative position of these two poles in the frequency domain, and hence change their individual contribution to the transient behaviour of the line currents. Theoretically then, it should be possible to position the pole associated with the controller sufficiently far into the left hand plane such that its effect on the transmission line currents is negligible.

The crosses in Fig. 2 show the location of the system poles corresponding to  $K1 = 1.74$ ,  $K4 = 5.0$ ,  $fbg = 0.1$ ; this combination ensures that the pole associated with the controller has a time constant equal to approximately one tenth of that of the pole associated with the transmission line.

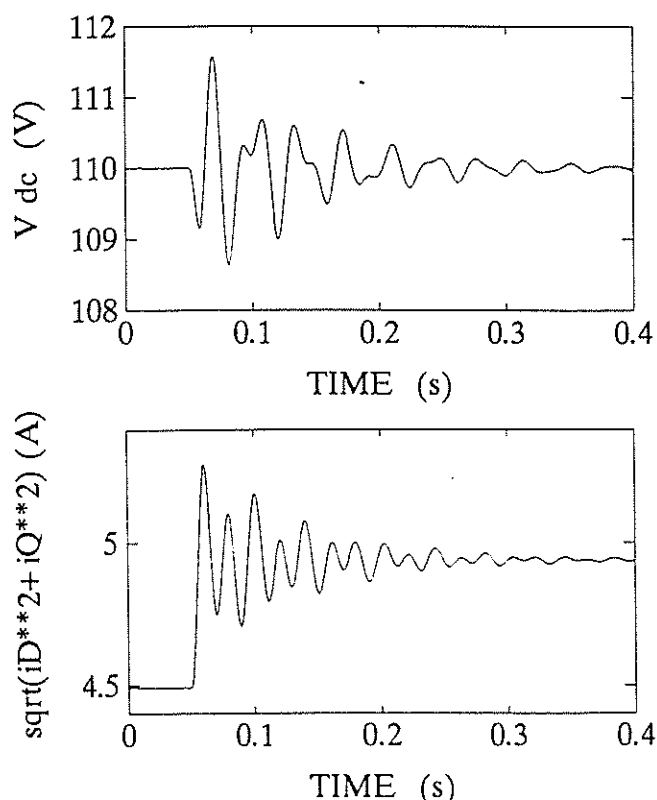


Fig. 3. Transient behaviour of the system with controller gains  $K1 = 1.0$ ,  $K4 = 50.0$ ,  $fbg = 0.01$

#### Transient Studies

The dynamic behaviour of the system derived from the small signal analysis in Fig. 2 is confirmed by time domain transient simulation of the full non linear continuous model of the system. Fig. 3 shows this transient response following a 10 percent increase in the magnitude of  $V_s$  and  $V_r$  for the combination of controller gains  $K1 = 1.0$ ,  $K4 = 50.0$ ,  $fbg = 0.01$  which correspond to the poles denoted by the squares in Fig. 2. The response of the capacitor voltage  $V_{dc}$  in Fig. 3 clearly shows a high order oscillation due to the contribution of both poles. Both frequency components are significant in the response since both poles are close to the imaginary axis in Fig. 2. The high order dynamics are also clearly evident in the transmission line currents.

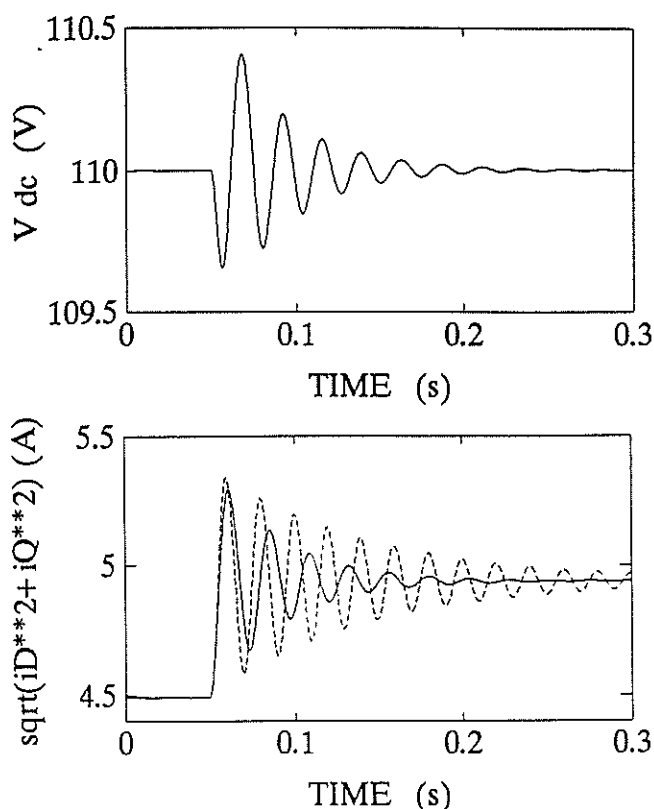


Fig. 4. Transient behaviour of the system with controller gains  $K1 = 1.74$ ,  $K4 = 5.0$ ,  $fbg = 0.1$

Fig. 4 shows the system response to the same disturbance as Fig. 3, for the combination of controller gains corresponding to the crosses in Fig. 2, and clearly shows that the responses of the capacitor voltage and the line currents are now predominantly second order in nature. Thus by positioning the pole associated with the controller sufficiently far into the left hand plane, it is possible to minimise the contribution of the controller pole to the dynamic behaviour of the line current. However Fig. 2 showed that in addition to the appearance of a second pole due to the introduction of the controller, the original pole corresponding to the transmission line is shifted from its position in the uncompensated system. This movement of the transmission line pole away from its position in the uncompensated system corresponds to a change in the natural frequency of the line as a result of the introduction of the compensator.

This change in frequency is evident in the current transient of Fig. 4, which is compared to the current response following an identical disturbance to a conventional R-L transmission line. This conventional transmission line has its inductive reactance  $X_L$  reduced to correspond to the compensated value  $X_L - X_c$  of the transmission line in Fig. 1. The uncompensated transmission line current (dashed curve) shows a 50 Hz transient which decays according to the line's R-L time constant, while the current transient of the controlled system (solid curve) decays more rapidly and at a lower frequency.

#### POWER SYSTEM RESONANCES

The results of Figs. 3 and 4 and other studies indicate that it is possible to identify the dynamics of the system of Fig. 1

and to design gains to minimise the contribution of the controller dynamics to the transient behaviour of the currents. However these studies have also indicated that the natural frequency of the transmission line is changed due to the introduction of the controller, and thus the system has the potential to have a detrimental effect on power system resonances. In order to investigate this possibility the linearised model is used further to determine the nature of the transfer function between the transmission line voltages and currents.

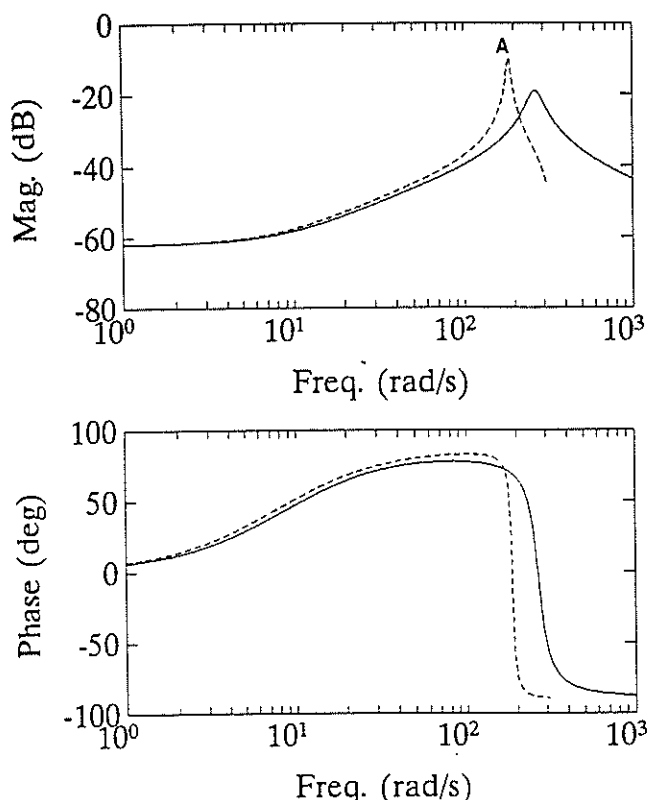


Fig. 5. Comparison of transfer function between  $\Delta v(s-r)D$  and  $\Delta i_D$  for CSC system and conventional capacitance

The solid curve of fig. 5 shows the magnitude and phase response of the linearised transfer function between the d-axis transmission line voltages and currents of the controlled capacitor system. The dashed curve shows the magnitude and phase response for the same line parameters, but with the compensation  $X_c$  provided by conventional capacitors; the result shows a sharp resonant peak at 186 rad/s (point A) which corresponds to the resonant frequency  $1/\sqrt{LC} = 128$  rad/s (20.4 Hz) of the line in the stationary abc reference frame. The solid curve shows that the line compensated with controlled series capacitance has no resonant peak at this frequency, but rather has a slightly more damped resonant peak at a frequency of 267 rad/s corresponding to a frequency of 47.7 rad/s (7.6 Hz) in the stationary abc frame.

The results of Fig. 5 indicate that although the introduction of controlled series capacitance (CSC) does not produce a classic LC resonance, the effect of the control results in a similar type of resonant peak at a subsynchronous frequency. The position of this resonant peak however depends on the choice of controller gains. Fig. 5 also indicates that the line currents and voltages at this resonant frequency are in phase as is the case with the LC resonance

phenomenon, and as a result it may be possible for the controlled series capacitance to excite subsynchronous oscillations elsewhere in the power system.

## CONCLUSION

This paper has presented an analysis of an advanced series compensator based on a voltage source inverter. Linearised analysis of the system has demonstrated the effect that the controller gains have on the transient behaviour of the system and shown that the controlled system could result in resonant behaviour similar to that found with conventional series capacitors.

## APPENDIX

$$\begin{aligned} V_s = V_r = 220 \text{ V} \quad \delta = 65^\circ \quad |S_c(t)| = \sqrt{2}^- \\ V_{dco} = 110 \text{ V} \quad V_{ref} = V_{dco}/fbg \quad \omega_{ref} = 10 \quad K2 = 31.42 \\ R = 1.49 \Omega \quad X_L = 51.55 \Omega \quad X_c = 8.59 \Omega \end{aligned}$$

## ACKNOWLEDGEMENTS

The authors gratefully acknowledge the financial support of the Foundation for Research Development and the University of Natal.

## REFERENCES

- [1] "Flexible AC Transmission Systems (FACTS): Scoping Study, Vol. 2, Part 1: Analytical Studies", EPRI Report EL-6943, Sept. 1991.
- [2] Gyugyi L, "Solid State Control of Electric Power in AC Transmission Systems", International Symposium on 'Electric Energy Conversion in Power Systems', Invited Paper, No. T-IP.4, Capri, Italy, 1989.
- [3] Gyugyi L, "Dynamic Compensation of AC Transmission Lines by Solid State Synchronous Voltage Sources", Proceedings of 1993 IEEE Power Engineering Summer Meeting, No. 93 SM 434-1 PWRD, Vancouver, Canada, July 1993.
- [4] IEEE Subsynchronous Resonance Working Group: "Reader's Guide to Subsynchronous Resonance", IEEE Transactions on Power Systems, Vol 7, No 1, Feb. 1992.
- [5] Rigby B S, Harley R G, "Initial Investigations into Converter Based Series Compensation", Proceedings of the Fourth Southern African Universities Power Engineering Conference SAUPEC, pp. 75-79, Cape Town, South Africa, January 1994.
- [6] Ooi B T and Wang X, "Voltage Angle Lock Loop Control of Boost Type PWM Converter for HVDC Application", IEEE Transactions on Power Electronics, Vol. 5, No. 4, April 1990.
- [7] Ooi B T, Dai S-Z and Wang X, "Solid-State Series Capacitive Reactance Compensators" IEEE Transactions on Power Delivery, Vol 7, No. 2, April 1990.
- [8] Wang X, Dai S-Z and Ooi B T, "A Series Capacitive Reactance Compensator Based on Voltage Source PWM Converter", IEEE IAS Conf. Rec., 1991, pp. 918-924.
- [9] Harley R G, Rigby B S and Jennings G D, "Design of a Controlled Converter which Emulates a Series Capacitive Compensator for Long Power Lines", Proceedings of the International Conference on Power Electronics and Motion Control PEMC'94, pp. 213-218, Warsaw, Poland, September 1994.

# A Development System for Automated Generation of Hard Real-Time Control Code for Motion Control Systems

M.C. Randelhoff, C.E. Kleinhans, R.G. Harley, D.C. Levy\*

Electrical Engineering, University of Natal, South Africa

\*Department of Electrical Engineering, University of Sydney, Australia

## ABSTRACT

A motion control development system (MCDS) has been developed at the University of Natal to allow control algorithms to be entered in block diagram form, which are then transformed to executable code. The intention is to allow the design engineer to produce real-time software that will run on the controller hardware with minimal use of programming. This paper briefly describes the software components of the MCDS.

Test code for a current source inverter (CSI) fed squirrel cage induction motor (SCIM) was implemented using the software tools of the MCDS. This paper demonstrates the correct operation of the MCDS by comparing simulated and measured results for the SCIM under field oriented control (FOC) coded by hand, and the results obtained by the code automatically generated using the MCDS.

## INTRODUCTION

High speed digital systems have provided the means to produce accurate, low cost AC machine controllers. These first became available with the advent of microprocessors in the late 70's. The major benefits have come as the power of the microprocessors has increased dramatically while the cost has diminished tenfold. The complexity of the newly applied control algorithms has matched the increased power of the microprocessor such that multiprocessor computing systems are increasingly being used. This has demanded that the motion control engineer should not only understand the control algorithms but also the structure of microprocessor systems and become skilled in programming them.

A Motion Control Research Group has existed in the Department of Electrical Engineering at the University of Natal since 1988 with the main objective of investigating and designing programmable software controllers for electronically controlled AC motors that would achieve the same high speed dynamic performance as equivalent DC motor systems. This group needed a flexible platform on which to develop software algorithms.

The MCDS allows control algorithms to be entered in block diagram form, which it then transforms to executable code, and places it on one or more microprocessors to achieve the computation performance necessary to meet specified controller sampling rates.

## THE MOTION CONTROL DEVELOPMENT SYSTEM (MCDS)

The software tools of the MCDS assist in the design of the hard real-time software for a transputer based motion control platform. The intention is to allow the design engineer to produce hard real-time software that will run on the controller hardware with a minimal use of programming. This requirement is addressed by the following tools (Figure 1):

- (1) a visual programming interface (VPI) which allows the design of control algorithms in a block diagram format;
- (2) a functions library that provides a collection of real-time software functions that are typically used in motion controllers, including blocks such as integrators, differential controllers and peripheral device drivers;
- (3) a function profiling program that determines the real-time behaviour of new library functions by analysis of the code. This program determines the worst case execution time of the function block;
- (4) a compile time scheduling and hardware optimisation program (MAST) that decides where and how to schedule code blocks for multiprocessor systems. This utility must permit multirate sampling systems;

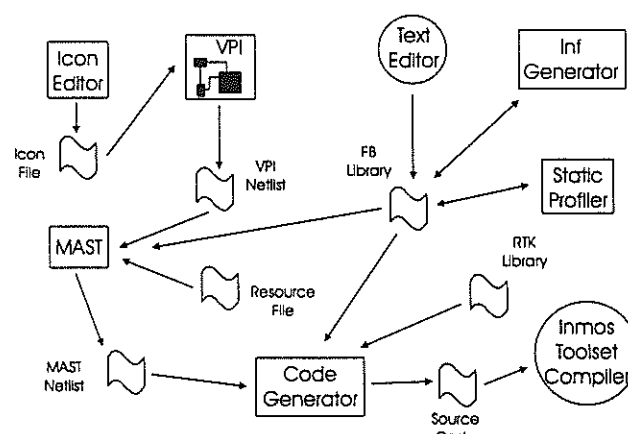


Figure 1: Motion control development system software

- (5) high level language program generator that produces C code for implementation on the transputer controller. The C code is compiled using a commercial compiler, and is loaded onto the controller using configuration and downloading tools;
- (6) there are other miscellaneous tools, including a network analyser that analyses the hardware components of the controller, and a crossbar configuration tool that connects the components.

### GENERATING THE CONTROL CODE FOR FOC OF A CSI-FED INDUCTION MOTOR

Control code was generated for a CSI-fed SCIM under *indirect* FOC. This control algorithm was investigated by another member of the research group at Natal [1], using a new simulation environment called CASED (Computer Analysis and Simulation of Electrical Drives). The "flux model" function block in Figure 2 (which describes the control algorithm) was executed at a significantly higher rate (both in the simulation and practical implementation) than the rest of the control algorithm; this was necessary to ensure that the rotor flux was calculated correctly. Kleinhans [2] found that the optimum calculation rate for the flux model was 5 kHz, while the rest of the algorithm was calculated at 1 kHz. The process of producing the controller code using the MCDS requires a number of phases, starting with the capturing of the control algorithm.

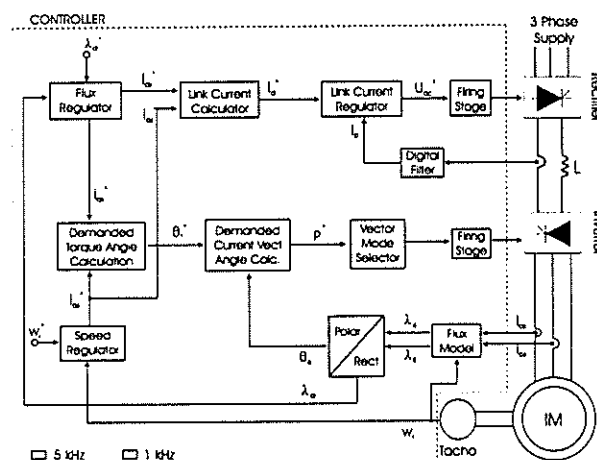


Figure 2 CSI-fed SCIM under FOC control block diagram

#### (a) Capturing the Control Algorithm Into the Visual Programming Interface (VPI)

The control block diagram illustrated in Figure 2 is captured into a format that can be used by the development system using the VPI. Figure 3 illustrates the VPI interface and the captured diagram for the CSI fed drive. There are several differences between the control block diagram and the VPI diagram since a schematic diagram such as that in Figure 2, omits a number of implementation details that are necessary

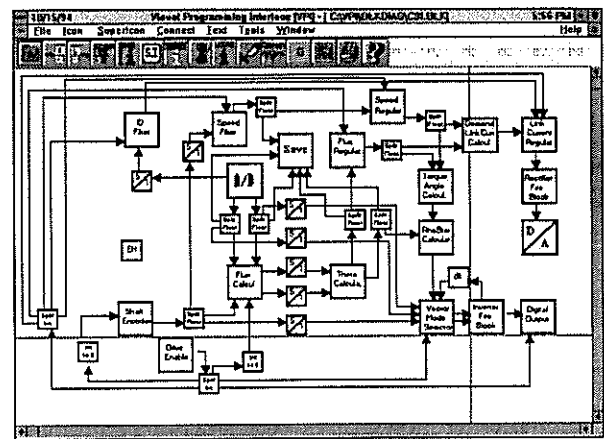


Figure 3 The control algorithm for the CSI-fed SCIM captured in the VPI

both for the manual and automated scheduling tool (MAST) and the code generator. The VPI diagram includes:

- (1) I/O devices which are necessary for the physical implementation;
- (2) information for MAST in order to schedule the flux model, the A/D and the shaft encoder to run at 5 kHz. The down and up-sampler blocks indicate relative sample rates (these blocks are indicated by "1/5" and "5/1" respectively);
- (3) splitter blocks which multiplex data streams are required in order to conform to the modelling requirements of the scheduler;
- (4) an Event Handler block which is required to tie the execution of the code to an external clock.

Once the blocks are connected an output netlist file is generated. This netlist is passed to the scheduling tool (MAST) so the function blocks can be allocated execution time.

#### (b) Profiling the Control Algorithm Function Blocks

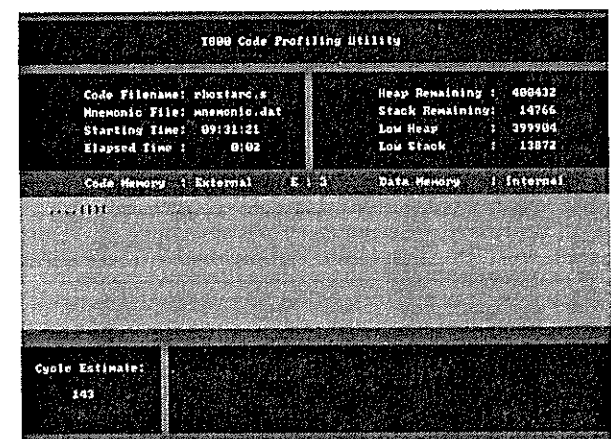


Figure 4 The Completed Profile of the Demanded Current Vector Angle Calculator

MAST requires the worst case execution times for all the controller function blocks in order to generate a schedule that guarantees the correct and timeous execution of the control code. The worst case execution time of each function block, for a particular processor (in this case the T800 transputer), is calculated in CPU cycles, using the Code Profiling tool (Figure 4). To ensure that a valid execution time is obtained, the content of the controller function blocks is restricted. Function blocks are not permitted to have run-time determined loops (such as *while* loops) or to engage in interprocessor communication.

### (c) Scheduling the Controller Code using MAST

The manual and automatic scheduling tool (MAST) (Figure 5) generates an execution profile for the controller code at compile time. MAST requires the output netlist of the visual programming interface (VPI), the available controller hardware, and the worst case execution times for each of the function blocks.

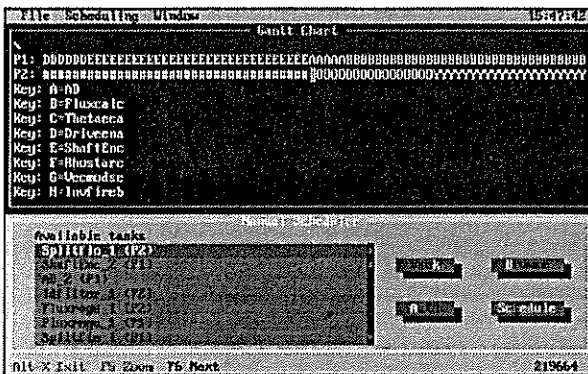


Figure 5 The MAST user interface implementing the CSI-fed FOC algorithm

Mast calculates a static schedule for an algorithm automatically, but it is also interactive and permits intervention when the user discerns that a more effective schedule can be obtained by alternative function placements. The MAST output netlist is used by the code generation tool to produce the controller code.

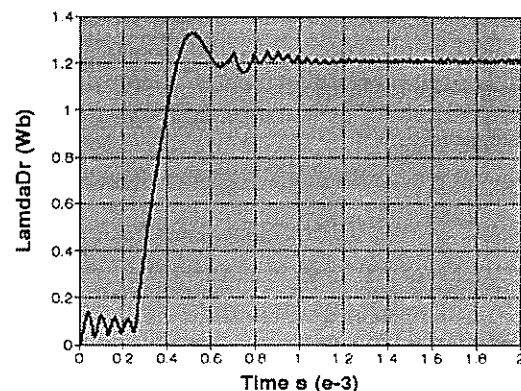
### (d) Generating the Controller Code

The code generator produces high level C source code, based upon the output netlist of the scheduling tool and the source code of the controller function blocks. In multi-processor systems a C program is generated for each of the processors. These processors communicate through calls to communication functions, which pass the data from one processor to another. The generator produces *link* files for each of the programs, a *configuration* file which is required by the C compiler for multiprocessor configurations, and a *makefile* which invokes the high level compiler. The MCDS uses the Inmos ANSI C toolset to compile, link and configure the C source code for the controller. Once the compilation process is complete then the controller code is downloaded onto the transputer network for execution.

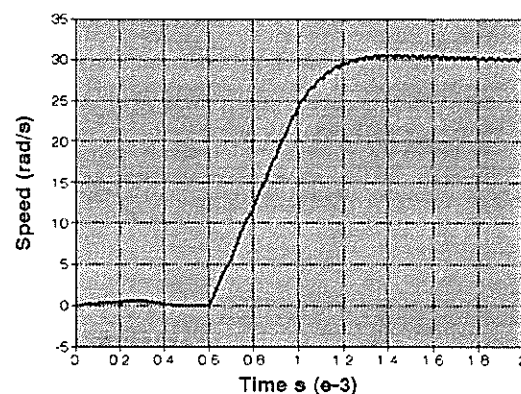
## RESULTS

To prove that this code executes correctly, it is necessary to show that the FOC algorithm, implemented by the MCDS, responds in the same manner as the FOC algorithm implemented using control code that was written manually. Furthermore, it is necessary to show that these results are expected, as a consequence of understanding the basic theory of FOC, and that they are similar to those results obtained from the simulation of a CSI fed SCIM.

The graphs shown in Figures 6-8 reflect the response of the CSI-fed IM under control of the algorithm depicted in Figure 2, to a step change in the commanded speed ( $\omega_r^*$ ). The data for all the graphs in this section was stored in memory during the first two seconds of execution of the control algorithm, after which it was written to disk. Figure 6(a) plots the simulated machine speed ( $\omega_r$ ), while Figure 6(b) depicts the simulated flux linkage ( $\lambda_{dr}$ ) for the same step in commanded speed.



(a)

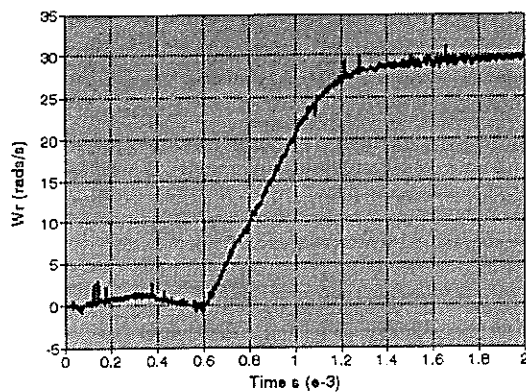


(b)

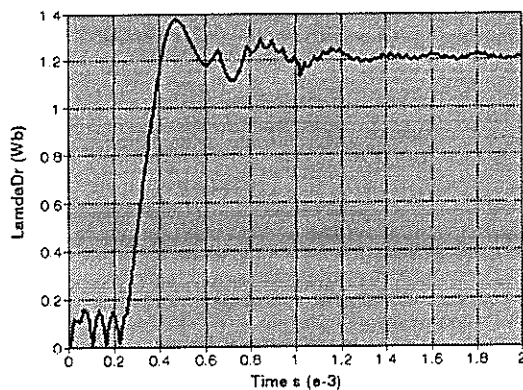
Figure 6 Simulated response of a CSI FOC induction motor to a step command in speed

A number of other state variables of the control algorithm could be graphed to illustrate that the system is operating correctly, but the graphs shown are

considered sufficient since it is not the object of this paper to be a treatise on CSI-fed FOC of IM.



(a)



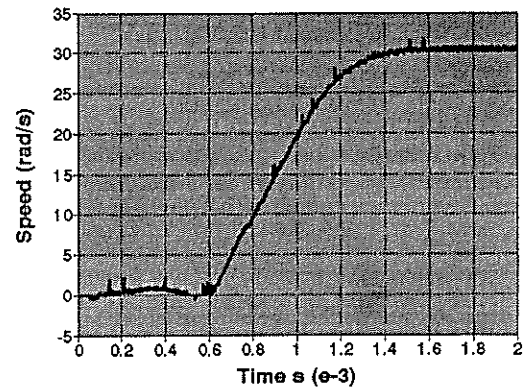
(b)

Figure 7 Measured response of a CSI FOC induction motor to a step command in speed. Controller code automatically generated

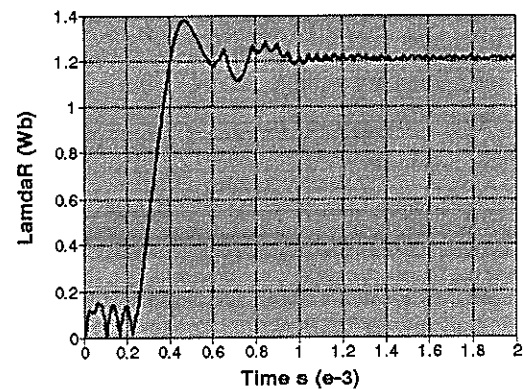
The state variables graphed for the simulation in Figure 6, are graphed in Figure 7 for the controller code generated automatically by the MCDS. The data was captured for the same duration as for the simulation (2 seconds).

The close correlation between the measured responses in Figure 7 of the automatically generated controller code, and that of the responses in the CASED simulation is indicative of the fact that the FOC algorithm for the induction motor is operating correctly. It remains to be shown that the automatically generated code produces results similar to those obtained by writing controller code manually. The results for the manually generated code are documented in Figure 8. Figure 7(a) and Figure 8(a) depict the actual speed responses of the induction machine. The minor differences between the plots in Figures 6, 7 and 8 can be ascribed to limited tachometer resolution, noise in the transmission line and in the device driver board of the transputer controller, and more significantly machine parameter inaccuracies. Figure 7(b) and Figure 8(b) depict the actual flux linkages of the induction machine. As in the case of the speed responses

there are differences between the two plots depicting the flux linkages and these can also be ascribed to noise.



(a)



(b)

Figure 8 Measured response of a CSI FOC induction motor to a step command in speed. Controller code manually generated

## CONCLUSION

The speed step response for the CSI-fed induction machine under FOC correlate closely for simulation, handwritten and automatically generated code. The small differences that exist in the results of the automatically and hand written code can be ascribed to mainly to system parameter inaccuracies and does not affect the validity of the code.

## REFERENCES

- [1] Kleinhans C, Diana G, Harley R, McCulloch M, Randelhoff M, Woodward D, "Analysing a CSI-Fed Field Oriented Controlled Induction Motor Using a New Simulation Package CASED", *Conference Proceedings of the IEEE Industrial Electronics Society, IECON*, 1994, Bologna, Italy, paper ref. No EP237P102.
- [2] Kleinhans C, Diana G, Harley R, McCulloch M, "The Application of CASED as a Simulation Tool for the Design and Analysis of Variable Speed Drives", *Conference Proceedings of the IEEE Industrial Applications Society Annual Meeting, IAS*, 1994, Denver, Colorado, pp 750-757.

# LOAD CURTAILMENT COST MODELLING OF ELECTRICAL ARC FURNACES IN AN INTEGRATED STEEL PLANT

F.G.T. Radloff, I.E. Lane

Centre for New Electricity Studies University of Pretoria

**Abstract:** - This paper proposes a method of calculating the cost of unserved energy to the customer as a result of load curtailment. The calculation is done by using a generalised model which is non process specific. Finally it is shown how this information may be used to help optimise the maximum demand setpoint.

## 1. INTRODUCTION

Large integrated steel plants usually have a maximum demand controller to limit the demand of the plant to an economic level. Since the electrical arc furnaces are large consumers of electricity in these plants and because they can be easily controlled, they are frequently targeted for maximum demand control purposes.

To accurately determine the optimum level of maximum demand setpoint, the cost of curtailment needs to be known. Previous studies have been done to develop so-called "customer damage functions" [1],[2],[3]. These strategies rely heavily on general indexes, customer response, and surveys performed to evaluate the cost to the customer.

This study aims to provide a simple way of modelling the complex relationship between furnace stoppages and the cost implications this can have on the rest of the plant. This is done without incorporating customer perceptions, which may be distorted.

## 2. PLANT LAYOUT

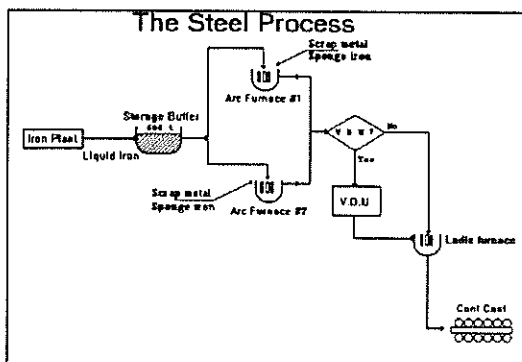


Figure 1

The steel plant considered has two electrical arc furnaces and a continuous caster. The plant also has a liquid iron plant which helps to supply the furnaces with raw material.

Due to the stochastic nature of the furnace operation it is practically impossible to continually match the production of the furnaces to the requirements of the continuous caster. Correspondingly a buffer (ton-dish) is required between the furnaces and the continuous caster to prevent stop-start operation.

Curtailling the furnaces (through maximum demand control) reduces the production rate (tons/hour) of the

furnaces (see section 5.2). If this happens the continuous caster might be interrupted due to lack of steel, which in turn reduces the production rate of the whole plant.

## 3. ELECTRICITY PRICING

### 3.1. Previous (old) tariff

The old tariff employed at the steel plant was a two-part tariff system having the following characteristics:

1. Energy was priced at a fixed rate which was not related to the time of day.
2. Demand charge was priced fairly high and amounted to nearly 50% of the electricity bill. Two time-slots were introduced. A so-called day tariff and night tariff. Demand was discounted during the night-tariff periods (30 MW increase in demand at no extra cost).

### 3.2. New (time differentiated) tariff

The steel plant was placed on a time-differentiated tariff sometime during the course of 1994. This tariff structure is similar to the Eskom T1 tariff employed widely throughout South-Africa:

1. A time differentiated energy charge applies, three different time-periods are identified (Eskom T1).
2. The demand charge (R/KW) is considerably lower. In addition, the steel plant pays only for that value of demand it contributes to the host city's monthly demand peak.

The result of pricing demand in this way is that the steel plant aims to have the inverse of the city profile (high during city lows and vice versa).

## 4. REQUIREMENTS OF THE MODEL

The model should be able to:

- Give operators an indication of the production which is possible under a chosen setpoint profile.
- Give an indication of the number of hours the furnaces will be interrupted.
- Use the setpoint profile as input and give the cost of unserved energy as output.
- Give an indication of the savings which result from a chosen setpoint profile.
- Be easily maintainable and adaptable to variations in operating pattern.

## 5. GENERALISED MODEL

Due to the large number of variables involved, the complex non-linear relationship between these and the stochastic nature of the steel making process, an exhaustive analytical approach was not favoured.

Instead a more general model, capable of being used in a number of other fields, was developed.

### 5.1. Cost components

A simplified representation of an industry and the different cost elements associated with production is shown in Figure 2.

Material cost is the cost of the raw materials used.

The energy needed for production may be supplied by different sources. In the case of steelmaking, energy is usually supplied via electricity, coal and oxygen [5],[6],[11].

Consumables refer to any material which experiences wear and consequently needs to be replaced regularly.

No production process is ideal and consequently has losses. The afore-mentioned costs may be collectively grouped as variable cost.

In addition to the variable cost, any industry has fixed costs. Examples include salaries, interest on capital, rent of equipment or premises, etc.

The price of the final product is subsequently composed of a variable cost component, a fixed cost component and a profit component.

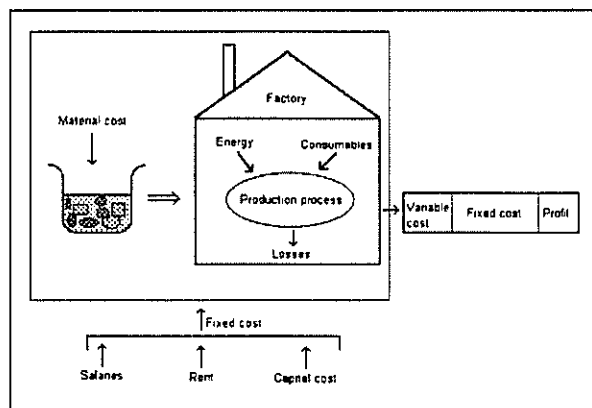


Figure 2

### 5.2. Production vs. demand setpoint

To manufacture a certain product (like a ton of steel) a fixed amount of energy is required. Mathematically this may be modelled as  $E = k \cdot S$

Where:

$E$  = Energy

$k$  = Constant

$S$  = Production output.

Since power is the rate of energy consumption, it follows that power can be related to the rate of production in the following way:

$$P = \frac{k \cdot S}{t} \text{ thus } P \propto \frac{S}{t}.$$

It becomes clear that the demand setpoint places an *upper limit* on the production rate possible. The efficiency of operators, the down-time caused by

breakdowns, etc. all contribute to a lower product throughput.

One way of incorporating the effect of random factors such as these, is to use stochastic modelling to obtain a relationship between demand setpoint and production throughput [8],[9],[10].

An alternative method is to obtain actual data of production vs. demand setpoint. An average value of production vs. setpoint, for every setpoint should be obtained. The intricacies of the production process are conveniently hidden. This may be desirable in many cases, since the process may be difficult to model and could needlessly complicate modelling the cost of unserved energy.

### 5.3. Cost of curtailment

Curtailment resulting in production loss, is more expensive than curtailment without production loss. A summary of the cost and savings due to curtailment is shown in Table 1.

Table 1

SAVINGS		COST
	TARGET MET	
• demand charge		• Energy • Consumables
	TARGET NOT MET	
• Demand charge • Variable cost • Energy		• Energy • Consumables • Profit • Fixed cost

Based on the table and discussion above, a model giving the savings and cost due to curtailment may be constructed.

#### COST MODEL:

IF  $P_P \geq P_T$  THEN:

$$\text{CUE} = (K_{\text{Loss}}) \cdot (ht) \cdot (\text{Energy cost}) + (K_{\text{Cons}}) \cdot (ht) \cdot (\text{Consumable cost})$$

IF  $P_P \leq P_T$  THEN:

$$\begin{aligned} \text{CUE} = & (K_{\text{Loss}}) \cdot (ht) \cdot (\text{Energy cost}) + \\ & (K_{\text{Cons}}) \cdot (ht) \cdot (\text{Consumable cost}) + \\ & \left( \frac{\text{Fixed cost}}{\text{Unit}} \right) \cdot (\text{Units not produced}) + \\ & \left( \frac{\text{Profit}}{\text{Unit}} \right) \cdot (\text{Units not produced}) \end{aligned}$$

#### WHERE:

$P_T$  = Production target.

PP = Predicted production target.

ht = Total number of hours curtailed (expected).

CUE = Cost of unserved energy

Kloss = The rate at which the process loses energy.

KCons = The rate of consumable consumption.

#### SAVINGS MODEL:

IF  $P_P \geq P_T$  THEN:

$$\text{Saving} = (\text{Demand reduction}) \cdot (\text{Demand charge})$$

IF  $P_P \leq P_T$  THEN:

$$\begin{aligned} \text{Saving} = & (\text{Demand reduction}) \cdot (\text{Demand charge}) + \\ & \left( \frac{\text{Variable cost}}{\text{Unit}} \right) \cdot (\text{Units not produced}) + \\ & \left( \frac{\text{Energy cost}}{\text{Unit}} \right) \cdot (\text{Units not produced}) \end{aligned}$$

Comparing the cost of unserved energy to the savings, yields the required optimum economic setpoint for the maximum demand controller.

## 6. CUSTOMISED MODEL

Due to the complex interaction between the various factors described in section 2, an averaged-based approach was favoured, since the best effort of analytically modelling the plant behaviour to date [6], proves to be mathematically very involved and only  $\pm 60\%$  accurate.

### 6.1. Assumptions (operating conditions)

The values of production rate vs. setpoint obtained, apply to a certain type of operating pattern. The nature of this operating pattern is briefly outlined:

1. A constant ratio of liquid iron vs. scrap is loaded into the furnaces for each melt.
2. A constant amount of oxygen is blown into the furnaces during each melt
3. The primary objective of the furnaces is to melt the steel. Refinement and quality assurance is done at the vacuum degassing unit.
4. The rate of refractory and electrode consumption is constant.
5. The rate of heat loss when a furnace is curtailed, is constant.

### 6.2. Incorporating process specific constants

An average production rate in tons/hour was determined for each value of maximum demand setpoint. A representation of the production rate vs. setpoint is given in Figure 3.

A marked drop-off in production throughput can be observed below 90 MW. This is caused by the forced staggering of furnaces below 90 MW.

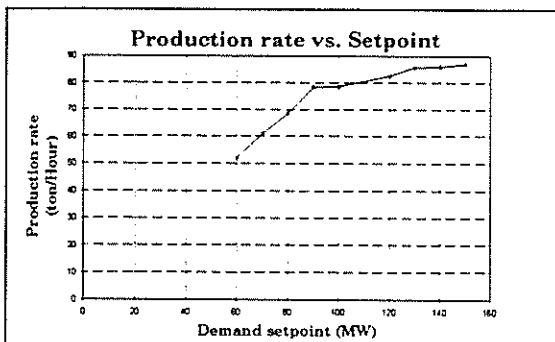


Figure 3

Figure 4 and Figure 5 present the results of the simulation under the old tariff structure (two step setpoint profile - day/night).

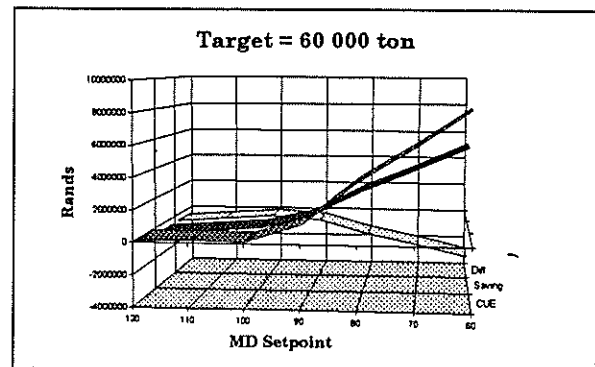


Figure 4

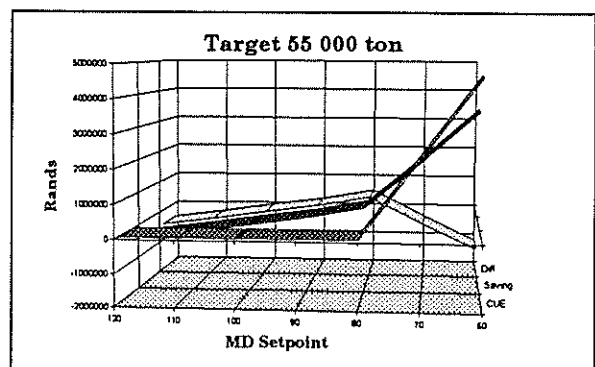


Figure 5

Figure 6 and Figure 7 give the results of the simulation using a multi-step setpoint profile possible under the new tariff.

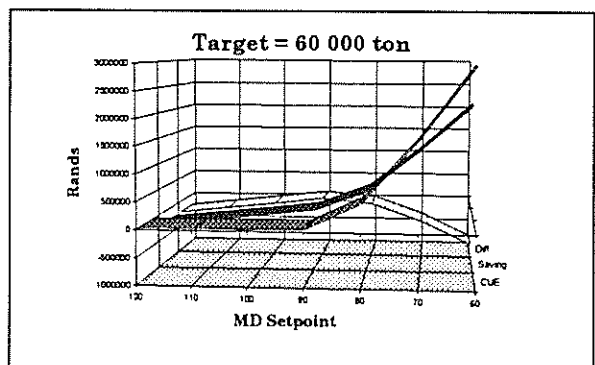


Figure 6

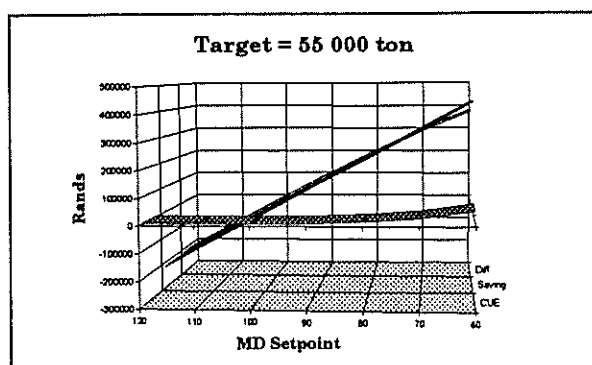


Figure 7

## 7. DISCUSSION OF THE RESULTS

### 7.1. Accuracy and suitability of the model

The accuracy of the model was tested by comparing the production predicted by the model to the actual production at the plant. A two-week period during which no major breakdowns were experienced, was considered. The predicted production was found to be 29 252 tons. This compared favourably with the 29 550 tons of actual production during this period (accuracy of 98 %).

One of the major advantages of this model is its simplicity and the ease with which this model may be applied to other plants and processes.

Unfortunately this simplicity also gives rise to one of the major shortcomings of the model, namely that changes in the production or operating pattern can only be accurately evaluated after the event (typically at the end of the month).

Until a better understanding of the steel-making process and the various factors influencing this process is gained, this type of approach is recommended to model the cost of unserved energy to the customer.

### 7.2. Interpretation of results

A production target of 60 000 ton (Figure 4) is close to the maximum capacity of the plant. Consequently there is very little opportunity to save money by reducing demand. An optimum setpoint seems to be 100 MW (100 MW in day-time and 130 MW during night-time). At this level the savings due to demand reduction are zero and the cost of unserved energy is also zero (the best case).

Figure 5 shows how the situation changes when the production target is lowered to 55 000 tons and spare capacity becomes available. The optimum setpoint is now 80 MW (day-time), which represents a monthly saving of R 531 866.00. Beyond this point the cost of unserved energy increases dramatically due to reduced production and overshadows the savings possible.

Figure 6 shows that a setpoint of 90 MW (billing setpoint) is the optimum under the new tariff. The reduction of 10 MW represents a monthly saving of R

108 000.00. In addition the overall city-setpoint will be reduced by 10 MW. This is a good example of a win-win situation created between a supplier and consumer through the use of innovative pricing of electricity.

Figure 7 reflects a production target of 55 000 ton. The huge advantage provided by the new tariff can be clearly seen. Even at a setpoint of 60 MW the savings are still substantially larger than the associated cost.

## 8. CONCLUSION

The model presented can be a valuable tool to help industries in their efforts to optimise their MD setpoints.

More research in this field is required to help refine and improve the generalised model suggested here.

Additional research is needed to establish process specific models for the integrated steel plant considered. These (more detailed) models may be used to investigate aspects such as overall energy balance optimisation (electricity, coal and oxygen), and process scheduling to increase availability of the furnaces.

## 9. REFERENCES

- [1] Wacker, R. Billinton, "Customer costs of electric service interruptions." Proceedings of the IEEE, vol. 77, no. 6, June 1989.
- [2] Subramaniam, R. Billinton, G. Wacker, "Factors affecting the development of an industrial customer damage function", IEEE Trans. Power App. Syst., vol.104, pp.3209-3215, 1985.
- [3] Billinton, G. Wacker, R.K. Subramaniam, "Factors affecting the development of a commercial customer damage function", IEEE Trans. Power App. Syst., vol.1, pp.28-33, 1986.
- [4] F.C. Schweppe; M.C. Caramanis; R.D. Tabors; R.E. Bohn; "Spot Pricing of Electricity"; Kluwer Academic Publishers 1988.
- [5] T.B. Johansson; B. Bodlund; R.H. Williams; "Electricity: Efficient End-Use and New Generation Technologies, and their Planning Implications"
- [6] B.J. de Vos, "Optimisation of Raw Material Addition for an Oxygen-blowing Arc Furnace". Faculty of Industrial Engineering, University of Pretoria, 1993.
- [7] C.R. Taylor and C.C. Custer, "Electric Furnace Steelmaking", Iron and Steel Society (USA), 1985.
- [8] F.D. Galiana, E. Handschin, A.R. Fiechter, "Identification of Stochastic Electric Load Models from Physical Data", IEEE Trans. on Automatic Control, Vol. ac 19 No. 6 Dec. 1974.
- [9] C. Alvarez, R.P. Malhame, A. Gabaldon, "A Class of Models for Load Management Application and Evaluation Revisited", IEEE Trans. on Power Systems, Vol. 7 No. 4, Nov. 1992.
- [10] Y. Manichaikul, F.C. Schweppe, "Physically Based Industrial Electric Load", IEEE Trans. on Power Apparatus and Systems, Vol. PAS-98, No. 4 July/Aug. 1979.
- [11] K-H. Klein, G. Paul, "Reflections on the Possibilities of Cost Savings in Electric Arc Furnace Steel Production", I&SM-25, January 1989.
- [12] A.P. Sanghvi, "Measurement and Application of Customer Interruption Costs/Value of Service for Cost-Benefit Reliability Evaluation: Some Commonly Raised Issues", IEEE Trans. on Power Systems, Vol. 5, No. 4, Nov. 1990.

### Authors:

Mr. F.G.T. (Gustav) Radloff, Prof. I.E. (Ian) Lane.  
Centre for New Electricity Studies, Electrical and Electronic Engineering, University of Pretoria.

# THE ROLE THAT LOAD ANALYSIS OF ELECTRICAL ARC FURNACES HAS TO PLAY IN A STEEL PLANT

M M Ferreira, I E Lane  
Potchefstroom University for C.H.E. & University of Pretoria

## ABSTRACT.

A probabilistic analysis of joint demand density of electric arc furnaces and the rest of the plant load reveals a wide variation when both loads are statistically independent. Simulations of perfect complimentary scheduling and of complimentary maintenance scheduling indicate that the maximum demand setpoint can be set substantially lower due to the narrower load variation without loss of production when such complimentary scheduling is applied. The plant implemented complimentary maintenance scheduling and realised very significant savings of their electricity demand charge account. These savings were achieved because load analysis helped to identify the cause of unacceptably high plant load variation.

## 1. INTRODUCTION.

In an integrated steelworks which is billed on a two-part tariff (tariff E) and a single point-of-supply basis, it is necessary to understand the nature and interaction of major end-use components of load, to minimise electricity cost.

In the integrated steelworks under study, major end-use components of load have been classified as:

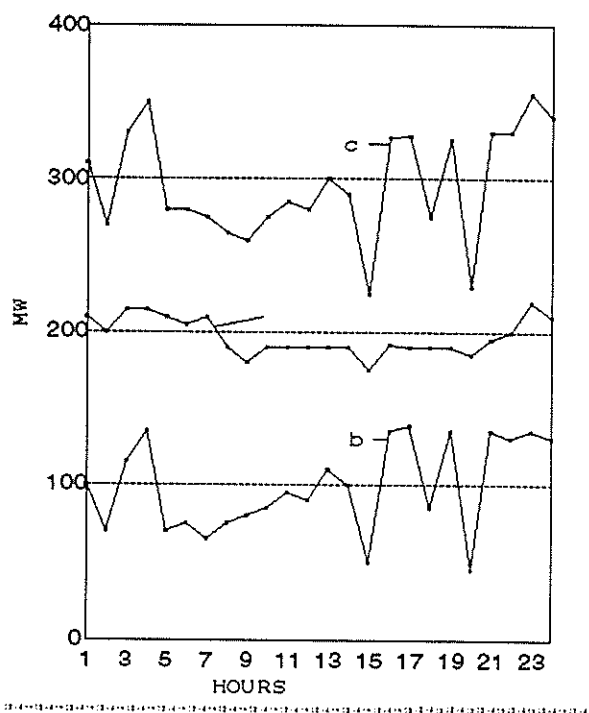
- i. electric furnaces
- ii. steel processing

Figure 1 reveals the characteristic make-up of the system (total) load for the integrated steelworks, disaggregated into the two major components. From figure 1 it can be seen that steel processing (component a) is primarily contributing to the load level and behaves like a base load with a good load factor. The electric furnaces (component b) on the other hand, have more variability in the load, and are the most significant contributor to the shape of the load profile (c).

The random variations in system load during the weekday hours from 07h00 to 23h00 must be analysed to establish the potential for electricity cost savings in the demand charges. This paper focuses on the potential demand charge saving through maintenance scheduling of the electrical arc furnaces.

## 2. MAINTENANCE SCHEDULING AND ELECTRICITY COST.

The monthly demand density plots in figure 2 are plotted for the hours during which demand charges are applicable under tariff E. The average demand is also shown for each weekday. Fridays are the highest and Mondays second highest. The bunching of hours close to the maximum demand on Fridays and Mondays is evident from figure 2. For a typical month it was found that 66% of the total outage time due to load curtailment on the furnaces occurred on Friday. Both the electric furnaces and other steelwork process plants prefer not to perform planned maintenance on Mondays or Fridays.



**Figure 1:** Steelworks load profile for one day

Using actual demand density data for the furnaces and steel processing plant, three simulations were performed, viz:

## 2.1 SIMULATION #1

The lower mean weekday hour values of the arc furnaces are combined with the higher mean weekday hour values of the steel processing plants, and vice-versa. This amounts to near perfect complementary scheduling of electric furnace loads so that furnace peaks occur in steel processing valleys, and furnace valleys occur during processing peaks.

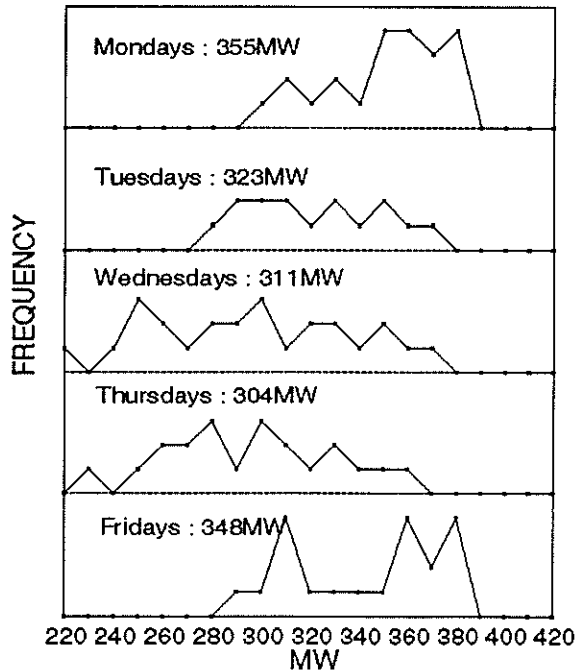


**Figure 2:** Density plots for demand chargeable hours.

The mean weekday hourly power values for the arc furnaces and the steel processing plants for a month are defined by the two relations

$$Pa_n = \frac{(\sum_{i=1}^H E_{af})}{H} \quad n=1, \dots, wd$$

where

$$\begin{aligned} E_{af} &= \text{Electrical Energy in MWh} \\ H &= \text{amount of peak hours per day (16)} \\ wd &= \text{amount of weekdays (23/month)} \end{aligned}$$

and

$$Pr_n = \frac{(\sum_{i=1}^H E_{rw})}{H} \quad n=1, \dots, wd$$

where

$$E_{rw} = \text{Electrical Energy in MWh for the the rest of the works (steel processing plants)}$$

The combined weekday values for the total works are given by

$$Tl_n = Pa_i + Pr_j$$

where

$$\begin{aligned} i &= \min, \dots, \max \\ j &= \max, \dots, \min \end{aligned}$$

Figure 3 shows the actual (T) monthly demand density and the simulation #1 (T1) monthly demand density. The peak loads for the two curves are  $T = 380$  MW and  $T1 = 340$  MW. It would be difficult to implement complementary scheduling in practice, but it does give an indication of the improvement potential of an 'ideal' situation so that improvements due to practical approach can be gauged in terms of the 'ideal'.

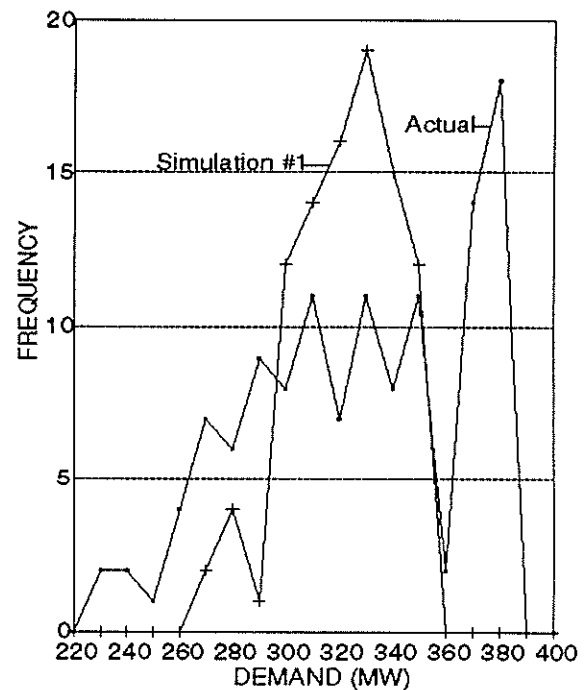


**Figure 3:** Comparison of actual and simulated ("ideal") demand density.

## 2.2 SIMULATION #2 AND #3.

For a given time period  $t$  (which could be a day, week, month, year, etc), composed of hours during which demand charges are applicable  $t = 1, 2, \dots, N$ , the system load profile is given by the sum of the two dependent (if load control is applied) random variables,

$$T_t = F_t + R_t$$

where

$F_i$  = Random variable for the electrical arc furnaces,

$R_i$  = Random variable for the rest of the works.

The purpose here is to develop two conceptual probability distribution simulation models. With the use of joint distributions, simulation #2 will represent the conceptual actual weekday demand density for the total works, while simulation #3 will represent the conceptual rescheduled weekday demand density for the total works.

We assume that the two random variables are independent, individual loads are independent of each other, and that each individual load is independent over time; these assumptions are valid because no load control is applied in both the simulation models.

The distributions for the two independent variables are  $p(F_i)$  and  $p(R_i)$ . Thus if  $p(F_i, R_i)$  is the joint density associated with specific values  $F_i$  and  $R_i$  of two random variables, then

$$p(F_i, R_i) = p(F_i)p(R_i)$$

If  $F_i = 100$  MW and  $R_i = 200$  MW, the probability of having  $T_i = 300$  MW would be given by the product of the individual probabilities,

$$\Pr(F_i = 100, R_i = 200) = \Pr(F_i = 100)\Pr(R_i = 200)$$

The data set (month) was divided into weekdays and weekday hours where demand charges are applicable under tariff E.

Simulation #2 is the probability that any weekday hour value can occur for the month for the joint distribution of the two random variables. The conceptual probability distribution for actual weekdays is defined by the relation

$$p(T2_i) = p(F_{w,i})p(R_{w,j})$$

where

$k = 1, \dots, n$  ( $i^*j$ ),

$i, j = 1, \dots, \text{amount of weekday-hours for the month for a specific weekday,}$

$w = \text{Monday}, \dots, \text{Friday}$

For simulation #3 the days of the electric furnaces were rescheduled as follows:

Was                      Becomes

Monday      Thursday

Tuesday      Friday

Wednesday      Wednesday

Thursday      Monday  
Friday      Tuesday

The conceptual probability distribution for rescheduled weekdays is defined by the relation

$$p(T3_i) = p(F_{w1,i})p(R_{w,j})$$

where

$w1 = \text{Thursday, Friday, Wednesday, Monday, Tuesday}$

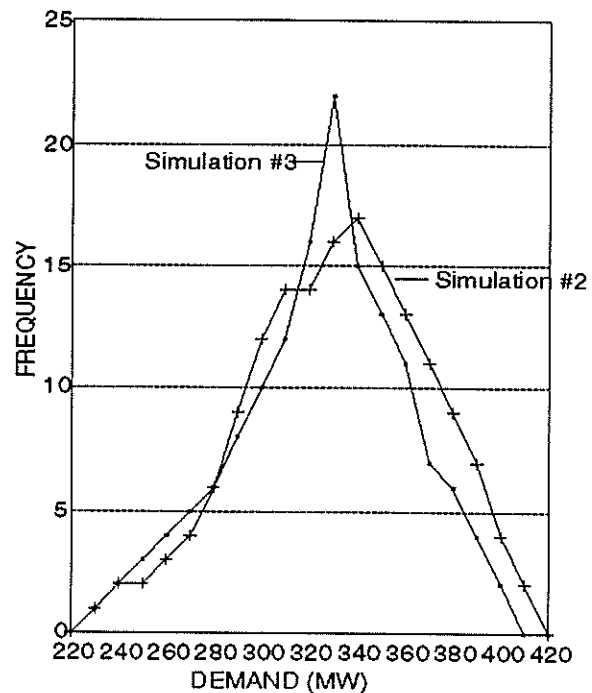


**Figure 4:** Simulated demand densities (demand chargeable hours only)

Figure 4 shows the density plots for the two simulation models. It is evident that the simulation #3 situation leads to a sharper and narrower demand density plot for the system.

With the use of statistical theory, the mean, variance and standard deviation is calculated for the two simulation models.

The mean ( $m$ ), variance ( $s^2$ ) and standard deviation ( $s$ ) for the probability distributions  $T2$  and  $T3$  is given by

$$M2 = \frac{(\sum T2_k^n)}{n}$$

$$M3 = \frac{(\sum T3_k)}{n}$$

$$s2^2 = \sum \frac{(T2_k^n - w2)^2}{(n-1)}$$

$$s3^2 = \sum \frac{(T3_k^n - w3)^2}{(n-1)}$$

Table 1 represent the calculated values for three months

	w2	s2	w3	s3
Feb. 1992	295 MW	36 MW	295 MW	25 MW
Mar. 1992	324 MW	33 MW	324 MW	23 MW
Apr. 1992	328 MW	45 MW	328 MW	33 MW

**Table 1:**

It is clear from table 1 that the standard deviation values for T3 are smaller than those of T2, which means that for T3 the distribution of MW values are closer to the mean than in the case of T2. The values of both T2 and T3 tend to be concentrated around the mean, so both T2 and T3 are normal distributions. With the use of the scaling relationship for the standard normal curve,

$$z = \frac{T - \mu}{\sigma}$$

$$T = z * \sigma + \mu$$

The mean values for the two distributions are the same for each month. Then for the same point on both the distribution curves, T3 will always be s3 - s2 MW smaller than T2.

The conclusion is made that the maximum demand setpoint for the conceptual rescheduled weekday distribution model would be respectively 10 MW less than the actual weekday distribution.

The simulations demonstrate that rescheduling of maintenance would allow considerable savings in electricity cost, provided that it is feasible to perform planned maintenance on electrical furnaces on Mondays and Fridays in preference to the middle weekdays.

### 3. RESCHEDULING OF MAINTENANCE DAYS FOR THE ELECTRIC ARC FURNACES.

After the simulation result was put before management, they decided to implement the recommended maintenance schedule for the electric arc furnaces. The preventive maintenance days for the various furnaces were rescheduled from Tuesdays and Thursdays to Fridays and Mondays. To confirm the savings and contribution to lower maximum demand setpoint for the total works, the probability distribution values for the actual load for two months were calculated.

The statistical values for the two months are shown in table 2

	m	s
June 1993	278 MW	17 MW
July 1993	305 MW	24 MW

**Table 2:**

If we compare the standard deviation of the actual rescheduled distribution values of the two months with the two simulations, T2 and T3 for the three months, we would see that the standard deviation for the actual rescheduled distribution is closer as was the case with simulation T3.

This indicates that a lower maximum demand setpoint for the total works with the rescheduled maintenance days is possible without additional loss of production due to unserved energy.

### 4. CONCLUSIONS.

Simulations have been used to demonstrate that rescheduling of maintenance would allow considerable savings in electricity cost. If the saving can be repeated on a monthly basis for simulation #3 it would amount to R2.5 million per annum, without additional loss of production. This is 55% of what could be saved with 'ideal' complementary scheduling (as described for simulation #1). Similar savings were achieved because the plant management responded to the results of the load analysis by implementing complementary maintenance scheduling on the electric arc furnaces.

### 5. REFERENCES.

- [1] Cohen, S.S.: "Practical Statistics, pp. 14-50, 162-165, 1988
- [2] Box, G.E.P., Hunter, W.G., Hunter, J.S.: "Statistics for Experimenters", pp. 21-83, 1978
- [3] Billinton, R., Allan, R.: "Reliability Evaluation of Engineering Systems", pp. 5-35, 124-167, 1987

# LOAD MANAGEMENT SCENARIO AND CONSTRAINT MODELLING BASED ON STEEL PLANT PRODUCT SCHEDULING AND FEEDSTOCK SWITCHING

W. Mulder and I.E.Lane

Centre for New Electricity Studies  
Department of Electrical and Electronic Engineering, University of Pretoria, South Africa

## ABSTRACT

The problem of load management of the arc furnaces in a steel plant is addressed in this paper. The development of a furnace model relating furnace fuel with energy consumption is presented. This constitutes an improvement on existing models in that it is more simple and seemingly more accurate. Remaining constraints on the accuracy of the model are addressed. The constraints of managing load by rescheduling production are explained and illustrated.

## 1 INTRODUCTION

Load management is gaining importance in the operation of energy intensive industries. With rising electricity costs load management has become an important and viable option to keep production costs as low as possible.

In the case of foundries, 61% of the total electrical energy used to produce iron castings is used in the melting process and more specifically, by the arc furnaces. Of the total energy consumed directly for the purposes of production (80%), this constitutes in excess of 76% [1].

A significant portion of the cost reduction in the load management scenario in a steel plant can thus be obtained by focusing the load management efforts on the arc furnaces. The feasibility of this is further underlined by the fact that the load presented by the continuous caster at the steel plant examined, presented the load manager with a constant load that cannot be shifted or reduced without seriously impairing production.

On the site that forms the basis of discussion in this paper the important upstream energy consumer is the Corex plant that produces liquid iron at a fixed rate of 40 ton an hour (28 000 ton/month). The energy for this, however, is primarily provided by coal (Corex) and gas (which are both time-of-use independent) [2]. The liquid iron has an effect on the arc furnace energy consumption and it's energy cost must therefore be included in the furnace energy cost.

In managing the load of the two arc furnaces at the steel plant examined, the options of load scheduling and

altering production mix were examined. The aim of both approaches being to lower the maximum demand of the plant during peak periods and to shift some of the electrical energy consumption from peak periods to off-peak periods.

## 2 THE LOAD MODELLING PROBLEM

One of the empirical factors in considering the application of load management, is the ability to accurately assess what the effect of such load management will be. This necessitates load models that fulfill the following requirements: First, they should accurately model (only) the relevant processes influencing electrical energy consumption. Secondly, they must provide the necessary information to evaluate the benefits obtained from load management [3].

### 2.1 Existing Furnace Model

The existing model for the steel plant considered for the purposes of the paper was developed by De Vos [4] and consists of energy calculations based on a comprehensive mass balance for the process in the arc furnace. The energy calculations are very cumbersome (over 113 equations) and only approximately 60% accurate.

### 2.2 Developed Model

In developing a new model from basic principles the aim was to concentrate only on fuel elements in the mass balance that influences energy consumption [5], [6], [7], [8]. Energy processes that were taken into account in the model, are:

- (i) Energy to heat material
- (ii) Energy to change material's phase (melt fuel)
- (iii) Energy created by the exothermic reaction of oxygen with silicon and carbon.
- (iv) Energy released by electric arcs

The assumption was made that the only significant elements (for the purposes of energy calculations) in the furnace fuel (due to either quantity or reaction) are Fe, Si, C, CaO and MgO. The energy required to heat these elements from ambient temperature to tap temperature T<sub>2</sub>,

$$\Delta H^\circ = \Delta H^\circ_f + \int_{T_{298}}^{T_2} [C_{p_i} - C_{p_r}] dT \quad (1)$$

where  $C_p$  (heat capacities of the elements or compounds) is calculated with (2) [8].

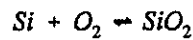
$$C_p = a + bT + cT^{-2} \quad (2)$$

Energy required to heat  $x$  ton of a compound, is

$$\Delta E = \frac{1000x}{n} \times \Delta H^\circ \quad (3)$$

... $n$ : molar mass of element

The exothermic reaction of oxygen with carbon can form either CO or CO<sub>2</sub>. By calculating Gibbs energies the formation of CO<sub>2</sub> is predicted. The exothermic reactions taking place are:



To calculate the energy released by these reactions the exothermic energy released (negative) is added to the positive value of energy that was consumed in heating the elements to the temperature at which they react:

$$\Delta H^\circ = \Delta H^\circ_f + \int_{T_1}^{T_2} [C_{p_r} - C_{p_n}] dT \quad (5)$$

These calculations are made for silicon and carbon in the liquid iron ( $T_1 = 1473$  K) as well as in the rest of the fuel mix ( $T_1 = 298$  K)

The total amount of energy thus released in the furnace is calculated with equation (3) where  $x$  is the total carbon and silicon masses respectively (in liquid iron and the rest of the mix respectively) and  $n$  is 28 (Si) and 12 (C) respectively. These total masses are calculated as follows:

In liquid iron (for carbon):

$$x(Si) = f(Si_{li}).m(li)$$

and in the rest of the mix:

$$x(Si) = f(Si_{pi}).m(pi) + f(Si_{si}).m(si) + f(Si_{spi}).m(spi)$$

.... $f(Si_K)$ : fraction Si (mass) in K

.... $m(K)$ : mass of K in furnace

.... $K =$  li : liquid iron

pi : pool iron

si : scrap iron

spi : sponge iron

The calculation for carbon is similar.

The total energy consumed (kJ) in the furnace is thus:

$$Q = \sum [HEATING ENERGY] + \sum [MELTING ENERGY] - \sum [EXOTHERMIC ENERGIES] \quad (6)$$

The electrical energy thus required for the furnace load is:

$$kWh = \frac{Q}{3600} \quad (7)$$

### 2.3 Other Energy Considerations

The cost of energy consumed by the Corex has to be taken into account. This cost is fixed (the Corex plant produces liquid iron at a constant rate and is heated by coal and oxygen). This has to be compared to the energy saved in the furnace by the addition of liquid iron:

$$1000x \times [\Delta H^\circ_{298K} - \Delta H^\circ_{1498K}] kJ \quad (8)$$

.. $x$  : tons liquid iron

The further potential saving in furnace energy consumption due to exothermic reactions, is:

$$\Delta H^\circ_{Si} \times 0.004x + \Delta H^\circ_c \times 0.042x kJ \quad (9)$$

The minimum amount of oxygen needed to react with silicon and carbon to produce steel with no silicon (required silicon for steel grade is added afterwards) can be calculated with the formula:

$$M_O = \left[ \left[ \frac{M_{Si}}{n_{Si}} \times 2 \right] + \left[ \frac{M_C}{n_C} \times 2 \right] \right] \times 16 \times 1000 kg O_2 \quad (10)$$

$n_{Si}$  and  $n_C$  are the molar masses of silicone and carbon.  $M_{Si}$  and  $M_C$  are the masses of silicone and carbon in the furnace that react with oxygen (values in tons).

The total energy cost is therefore:

$$Total Cost = M_O \times C_O + \frac{Q}{3600} \times C_{elec}(t) + M_{li} \times C_{li} \quad (11)$$

## 3 RESULTS

(1) The model was tested for a month's data. The energy consumptions for 448 furnace loads were calculated and compared with actual energy consumptions. The developed model proved to be 95.12% accurate with a standard deviation of only 12.04% [9]. This constitutes a significant improvement on the existing model.

(2) At present power consumption per melt stays relatively constant as melting time decreases proportionally with decreased energy consumption due to feedstock switching (figure 1). Reduced energy consumption does create the possibility of lower power consumption if melting time is kept constant.

Due to power on time being (i) short enough so that furnaces do not operate simultaneously and (ii) longer than the measuring interval for maximum demand, maximum demand is not significantly decreased by increasing furnace liquid iron content

(less than 1 % for a 30t liquid iron increase) unless the melt is controlled to lengthen melting time (not at present the case).

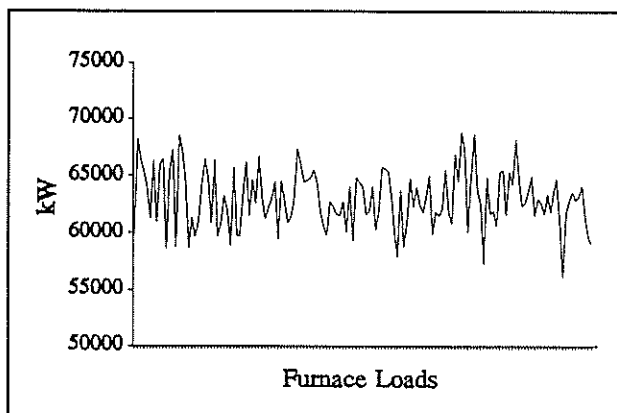


Figure 1 The average power consumption per melt.

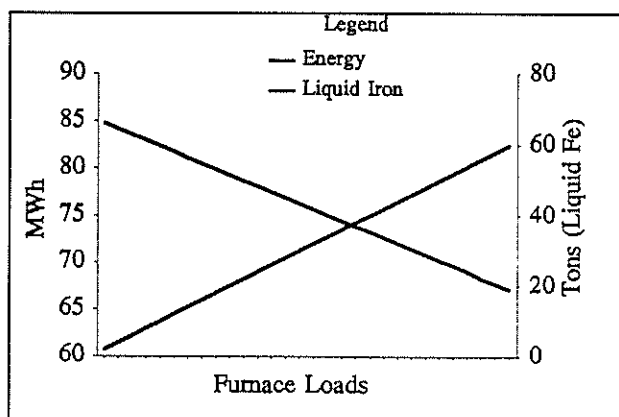


Figure 2 The reduction in energy consumption with the increase in the percentage liquid iron in the furnace.

- (3) The only fuel that has a significant effect on energy consumption (kWh) is the liquid iron which decreases energy consumption linearly as it is increased. When the plant has no spare capacity, the reduction in energy consumption is directly proportional to a shortening in melting time resulting in constant power consumption (kW). When the plant does have spare capacity, the rate of power input can be reduced in peak hours to reduce maximum demand.
- (4) All the Corex produced liquid iron is not used. By increasing liquid iron content of furnaces to better utilise the Corex, furnace energy consumption is reduced by 23.56 %.

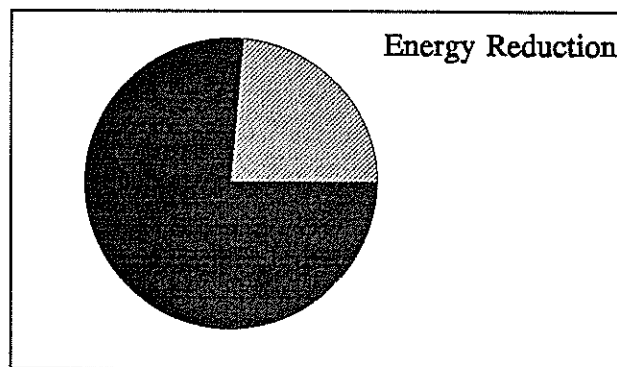


Figure 3 The percentage of present average electrical energy consumption reduced by using all available liquid iron.

This is a clear saving as excess liquid iron is allowed to solidify and its energy is thus lost.

#### 4 LOAD SCHEDULING

The steel plant examined has a special electricity tariff with maximum demand charge the dominant cost factor. Maximum demand is measured when the city experiences maximum demand (predicted to be in the periods 08:00 - 12:00 and 18:00 - 21:00 for weekdays).

The potential benefit from load scheduling was calculated for the ideal case:

- (1) Orders are known long enough in advance so that similar products can be produced together (no stoppages).
- (2) Maintenance is performed during peak periods.
- (3) Present monthly plant production is applicable.

Under these circumstances all load can be scheduled to fall outside the maximum demand risk periods. Resulting reduction in maximum demand charge is:

summer tariff: R 0.526 million  
winter tariff: R 0.584 million

#### 5 CONSTRAINT MODELLING

The constraints referred to are not physical constraints such as the maximum liquid iron that can be added to a furnace load. The more fully the production capacity of a steel plant is utilised, the less the opportunity for rescheduling load to off-peak periods becomes. To model this constraint, the formulae and values given in Appendix A were used. The results are given in figure 4. The results show the potential benefit that can be derived from load rescheduling in terms of energy cost. The increase in the advantage of load rescheduling as the plant is utilised to less of its full potential is evident. When the furnaces are on for less than 30 % of the week, producing even less hours a week does not improve the effectiveness of load rescheduling as the entire load can already be scheduled to off-peak periods.

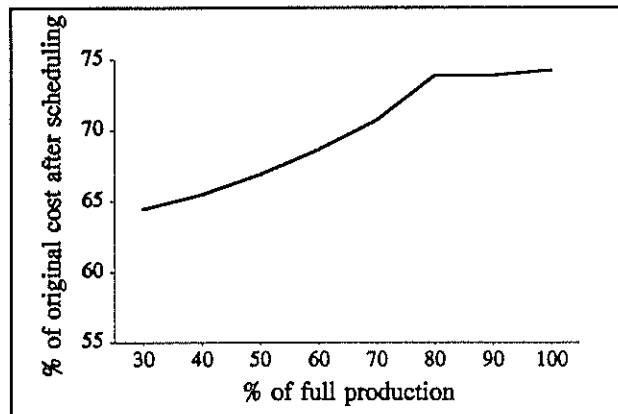


Figure 4 The energy cost after rescheduling (as a percentage of original cost) increases as the plant operate nearer to full production.

## 6 CONCLUSIONS

- (1) The load model of a furnace can be dramatically simplified if it's only purpose is the calculation of electrical energy costs.
- (2) The developed model gives an accurate indication of energy consumption.
- (3) The accuracy of the furnace model is limited by the human factor (the furnace operator greatly influences energy consumption).
- (4) The more fully the plant is utilised for production (time wise), the less is the opportunity reduce energy cost by load rescheduling.
- (5) If the plant does not have spare capacity maximum demand cannot be significantly reduced by fuel switching.
- (6) If the plant has spare capacity maximum demand can significantly be reduced by increasing liquid iron content per melt while reducing power input (to keep melting time constant).
- (7) Monthly energy consumption can be reduced by using all the liquid iron the Corex produces.

## 7 NOMENCLATURE

$\Delta H^\circ$ :	standard heat of transformation
$\Delta H^\circ_f$ :	standard heat of formation
$C_{pl}$ :	heat capacity (liquid phase)
$C_{ps}$ :	heat capacity (solid phase)
$C_{pT1}$ :	heat capacity (material at temperature T1)
a, b, c :	standard constants
$\Delta E$ :	energy required
n :	molar mass of element
Q :	total energy consumed
x :	tons of material
$M_{si}$ :	mass of silicon in furnace
$M_c$ :	mass of carbon in furnace
$M_o$ :	mass of oxygen in furnace
$C_o$ :	oxygen cost (R/kg)

$C_{elec}$ :	electricity cost (R/kWh)
$M_{li}$ :	mass liquid iron used (t)
$C_{li}$ :	liquid iron cost (R/t)
$T_1$ :	feedstock temperature (K)
$T_2$ :	tap temperature of metal
$T_{298}$ :	room temperature (K)
T :	temperature (K)

## 8 REFERENCES

- [1] E.L. Kotzen, P.J. Powers and A.J. Wagner. "Foundry Energy Management". American Foundrymen's Society, 1982.
- [2] F.G.T. Radloff. "Load Management Strategies for an Integrated Steel Plant". Student Report, Centre for New Electrical Studies, University of Pretoria, 1994.
- [3] C. Alvarez, R.P. Malhamé and A. Gabaldon. "A Class of Models for Load Management Application and Evaluation Revisited". IEEE, Transactions on Power Systems, Vol. 7, No. 4, November 1982.
- [4] B.J. de Vos. "Optimisation of Raw Material Addition for an Oxygen-blowing Arc Furnace". Dissertation for the degree M.Eng (industrial), Faculty of Industrial Engineering, University of Pretoria, 1993.
- [5] J.W. Brown and R.L. Reddy. "Electric Arc Furnace Steelmaking with Sponge Iron", The Metals Society, Ironmaking and Steelmaking, Vol. 1, 1979.
- [6] W.L. Masterton, E.J. Slowinsky and C.L. Stanitski. "Chemical Principles". Saunders, 1985.
- [7] O. Kubaschewski and C.B. Alcock. "Metallurgical Thermochemistry". Pergamon, 1979.
- [8] I. Coudurier, D.W. Hopkins and I. Wilkomirsky. "Fundamentals of Metallurgical processes". Pergamon, 1985.
- [9] A.G.W. Steyn, C.F. Smit and S.H.C. du Toit. "Moderne statistiek vir die praktyk". JL van Schaik, 1984.
- [10] Lj. Geric and G. Strbac, "Load Management in Industries with Automated or Periodic Technological Processes," International Journal of Power and Energy Systems, Vol. 14, No. 2, 1994.

# INNOVATIVE ELECTRICITY PRICING AND ENERGY MANAGEMENT IN INDUSTRY

JG Roos   IE Lane   EC Botha  
University of Pretoria, South Africa

**Abstract.** It is the aim of electricity supply utilities to sell more kWh of energy, but at the same time they have to face the fact of running out of capacity, which implies the need to erect new power generation plants at high cost. On the other side energy-intensive consumers of electricity have to cope with the burden of high energy bills each month. If these two parties can arrange a specialised pricing agreement between them, a win-win situation can be created from which both parties will benefit. The supply utility can defer the erection of the new generation plant, while the electricity bill of the energy-intensive customer can be lowered. This paper will cover these innovative pricing agreements between supply utilities and consumers which imply sophisticated load management mechanisms to be performed by the consumers.

## 1. INTRODUCTION

Every actor in an energy system, whether it be a residential, commercial, industrial or mining energy consumer or the electric supply utility, wants to maximise his profit and minimise the costs for purchased or delivered electrical energy and power. One of the great expenses of supply utilities is the expansion of their capacity in the form of new power generation plants to be erected. Utilities are therefore willing to promote Demand Side Management (DSM) measures and arrange special pricing agreements with their energy-intensive customers in order to defer the erection of these power plants. Energy-intensive consumers, mainly in the industrial and mining sectors, are sensitive to the high costs of electrical energy and power, and are willing to perform DSM measures in order to reduce their monthly energy bill. A special pricing agreement between the energy-intensive consumer and the supply utility will thus serve as an incentive to the customer to perform the DSM measures on his plant. To maximise their financial benefits which will emanate from the pricing agreements, the consumers would have to implement sophisticated load management mechanisms, like dynamic maximum demand setpoint control, load scheduling, load shifting, fuel switching, etc. The load management programs will change the load profile of the consumers to result in valley-filling and peak-clipping. Time-of-use (TOU) tariffs have been proved to be of the most effective programs of load management [1]. The special pricing agreements will therefore be based on TOU tariffs which may exist between the consumer and the supply utility.

This proposed energy management system where the interests of both these parties are integrated, will be discussed in the next section. To realise such an integrated energy management system, it will be necessary to apply artificial intelligence in the form of knowledge-based systems and artificial neural networks (ANN) in this power system. This will be discussed in the ensuing section. A case study which is currently performed at a major steel manufacturing company in Pretoria is discussed next, where an innovative pricing agreement was arranged between the steel works and the city council of Pretoria.

## 2. INTEGRATED ELECTRICAL ENERGY MANAGEMENT SYSTEMS (IEEMS)

For both the energy-intensive consumer and the supply utility to benefit from the special pricing agreement between them, an energy management system has to be implemented, where the interests of both parties are integrated. Unlike a human being, who is an excellent example of a cybernetic control system due to its intelligent nature, this proposed integrated energy management system has to rely on computer-based artificial intelligence to act as a cybernetic control system, which will be adaptable to changes in its environment and will have the abilities of internal feedback and the exchange of information and energy.

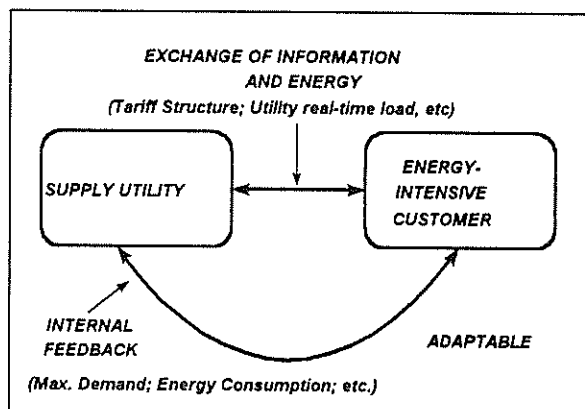


Figure 1 : Block Diagram of a Cybernetic IEEMS

Figure 1 shows a block diagram of the proposed IEEMS which will act as a cybernetic control system. Due to the software-driven nature of the system, it will be adaptable to changes in the environment, like changes in company policy etc.; there will be an exchange of energy between the two parties, like the supply and absorption of active and reactive power; there will be an exchange of information between the two parties, like the relay of

real-time tariffs and the utility's instantaneous load, the status of the utility's cogeneration plants (in the case of some municipalities), etc.; the system will exhibit the feature of internal feedback, like the monthly energy bill which will serve as a barometer to the consumer and upon which he would have to react.

### 3. ARTIFICIAL INTELLIGENCE IN POWER

Due to the complex nature of the decision-making process and control at the consumer's side of the proposed IEEMS, it can only be managed as a cybernetic control system with the help of computer-based artificial intelligence. The block diagram in figure 2 shows a typical layout of an IEEMS. The aim of the manufacturing plant is to meet its production request at the lowest cost possible. To achieve this, the company's production management system and its energy management system should be integrated to some extent so that optimisation of the production process on the one side as well as the energy management process on the other side can complement each other.

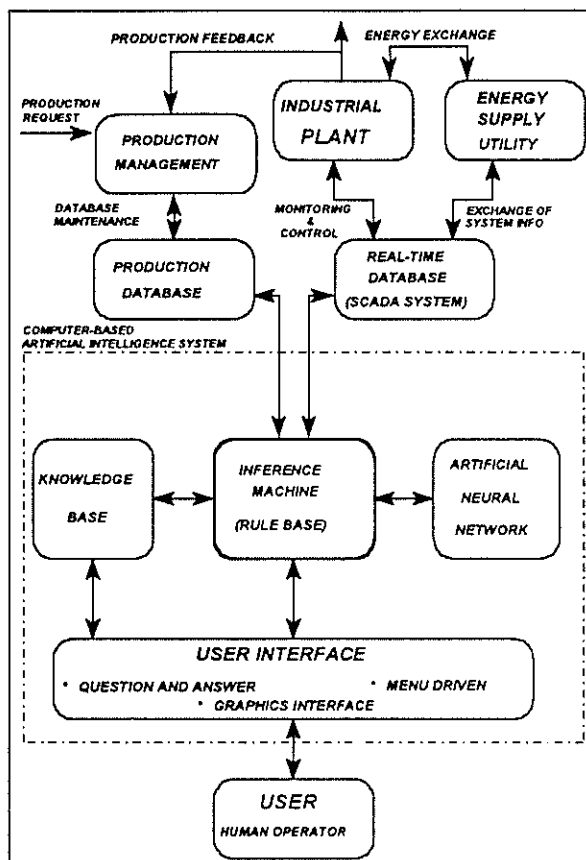


Figure 2 : Artificial Intelligence in the IEEMS

In a manufacturing plant the monitor and control functions are usually performed by dedicated PLCs connected to a SCADA system. The same SCADA system can, however, be used as medium to exchange information between the plant and the supply utility, like the transmitting of real-time pulses (power

measurements) which represent the instantaneous load of the utility, etc.

Information from the plant and utility variables, as well as production information like daily/weekly/monthly production requests and actual production feedback, should be fed to a computer-based artificial intelligent system. The short to long term decisions (hourly to monthly) which have to be made by human operators and plant managers can be alleviated with the aid of a knowledge-based expert system. Some control decisions, like the dynamic setpoint control of the maximum demand (MD) controller, may e.g. depend on the forecasted load of the utility one hour in advance.

Several methods exist to forecast the utility's load in the short term (1-24 hours), like multiple linear regression, stochastic time series, general exponential smoothing, state space methods, artificial neural networks (ANN) and with a knowledge-base approach [2]. During recent years much success have been reported with the ANN method [3,4] and the knowledge-base technique [5,6], with errors of as low as 1%. It will therefore be convenient to perform load forecasting by an artificial intelligent method (ANN or knowledge-based) due to the artificial intelligent infrastructure which will exist at the plant control centre.

### 4. INDUSTRIAL CASE STUDY

#### 4.1 Innovative Pricing Agreement

To investigate the feasibility of the proposed IEEMS, a major steel manufacturing company in Pretoria is taken as a case study. The steel plant can be rated as an energy-intensive consumer which contributes up to 13% of the city of Pretoria's load. Recent negotiations between the steel plant and the city council (supply utility) resulted in an innovative pricing agreement between the two parties. Where the energy (kWh) was previously supplied at a constant tariff, the new energy tariff is based on a time-differentiated tariff. The new energy tariff is almost 2 times higher during the ESKOM T1 standard period and almost 3 times higher during the peak period. The steel plant should now react to this by implementing proper load scheduling and load shifting measures and to investigate the possibility of fuel switching (alternative energy carriers) during these expensive periods. It has been reported that the scheduling of a steel plant has been performed with the aid of a knowledge-based system [7].

The new maximum demand (MD) tariff promises to have a great impact on the plant's electricity bill. It is based on the actual contribution of the plant to the city's monthly MD from ESKOM. For purposes of this paper the level of cogeneration of the city council is taken as constant through a 24 hour period. Figure 3 presents the

principle of this new MD tariff schematically, where the customer's contribution to the utility's peak is shown. If the steel plant can thus predict the day and hour when the city will have its monthly MD from ESKOM, it can in advance take the necessary measures to minimise the plant's demand during that predicted period, which can result in tremendous savings on its electricity bill.

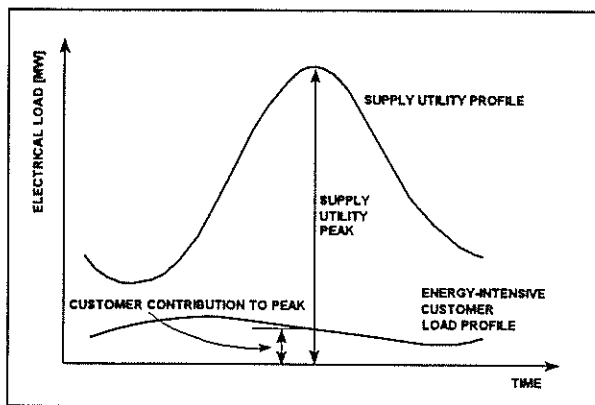


Figure 3 : Principle of the new MD tariff

#### 4.2 Dynamic MD Setpoint Control

To maximise its benefit from the new MD tariff, the plant should alter the setpoint of its MD controller dynamically through a 24 hour period. Figure 4 shows load profiles over two days taken from the customer (steel plant), the city demand (without the customer), the total demand taken from ESKOM (utility) and the monthly utility peak (MD taken from ESKOM). According to the new tariff, the customer can increase its demand anywhere during the 24 hour period provided that he does not create a new utility peak. From the figure it is evident that this extra power is available between the city without the customer's load profile and the horizontal line which depicts the utility peak.

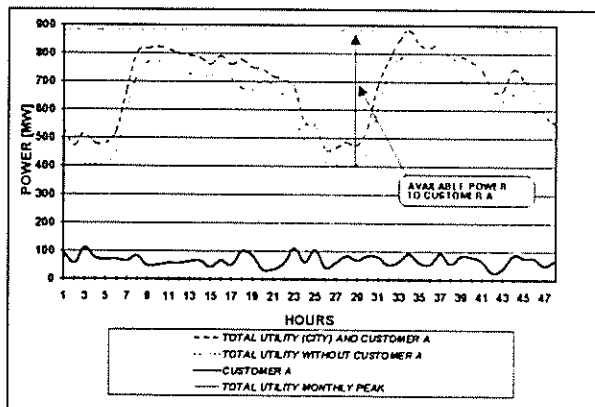


Figure 4 : Load Profiles over Two Days

Figure 5 shows this available power to the customer in an inverse load duration curve (ILDC) format during peak and standard hours, as well as the actual load of the consumer. In the first case (top ILDC in figure) the plant did not take any measures to decrease its contribution (92

MW) to the utility's MD, and therefore its actual load profile lies underneath the available profile. The two curves coincide only at one point (92 MW) at the left hand side of the chart, which corresponds to the monthly peak of the city. If the plant, however, decides to decrease its contribution from 92 MW to say 60 MW, the inverted LDC slides down and evidently cuts into the actual load profile. This implies load shifting or load curtailment for the part of the actual load which lies above the available power curve, and these parts are encircled in the figure.

The MD setpoint should therefore be dynamically controlled along the slope of the inverted LDC for that hours where the actual load has to be curtailed. (In the encircled part of the chart). It is evident from the illustration that the load need not to be curtailed for the greatest part of the peak period, and never during the standard periods. This is obviously a great improvement from the previous MD tariff, where the load had to be curtailed for longer periods during both the peak and standard periods. This new tariff, however, implies that the setpoint of the MD controller should be updated at least every hour.

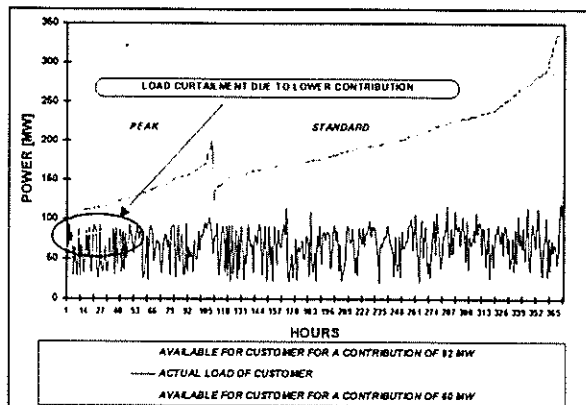


Figure 5 : ILDCs of Available Power

The decision the plant must now deal with is how far it can decrease its contribution to the utility's MD. This decision-making relies on a cost optimisation exercise. The lower the contribution, the lesser is the MD cost component in the electricity bill. However, the lower the contribution, the more load has to be shifted or curtailed, which implies increasing costs mainly from the production side because arc furnaces, for example, must shut down more frequently. This cost of unserved energy, however, is not quantified yet, and therefore the cost optimisation procedure cannot yet be executed.

For this dynamic MD setpoint control to be implemented successfully, the plant need to know in advance what the load profile of the city will look like. Short term load forecasting (1 hour ahead) is necessary to enable the plant managers, who are aided with the knowledge-based system, to set the MD controller setpoint for the next hour.

### 4.3 Load Forecasting Using ANN

As was mentioned earlier, during recent years artificial neural networks (ANN) achieved great successes in short term load forecasting [3,4]. Because the load of the city is very much weather dependent, the load forecasting procedure should take environmental temperature into account. ANNs can take weather data as input, and will thus be able to forecast the city load one hour in advance as a function of the current and recent temperatures. However, due to thermal storage capacities in city buildings, for example, the city load may be higher than normal if the city experienced, for example, two previous cold days, even if the target day is sunny. For this reason the neural network should take at least the two previous days' average temperatures into account. For the shorter term effect the neural net may take the previous say three hours' temperatures into account, should a sudden cold front reach the city.

Other inputs to the proposed ANN will be the current city load (without the steel plant), six previous half-hourly load inputs (load at  $h-1/2$ ,  $h-1$ , ...), and an input which will present the time of the day (06h00-20h00). A certain analog level at the input will present a certain hour of the day. Experimental work is still to be performed in this regard. Figure 6 shows the structure of the proposed neural network with which there will be experimented.

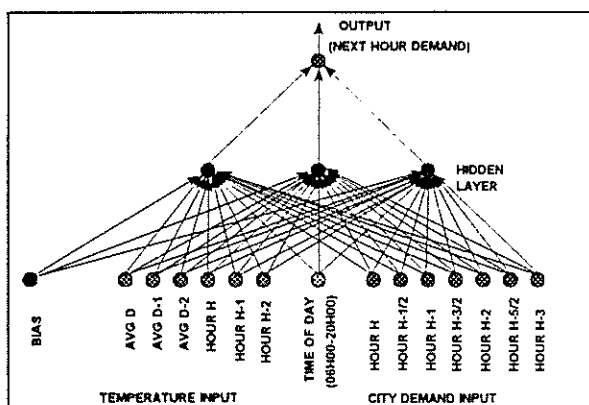


Figure 6 : Neural Net Structure for Load Forecasting

Processed historical data of the city load (1989-1994) indicates that the load profiles can be categorised in three seasons, namely summer (Nov, Dec, Jan, Feb), winter (May, Jun, Jul, Aug) and transition (Sep, Oct, Mar, Apr). Mondays to Thursdays exhibit similar profiles, while Fridays, Saturdays and Sundays differ to some extent from them. This means that four nets per season will be trained, and therefore twelve nets in total will be used for load forecasting. Public holidays' profiles mainly display as Sundays and will be treated that way.

### 5. SUMMARY

An Integrated Electrical Energy Management System is proposed where the interests of both the electrical supply utility and the energy-intensive consumer are integrated to create a win-win situation. Innovative pricing agreements between the two parties imply sophisticated load management measures to be performed by the consumer to maximise his benefits. With the aid of computer-based artificial intelligence these load management options can be performed by human operators and plant managers. A case study of a steel manufacturing company is described, illustrating the new innovative pricing agreement and more benefits if dynamic MD setpoint control can be performed. To implement this type of control, load forecasting has to be done and for its implementation artificial neural networks are proposed.

### 6. REFERENCES

- [1] Sheen, J-N, Chen, C-S and Yang, J-K: "Time-of-use pricing for load management programs in Taiwan Power Company", IEEE Trans. on Power Systems, Vol. 9, No. 1, pp. 388-395, February 1994.
- [2] Mogram, I, Rahman, S: "Analysis and evaluation of five short-term load forecasting techniques", IEEE Trans. On Power Systems, Vol. 4, No. 4, pp. 1484-1491, October 1989.
- [3] Lu, C.N., Wu, H.T. and Vemuri, S: "Neural network based short term load forecasting", IEEE Trans. On Power Systems, Vol. 8, No. 1, pp. 336-342, February 1993.
- [4] Chen, S-T, Yu, D.C. and Moghaddamjo, A.R.: "Weather-sensitive short term load forecasting using nonfully connected artificial neural networks", IEEE Trans. On Power Systems, Vol. 7, No. 3, pp. 1098-1105, August 1992.
- [5] Rahman, S, Hazim, O: "A generalised knowledge-based short term load forecasting technique", IEEE Trans. On Power Systems, Vol. 8, No. 2, pp. 508-514, May 1993.
- [6] Rahman, S, Bhatnagar, R: "An expert system based algorithm for short term load forecast", IEEE Trans. On Power Systems, Vol. 3, No. 2, pp. 392-399, May 1988.
- [7] Stohl, K, Snopek, W, Weigert, Th and Moritz, Th: "Development of a scheduling expert system for a steel plant", Proceedings of the IFAC Workshop on Expert Systems in Mineral and Metal Processing, Finland, pp. 39-44, 26-28 August 1991.

### 7. ADDRESS OF AUTHOR

Mr JG Roos, Department of Electrical and Electronic Engineering, University of Pretoria, Pretoria, 0002.  
E-mail : Johan.Roos@ee.up.ac.za

# INTEGRATED ELECTRICITY END-USE PLANNING IN DEEP LEVEL MINES

GJ DELPORT IE LANE

Centre for New Electricity Studies  
Department of Electrical and Electronic Engineering, University of Pretoria, South Africa

## ABSTRACT

The question arises: 'Is there a tariff that gives a mine enough incentive to convert to that tariff and to do load management which helps to keep the cost of electricity low by impacting on the national load profile?' In this paper a comparison between Eskom's tariff E and tariff T1 is given from this perspective with the help of simulations. The results are critically evaluated and conclusions are made.

## NOMENCLATURE

$$\sum_{i=1}^{80} E_{TM(\text{coal sim})\text{High}}(i) = \text{the sum of the calculated energy used by the total mine for the separate simulations during the 80 high demand hours of one week}$$

$$MD_{TM(\text{coal sim})\text{High}} = \text{calculated maximum demand for the combined simulation}$$

## 1 INTRODUCTION

The purpose of the time differentiated tariff, tariff T1, offered by Eskom to large power users is to provide an incentive to shift load from the peak hours to the standard and off-peak hours. The mines would not accept the new time differentiated tariff if they are going to pay more for electricity. One way to find out if a mine is going to pay more for electricity is the use of simulation. If the simulation methodology and load modelling are in place [1] [2] [3] and the mine's configuration is programmed into the simulation certain 'what-if' simulations can be done. After determining the end-user group(s) to target for load shifting [3], the possible load shifting per end-user group in the mine is simulated. For this paper the mine winding system end-user group and the underground water pumping system end-user group are the targets for the simulation.

## 2 TARIFF E

The possible maximum demand reduction results for the separate simulations of the mine winding system end-user group and the underground water pumping system end-user group are given in table 1. The results of the combined mine winding and underground water pumping systems simulation are given in table 2.

It is important to note that the aim for a demand charge tariff, like tariff E, is to strive for a load factor of 1 during the high demand hours per day.

Table 1 The maximum demand reduction results of the separate simulations for tariff E.

	Mine winding system	Underground water pumping system	Total
Maximum demand	4.14 MW	5.94 MW	10.08 MW

Table 2 The maximum demand reduction results of the combined simulation for tariff E.

	Combined simulation	Price of electricity	Saving (R × 1000)
Maximum demand	7.74 MW	R 32.22 / kW	249.38

The load duration curves of the separate simulations are given in figure 1 and figure 2 and that of the combined simulation in figure 3. From these figures the attempt made by the simulation to achieve a load factor of 1 during the 80 high demand hours is clearly visible. The simulation of the mine winding system end-user group is the least successful, figure 1, because the buffers and capacity of the existing mine winding system limits any further load shifting. The load profile for the underground water pumping system end-user group after simulation, figure 2, almost reaches a load factor of 1 during the 80 high demand hours of the week. Again, the capacities of the storage dams do not allow any further load shifting.

The combined simulation of the two targeted end-user groups takes much longer than the two separate simulations together. The main reason for this is the extra number of control rules that must be adhered to during the combined simulation. The minimum theoretical maximum demand possible, for the combined simulation can be calculated (predicted) from the available results from the separate simulations of the mine winding system end-user group and the underground water pumping system end-user group. The lowest maximum demand for a load factor of 1, is calculated with equation 1, [3].

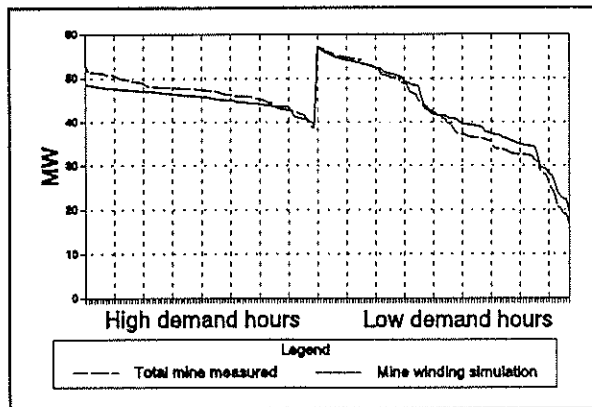


Figure 1 The load duration curves after the mine winding system simulation for the high and low demand hours for tariff E (one week).

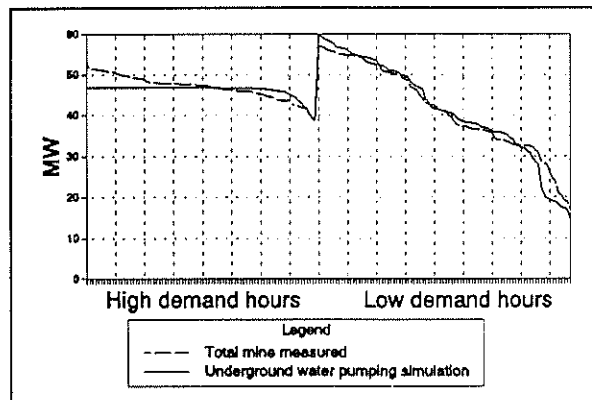


Figure 2 The load duration curves after the underground water pumping simulation for the high and low demand hours for tariff E (one week).

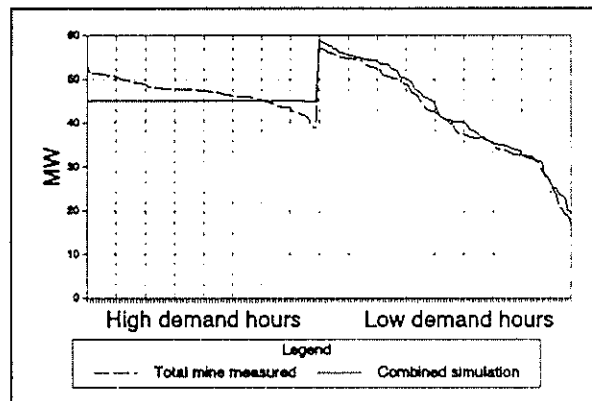


Figure 3 The load duration curves after the combined simulation for the high demand and low demand hours for tariff E.

$$\begin{aligned}
 MD_{\text{Total sim}} &= \frac{\sum_{i=1}^{80} E_{\text{Total sim}}(i)}{80 \times 1} \\
 &= \frac{3\,575.60}{80} \\
 &= 44.70 \text{ MW}
 \end{aligned}$$

The separate simulations are used to take the process limitations and constraints into account when calculating the possible load shifting from the 80 high

demand hours to the 88 low demand hours in a week. The maximum demand calculated is 44.70MW, only 0.40MW less than the combined simulation. A summary of the maximum demands for the tariff E case study is given in table 3. Table 4 gives the total possible saving per month if the mine is on tariff E and the two targeted end-user groups, mine winding and underground water pumping, are instrumented.

Table 3 Summary of the resulting maximum demands for the tariff E measured, simulated and calculated data.

	Maximum demand in MW
Measured maximum demand	52.84
Expected maximum demand reduction for the combined simulation	10.08
Expected maximum demand for the combined simulation	42.76
Actual maximum demand reduction for combined simulation	7.74
Actual maximum demand for the combined simulation	45.10
Calculated maximum demand for the combined simulation	44.70

Table 4 Summary of the total possible saving per month if the mine is on tariff E.

	Measured		Simulated		Saving (R × 1000)
	Value	Cost (R × 1000)	Value	Cost (R × 1000)	
Maximum demand MW	52.84 MW	1 702.61	45.10 MW	1 453.12	249.38
Energy consumption MWh	32 080 MWh	1 915.18	31 805 MWh	1 904.73	10.45
Total saving					259.83
Total saving per year					3 117.96

### 3 TARIFF T1

Table 5 and table 6 give the simulation results for the combined simulation if the mine is on tariff T1 for the low demand (summer) months and the high demand (winter) month respectively.

The load duration curves of the separate mine winding simulation and the underground water pumping simulation are given in figure 4 and figure 5 respectively. The load duration curves for the 85 high demand hours of the total mine measured and the total mine after the combined simulation are given in figure 6. The noticeable reduction in the use of standard energy is due to the standard time on Saturday from 07:00 to 12:00.

The minimum theoretical maximum demand possible, for the combined simulation from the available separate simulations of the mine winding system end-user group and the underground water pumping system end-user group is calculated as 43.82MW. This is 2.72 MW less than the actual simulation. The reason for this is that the combined simulation under the time differentiated tariff does not want to achieve

a load factor of exactly 1. The simulation tries to shift load from the peak time to the standard time and the off-peak time, as well as from the standard time to the off-peak time. This is the first priority of the simulation. This can be seen in figure 6 where the load duration curve of the combined simulation does not stay constant at 46.54 MW. No more load shifting is allowed by the simulation because the saving in peak energy cost is less than sum of the cost of the standard energy and the higher maximum demand cost.

Table 5 Summary of the cost involved for the case study for tariff T1, low demand.

	Measured		Simulated		Saving (R × 1000)
	Value	Cost (R × 1000)	Value	Cost (R × 1000)	
Maximum demand	52.84 MW	514.66	46.54 MW	453.30	61.36
Peak time energy consumption	6 042 MWh	886.38	4 615 MWh	811.32	75.07
Standard time energy consumption	12 213 MWh	1 201.76	11 627 MWh	1 134.26	67.50
Off-peak time energy consumption	14 825 MWh	837.61	16 674 MWh	879.93	- 42.32
Total per month		3 440.42		3 278.81	161.61
Total saving for 6 months					969.68

Table 6 Summary of the cost involved for the case study for tariff T1 high demand.

	Measured		Simulated		Saving (R × 1000)
	Value	Cost (R × 1000)	Value	Cost (R × 1000)	
Maximum demand	52.84 MW	671.71	46.55 MW	603.67	68.04
Peak time energy consumption	6 071 MWh	890.95	4 642 MWh	907.06	83.90
Standard time energy consumption	12 327 MWh	1 349.79	11 634 MWh	1 273.92	76.87
Off-peak time energy consumption	14 681 MWh	923.46	15 423 MWh	970.11	- 46.65
Total per month		3 835.90		3 664.75	181.15
Total saving for 6 months					1 086.92

#### 4 CONCLUSIONS

From table 7 it can be concluded that if the mine is on a two-part tariff (demand energy tariff) the possible saving consists 95.98% of possible saving from the demand charge while the time differentiated tariff demand charge contributes only 37.97% to the saving. In other words the diminishing return on investment has a bigger influence on the two-part tariff than on the time differentiated tariff.

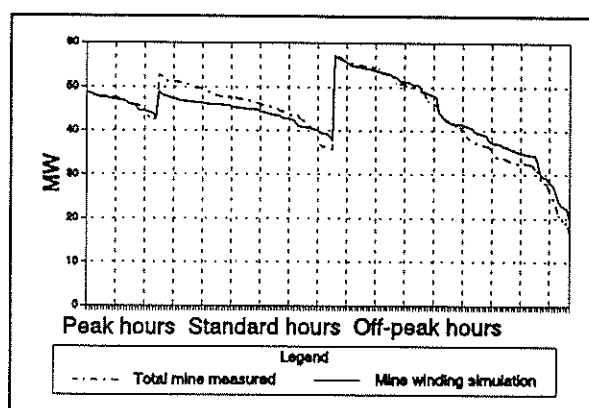


Figure 4 The load duration curves after the mine winding system simulation for the peak, standard and off-peak hours for tariff T1 (summer week).

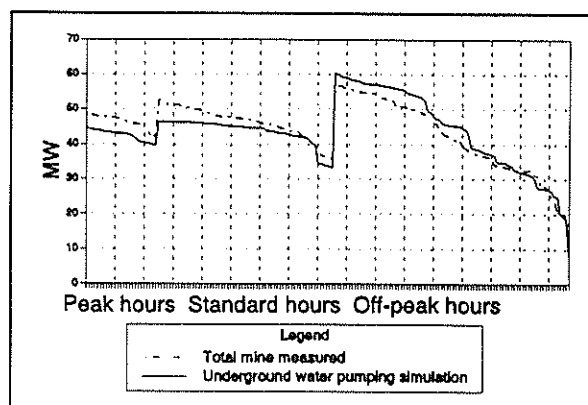


Figure 5 The load duration curves after the underground water pumping simulation for the peak, standard and off-peak hours for tariff T1 (summer week).

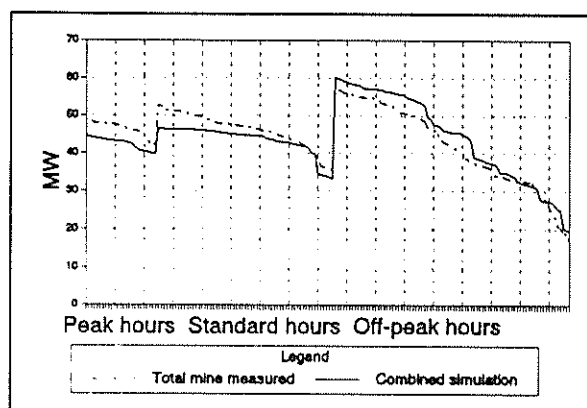


Figure 6 The load duration curves for the combined simulation for the peak and standard and off-peak demand hours for T1 (summer week).

If the mine decides to change to tariff T1 an average of R 17 190 higher electricity account per month is possible, without any changes in the current configuration or operation of the mine. With the combined simulation, an average saving per month of R 171 384 can be achieved (table 8), therefore a total actual average saving of R 154 194. If the mine does not change their electricity tariff and keep the two-part tariff they can save a possible R 259 830 (table 8).

The electricity supply industry does not have a tariff available that gives the mine enough incentive to change to that tariff and save on their electricity account with load management. If, for example, the time differentiated tariff T2, could be made available to the mine, it can benefit both the mine and the electricity supply industry. This tariff does not have an explicit maximum demand charge. The energy charges are the same as for tariff T1 except for a higher peak energy charge (the excess can be seen as a demand component).

**Table 7** Summary of the maximum demands, energy consumptions and cost involved for the case study.

	Maximum Demand		Energy		Total saving per month (R x 1000)
	Saving (R x 1000)	% of total saving	Saving (R x 1000)	% of total saving	
Tariff E	249.38	95.98	10.45	4.02	259.83
Tariff T1 (low demand)	61.36	37.87	100.26	62.03	161.61
Tariff T1 (high demand)	68.04	37.56	113.12	62.44	181.15

**Table 8** Summary of cost involved for the case study.

	Saving per month for the 6 low demand months per year (R)	Saving per month for the 6 high demand months per year (R)	Total saving per year (R)	Average saving per month (R)
Tariff E	259 830	259 830	3 117 960	259 830
Tariff T1	161 613	181 154	2 056 602	171 384

From all the time differentiated figures in this paper, figures 4 to 6, it can be seen, before and after simulation, that the mine always peaks during the standard energy time. The simulation can therefore not move more load to the standard energy time, because the money saved on peak energy is less than the cost in standard energy time and the maximum demand component that is a result of the load shifting. The end-user group configuration may still allow more load shifting, from peak to standard time, but it is not viable from an electricity cost point of view on tariff T1. If the mine can pay under a time differentiated tariff with no demand charges in the standard period, more load shifting would be done and both the mine and the electricity supply industry would benefit from the lower overall resource costs.

This case study emphasises the diminishing return on investment that takes place with the possible saving on maximum demand costs, if more than one end-user group is targeted for electrical energy cost optimisation. This was shown with an actual combined simulation of the two end-user groups, mine winding and underground water pumping and confirmed with a mathematical calculation. Therefore, when the return on investment period for each additional end-user group is calculated, it is very important to include the diminishing return on investment factor.

In this case study no other capital investment is only necessary, for the instrumentation of the two targeted end-user groups regardless of the applicable tariff structure. This provided a fair basis for comparison. It must be emphasised that none of the simulated scenarios would be possible in practice without an efficient energy measurement, control and information system.

## 5 REFERENCE LIST

- [1] Delpont GJ, Lane IE; (1994) A Simulation Model for Integrated Mine Energy Systems Planning; Paper presented at the 13th IASTED (International Association of Science and Technology for Development) International Conference on Modelling, Identification and Control. Grindelwald, Switzerland.
- [2] Delpont GJ, Lane IE; (1993) Load Audits and Simulations to Develop DSM Options in the Mining Sector. Paper presented at DSM Participants Seminar, DMEA.
- [3] Delpont GJ; (1994) Integrated Electricity End-use Planning in Deep Level Mines; Thesis, University of Pretoria, Pretoria.

## 6 ACKNOWLEDGEMENTS

The authors thank the Department of Mineral and Energy Affairs for supporting this research effort. We also thank the management of the mine for their participation in the load research described in this paper.

## 7 ADDRESS OF AUTHORS

Centre for New Electricity Studies  
Department of Electrical and Electronic Engineering  
University of Pretoria  
PRETORIA  
0002  
e-mail: johan.delpont@ee.up.ac.za

## Residential Load Modelling Using Cooking Appliance Proclivity, Availability and Usage Functions

J.P.G. Engelbrecht, I.E. Lane

Centre for New Electricity Studies  
 Department of Electrical and Electronic Engineering  
 University of Pretoria  
 Pretoria, South Africa

**Abstract**

The proposed model uses the concepts of availability, proclivity and usage functions to determine the electrical load due to residential consumption. Availability statistically estimates the number of appliances available in a house and proclivity is the probability that a certain appliance will be used at a certain time of the day. Usage functions give the typical energy consumptions of the different electrical loads as a function of time.

**1. INTRODUCTION**

In this study electrical energy consumption prediction for food preparation using computer simulations is based on four loads, i.e. the stove, oven, microwave oven and frying pan. A survey was conducted at 22 high-cost households to obtain information that is used in the simulations[6]. This information is not considered to be peculiar to this area only but indicative of most high-cost dwellings encountered. More loads will be used while food is prepared e.g. the geysers. These loads are treated separately in the model and will not be considered here.

Various approaches used for load modelling are described in [1,2,3 and 4]. The model used herein is based on the same principle as the model described by Walker and Pokoski in [1]. It makes use of a specific relationship between physical equipment and load on a per household basis. Each item of equipment is treated as an individual load with a different:

- frequency of usage;
- proclivity;
- duration of usage;
- device penetration (availability);
- usage level and
- usage pattern.

Inputs are generally obtained from surveys but they can be obtained from actual load measurements[1].

In this paper, the working principle of the model is

described and an after diversity load profile for food preparation for the surveyed households for a day is generated. This load profile is compared to measured load data. Then, three different simulations are compared to the original usage simulation. The simulations are as follows:

- **Original usage simulation:** The original electricity usage of the surveyed customers as determined by the survey is generated and compared to measured data. This will be used as the reference technique. All appliances are switched on at a certain setting and are kept at this setting for the remainder of the cooking cycle. Cycles are different for each day of the week.
- **Time and duration of use simulation:** The stoves are switched on at their highest setting for 20 minutes and then turned down to half-setting for the remainder of the cycle.
- **Seasonal swing simulation:** The effect that seasonal swing will have due to temperature change assuming that the frequency of usage, proclivity and availability stay the same.
- **Low-cost dwelling simulation:** In this simulation the cooking load profile for 22 low-cost households is generated.

**2. WORKING PRINCIPLE OF THE MODEL**

The model combines the loads due to individual appliances. The load on each appliance is calculated during each period and the loads for all appliances are added. A number of computer simulations are totalled and then scaled to the required number of residences.

Figure 1 shows the proclivity function for the stoves for a weekday, Saturday and a Sunday respectively. This is a probability density function and represent the probability that the stove will be used at a certain time of the day given that it is available. This discrete random variable proclivity function is

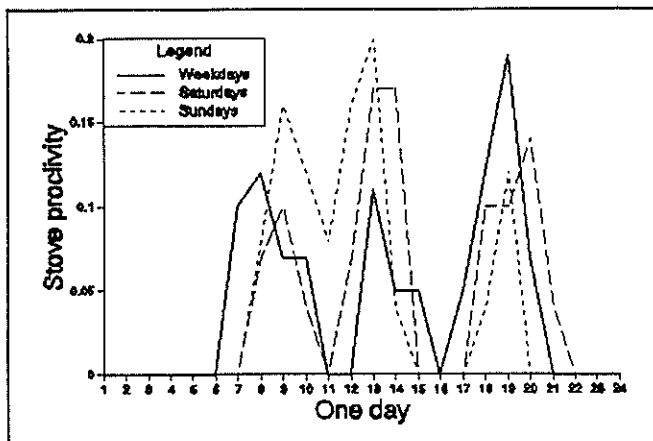


Figure 1. Proclivity function for the stoves.

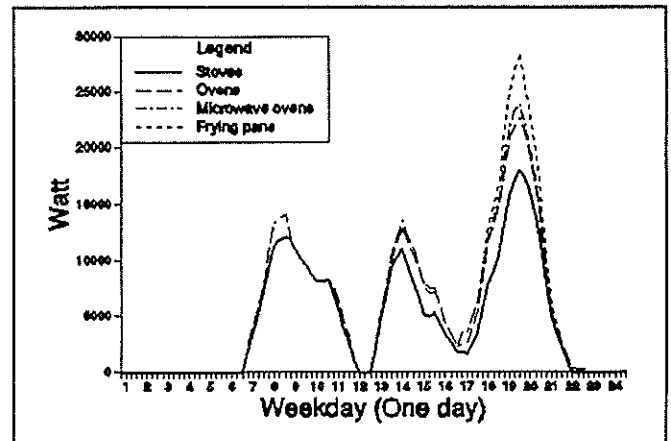


Figure 3. Stacked load profile.

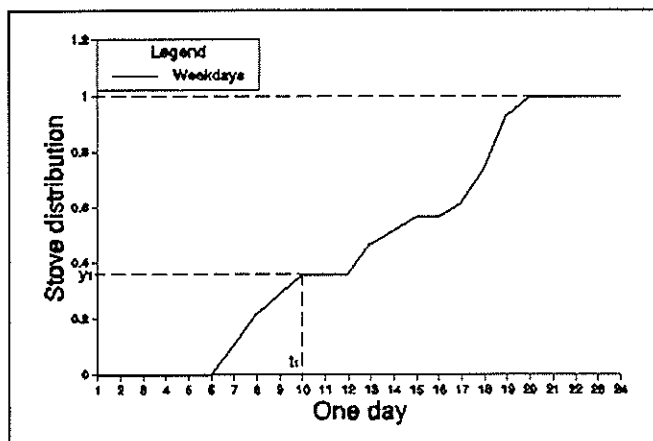


Figure 2. Cumulative probability distribution function.

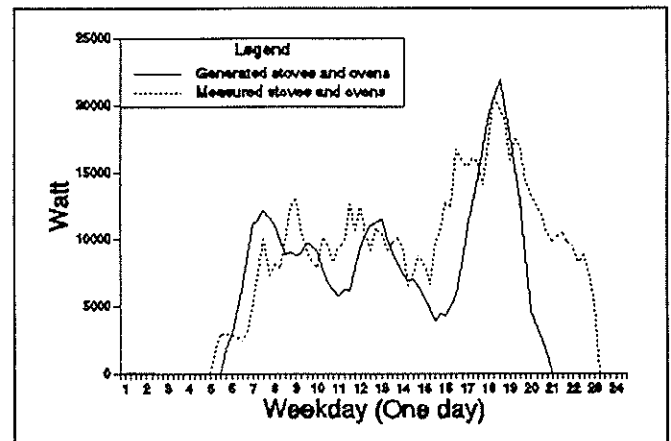


Figure 4. Generated and measured load profiles.

numerically integrated, i.e. summated, and for each interval  $i=1$  to  $n$  plotted against time. The result is a curve as depicted in figure 2. Since all possible outcomes have been included the summation must equal unity. This curve is known as the cumulative probability distribution function[7]. This distribution indicates the probability of the appliance being on at a certain time or during a certain time interval.

A random number generator generates a number between 0 and 1, say  $y_1$ .  $y_1$  then indicates the probability of the appliance being on at time  $t_1$  (refer to figure 2). A load profile is then constructed by placing the usage function of the stove, starting at time  $t_1$ , in the stove total load profile. This is repeated a number of times to achieve a flat random number distribution and a total load profile for stoves is constructed.

### 3. ORIGINAL USAGE SIMULATION

Figure 3 shows the stacked generated load profile

for the four loads. Note that the stove is the main contributor to energy consumption and determines the load profile. Figure 4 compares the generated load profile to measured load data. Variations between the generated and measured loads will reduce if larger numbers of households participate and more accurate usage patterns for individual devices are used.

### 4. TIME AND DURATION OF USE SIMULATION

For this simulation the stoves are switched on at their highest setting for 20 minutes and then turned down to half-setting for the remainder of the cooking cycle. It is estimated - for this study - that small to medium portions of food can be brought to boil in approximately 20 minutes. This time is a function of type of food, cooking methods, utensil and plate thermal diffusivity, thickness and shape. Thermal contact resistance between plate and utensil is ignored. Ambient temperature is taken as 20°C. The problem is reduced to a one dimensional heat flow

system by assuming that the cooking utensil is at constant temperature. This is justified by the fact that the utensil thermal diffusivity defined by equation 1[5] is large and the emissivity is small.

$$\alpha = \frac{k}{\delta c} \quad (1)$$

where:  $\alpha$  = thermal diffusivity ( $\text{m}^2/\text{s}$ );  
 $k$  = thermal conductivity ( $\text{W}/\text{m}/\text{K}$ );  
 $\delta$  = density ( $\text{kg}/\text{m}^3$ );  
 $c$  = specific heat of material ( $\text{J}/\text{kg}^\circ\text{C}$ ).

Figure 5 shows the generated load profile for this simulation. It is assumed that the proclivity and duration of usage stay the same for the households. It is evident from this figure that this method of cooking reduces the load profile.

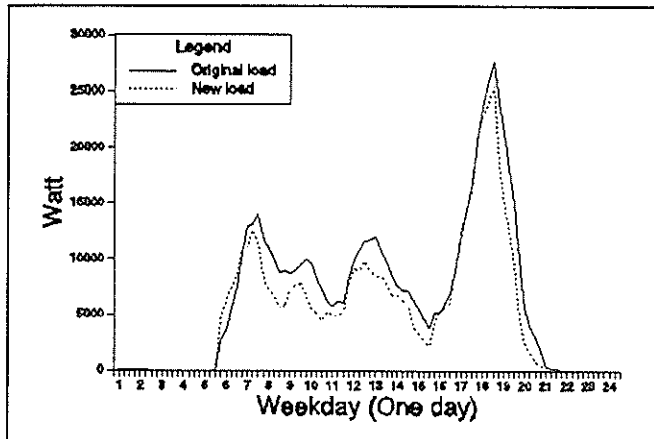


Figure 5. Load profiles for time and duration of use simulation.

## 5. SEASONAL SWING SIMULATION

The effect of a lower ambient temperature during winter months will have an adverse effect on the domestic food preparation load profile. Assuming that the frequency of usage, proclivity and availability remain unchanged, the load profile shown in figure 6 is generated for this simulation. The additional power required to prepare the food is calculated from Newton's law of cooling and convection (equation 2) and equation 3 deduced from Stefan-Boltzmann law of thermal radiation[5]. Only natural heat convection is considered.

$$Q = hA(T_1 - T_2) \text{ [W]} \quad (2)$$

where:  $h$  = convection heat-transfer coefficient ( $\text{W}/\text{m}^2/^\circ\text{C}$ );  
 $T_1$  = temperature of utensil ( $^\circ\text{K}$ );

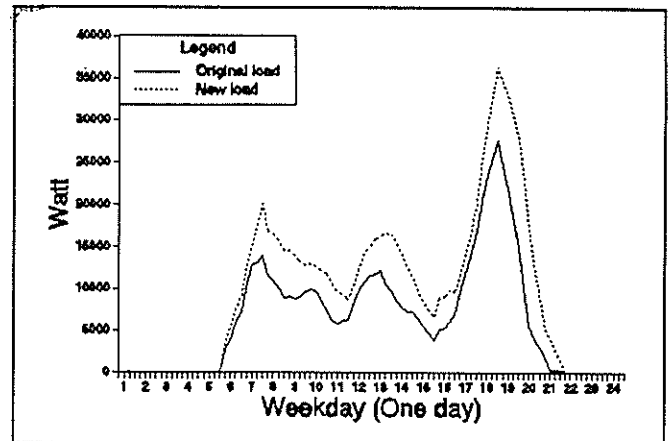


Figure 6. Load profiles for seasonal swing simulation.

$T_2$  = temperature of surrounding air ( $^\circ\text{K}$ ).

$$Q = \epsilon \sigma A (T_1^4 - T_2^4) \quad (3)$$

where:  $\epsilon$  = emissivity;  
 $\sigma$  = Stefan-Boltzmann constant  
 $= 5.669 \times 10^{-8} \text{ [W}/\text{m}^2\text{K}^4]$ ;  
 $T_1$  = temperature of utensil;  
 $T_2$  = temperature of surrounding air.

By assuming that the outer surface of the cooking utensil is in contact with an infinite heatsink (surrounding air) at a temperature of  $5^\circ\text{C}$  for winter months the total heat loss can be calculated. The total heat loss is the sum of the convection and radiation components from the side and the top of the utensil. The problem is reduced to a one dimensional system with the assumption that the cooking utensil is at constant temperature.

The lower ambient temperature results in a sharp load increase. The ambient temperature for summer months is taken as  $20^\circ\text{C}$ .

## 6. LOW-COST DWELLING SIMULATION

In this simulation the cooking load profile for 22 low-cost dwellings will be constructed. Assumptions are based on future electrification programmes for rural areas and townships planned by the Government and ESKOM and are as follows:

- low-cost dwellings only have one hot plate and no stove or oven or a combination thereof;
- each dwelling has one kettle;

- no other electrical food preparation devices are used;

Furthermore, it is assumed that the proclivity, availability, frequency and duration of usage for purposes of this study are the same as for high-cost dwellings. This assumption is influenced by geographical location, social welfare and human behavioral characteristics. It is expected that these functions will change significantly from one geographical area to the next.

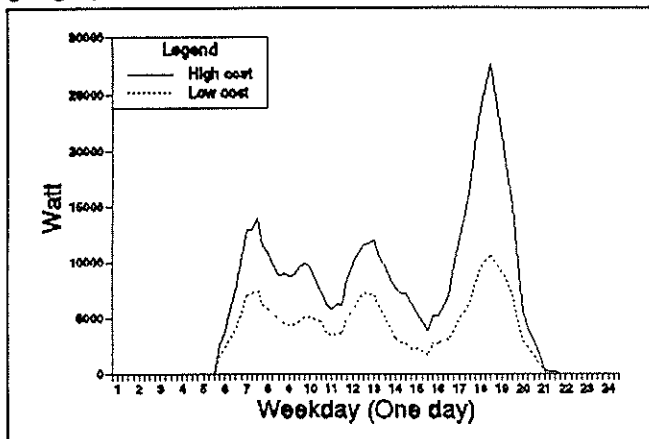


Figure 7. Generated load profile for low cost dwelling simulation.

Figure 7 shows the generated load profile. Note that the load is significantly lower than high-cost dwellings as could be expected. The load factor remains essentially constant.

## 7. SUMMARY AND CONCLUSIONS

A domestic load profile simulation model has been introduced and used to generate load profiles for 22 households in the high-income group. Four simulations were done and generated and measured load data were compared. It should be remembered that people's availabilities and proclivities are functions of many other factors such as social trends, national economy, political situation and the price of electricity. Although the model and modelling concepts are not complete, comparisons between generated and measured load data indicate the usefulness of the concept.

Load changes due to social, demographic and reconstruction changes can be predicted by the implementation of modified and appropriate availability, proclivity and usage functions. This can then be used for power reticulation and system expansion planning.

Insulation of cooking utensils was considered but it had a limited effect. DSM options should rather focus on more energy effective utensils which retains its thermal energy longer and is divided internally in sections so that more than one type of food can be prepared in it at the same time. The stored thermal energy can be utilised to complete the cooking while the stove is switched off before it is usually done. The cooking load profile for high-cost dwellings would therefore tend to the low-cost dwelling profile because the stoves are the main contributor to energy consumption.

Models to evaluate weather sensitivity must be incorporated in the simulation program.

## REFERENCES

- [1] C.F. Walker and J.L. Pokoski, "Residential Load Shape Modelling Based on Customer Behaviour", IEEE Trans. on Power Apparatus and Systems, Vol. PAS-104, No. 7, July 1985, pp. 1703-11.
- [2] C.W. Cellings and B.W. Taylor, "Electrical Load Curve Synthesis - A Computer Simulation of an Electrical Load Shape", IEEE Trans. on Power Apparatus and Systems, Vol. PAS-100, January 1981.
- [3] S.L. Corpening, N.D. Peppen and R.J. Ringlee, "Experience with Weather Sensitive Load Models for Short and Long-Term Forecasting", IEEE Trans. on Power Apparatus and Systems, Vol. PAS-92, December 1973, pp. 1966-1972.
- [4] P. Gupta and K. Yamada, "Adaptive Short-Term Forecasting of Hourly Loads Using Weather Information", IEEE Trans. on Power Apparatus and Systems, Vol. PAS-91, October 1972, pp. 2085-2094.
- [5] J.P. Holman, "Heat Transfer, SI Metric Edition", McGraw-Hill Book Company, 1989, pp. 1-130.
- [6] Wenelek Questionnaire; Conducted by the University of Pretoria Final Year Students, June 1993.
- [7] R. Billinton, R.N. Allan, "Reliability Evaluation of Engineering Systems: Concepts and Techniques", Plenum Press, New York, 1987, pp. 25-34, 124-128.

# SYSTEM ANALYSIS AND DESIGN OF AN INTELLIGENT DECENTRALISED DOMESTIC LOAD CONTROLLER

GL VAN HARMELEN

IE LANE

Centre for New Electricity Studies, Department of Electrical and Electronic Engineering, University of Pretoria, Pretoria, South Africa

## ABSTRACT

Current development in the software and micro-electronic fields has greatly fuelled the growth of dedicated electronic energy management systems for the implementation of DSM options. This paper deals with the proposed future generation of controllers which will introduce "self-learning", thus closing the loop and introducing self-optimisation. This is advantageous as tariff rates and structures are bound to change as time progresses, and as domestic behavioural and usage patterns are influenced by a large variety of external factors (e.g. weather, visitors)

## INTRODUCTION

There are two important problems associated with the effective use of "changing system condition" power. Firstly, the signal data (e.g. price) must be delivered to the consumer in a timely fashion. Secondly, the consumer must interpret the data and apply it to his appliance operation. Since most consumers do not come close to understanding even this terminology, they are not likely to implement these options correctly. There is thus a substantial requirement for automation technology which will assist the consumer electronically, while implementing utility inspired load curtailment strategies [1].

It is primarily as this home-automation assistant that a network of intelligent, distributed load control devices is proposed in this paper. In this type of system, each node in itself contributes to the intelligence of the entire system and is completely self sufficient. There is therefore no central point of intelligence. This structure will also reduce the computational complexity per node, increase the total system robustness and enable the latest control technology to be shipped with the latest end use devices (i.e. upgrade-ability). As well as making the system extremely robust (e.g. if a single node fails, the rest of the system can continue functioning) it also has a direct practical advantage, in that these electronics should be built into the end-use devices. This greatly reduces the need for software and hardware upgrades, as the latest control algorithms come shipped with the newest end-use device that the consumer purchases [2,3].

The problem is therefore to design a system where only state information is available to all nodes. This leads to an object oriented approach being used for the network of decentralised load controllers [9]. The structure thus dictates that commands for controlling devices are not distributed over the network. If this was so, and this is normally the way control systems used to operate, it would mean that when technology changed in a node, some other controlling node would have to be made aware of that fact. If however only state variables are transmitted over the network, this would not have to be the case.

## OBJECT ORIENTED CONTROL APPROACH

In conventional programming lingo, an object is a piece of software which can operate independently and has contained within itself, both the code (i.e. methods), as well as the data which it requires in order to perform a specific task. This bundling together of data and methods is called encapsulation and forms precisely the methodology used in the decentralised controller network as discussed here.

Each node contains the methods (program) as well as the data (from sensors and state information received over network) in order for it to perform a specific task.

This is different from the conventional approach which is shown in Fig. 1 where a centralised controller sends commands, and retrieves information, to and from each of its remotely located nodes.

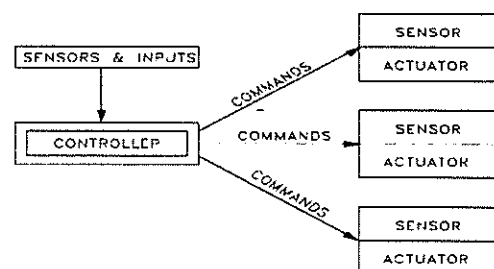


Fig. 1: A conventional controller network.

In this case, it is obvious that, should the central controller go down or one of the communication channels fail, the system could stop operating altogether.

In an object oriented approach however, this would not necessarily be the case as each node is largely self sufficient. Furthermore, default values may be used in those cases where the network fails to deliver a required state variable. Furthermore, through the mechanism of inheritance, one can create sub-networks of controllers, which contain some or all of the functionality of the controllers from which they were built originally. These two object oriented features (encapsulation and inheritance), which are present in the proposed network of controllers, have become the keys to greater productivity, higher reliability, and ease of building software applications [7], and should apply directly to the controller network presented here. Fig. 2. shows a block diagram of such a decentralised controller network.

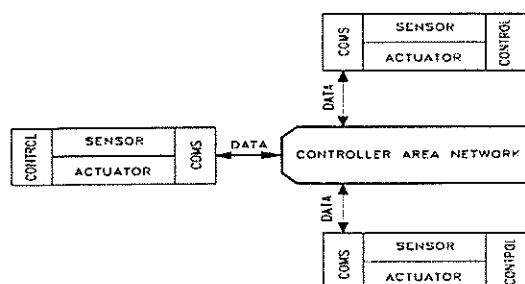


Fig. 2: An Object Oriented Controller Network

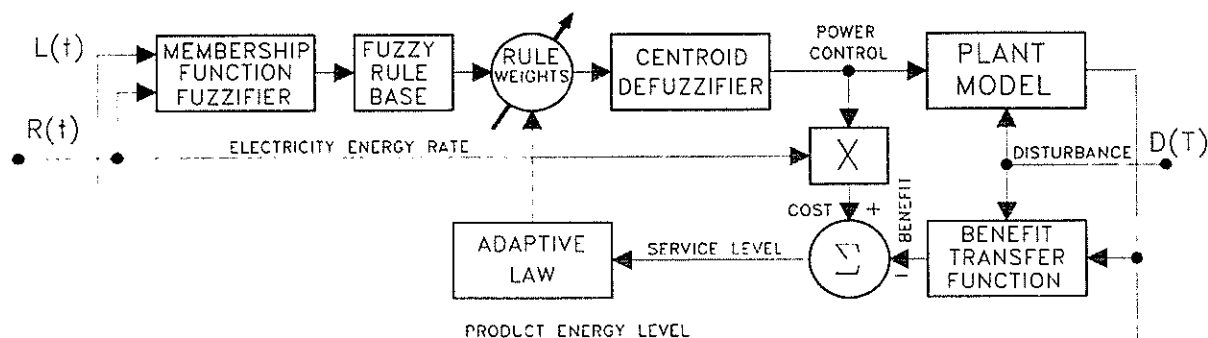


Fig. 3: Block diagram of the adaptive fuzzy logic controller.

#### RULE-WEIGHT OPTIMISATION BY STEEPEST DESCENT GRADIENT METHOD

In order to maximise the service level function we minimise  $f(\mathbf{K})$ , where  $f(\mathbf{K}) = -\text{service level}(\mathbf{K})$ , where  $\mathbf{K}$  is a column vector of  $N$  weights which apply to the individual fuzzy logic controller rules. The gradient of  $f(\mathbf{K})$ , is a vector defined as follows :

$$\text{grad } f(\mathbf{K}) = (f_1, f_2, \dots, f_N) \quad (1)$$

where the partial derivatives

$$f_i = \frac{\partial f}{\partial K_i} \quad (2)$$

are evaluated at the point  $\mathbf{K}$ .

Due to the object oriented feature of this type of control network, each of the nodes are independent, and can be modified or upgraded separately, without interfering with the rest of the network.

#### AN ADAPTIVE FUZZY LOGIC CONTROLLER

The block diagram of an adaptive fuzzy logic controller which could function as one type of decentralised intelligent load controller is shown in Fig. 3 [5].

In order to facilitate controller development, a linear differential equation model for a hot water cylinder was used during simulations for the results produced in this paper. The adaptive fuzzy logic controller had adjustable weights by which the firing strengths of each rule of the rules were scaled. These weight factors vary between 0 and 2 with 1 being the base case [6]. The weights are adapted so as to maximise the service level function which gives the least cost for the most benefit. The cost is calculated from the current rate of electricity, a capital outlay component and losses, whereas the benefit is calculated from the difference between requested and received comfort components (comfort in this sense means an amount of end-use product, such as boiled water) [4].

The gradient vector points locally towards the direction of the greatest rate of increase of  $f(\mathbf{K})$ . Hence  $-\text{grad } f(\mathbf{K})$  points locally in the direction of greatest descent. The optimisation therefore involves starting at a point  $\mathbf{K}_0$ , and searching along a line in the direction  $-\mathbf{G}/|\mathbf{G}|$ , where  $\mathbf{G} = \text{grad}(\mathbf{K}_0)$ . If  $\mathbf{K}_1$  is the local minimum in this direction, it will be situated at a new point  $\mathbf{K}_1 = \mathbf{K}_0 + t\mathbf{S}$ , with  $\mathbf{S}$  being the search direction given by  $-\mathbf{G}/|\mathbf{G}|$ .

The value of  $t$  is estimated by a Lagrange quadratic interpolation. This interpolation estimates where the minimum of the function  $f(\mathbf{K})$  is, along the direction vector  $\mathbf{S}$  from the point  $\mathbf{K}_0$ . This procedure is continued iteratively until the global minimum is found.

## FUZZY LOGIC IMPLEMENTATION

The fuzzy logic controller (FLC) proposed here has 17 rules where each rule has the following format :

$$\begin{aligned} R_1 : & \text{IF } x=A_1 \text{ AND } y=B_1 \text{ THEN } z=C_1 \\ R_2 : & \text{IF } x=A_2 \text{ AND } y=B_2 \text{ THEN } z=C_2 \end{aligned} \quad (3)$$

with  $x$  being price,  $y$  being temperature, and  $z$  being the power output to the element of the hot water cylinder.  $A$ ,  $B$  and  $C$  are linguistic variables describing the input and output membership functions on which the rule set operates.

All the rules may be read off from the fuzzy associative memory representation shown in Table 1.

Table 1: Fuzzy associative memory representation

	LL	SL	N	SH	LH
LL	LH	LH	LH	LH	LH
SL	SH	LH	SH	N	SH
N	SH	SH	N	SL	SL
SH	SL	N	SL	LL	SL
LH	LL	LL	LL	LL	LL

The horizontal axis represents price, whereas the vertical axis represents temperature. Readings contained within the matrix represent the power output of the element. The membership functions for the price universe of discourse are shown in Fig. 4 and all universes exhibit this same format.

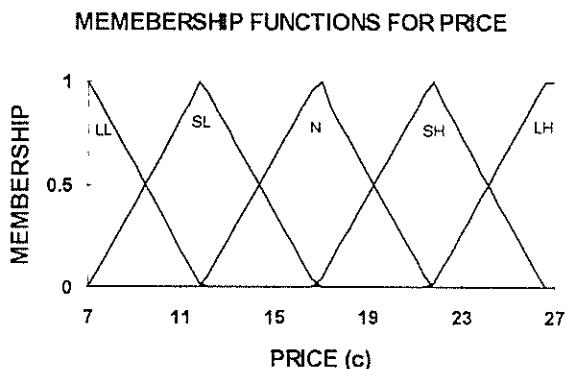


Fig. 4: Membership functions for price.

The inputs to a FLC are usually measured by sensors which are single valued sets and are called crisp values. They may therefore be treated as fuzzy singletons and the firing strengths for the example in eq. 3 may be expressed as

$$\begin{aligned} \alpha_1 &= K_1 \bullet (\mu_{A_1}(x) \wedge \mu_{B_1}(y)) \\ \alpha_2 &= K_2 \bullet (\mu_{A_2}(x) \wedge \mu_{B_2}(y)) \end{aligned} \quad (4)$$

where  $\mu_{A_i}(x)$  and  $\mu_{B_i}(y)$  play the role of the degrees of partial match between the user-supplied data and the data contained in the rule base. The  $K$ 's in eq. 4 represent the adaptive rule weights. In this implementation, fuzzy reasoning of the first type was used which is associated with Mamdani's minimum operation rule as a fuzzy implication function [8]. In this mode of reasoning, the  $i$ 'th rule leads to the control decision

$$\mu_{C_i}(w) = \alpha_i \wedge \mu_{C_i}(w) \quad (5)$$

which implies that the membership function  $\mu_C$  of the inferred consequence  $C$  is pointwise given by

$$\begin{aligned} \mu_C(w) &= \mu_{C_1} \vee \mu_{C_2} \\ &= [\alpha_1 \wedge \mu_{C_1}(w)] \vee [\alpha_2 \wedge \mu_{C_2}(w)] \end{aligned} \quad (6)$$

To obtain a deterministic control value, the centre of area method of defuzzification was employed [8]. This method generates the centre of gravity of the possibility distribution of the control action.

In the case of a discrete universe, this method yields

$$z_0 = \frac{\sum_{j=1}^n \mu_z(w_j) \bullet w_j}{\sum_{j=1}^n \mu_z(w_j)} \quad (7)$$

where  $n$  is the number of quantization levels of the output [8].

## RESULTS

From the surface response plot shown in Fig. 5, it can be seen that the controller behaves identically to a normal geyser controller (i.e. when water is hot, power input is low, and vice-a-versa), except when electricity prices deviate from normal (N). When prices are low (SL), the controller tends to add additional energy to the water, and when the prices are high (SH), less energy is added and therefore the tank tends to run cooler.

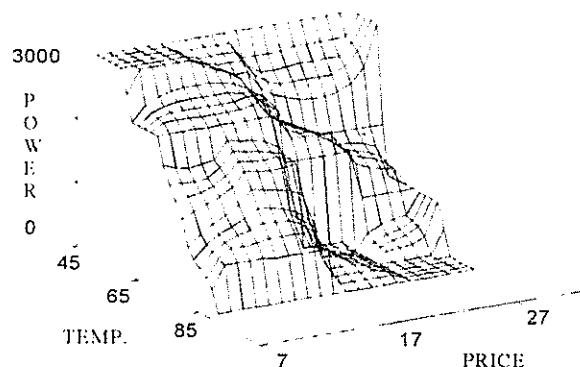


Fig. 5: Surface response plot of the optimised fuzzy logic controller.

In order to obtain the surface response plot shown in Fig. 5, the optimised weight vector was used as

weighting factor for the contribution of each of the rules. This weight vector was obtained from the steepest descent gradient search algorithm [10], using the service level function as optimisation indicator [4].

The adaptive FLC showed a more than 25% increase in performance over the standard fuzzy logic controller of Table.1, and more than an order of magnitude in performance over a standard hysteresis controller. These observations were made using the service level function as evaluation parameter [4].

The average tank temperatures for a three price range TOU tariff are shown in Table 2. These differences in controller setpoints demonstrate that the controller indeed controls the temperature setpoint in response to the price, while still maintaining an acceptable comfort level.

*Table 2: Tank Operating temperatures under varying tariffs.*

Energy Rate	Average Temp.
13	75
18	65
23	55

## CONCLUSION

In this paper, an adaptive fuzzy logic controller for use as a decentralised intelligent load controller was shown. (only data being sent to it from other control nodes e.g. price of electricity). Each controller in such a network exercises only local control, in this way, the controllers form an object oriented control network which means greater robustness, versatility and ease of upgrade.

The adaptive FLC proposed here showed a 25% increase in performance over the conventional FLC, and an order of magnitude increase in performance over a hysteresis controller. The adaptive FLC however exhibits the added advantage of being able to adapt continuously should it's environment, and therefore the optimum operating point, change.

Future work entails testing these simulations on actual devices in actual homes, as well as including the control of other types of devices (e.g. fridges, lights). The combined effect of a whole group of such controller networks should also be evaluated.

## NOMENCLATURE

FLC	Fuzzy Logic Controller
$\mu$	membership function
<b>K</b>	rule weight column vector
$x, y$	crisp sensor inputs
$z$	crisp control output
$w$	output control universe of discourse

$x \wedge y$	intersection : minimum ( $x, y$ )
$x \vee y$	union : maximum ( $x, y$ )
$\alpha_i$	rule <sub>i</sub> firing strength
$R_i$	i'th rule
LL	large low
SL	small low
N	normal
SH	small high
LH	large high
<b>W</b>	weight vector
sl	service level function
<b>S</b>	search direction vector
<b>G</b>	gradient vector

## REFERENCES

1. Whitaker, M., Whitaker, R., Rabl, V., Lannus, A : "Integrated home automation", in EPRI Journal, pp. 25-31, December 1989.
2. Van Harmelen, G.L., Lane, I.E., Hancke, G.P. : "System impact of decentralised AI controllers operating on domestic devices in the intelligent home", in Proc. of IEEE International Measurement Technology Conference (IMTC-94), pp. 10-15, Hamamatsu, Japan, 10-12 May 1994.
3. Machiels, M. : "GIDE A decentralised load management system", in Proc. of Conference on Advanced Technologies for Electric Demand Side Management, Sorrento, Italy, Vol. 2, pp. 1.15-1.35, 2-5 April, 1991 [21]
4. Van Harmelen, G.L., Lane, I.E. : "Comfort-Cost Analysis for the Optimisation of Domestic Load Controllers", to be published in proceedings of 5th South African Universities Power Engineering Conference (SAUPEC-95), University of Pretoria, Pretoria, 19-20 January 1995.
5. Qin, S.J., Borders, G. : "A multiregion fuzzy logic controller for non-linear process control", in IEEE Trans. on Fuzzy Systems, Vol. 2., No. 1., February 1994.
6. Cox, E. "Adaptive fuzzy systems", in IEEE Spectrum, February 1993, pp. 27-31.
7. Atkinson, I., Atkinson, M., Mitchel, E. : Using Microsoft C/C++ 7, Que Corporation, Prentice Hall Computer Publishing, 1992, pp 412-417.
8. Lee, C.C. : "Fuzzy Logic in Control Systems: Fuzzy Logic Controller, Part II", in IEEE Trans. on Systems, Man, and Cybernetics, Vol. 20, No. 2, March/April 1990, pp. 419-435.
9. Raji, R.S. : "Smart Networks for Control", in IEEE Spectrum, pp. 49-55, June 1994.
10. Mathews, J.H. : Numerical Methods for Mathematics, Science and Engineering, 2nd Edition, Prentice Hall International, pp. 400-422, 1992.

# IMPROVEMENT OF QUALITY OF ELECTRICITY SUPPLY

A van Zyl J H R Enslin  
University of Stellenbosch

R Koch  
TRI/Eskom

R Spée  
Oregon State University USA

## ABSTRACT

This paper introduces a single power electronic converter device that is capable of harmonic and/or flicker compensation. The proposed device is an extension of the Harmonic Isolator. A voltage source inverter injects a voltage, which has a harmonic component for harmonic isolation and a fundamental component for flicker compensation, in series with a shunt passive filter. This new device is called a *Power Quality Manager (PQM)*. Simulation results are presented of the *PQM* operated as Harmonic Isolator and Flicker Compensator.

## 1. INTRODUCTION

Power Quality problems can be associated with a variety of phenomena which affect the voltage waveform supplied to utility customers. These phenomena, caused by the interaction of load and network characteristics, include: harmonics, flicker, poor voltage regulation, voltage dips and voltage unbalance. Harmonic voltage distortion in the utility network is caused by loads such as diode and thyristor converters which draw non-sinusoidal currents. Flicker is caused by loads such as mills, arc furnaces and pumps, which draw fluctuating currents at frequencies which correspond to the range of sensitivity of the human eye to changes in light intensity. Dynamic compensation can both contribute to the pool of solutions to these problems, and has the potential of enhancing the effectiveness of existing compensators.

The *PQM* is based on the Harmonic Isolator and it is of interest to trace the evolution of the Harmonic Isolator. Passive filters consisting of a bank of tuned LC filters and/or a high-pass filter are widely used to suppress harmonics. However, passive filters have the following disadvantages: the source impedance strongly affects filtering characteristics, a low impedance path for unwanted harmonic currents is created and there is a possibility of parallel or series resonance between source and active filter leading to excessive harmonic source or filter currents. To solve these problems associated with shunt passive filters, shunt active filters using PWM inverters have been studied and developed in recent years[6]. However, disadvantages relating to the high capital costs as well as the difficulties of constructing a large-rated current source with a rapid current response have not yet been resolved[4].

## 2. HARMONIC ISOLATION

An alternative to active harmonic compensation is the improvement of the filtering characteristics of the passive filter. The impedance of the shunt passive filter should be lower than the source impedance at

harmonic frequencies to provide a low-impedance path for harmonic currents. Hence, the higher the source impedance, the better the filtering characteristics. However, the source impedance should exhibit a negligible amount of impedance at the fundamental frequency so that it does not cause any appreciable fundamental voltage drop. These two requirements, which contradict each other, can be satisfied by inserting an active impedance in series with the ac source, exhibiting zero impedance to fundamental frequency components and a high impedance,  $K_h$ , to harmonic components[4]. This is shown in Figure 1.

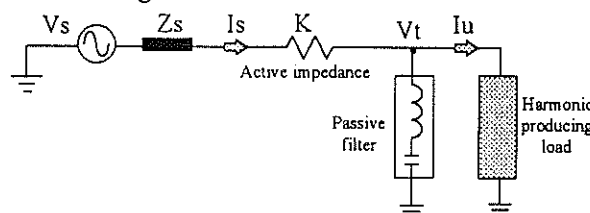


Figure 1 Harmonic Isolation

Series and parallel resonance phenomena can also be eliminated in this way. The filtering characteristics, expressed as the ratio of the harmonic content of the source current to that of the load current,  $i_{sh}/i_{uh}$  [dB], is shown in Figure 2 for an active impedance of zero, 2,5 and 5 per unit.

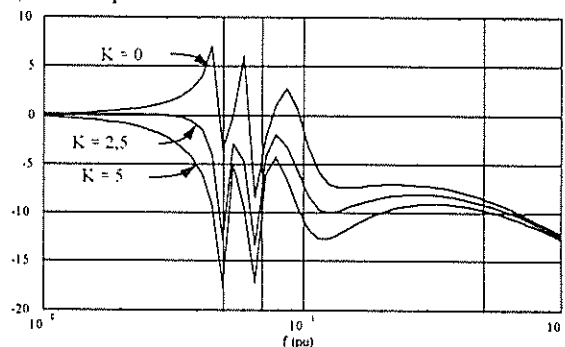


Figure 2 Improvement in filtering characteristics of passive filter by adding active impedance

The active impedance can be realized by injecting a voltage proportional to the harmonic component of the source current:  $V'_{oh} = K_h \times I_{sh}$ , which requires the determination of the harmonic component of the source current,  $I_{sh}$ . This can be achieved by using either the Instantaneous Reactive Power Theory (IRPT) introduced by Akagi[4] or the Synchronous Reference Frame (SRF) approach suggested by Divan[1]. The voltage can be injected through a transformer by using a voltage source inverter. This approach to harmonic compensation, which combines the use of a conventional passive filter and an active filter is commonly known as a Harmonic Isolator [4]. The active filter can be inserted in series with the line

or in series with the passive filter. In the first case there are some disadvantages [6]: the active filter has to be designed for the total source current, in case of load overcurrent, it affects the active filter and a failure in the active filter affects the supply of the load. In the shunt configuration, the current rating of the active filter is the harmonic load current plus the fundamental reactive current of the passive filter, and failures in the active filter do not affect load supply. Both configurations have the same effect on the filtering characteristics of the passive filter and the control strategy is the same.

### 3. CONCEPT OF UNIFIED POWER QUALITY MANAGEMENT

Several converter based devices have been designed to compensate for different Power Quality problems. Due to the high cost of high power converters, it is important to be able to compensate for more than one problem with a single converter device[2]. The extension of the characteristics of the Harmonic Isolator to include flicker compensation is proposed here. This new device will be referred to as a *Power Quality Manager (PQM)*. A simplified diagram of the PQM embedded in a radial network with a harmonic producing load is shown in Figure 3.

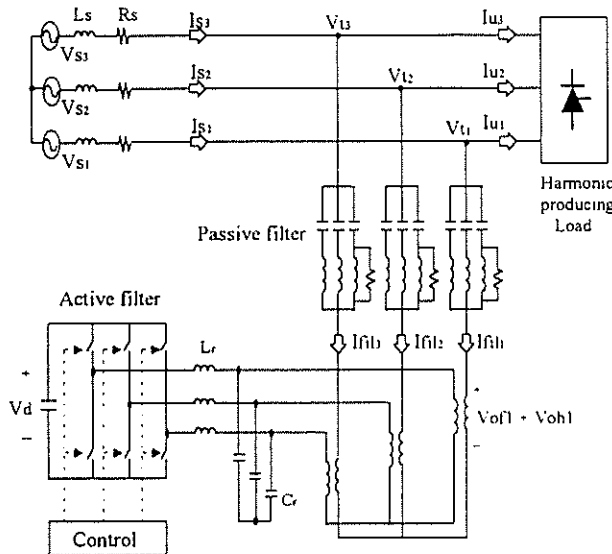


Figure 3 The PQM embedded in a radial network

The active filter injects a voltage in series with the passive filter. This voltage has a harmonic component providing harmonic isolation and a fundamental component for flicker compensation. The terminal voltage  $V_t$  is determined by the voltage drop across the source impedance.  $V_t$  can be regulated by controlling the component of  $I_s$  that is  $90^\circ$  out of phase with  $V_t$  ( $I_{sq}$ ).  $I_{sq}$  can be controlled by changing the fundamental component of the current through the passive filter,  $I_{fil}$ . At the fundamental frequency, the impedance of the passive filter is equivalent to a capacitor. This is shown in Figure 4.

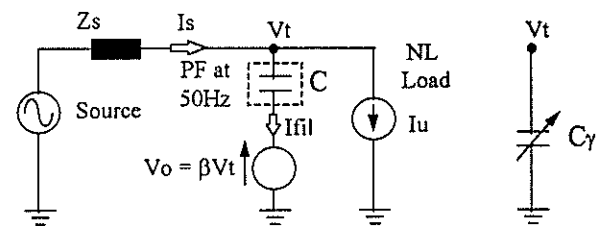


Figure 4 Simplified equivalent circuit at fundamental frequency

$I_{fil}$  can be controlled by modulating the equivalent capacitance of the passive filter seen by the circuit. This can be achieved by varying the voltage drop across the capacitor by injecting a voltage at fundamental frequency,  $V_{of}$ , which is in-phase with  $V_t$ , i.e.  $V_{of} = \beta \times V_t$ . By doing this  $i_{fil}$  becomes:

$$i_{fil} = C \frac{d}{dt} (v_t - \beta v_t) = (1 - \beta) C \frac{dv_t}{dt} \quad (1)$$

The equivalent capacitance of the passive filter at fundamental frequency is the following:

$$C_\gamma = (1 - \beta) C \quad (2)$$

The value of  $\beta$  required to keep the rms value of  $V_t$  at the reference level,  $V_{ref}$ , is determined open-loop every half cycle as follows:

$$\beta = \beta_o + (V_{ref} - V_{rms}) \left[ \frac{\Delta V_{rms}}{\Delta \beta} \right]^{-1} \quad (3)$$

where  $\beta_o$  is the value of  $\beta$  over the previous half cycle. The ratio  $\Delta V_{rms} / \Delta \beta$  was determined through simulations. The calculation of  $V_{rms}$  is based on a moving window concept[3]. The rms value of  $V_t$  is calculated every  $\delta T$  (taken as  $100\mu s$  in the simulations) based on the values of  $V_t$  over the previous 10ms, as follows:

$$V_{rms} = \sqrt{R_{uu}[0]} = \sqrt{\frac{1}{N} \sum_{i=1}^N V_i V_i} \quad (4)$$

with  $N$  the number of points in the window

$R_{uu}$  the autocorrelation of  $V_t$

The output voltage of the active filter,  $V_o$ , has two components: a fundamental component,  $V_{of}$ , used for flicker compensation, and a harmonic component,  $V_{oh}$ , used for harmonic isolation. From superposition it follows that the Harmonic Isolator and Flicker Compensator can be operated independently. A block diagram of the controller is shown in Figure 5.

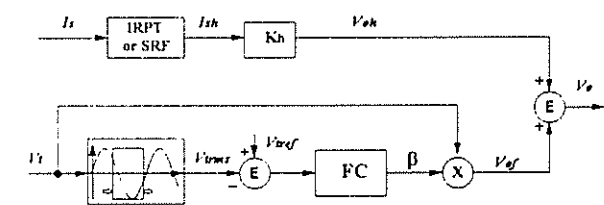


Figure 5 Block diagram of the PQM controller

#### 4. SIMULATION RESULTS

The concept of the PQM has been verified through simulations. The operation of the PQM as Harmonic Isolator is illustrated in Figure 6. The supply voltage,  $V_s$ , is a 80kV sinusoidal source and the load current is that of a six-pulse controlled rectifier that supplies a 200A dc current to the load. The load current contains harmonics of the order  $6n \pm 1$ ,  $n=1,2,3,\dots$ . Other circuit parameters are given in Table 1.

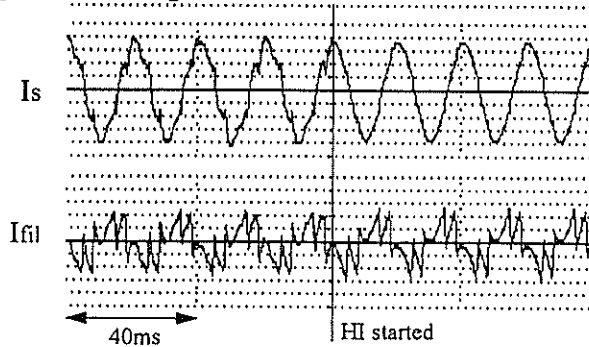


Figure 6 Operation of PQM as Harmonic Isolator

Table 1 Circuit parameters

$Z_s$		$L_s = 64.9\text{mH}$	$R_s = 12.4\Omega$
5th	$C_5 = 510\text{nF}$	$L_5 = 795\text{mH}$	$Q = 20$
7th	$C_7 = 470\text{nF}$	$L_7 = 440\text{mH}$	$Q = 20$
HPF	$C_h = 1\mu\text{F}$	$L_h = 83.7\text{mH}$	$R_h = 579\Omega$

The reduction in harmonic content of the source current can clearly be seen when the Harmonic Isolator is started. These results were achieved with an active impedance of 5 per unit and a device rating of 9% of the load rating (1MVA).

The operation of the PQM for flicker compensation is shown in Figure 7. The reactive power drawn by the load is modulated at a frequency of 4Hz between 2MVA and 6MVA, a fluctuation of 33% of the load power rating. This causes a modulation in the rms value of the terminal voltage  $V_t$ . When the flicker compensator is started the amplitude of the modulation in voltage is decreased considerably. These results were achieved with a device rating of 1MVA, the same as that required for harmonic isolation.

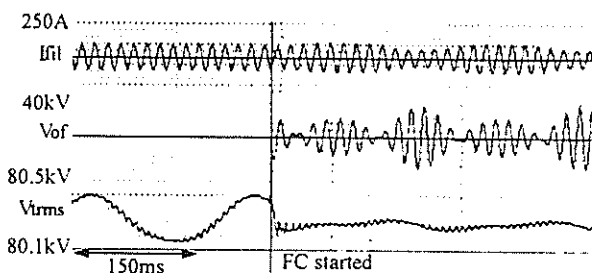


Figure 7 Operation of PQM as flicker compensator

When both the flicker control and harmonic isolation functions of the PQM is in use, the output voltage of the active filter becomes:

$$V_o = V_{oh} + V_{of} = K_h \times I_{sh} + \beta \times V_t \quad (5)$$

The injected voltage  $V_o$  has both a fundamental and harmonic component as shown in Figure 8.

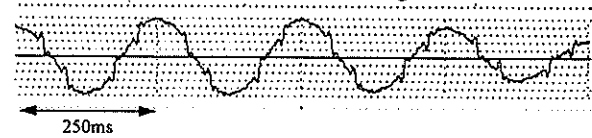


Figure 8 Injected voltage ( $V_o$ ) for harmonic and flicker compensation

The passive filter has a substantial influence on the power rating of the PQM [7] and therefore the passive filter must be optimally designed for the system.

#### 5. IMPLEMENTATION

The next step is to implement this controller into existing converter hardware. For laboratory testing, a DSP based controller will be used to control an existing medium power three phase converter (10kVA)[5]. Open loop current and voltage waveforms generated by the existing hardware is shown in Figure 9.

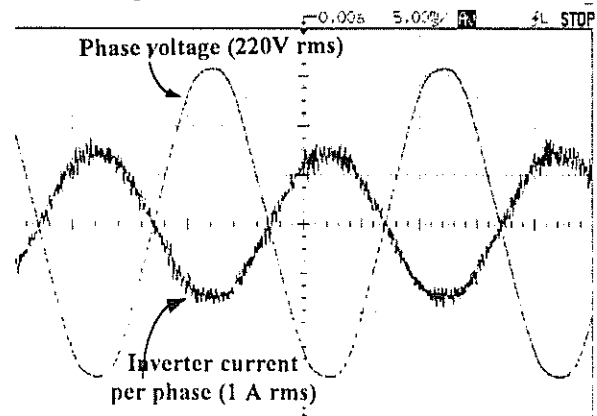


Figure 9 Inverter mode operation of existing hardware

The controller developed through simulation will be implemented on the existing hardware. The hardware implementation of the controller features a modular design with separate A/D converter and CPU boards. This allows for easy upgrade when the need arises for faster sampling rates or more complex control algorithms. Two control loops are used, an inner low-level control loop for the power converter and an outer loop that determines the converter reference signal. The inner loop control is done with a Intel80C196 microcontroller which allows for advanced PWM control schemes. The outer loop control is done by a TMS320C31 floating point CPU based inside a 486 PC. High voltage isolation from the power electronics is provided by an optic fibre link. The inverter status and all current and voltage

signals are available to both the inner and outer loop controllers.

## 6. APPLICATION

The PQM is being developed to be used for improvement of Quality of Electricity Supply on radial distribution lines. The proposed system is versatile in the sense that it can be used dedicatedly for either harmonic isolation or flicker compensation or the functions can be superimposed, depending on the type of compensation required. The amount of compensation required determines the power rating of the device. Partial harmonic isolation can be used in conjunction with partial flicker compensation to utilize the device to its full rating.

The potential applications of permanently installed dynamic compensators for improvement of supply quality are the subject of published studies which range from industrial customer installations to utility power capacitors. Specific application of smaller dynamic compensators such as the PQM can be found on weak rural networks which are required to feed both small industries with disturbing equipment, and other customers. An example would be remote saw mills which give rise to customer complaints of light flicker. The cost of increasing the network fault level to satisfy quality requirements may be inhibitive and/or untimely when related to load growth patterns in the area. The PQM can be made portable and relocated as problems arise on different sites in the network. By installing a portable dynamic compensator, network strengthening can be delayed until the economic benefits derived from increased customer power demand are more favourable. The portable compensator would then be available for installation at another site which may be experiencing another type of quality problem.

## 7. CONCLUSIONS

The concept of a unified approach to Power Quality Management, whereby the Power Quality problems of harmonic interference and/or flicker in voltage can be addressed by a single power electronics converter, has been investigated through simulations. The successful operation of a Harmonic Isolator has already been shown experimentally [4,2] and the incorporation of a fundamental component in the output voltage for flicker compensation has been verified through simulations. It will be evaluated experimentally on a 10kVA laboratory prototype. The device will be installed in series with a passive filter, thus failure in the device will not disrupt power flow across the distribution line and the power rating of the device can be optimized.

## 8. REFERENCES

- [1] Bhattacharya, D.M. Divan, B. Banerjee, "Synchronous Frame Harmonic Isolator using Active Series Filter", *EPE Firenze*, 1991.
- [2] J.H.R. Enslin, J. Zhao, R. Spée, "Operation of Unified Power Controller as Harmonic Isolator", *PESC '94*, pp.169-176, 1994.
- [3] G.L. van Harmelen, J.H.R. Enslin, "Real-Time Dynamic Control of Dynamic Power Filters in Supplies with High Contamination", *IEEE Trans. Power Elec.*, vol. 8, no. 3, pp. 301-308, July 1993.
- [4] H. Fujita, H. Akagi, "A Practical Approach to Harmonic Compensation in Power Systems - Series Connection of Passive and Active Filters", *IEEE Trans. Ind. Appl.*, vol. 27, no. 6, pp. 1020-1025, Nov./Dec. 1991.
- [5] P. Randewijk, J.H.R. Enslin, "Inverting DC Traction Substation with Active Power Filtering Incorporated", *Proc. of the SAIEE PEDS '94*, pp.102-110, 1994.
- [6] N. Balbo, L. Malesani, et al., "Hybrid Active Filter for Parallel Harmonic Compensation", *EPE 1993*, pp. 133-138, 1993.
- [7] F.Z. Peng, H. Akagi, A. Nabae, "Compensation Characteristics of the Combined System of Shunt Passive and Series Active Filters", *IEEE Trans. Ind. Appl.*, vol. 29, no. 1, pp. 144-152, Jan./Feb. 1993.

## 9. ACKNOWLEDGEMENTS

The authors express their sincere gratitude to ESKOM, who supported this research financially and technically.

## 10. LIST OF SYMBOLS

$K_h$	active impedance
$i_s$	source current
$i_{fil}$	current through passive filter
$i_u$	load current
$V_o$	injected voltage
$V_i$	terminal voltage across load
$\beta$	gain for flicker compensation
$C$	capacitance of passive filter at 50Hz
$C_\gamma$	equivalent capacitance of passive filter
IRPT	Instantaneous Reactive Power Theory
SRF	Synchronous Reference Frame
PQM	Power Quality Manager
$R_{uu}$	autocorrelation of voltage

# Neural Networks for Nonintrusive Appliance Load Monitoring

J. Vermaak and I. E. Lane

*Centre for New Electricity Studies,  
Department of Electrical and Electronic Engineering,  
University of Pretoria, Pretoria, 0002, South Africa*

## ABSTRACT

This paper investigates the application of various pattern recognition techniques for nonintrusive appliance load monitoring. Discriminative features are extracted from appliance specific voltage and current waveforms, calculated from the appropriate signals before and after detecting a step change in the aggregate supply. In the case of the responsive appliances (those that react immediately upon a switching event), these signatures can be obtained by controlling the switching of the specific device, labelled, and used to train a neural network classification system. For the non-responsive appliances, the classifier training has to be preceded by a process of clustering, to exploit the natural groupings in the data and label the unknown feature vectors.

## 1 Introduction

The switching of appliances within a residence are reflected by step changes in the total power consumption, as measured at the point of supply. Following from Kirchoff's law of current superposition, the subtraction of the current waveform before the transition from that after, yields an appliance specific current waveform. In this way the load can be disaggregated, and information relating to any specific appliance can be obtained, thus forming the basis for nonintrusive appliance recognition and monitoring.

The subsequent sections of this paper will present and discuss the various components and subtasks

of a nonintrusive appliance recognition and load monitoring system.

## 2 Data Acquisition

The voltage and current waveforms of the aggregate supply are measured by Hall-effect transducers. These sensors have a high bandwidth, and assure that all the frequency information present in the waveforms are preserved. This is important for the subsequent feature extraction. These signals are then amplified and sampled, the samples being converted to digital values by a 12-bit A/D converter, before being stored in the memory of a PC. Following from the Nyquist criterium [1], the sampling frequency should be at least twice the highest frequency of interest within the sampled signals.

It is important for the data acquisition to continue without interruption, in order not to miss any power transition in the aggregate supply. For this reason the samples are transferred to the PC memory via direct memory access (DMA), leaving the CPU free to process the data.

## 3 Preprocessing the Data

During preprocessing, the data is processed in such a way as to minimize the effect of external influences, and present it in such a form as to facilitate the effective further processing of the data. External influences corrupting the data includes environmental and transducer noise, measuring nonlinearities, quantization errors, etc.

The most important external influence in a nonin-

trusive monitoring system, is the variation of the line impedance as a result of the loading of the line, temperature variations, etc. Because of this, it is necessary to normalize the current signal to a fixed line voltage, usually the nominal value ( $U_n$ ). Because the impedance essentially stays the same, this can be done by multiplying each current sample by  $U_n/U$ , where  $U$  is the actual voltage RMS value.

Finally, in order to aid the step detection (discussed in Section 4), the current RMS value is calculated from the aggregate current waveform every three cycles. This ensures that no step change, however short in duration, goes undetected by the system.

## 4 Segmenting the Data

Segmentation of the data involves the extracting of appliance specific voltage and current waveforms from the aggregate supply signals. As the aggregate waveforms encapsulate those of all the appliances currently on, appliance specific waveforms can only be isolated by examining the waveforms before and after the step changes in the aggregate supply. Thus, segmentation involves two steps: step detection, and processing of the waveforms before and after the detected step change.

Step changes are best observed as changes in the total RMS current. The step change detection algorithm was inspired by Sultanem [2], and is described in the points below.

- A revolving type memory buffer keeps the last three measured values of the total RMS current,  $I_0$ ,  $I_1$  and  $I_2$ , where  $I_2$  is the last calculated value.
- The difference  $I_2 - I_1$  is continuously tested.
- If  $(I_2 - I_1) > \delta$ , where  $\delta$  is the detection threshold,  $I_0$  is stored in memory and time is given for the RMS current ( $I$ ) to stabilize in order to assure that the transient is completed (i.e.  $(I_2 - I_1) < \delta$ ).
- The event is then characterized by  $dI = I_2 - I_0$ .

Following from the law of current superposition, an appliance specific current waveform can be calculated by subtracting the current waveform after

the detected step change, from that before. This is equally true for on- and off switching events, a change in sign of the current signal being the only discriminating factor. Because the voltage waveform remains a fairly constant sinusoid, it can be used together with the derived current waveform to yield the appliance specific waveforms. Care has to be taken in order to preserve the phase information between the voltage and current signals.

## 5 Feature Extraction

During feature extraction, appliance specific signatures are extracted from the calculated voltage and current waveforms. This process reduces the dimensionality of the data (only a small number of values are used to represent the original waveforms), resulting in a representation highlighting the discriminative properties of the data, thus expressing the specific characteristics of the generating process.

A vast number of features are available for non-intrusive monitoring applications. Some of these are summarized in the points below.

- The features most frequently appearing in the current literature, are the power components, as calculated by the classical power definition. Other, more accurate, power definitions that can also be used as features, include the Budeanu [3], Czarnecki [4] [5], and time-domain [6] approaches.
- Frequency features, such as harmonic content, harmonic distortion, etc.
- Plotting the current waveform against the voltage waveform, yields the impedance contour for the specific appliance. From these contours various shape- and moment based features can be derived, as described in [7].
- A variety of other miscellaneous features, such as power factor, etc. These are really only limited by the imagination of the system designer.

As a final point, it can be said that the goodness of a specific feature can be quantified as the measure of distinctness it introduces in the data obtained

from different classes (appliances). There is no clear cut answers here, as this quality is dependent on the nature of the appliances to be recognized, the environmental conditions, and the optimal group of features is usually determined by trial.

## 6 Classifier Training

In order for a nonintrusive monitoring system to be able to track the usage of appliances, it has to be trained to recognize these appliances from their characteristic signatures. In terms of the training of the classifier system, there are essentially two types of appliances; the responsive, and the non-responsive appliances. The responsive appliances are those that react immediately upon a switching command, and includes devices such as kettles, food mixers, televisions, vacuum cleaners, etc. The state of operation of the non-responsive appliances, however, is regulated internally. Devices characterized by this behavior are for example refrigerators, washing machines, dishwashers, etc.

A system for the acquisition of training samples for the responsive appliances is shown in Figure 1. It consists of a master unit, also situated at the point of supply, and a number of smartplug units (SPUs), each installed at an appliance for which characteristic data needs to be obtained. The switching of the SPUs are controlled by the main unit, resulting in step changes in the aggregate supply that can easily be verified. Appliance specific waveforms and the subsequent features can be extracted according to the methods discussed in Sections 4 and 5. Because the source of the characteristic signature is known, these feature vectors can be labelled accordingly.

The labelled signatures are now presented to a classifier system, the parameters of which are adjusted until the error between the desired and actual output is minimized, the desired output being that every sample be correctly classified. To this end, during training, the classifier forms decision regions within the feature space, based on the nature of the samples presented. This type of training is called supervised, because the training samples are labelled. One such classifier system that consistently attains high success rates in pattern recognition applications, is artificial neural networks. These have proven to be robust classifiers, subject to a variety of external influences.

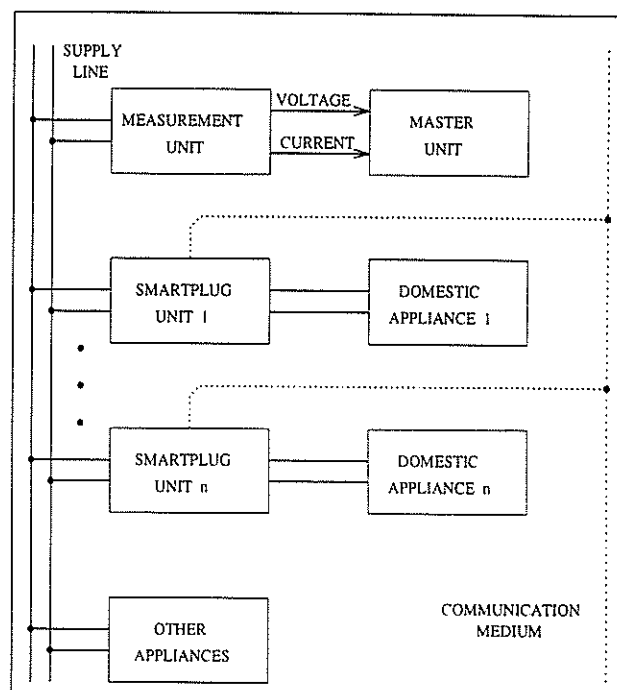


Figure 1: Smartplug system for the acquisition of training samples for the responsive appliances.

The theory and various applications of neural networks are extensively investigated in the literature [8] [9] [10] [11].

It is important to mention at this stage that the success of the classifier system is largely dependent on the measure of distinctness induced by the features chosen to represent the original data. No amount of improvement or tweaking of the classifier can make up for the loss suffered by using unsuitable features, in terms of discrimination.

The non-responsive appliances are harder to deal with, because appliance characteristic signatures cannot be obtained in a controlled manner, as was the case with the responsive appliances. This problem can, however, be solved, by following the steps listed below.

1. Log appliance signatures (feature vectors) as extracted from the normal switching events over a period of time, say 24 hours.
2. Perform a clustering procedure [12] on the data in order to isolate the natural groupings of the data. Each distinct grouping will be the result of the switching of a specific appliance.

3. Isolate the groupings of interest, label the samples, and use the samples to train a classifier system in the same manner as for the responsive appliances.

## 7 Monitoring Implementation

As soon as the classifier systems for both the responsive and non-responsive appliances have been trained, they can be implemented in order to track the behavior of appliances in real time. Appliance signatures are computed from the detected step changes, now resulting from the natural usage and/or switching patterns of all the devices within the residence. These signatures are labelled by the classifiers and presented together with a confidence measure; an indication of the correctness of the classification process. This is especially important when the classifiers encounter signatures of appliances not presented during the training phase. The labelled switching events can now be logged, yielding information for the determining of usage patterns, end-use energy efficiency, success of load control algorithms, and a variety of relating load monitoring information.

## 8 Conclusion

In this paper it was shown that it is possible to develop a system that is able to track the usage of various appliances within a residence by monitoring the point of supply alone. The system has to be trained to recognize these appliances. It was shown that, for the responsive appliances, training is supervised, because of the availability of labelled samples. For the non-responsive appliances, however, no labels are available, and the process of training is preceded by clustering to isolate the natural groupings in the data.

## REFERENCES

- [1] A.V.Oppenheim and R.W.Schafer. *Discrete-Time Signal Processing*. Prentice-Hall International, Inc., Englewood Cliffs, New Jersey, 1989.
- [2] F.Sultanem. Using appliance signatures for monitoring residential loads at meter panel level. *IEEE Transactions on Power Delivery*, 6(4):1380-1385, October 1991.
- [3] C.I.Budeanu. The different options and conceptions regarding active power in non-sinusoidal systems. *Rumanian National Institute (Bucharest, Rumania)*, (4), 1927.
- [4] Leszek S.Czarnecki. Active, reactive, and scattered current in circuits with nonperiodic voltage of a finite energy. *IEEE Transactions on Instrumentation and Measurement*, 37(3):398-402, September 1988.
- [5] Leszek S.Czarnecki. Powers in nonsinusoidal networks: Their interpretation, analysis, and measurement. *IEEE Transactions on Instrumentation and Measurement*, 39(2):340-345, April 1990.
- [6] J.H.R.Enslin. Digital signal processing in electrical power systems: Calculation of power under non-sinusoidal voltage and current conditions. *The Transactions of the SA Institute of Electrical Engineers*, pages 17-24, July 1988.
- [7] A.Khotanzad and J.Lu. Classification of invariant image representations using a neural network. *IEEE Transactions on Acoustics, Speech and Signal Processing*, 38(4):1028-1038, June 1990.
- [8] R.P.Lippmann. An introduction to computing with neural nets. *IEEE ASSP Magazine*, 2:4-22, April 1987.
- [9] W.Y.Huang and R.P.Lippmann. Neural nets and traditional classifiers. In D.Z.Anderson, editor, *Neural Information Processing Systems*, pages 387-396, Denver, Co, 1988. AIP.
- [10] B.Irie and S.Miyake. Capabilities of three-layered perceptrons. In *International Conference on Neural Networks*, pages I-641 - I-648, San Diego, July 1988. IEEE.
- [11] R.L.Watrous. Learning algorithms for connectionist networks: Applied gradient methods of non-linear optimization. In *International Conference on Neural Networks*, pages II-619 - II-627, San Diego, July 1987. IEEE.
- [12] R.O.Duda and P.E.Hart. *Pattern Classification and Scene Analysis*. Wiley, New York, 1973.

# DEVICE LEVEL MODELLING OF THE RISK OF UNSERVED ENERGY FOR THE DOMESTIC HOT WATER HEATER

B Rautenbach

I E Lane

University of Pretoria, South Africa

**ABSTRACT** - Unserved energy for a domestic water heater is presented as a function of heater mounting and size, rate of flow and thermostat setting. The domestic hot water heater is modelled with a reduced set of the Navier-Stokes equations for diffusive and convective flow, and simulated on digital computer by employing the QUICKEST method. With the assumption that the rate of extraction of hot water is coupled with the thermostat setting, the model is used to simulate various combinations of the above parameters. These results are combined with typical water usage patterns for different households and show how the risk of unserved energy increases for smaller heaters, lower thermostat setting, and for horizontal heaters compared to vertical heaters, with external control applied to the hot water load.

## NOMENCLATURE

$c$	Courant number ( $u \Delta t / \Delta x$ )
$C_p$	Specific heat of water [4.2 kJ/kg·°C]
$m$	Mass of water inside the heater [kg]
$m'$	Rate of water extraction from the heater [l/s]
$num$	Number of control-volume cells
$Q(t_n)$	Amount of energy inside the water heater [kJ] at time $t_n$
$Q_{dem}$	Energy extracted from the water heater [kJ]
$Q_{stored}$	Stored energy in the water heater [kJ]
$S$	Source term [W/m <sup>3</sup> ]
$T_c$	Threshold temperature for cold water [°C]
$T_i$	Temperature of $i$ th control-volume cell
$T_{inlet}$	Inlet water temperature [°C]
$T_{therm}$	Thermostat setting [°C]
$T_{out}$	Outlet water temperature [°C]
$t$	Time coordinate [s]
$\Delta t$	Time step [s]
$u$	Horizontal velocity [m/s]
$x$	Horizontal spacial coordinate [m]
$\Delta x$	Step size in $x$ direction [m]
$\alpha$	Generalized diffusion parameter
$\Gamma$	Generalized diffusion coefficient [m <sup>2</sup> /s]
$\Delta$	Difference operator
$\rho$	Density [kg/m <sup>3</sup> ]
$\phi$	Generalized scalar dependent variable
$i$	Horizontal spatial grid index
$l$	Left face of control volume
$n$	Time level
$r$	Right face of control volume
$*$	Space-time average

$CURV$ , Curvature at left control volume face

$GRAD$ , Gradient at left control volume face

QUICK Quadratic Upstream Interpolation for Convective Kinematics

QUICKEST QUICK with Estimated Streaming Terms

## 1. INTRODUCTION

The risk of unserved energy for a domestic hot water heater can also be described as the risk of drawing cold water when hot water is demanded. The mounting (horizontal or vertical) and size of the heater, the amount of water drawn from the heater and the thermostat setting have the most important influence on this risk. These parameters will be discussed in this paper.

The QUICKEST algorithm (Quadratic Upstream Interpolation for Convective Kinematics with Estimated Streaming Terms) is used to solve the energy equations that govern the temperature profiles inside the hot water heater [1]. It is based on local upstream-weighted quadratic interpolation in estimating numerical control-volume cell face values and gradients of all field variables undergoing simultaneous convection and diffusion.

The influence of the different parameters on the risk of unserved energy is evaluated in the simulations by drawing the total amount of hot water from the heater. The profile of the outlet temperature then serves as the yardstick for measuring the risk of unserved energy. It is assumed that the threshold temperature when the water becomes too cold ( $T_c$ ) is 45°C.

The amount of energy left in the heater at  $T_c$  is calculated for various combinations of the above parameters. The time expired until  $T_c$  is reached is also noted. In order to couple these results with risk of unserved temperature, we need to compare the amount of energy available with the amount demanded. The demand of hot water is a very random process, but for the purpose of this exercise the only interest lies in typical demand values for different applications of hot water (shower, wash hands, etc.) [2].

## 2. DEVELOPMENT OF THE MODEL

A one dimensional model is used for the hot water heater, because the convective term, when water is drawn, dominates in only one direction. The general differential equation for unsteady convection and diffusion of a scalar  $\Phi$  is [3]

$$\frac{\partial(\rho\Phi)}{\partial t} + \text{div}(\rho u\Phi) = \text{div}(\Gamma \text{grad}\Phi) + S \quad (1)$$

where  $\rho$  is the density of the specific property  $\Phi$  (or temperature in our case),  $u$  is the convecting velocity,  $\Gamma$  is the diffusion coefficient, and  $S$  is the source term. The one-dimensional simplification of Eq. (1) is

$$\frac{\partial\Phi}{\partial t} = -\frac{\partial(u\Phi)}{\partial x} + \frac{\partial}{\partial x}(\Gamma \frac{\partial\Phi}{\partial x}) + S \quad (2)$$

The four terms are the unsteady term, the convection term, the diffusion term, and the source term. Eq. (2) can be integrated in time from  $t$  to  $t + \Delta t$  and in space, across a control-volume cell of constant mesh size  $\Delta x$ , from  $- \Delta x/2$  to  $+ \Delta x/2$ , giving

$$\frac{\overline{\Phi_i^{n+1}} - \overline{\Phi_i^n}}{\Delta t} = \frac{(u\Phi)_l - (u\Phi)_r}{\Delta x} + \frac{(\Gamma \partial\Phi/\partial x)_r - (\Gamma \partial\Phi/\partial x)_l}{\Delta x} + S^* \quad (3)$$

where the overline represents spatial average, the  $\Phi$  terms on the right are time averages, and  $S^*$  is a space-time averaged source term. The subscripts  $l$  and  $r$  represent the left and right face respectively of the control-volume cell. Figure 1 depicts the control-volume cell for the one-dimensional case.

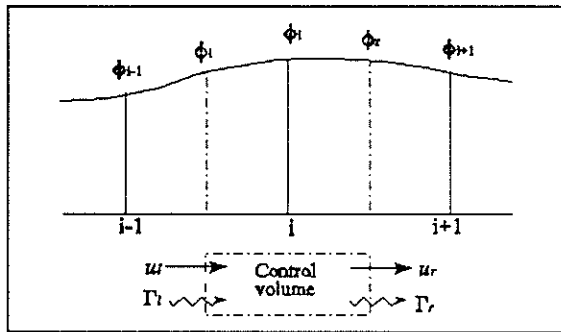


Figure 1: One-dimensional control volume.

The finite-difference QUICKEST algorithm corresponding to Eq. (3) is

$$\begin{aligned} \Phi_i^{n+1} = & \Phi_i^n + c_l \Phi_l^* + c_r \Phi_r^* \\ & + \left[ \alpha_r \left( \frac{\partial\Phi}{\partial x} \right)_r - \alpha_l \left( \frac{\partial\Phi}{\partial x} \right)_l \right] \Delta x \\ & + \Delta t S_i^* \end{aligned} \quad (4)$$

where

$$\begin{aligned} \Phi_l^* = & \Phi_{LIN} - c_l \text{GRAD}_l \frac{\Delta x}{2} \\ & + \left[ \frac{\alpha_l}{2} - \frac{1}{6}(1 - c_l^2) \right] \text{CURV}_l \Delta x^2 \end{aligned} \quad (5)$$

and

$$\left( \frac{\partial\Phi}{\partial x} \right)_l = \text{GRAD}_l - c_l \text{CURV}_l \frac{\Delta x}{2} \quad (6)$$

with

$$\Phi_{LIN} = \frac{1}{2}(\Phi_i + \Phi_{i-1}) \quad (7)$$

$$\text{GRAD}_l = \frac{\Phi_i^n - \Phi_{i-1}^n}{\Delta x} \quad (8)$$

$$\text{CURV} = \begin{cases} \frac{\Phi_i - 2\Phi_{i-1} + \Phi_{i-2}}{\Delta x^2}, & \text{if } u_l > 0 \\ \frac{\Phi_{i+1} - 2\Phi_i + \Phi_{i-1}}{\Delta x^2}, & \text{if } u_l < 0 \end{cases} \quad (9)$$

$\Phi_{LIN}$  is the usual linear interpolation,  $\text{GRAD}_l$  represents the average gradient, and  $\text{CURV}_l$  is the upstream-weighted finite difference approximation for the second derivative. Eq. (6) represents the time-averaged gradient. The  $c$ 's represent Courant numbers  $u\Delta t/\Delta x$ , and  $\alpha$ 's are diffusion parameters  $\Gamma\Delta t/\Delta x^2$ . By choosing temperature as the variable, these equations are used to model a hot water heater. For a more detailed explanation of the derivation of the equations refer to [1].

### 3. PRACTICAL RESULTS

In order to test the algorithm the outlet temperature of a vertically mounted, 3 kW, 150 litre domestic hot water heater was measured. The flow rate of the inlet water was 0.2 l/s. Figure 2 shows the close correlation between the simulated (QUICKEST) and actual results. This proves the accuracy of the simulation under conditions of convective flow.

### 4. SIMULATION RESULTS

It was assumed that the rate of extraction of hot water is directly coupled with the thermostat setting in the hot water heater. With a higher thermostat setting, the hot water would be drawn at a slower rate. Simulation results were then obtained for different mountings and heater sizes for two scenarios.

#### 4.1. Scenario 1

Both vertically and horizontally mounted water heaters, of three different sizes (100, 150 and 200 litres), were simulated. The thermostat setting was 55°C and the rate of water extraction 0.20 litres per second. The results are graphically depicted in Figures 3 and 4.

The difference in stratification between vertically and horizontally mounted hot water heaters can clearly be seen in the resulting graphs. The steeper descent in outlet temperature demonstrates the higher degree of stratification in vertically mounted hot water heaters.

#### 4.2. Scenario 2

The simulations of scenario one were repeated, but with a higher thermostat setting of 65°C and subsequently (assumption) a slower rate of hot water extraction of 0.15 litres per second.

The amount of energy inside the water heater was calculated for each time step  $t_n$  in the following manner

$$Q(t_n) = \sum_{i=1}^{num} \frac{m}{num} C_p T_i \quad (10)$$

For the vertically mounted water heaters between 94% and 96% of the available energy was extracted before  $T_c$  was reached. This changed to between 83% and 87% for the horizontally mounted water heaters. These figures can be used in calculations of the risk of unserved energy on the system level for various communities [4].

### 5. RISK EVALUATION

The risk of unserved energy, for a household in general, is not only a function of the physical parameters as described above. It is also dependent on the usage of hot water (by the household) and the type and amount of control applied to the water heater.

The control applied to the water heater and the physical parameters of the water heater influence the amount of stored energy in the water heater. For the purpose of this exercise we assume that external control disallows the operation of the heater element for the period under consideration. This could be the case during peak system load periods [5]. Also, it is assumed that the water in the heater is at maximum temperature (thermostat setting) at the starting time.

The amount of stored energy in the water heater (that can be extracted before unserved energy is experienced) is then

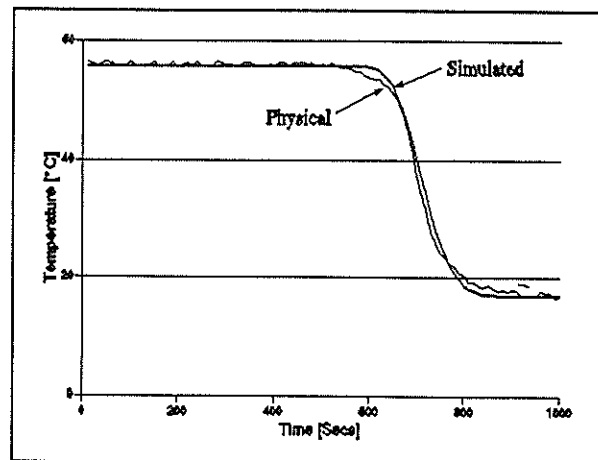


Figure 2: Simulated vs. actual temperature profiles (vertical hot water heater).

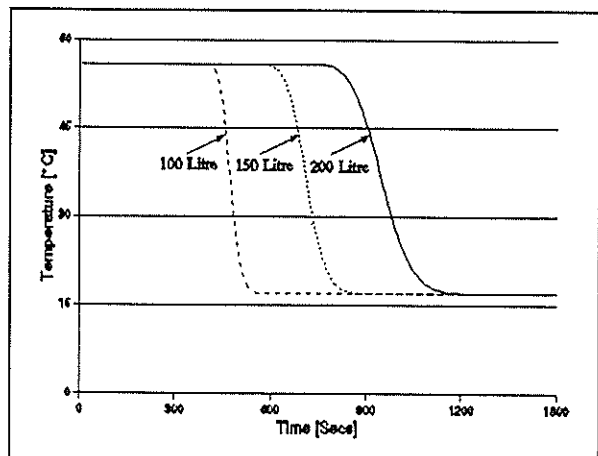


Figure 3: Simulated outlet temperature profiles for vertical hot water heaters (scenario 1).

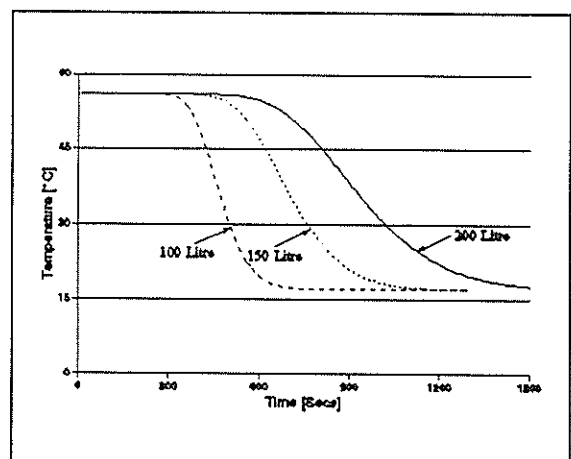


Figure 4: Simulated outlet temperature profiles for horizontal hot water heaters (scenario 1).

$$Q_{\text{stored}} = mC_p(T_{\text{therm}} - T_c) \quad (11)$$

The amount of stored energy for the different water heater configurations can be found in Table 1.

If the amount of energy demanded exceeds the stored amount (Table 1) then unserved energy will be experienced. Physically this means that  $T_{\text{out}}$  will fall below  $T_c$ . Obviously the usage of hot water depends on the type of household. To demonstrate this effect three types of households were chosen with low, average and large usage patterns. For the purpose of this evaluation we chose the following households: two adults, two adults with two children, and two adults with four children.

We assume that half of the children bath and one of the grown-ups shower during the period under consideration, and that the average use of the washbasin is twice per person during the period under study.

Then, using draw sizes for bath, shower and sink of 60, 40 and 4 litres respectively, Table 2 shows the results for scenario 1 [2]. A '✓' denotes hot water at all times, while a 'x' shows that cold water was drawn. The first column shows the water heater configuration in size (100, 150, 200) and mounting (vertical or horizontal).

For scenario 2 the picture changes slightly. Assuming that the amount of energy drawn is the same as in scenario 1 (which is in line with the assumption that a higher thermostat setting causes a lower rate of extraction), the results are shown in Table 3.

## 6. DISCUSSION OF SIMULATION RESULTS

When evaluating the results shown in the above tables, it is necessary to remember that a very excessive draw schedule was used for the various households. The control applied also prevented any replacement of energy to the water heater. However, these simulations do serve a purpose in that they give an idea of the influence of the physical parameters of a domestic hot water heater on the risk of unserved energy.

The size of the water heater had a very predictable influence on the risk of unserved energy. The larger the water heater, the more energy could be stored, and the more could be extracted. However, when the amount of energy required exceeded the amount available, there was still unserved energy.

The influence of the thermostat setting, with our assumption that it is coupled with the draw rate, also correlated with what was expected. The higher

**Table 1:** Values of stored energy for different water heater configurations.

Size [Litres]	Scenario 1 Energy [kJ]	Scenario 2 Energy [kJ]
100	15960	20160
150	23940	30240
200	31920	40320

**Table 2:** Risk of unserved energy for different water heater configurations for scenario 1.

	Low	Medium	Large
100h	✓	x	x
100v	✓	x	x
150h	✓	x	x
150v	✓	x	x
200h	✓	x	x
200v	✓	✓	x

**Table 3:** Risk of unserved energy for different water heater configurations for scenario 2.

	Low	Medium	Large
100h	✓	x	x
100v	✓	x	x
150h	✓	x	x
150v	✓	✓	x
200h	✓	✓	x
200v	✓	✓	✓

thermostat setting in scenario 2 caused a higher amount of available energy in the water heaters. For example, the large family did not experience unserved energy with the largest vertical water heater with a higher thermostat setting.

The most interesting result was that the mounting of the water heater had an influence on the risk of unserved energy. In both scenarios there was a case where a certain size horizontal water heater produced cold water, while the vertical one did not.

One physical parameter that was not investigated here is the losses through the tank walls. Calculations are not included in this paper, because the effect of losses on the risk of unserved energy is minimal. The percentage of energy lost during the period under consideration ranged from 2% for the 100 litre tank, to 1.8% for the 200 litre tank.

## 7. CONCLUSIONS

The simplifying assumptions in this paper need qualification. The worst case scenario was presented, where no energy was allowed to be replaced, and heavy draw schedules were applied to the water heaters. This could be the case on an extremely cold day in winter. During the summer, however, this would not be the case. The amount of control applied should be less, resulting in a reduced risk of unserved energy for the domestic customers in general.

With this in mind, it was shown how, under external control conditions, an increase in water heater size and thermostat setting might reduce the risk of unserved energy. Importantly, it was also shown that this risk is less for a vertically mounted water heater compared with a horizontally mounted one of the same size.

One option to reduce the risk of unserved energy under control conditions would be to install only large water heaters, with high thermostat settings. This option would however be economically unpopular, not only because of the high initial investment, but also because of the high resulting electricity account for the household.

A more viable option would be to promote the installation of vertically mounted water heaters. In South Africa the majority of installed domestic hot water heaters are horizontal [6].

A third option would be to control the hot water load intelligently. One method would entail controlling different types of households (and different usage patterns) separately. Control could also be applied according to hot water heater size (storage capacity and element rating). Another method which is

currently under investigation by the author, is to use the storage capability of a hot water heater to store the correct amount of energy before peak load periods, and to still control during these periods [7].

If control of the domestic hot water load is planned on a nation-wide scale, consideration should be given to those municipalities who have already invested in a control system, and who would not happily change to another. The control strategy should therefore be compatible with various control systems.

In the opinion of the author the risk of unserved energy will never be zero due to the random nature of the demand of hot water. For the supply authority there will always be a compromise between the amount of control applied to the hot water load, and the amount of complaints received due to unserved energy.

## REFERENCES

- [1] Minkowycz, W. J. *et. al.*: "Handbook of Numerical Heat Transfer" pp. 347-378, John Wiley & Sons, 1988.
- [2] Schultz, W. W. and Goldschmidt, V.W.: "Energy Performance of a Residential Electric Water Heater" ASHRAE Transactions, No. 2630, pp. 310-334.
- [3] Patankar, S. V.: "Numerical Heat Transfer and Fluid Flow" pp. 11-21, Hemisphere Publishing Corporation, 1980.
- [4] Smit, J. J. and Lane, I. E.: "Calculation of the Risk of Unserved Energy" Centre for New Electricity Studies, Department of Electrical and Electronic Engineering, University of Pretoria, Pretoria, South Africa, October 1994.
- [5] Malan, J. G.: "Load Management in a Metropolitan Supply Authority" Municipal Engineer, pp. 21-29, April 1993.
- [6] Beute, N.: "Domestic Utilization of Electrical Grid Energy in South Africa" Ph.D. Thesis, University of Potchefstroom, 1993.
- [7] Rautenbach, B. and Lane, I. E.: "A Minimum Discomfort-Minimum Energy Controller Model for Domestic Water Heating" SAUPEC-94, Proceedings of the Fourth Conference, Cape Town, January 1993.

## AUTHORS' ADDRESS

Centre for New Electricity Studies, Department of Electrical and Electronic Engineering, University of Pretoria, Pretoria 0002.

# THE DEVELOPMENT OF A LOW COST REFRIGERATOR FOR LOW INCOME HOUSEHOLDS

Thomas Baker.

Charles Dingley.

University Of Cape Town, South Africa.

Having recognised the need that has arisen in South Africa for low cost refrigerators, it was decided to attempt to develop a low-cost refrigerator as a fourth year thesis project.

The proposed cooling method was to use thermo-electric cooling devices, because in many ways, these devices are ideal for this application. Thermo-electric coolers were chosen because they are lightweight, small, have no moving parts and are cheap and reliable.

A prototype was designed, built and tested and this paper will give an overview of the work done and results obtained. The paper will also make mention of a few issues surrounding the subject of low cost refrigeration.

## 1. INTRODUCTION.

In South Africa at the moment, one of the major priorities of both the government and ESKOM is that of electrifying the townships and rural areas. This will allow people who have historically not had access to electricity the opportunity to benefit from this cheap, clean energy source. At present, the RDP is committed to electrifying 500 000 homes per year in the next 5 years.

One of the biggest benefits of having access to electricity is that of refrigeration. Refrigeration allows the user to keep food fresh for longer which means that the user needs to go shopping for food less often, thus saving both time and money spent travelling. Beverages can also be kept cool which greatly increases their enjoyment.

Although there are several refrigerators on the market, they are often unaffordable for the people at whom the electrification scheme is aimed.

Thus, having identified this need, it was decided to focus the effort of this project on developing a low cost refrigerator, with the need of the above mentioned consumers in mind. It was reasoned that

because the unit's prime function would be to keep food fresh, it would not need to have a freezer compartment and thus a smaller refrigeration unit would be required resulting in a lower initial cost.

The most common method of cooling household refrigerators is the compression-expansion cycle. Although efficient, this method of cooling requires expensive machinery to operate and so it was decided to examine other methods of cooling for this project to keep the initial cost low.

Another method of cooling is that of thermo-electric cooling which is much cheaper than the conventional cycle. Thus, it was decided to investigate the viability of using thermo-electric (TE) cooling for the application of low cost refrigeration.

The main body of this paper will further discuss the need for and requirements of a low cost refrigerator for the South African market, followed by a section dealing with the prototype built. It will end by discussing the testing and results.

## 2. WORK DONE AND AREAS COVERED.

### 2.1. The need for and requirements of a low cost refrigerator.

At the start of the project, a few appliance retailers were visited to determine the cost of small refrigerators. It was found that a refrigerator of 60 litres was priced at R800, while a 140 litre model was priced at R950 (these prices were on cash terms).

For the people at whom the RDP's electrification scheme is aimed, such a new refrigerator would cost up to a month's income, or require getting into debt. This places refrigerators out of many people's financial reach.

A small survey (12 people) was conducted to get the views of a sample of how the potential customers felt about this issue. The questions asked were to try to

gauge the extent to which a refrigerator makes a difference in a low-income household.

People interviewed who owned refrigerators said that they needed to purchase fresh food 2 to 3 times a week, compared to almost every day in households which did not own refrigerators. In either case the mode of transport was by foot or taxi (a taxi trip would cost 2 to 4 rands each way). The time spent shopping for food ranged from 1 to 3 hours, depending on transport time. It should be mentioned that in some cases food shopping was done on the way to and from work.

In response to some other questions asked, people felt that if the price was low enough, not having an ice box would be acceptable. Most people felt that for a small, simple refrigerator of around 80 litres a price of R400-500 would be reasonable. Everybody interviewed agreed on the need for low cost refrigeration.

The next area to be considered is the design of the refrigerator. The primary requirement would be that the refrigerator needed to be as cheap as possible while still satisfying constraints such as maintaining the required temperature, having a reasonable sized volume, being reliable, rugged etc.

To achieve a low initial cost, the design needs to utilise cheap materials and parts. Using standard parts and materials would in most cases keep the price lower. The design also needs to be cheap to manufacture to avoid large labour costs if it were ever to be mass produced. As for the cooling mechanism, it was reasoned that if the initial purchase price was low enough, a lower efficiency might be acceptable.

The designer needs to determine an optimum size for the refrigerator. Naturally, a small refrigerator would cost less, but it may then be too small to be useful. The minimum size needs to be large enough to allow storage of beverage and milk bottles, and to allow space for storage of fruit and meat.

The required temperature for storing meat and milk is a maximum of 7°C (Hull: 1933) if storage of longer than two days is required. Deterioration of foods is due mainly to micro-organisms, whose growth rate is very dependant on temperature. Thus, it is important not to exceed this temperature. It was recognised by Papst (1929 & 1931) that bacteria remain dormant for a time and then find it possible to grow. This dormant time depends on their temperature. If meat and milk are kept below 7°C this dormant time is approximately two days. After that they grow quickly.

Other desirable characteristics include reliability, low running costs, being lightweight (making it easy to transport) and robust.

## 2.2. The prototype built.

To cool the cabinet, thermo-electric coolers (TECs) were used. TECs are heat pumps and have a number of desirable characteristics, making them ideal in some ways for this application. They are small (the TECs used for the prototype were 40x40x3 mm in size), lightweight, reliable (MTBF > 22 years), have no moving parts, and are cheap (the TECs used for the prototype cost R38.50, bought from a company who imports them in bulk). Their main disadvantages are that they are inefficient and they require a large DC power supply (the ones used in the prototype required 12V and 5-6 A each).

TECs utilise the *Peltier effect* for their cooling action. The principle is as follows: In the same way that a thermocouple produces a voltage when exposed to a temperature difference (due to the junction of two different metals), TECs produce a cooling effect due to the voltage applied across N and P-type semiconductor material. For more information on their operation, the reader is referred to "Circuits, Devices and Systems" by Ralph J. Smith, Fourth edition (Wiley), page 566, or to "Thermodynamics: An Engineering Approach" by Cengel & Boles (McGraw Hill) pp 519-521.

TECs are not manufactured in S.A. and so it would have been necessary to import some for the prototype.

Fortunately a company in Johannesburg was found which uses TECs for manufacturing water coolers. This company imports TECs in large numbers from the USA and kindly supplied two TECs rated at 51.4 Watt of heat pumping capacity at their cost price of R38.50. (TECs come in sizes ranging from 1.2W to 125W and 51.4W is the size used by the company above).

The cabinet was constructed from sheet plastic and used polystyrene foam as insulation. In the event of the refrigerator being mass produced it is suggested that the cabinet be made from blow moulded polyethylene which would then have its walls filled with foam which could be injected. A plastic cabinet would be cheap and easy to manufacture and would also be tough and corrosion resistant. The prototype volume was 80 litres.

A simple temperature control mechanism was designed and built and was set to regulate the inside temperature between 3°C and 6°C.

The TECs were installed in the cabinet wall with large heat sinks on either side. The warm heat sinks were fitted with a fan to increase heat dissipation. The outside heat sinks needed to be kept as cool as possible because the efficiency of the TECs decreases as the change in temperature across the plates increases.

For the DC power supply, a step down transformer was used which was then rectified using a diode (full wave) rectifier which was smoothed using capacitors.

To reduce the current required from the transformer, the TECs were connected in series.

Once the prototype was working, it was tested to see how the TECs performed. The results were not as good as was hoped for. This was due to two reasons: firstly, it was initially assumed that the inside heat sinks needed to be at the required air temperature. On testing however, even when the inside heat sinks were at their lowest temperature of 4.5°C, the air temperature was at 9°C. On consulting refrigeration specialists, it was discovered that the cool heat sink would need to be at around 0°C to maintain an air temperature of 5°C in which case the cooling power required would have been under-designed for.

Although this was true to a certain extent, the TECs were rated to pump 51.4 W each, while it was calculated that the insulation would only let in 30W of heat from the surroundings. It was known that the TECs' performance decreased with the temperature difference but it was not expected to drop that much. Thus, the second reason was that the TECs' performance dropped considerably with the temperature difference.

### 3. CONCLUSION AND DISCUSSION.

Firstly, it was noted that the assumption that not having an ice-box would save costs is not correct because to have the low air temperatures desired, the inside heat sink needs to be around 0°C anyway. In this case, the inside heat sink could be designed to form the outer casing of an ice box making this an additional feature.

The tests done showed that more TECs would be required to reach the lower temperatures desired. Although they are cheap enough to install more this implies that more power is used by the refrigerator.

The problem with using TECs that became apparent is their poor heat pumping performance at the temperature difference required for the operation of refrigerator. A typical compression-expansion cycle

operates with a coefficient of performance of approximately 3 (i.e. it pumps 3 watts of heat for every watt of electricity it uses) compared to a figure of 0.25 calculated for the TECs operating in the prototype. In other words a TE cooled refrigerator would consume 12 times more electricity than a conventionally cooled refrigerator.

For the prototype, it was calculated that with the extra TECs installed to cool the air to 5°C, it would draw 150W of electricity. A conventional cycle would thus require no more than 15W to do the same job. The energy difference is thus in the region of 135W.

Assuming an electricity cost of 20 cents per kWh, this means an additional cost of around R20 per month for the consumer. It is estimated that the (equipment) costs for a TE cooled refrigerator would be around R575, made up as follows:

TECs (for 150W power)	» R150
Heat Sink & Fan	» R100
Transformer	» R200
Cabinet	» R 75
Control & DC Rectification	» <u>R 50</u>
Total	<u>R575</u>

These prices assume that these items are bought in large quantities making them cheaper. It should also be noted that this total also neglects labour costs.

As mentioned earlier, a similar sized refrigerator would cost R800 from a retailer. Thus in less than a year, the price difference would be made up in the cost of the electricity and thus it was finally concluded that TE cooling would not be suitable for low cost refrigeration.

A question that needs to be asked is how much the ex-factory cost of conventional refrigerators actually is. If a retailer can sell a refrigerator of almost double the volume of the prototype, at less than double the cost for R950, and still make enough profit to make that price viable, it can be speculated that the cost of the refrigerator when it left the factory was a few hundred rands less (considering that it probably went through a number of "middle men" first, each adding their own mark up).

Therefore, even if TEC cooling was viable, by the time the refrigerator reached the consumer it would probably not be sold for significantly less (if at all less).

It is commendable that both the government and ESKOM are putting so much effort into electrification, but perhaps they should be looking into

ways of addressing the problem of low cost appliances. One possible solution would be to use their resources to get a basic simple refrigerator from the manufacturers directly to the consumers - while not robbing the retailers (who would then continue to sell the more advanced models that they already sell) of their livelihood.

Unless somebody with the financial or political capacity does something to resolve this problem (with a social, non profit motivation), it will probably go unsolved. History is proof of this. What will probably *continue* to happen is that a number of retailers will make a large profit from selling normal priced refrigerators to people who can afford them, while large numbers of people who cannot afford the cost of a new refrigerator will have to continue to live without refrigeration.

## REFERENCES

Hull, H.B. "Household Refrigeration" *Nickerson & Collins Co.* pp 51, 1933.

Papst A.M. "Milk in the household refrigerator" - *Ice and Refrigeration*, v76, pp14-15 Jan 1929.

Papst A.M.- "Meat keeping in Home refrigerators studied in varying conditions" *Yearbook of agriculture*, pp 369-370, 1931.

## Address of Author

Mr Thomas Baker  
c/o Mr C.E. Dingley  
University of Cape Town  
Private Bag  
Rondebosch  
7700

# CALCULATION OF THE RISK OF UNSERVED ENERGY

J.J. Smit and I.E. Lane

Department of Electrical and Electronic Engineering  
University of Pretoria  
Pretoria, South Africa

**Abstract:** - This paper proposes a method to calculate the risk of cold water (risk of unserved energy) for a group of consumers whose hot water storage heaters are being controlled by means of a load control algorithm. The risk calculation is achieved by using a probabilistic demand/supply model.

## Nomenclature

$t_c$	Time period of applied control action
$E_u(t+t_c)$	Stored energy at time $t+t_c$ [kJ]
$E_u(t)$	Stored energy at time $t$ [kJ]
$\dot{Q}$	Nett heat flow from tank [kJ/s]
$\dot{m}$	Water flow rate from tank [kg/s]
$P(t)$	Power input into the tank [kW]
$\Delta E_u$	Water usage/change in stored energy [kJ]
$K$	Percentage of useful stored energy in a particular model of hot water storage heater
$\Delta E_{\max}$	Maximum amount of available stored energy that can be withdrawn from a particular model of hot water storage heater [kJ]
$m$	Mass [kg]
$C_p$	Specific heat capacity [kJ/kg.°C]
$T_{\text{therm}}$	Average thermostat setting [°C]
$T_{\text{inlet}}$	Average inlet water temperature [°C]
$T_{\text{out}}$	Outlet water temperature [°C]
P.d.f.	Probability distribution function
$f(E)$	P.d.f. for $\Delta E_s$
$g(E)$	P.d.f. for $K \cdot \Delta E_{\max}$
$P_0$	Occupance probability for a working family (no children)
$P_2$	Occupance probability for a working family (2 children)
$P_4$	Occupance probability for a working family (4 children)
$P_a$	Occupance probability for a 100 litre horizontal hot water storage heater
$P_b$	Occupance probability for a 150 litre horizontal hot water storage heater

$P_c$	Occupance probability for a 200 litre vertical hot water storage heater
$P_u$	Probability of unserved energy
$n$	Number of houses
$\mu_t$	Mean value of the combination of a number of normalised normal distributions
$\sigma_t$	Standard deviation of the combination of a number of normalised normal distributions

## 1. Introduction

Controlling the domestic hot water storage heaters of consumers is a practise that has been around for a number of years. Various aspects of this practise have been investigated [1,2,3,7]. Yet, no mention could be found of the effect of such a control strategy on the lifestyle of the consumer. In this paper we will develop a method by which we can quantify this effect. This method will be: The calculation of the risk of unserved energy<sup>1</sup>.

## 2. Theory

The following equations govern the energy balance in a hot water storage heaters.

$$E_u(t + t_c) = E_u(t) - \int_0^{t_c} \dot{Q} \cdot dt + \int_0^{t_c} P(t) \cdot dt$$

$$\Delta E_u = \int_0^{t_c} (\dot{Q} - P(t)) \cdot dt \quad (1)$$

<sup>1</sup> When a control algorithm causes a consumer's hot water supply system to yield cold water, we can say that the supply authority failed to serve the consumer with the required energy. The risk of unserved energy is thus nothing more than the risk of having cold water.

$$\int_0^{t_c} \dot{Q} \cdot dt - \int_0^{t_c} P(t) \cdot dt > K \cdot \Delta E_{\max} \quad (2)$$

$$\Delta E_u > K \cdot \Delta E_{\max}$$

$$\dot{Q} = \dot{m} \cdot C_p \cdot (T_{\text{out}} - T_{\text{in}}) \quad (3)$$

$$\Delta E_{\max} = m \cdot C_p \cdot (T_{\text{therm}} - T_{\text{inlet}}) \quad (4)$$

Suppose we have a hot water storage heater, with the maximum amount of energy, stored in the water. In order to receive cold water from this water heater, we need to fulfil two conditions:

- More energy must be withdrawn from the heater in a certain period, than can be replaced by the electrical heating element over that same period (i.e.  $\Delta E_u$ , as defined in eq. 1, must be positive).
- To take into account the stratification properties of the hot water storage heater,  $\Delta E_u$  must be greater than  $K \cdot \Delta E_{\max}$  (over a time period  $t_c$ ).  $\Delta E_{\max}$  represents the maximum amount of stored energy, that can be withdrawn from the water heater, at the beginning of  $t_c$ . The constant  $K$  represents the percentage of  $\Delta E_{\max}$  that can be withdrawn, before the water temperature goes below the level we perceive as cold.

Both water usage and control actions are random events and we can thus generate a probability distribution function (hereafter called p.d.f.), for  $\Delta E_u$ . In this paper, the effect of  $P(t)$  is ignored, by assuming that the element is switched off for the whole period in question ( $t_c$ ). This is representative of the 'worst case' control condition which supply authorities would apply if the system power consumption peak exceeds the control demand setting for a period  $t_c$  and the water consumption peak coincides with the power consumption peak.

The water heater model constant  $K$ , in eq. 2, is determined only by the physical dimensions of the hot water storage heater and the mounting orientation [8].  $\Delta E_{\max}$  is dependent on the holding capacity of the heater as well its thermostat setting ( $m$  and  $T_{\text{therm}}$  in eq. 4). Because different consumers

have different hot water requirements they use different hot water storage heater models. We can therefore also generate a p.d.f. for  $K \cdot \Delta E_{\max}$ .

If we plot the p.d.f. for  $K \cdot \Delta E_{\max}$  together with the one for  $\Delta E_u$  (consumption) on the same axis (as shown in figure 3), we can determine the probability that  $\Delta E_u > K \cdot \Delta E_{\max}$  for a group of consumers, as follows [5]:

$$P_u = \int_0^E f(E) \cdot \left( \int_0^E g(E) \cdot dE \right) \cdot dE \quad (5)$$

$$= \int_0^E \int_0^E f(E) \cdot g(E) \cdot dE \cdot dE$$

With  $f(E)$  being the p.d.f. for consumption/demand ( $\Delta E_u$ ) and  $g(E)$  the p.d.f. for storage/supply ( $K \cdot \Delta E_{\max}$ ).

The control period  $t_c$  is defined as a period around the peak times of power consumption.

### 3. Results

Suppose there exists a population with properties as given by tables 1, 2, 3, and 4.

**Table 1:** Demographic and consumption data for 300 households.

Consumer class	No.	Ave. water usage (L): (1 hour over peak periods)	Probability of class occurring
Working family (no children)	45	23	$P_0 = 0.15$
Working family (2 children)	165	41	$P_2 = 0.55$
Working family (4 children)	90	53	$P_4 = 0.3$

The 'Ave. water usage' column in table 1 represents the average water usage, for one hour, over peak periods, for different classes of consumers. Tables 2, 3 & 4 lists the data pertaining to distribution of hot water storage heaters in the same three consumer classes. Here 'no.' implies the amount that is present in the total

population, 100h represents the size and mounting orientation of the hot water storage heater (h=horizontal, v=vertical).

**Table 2:** Hot water storage heater data for 100 households (Working family - no children)

Capacity (L) & orientation	No.	K.	Mean $E_{\max}$ (kJ)	$P_a, P_b$ & $P_c$
100h	35	0.83	16800	0.35
150h	55	0.85	25200	0.55
200v	10	0.96	33600	0.10

**Table 3:** Hot water storage heater data for 100 households (Working family - two children)

Capacity (L) & orientation	No.	K.	Mean $E_{\max}$ (kJ)	$P_a, P_b$ & $P_c$
100h	15	0.83	16800	0.15
150h	65	0.85	25200	0.65
200v	20	0.96	33600	0.20

**Table 4:** Hot water storage heater data for 100 households (Working family - four children)

Capacity (L) & orientation	No.	K.	Mean $E_{\max}$ (kJ)	$P_a, P_b$ & $P_c$
100h	2	0.83	16800	0.02
150h	50	0.85	25200	0.50
200v	48	0.96	33600	0.48

### 3.1 P.d.f.'s for water usage ( $\Delta E_u$ )

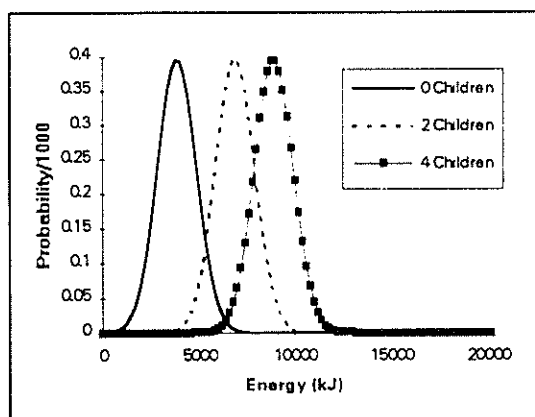


**Figure 1:** P.d.f.'s for water usage ( $\Delta E_u$ ) for three consumer classes.

The p.d.f.'s for water usage ( $\Delta E_u$ ), were modelled using normal distributions. The mean values of these distributions were obtained from the average water usage (for a period of 1 hour over peak periods) for each consumer class, given in table 1. The standard deviations of these water usage p.d.f.'s were assumed to be approximately 6 litres (1008 kJ) for each class. The resulting p.d.f.'s are shown in figure 1.

### 3.2 P.d.f.'s for hot water storage heaters ( $K \cdot \Delta E_{\max}$ )

The p.d.f.'s for  $K \cdot \Delta E_{\max}$  not only depends on the information given in tables 2, 3 & 4 but also on the thermostat settings of the hot water storage heaters. If we assume that the thermostat settings are distributed normally around a mean value of 65°C, with standard deviations of 2, 3, & 5°C respectively, the normalised p.d.f.'s for the different water heater models can be shown to be those given in figure 2.

The total p.d.f. for  $K \cdot \Delta E_{\max}$  for each consumer class is a combination of the three water heater p.d.f.'s shown in figure 2. The combination of these p.d.f.'s is achieved by taking a trial sample of  $n$  houses, and using the multinomial formula (eq. 6) to find all the possible combinations of water heaters for these five houses.

$$(P_a + P_b + P_c)^n = 1.0 \quad (6)$$

If we take a representative trial sample of 5 houses, from the consumer class with no children (table 2), then according to the multinomial theorem (eq. 6), we get an equation whose terms are shown in table 5 [9]. Also shown in table 5 are the probability of occurrence for each term, calculated with the given values of  $P_a$ ,  $P_b$  and  $P_c$ . The energy value associated with each term represents the mean value of the p.d.f. that is obtained by combining the five p.d.f.'s for each term. The combination of the five p.d.f.'s in each term is accomplished using the following well known equations:

$$\mu_i = \sum_{n=1}^i \mu_i \quad (7)$$

$$\sigma_t = \sqrt{\sum_{n=1}^i \sigma_i^2} \quad (8)$$

**Table 5:** Probabilities and loads for a 5 house sample

Term	Value (P)	Load (kJ)
$P_a^5$	0.0052522	13944
$P_b^5$	0.0503284	21420
$P_c^5$	0.0000100	32256
$5 P_a^4 P_b$	0.0412672	15439.2
$5 P_a^4 P_c$	0.0075031	17606.4
$5 P_a^3 P_b^4$	0.1601359	19924.8
$5 P_b^4 P_c$	0.0457531	23587.2
$5 P_a^3 P_c^4$	0.0001750	28593.6
$5 P_b^3 P_c^4$	0.0002750	30088.8
$20 P_a^3 P_b^3 P_c$	0.0471652	19101.6
$20 P_a P_b^3 P_c^3$	0.1164625	22092
$20 P_a P_b P_c^3$	0.0038500	26426.4
$10 P_a^3 P_b^2$	0.1296969	16934.4
$10 P_a^3 P_c^2$	0.0042875	21268.8
$10 P_a^2 P_b^3$	0.2038094	18429.6
$10 P_b^3 P_c^2$	0.0166375	25754.4
$10 P_a^2 P_c^3$	0.0012250	24931.2
$10 P_b^2 P_c^3$	0.0030250	27921.3
$30 P_a^2 P_b^2 P_c$	0.1111688	20596.8
$30 P_a^2 P_b P_c^2$	0.0202125	22764
$30 P_a P_b^2 P_c^2$	0.0317625	24259.2
<b>TOTAL:</b>	<b>1.00000000</b>	

The area under the specific p.d.f. must be equal to the calculated probability. In order to make the generated p.d.f.'s relevant to a single household, we must translate the p.d.f. by dividing its mean value by five. Figure 2 shows the five p.d.f.'s and the resulting combined p.d.f., translated to be specific to one household, for the term  $30 P_a^2 P_b^2 P_c$  in table 5. Only four p.d.f.'s are visible because the two p.d.f.'s for 150h and the two p.d.f.'s for 200v are plotted over each other.

Using the method described above, we now have 21 combined p.d.f.'s (one for each term of table 5). These 21 distributions must be combined to yield a p.d.f. that is representative of the total population for the class '0 Children'. The 21 distributions can be combined by dividing the energy axis into small intervals, integrating the p.d.f.'s over each interval and adding the results.

The total p.d.f. for the class of consumer '0 Children' is shown in figure 3 together with the p.d.f. for water usage ( $\Delta E_u$ ). This same method can be used to generate p.d.f.'s for the classes '2 Children' and '4 Children'.

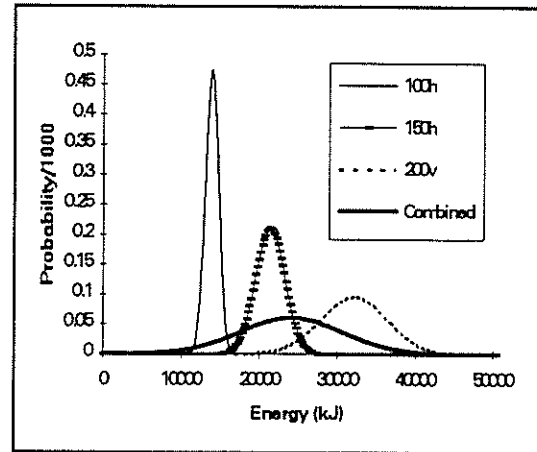


**Figure 2:** Individual & combined p.d.f.'s for the term  $30 P_a^2 P_b^2 P_c$  in table no. 5

### 3.3 Scenarios

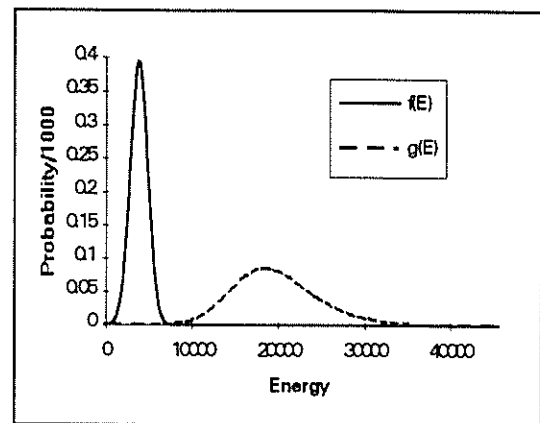


**Figure 3:**  $\Delta E_u$  and  $K \cdot \Delta E_{\max}$  p.d.f.'s for a working family with no children

Using eq. 5 we can calculate the risk of unserved energy for a working family with no children, from the p.d.f.'s for  $\Delta E_u$  ( $f(E)$ ) and  $K \cdot \Delta E_{\max}$  ( $g(E)$ ) shown in figure 3 as  $P_u = 0.364\%$ . Applying the same technique to the classes '2 Children' & '4 Children' we can calculate their risk of unserved energy as:  $P_u = 1.695\%$  &  $P_u = 2.894\%$ .

The risk was calculated for another four scenarios. In scenario 4 the control period was increased, in scenario 5 distribution of

water heaters was altered and in scenario 6 we lowered the thermostat setting. In scenario 7 we calculated the risk for a group of consumers who occupied a block of houses in a totally random fashion. The results are summarised in table 6.

**Table 6: Results**

Scen No.	$t_c$ (hours)	Water heater	Therm. setting	$P_u$ (%)
1	1	table 2	65°C	0.364
2	1	table 3	65°C	1.659
3	1	table 4	65°C	2.894
4	1.5	table 4	65°C	10.27
5	1	table 2	65°C	6.103
6	1	table 4	60°C	5.391
7	1	Comb.	65°C	13.10

#### 4. Discussion of results

The risk of unserved energy calculated in scenarios 1, 2 & 3 serves as a basis for discussion. Scenarios 4, 5 & 6 proved the ability of the developed risk calculation method to accurately predict the trend in the risk of unserved energy, when different components and constants of the hot water supply system are varied.

Scenario 7 highlighted the value of good advice, given by supply authorities to customers whose hot water storage heaters are being controlled. A consumer that has been given good advice by the supply authority will be aware of the effect of hot water storage heater capacity and thermostat setting on his risk of unserved energy. He would therefore choose a water heater model with the correct capacity and adjust his thermostat setting so as to minimise his risk of unserved energy. This type of consumer is modelled in scenarios 1, 2 & 3. An uninformed consumer would randomly choose his water heater model and thermostat setting with no regard to his family size and water usage. This type of consumer is modelled in scenario 7. From table 6 it is clear that this type of consumer will have a significantly higher risk of unserved energy compared to the informed consumer. The value of advice is of importance to all supply authorities but especially to those who has to supply mass housing projects. Unhappy consumers may

resort to drastic measures such as picketing or even rent boycotts - a situation any supply authority wants to avoid.

#### 5. References

- [1] Rautenbach, B. and Lane, I.E.: "A Minimum Discomfort - Minimum Energy Controller Model for Domestic Water Heating" Saupec-94, Proc. of the Fourth South African Univ. Power Engineering Conf., Cape Town, Jan. 1994.
- [2] Malan, J. G.: "Load Management in a Metropolitan Supply Authority" Municipal Engineer, pp. 21-29, Apr. 1993.
- [3] Beute, N.: "Domestic Utilisation of Electrical Grid Energy in South Africa" PhD Thesis, Univ. of Potchefstroom, 1993.
- [4] Schultz, W.W. and Goldschmidt, V.W.: "Energy Performance of a Residential Water Heater" ASHRAE Transactions, No. 2630, pp 310-331, 1976.
- [5] O'Connor, P.D.T.: "Practical Reliability Engineering" Second Edition, John Wiley & Sons, Chap. 4, pp 101 - 104.
- [6] Smit, J.J.: "Calculation of the Risk of Cold Water" Student Paper, C.N.E.S., Dept. of Electrical and Electronic Engineering, Univ. of Pretoria, Pretoria, South Africa, Jun. 1994.
- [7] Van Harmelen, G.L. and Lane, I.E.: "An object orientated approach for determining the system response of centralised and decentralised domestic load control options", Proc. of the Thirteenth IASTED International Conf., Modelling, Identification and Control, Grindelwald, Switzerland, 21-23 Feb., 1994, pp. 120 - 123.
- [8] Rautenbach, B.: "Device level modelling of the risk of unserved energy for the domestic hot water heater", Student Paper, C.N.E.S., Dept. of Electrical and Electronic Engineering, Univ. of Pretoria, Pretoria, South Africa, Jun. 1994.
- [9] Townsend, M.: "Discrete mathematics: Applied combinatorics and graph theory", The Benjamin/Cummings Publishing Company, Inc., 1987, Chapter 2, pp. 70 & 87.

# INSULATOR POLLUTION MONITOR: CALIBRATION RESULTS

P. Davel

J.P. Holtzhausen

W.L. Vosloo

University of Stellenbosch  
South Africa

## ABSTRACT

An insulator pollution monitoring apparatus has been developed at the University of Stellenbosch to determine the surface conductivity of the pollution layer on an insulator using artificial wetting of the pollutant. The new artificial wetting procedure proposed eliminates the traditional problems of non-repeatability and loss of pollutant. The new measuring procedure introduces extra environmental parameters that need to be established in order to perform the pollution severity analysis.

## INTRODUCTION

An insulator pollution monitoring apparatus (IPMA) has been developed at the University of Stellenbosch. The IPMA is based on the PME device constructed by CESI for installation in Thailand [1]. Previous experience was gained with the installation of a functionally similar device installed at Koeberg Nuclear Power Station during 1989 and 1990 [2].

IPMA is a device designed to monitor the pollution conditions of high voltage insulators in the field. The insulators under test are not however actually in service, but are suspended from the IPMA structure at a location adjacent to the power line of interest. This approach has the advantage of allowing different types of insulators to be evaluated for use at a particular site. Site assessment of remote areas is also possible.

An excellent correlation between the surface conductivity of the pollution layer, as determined by the current IPMA, and the ESDD of the pollution layer on the insulator has been established [3]. These results are summarized later in this paper.

The previous IPMA, installed at Koeberg did not give entirely satisfactory results. This problem was again apparent during the calibration procedure for the current IPMA [4]. In order to overcome the measurement problems, the physical processes occurring during a test were considered. Based on observations of the condition of the pollution layer on an insulator before and after testing, the testing philosophy was altered to minimize the effect of the test. The alterations did, however, result in a more

complicated measurement and interpretation algorithm. The modifications to the testing algorithm do, however, result in a much improved long term performance.

## DESIGN FEATURES

The IPMA is a self-contained device that has been designed as a stand-alone, integrated insulator test system. The only external connections required are a 220 V, 50 Hz power source and a water point. These features make IPMA ideal for investigations into the pollution conditions in remote areas.

All the important mechanical and electrical components are housed within the body of the IPMA device. The shell is made of a durable polymer material. This structure provides protection from the environment to the sub-systems housed within. These include a steam generator, transformer, single phase motor, hot air blowers and control circuitry. A basic schematic outline of IPMA is presented in Figure 1.

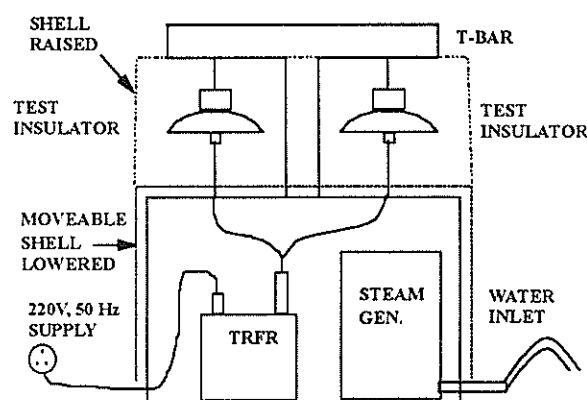


Figure 1 General layout of IPMA showing location of major sub-systems

The current sensors are housed in the T-bar on top of the IPMA and the power supply cables and output signals run down the leg of the "T" to interface with the data and control cable in the enclosed cabinet. In the current configuration, the controller is housed outside the IPMA, for instance in a substation building where a personal computer can be used to change the test parameters via the software interface. However,

there is no functional necessity for this configuration, as the adjustments could just as easily be performed via a laptop computer communicating with the controller housed inside the shell of the IPMA.

The insulators to be tested are suspended beneath stand-off insulators from the T-bar shown in Figure 1. During tests, the motor inside the shell raises the moveable shell by means of a helical screw mechanism so as to seal the environment containing the test insulators. The environmental conditions affecting the behaviour of the insulators can thus be controlled and monitored. The transformer is interfaced to the mains by means of a dedicated thyristor control circuit to ensure that switching occurs at the correct point on the voltage wave and that the energisation lasts for the correct number of cycles.

The tests are performed using a 220 V/ 3 kV, 4 kVA transformer. The 3 kV voltage is far below the normal operating voltage of the insulators in question, but because the test parameter is the ratio of current to voltage, this is not an important factor. The 3 kV voltage level does, however, provide significant advantages. The smaller currents produced through the pollution layer lead to greatly reduced heating effects ( $I^2R$  losses) and much simpler current sensors, both from the point of view of measurement and safety in the case of insulation failure. Furthermore, the reduced voltage level implies smaller clearances within the device which results in a significant space saving (a factor of  $\pm 12$ ). This, along with a smaller transformer, leads to a significant cost saving in relation to previous designs based on this principle. The dimensions are  $1.38 \times 1.01 \times 0.61$  m. This can easily be transported and erected using nothing more than a standard vehicle hydraulic hoist.

## TESTING PROCEDURE

IPMA operates according to the parameters set in the logger via the software interface. However, all the tests follow the same general sequence:

Once the logger's internal clock routine detects that a specified test starting time is reached, it triggers the high pressure steam generator. Once the steam pressure has reached a preset level, the logger is polled. At this stage the shell is raised. The hot air blowers are activated for a period. This enables all tests to start with approximately uniform environmental conditions. At this stage the *maximum current* settings for each channel are set to zero. The steam generator is activated again until the *steam ready* signal is received. The logger asserts the relay which opens the steam valves for the specified amount of time and then shuts off. After a specific delay, the transformer is energised for 5 cycles. Simultaneously, the currents, voltage and any appropriate environmental variables

are logged. If either of the currents logged is less than 95% of the previous maximum for that channel, the test halts. If not, the maxima are set to the new values and the steam release and measurement cycle repeats. If no decrease is determined before the specified maximum number of iterations is performed, the test halts at this point. The insulators are first dried off before the shell is lowered to once again expose the insulators to environmental conditions.

The logger can accommodate the data from approximately 450 tests in its current form. This represents five tests per day for three months. At this stage only the currents and voltage are logged. If environmental parameters are introduced, the maximum interval between resetting will obviously decrease.

## CALIBRATION RESULTS: 1

The IPMA was originally designed to only measure current and voltage. In this configuration, excellent correlation was achieved between the initial conductivity measured on the insulator, i.e. the first test performed, and the Equivalent Salt Deposit Density (ESDD) measured. The results of this calibration can be seen in the curves in Figure 2.

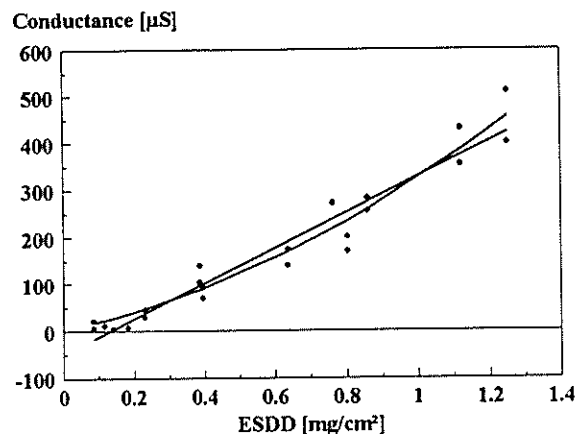


Figure 2 Calibration curve for first time IPMA tests showing conductance vs. ESDD

There is a clear correlation between the conductance and ESDD. Hence, in the absence of skilled personnel or equipment such as measuring flasks, distilled water, etc, IPMA can be used to give an accurate indication of the ESDD of insulators at a particular site. Note that although conductance and not conductivity is plotted as the ordinate, the tests were all performed using the same type of U70 toughened glass insulator, and hence the two measurements are equivalent.

The problem with the above testing technique, is that the results are not repeatable over time. Figure 3 shows that, if the same insulator is tested repeatedly,

there is a steady decrease over time for both insulator types and transformers considered.

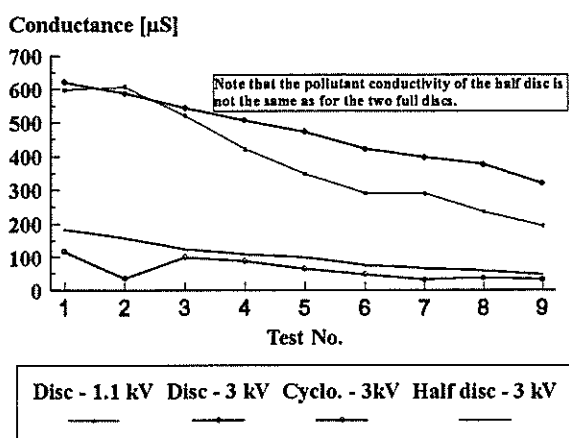


Figure 3 Decrease of IPMA readings over time

This gross influence of the testing procedure on the pollution layer is clearly unacceptable for an insulator pollution monitor. As a result of the problems shown in Figure 3, it was necessary to modify the operating routine.

#### ANALYSIS OF PHYSICAL PROCESSES

The first step to determine the cause of the problem was to visually inspect the insulators after a series of tests. It seemed as if some of the pollutant became redistributed along the lower rim of the insulator. ESDD measurements on similar insulators before and after testing showed that there was no significant loss of pollutant. This fact is illustrated in Table 1.

Table I Table of ESDD readings from similar insulators before and after IPMA tests

ESDD BEFORE IPMA TESTING	ESDD AFTER IPMA TESTS
1.54	1.54
2.22	2.24
1.10	1.11
1.61	1.62

The physical process that accounts for the rise in the conductance of the pollution layer is the condensation of water from the air onto the insulator. Standard reference works on heat transfer confirmed that the two

crucial environmental parameters governing this process are humidity and temperature [5]. Monitoring of the conditions inside the IPMA shell during a test indicated that the air became saturated, i.e. a relative humidity (%RH) of 100 % was achieved. However, a relative humidity of approximately 80 % produces sufficient moisture deposition to cause a meaningful increase in conductivity [6].

#### CALIBRATION RESULTS: 2

The operation routine of the IPMA was adapted to achieve a final relative humidity reading of approximately 80 - 90 %. The environmental variables during a test were logged and the results are displayed in Figure 4.

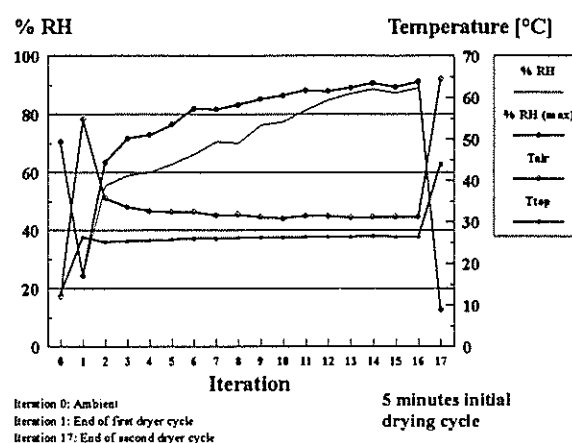


Figure 4 Behaviour of environmental parameters during IPMA test

It is clear that the humidity levels reached are within bound, i.e. the air does not become saturated. Furthermore, the insulator temperature is lower than the air temperature and the difference remains roughly constant. Hence, the possibility of having a wet bulb temperature higher than the insulator temperature always exists. Under quasi-static environmental conditions, the mass of condensate deposited on the surface of an insulator per unit area is given by Equation 1 [6].

$$m = \sqrt{\frac{2 \cdot p \cdot \kappa}{\lambda} \cdot (T_w - T_i) \cdot t_\delta} \quad (1)$$

The important parameters in Equation 1 are the insulator temperature,  $T_i$ , the wet-bulb temperature,  $T_w$ , and the time interval,  $t_\delta$ .  $T_i$  can be determined directly by measurement. However the wet bulb temperature is dependent on the air temperature, or dry-bulb temperature, and the relative humidity of the air. The relationship between  $T_w$  and these two parameters is best described by means of a

psychrometric chart. An example of a representation of a psychrometric chart, generated by a program to calculate the wet-bulb temperature iteratively, is shown in Figure 5.

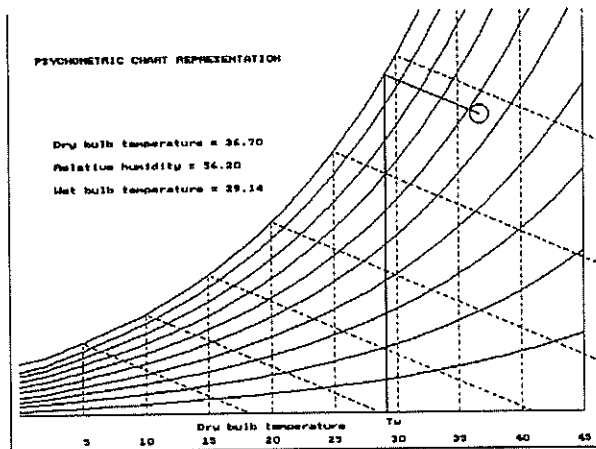


Figure 5 Representation of a psychrometric chart as used to calculate the wet-bulb temperature

In order to achieve repeatable results, the relationship between the leakage current that flows on the insulator and the amount of water deposited during the test should be constant for a given pollution condition. Figure 6 shows the results of a number of tests performed on a toughened glass insulator polluted according to IEC specifications [7] and tested in IPMA over a period of days. The mass of deposited water was calculated using Equation 1.

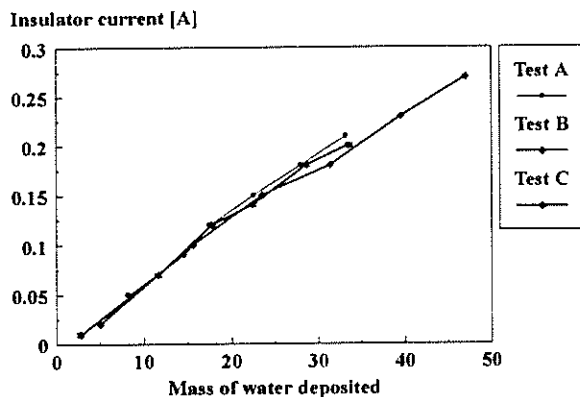


Figure 6 Calibration curves for single toughened glass insulator

As can be seen, the curves are almost co-incident which implies that the tests are repeatable. Further research is continuing so that a calibration curve, equivalent to Figure 2, can be drawn up that accommodates the new testing philosophy. It is anticipated that the slope of the line will be proportional to the pollution severity of the contaminant layer.

## CONCLUSIONS

An insulator pollution monitoring apparatus has been designed that seems to offer an excellent chance to avoid the pitfalls of previous testing algorithms. Hence, the advantages of using surface conductivity as the test parameter can be maintained, while at the same time achieving a non-destructive test.

The changes in the testing philosophy do result in a substantially more involved measurement and analysis routine. This tends to nullify the advantage of simplicity achieved with other conductivity based testing algorithms.

Research is continuing into the behaviour of the environmental conditions between each iteration. The humidity and temperatures are not constant, and thus the linearized approach followed in this paper may not necessarily be accurate. The environmental effects, as well as to a new calibration curve based on the new testing algorithm, are the subject of continuing study.

## REFERENCES

- [1] Bertazzi A., Perego G., Sampaoli G., Vachiratarapadorn Y., Eamsa-ad V., "A Device for the Automatic Measurement of Surface Conductivity of Insulators", Proc. Sixth ISH, paper 47.41, New Orleans, August/September 1989.
- [2] Holtzhausen J.P., Smith J.M., Potgieter O.C.T., "Insulator Pollution: Monitoring of Leakage Currents During Artificial and Site Test Conditions", Proc. SAUPEC 90 Jan 1990, paper 3.4.
- [3] Davel P., Holtzhausen J.P., Vosloo W.L., "The Commissioning and Performance of a New Insulator Monitoring Apparatus", Proc. SAUPEC - 94, Jan 1994, p 211 - 214.
- [4] Davel P., Holtzhausen J.P., Vosloo W.L., "Low Voltage Measurement of the Pollution on High Voltage Insulators", Proc. 29th UPEC 1994, p 798 - 801, Sept 1994.
- [5] Incropera F.P., De Witt D.P., Fundamentals of Heat Transfer, John Wiley and Sons, p 468, 1981.
- [6] Orbin D.R.H., Swift D.A., "Surface Resistivity of a Cool Polluted Insulator when Exposed to Warm Ambient Air", Proc. 4th International Conference on Properties and Applications of Dielectric Materials, Brisbane Australia, paper No. 7244.
- [7] Revision of IEC publication 507, "Artificial Pollution Tests on High Voltage Insulators to be Used on A.C. Systems", January 1987.

## DESIGN AND REALISATION OF AN AUTOMATED IMPULSE TEST FACILITY

G. Kwasnik

Department of Electrical Engineering, Technikon Witwatersrand

### Abstract:

When performing either current or voltage tests on high voltage or lightning protection equipment it is important that the tests are performed in a reliable and repeatable manner with the safety of the operator and measuring equipment being of the utmost importance.

In order to perform such testing it is often necessary for the operator to remain close to the impulse generator and device under test (DUT) in order to trigger and monitor the impulses as well as record residual and clamping voltages.

In order to overcome these hazards and speed up the testing, the project design automates the impulse setup, to ensure that it is intrinsically safe without losing any testing ability.

### Introduction :

In recent times the study of lightning strikes, corona and other such large voltage impulses have come to the fore front by virtue of necessity of both research and everyday environmental occurrences. The research laboratory environment call for more constant creation, production, monitoring and measuring of high voltage impulses. The provision of a fully automated, repetitive impulse generating facility is the end objective.

Studies of transient disturbances on a transmission system have shown that lightning strikes and switching operations are followed by a travelling wave of a steep wave front. An impulse voltage is a unidirectional voltage which rises rapidly to a max value and then decays slowly to zero.

The wave shape is defined in terms of the time taken to reach the peak value and the time taken for the wave to decay to 50 % of its peak value.

The combination of computer programme, feedback monitoring and physical impulse voltage generation facilitates the repetitive test facility so required.

### Main :

A. Design and implementation of the control system for the operation of the high voltage Transformers.

The selection of magnitude reference voltage, relates directly to the type, turns ratio and construction of the source transformer. Depending on the reference voltage the data base is consulted for the high voltage transformer characteristics. The base low voltage value is set, the control feedback computer circuit energises the DC motorised potentiometer until the nett value is zero. The AC output high secondary voltage is now set up. The secondary high voltage is enlarged via a double circuit, rectified and switched automatically computer controlled as required. Control of low voltage potential on the HV transformer so that repetitive impulses may be generated. is in the method realised.

Besides the theoretical calculation and setting of the primary and secondary circuitry values, voltage and current transducers are required to measure, monitor and facilitate the recording of these values by the computer.

Values of interest will be both primary voltage and current values, secondary voltage and current values, specifically the current in the secondary windings of the transformer. The transducer is required to have sufficient bandwidth to detect high  $di/dt$  values so that effective protection may be included.

Additional environmental variable elements monitored and recorded are Relative Air Density. Temperature and Relative Humidity. External probes are mounted in the near vicinity of the DUT, by means of analogue/digital and input/output cards in the PC these values so that effective protection may be included.

Set up protection is of paramount importance and the following procedures to the high voltage transformer automated set up are monitored.

1. The potentiometer setting - on, off, up, down and feedback control of the DC drive.
2. The sequence of setting up procedures.
3. Breakdown voltages ie.  $\Delta V / \Delta T$
4. The limits of maximum voltage and current as calculated by data base and transformer characteristic criteria.

The software design facilitates the flexibility between transformers, their protection and characteristics.

#### **B. Automated triggering of the impulse generator.**

In large impulse generators, the spark gaps generally consist of spherical electrodes of such size that the spacing for the maximum voltage does not exceed a sphere diameter. The relatively uncontrollable method of tripping an impulse generator, is to set the lowest spark gap to breakdown at a predetermined value. The tripping in this case is reliant on the first gap breakdown - not always accurate.

The method presently under investigation is the controlled tripping method utilizing a three electrode gap at the first stage spark gap. The charging voltage achieved from the high voltage transformer is placed over the outer electrode spheres. The central electrode should be biased at some intermediate voltage between the two outer electrodes. The electrode system is so balanced that it withstands the charging voltage by a small margin and the tripping of the generator is effected by applying a short duration voltage pulse to the central electrode. With this method the tripping time of the generator can be accurately controlled by the tripping pulse.

Tripping could also be facilitated by affecting an alternating current to the central electrode, ie. the system would trip at/near the peak of the wave. The various voltage spark gaps are facilitated with the automated movement of the outer electrodes equally in and out equi-spaced either side of the central electrode. In order to ensure consistent charging across the sphere gaps, a set of high resistances are connected across the gaps. These resistances are equivalent in all ways.

The tripping is initiated by applying an impulse above  $+1/5$  of the charging voltage, this voltage is applied through a capacitor. During the charging of the generator the anode of the thyristor is maintained at the positive voltage of  $+1/5$  of the charging voltage, a negative bias applied prevents the conduction through this component. Should the bias be neutralised momentarily, the thyristor conducts and a negative  $1/5$  of charging voltage exists at the anode. The output of the impulse generator is therefore controlled by the switching of this negative bias.

#### **C. Automated Measurement of the Impulse and Recorded Wave Shapes.**

Measurement of the impulse wave shape and peak magnitude will be done using a fast (band width 500MHZ) digital oscilloscope

together with calibrated high current and voltage probes having the equivalent bandwidths.

The following data must be presented on both the user and the control system so that the following impulse may be performed at the required interval as well as ensuring the correct impulses magnitude.

Firstly the oscilloscope would have to be controlled by the PC to ensure that the correct channel and time-base setting would be made for the measurement selected on the PC.

The acquired information would have to be downloaded from the oscilloscope to the PC for viewing and analysis. It must be ensured that the effective earthing and protection of both the PC and the scope is implemented. This would involve earthing strategies set out by IEC 81.

#### **D. Earthing and Capacitor Discharge.**

It is essential that the impulse generator and circuitry will have a device to earth and / or discharge the capacitors when not in operation. The device will be based on the design of an electrically operated arm, automatically controlled, applied to the charging point of the generator. Therefore all capacitors will discharge through various stage resistors. The earth point of the impulse generator should be situated at the base of the condenser columns with an earth rod or rods driven into the ground.

If the resistance to ground is not of an acceptable low level, it may set up dangerous potentials between various parts of the building. To prevent/avoid any such problem occurring the building structure should be earthed to the same earth rod.

#### **E. Central and Monitoring by the PC**

A/D and I/O cards in the PC will be used to control the transformer and impulse triggering. This will involve subtle earthing and screening typographies which will prevent interference with the measurement, user and measurement safety.

Protection levels for the transformer voltage, current and  $di/dt$  would need to be set to ensure that the transformer is correctly protected on both the high and low voltage sides.

The idea is that the user can type in the required impulse level, time duration between impulses and allow the system to perform the impulses as specified while at the same time being confident of human and equipment safety. Records of each impulse, recorded residual and clamping voltages will be kept for each impulse test set.

In order to ensure repeatable impulses a control system will need to be implemented which controls the wave shaping circuitry as well as the triggering mechanism in order to take into account spark gap denudation and temperature increases in the low inductance resistors and capacitors.

The control system would have to continually monitor Relative Air Density and Temperature to ensure standardisation of measurements.

#### **Conclusion:**

It should be stressed that the current impulses of the peak magnitudes exceeding 40KA and voltage impulses of 20KV plus will exist and that a large portion of the project design involves making the test setup robust to such conditions.

Effective earthing strategies in order to perform correct measurements of transients in having rise times in the order of microseconds will also have to be finalised and implemented due to inductive and skin effect problems associated with such measurements. The design, implementation and calibration of the transducers to monitor and control such fast transients will also involve extreme care.

## 5. References

- (1) Lewis WH. "Recommended power and signal grounding for control and computer rooms". Transactions of the IEEE, vol. 1A-21, no 6, November/December 1985, pp 1505-1516.
- (2) Barnes JR. "Electronic system design - Interference and noise control techniques", First edition, Prentice Hall, 1987.
- (3) IEC (1993). "IEC 81, sec 57 Lightning protection against LEMP. Part 1. General Principles" Released for discussion, IEC Geneva, May 1993.
- (4) SABS (1988). "SABS 1474-1988. Uninterruptable Power Systems." SABS, Pretoria 1988.
- (5) Melia R, Jandrell IR, Van Coller JM, Phillips AJ, Reynders JP "Development of a combination generator for lightning simulation", Proceedings of the fourth Southern African Universities Conference, Cape Town, January 1994.

# AN ASSESSMENT OF VFT V-t CURVES GENERATED IN MIXTURES OF SF<sub>6</sub> AND N<sub>2</sub> GAS IN A 180/110 mm COAXIAL TEST GAP

D A Reynders    R J Traynor    S D Nielsen    I R Jandrell    J P Reynders

Electric Power Research Group  
University of the Witwatersrand

## 1 Abstract

Volt - time curves are plotted for pure SF<sub>6</sub> and a SF<sub>6</sub>/N<sub>2</sub> = 50%/ 50% mixture at one bar absolute pressure under Very Fast Transient conditions. Due to remote measurement, amplitude corrections of either 2,35% or 10,05% had to be made depending on when breakdown occurred. A time correction of -6 ns was also necessary. The tails of the curves tend towards the critical breakdown voltages for the respective gases. This means that even under VFT conditions, the DC critical voltage, which is easy to predict, is valid. It appears that the breakdown mechanisms may be different for the two gases tested.

## 2 Introduction

Disconnecter generated VFTs in Gas Insulated Systems (GIS) can cause breakdown if the insulation co-ordination is not done correctly. For good insulation co-ordination, Volt - time (V-t) curves are needed for all the components in the system of interest. It has been shown in the past that lightning V-t curves cannot be extrapolated to faster times for VFTs [6]. Thus experimental work is necessary.

It was stated by Boggs [4] that VFTs rarely exceed 2 pu in service, however, since VFTs are routinely applied to a system, this low value is important. Luxa stated that the presence of defects in a system could cause breakdown at lower voltages than the lightning withstand voltage [5].

It is suspected that since nitrogen (N<sub>2</sub>) is much less susceptible to surface roughness than SF<sub>6</sub>, gas mixtures might give superior performance under VFT conditions where roughness plays a significant role. The test gap used was an industrial grade 180/110 mm GIS duct. The system was stressed with negative VFTs.

To compensate for remote measurement, a computer simulation was run to obtain correction factors for this known error and to look for other possible errors. The simulation was done using the Alternative Transients Program (ATP) [1].

## 3 Generation of VFTs in a GIS Geometry

VFTs are high frequency (up to 300 MHz) oscillations generated when small capacitive currents are switched by a disconnector operation. During disconnector operation (especially during closing), pre-striking and re-striking occurs between the disconnector electrodes (when the critical field is exceeded) resulting in a voltage collapse in two to twelve nanoseconds [3] depending on the disconnector design. When the disconnector voltage col-

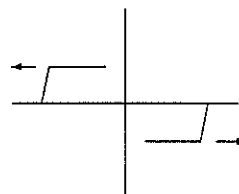


Figure 1: Travelling Waves

lapses, travelling waves are transmitted from the switch in either direction along the GIS (figure 1). At any impedance discontinuity, (eg a spacer or a change in GIS diameter) part of the travelling wave is reflected and part is transmitted. These reflections sum to form a VFT. The shape of a VFT is dependent on the GIS geometry, the supply voltage and gas pressure in the disconnect chamber.

One of the dominant factors in determining the wave shape is the disconnector arc impedance.

## 4 VFT V-t curves

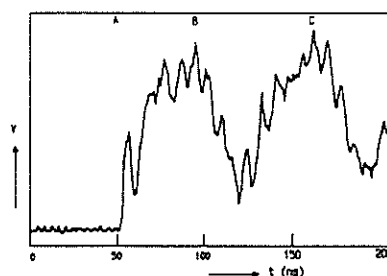


Figure 2: VFT measurement

A VFT V-t curve plots breakdown voltage vs time to breakdown. Breakdown voltage is defined as the highest voltage up to the point of breakdown (the IEC 60-2 method [6]). Figure 2 illustrates this in an exaggerated fashion. If breakdown occurs between the points A and B, the voltage at the point of breakdown is taken. For breakdown between B and C, the highest previous voltage is taken (ie the voltage at point B). After C, voltage C is used. The time to breakdown is defined as the time when the breakdown arc crosses the gap. This occurs when the curve starts to drop towards ground and NOT when the curve crosses the zero volts level. Once all the points have been plotted, a line is drawn through the lowest of these points.

## 5 Experimental Setup

The test pole used is shown in figure 3. The test

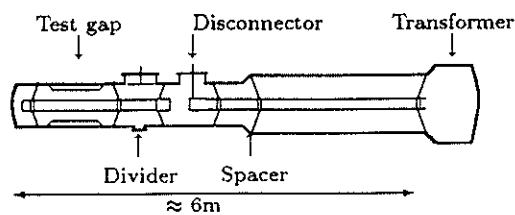


Figure 3: The Test Pole

pole's configuration models a real situation with a charged section (source) switching on to a short uncharged section (circuit breaker). The pressure in the test gap was lower than the rest of the system. This, together with the narrow test gap ensured breakdown in the gap.

### 5.1 Measurement equipment

Both the capacitive voltage divider and the oscilloscope had bandwidths of 500 MHz. This is necessary since the high frequency components ( $\approx 300$  MHz) need to be measured accurately. To reduce interference, the measurement lead and oscilloscope were shielded.

### 5.2 Experimental procedure

The voltage was be incremented in steps of 10kV from 60% to 140% of the critical value. Between breakdowns, a five minute recovery time was allowed. The critical value was calculated from the streamer criterion. The predicted breakdown values for the gas mixtures tested at one bar absolute are (calculated according to Baumgartner, assuming a smooth conductor [2]):

Pure SF <sub>6</sub>	253.5 kV
SF <sub>6</sub> /N <sub>2</sub> 50%/50%	220.7 kV

## 6 Simulation

At different points along the duct, VFTs will not look the same at any time instant [8]. Measurement cannot take place at the point of breakdown, since this would damage the divider. Simulation would ensure that amplitude and time corrections could be made to the remote measurements. The simulation was done using ATP.

### 6.1 Model

To obtain reasonably accurate correction factors, the test pole (figure 3) must be modelled correctly. A distributed parameter model was chosen. The duct was broken up into homogeneous sections (constant geometry) and each section modelled in terms of electrical parameters (R, L and C) and length. The following assumptions were made :

- Axial flashover occurs in the disconnector chamber when the potential is at a maximum, ie at the supply peak. The entire simulation lasts  $1\mu s$ , thus the voltage (normally 50Hz) can be assumed constant over this time interval.
- Radial flashover occurs in the middle of the test duct.

### 6.2 Arcs

One of the most difficult components to model is an arc. Toepler's spark law only describes the initial development [3] (plasma formation) and not the portion of interest for VFTs. It was felt intuitively that as an arc develops, its diameter increases, thus reducing its resistance (damping). Thus an exponentially time decaying resistance was chosen.

Capacitive coupling while the disconnector was open was taken into account by a small capacitor across the chamber.

## 7 Comparison of real and simulated VFTs

For correction purposes, the magnitudes of the simulated and measured VFTs compared to within 1%. However, the times of the peaks differed by as much as 25% which means that the model is not perfect. The comparison is not as good for the troughs which also suggests that the model is not quite correct. After about the fourth peak (it figure 4, the measured VFT starts to go into resonance mode and then the simulation loses accuracy. The following correction factors were obtained from the simulation:

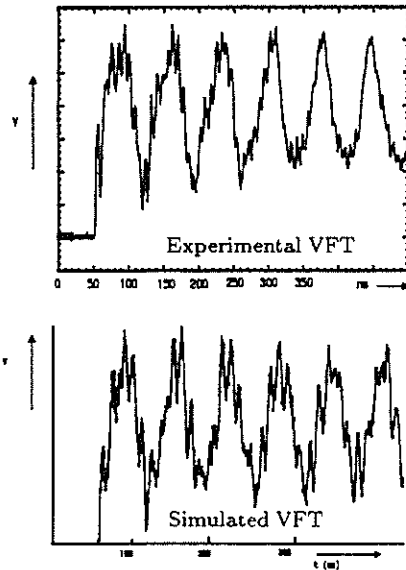


Figure 4: Experimental and Simulated VFTs

Amplitude Correction			Time Correction
Before 1st Peak	1st - 2nd Peak	After 2nd Peak	
Read Off Graph	+ 2%	+ 10%	- 6 ns

The VFT at the measuring point differs from that at the measuring point by a variable amount. This means that the exact geometry used must be accurately simulated because the correction factors depend strongly on the geometry. The 6ns time correction is due to travelling wave phenomena.

An error due to pre-charging as suggested by Nielsen [7] has been neglected since it is believed to be negligibly small in this work.

## 8 Experimental results

V-t curves for both pure  $\text{SF}_6$  and the mixture are plotted together for comparison in figure 5.

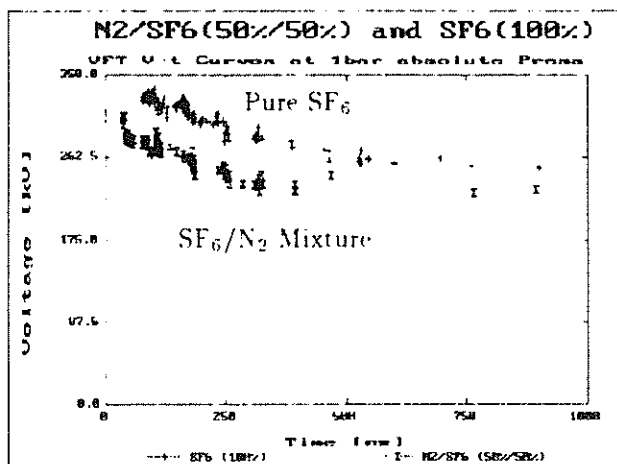


Figure 5: VFT V-t Curves

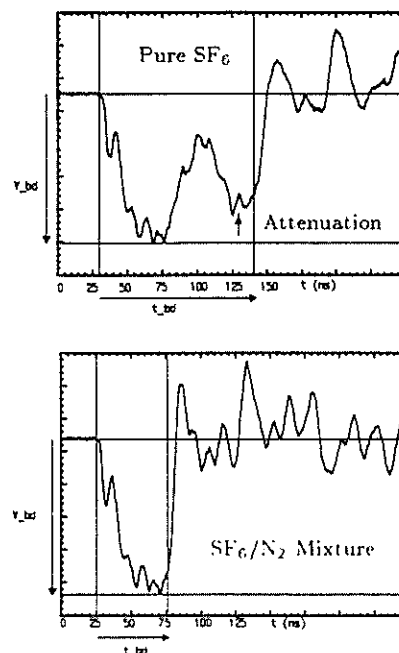
Interesting to note is that both the tail of the pure  $\text{SF}_6$  curve and that of the  $\text{SF}_6/\text{N}_2 = 50\%/50\%$  mix-

ture curve tend towards the predicted critical voltage for the respective gas compositions. This means that the minimum critical voltage is just about constant throughout the frequency spectrum (DC to VFTs) under smooth surface conditions. This enforces the economic advantage of mixing a cheap gas ( $\text{N}_2$ ) with  $\text{SF}_6$  from an electrical performance point of view.

The pure  $\text{SF}_6$  curve has an almost linear upward trend while the  $\text{SF}_6/\text{N}_2$  curve has a more exponential shape.

### 8.1 Pre-breakdown Attenuation in $\text{SF}_6$

Figure 6 shows that when breakdown occurs, there is an attenuation of the  $\text{SF}_6$  VFT just before breakdown while this is not the case for an  $\text{SF}_6/\text{N}_2 = 50\%/50\%$  mixture. The attenuation was consistent

Figure 6: Pre-breakdown Attenuation in Pure  $\text{SF}_6$ 

in pure  $\text{SF}_6$  while it never happened in the mixture. This could have to do with the development of a plasma channel before breakdown. The channel could be formed by negative ions (the result of  $\text{SF}_6$ 's electronegativity) moving across the gap. The same should have been observed in the mixture though to a lesser extent, so this might not be the case.

The lack of attenuation in the mixture could be because of the high number of energy levels present in  $\text{N}_2$ . This merits further investigation.

The voltage collapse is slightly faster in the mixture. It appears to be a function of the breakdown arc characteristics. It could be that an arc develops faster in a mixture than in pure  $\text{SF}_6$ ; ie its resistance drops faster to a negligible value.

## 8.2 Comparison with other results

Curves generated by Nielsen [7] and Modry [6] were essentially flat with an upturn at about 50 ns. While curves for positive VFTs should be flatter than that for negative ones [5], it is felt that these results are excessively so. It is believed to be due to the capacitive divider that was used. No published VFT V-t curves for SF<sub>6</sub>/N<sub>2</sub> mixtures were available for comparison.

## 9 Conclusions

- For the purpose of obtaining accurate correction factors for voltage and time measurement for VFT V-t curves an accurate model must be used. Voltage corrections of +2,35% and +10,05% needed to be made for breakdowns occurring between the first and second peaks and after the second peak respectively. A time correction of -6ns was made.
- For long times to breakdown (500ns), both the pure SF<sub>6</sub> VFT V-t curve and that for the mixture tend towards the predicted critical field breakdown level.
- Errors that still exist are those due to inaccurate pressure and hence gas mixture measurements. These are probably quite small but could make a difference of a percent or two. Pre-charging of the test gap could result in a one or two percent measurement error.
- Unlike previous results for SF<sub>6</sub>, the VFT V-t curves are not flat. The SF<sub>6</sub>/N<sub>2</sub> mixture gave results that almost tracked those for pure SF<sub>6</sub> at a reduced voltage, except for the slope of the curve which is more exponential. This steeper slope at higher voltages is significant for insulation co-ordination because it means that for fast breakdown to occur, very high voltages are required.
- To gain a fuller understanding the performance of gas mixtures under VFT conditions, curves need to be generated at higher pressures (closer to those used in industry) where small surface imperfections become more significant.

## References

- [1] 'Alternative Transients Program Rule Book', Leuven EMTP Center Belgium, 1987.
- [2] Baumgartner R G. 'Dielectric characteristics of mixtures of sulphur hexa-fluoride (SF<sub>6</sub>) and nitrogen (N<sub>2</sub>)'. IEE Publication no. 118 September 1974 pp 366-369.
- [3] Boeck W, Witzmann R. 'Main influences on the fast transient development in gas-insulated substations (GIS)'. 5th International Symposium on High Voltage Engineering, Braunschweig Germany Aug, 1987.
- [4] Boggs S A, Fujimoto N, Chu F Y, Krenicky A, Plessl A, Schlicht D. 'Disconnect switch induced transients and trapped charge in gas-insulated substations'. IEEE Trans. on Power Apparatus and Systems vol PAS-101 Oct 82.
- [5] Luxa G, Kynast E, et al. 'Recent research activity on the dielectric performance of SF<sub>6</sub>, with special reference to very fast transients'. CIGRE' Session 15-06 1988.
- [6] Modry R. 'Insulation performance of SF<sub>6</sub> gas insulated switchgear (GIS) stressed with high frequency oscillating transients'. MSc Thesis Department of Electrical Engineering, Wits 1986.
- [7] Nielsen S D, Wardley H. 'Breakdowns in a coaxial gap due to disconnect transients and simulation of VFTs using ATP'. 4th year project, Department of Electrical Engineering, WITS Nov 1990.
- [8] Nielsen S D, Jandrell I R, Reynders J P. 'Assessment of the errors in the measurement of VFT V-t curves due to the geometry of the system and the location of the voltage measurement point'. 8th International Symposium on High Voltage Engineering, Yokohama Japan, Aug 1993.

## 10 Address of Author

D A Reynders  
Electric Power Research Group  
University of the Witwatersrand  
Pvt Bag 3  
WITS 2050.

# A LIFE MANAGEMENT PROGRAM FOR THE STATOR WINDING INSULATION OF ESKOM'S POWER GENERATORS

H van der Merwe  
ESKOM Technology Group (T-R-I)

P Rasekhi  
Witwatersrand Technikon

## Abstract

World-wide, financial and environmental factors are necessitating the life management and life extension of power generating facilities.

Because of this, Eskom - TRI (Technology Research & Investigations) is developing a life management program for the stator winding insulation of its power generators. As part of this program, the quadratic-rate partial discharge test of Electricité de France is being evaluated.

Initial experience has confirmed the claimed ability of this test to quantify the difference in insulation system condition between an old and a new stator winding. Trending the results of these tests over time will point out those generators at risk of in-service failure, allowing for scheduled and budgeted stator winding repair procedures.

## 1. Introduction

World-wide, financial and environmental factors are necessitating life management and life extension of power generating facilities nearing the end of their design life. Plant managers can therefore expect an increasing incidence of in-service equipment failure in years to come.

To address this issue, the Technology Research & Investigations division of Eskom's Technology Group (TRI) is developing a life management program for the stator winding insulation of its power generators. The integrity of stator winding insulation in high voltage generators is a crucial parameter in the estimated total reliability of a power generating unit.

## 2. Conventional insulation assessment tests

The following tests are often used to assess the insulation condition of motor and generator stator windings (the measured parameters are bulk/volume indicators of insulation condition):

### 2.1 Direct voltage tests:

- IR (insulation resistance) — gives a general indication of the voltage withstand capability of the insulation system under test.
- PI (polarization index) — gives an indication of the moisture content of the insulation system under test.

### 2.2 Industrial frequency voltage tests:

- HIPOT (overvoltage) and leakage current — gives a Go/NoGo (no-flashover/flashover) indication of insulation condition.
- Capacitance and capacitance change — gives an indication of the void content of the insulation system under test, as well as winding pollution.

- Dissipation factor ( $\tan\delta$ ) and  $\tan\delta$  tip-up — is a measure of solid insulation loss and certain types of partial discharge activity (see next section on the latter).

## 3. Partial discharge detection

Partial discharges (PD) are localized electrical discharges/flashovers inside insulating media, restricted to only parts of the dielectric under test, [1981 IEC 270 standard].

Detection of PD is widely seen as an effective method by which the condition of high voltage insulation systems can be assessed. Increased sensitivity and a greater degree of anomaly localization than with conventional bulk indicators, can be achieved.

PD pulses can be categorized as:

- *Internal discharges* (Discharges inside the winding groundwall insulation, caused by flashovers of included air voids. During manufacturing, some voids invariable remain after insulation curing. Excessive temperatures & core vibration can cause groundwall delamination).
- *Slot discharges* (Discharges in any gap or bad contact between the winding groundwall and the stator core teeth. Due to ex. an increase in corona varnish resistivity, loose/damaged side-packing, loose slot wedges and loose overhang wedges/spacers/supports).
- *Corona discharges* (Air ionization between the overhang portion of the winding and the core, in areas of high voltage gradient. Due to lack/deterioration of stress-grading tape/paint).
- *Surface discharges* (Tracking on the surface of winding overhangs, due to ex. pollution).

Across the world, many different methods for the detection of these PD pulses in the stator winding insulation of high voltage generators, have been developed and are being employed.

## 4. The EDF partial discharge method

The effectiveness of the Electricité de France (EDF) method for stator winding insulation condition assessment, with specific emphasis on turbo generators, is currently being investigated in a technical exchange agreement between Eskom and EDF.

This method has also been discussed in [Audoli, 1-3] and [Van der Merwe, 4]. It basically entails off-line electrical quadratic rate PD measurements taken from the machine terminals, using a range of relatively low center-frequency narrow band filters.

Each phase winding is in turn stressed with AC voltage up to a maximum of 1.2 times the relevant phase to

ground voltage. The remaining phase windings of the machine are grounded to the magnetic core in each case.

Coupling capacitors of 0.1  $\mu\text{F}$  and 250 pF at each end of the energized winding (refer to Fig. 1) allows electrical detection of discharges in the winding insulation.

#### 4.1 The advantages of off-line partial discharge tests

- Noise interference that would be generated by normal operation of the machine (i.e. arcing at field-winding slip rings and rotor/shaft grounding brushes), are absent.
- Electromagnetic coupling of and attenuations between energized phases is prevented, since only one phase is tested at a time, during which the other two phases are grounded.
- Because tests are taken from the machine terminals, the procedure is non-intrusive (insulation integrity is not affected).
- As no permanent PD couplers are installed, the test set is completely portable. A large number of generators can therefore be tested with one set, resulting in low required capital layout.
- Since the entire winding under test is energized with the same level of voltage, from line side to neutral side, it is possible to compare the winding insulation condition of the two sides.
- A variable test voltage can be applied. This allows for PD development with voltage, including PD inception and extinction voltages, to be verified.

#### 4.2 The quadratic-rate measured quantity

Phenomena like mutual electromagnetic coupling, attenuation, resonance and traveling waves, complicate the interpretation of PD test data on high voltage stator winding insulation systems. Furthermore, due to the intricate geometry of these windings, internal-, slot-, corona- and surface discharges can at certain voltages occur simultaneously.

Measurement of the highest/peak PD magnitude is therefore not adequate to determine the harmfulness of each discharge phenomena. It can only detect the discharge phenomenon that results in the highest magnitude pulse at the winding terminals, at any given stage.

Instead, an indication of the combined electrical energy content of any discharge type or combination of discharge types at any stage, can be provided through measurement of the charge quadratic rate quantity. The basic charge quadratic rate (QR) quantity is given in coulombs squared per second or

$$\text{QR} = Q^2/t, \text{ expressed in } C^2/s.$$

Typical PD levels in the solid insulation system of high voltage generators and motors are very high compared to for instance the paper and oil insulation system of most transformers. The PD quadratic rate quantity for these machines is therefore expressed in decibels (db).

For the 10 kHz measurement:  $0\text{db} = 10^{-9}C^2s^{-1}F^{-1}$ , whilst for the 130 kHz measurement:  $0\text{db} = 10^{-16}C^2s^{-1}$  [Audoli, 2]. To make the results of one machine comparable with that of another machine of the same voltage rating, the 10 kHz measurement is normalized by dividing the measured quadratic rate PD quantity with the phase capacitance of the winding.

Note that an increase of 3db corresponds to a doubling of the linear quadratic-rate quantity. The relevant formula is therefore:

$$\text{Quadratic Rate}_{\text{db}} = 10 \log(\text{Quadratic Rate}_{\text{linear}} / 10^{-16} C^2 s^{-1})$$

or

$$\text{Quadratic Rate}_{\text{linear}} = 10^{-16} C^2 s^{-1} \cdot 10^{\text{Quadratic Rate}_{\text{db}}/10}.$$

#### 4.3 The 10 kHz and 130 kHz selective measuring frequencies

A PD pulse occurring in stator winding insulation, generates a propagating Dirac-type current impulse (i.e. with a very wide-band frequency spectrum) in the winding conductor. Because of the inherent low-pass filter characteristic of any stator winding insulation system, the higher frequency components of such a pulse are attenuated more than the lower frequency components whilst travelling to the measuring terminal.

It is clear that the so-called reach of a specific measurement frequency is of great importance when interpreting the test results. A low measurement frequency has a long reach and a high measurement frequency a short reach.

In the EDF method, measurement of discharges in a narrow frequency band, centered around 10 kHz, enables assessment of the winding insulation condition as a whole. Measurement of discharges in a narrow frequency band, centered around 130 kHz, enables assessing the winding line side and winding neutral side insulation condition separately (only discharges originating a few bars away from the measuring terminal on the line or neutral side of a phase winding, still contain measurable energy in this band when picked up by the discharge detector).

#### 4.4 Interpretation of quadratic-rate partial discharge levels and discharge waveforms

The criteria used for insulation diagnosis are typically as follows:

- Development of discharge levels over time (i.e. between sets of measurements, typically a few years apart) at the measuring frequencies of 10 kHz and 130 kHz respectively. This process is called data trending.
- The difference in discharge levels detected by the 130 kHz measurement, at the line and neutral ends of the winding respectively.
- Consistency of the test results between phases.
- Development of PD with increasing test voltage (including the PD inception and extinction voltages).

- Identifying the dominant discharge phenomenon at different test voltage increments. This is accomplished by studying the PD graphs on an oscilloscope, using the guidelines of [Cigre, 5].
- The decrease (if any) in PD level with voltage application time, due to the neutralisation of internal groundwall voids.

#### 4.5 Suppression of noise interference

Because the PD test is conducted off-line, noise interference originating in the machine itself, are absent. Noise coming from other external sources (i.e. arc welding and operating machinery) however still need to be blocked or suppressed.

The following methods are utilized to achieve this:

- The HV supply cable and the signal cables are screened.
- An oscilloscope is used to visually differentiate noise from real PD signals. Noise patterns remain constant with increasing test voltage and could also be identified at lower voltages (before PD inception and using the guidelines of [Cigre, 5]).
- The size of the coupled-noise window (antenna effect), formed by the HV cable, winding under test, earth cable and HV power supply, are minimized by laying out the HV cable and HV power supply earth cable as close to each other as possible.

Directionality of coupled noise can be investigated by changing the cabling layout so as to rotate the window mentioned above through ninety degrees.

- The generator frame and terminal chambers give a noise shielding effect similar to that of a Faraday cage.
- The narrow-band filters used in the quadratic-rate PD measurement makes this method inherently more robust to noise interference than methods using wide-band filters.
- Because the typical PD levels of generator and motor stator winding insulation systems are relatively high, noise suppression during field measurements is much less of a problem than with for instance paper and oil insulated transformers.

#### 4.6 Partial discharge test setup

A diagram of the basic test setup used for the quadratic-rate PD test, is given in Fig. 1.

In this figure:

- The *HV transformer* is typically a series or parallel resonant test set, used to energize the winding under test to 1.2 times the relevant phase to ground voltage.
- The *Quad Rate Measurer* is the quadratic rate PD detector, equipped with the selective filters and a true RMS voltmeter.
- The *Relay Box* contains high frequency blocking impedances connected to earth, and relays (the latter is used to switch the desired signal through to the discharge detector). Closing only relay A for instance, will switch all discharge signals passed by the 0.1  $\mu\text{F}$

capacitor on the line side of the machine winding, through to the discharge detector.

- The *Oscilloscope* is used as an auxiliary tool, to help visualizing the discharge phenomena (including noise pulses) picked up by the discharge detector.

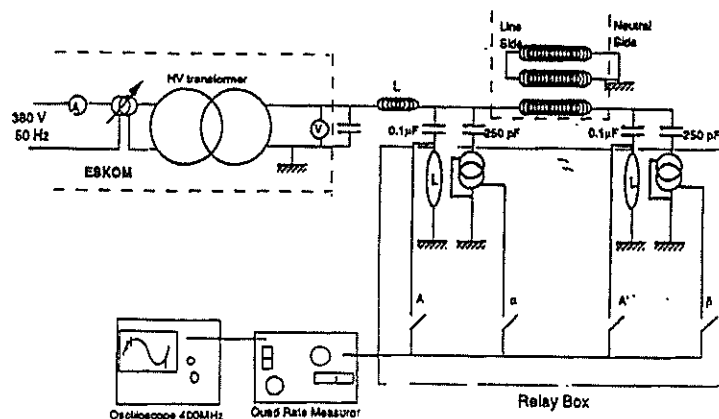


Figure 1 Diagram of test setup used for quadratic rate PD tests on generator stator winding insulation

#### 4.7 On-site tests on generators

Quadratic-rate PD tests on a number of Eskom's turbo generators have been completed. The experience gained through tests on one of these generators will be discussed briefly.

A 12 kV, 50 MW gas-turbine generator was tested shortly before commencement of a planned stator rewind for strategic reasons. This generator was used for short term peaking generation as well as synchronous condenser operation. The winding was more or less 17 years old at the time of test.

At the inception voltage of internal discharges (about 4.6 kV), considerably higher discharge levels for the 130 kHz measurement were detected from the line side terminal than from the neutral side terminal. This was true for all three phase windings of the machine, although levels for the individual phases were not consistent.

It can therefore be concluded that electrical aging of the groundwall insulation had taken place on the line side of all three phase windings.

Table 1 shows the 130 kHz discharge levels detected at the line and neutral side terminals of each phase winding, at 4.6 kV.

	130 kHz, line	130 kHz, neutral
Red phase	37	28
White phase	32	26
Blue phase	30	23

Table 1 Discharge levels (db) at 4.6 kV (old winding)

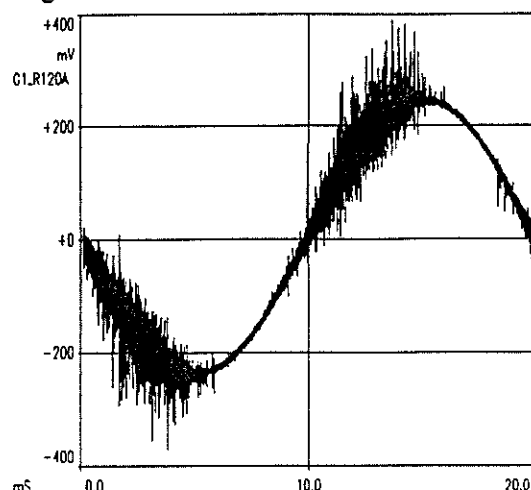
Above 7 kV, exceptionally high slot discharge levels caused saturation of the discharge detector. Note that the rated working voltage of this machine under steady-state conditions is already 7.6 kV.

The gas-turbine generator described above was re-tested after completion of the full stator rewind. The absolute level of discharges shown in table 2 below are relatively low for the associated voltage level and are also much lower than was measured at the same voltage level on the old winding (refer to table 1 above). Discharge levels for line and neutral sides of the winding are essentially the same.

	130 kHz, line	130 kHz, neutral
Red phase	14	15
White phase	17	19
Blue phase	12	12

Table 2 Discharge levels (db) at 4.6 kV (new winding)

A PD graph over one 50 Hz cycle of test voltage, captured at maximum test voltage on the new winding, are given below.



PD graph for maximum test voltage (PD and 50 Hz not to the same scale)

#### 4.8 Laboratory tests on stator bars

Laboratory based quadratic-rate PD tests are currently underway on individual stator bars (both old and new). A series of winding anomalies are artificially introduced and before and after measurements are taken.

Experience gained through these research tests should lead to a better understanding of the PD phenomena involved, allowing better assessments of in-service stator windings to be made.

#### 5. Localization of winding anomalies

The EDF quadratic-rate PD test and other conventional off-line tests, taken from the machine terminals, will be used to fingerprint and trend the stator winding insulation condition of all Eskom's generators.

High risk generators identified during this process should be monitored more closely and a suitable refurbishing procedure should be identified and budgeted for. An expanded monitoring program for the relevant generators could involve special visual inspections, decreasing the time span between successive off-line tests or introducing more localized on-line PD tests. Examples of the latter are the TVA probe [Sedding, 6] and the stator slot

coupler method originated by Ontario Hydro [Sedding, 7].

#### 6. Discussion and conclusions

The development of a condition monitoring program for the stator winding insulation of Eskom's power generators has been highlighted. The novel aspects of the EDF quadratic-rate PD detection method have been described.

Initial experience, gained through a number of measurements on Eskom generators, practically confirm the claimed ability of the EDF method to quantitatively indicate the difference in insulation system condition between an old and a new stator winding. A series of measurements over time (including conventional bulk indicators) is needed however, to obtain an accurate insulation degradation curve/trend for a specific stator winding.

These tests, possibly coupled with more localized on-line PD tests in special cases, will allow properly scheduled and budgeted stator winding repair procedures, such as rewedging and rewinding, to be carried out.

#### 7. References

1. Audoli, A and Drommi, JL: "Analysis of partial discharges measurements and generator technology evolution", Proceedings of the 3rd International Conference on Properties and Applications of Dielectric Materials (ICPADM), Tokyo - Japan, July 1991, pp. 687 - 690.
2. Audoli, A and Drommi, JL: "Generator and motor stator monitoring based on partial discharge quadratic rate measurement", IEEE International Symposium on Electrical Insulation, Baltimore, June 1992, pp. 359 - 362.
3. Audoli, A and Merigot, C: "Use of dielectric tests as an aid for hydro generator maintenance", Conference record of the IEEE International Symposium on Electrical Insulation, Toronto - Canada, June 1990, pp. 379 - 382.
4. Van der Merwe, H et al.: "Initial experience with quadratic rate partial discharge tests on the stator winding insulation of power generators in South Africa", Proceedings of the 4th International Conference on Properties and Applications of Dielectric Materials, Brisbane - Australia, July 1994, pp. 594 - 597.
5. Cigre Working Group 21 03 - Electra no 11, "Recognition of discharges", December 1969, pp. 61 - 98.
6. Sedding, HG and Stone, GC: "Discharge locating probe for rotating machines", Proceedings of the 19th Electrical/Electronics Insulation Conference, Chicago - USA, September 1989, pp. 225 - 227.
7. Sedding, HG et al.: "Measurement of partial discharges on operating turbine generators with a novel wide band coupler", Proceedings of the 3rd International Conference on Properties and Applications of Dielectric Materials, Tokyo - Japan, July 1991, pp. 773 - 776.

#### 8. Address of author

Mr P Rasekhi, Mr H van der Merwe, Eskom (T-R-I), Private Bag 40175, Cleveland, 2022

# BAD DATA REJECTION IN A LINEAR PROGRAMMING BASED POWER SYSTEM STATE ESTIMATION

R.Zivanovic  
Pretoria Technikon

A.Petroianu  
University of Cape Town

The properties of Linear Programming State Estimation (LPSE) in bad data rejection are explored and assessed. Comparison between Linear Programming and Weight Least Square techniques, in terms of treating bad data are presented. A new reweighting strategy for LPSE is developed. This strategy succeeds in treating multiple interacting bad data.

## 1. Introduction

The most common solution for a power system state estimation is based on the Weighted Least Square (WLS) technique. The bad data in WLS algorithm are rejected by using residual analysis methods [1].

The Linear Programming State Estimator (LPSE) uses as a criterion the weighted sum of the absolute value of the estimation residuals, and it is an alternative approach to WLS [2,3]. The LPSE belongs to the group of estimators based on nonquadratic estimation criteria [1]. The LPSE's ability for automatic bad data rejection, although effective in most of the practical situations, may fail in some cases. This is mainly caused by the existence of many leverage points in the measurement regression model [4,7].

In the first part of the paper the LPSE problem is formulated. Details about algorithm are given in [2]. In the second part comparison between LPSE and WLS state estimator is presented. This comparison gives a better understanding of the problems created by bad data in state estimation. In the last part of the paper a new bad data rejection algorithm for LPSE is developed and tested.

## 2. Review of the LPSE

The relationship between measurements and states is represented by:

$$z = Hx + v \quad (1)$$

where  $z$  -  $M \times 1$  vector of system measurements,  
 $x$  -  $N \times 1$  state vector,  
 $H$  -  $M \times N$  matrix,  
 $v$  -  $M \times 1$  vector of measurement errors.

The goal of state estimation problem is to determine the state vector  $x$ , which minimises the errors  $v$ .

In LPSE the objective function is the weighted sum of absolute values of the measurement residuals. By introducing the slack variables  $S_i$  (for  $i = 1, \dots, M$ ), the LPSE problem can be formulated as [2]:

$$\min \sum_{i=1}^M C_i (2S_i - \sum_{k=1}^N H_{ik} x_k) \quad (2)$$

$$\text{subject to } Hx - S \leq z, \quad x \geq 0 \text{ and } S \geq 0. \quad (3)$$

where  $C_i = R_i^{-1} = 1/\sigma_i^2$  represents the weight  $i$  (inverse of variance for normally distributed error of measurement  $i$ ).

The LPSE method tends to automatically reject bad data in the measurements [2,3]. It gives a solution in which  $N$  measurements out of  $M$  are exactly satisfied, i.e. the corresponding estimation residuals are null. However, in some cases the set of measurements that are exactly satisfied may not be all correct [4].

## 3. Bad Data Rejection Properties of LPSE versus WLS State Estimation

In order to derive the properties of LPSE, let partition the basic measurement equation (1) in the following way:

$$\begin{bmatrix} z_t \\ z_s \end{bmatrix} = \begin{bmatrix} H_t \\ H_s \end{bmatrix} \cdot x + \begin{bmatrix} v_t \\ v_s \end{bmatrix} \quad (4)$$

where  $t$  - subscript refer to those measurements that are exactly satisfied by the LPSE ( $N$  measurements),  
 $s$  - subscript refer to the remaining  $M-N$  measurements suspected to be inaccurate and rejected by the LPSE.

The measurement residuals can be written as:

$$\begin{bmatrix} r_t \\ r_s \end{bmatrix} = \begin{bmatrix} z_t \\ z_s \end{bmatrix} - \begin{bmatrix} H_t \\ H_s \end{bmatrix} \cdot \hat{x} \quad (5)$$

where  $r_t$  -  $N \times 1$  residual vector of measurements from subset  $t$  ( $r_t=0$  because  $t$  measurements are fully satisfied),  
 $r_s$  -  $(M-N) \times 1$  residual vector of measurements from subset  $s$ ,  
 $\hat{x}$  - state estimate vector.

Substituting equation (4) into (5) we have:

$$\begin{bmatrix} 0 \\ r_s \end{bmatrix} = \begin{bmatrix} H_t \\ H_s \end{bmatrix} \cdot (x - \hat{x}) + \begin{bmatrix} v_t \\ v_s \end{bmatrix} \quad (6)$$

Eliminating the state estimation error  $(x - \hat{x})$ , the equation (6) can be reduced to the following:

$$r_s = -H_s H_t^{-1} v_t + v_s \quad (7)$$

Based on the known statistical properties of the measurement errors (normal distribution with known variance),

the corresponding statistical properties of the estimation error ( $\mathbf{x} - \hat{\mathbf{x}}$ ) and the residuals  $\mathbf{r}$ , can be evaluated [4,5].

From the other side the measurement residual vector  $\mathbf{r}'$ , based on WLS estimation algorithm [6], is by definition:

$$\mathbf{r}' = \mathbf{z} - \mathbf{H}\hat{\mathbf{x}} = \mathbf{W}\mathbf{v} \quad (8)$$

where  $\mathbf{W}$  -  $M \times M$  residual sensitivity matrix [6].

Bad data detection and identification is based on Hypothesis Testing Identification (HTI) [6]. Using the same notation as in (4), the equation (8) can be partitioned as follows:

$$\begin{bmatrix} \mathbf{r}'_t \\ \mathbf{r}'_s \end{bmatrix} = \begin{bmatrix} \mathbf{W}_t & \mathbf{W}_s \\ \mathbf{W}_t & \mathbf{W}_s \end{bmatrix} \begin{bmatrix} \mathbf{v}_t \\ \mathbf{v}_s \end{bmatrix} \quad (9)$$

In this case the subscript  $s$  refer to the maximum number ( $M-N$ ) of suspected measurements (from detection test), and the subscript  $t$  indicate an  $N \times 1$  vector containing the smallest residuals. We can write the lower part of the equation (9) as:

$$\mathbf{r}'_s = \mathbf{W}_{ss}\mathbf{v}_s + \mathbf{W}_{st}\mathbf{v}_t = \mathbf{W}_{ss}\mathbf{v}_s + \mathbf{e} \quad (10)$$

In HTI method a vector  $\mathbf{v}_s$ , containing bad data, is estimated for a given vector  $\mathbf{r}'_s$ , and noise  $\mathbf{e} = \mathbf{W}_{st}\mathbf{v}_t$ , by using least square approach:

$$\hat{\mathbf{v}}_s = \mathbf{W}_{ss}^{-1}\mathbf{r}'_s \quad (11)$$

The corrected state vector  $\hat{\mathbf{x}}^c$  will be obtained using the corrected measurement vector  $[\mathbf{z}_s - \hat{\mathbf{v}}_s \quad \mathbf{z}_t]^T$ . Based on the fact that the residuals of the corrected measurements are equal to zero

$$\mathbf{r}_s^c = \mathbf{W}_{ss}(\mathbf{v}_s - \hat{\mathbf{v}}_s) + \mathbf{W}_{st}\mathbf{v}_t = 0 \quad (12)$$

the corrected state vector  $\hat{\mathbf{x}}^c$  is obtained through  $\mathbf{z}_t$  only [6].

Further we can prove that the vector of error estimates  $\hat{\mathbf{v}}_s$  is the same as the vector of residuals  $\mathbf{r}_s$  in LPSE (substituting (10) into (11) we obtain equation (7)):

$$\hat{\mathbf{v}}_s = \mathbf{W}_{ss}^{-1}\mathbf{W}_{st}\mathbf{v}_t + \mathbf{v}_s = -\mathbf{H}_s\mathbf{H}_t^{-1}\mathbf{v}_t + \mathbf{v}_s = \mathbf{r}_s \quad (13)$$

The statistical properties of the corrected state estimation error ( $\mathbf{x} - \hat{\mathbf{x}}^c$ ) and the error estimates  $\hat{\mathbf{v}}_s$ , obtained in HTI, are the same as the statistical properties of estimation error and residuals  $\mathbf{r}_s$  in LPSE respectively [5,6].

In conclusion the bad data rejection of LPSE is giving the same result as HTI method in WLS estimation.

#### 4. Problems Related to Bad Data Rejection

From the equation (7) (or (13)) results that the source of error could be  $\mathbf{v}_t$  and/or  $\mathbf{v}_s$ . The following situations will be considered:

- The measurements with gross error belong to subset  $s$ ; the result of LPSE is not corrupted. The measurements with gross error correspond to the flagged residuals in HTI (residuals larger than statistical threshold).
- The measurements with gross error belong to subset  $t$ ; the result of LPSE is corrupted. The measurements with gross error do not correspond to the flagged residuals in HTI.

- The measurements with gross error belong to subsets  $s$  and  $t$ . The state estimate is corrupted, and the flagged residuals do not correspond to the bad data.

In the situation a) the gross error rejection of the LPSE is automatic. In the situations b) and c) the LPSE always fail in rejection of bad data. The reason for the situations b) and c) are the critical measurements and/or bad leverage points in state estimation regression model.

The critical measurement is the one whose deletion will cause the system to become unobservable. The leverage points are those points which are far away from the bulk of the data points in the factor space [7]. In the regression model of the power system state estimation, the factor space is represented by the matrix  $\mathbf{H}$ . To be good or bad leverage point depends upon whether the metered value, which corresponds to the leverage point, is valid or not.

Correct detection of bad data in the situations b) and c) may be obtained, in some cases, by utilising the linear estimation (regression) model (7) or (13), as shown in [4,5]. The gross errors in the subset  $t$  can be easily identified as long as the subset  $s$  is cleared from any bad data (the situation b)). In estimating  $\mathbf{v}_t$  the model (7) or (13) is assumed, and the weighted least square algorithm is applied:

$$\hat{\mathbf{v}}_t = (\mathbf{M}^T \mathbf{R}_s^{-1} \mathbf{M})^{-1} \mathbf{M}^T \mathbf{R}_s^{-1} \mathbf{r}_s \quad (14)$$

where  $\mathbf{M} = -\mathbf{H}_s \mathbf{H}_t^{-1}$ ,

$\mathbf{R}_s^{-1}$  - the inverse of the variance matrix of measurement errors for subset  $s$ .

In the situation c) the subset  $s$  is contaminated with bad data, so the statistical model (7) or (13) is biased. The masking effect of bad data in subset  $s$  make the identification of any gross errors in subset  $t$  unreliable. However, we can employ hypothesis test based on the following residual:

$$\mathbf{r}_p = \mathbf{r}_s - \mathbf{M}\hat{\mathbf{v}}_t \quad (15)$$

in weighted or normalised form [5]. Sometimes this technique cannot succeed due to rank deficiency of matrix  $\mathbf{M}$  and/or bad leverage points in the factor space of regression model (7) or (13), as shown in [5].

In a power system, the leverage points in the factor space associated with  $\mathbf{H}$  (and  $\mathbf{M}$ ), result from measurements of the following types [7]:

- line flows and bus injections associated with lines that are relatively short compared to the others,
- bus injections at nodes that have a large number of incident lines.

The entries of the matrix  $\mathbf{H}$  associated with such measurements become large.

#### 5. The Reweighting Algorithm for Bad Data Rejection

The estimates of the state vector obtained by using LPSE, satisfies  $N$  measurements exactly, and the corresponding residuals are equal to zero. As we show in section 4 the re-

siduals of the measurements associated to bad leverage points may be zero in some situations. It means that the LPSE satisfies bad data exactly. In this case more than half of the measurement residuals from subset  $s$  ( $M-N$  redundant measurements which are rejected by LPSE) are larger than statistical threshold. It means that more than half of the redundant measurements are detected as bad data. This is an indicator that the result of LPSE is corrupted with bad data, because the largest possible number of bad data that any estimator can handle is equal to half the number of redundant measurements [7]. Certainly this is true if we consider the full regression model, i.e. each measurement is function of all state variables.

To correct the biased LPSE result the weights of all measurements from subset  $t$  are lowered, alleviating their contribution to the solution. The weights of the measurements from the subset  $s$  are replaced with the associated values of residuals  $r_s$ . These residuals represent the distances of the wrong solution point to the measurement hyperplanes. This reweighting strategy move away the solution point from bad leverage points by giving the larger weights to the data far away from the bad leverage points.

The following algorithm describes the steps involved in the proposed bad data rejecting method:

- run the LPSE and obtain the residual vector  $r_s$ ;
- find the number of bad data from the subset  $s$  using some statistical threshold; if the number is less than  $(M-N)/2$  stop, bad measurements are rejected; otherwise go to step c);
- change the weights of the measurements in subset  $t$  to some small value (say 0.01), and weights of the measurements in subset  $s$  to  $r_s$ ; go to a).

The regression model of the power system state estimation is specific, because of the sparse matrix  $H$  (Jacobian). It means that a measurement is not a linear combination of all the state variables, but only of some of them. This property induces some differences in step b) of the above algorithm [7].

## 6. Numerical Examples

### 6.1. Linear Regression Example

In the first example the goal is to estimate the slope  $x_1$  and the intercept  $x_2$  of a straight line  $z = x_1 h + x_2$ , which fits 5 data points, given in Table I.

Table I: Data points ( $z$ ,  $h$ ) and the results for the first regression example

$i$	$z_i$	$h_i$	$r'_{w_i}$	$r'_{N_i}$	subset	$\hat{v}_{s1}$	$r_{s1}$
1	1.5	3	-1.44	-1.85	s	0	0
2	6	4	2.67	3.27	s	4	4
3	2.5	5	-1.21	-1.43	s	0	0
4	7.5	15	-0.07	-0.09	t		
5	8	16	0.04	0.07	t		

The second measurement is a bad measurement (6 instead of 2). The line fitted by using WLS is  $z = 0.39h + 1.78$ . The line is shown in Figure 1 together with data points. Table I shows that the weighted residuals  $r'_{w_i} = r'_i / \sigma_i$  (where  $\sigma_i = 1$ ), and normalised residuals  $r'_{N_i}$  clearly detect the bad measurement; its value is larger than the chosen threshold, 2.5. The error  $\hat{v}_{s2}$  is estimated using least square technique (11), and the corrected solution is obtained,  $z = 0.5h$ . From the other side the LPSE automatically reject bad data point 2 as shown in Figure 1. The LPSE results are the same as the corrected WLS results. The additional result obtained from LPSE are the residuals of the subset  $s$  (equal to error estimates).

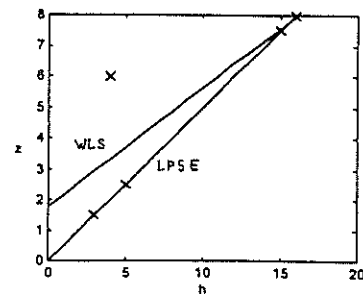


Figure 1: WLS and LPSE in the presence of a single bad data

In the second example two leverage points (they are far from the others in the  $h$ -axis) have wrong values for  $z$  ( $z_4=z_5=1.5$  instead of 7.5 and 8 respectively). These bad data points are clearly indicated in Figure 2 and Table II.

Table II: Data and the results for the second regression example

$i$	$z_i$	$h_i$	$r'_{w_i}$	$r'_{N_i}$	subset	$r_{s1}$	$\hat{v}_{u_i}$
1	1.5	3	-0.5	-0.65	s	-0.54	
2	2	4	0.03	0.04	t		0.05
3	2.5	5	0.57	0.67	s	0.54	
4	1.5	15	-0.07	-0.09	s	-0.04	
5	1.5	16	-0.03	-0.04	t		-0.06

The WLS fitted line is  $z = -0.04h + 2.11$ , and it is shown in Figure 2. Table II shows that neither the weighted residuals nor the normalised residuals are able to detect bad data. The error data belong to subset  $s$  and subset  $t$  (as discussed in section 4) and the estimator is subject to the masking effect of the multiple interacting bad data. The LPSE also fails to reject the error. Its fitted line is  $z = -0.04h + 2.17$ ; indicated in Figure 2 with LP1. Because the error data belong to both subsets ( $s$  and  $t$ ) bad data identification technique (14) fails, as shown in Table II, column  $\hat{v}_{u_i}$ .

The reweighting algorithm, as explained in the section 5, uses the residuals  $r_{s1}$  (see Table II) for the weights of suspected data (subset  $s$ ), and the value 0.01 for the weights that belong to subset  $t$ . These weights force the LPSE algorithm to find the correct fitting line (LP2 in Figure 2).

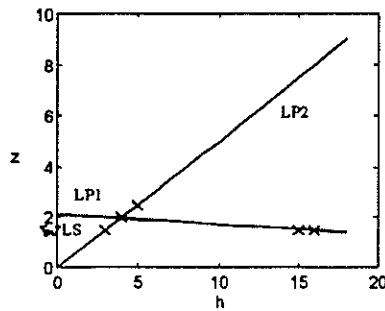


Figure 2: WLS estimator and LPSE in the presence of two bad leverage points

### 6.2. Example of a 3-bus DC model

A 3-bus power system is shown in Figure 3. The system is modelled using DC model. All lines are assumed to have zero resistance and reactance equal to 1 pu. The problem is to estimate two bus voltage phase angles  $x_1$  and  $x_2$  ( $x_3$  is considered zero for the reference node 3) from a set of 6 active power measurements. The measurements are disposed in the way shown in Figure 3. The linear regression model in the matrix form is  $z = Hx + v$ , with

$$H = \begin{bmatrix} 1 & -1 & 1 & 0 & 1 & 1 \\ -1 & 1 & 0 & 1 & -2 & 1 \end{bmatrix}^T \quad (16)$$

If we shorten line 2-3, by increasing its susceptance to 2 pu, the points 4, 5 and 6 in the factor space will move away from the rest of the data, and the associated rows of  $H$  become  $[0 \ 2]$ ,  $[1 \ -3]$ , and  $[1 \ 2]$  respectively. In that way we create the leverage points.

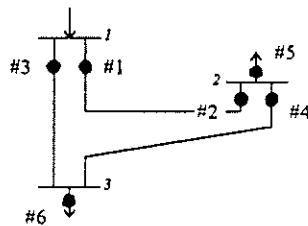


Figure 3: 3-bus power system

All true measurements are equal to zero. Two bad data points have been introduced at measurements 1 and 5 with a value 1 for both. The LPSE automatically reject these two errors if the  $H$  matrix is equal to (16). But if we introduce the leverage points, as explained above, the estimates of LPSE and WLS estimator are wrong. The data points 1 and 5 mask each other in both  $r'_{wi} = r'_i / \sigma_i$  ( $\sigma_i = 1$ ) and  $r'_{Ni}$  values, as shown in Table III. The bad data points are classified in both subsets (s and t). The error estimates  $\hat{v}_{ti}$  are wrong.

The residuals  $r_p$ , calculated using (15), can indicate the bad data point 1 (shown in Table III). One possibility is to eliminate that measurement by lowering its weight, and then obtained another LPSE solution [5]. In our example that technique will succeed, but in some cases the technique will fail [5]. This technique will fail if we change the value for

bad measurement 5 to 2 in our example. The value for bad measurement 1 stay the same.

Table III: Data and the results for 3-bus DC power system

i	$z_i$	$r'_{wi}$	$r'_{Ni}$	subset	$r_i$	$\hat{v}_{ti}$	$r_p$
1	1	0.53	0.6	s	0.4		0.64
2	0	0.46	0.52	s	0.6		0.36
3	0	-0.3	-0.34	s	-0.4		-0.29
4	0	0.32	0.37	s	0.4		0.14
5	1	0.21	0.31	t		0.5	
6	0	0.02	0.04	t		-0.14	

In both cases we can implement the reweighting procedure, as explained in the section 4, and find the true solution in second LPSE iteration.

### 6. Conclusions

The results of the study reported in this paper lead to the following conclusions:

- The WLS state estimator with post-processing of bad data (HTI method) is giving the same result as LPSE. Automatic rejection of bad data in LPSE is not a real advantage over WLS estimator, as claimed in [2,3].
- The multiple interacting bad data, differently called multiple bad leverage points are the most critical for any kind of state estimator. WLS estimator and LPSE always fail in rejecting that kind of bad data.
- A simple reweighting strategy for treating bad data in LPSE has been proposed in the paper. The strategy succeeds in treating the multiple interacting bad data.

### 7. Acknowledgement

The authors gratefully acknowledge the financial assistance granted by ESKOM in support of this project.

### 8. References

- [1] E.Handchin at all., "Bad Data Analysis for Power System State Estimation", IEEE Trans.on PAS, Vol.94, No.2, March/April 1975, pp. 329-337
- [2] M.R.Irving at all., "Power System State Estimation using Linear Programming", Proc.IEE, Vol.125, No.9, Sept.1978, pp. 879-885
- [3] W.Kotiuga and M.Vidyasagar, "Bad Data Rejection Properties of Weighted Least Absolute Value Techniques applied to Static State Estimation", IEEE Trans.on PAS, Vol.101, No.4, April 1982, pp. 844-853
- [4] D.M.Falcao and S.M.de Assis, "Linear Programming State Estimation: Error Analysis and Gross Error Identification", IEEE Trans.on PWRs, Vol.3, No.3, August 1988, pp.809-815
- [5] A.Abur, "A Bad Data Identification Method for Linear Programming State Estimation", IEEE Trans.on PWRs, Vol.5, No.3, August 1990, pp.894-901
- [6] L.Mili at all., "Hypothesis Testing Identification: A New Method for Bad Data Analysis in Power System State Estimation", IEEE Trans.on PAS, Vol.103, No.11, November 1984, pp.3239-3252
- [7] L.Mili at all., "High Breakdown Point Estimation in Electric Power Systems", Proc.of Int.Symp.on Circuit and Systems, New Orleans, May 1990, pp.1843-1846

# OBJECT ORIENTATED SOFTWARE PACKAGE FOR FAULT ANALYSIS

Lulamile Mzamo

Silviu Darie

Department of Electrical Engineering  
University of Cape Town,  
Rondebosch, 7700, Republic of South Africa

## ABSTRACT

Using the Borland Pascal 7 with Objects a graphical editor and a user friendly package for short circuit current analysis has been created. The package is called FanaW. The program's Editor contains a number of standard electrical symbols to introduce the power network. This is an integrated graphics environment for power systems fault analysis. The program allows to calculate any kind of fault in a power network from 1 cycle to steady state period of time. The package has been tested for different network structures, and the results were compared with the EDSA package. Good results were obtained with less than 0.5 % deviation.

**Keywords:** Power System, Faults Calculation, Object Orientated Software, Windows.

## 1. INTRODUCTION

Fault analysis is one of the most important fields in Power Systems engineering. One of the major reasons for this is the amount of damage that an unexpected fault can cause to a power system. It is often practice that the calculations done in calculating the short circuit currents are only those for steady state conditions. Another factor that is most of the times ignored in fault calculations is the influence that a transformer winding has on the phase of branch currents and thus voltages in a system. The paper deals with the fault calculation in power network by considering the power transformer phase shift due to the winding type, the electrical machines contribution to the fault, and performing the faults calculations in the transient and steady state period. The package that has been designed is installed in the electrical engineering computer network

## 2. PHASE CHANGES DUE TO TRANSFORMER WINDING TYPE

The phase changes due to the power transformer winding methods occur only in the power transformer with a delta and Wye and a Delta and Wye-ground connection style.

In the program the above requirements have been implemented in the following steps:

1. Initialise the matrix. This is done by making all of the elements of the matrix  $0 + j0$ .
2. Formulate the matrix in this form

If (transformer primary and secondary winding are the same) or (none of the winding is delta) then

corresponding element =  $1 + j0$

else

if (voltage at I > voltage at j) then

$$V_{rel\ j} = \frac{\sqrt{3}}{2} + j0.5$$

$$V_{rel\ j} = \frac{\sqrt{3}}{2} - j0.5$$

else

$$V_{rel\ j} = \frac{\sqrt{3}}{2} - j0.5$$

$$V_{rel\ j} = \frac{\sqrt{3}}{2} + j0.5$$

3. Complete the matrix, using the method below
  - i. find  $V_{rel\ ij} = 0 + j0$ ;
  - ii. If found then do the following  
find k such that  $V_{rel\ ik}$  and  $V_{rel\ kj}$  are not equal to  $0 + j0$   
 $V_{rel\ ij} = V_{rel\ ik} \times V_{rel\ kj}$   
goto I
  - iii. if no  $V_{rel\ ij} = 0 + j0$  then  
matrix is complete.

## 3. MACHINE CONTRIBUTION TO FAULT

The types of the machines to be considered are:

1. Generic machine: This is the most probable industrial machine load type: it is a combination of a synchronous and induction machines, 25 % synchronous motors and 75 % induction machine load, [1];
2. Induction machine;
3. Synchronous machine;
4. Reactor connected machine: This machine is connected to a bus via a reactor.

According to [1] the practical approximations to these machine impedance are:

#### First cycle impedances

1. For generic machines:  
 $x'' = 0.28 \text{ pu}$  for  $S_r < 50 \text{ Hp}$   
 $= 0.2 \text{ pu}$  for  $S_r \geq 50 \text{ Hp}$
2. For Induction machines  
 $x'' = 0.28 \text{ pu}$  for  $S_r < 50 \text{ Hp}$   
 $= 0.2 \text{ pu}$  for  $S_r \geq 50 \text{ Hp}$
3. Synchronous Machine  
 $x'' = 0.2 \text{ pu}$  for  $S_r \geq 250 \text{ hp}$

4. Reactor connected machines:  
 Their impedance depends on the reactor impedance.

#### Interrupt cycle impedances

Interrupt cycle impedance can be calculated from the first cycle impedance by using multiplying factors for impedances. Below are these multiplying factors.

Source Type	Multiplying factor k
Power Utility	1.
Generators	1
Synchronous motors	1.5
Induction motors	
> 250 Hp	1.5
> 50 Hp	3
< 50 Hp	Neglect

## 4. TRANSIENT CHARACTERISTICS OF FAULT CONDITIONS

In order to calculate the transient fault currents the Multiplying factors are used. The multiplying factors depend on the equivalent impedance at the fault point and the cycle number at which the fault is occurring. These factor can be found from [2] as graphs or as an approximated formula from [3]:

$$MF = \sqrt{1 + 2e^{-4\pi \frac{R}{X} t}}$$

with t in cycles

## 5. FanaW

A software package called FAnaW in windows platform has been designed and implemented. This package has the following features:

- An object orientated software written in Windows;
- Mainmenu drive orientated.
- Allows to perform any kind of fault according to IEEE and IEC standards

### 5.1 Entering of data:

Bus data

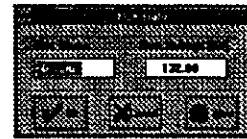


Figure 1. Bus Data Editor

Branch data

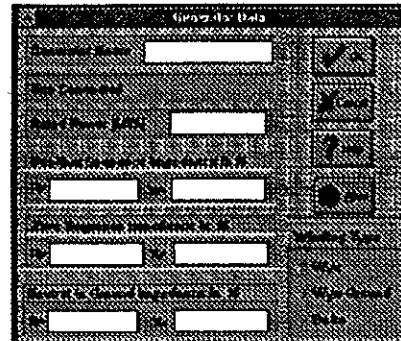


Figure 2. Branch Data Editor (Generator)

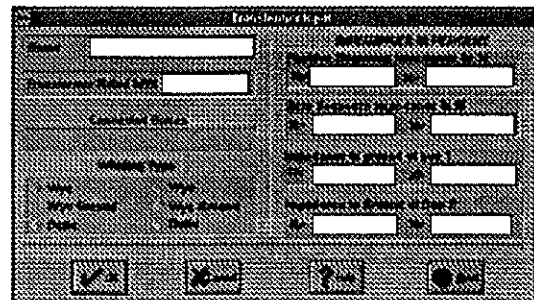


Figure 3. Branch Data Editor (Transformer)

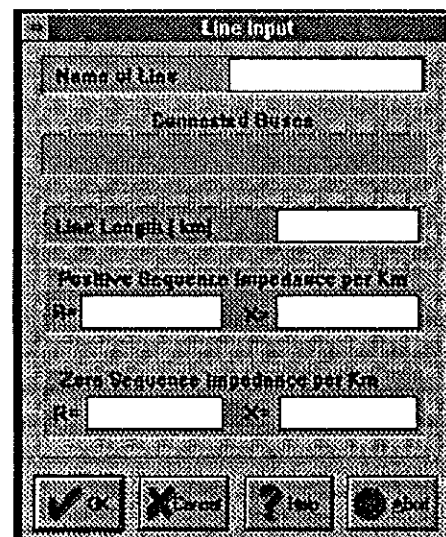


Figure 4. Branch Data Editor (Line)

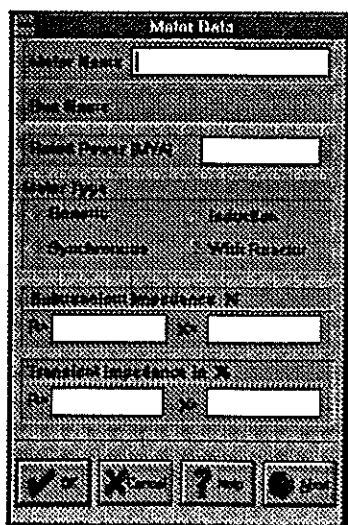


Figure 5. Branch Data Editor (Motor)

This is very simple and is done by using the FANaW windows editors

## 5.2 Preferences

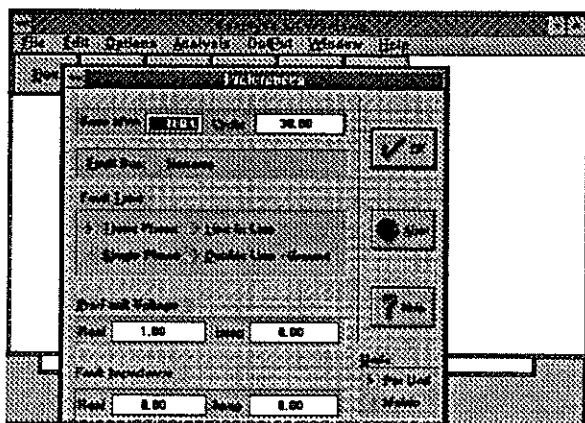


Figure 6. Fault Conditions.

This includes the fault point impedance, prefault voltages, base MVA, the cycle to be analysed, the fault type, the system of units etc.

## 5.3 Saving and retrieving the network.

This is window menu driven.

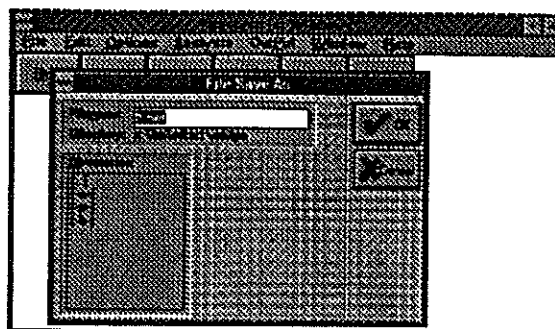


Figure 7. File Save Window.

## 5.4 Fault Analysis

- Choose the fault bus by clicking on the Short button and clicking on the bus on the one line diagram displayed on the screen.
- Choose RUN from the ANALYSIS Submenu.
- Choose Output choice needed from the OUTPUT submenu.

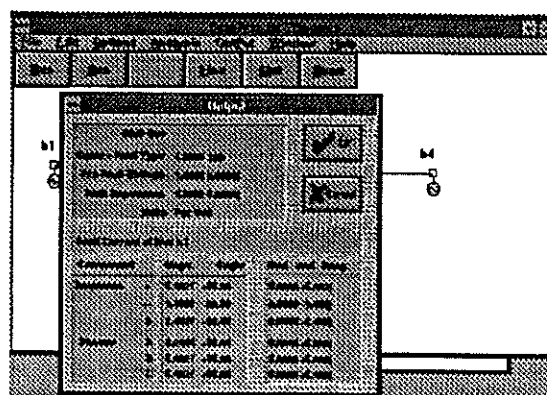


Figure 7. Fault Currents Output Window

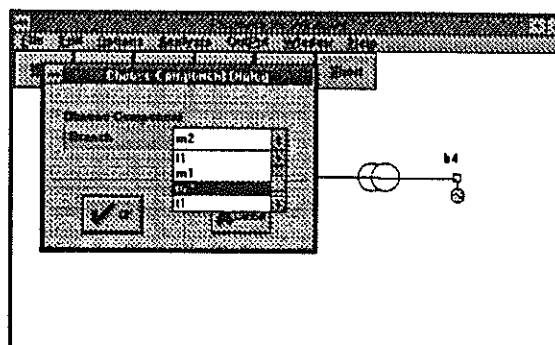


Figure 8. Window for choosing a branch

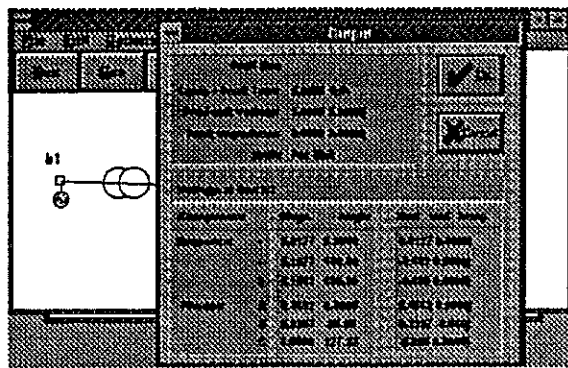


Figure 9. Output window for Bus Voltage

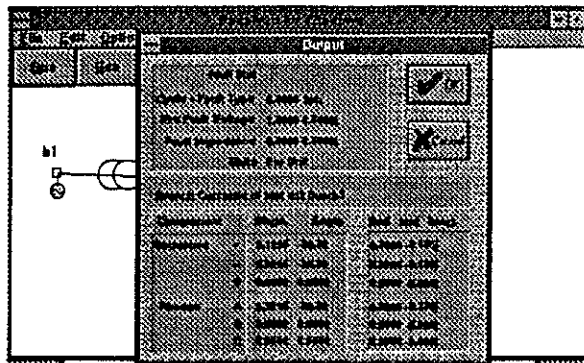


Figure 10. Output Window for Branch Currents.

## 6. PROGRAM DESCRIPTION

The program FAnaW is written in Borland Pascal V7.0 for windows; it contains 5439 lines and the resource code. The program has 23 units and is object orientated. The following objects were used in developing the software:

**Papplication:** This object manages the interface between the program and the windows environment;

**PWindow:** This maintains the screen display and this is controlled by Papplication.

**PCollection:** These are linked lists of the components. There is one PCollection for each component type. These are connected to PWindow.

**Pcomponent:** This is the parent for the components in the network. This has only one field, the name.

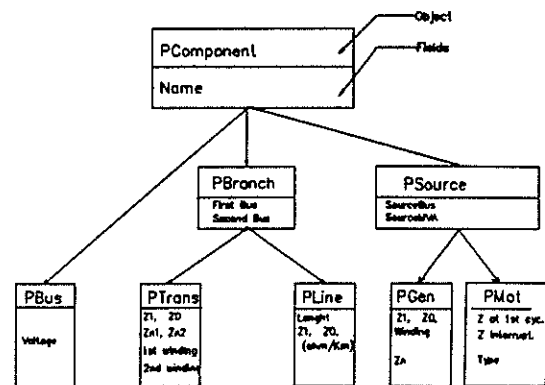


Figure 11. Network components hierarchy

## 7. CONCLUSIONS

A user-friendly software package in windows platform has been designed and implemented in the electrical Engineering computer network at U.C.T. The package has been tested against EDSA and has a less than 0.1 % deviance from EDSA.

## 8. REFERENCES

- [1] ANSI/IEEE Str 141-1986, IEEE recommended practice for electric power distribution in industrial plants (Red Book)
- [2] ANSI/IEEE c37.5-1979, IEEE Guide for calculation of fault currents for application of ac High Voltage Circuit Breakers rated on total current basis.
- [3] Glover, J.D., Sarma, M. Power System Analysis and Design with personal computer Applications. PWS-Kent Publishing company, Boston, 1987

# UNIT CONNECTED BACK-TO-BACK PUMP STORAGE SCHEMES

T A Rae   R G Harley   G D Jennings   M T Wishart\*

Department of Electrical Engineering, University of Natal, South Africa

\*Electrical Technology; ESKOM Technology, Research and Investigations, South Africa

## ABSTRACT

Conventional High Voltage Direct Current (HVDC) has advantages in long distance transmission, and of decreased stability problems which limit High Voltage Alternating Current (HVAC) transmission, but in turn introduces other complexities. Unit Connection is a refined HVDC scheme which rectifies the power of each turbo-generator individually before connecting it to the DC line. The general aspects of the Unit Connected scheme are presented along with the advantages and disadvantages of this scheme, connected in a back-to-back configuration coupled with a pump storage scheme. An initial cost study is included to evaluate the financial aspects of this scheme.

## 1. INTRODUCTION

Historically electrical power was generated and distributed in DC, and therefore utilized in this form. The advent of AC and the transformer allowed AC power to be transmitted over long distances at a higher voltage, but brought with it the concepts of synchronism between the sending and receiving ends, and thus the problems of maximum power transfer. The use of a HVDC line eliminates the synchronism problems and to a large extent the transmission distance limitations.

The conventional HVDC connection is given in Fig.1 where a four machine set is connected to the common AC bus, to which the filters are attached. The rectifiers are connected in series on the DC side, in a two pole (positive and negative) configuration, where the star-star and star-delta transformers create a 30° phase shift necessary for twelve pulse operation.

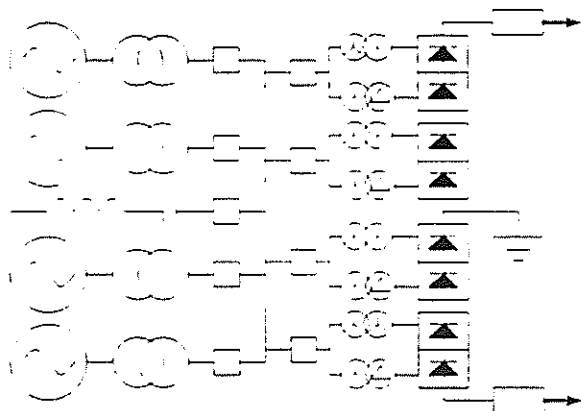


Figure 1: Conventional HVDC Scheme

The configuration may be altered such that each generator is connected to a single rectifier which in turn is connected in a series or parallel configuration on the DC side, in a similar manner as a conventional HVDC connection. Such a connection is referred to [1] as a *Unit Connected Scheme* as each generator is matched to a single rectifier, thus creating a module or individual *unit* as shown in Fig.2.

## 2. GENERAL UNIT CONNECTION

### 2.1 Basic Connections

#### Unit Connection

Comparing the Unit Connected scheme in Fig.2 with the conventional HVDC scheme in Fig.1, one voltage transformation step, the AC filters, and most of the AC switchgear and busbars at the rectifier station are eliminated, by directly connecting each generator to its two converter transformers; this eliminates the need for the generators to run in synchronism as there is no longer a common AC bus. The on-load tap-change transformers can also be eliminated due to the rectifier converter voltage control being exercised by the generator excitation control.

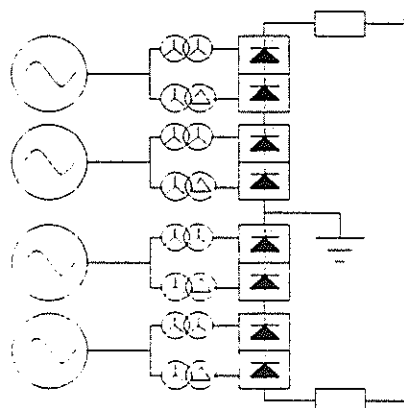


Figure 2: Series Unit Connection

The reduction in AC equipment leads to significantly reduced capital cost as well as reduced operating costs due to smaller station losses [1]. The avoidance of low order harmonic resonances, due to the absence of AC filters, results in a significant improvement in reliability. The possibility of variable speed operation to optimize the efficiency of hydro sets under different load conditions and water heads occurs due to the individual matching of each generator to its turbine.

The disadvantage of such a Unit Connection is that the converter current harmonics are injected into the

generator stator winding creating ripple torques and generator voltage distortion.

The optimum transmission voltage for the transmission distance and rated power is determined by the DC side connection of the rectifiers, i.e. in either a series or parallel connection, or even a combination of these.

### Series Topology

The series connection (Fig.2) of the rectifier units on the DC side results in the simplest control and protection strategies as the same direct current flows through all the converters; this yields an economical design due to the moderate DC voltage of each rectifier unit. No earth current flows in the case of an outage. The inverter station must be able to cope with a varying DC voltage due to partial load.

### Parallel Topology

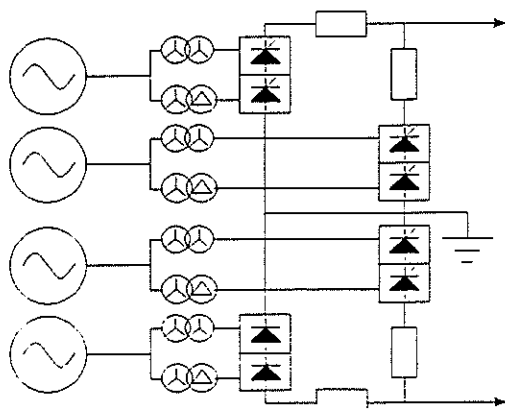


Figure 3: Parallel Unit Connection

The above parallel connection (Fig.3) results in complex control requirements due to each rectifier requiring its own current control, as well as a balance control to suppress power oscillations. The outage of a rectifier causes an equivalent earth current. Transmission voltage is all at its maximum value, thus the inverter station does not require any specific design requirements.

### Group Connection

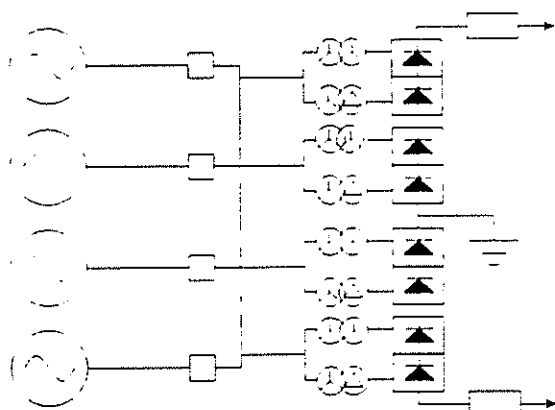


Figure 4: Group Unit Connection

Fig.4 displays the so-called group connection scheme which consists of a direct connection of the rectifiers with the generator transfer bus; and is thus not a true Unit Connected scheme but rather a Direct Connected scheme. The advantage of this connection is that the matching of the generator to its converter is no longer required, and the flexibility of operation and maintenance is enhanced. However some form of common speed control is required to ensure that the generators remain stably in synchronism.

### 2.2 Variable Speed

Traditional synchronous generators are run at constant synchronous speed, however, in the unit connection scheme of Fig.2 or Fig.3, it is possible to run each generator at a different speed from synchronous speed; which allows each turbine to be run at a particular value of speed which ensures maximum efficiency at any particular load value.

### Hydro Turbine Efficiency

The hydro power available from the water head (above the hydro-turbine) is determined by the following equation:

$$P = \rho g Q H$$

where  $\rho$  is the density of water  
 $g$  is the gravitational constant  
 $Q$  is the flow rate in  $\text{m}^3/\text{s}$   
 $H$  is the head of water above the turbine

$\rho$  and  $g$  are constant, and for a certain dam water level  $H$  is also constant, thus turbine power is varied by adjusting the water flow rate  $Q$ , which determines turbine shaft speed. Thus for a specific head the power delivered is directly related to the turbine speed. The efficiency of the turbine is a function of its speed and thus allowing the turbine speed to vary with the power requirement ensures a maximum conversion of energy due to the increased turbine efficiency.

In the pumping mode the speed of the motor (pump) determines the power drawn from the supply. Thus any form of speed control will determine the pumping load, and therefore ensure a maximum conversion from electrical to hydro power due to the increased efficiency of the turbine/pump.

### 2.3 Thyristor and Diode Rectifier

In the unit connected scheme, the thyristor rectifier is assigned, as with conventional HVDC, a constant current mode of operation, and the inverter is assigned a constant voltage mode of operation. The thyristor firing circuits provide rapid control, which when combined with the excitation control of the generator present a high speed control mechanism. This high speed control can be utilized to control any power oscillation around a desired operating point.

Alternatively, the rectifier may be composed of diodes which offer the highest degree of simplification of the sending end and the best economical benefit due to the saving of the firing controls and in the cost of the semi-conductors themselves. In this case the rectifier is assigned the voltage control (instead of the conventional current control) and the inverter the current (instead of voltage) control due to the uncontrolled action of the diode. The generator excitation control becomes the only means of voltage control at the sending end, and thus in the case of line faults, generator breakers and fast de-excitation has to be relied upon to extinguish the fault currents and protect the rectifier diodes. This relatively slow method of protection limits the use of diodes to low power applications as longer fault durations and higher fault levels occur [2].

### 3. PUMP STORAGE

The first obvious application of unit connection is to pumped-storage schemes, due to an increased ease of control for the generating and pumping mode, and the possibility of variable speed operation to increase the overall conversion efficiency.

#### 3.1 Conventional Pump Storage

The pump storage scheme is the only energy conversion system, totally controllable by the supply authority, which is found to be practical [3]. The efficiency of the pump storage scheme is calculated via the *conversion loss* ( $L$ ), which is the difference between the *pumping energy* ( $E_p$ ) and the *energy generated* ( $E_G$ ):

$$E_p = E_G + L$$

$$\frac{E_G}{E_p} = E_p - \frac{L}{E_p} = \eta$$

Thus any increase in the pumping and or generating efficiency increases the overall conversion efficiency by decreasing the conversion loss ( $L$ ).

#### Operating Advantages

Pump storage plants have all the operating advantages of conventional hydro plants arising from the quick starting, loading and high availability. There are additional advantages particularly if added to a predominately thermal system; such as a certain amount of reserved spinning capacity, handling of substantial short-term load swings, reduced thermal loading and system frequency control due to quick loading and unloading of the pump storage plant.

#### Disadvantages

The conventional pumped-storage scheme requires synchronization of the generator-motor to the system frequency for generation and pumping. The starting (pumping) of the conventional scheme is difficult due

to the magnitudes of the starting currents drawn causing voltage dips and frequency variations. The electrical power to the motor cannot be controlled in the pumping mode and is determined by the pump/motor characteristics.

#### 3.2 Unit Connection Back-to-Back Pump Storage

Conventional pump storage plants cannot control the pumping load, and the motor operates at a power determined by the pump-turbine characteristics, regardless of the system requirements. A variable speed pumping unit can easily control the pumping load by changing the rotational speed, via the control presented by the back-to-back DC link. The variable speed pumping units can thus be operated at a power determined by the grid requirements.

In the case of a pump storage scheme the net head fluctuates due to the pumping or generating action filling or emptying the upper reservoir. The variable speed unit has a broader operational range in the pumping and generating mode which results in a higher efficiency over the entire generating and pumping mode. The increase in efficiency is achieved by the shifting of operating conditions towards the optimum design point by varying the speed.

In the conventional system, power is controlled by the guide vanes, while the speed of the generator is kept constant by the synchronizing force of the grid and therefore the power output response is slow due to the large inertia giving long time constants. The variable speed Unit Connected back-to-back system responds quickly to power commands because the power is controlled on the generator side by the back-to-back converters by the use of the flywheel effect. The difference between the generator power and the turbine power is derived from or compensated by the decrease or increase in speed, hence the flywheel effect. This change of speed is not reflected onto the system frequency due to the asynchronous tie formed by the back-to-back converter.

The variable speed operation of the reversible Unit Connected back-to-back scheme has the following advantages:

#### Electrically

The improvement in the ability to adjust the power system frequency even in the pumping mode (off-peak times), a great improvement in the power system stability due to the asynchronous tie formed by the DC link, quick response of active power by the flywheel effect, elimination of pump starting systems due to the control possible with the DC bridge, and the power electronics are at the generator voltage, leading to an economical converter design.

#### Hydraulically

The possibility of variable power and discharge in the

pumping mode, improvement in hydraulic efficiency in the generating and pumping mode and thus an overall increase in conversion efficiency, broader partial load and operating head range in the generating mode.

### 3.3 An Alternative Variable Speed Scheme

An alternative form of speed control is being developed for use on a pumped storage scheme in Japan. The rotor windings of the generator are replaced by a new three-phase windings. The rotor windings are designed to generate a rotating magnetic field around the rotor by excitation with low frequency AC current supplied by a cycloconverter [4], [5]. Thus the operating frequency can be varied by injecting a low frequency AC voltage on to the rotor instead of conventional DC. Although this scheme shows much promise, a comparison between this and the Unit Connected scheme is outside the scope of this paper.

## 4. ECONOMIC ASSESSMENT

### 4.1 Operational Costs

Negatively; the Unit Connection scheme (Fig.2) cannot directly supply local loads, due to the variable speed, however this may be overcome with the use of a small local converter, or in a back-to-back scheme a transformer may be used to supply the station auxiliaries and any local load. The generator and rectifier ratings must be matched to avoid the over-dimensioning of components, which reduces efficiency.

Positively; the elimination of one transformation level and the AC filters result in a substantial reduction in the station losses. A compact design of the turbine and generator results from a custom design for variable speed operation (and thus higher speeds if necessary).

The overall optimization depends on the special characteristics of each scheme and is likely to vary from one application to another.

### 4.2 Capital Costs

Precise cost comparisons between a unit connected HVDC and a conventional scheme can only be made for the same specific project. The following cost figures [1] are obtained from the cost breakdown of a conventional HVDC rectifier station minus the well known components that can be eliminated for a unit connection station generating at standard fixed frequencies. The group connection presents a saving of 32.5% [1] and the fixed speed Unit Connected scheme a saving of 39.0%. The savings are mainly due to the savings in the generator transformers, converter transformers, the AC switchgear, capacitors and AC filters; the only increase in capital cost is an increased generator cost to handle the converter harmonics. The unit connection scheme has a clear advantage irrespective of the inherent inaccuracies in the estimate [1]. No capital cost estimates are available for a variable frequency unit connection scheme.

## 5. FURTHER APPLICATIONS

Unit Connected schemes are also viewed as very attractive solutions, due to their flexibility of operation and to the possibility of a compact and light design, for large remote hydro stations with large units, or low power remote gas powered stations with isolated turbines.

## 6. CONCLUSION

The main disadvantage of the Unit Connection scheme is that converter created harmonic currents are injected directly into the generator and these create additional heat losses and ripple torques. The generator operation with variable speed needs further investigation to assess thermal capabilities at higher speed ranges. Due to the absence of AC filters the converter operates at a lower power factor.

The Unit Connection variable speed operation is of particular interest with reversible pump turbines (pump storage) due to the possibility of increased efficiency in the generating and pumping mode. On-load tap-changers are eliminated due the voltage control being performed by the generator excitation. The Unit Connection scheme is less susceptible to disturbances and therefore simpler to operate. The back-to-back connection of the inverter and converter results in a economical design due to the power electronics being at generator voltage. The above advantages outweigh the several disadvantages presented by the Unit Connection scheme.

The back-to-back Unit Connection scheme has an obvious application to the pumped storage scheme, however it may be applied to any HVDC scheme.

## REFERENCES

- [1] Arrilaga, J., Bowles, J.P., Campos Barros, J.G., Kanngiesser, K.W. and Ingram, L.: "Direct Connection of Generators to HVDC Converters: Main Characteristics and Comparative Advantages" *Electra*, pp.19-39, August 1993
- [2] Hungsasutra, S., Mathur, R.M.: "Unit Connected Generator with Diode Valve Rectifier Scheme" *IEEE Transactions on Power Systems*, Vol. 4, No. 2, pp 538 - 542, May 1989
- [3] Brown, G.: "Hydro Electric Engineering Practice", Blackie and Son Limited, 2<sup>nd</sup> edition, Glasgow and London, 1970
- [4] Tanaka, J.: "An 82 MW variable speed pumped-storage system" *Water, Power and Dam Construction*, pp.25-26, November 1991
- [5] Kita, E., Nishi, M., Saito, K., Bando, A.: "A 400MW adjustable speed pumped-storage system" *Water, Power and Dam Construction*, pp.37-39, November 1991

# CONSIDERATION OF THE USE OF LPATS FOR OPTIMISATION OF TRANSMISSION LINES

MG Redelinghuys, WC van der Merwe, IR Jandrell\*

Transmission Substation Technology  
Eskom, South Africa

\*Department of Electrical Engineering  
University of the Witwatersrand, South Africa

## ABSTRACT

LPATS (Lightning Position and Tracking System) was installed for Eskom early in 1993 for the purpose of monitoring and logging lightning in Southern Africa. Data for a first lightning season has been extracted from the system and analysed. This paper presents results of these preliminary studies. System limitations are discussed in this context. The results of the preliminary analysis indicate the usefulness of LPATS as a design tool in the optimization of transmission lines.

## 1) INTRODUCTION

South Africa has been actively involved in the study of lightning for many years. A large portion of lightning data has been collected using lightning flash counters. This method of detection has the disadvantage, in a large country like South Africa, of high operating costs due to large distances to be travelled in collecting counter data. With the advent of lightning location systems it was seen that such a system was vital for the progression of lightning research in South Africa. Early in 1993 a Lightning Position and Tracking System (LPATS) was installed for Eskom.

The system has been operational and logging data since October 1993. A preliminary analysis of data from a first lightning season has been completed. The analysis comprised grouping data according to polarity, amplitude, multiplicity, time and distance between strokes, ground flash density and time of day. Comparisons of LPATS data with data recorded from strikes to the 60m CSIR lightning research tower, which stands at an altitude of 1400m above sea level, have been made.

Although preliminary results have proved encouraging they have also highlighted a number of limitations of the installed system. The limitations include loss of subsequent stroke data and deviations in the ground flash density figures produced by LPATS from maps produced from flash counter readings. A comparison of the LPATS data with that recorded by the

instrumented lightning mast show deviations in location from a few hundred metres to over a kilometre.

Despite the present limitations LPATS has the potential to be a powerful engineering tool. Eskom's prime objective for the system is in the area of optimization of transmission lines. It is believed that LPATS will play a role in both the design stage and performance monitoring of various insulation co-ordination practices implemented on transmission lines.

In order to fully understand the system's limitations and advantages, a brief overview of the LPATS system components and operation is given in the next section. Thereafter, some results of the analysis of one season of lightning data is presented, and future utilisation of the system is discussed.

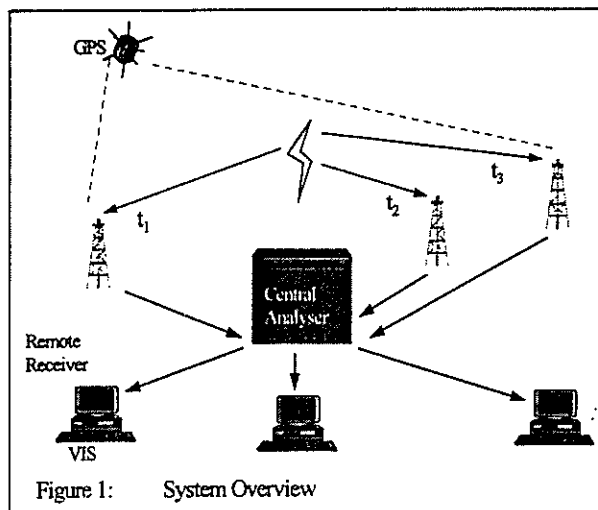
## 2) SYSTEM COMPONENTS AND OPERATION

LPATS comprises four main components:

- Remote Receivers - responsible for lightning stroke detection.
- Central Analyser - processes all lightning data and calculates stroke location.
- VIS (Video Information System) - user interface for easy access to lightning data.
- GPS Satellite - ensure system clocks are all synchronised and system timing is accurate.

The operation of the system is illustrated in Figure 1 and can be summarised in the following steps :

1. A lightning stroke generates an electromagnetic signal which radiates outward from the source and is detected by the remote receivers.
2. The remote receivers detect the lightning stroke waveform and attach a time stamp to the stroke. This time stamp corresponds to the peak of the detected waveform. The receivers also record the stroke amplitude, polarity and whether it is a cloud or ground stroke.



3. This information is then transmitted to the Central Analyser for processing.
4. The Central Analyser receives the reports from all the stations and uses this data to calculate the stroke location, using a "time of arrival" method. The stroke location, amplitude, time etc. are compiled into a complete report for each lightning stroke.
5. The report from the Central Analyser is sent to the Video Information System for access by the user.
6. In order to ensure that all data is accurate the timing of the system and the synchronisation of the receiver stations has to be exceptionally precise. GPS satellites are used to synchronise system clocks to achieve an accuracy of better than 1 millisecond.

LPATS detects and displays each lightning stroke in this manner. As the data is displayed it is archived so that it can be accessed at a later time. It is this archived data that is used for the study.

### 3.) PRELIMINARY RESULTS

The preliminary results can be classified according to two main areas of study:

1. To determine the accuracy of the system.
2. To produce lightning statistics for transmission line design purposes

#### 3.1) ACCURACY OF THE SYSTEM

In order to obtain an indication of system accuracy a joint project between Eskom and CSIR was established. Stroke data from LPATS was compared with corresponding stroke data obtained from lightning strikes to the CSIR lightning mast. For the 1993-1994 lightning season a total of three strokes were recorded as having struck the tower. Details of the strikes i.e. amplitude, time and location comparing LPATS data to CSIR mast data are given in Table 1.

Table 1: Data for strikes to CSIR lightning mast

Date	Time	Tower Peak Current	LPATS Peak Current	LPATS Position deviation (from tower)
12/02/94	17:33:28	-34.2kA	-34kA	1100m
3/03/94	15:35:21	-40.0kA	-39kA	600m
21/04/94	18:29:33	-13.4kA	-15kA	500m

As can be seen from Table 1 the difference in peak amplitude readings was from 0.58 % to 10.67 %. The distances of the strokes from the tower varied from as little as 500m to 1.1km.

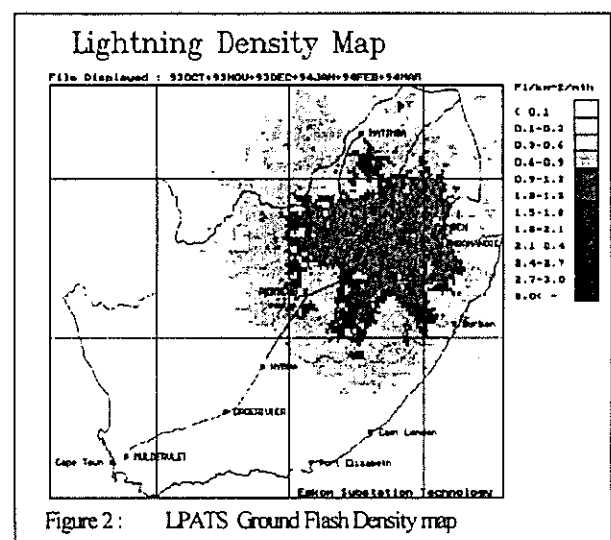
#### 3.2.) LIGHTNING STATISTICS

The following lightning statistics extracted from the data for the 1993-1994 lightning season are of interest:

- Ground flash density.
- Stroke amplitude distribution.
- Distribution of multiple stroke flashes .

##### 3.2.1.) Ground Flash Density

A plot of the ground flash density for the 1993-1994 lightning season is given in Figure 2. Comparing this data to the plot produced by the CSIR [1], using flash counters, a good general correlation between data can be observed. The main peak lightning areas indicated on the CSIR map are also evident in the LPATS plot.



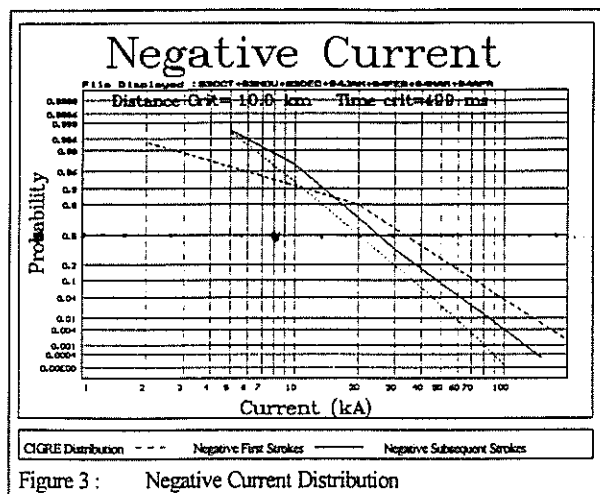
However, there is one area, in the Northern and Eastern Lesotho area, where LPATS does not detect as high a ground flash density as the flash counters. Two possible reasons have been proposed for this phenomenon :

- LPATS does not detect the lightning that occurs in this area (due to poor alignment of remote receivers).
- As the LPATS ground flash density data only represents one lightning season while the CSIR maps contain over 10 years of recorded data, we

may be observing a phenomenon that is specific to this lightning season only.

### 3.2.2.) Stroke Amplitude Distribution

Figure 3 shows stroke current amplitude distribution for negative first and subsequent strokes recorded by LPATS. The CIGRÉ current amplitude distribution for negative first strokes [2] has also been included in Figure 3 for comparison.

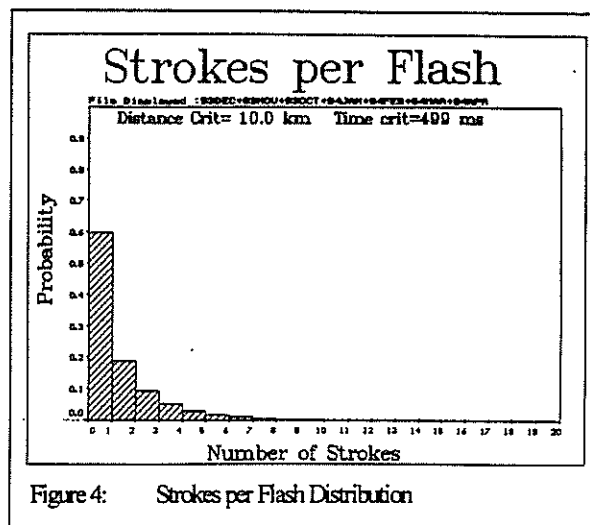


It can be seen from Figure 3 that the distribution of negative first strokes and that of subsequent strokes follow the same general trend, running parallel to each other. The LPATS negative first stroke distribution does not however, correspond to the CIGRÉ curve at current amplitudes of less than 15kA. For amplitudes greater than 15kA there is a better correlation between the CIGRÉ curve and the LPATS data. The mean current amplitude indicated by LPATS is 25kA for negative first strokes which is lower than the CIGRÉ mean of 31kA.

The deviation of the LPATS data from the CIGRÉ distribution at currents less than 15kA could possibly result from LPATS's inability to adequately detect low amplitude strokes. In order for a stroke to be registered by the system it has to be detected by at least 3 remote receivers. Low amplitude strokes may not have sufficient intensity to be detected by 3 receivers.

### 3.2.3.) Distribution of Multiple Stroke Flashes

A distribution for the number of strokes per flash is shown in Figure 4. From the plot it can be seen that LPATS records over 60% of all flashes as containing only a single stroke. This does not correlate with published data which gives the number of single stroke downward flashes as being approximately 45% and the mean number of strokes per flash as being 3 [2], [3].



The reason for the large discrepancy is believed to lie with the data communication transmission rate between the remote receivers and the central analyser. The data transmission rate is believed to be inadequate to deal with the vast number of strokes occurring which results in some subsequent stroke data being lost.

The preliminary analysis of LPATS data has already provided some useful information on the system and on lightning behaviour in South Africa. One of the most important results of the study however, has been the demonstration of the potential power of the system as an engineering tool. In order to provide some indication of the systems potential details of the envisioned utilisation of LPATS will be described.

## 4.) FUTURE UTILISATION OF LPATS

The primary role of LPATS will be in the establishment of a comprehensive lightning database from which lightning statistics and engineering design parameters can be extracted. The information provided by LPATS is extensive, for each lightning stroke the exact geographical location, the stroke amplitude, polarity, and time of occurrence are provided. In order to be useful to engineers, however, statistical analysis of this data is essential. Some of the information to be extracted includes:

- Ground flash density plots
- Lightning current amplitudes
- Strokes per flash
- Time between strokes
- Distance between strokes
- Time of day of occurrence

These parameters will then be available to be used in design calculations.

A second function to be served by LPATS will be performance monitoring of various insulation co-ordination practices on transmission lines. An example of this would be a case where the tower footing resistance of a particular line has been reduced by the use of earth electrodes at the towers. LPATS could be used to monitor the performance of the line by observing the number of lightning strikes which occur in the region of the line compared to the reported outage rate of the line. In this way the effect of reduced tower footing resistance on line performance could be quantified.

## 5.) CONCLUSION

The installation of the Lightning Position and Tracking System in South Africa has opened up a new avenue for lightning research in this country. The system is able to record large quantities of lightning data which is essential for meaningful statistical data analysis. The extensive data supplied by the system, for each lightning stroke, provides a large scope for data analysis.

The analysis results of the first season of lightning data have established some confidence in the system. This has been achieved by the general correlation of the ground flash density data. The results have also raised questions concerning the limitations of the current system in South Africa. The inconsistencies indicated in the study results include:

- Possible loss of lightning data in certain areas of South Africa.
- The possible inability of the remote receivers to detect low amplitude strokes sufficiently.
- Possible loss of some subsequent stroke data.

These limitations must be investigated in more detail to properly evaluate the systems performance. It must be considered, however, that the system has only been in operation for a relatively short time and the data collected thus far is not sufficient to yield any truly conclusive results as yet.

One of the most important results of the study has been to provide insight into the potential role of LPATS in transmission line optimisation and monitoring. This will be achieved by the establishment of a LPATS lightning database and by using LPATS to monitor insulation practices on transmission lines. In this way it is believed that LPATS will prove to be an invaluable tool in the area of lightning research.

## 6.) REFERENCES

- [1] Lightning Ground Flash Density Map of Southern Africa, prepared by The Division of Energy Technology, CSIR, South Africa.
- [2] Working Group 01 of Study Committee 33, "Guide to Procedures for Estimating Lightning Performance of Transmission Lines", CIGRE Paris Conference, October 1991
- [3] Anderson RB, Eriksson AJ, "Lightning Parameters for Engineering Application", Electra No.69, pp65-102, March 1980.

## 7. ADDRESS OF AUTHOR

Mrs MG Redelinghuys, Eskom, Transmission Substation Technology, Megawatt Park, D3Z40, P.O. Box 1091, Johannesburg 2000.

# EXPLORATORY DESIGN OF A SOUTHERN AFRICAN GRID FOR THE YEAR 2025

R J Ahlschlager  
University of Cape Town, SA

C E Dingley  
University of Cape Town, SA

## ABSTRACT

This paper outlines an exploratory design of a Southern African power grid for the year 2025. This grid should be capable of meeting the basic energy needs of the region's projected 520 million people.

The paper describes three steps in the development of a regional power grid: developing load forecasts; generation scenarios; and possible grid configurations.

From the research work it can be concluded that firstly, development of a grid would be vital for future socio and economic development. Secondly, a distinct grid pattern emerges for the region.

## 1. INTRODUCTION

Africa is a land richly blessed with an abundance of natural resources, yet the majority of its people live in poverty.

It is a widely held and popular view that an electricity supply grid, spanning the sub-continent, could make the best use of the region's resources. It would ensure that each country in the region would be given access to cheap and abundant energy and, in addition, provide a means of building trust, unity and economic inter-dependence between countries.

The region referred to here consists of all the eighteen countries situated on and below the equator. The year 2025 has been chosen as it provides a time frame in which the effects of present political and economic policies on grid development can be neglected.

The structure of this paper is to first look at developing regional load forecasts for 2025 based on population projections, then to take the energy resources of the region and convert them to possible generating capacities. The load forecasts can thus be met by developing different generation scenarios. Using information obtained from studying country profiles and the generation scenarios, it is possible to develop different grid configurations.

It must be stressed that this work is purely exploratory and attempts to show the order of magnitude for a future grid scenario.

## 2. LOAD FORECASTS FOR 2025

By using population projections obtained from the World Bank [1], load forecasts for 2025 were developed for each country in the region.

### 2.1 Energy Calculations

Three load scenarios were developed by using different electricity consumption figures derived from present South American and Asian kWh/capita figures [2][3]. Values of 1,200, 1,600 and 2,000 kWh/capita have been used to represent the low, medium and high average regional energy demands respectively as shown in table 1. The figure of 1,200 kWh/capita represents an electricity consumption midway between present Asian levels (830 kWh/capita) and South American levels (1,500 kWh/capita).

Table 1: Regional Forecast Figures for 2025

Load Scenario Considered	Regional Electricity Demand	
	Average (kWh/capita)	Total (TWh)
Low Demand	1,200	620
Medium Demand	1,600	830
High Demand	2,000	1,040

Using the above values, the energy demand forecasts can be simply derived. To simplify calculations, countries were placed into categories depending on present per capita consumption levels, and each category was assigned an energy forecast value.

South Africa, being the major regional load centre was dealt with separately. Its demand was assumed to grow relatively slowly due to a predicted decrease of gold mine production over the next three decades and the fact that the South African economy is moving into a less energy intensive post industrial stage.

### 2.2 Calculating Maximum Demands

Maximum demands of each country were calculated by applying a load factor of 70 % to the previous energy forecasts. Total regional demand ranged from 110 GW for the low demand scenario to 180 GW for the high demand scenario. From table 2, it can be seen that the region has less than half of the required installed capacity (neglecting reserves or diversity) to meet even a low growth scenario for thirty years time. In addition, three major load centre emerge, with Zaïre

in the north-west, Kenya in the north-east and South Africa in the south. South Africa remains the major load centre, consuming just under half of the region's projected demand.

### 3. THEORETICAL GENERATING CAPACITY

Before a grid design can be developed, the major generation centres for the region need to be identified and the total potential capacity calculated. These capacities were calculated by converting energy resources into electrical energy.

#### 3.1 Converting Energy Resources

The resources considered were coal, natural gas, oil, hydro-electricity and nuclear power. The future development of solar power in Southern Africa is difficult to predict and has been excluded.

Hydro-electric potentials were obtained from various civil engineering publications, and thermal plant potentials were calculated from the proven recoverable reserve of the energy resources considered. The theoretical nuclear generating capacity developed was for a Pressurised Water Reactor (PWR) and was derived from known uranium resources. It must be stressed that the results obtained are merely speculative and are dependant on many variables such as calorific values, plant efficiencies, economic lifetimes and load factors, the amount of resource allocated to the electricity supply industry, and the percentage of an energy resource kept as a safety reserve margin.

Generating potentials can be divided into two broad categories, technically feasible potential and economically viable potential. Only technically feasible potentials are shown in table 2.

#### 3.2 Analysis of Potential Capacity

From this table it can be seen that the bulk of the available capacity in the region is in the form of hydro potential. Over 50 % of this potential is located in Zaïre and the bulk of it is situated at the Inga site on the Zaïre River. Other major rivers are the Zambezi, with sites at Kariba and Cahora Bassa, and the Kwanza River in northern Angola.

The other major source of potential in the region is the significant coal reserves located in Southern Africa, the bulk of which is located in South Africa.

### 4. GENERATION SCENARIOS

The demand from the load forecasts can met by utilizing some of the theoretically available generating capacity. System losses equivalent to 5 % of generator output power have been included in the analysis. Reserve capacity was not catered for and the effects of load diversity were assumed to be negligible.

#### 4.1 Generation Scenario Development Criteria

Different levels of self-sufficiency were used to develop the generation scenarios for the region as a whole. Three different levels of sufficiency were used, with a country being able to import either 10 %, 25 % or 50 % of its total demand.

When developing the generation scenarios, it was necessary to build from certain base assumptions. Initially only economically viable hydro capacity was considered, no gas was used, and coal and nuclear capacities were set to present installed levels.

**Table 2: Population Projections, Load Forecasts and Theoretical Generating Capacities**

Countries	Population in millions		2025 Load Forecasts			1993 Installed Capacity	Total Theoretical Generating Capacities				
	1991	2025	Low	Medium	High		Coal	Gas	Hydro	Nuclear	Total
Angola	10	27	3,100	4,300	5,500	520		1,500	23,000		24,500
Botswana	1	3	700	1,000	1,200	170	6,600				6,600
Burundi	6	14	1,600	2,200	2,800	40			800		800
Congo	2	6	1,000	1,400	1,800	120		700	11,000		11,700
Gabon	1	3	700	1,000	1,200	280		400	18,000	2,100	20,500
Kenya	25	73	12,600	17,300	22,100	660			6,000		6,000
Lesotho	2	3	500	700	900	5			500		500
Malawi	9	24	2,800	3,800	4,900	200			900		900
Mozambique	16	43	5,000	6,800	8,700	2,330	400	600	15,000		16,000
Namibia	1	3	700	1,000	1,200	360		500	1,600	13,000	15,100
Rwanda	7	17	2,000	2,700	3,400	60		500	600		1,100
South Africa	39	69	45,000	50,600	56,200	40,000	104,000	400	800	37,000	142,200
Swaziland	1	3	910	1,200	1,600	50	1,900		600		2,500
Tanzania	25	59	6,800	9,300	11,900	350	400	600	9,500		10,500
Uganda	17	48	5,500	7,600	9,700	160			2,800		2,800
Zaire	37	89	15,000	21,100	27,000	2,600	1,100		120,000	300	121,400
Zambia	8	21	5,000	6,700	8,500	1,600	100		12,000		12,100
Zimbabwe	10	18	4,000	5,700	7,300	2,000	1,400		3,800	200	5,400
Totals	217	523	113,000	144,400	176,000	51,405	121,600	5,200	227,900	52,600	400,600

## 4.2 Factors Influencing Scenario Development

Many factors, local as well as regional, will influence the type of resource used or effect the development of resources in each country.

Some of these factors are: the availability of finance to develop resources; the availability of water for thermal and nuclear plants; the amount of resources available for exploitation; the availability of skilled and educated personnel capable of operating some of the more advanced types of plants; and the environmental impact of developing the resource.

Hydro and gas plants have been given precedence over nuclear and coal for economic as well as environmental reasons. However, for some countries to maintain their required levels of self-sufficiency it was necessary to use these resources. Botswana and South Africa were notable examples of this, but imports of power were kept at maximum possible levels.

Development has been concentrated in those countries with abundant resources and where it is believed that those countries have the technical and financial ability to develop their resources. In the high demand scenarios, nuclear power was developed in order to take some of the burden off hydro power. Nuclear power development was confined to South Africa, Gabon and Namibia.

## 4.3 Analysis of a Generation Scenario

Table 3 shows one of the generation scenarios that was developed.

This scenario was created using the low demand scenario for the load forecast with an import limit of 10 % of maximum demand.

For this scenario, we see that hydro capacity is the major contributor of exported electricity, with Zaïre being the major exporter.

By examining other generation scenarios that were developed, it was discovered that the major load centres are located in the south (South Africa and Zimbabwe) and in the north-east (Uganda, Kenya and Tanzania). The major exporters of electricity are concentrated in the north-west (Gabon, Congo, Zaïre and Angola).

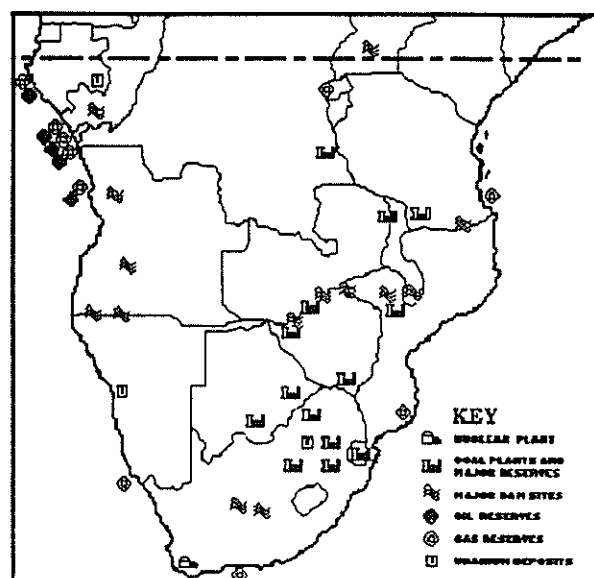


Figure 1: Key Energy Resources

Table 3: Generation Scenario assuming an import limit of 10 % of Maximum Demand

Countries	Coal MW	Gas MW	Hydro MW	Nuclear MW	Total Capacity MW	Low Load Scenario MW	Imports and Exports
Angola		1,000	5,000		6,000	3,500	2,500
Botswana	660				660	700	-40
Burundi			800		800	1,700	-900
Congo			3,000		3,000	1,300	1,700
Gabon			5,000		5,000	1,200	3,800
Kenya			6,000		6,000	13,700	-7,700
Lesotho			450		450	500	-50
Malawi			900		900	3,100	-2,200
Mozambique	160		6,440		6,600	5,100	1,500
Namibia		500	800		1,300	800	500
Rwanda		500	600		1,100	2,100	-1,000
South Africa	37,000		650	3,600	41,200	45,600	-4,400
Swaziland	300		600		900	900	0
Tanzania	180		6,000		6,180	6,900	-720
Uganda			2,800		2,800	6,000	-3,200
Zaïre			27,600		27,180	16,800	10,380
Zambia			4,900		4,900	4,800	100
Zimbabwe	690		3,200		3,890	4,200	-310
Total	39,000	2,000	74,740	3,600	118,860	118,860	0

### 3. GRID DESIGNS

From the previous section, we can see that one of the primary functions of a regional grid would be to transport large amounts of power from generating centres to major load sites. This requires the development of lines running from the north-west, eastward and southward.

Another aim of this grid is to supply every country with electricity, so the grid must interconnect with each country at least once.

#### 3.1 Developing Grid Designs

To develop different grid designs, the major load and generation centres need to be identified. Figure 1 shows where some of the region's key energy resources are located. We can see that a pattern emerges in their distribution.

The first can be clearly seen along Southern Africa's west coast where there are major load and generation centres fairly evenly distributed from Gabon to Cape Town. Another pattern that emerges is along Southern Africa's east coast with centres stretching from Kenya in the north-east to Swaziland. Finally, there is a central corridor running from Kananga in central Zaïre through the central African countries to Botswana in the south.

These three corridors can be connected together by links running from east to west. The first link is from Gabon, running through Zaïre to Kenya in the east. The South African link from Johannesburg to Cape Town completes the basic grid. This grid is shown in figure 2. The three power highways running from north to south can be clearly seen. In reality, a more interconnected grid would be desirable for security and energy trading reasons and so several interconnections have been included.

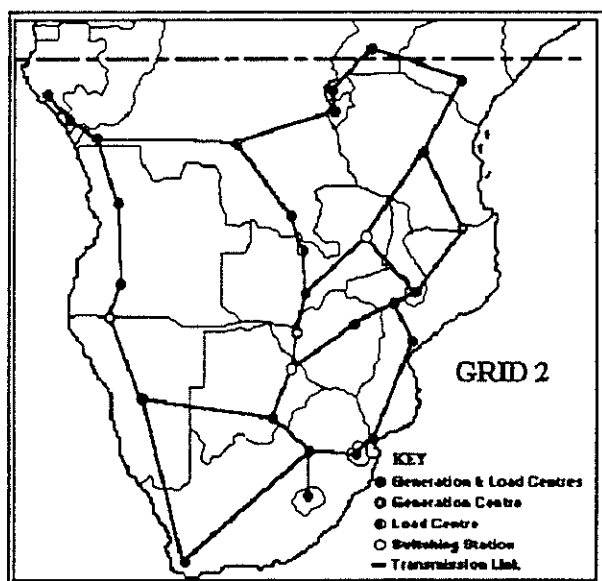


Figure 2: Transmission Network Design

This network would probably consist of mixed high voltage AC and DC lines. From table 3 it can be seen that in most cases, single 765 kV lines are sufficient, and for some links 400 kV lines can be used. But due to the stability constraints associated with long distance AC lines, it is quite likely that some of the lines would be DC. This would impose certain operational requirements in order to avoid the stability problems associated with parallel AC/DC systems.

### 4. CONCLUSIONS

Based on the research work done, a number of conclusions can be drawn:

- In order for the region to meet the basic energy needs of the population for thirty years time, the present installed capacity needs to be doubled.
- Significant potential does exist, but this is unevenly distributed through the region, and unless interconnections exist between generation and load centres, some countries will experience severe power shortages in the near future.
- A distinct grid pattern emerges which is dependent on the location of load and generation centres through the region.

We can see that a regional grid can provide access to electricity for all the countries in the region. It would facilitate the development of the region's most economical energy resources and provide access to markets for those countries with an excess of capacity.

In addition, for any grid development to be successful, greater emphasis needs to be placed on co-ordinated regional planning by utilities.

Finally, development of such a grid could help to build Southern Africa into the economic powerhouse that it has the potential to become.

### REFERENCES

- [1] World Bank: "World Development Report 1993", Hopkins University Press, London, 1993.
- [2] Eskom: "Statistical Yearbook 1993", Eskom Corporate Communication Department, 1993.
- [3] Dingley C E: "A proposal for the creation of a Southern African power authority". Cigre Southern African Regional Conference on Electric Power Systems in Sub-Equatorial Africa, Durban, May 1994.

### ADDRESS OF AUTHORS

Dept. of Electrical Engineering, University of Cape Town, Rondebosch, 7700.

Tel: (021) 650-2793 Fax: (021) 650-3465

# WRITING AN OBJECT-ORIENTED GRAPHICAL USER INTERFACE FOR ATP AS A PRE-PROCESSOR TO THE PROGRAM

T Orbach, IR Jandrell, B Dwolatzky  
Electric Power Research Group  
University of the Witwatersrand

## ABSTRACT

This paper discusses a graphical user interface (GUI) for the Alternative Transients Program (ATP), which is a High Voltage transient analysis package. The paper includes a description of a previous GUI for ATP, and an explanation of this GUI's limitations. The importance of designing modern GUIs to be as maintainable as possible is discussed with emphasis on using object-oriented programming and design. In addition, the object-oriented design of the GUI is presented, and is shown to be easily maintainable. The use of the MS Windows platform is explained, and the implementation of the GUI using modern Software Engineering quality principles is described.

## 1. INTRODUCTION

ATP or the Alternative Transients Program is a computer program written in Fortran, which is capable of simulating transient conditions and phenomena in power machinery and distribution networks. ATP can solve any network consisting of interconnections of resistances, inductances, capacitances, single and multiphase  $\pi$  circuits, distributed (or lumped) parameter lines, and certain other elements [1].

ATP was developed in the 1960's, and at the time made use of data cards to input information. The present version of ATP makes use of data files to input data. The data files have a very strict format, which if not adhered to causes errors that are often difficult to find. This form of user interface is extremely time consuming to use and to learn, as well as being very user-unfriendly.

Modern Graphical User Interfaces (GUIs) adhere to the IBM CUA (common User Access) guideline (which defines user interface components that should be consistent within and across applications [2]), while Windows applications generally adhere to the Microsoft Application Design Guide, which replaced IBM's CUA Guidebook as the general standard for GUIs. The Microsoft Design Guide was written in order to promote user interface consistency among Windows applications [2]. Another very important aspect of modern software including GUIs, is

maintainability. Any successful software will eventually enter a prolonged and costly maintenance phase [3], which will involve the GUI in every case.

In this paper we describe the design of a modern GUI for ATP in which general GUI standards and software maintainability have been emphasised.

## 2. THE PREVIOUS GUI FOR ATP

The user interface currently supplied by the BPA (distributors of ATP) is a GUI (called ATPDRAW), which runs under MS DOS. The interface is a pre-processor to ATP, and as such runs totally separately from ATP. It's design and implementation was based on the so-called 'structured approach' [4].

Structured programming and design involves breaking a program up into functions, which are separate from the application's data. This means that if the data is changed, the function code must also be changed. Every instance of the data being passed to a function within the program requires changing of the function code when the data is changed. Adding functionality to a structured program would involve understanding the entire program architecture (and details of the entire program), to ensure that all variables are taken into account. In structured programming, a common occurrence is that pieces of data flow unchanged or unwanted through the majority of the modules they pass through [5]. Object-oriented programming (OOP) and design (OOD), on the other hand, involves the encapsulation of both data and functions into entities called objects. This means that if a variable name is changed, only the object in which this variable is defined must be changed. Adding functions do not require an understanding of the entire program, only of a single object.

The fact that the ATPDRAW software was designed in a structured way makes it less maintainable than an equivalent GUI written in the object-oriented paradigm.

In a High Voltage application such as ATP, new functions are often added to the application as research progresses. The poor maintainability of the interface means that it will be difficult and very time

consuming to add the operation of these functions to the GUI (unless the original coder of the program is available to do this). Also if any problems are encountered with the GUI, it would again be difficult to correct these problems.

ATPDRAW is also not very flexible in functionality. A good example of this is that it does not allow for interfacing with a CAD package or database type files. This means that if a circuit was initially drawn on a CAD package and now requires an ATP simulation, it would have to be redrawn in the GUI. Another example is that, ATPDRAW comes with only 12 printer drivers, and if the user wishes to use any printer other than those specified, he/she has to write their own printer driver.

Other features of ATPDRAW are that it is interactive, menu driven, and works in a mouse driven environment [4]. The user's ability to learn an interface is crucial to its acceptance [6]. Since the GUI is graphical, it is relatively easy to use. It is however, still time consuming to learn how to use such a GUI, since it does not operate in a standard manner (such as programs which run on the Microsoft Windows platform). Regular users of ATP who are already accustomed to using the data file interface would therefore have to learn how to use this GUI as well, and this could be time consuming. Since most software users are accustomed to the MS Windows platform, an equivalent Windows GUI would not suffer from the same setback.

### 3. OOD/OOP AND GUIs

Object-oriented programming is a method of implementation in which programs are organised as co-operative collections of objects, each of which represents an instance of some class, and whose classes are all members of a hierarchy of classes united via inheritance relationships [7]. Object-oriented programming uses objects, not algorithms, as it's fundamental logical building blocks.

Object-oriented design is a method of design encompassing the process of object-oriented decomposition and a notation for depicting both logical and physical as well as static and dynamic models of the system under design [7].

In comparing the structure (or 'procedural') paradigm to the object-oriented paradigm, Wilde et al state that object-oriented methods provide better data abstraction and better information hiding, allowing for concurrency more readily, and respond better to changes in the real world [3].

Wilde et al also describe the goal of object-orientation as being to make change easier, stating that objects in the program match objects in the real world more closely, so real world changes should be easier to map to program modifications [3].

Graphical environments have an inherent complexity that makes them good candidates for the benefits of OOP [8]. This complexity also translates directly to the need for high maintainability of GUIs, which is provided by the object-oriented paradigm. As a result, OOP has caught on widely on platforms such as the Mac, Microsoft Windows, and the NeXT machine [8].

### 4. THE OBJECT-ORIENTED DESIGN OF THE GUI

This section describes our new GUI for ATP, called ATP for Windows. It is also a pre-processor to ATP, and must thus convert graphical information received from the user, to the data cards / data files needed to run ATP simulations.

ATP data cards all have a fairly similar structure to each other, but different types of cards such as Branch cards or Source cards, have a fixed structure within their own card type. This means that the data cards can be split up into definite types, which can then be used as objects or classes in the object-oriented approach of the interface.

This approach has led to the high level design seen in Figure 1.

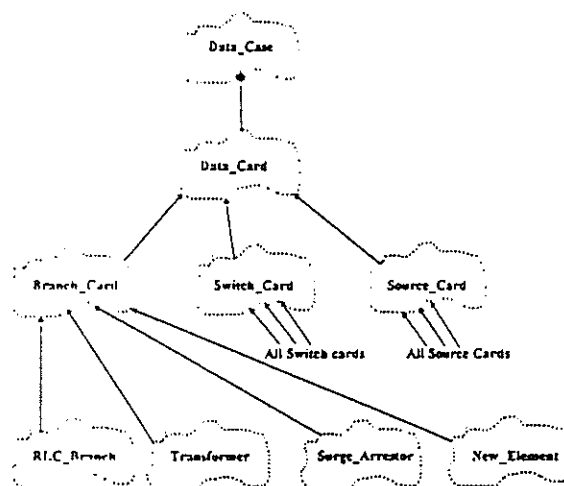


**Figure 1:** The Booch class diagram of the GUI design

In Figure 1, it can be seen that the *Data\_Case* class contains the *Data\_Card* classes. Each type of card (branch card, switch card etc.) inherits the general properties of the *Data\_Card* class, and each type of Branch card inherits the properties of the *Branch\_Card* class. This means that using virtual inheritance, one can write the *RLC\_Branch* class by using the general properties of the *Branch\_Card* class, overwriting the necessary virtual members of the *Branch\_Card* class, and adding whatever member functions necessary. An example of this functionality is the *PrintElement()* function. This function would be in the *Data\_Card* class, since all the elements are printed in the same manner. The *RLC\_Branch* class would then not need functionality for printing the element since this functionality is inherited from the base class.

Similarly, if at a later stage anyone wishes to add an element which is a branch card, he/she can do this, without knowing the internal workings of the rest of the program, by simply over-riding the relevant virtual members of the *Branch\_Card* class, and adding whatever member functions are required. In the same way, anyone can add any type of ATP element, such as source and switch, to the interface without understanding the rest of the program details, using inheritance.

This use of inheritance is one of the properties of object-oriented programming and design which makes OOP programs extremely maintainable. This type of structure will be used for the entire design, including the Object Windows Library (OWL) functions which are used in Borland C++ 4.0 programming for Windows.

## 5. IMPLEMENTATION

The GUI is being written using Borland C++ 4.0 (for Windows). This compiler includes built in classes with functionality for the MS Windows platform (Object Windows Library or OWL). This functionality will be used by inheriting classes from the relevant OWL classes, and over-riding the required methods.

In order to develop a successful GUI, it was decided that recent Software Engineering quality principles be used for the project. This means that the design involves the following stages:

- Documenting the User Requirements Specification, the User Reference Manual, the Technical Reference Manual, and the Product Test Specification and Plan.

- Coding of the GUI.
- Testing of the GUI.
- Final revision of documentation.

To date, the User Requirements Specifications, the User Reference Manual, and the Technical Reference Manual have been completed.

The final product will be a graphical user interface on the MS Windows platform, which is as flexible as possible, maintainable as possible, and will adhere to the principles of the IBM CUA, and Microsoft Application Design Guide, making it very usable. Although not every element in ATP will be available for simulation in ATP for Windows initially, due to the nature of the design, further elements should be easily added at a later stage. ATP for Windows will be capable of interfacing with CAD packages which work with the DXF format (such as AutoCad and Intergraph Microstation).

The general format of ATP for Windows can be seen in Figure 2.

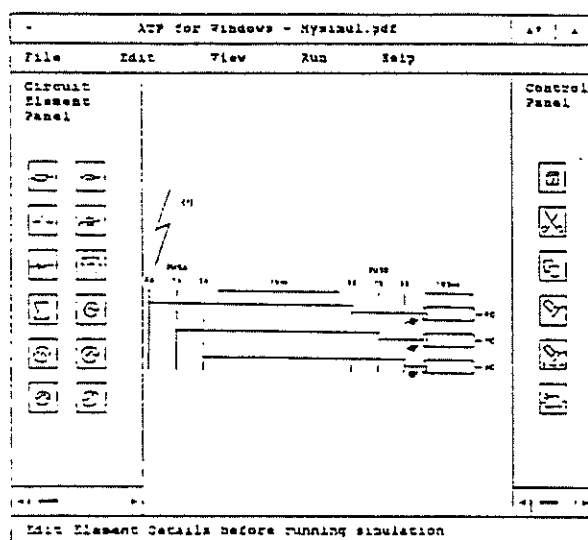


Figure 2: The general format of ATP for Windows

## 6. CONCLUSION

ATP is an example of a High Voltage software application which is commonly used in industry, but has an outdated interface. Other High Voltage applications suffer from similar setbacks, and many of these applications would benefit greatly from a graphical user interface.

One aspect of such software is that changes and additions are often made due to advances in research. This implies that it is extremely important to design modern High Voltage applications to be as maintainable as possible. This is especially true for GUIs. It is also important that GUIs in this field adhere to common GUI standards such as the IBM CUA and the Microsoft Application Design Guide.

As has been shown, ATP for Windows, should be extremely maintainable, flexible, and user-friendly. The goal of the design also includes making ATP for Windows easy to learn. To ensure that this is the case, ATP for Windows is being developed using object-oriented programming and design, for the MS Windows platform, whilst maintaining recent Software Engineering quality principles.

The use of the MS Windows platform has many other advantages over the DOS platform, including the inherent object-oriented nature of programming for Windows, and the fact that programs developed for the Microsoft Windows platform support almost all graphical displays (such as CGA, EGA, VGA, XGA and Hercules), as well as hundreds of displays and printers. This is due to the device drivers being part of Windows [7]. There is also the ability to cut and paste between programs using Object Linking and Embedding (OLE 2.0), which offers interesting possibilities of combining the interfaces of a number of Power Engineering and High Voltage tools in the Windows domain.

## 7. REFERENCES

- [1] Dommel HW. 'Reference Manual for EMTP', Leuven EMTP Center (LEC), pg1-1, 1992.
- [2] Lacob RI. 'Designing the user interface of an automated system for non-destructive testing (NDT) to take user limitations into Account', MSc Thesis, Dept of Elec. Eng., Wits University, Johannesburg. 1993.
- [3] Wilde N, Matthews, P, and Huitt, R. 'Maintaining Object-Oriented Software', IEEE Software, pp75-80, Jan 1993.
- [4] Hoidalén HK. 'ATP-DRAW User Manual', Bonneville Power Administration, June 1992.
- [5] Jamsa K A. 'Object-oriented Design vs. Structured Design - A Student's Perspective', ACM Sigsoft Engineering Notes, Vol9, No 1, pp43, Jan 1984.
- [6] Ege R. and Stary C. 'Designing maintainable, reusable interfaces', IEEE Software, pp24-32, Nov 1992.
- [7] Booch G. 'Object-Oriented Analysis and Design with Applications', Second Edition, Benjamin Cummings, 1994.
- [8] Urlocker Z. 'Object-oriented Programming for Windows', Byte, pp287-294, May 1990.

## 8. ADDRESS OF AUTHORS

Mr Tamir Orbach  
Electric Power Research Group  
Department of Electrical Engineering  
Private Bag 3  
WITS  
2050

# THE DEVELOPMENT OF AN INTEGRATED SET OF SOFTWARE TOOLS FOR USE IN THE DESIGN OF AN ELECTRICAL RETICULATION NETWORK

B Dwolatzky, AS Meyer  
Department of Electrical Engineering  
University of the Witwatersrand

The use of software tools in the design of electrical reticulation systems will help us to make better use of limited design expertise and will allow us to optimise the use of financial and other resources. This paper describes a conceptual framework within which a variety of software tools have been integrated. The design of the proposed software framework is based on the object-oriented approach. Implementation factors are also discussed.

## 1. Introduction

As we enter the late 1990's there are many challenges facing South Africa's engineering community. Where, for example, will we find the expertise to design the thousands of new electrical reticulation networks which will bring grid electricity to more than 3 million un-electrified urban and rural homes? And even if we did have the expertise, how will we ensure that the networks designed make optimum use of financial and other resources? At Wits University we believe that modern computer techniques have a key role to play in meeting these and other challenges raised by mass electrification.

In 1991 a research effort began in the Wits Department of Electrical Engineering with the aim of developing a set of software tools which would assist the designers of electrical reticulation networks. The functions to be carried out by these tools include:

- Voltage calculation - given the layout of a network and parameters such as ADMD, diversity factors and cable resistances, determine the expected voltdrop at each consumer's property;
- Optimum cable sizing - for a given network layout determine the cheapest set of cables which will ensure that each consumer has a supply voltage within a certain percentage of 230V (eg. 230V - 6%).
- Automatic cable routing - find the shortest and cheapest route for a cable connecting

two points in the network. 'Obstacles' such as private property, buildings and geographic features (eg. streams, rocky areas, etc.) are either avoided completely or are assigned a cost which is incurred if the cable passes through them.

- Medium voltage calculations - determine the effect on the LV network of voltdrops in the MV network. Changes caused by opening and closing sections of MV ring mains can also be investigated.

Software to carry out each of these functions (with the exception of automatic cable routing) is widely available and has been for many years. What then makes the work being done at Wits novel and valuable? The answer is integration. Our major objective in developing these, and other, tools was to ensure that they were tightly integrated into a common framework. In this paper we discuss this software framework.

## 2. Integration of the software tools

The integration of software tools is more than simply ensuring that data can be exchanged between them, although this is essential. Genuine software integration requires that there should be a single conceptual model lying at the heart of the set of tools. It is also important that any new tools developed in the future should fit within the same conceptual model.

In our application the core concept is a **network**. A network consists of **links**, **nodes** and **leaves**. In a radial network there is a single **root node** connected via **links** to a set of **nodes**. Each of these are connected to other nodes or to a **leaf**, which is the termination of that branch of the network. Associated with the concept of a network are certain basic functions. One must be able to add links, nodes and leaves to the network. One must also be able to delete them from the network. There must be various

"trace" functions. Given a certain node it must be possible to find all of the leaves attached to it. It must also be possible to trace back from any leaf in the network to the associated root node.

Within our conceptual model each of the components present in an electrical reticulation system are special cases of the above simple elements. In an LV network the transformer is a **root node**. The feeder and service cables are types of **links**. The nodes are kiosks or junctions, and the "leaves" of the network are the consumers. Special forms of the trace functions will allow us to answer questions like: Given that each consumer draws a certain load, determine the total load attached to a particular transformer. The association between conceptual network elements and physical electrical equipment might change according to one's view of network. For example, if one was working with the MV network an LV transformer might be seen to be a leaf rather than a root node.

Another important aspect which needs to be catered for within our conceptual framework is the accurate representation of the network geographically. What distinguishes our design tools from many others is that ours relates the layout of the network to the map of the area being electrified. To achieve this we defined a concept called **graphical element**. A graphical element has a unique location on the map and various display attributes (eg. colour, size, shape, etc.). It has associated with it functions to change some of these attributes (such as "change colour"), to draw itself on the map or to move itself to another location. Again we define special cases of this basic concept appropriate to our application. There are, for example, transformer elements and various types of cable elements. There are also graphical elements which have no association with the network. A building, road or text item might be represented on a map, but is not associated in any way with nodes, links and leaves.

Within our software an LV transformer, for example, is both a type of node and a type of graphical element. Being a node it has connections, via links, to other nodes. Being a graphical element it has a location on the map and a set of display attributes. In addition, as a transformer, it has attributes such as a KVA rating, a secondary voltage, a cost and a manufacturer. It can thus be seen how the conceptual framework we have defined models both the network and the map together with all of their elements.

### 3. Software Design of the framework

Having defined a general software framework we next needed to develop an appropriate software design. Our design was based on the object-oriented approach

[1]. All software design approaches require some decomposition of the application into simpler entities. In the so-called structured (or procedural) approach one would carry out a top-down decomposition of the application into an hierarchy of simpler and simpler functional entities. These entities operate on data structures which would be decided upon as a separate part of the design process. The object-oriented approach encapsulates both functional entities and data structures into "objects". Decomposing an application into a set of cooperating objects results in software systems which are highly flexible and maintainable. Each object in an object-oriented system is an instance of a "class". The relationship between objects and classes is similar to the relationship, in most general purpose programming languages, between variables and built-in data types. Object-oriented design therefore requires the specification of a set of appropriate classes. Classes are grouped into families in which certain classes inherit attributes and behaviour from others.

The conceptual model described in Section 2 leads naturally to a good object-oriented design. The class **transformer**, for example, is inherited from a **node** class and a **graphical element** class. It is not appropriate in a paper of this length to give a detailed account of the software design of the framework. Suffice it to say that we carefully mapped each of the elements of the conceptual model into a set of suitable classes.

### 4. Implementation of the framework

A software design specifies how various aspects of the software system should be implemented. Implementation, however, is limited by the constraints imposed by the available or preferred software languages and other tools. Our first implementation of the software framework, called CART 1.1, was carried out using the Intergraph MicroStation CAD system. Data was stored in dBase 3+ files and software functions were developed in both "mdl" (MicroStation's own programming language) and in C++. This implementation environment made it very difficult to retain the object-oriented nature of our design.

A second implementation, written completely in C++, was much closer to the 'pure' object-oriented design. A collection of general classes, such as **network**, **node**, **link** and **graphicalElement** were implemented. More specific classes, such as **transformer**, **cable** and **consumer** were inherited from these general classes.

Based on this software framework, tools for use in the design of reticulation networks were implemented.

Optimisation and cable routing were achieved by writing new procedures (or 'methods') for specific classes. These methods are easily implemented since underlying functionality (such as tracing through a network) was implemented as part of the behaviour of the general classes.

The drawback of this second implementation (called "the testbed") was that it did not have a CAD package as its front-end. A simple MicroSoft Windows interface was developed but the system had none of the drawing and display facilities found in a CAD package. The implementation was written to provide a demonstration of the effectiveness of the conceptual framework and the validity of the object-oriented design.

A third implementation, based on a specialised software tool called Geonet, is currently under development. This implementation should provide a usable and practical implementation of our proposed software framework.

## 5. Future Work

Although we haven't described in detail in this paper how software tools can be integrated within our general framework, the task of developing new tools has been progressing within our research team.

All of the tools outlined in Section 1 have been integrated within our "testbed" implementation. Other tools such as an on-line expert system for use in determining the size of 'non-standard' loads and a more advanced optimization module are currently under development.

By developing distinct software tools within a general and flexible conceptual framework we can achieve true integration.

## 6. REFERENCES

- [1] Booch G. 'Object-oriented Analysis and Design with Applications', Second Edition, Benjamin Cummings, 1994.

## 7. ADDRESS OF AUTHORS

Dr Barry Dwolatzky  
Department of Electrical Engineering  
University of the Witwatersrand  
Private Bag 3  
WITS  
2050

# The use of Perchloroethylene to Enhance the Thermal and Insulating Properties of Mineral Oil

M S A Minhas, D A Hoch, J P Reynders  
University of the Witwatersrand South Africa

## 1 Abstract

The results of an experimental investigation into the heat transfer, flame retardancy, partial discharge extinction and loss tangent properties of an optimum mixture of pure transformer oil with perchloroethylene are presented. This paper is a small extension of earlier work [1].

## 2 Introduction

The advantages of improving the heat transfer and flame retardant properties of a liquid dielectric are obvious.

A nonflammable transformer is needed in situations where the fire risk is high. Several liquids have been developed which show flame retardancy [2]. They are regarded as suitable for transformers used in high fire risk areas like office blocks, basements, high rise buildings and mines.

Partial discharges are recognised for their significant degradation of both the paper and the oil in oil-paper insulated systems. Ideally the liquid impregnant should be capable of extinguishing partial discharges and thereby increasing the life of the insulation. To this end the mixture of perchloroethylene and transformer oil as been investigated. An optimum mixture based on breakdown performance (35% perchloroethylene and 65% transformer oil) was employed [3][4][5].

The combination of a low flammable liquid with the totally nonflammable perchloroethylene has resulted in a liquid which satisfied the classical definition of nonflammable [6]. Mixtures of perchloroethylene have already been investigated but the loading of perchloroethylene was 75% by volume [2]. However, some other commercial liquids are highly purified perchloroethylene with proprietary additives (WECOSOL<sup>TM</sup>) and other are mixtures of perchloroethylene with chloroflouro carbons (FORMAL<sup>NF</sup>) [2][7]. The data available does not show the ability of these liquids to reduce partial discharges.

## 3 Experimental Procedures

Four series of tests, namely temperature rise, partial discharge, loss tangent measurements, and flame retardancy, were performed.

### 3.1 Experimental Setup

#### 1. Temperature Rise Test

The BS method was adopted [8][9]. Two 50 kVA 11kV/400V transformers were connected back to back and an auxiliary transformer, fed by an adjustable three phase transformer, was included in the circulating circuit, to give the adjustable circulating current up to 150% of load current. An oil filled pocket was placed 30 mm deep in the top oil to accommodate the thermometer to observe temperature. The RTDs and mercury filled thermometers are not reliable in a magnetic field and alcohol filled thermometers were used [9]. The winding temperature was measured by the resistance method after switching the supply off [8]. The test was performed on 100% and 150% load with pure mineral oil, 35% and 50% perchloroethylene mixtures.

#### 2. Partial Discharge measurements

A 22 kV CT with high partial discharge levels was used in this test. A standard partial discharge measurement circuit was used. The output of the detector was fed into a 500 MHz digital storage oscilloscope, where the discharges were displayed simultaneously with the power frequency voltage waveform. This arrangement made it possible to summate the discharges for a significant length of time.

The CT, taken out of service and already filled with mineral oil, was subjected to a partial discharge test. Then it was drained and flushed with  $C_2Cl_4$ , filled with the optimum mixture and the partial discharge test was repeated.

### 3. Loss Tangent Measurements

A simple liquid cell was used in conjunction with a commercial bridge for the measurement of  $\tan\delta$ .

### 4. Flame Retardancy Test

The flash point and fire point were observed by the method described in [10].

## 4 Experimental Results

### 4.1 Temperature Rise Test

A difference in the winding temperature rise of  $8^{\circ}\text{C}$  and  $11^{\circ}\text{C}$  lower than mineral oil was observed in 35% and 50% perchlorethylene mixtures respectively at 150% load. The results recorded are shown in Figure 1. The enhanced cooling of the winding has associated with it an increase in the tank temperature as is illustrated in Figure 2.

### 4.2 Partial Discharge Test

There was an increase in the partial discharge inception voltage (PDIV) as well as a decrease in the peak discharge magnitude. The increase in PIDV was 3,0kV (17%) and the peak discharge magnitude dropped from 23pC to 5pC at 27kV (the voltage chosen as reference voltage as it is 20% above normal line voltage). However, some occasional discharges were observed which reached about 20pC, but they were very infrequent and they appeared at an average rate of 2 discharges per minute (1 in 1500 cycles). Figure 3 shows the results of a partial discharge measurement in the transformer filled with oil. The pattern of partial discharges was fairly stable and there were no significant variations observed over 20 minutes. Figures 4 and 5 illustrate the discharge pattern in the 35% perchlorethylene mixture. Initially the discharge activity was at a higher level (Figure 4) and with the passage of time the magnitude decreased to a stable pattern as shown in Figure 5.

### 4.3 Loss Tangent Measurements

This work is still in a preliminary phase. Typically, the mixtures have loss tangent values which are 2,0 - 2,5 times greater than that of the pure mineral oil. This cannot be accounted for in terms of a difference in relative permittivity and must be attributed to an increase in leakage current. An enhanced charge carrier mobility is the most likely mechanism and further work is in progress.

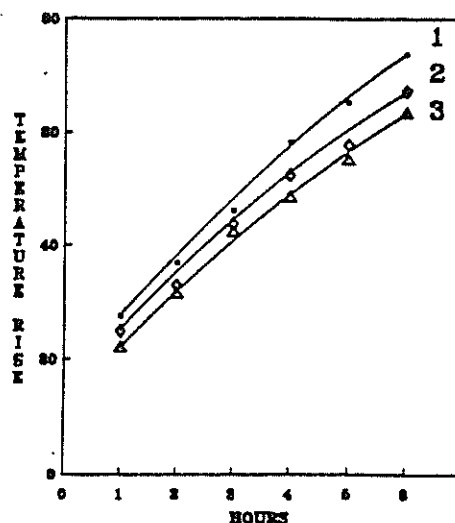


Figure 1: Winding temperature rise: 1 in pure mineral oil, 2 in the 35% perchlorethylene mixture and 3 in the 50% mixture.

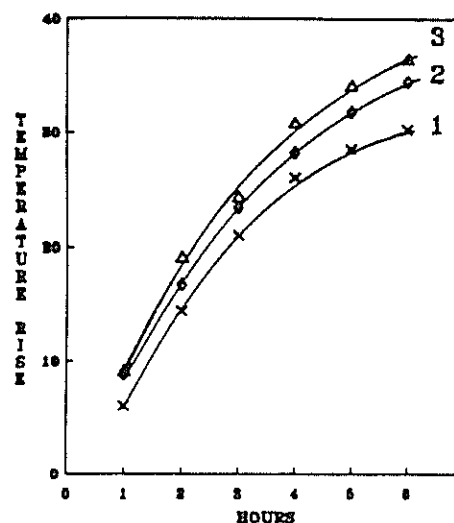


Figure 2: Oil temperature rise: 1 mineral oil, 2 35% perchlorethylene mixture, 3 50% perchlorethylene mixture.

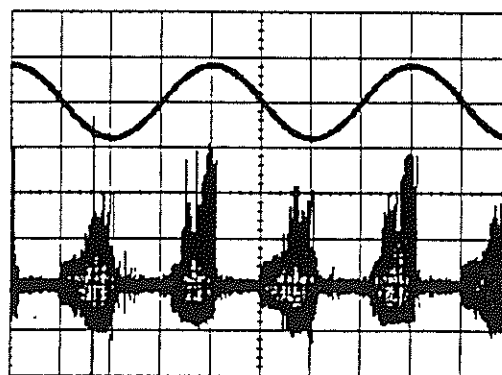


Figure 3: Partial discharge pattern in CT filled with mineral oil. PD 5 pC per vertical division

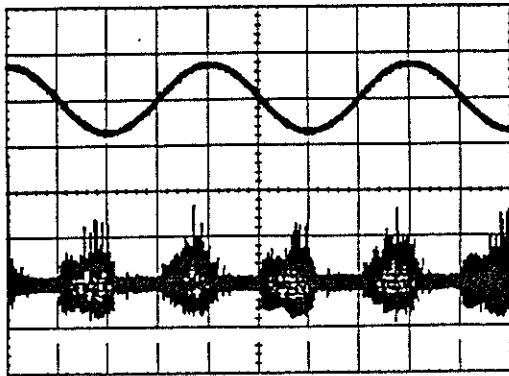


Figure 4: Partial discharge pattern in optimum mixture immediately after switching the supply on. PD 6 pC per vertical division.

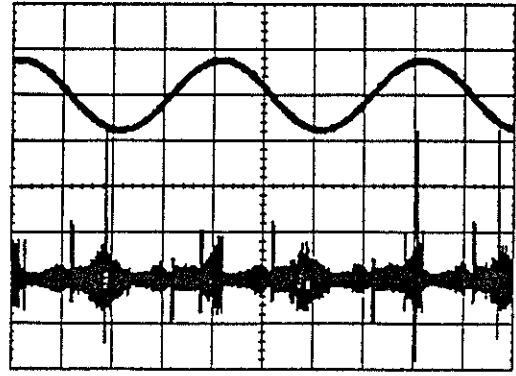


Figure 6: High value discharges in optimum mixture observed at 30 kV. PD wave 6 pC per vertical division.

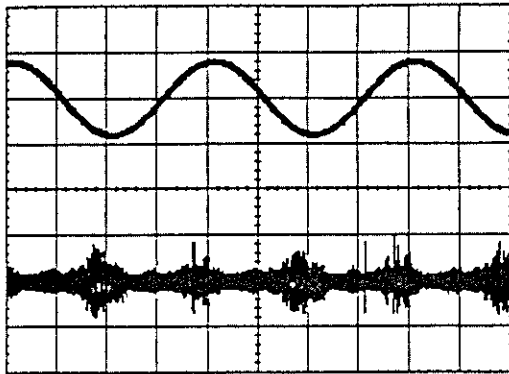


Figure 5: Partial discharges in optimum mixture after stabilisation. PD 6 pC per vertical division.

#### 4.4 Flame Retardancy Test Data

The BS Method was adopted (Cleveland open cup method) [10]. The results obtained are presented in Table 1.

### 5 Discussion

The fact that the heat transfer of the optimum mixture is better than oil is due to the lower viscosity of the mixture, which ensures faster liquid currents. Moreover, the mixture has an improved penetration in the paper and heat transfer from the conductor is enhanced, thereby reducing the temperature gradients in the liquid. The tank reaches a higher temperature and becomes more effective radiator.

The enhanced breakdown strength is due to the volatility of the highly electronegative perchlorethylene. The perchlorethylene molecule has a very high attachment rate constant ( $2,77 \times 10^{-8} \text{ cm}^3/\text{s}$ ) and an attachment cross-section of  $0,02 \times 10^{15} \text{ cm}^2$  as compared to other chloroethylenes. Hence the free electron attachment is significant below mean electron energy of 2eV at this energy level perchlorethylene can form three  $\text{Cl}^-$  ions which leads to an increase in breakdown strength because of an increase in electron attachment opportunities. This process of electron attachment is mainly observed below electron energy level of 2.5 eV beyond which little has been reported [11].

In the oil and perchlorethylene mixture two opposing mechanisms are at work. These two mechanisms, are firstly the generation of significant space charge due to the presence of an electronegative molecule, and secondly an increase in charge carrier mobility due to the decrease in viscosity. The first mechanism should lead to the reduction in average current. If

Table 1: Flame Retardancy Test

	Min. Oil	35% $\text{C}_2\text{Cl}_4$ Mix.	Pure $\text{C}_2\text{Cl}_4$
Viscosity	30	4,0	0,84
Flash point	150°	NTB	NTB
Fire point	165°	NTB	NTB

NTD: Not till boiling point

the charges have sufficiently low effective mobility due to field reduction at the place of activity, the second mechanism will tend to increase the current flow. The third phenomenon which could be observed in liquids with high volatility, is that the low boiling point and high volatility of these can facilitate the production of a bubble at highly stressed points. If the stress is high enough to cause discharges in the bubble, the large number of charge carriers will make high value discharges possible (Figure 6). These discharges will impart energy to the liquid in the form of heat at the bubble interface and will cause evaporation and increase in bubble size, which leads to more and more discharges. The growth is retarded by the enhanced heat transfer capabilities of the mixture.

## 6 Conclusions

1. The introduction of perchlorethylene in mineral oil makes it more volatile, lower the viscosity and improves the heat transfer.
2. The mixture of 35% perchlorethylene in 65% transformer oil exhibits the maximum dielectric strength.
3. The superior dielectric breakdown properties are reflected in superior partial discharge performance of the mixture.
4. The free electron attaching capability leads to reduced charge carrier mobility in mixture.
5. The high levels of loss tangent in the mixtures, compared with typical values for mineral oil need further investigation.
6. The improved heat transfer can help to dissipate the energy imparted by the discharges and can retard the bubble formation in the highly stressed regions.
7. Low boiling point perchlorethylene vapours inhibit fire by displacing oxygen.

## References

- [1] Minhas M S A, Hoch D A, Reynders J P, "Enhancing the flame, thermal and partial discharge performance of mineral oil." Proceedings of the 4th International Conference on Properties and Applications of Dielectric Materials. July 3-8, Brisbane, Australia. Paper 4231.
- [2] "The low flammability transformers". ERA report 87-0021, 1987.
- [3] Ruffini A, Hoch D A, Reynders J P, "Partial Discharge behaviour of Halogenated liquids." Sixth International Symposium on High Voltage Engineering 1989. Paper 319.
- [4] Hoch D A, Reynders J P, "The effect of Increasing concentration of perchlorethylene on the Electrical Performance of Mineral oil." 7th International Symposium on High Voltage Engineering, 1991.
- [5] Hoch DA, Reynders J P. "Partial Discharge Behaviour of Mineral oil/Perchlorethylene mixture." 8th International Symposium on High Voltage Engineering, 1993. Paper 24.04.
- [6] British Standard 2000 Part 34, 1986.
- [7] Draft ESI standard 35-00, Standard for Formal filled Transformers, May 1984.
- [8] British Standard 171 Part 2, 1978.
- [9] Franklin A C, Franklin D P, Butterworths, J&P Transformer Book, 1990.
- [10] British Standard 4689: 1986.
- [11] McCorkle D L, Christodoulides A A, Christophorou L G, "Electron Attachment of Halocarbons of interest in Gaseous Dielectrics." Fourth International Symposium on gaseous dielectrics, Knoxville, Tennessee. U.S.A. 1984.

## The Effect of Corona Activity on the Hydrophobic Surface Properties of Silicon Rubber Insulators

A E Dickson and J P Reynders  
Department of Electrical Engineering  
University of the Witwatersrand  
Johannesburg

### Abstract

It has been found that streamer and, to a lesser degree, glow corona on the surface of silicon rubber results in the temporary loss of its hydrophobic properties. The loss and recovery of the silicon rubber's hydrophobicity have been investigated. Processes that result in the temporary loss and subsequent regeneration of the hydrophobic properties of silicon rubber are also considered.

### 1 Introduction

For some time it has been known that silicon rubber (SR) insulators possess better insulation qualities than their glass and porcelain counterparts. This is especially true when the surface of the insulators becomes polluted [1]. The pollution layer on the surface of these insulators causes them to become hydrophilic under wet conditions eg mist and light rain.

The surface of these insulators becomes conductive and leakage currents flow between the conductor and earth. The heating inherent in leakage current creates dry bands and the resulting dry band arcing leads to damage of the insulator and may cause the insulator to fail.

The hydrophobic properties that silicon

rubbers possess, a low free surface energy [2], allows water to collect in droplets thereby reducing leakage current flowing on the surface of the insulator, and reducing the effects of dry band activity.

Dry band arcing and other electrical discharge phenomena cause the SR to lose its hydrophobicity. After a period where the electrical discharge is no longer present the SR may recover all of its original hydrophobicity.

This paper presents initial experimental evidence that compares the effects that both streamer corona and glow corona have on the hydrophobic surface of SR. The extent to which hydrophobicity has been lost and the time taken to hydrophobic recovery have been investigated. The experimental procedure has been completed using clean SR surfaces. Possible mechanisms that explain the loss and recovery of the SR hydrophobicity have been covered.

### 2 Measurement Technique

The degree of surface hydrophobicity can be quantified by the measurement of the contact angle that a water droplet forms on the surface of a solid material.

The surface contact angle and the surface

free energy are related by Young's equation:

$$\sigma_{SR} = \sigma_W + \sigma_A \cos \theta \quad \dots (1)$$

where  $\theta$  is the static contact angle and  $\sigma_{SR}$ ,  $\sigma_W$ ,  $\sigma_A$  are the surface free energy per unit area of the SR insulator, water and air respectively.

Equation 1 represents a dynamic representation of the forces at the point of contact. The water will alter its shape until these forces reach an equilibrium. When equilibrium is reached the contact angle,  $\theta$ , can be measured and gives an accurate representation of the level of hydrophobicity of the solid surface.

Figure 1 illustrates the energies and the surface contact angle of a hydrophobic surface.

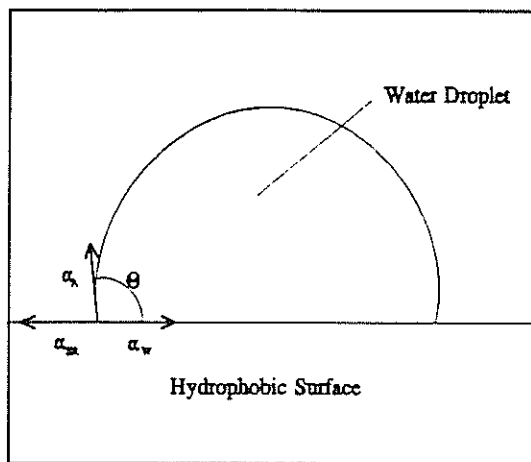


Figure 1: Surface Energies and Water Droplet Shape on a Hydrophobic Surface.

### 3 Experimental Setup

A SR paint was applied to a metal sphere with a diameter of 340mm. The sphere was energised so that corona formed on the surface of the SR paint.

#### Streamer Corona

The metal sphere was attached to the top of the HV bushing of a 140kV transformer and energised for 48 hours.

To create large streamer corona a voltage of 130kV was applied to the sphere. This created visible streamer corona around the surface of the sphere. The streamers were approximately 50mm in length.

#### Glow Corona

Visual glow corona was created around the surface of the sphere. The SR paint was exposed to the corona for 48 hours.

The glow corona was most stable when the entire experiment was conducted at a pressure of 0.1 Bar with an applied voltage of 7kV.

#### Recovery of Hydrophobicity

The recovery of hydrophobicity was measured using the previously mentioned contact angle method.

A 50μl distilled water droplet was placed on the surface of the SR paint. The water droplet was photographed through a microscope at regular intervals until the rate of recovery of the hydrophobicity had stabilised.

## 4 Experimental Results

A reduction of the SR hydrophobicity was found after both the glow and streamer corona were applied for 48 hours.

It was found that the high level of streamer corona reduced the contact angle to 32 degrees. Thereafter the SR

completely recovered its hydrophobicity at an exponential rate.

This result confirms the fact that the rate at which SR recovers its hydrophobicity can be modelled on a first order exponential system /2/. The time constant, defined as the time taken for the contact angle to reach 63% of the total change, was measured to be 90 minutes. This result compares favourably to that calculated in /2/.

The corona had caused discolouration of the paint at sites of prolonged streamer activity. This appeared to affect the colour pigment only and no difference was observed in the recovery of hydrophobicity at these sites compared to the rest of the surface.

The glow corona also caused a reduction in the level of the SR hydrophobicity. The contact angle was measured at 68

degrees shortly after the completion of the experiment.

Thereafter, the hydrophobic recovery rate followed that of the streamer corona case. No discolouration was observed with the glow corona. Figure 2 graphically illustrates the hydrophobic recovery rate of the SR after streamer and glow corona respectively.

## 5 Conclusion

Exposing SR insulators to prolonged periods of streamer and glow corona result in the temporary loss of its hydrophobic properties.

It is felt that the high energy photons present in streamer discharge phenomena have the ability to destroy the chemical bonds that give SR its hydrophobicity /2/.

These high energy photons are not present in glow corona /3/. However, it is felt that prolonged exposure to glow corona will provide sufficient energy to damage the chemical bonds.

The recovery of SR hydrophobicity is accredited to the migration to the surface, from the bulk, of low molecular weight polymer chains.

More extensive experimental work will need to be completed to assess the relative energies that cause the breakdown of the chemical structure of SR leading to loss of hydrophobicity.

## 6 References

1. Pingini A, Tomba A, "Set Up of a Method to Evaluate the Surface

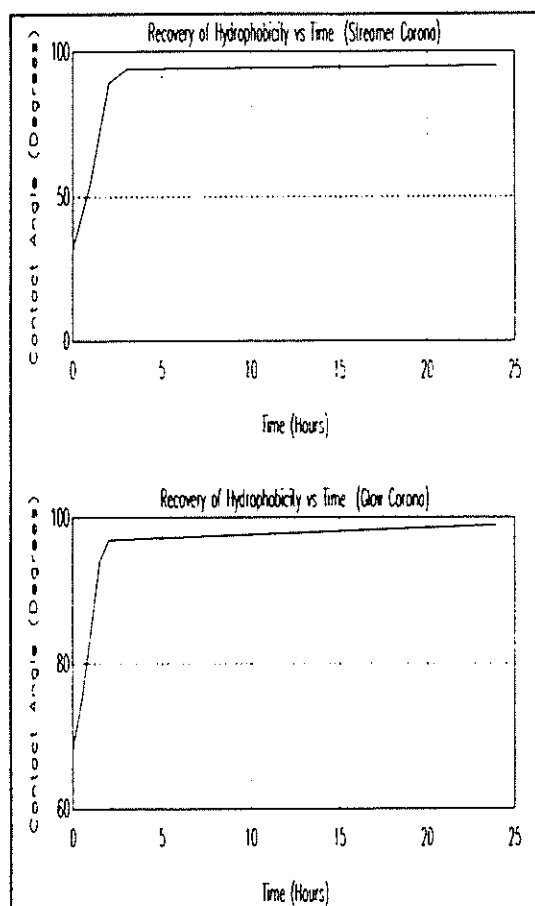


**Figure 2:** Rate of Hydrophobic Recovery after Streamer and Glow Corona.

Hydrophobicity of Insulators", 8th International Symposium on High Voltage Engineering, Yokohama, Japan, August 23-27, 1993, pp 29-32.

2. Bhana D K, Swift D A, An Investigation into the Temporary Loss of Hydrophobicity of Some Polymeric Insulators and Coatings", Proceedings of the 4th International Conference on Properties and Applications of Dielectric Materials, July 3-8 1994, Brisbane Australia, pp 294-297.

3. Loeb L B "Electrical Coronas: Their Basic Physical Mechanisms", University of California Press, Berkley and Los Angeles, 1965.

# THE USE OF NEURAL NETWORKS TO RECOGNISE ELECTRICAL SYMBOLS ON A TOWNSHIP MAP.

J.C Shapiro      B Dwolatzky      A.S Meyer  
University of the Witwatersrand, Johannesburg, South Africa

A project is presented whose aim is to develop a system that can recognise electrical symbols on a scanned-in township map. The design of reticulation networks inevitably involves merging the new network with an existing infrastructure, and the system proposed plans to automate a large part of this process which was previously performed manually. The use of Neural Networks to implement the Pattern Recognition is explored, and this technology is shown to be particularly suited to the task put forward. The integration of the proposed system with a larger software package is described and the envisaged usage of the final product is discussed.

## 1. INTRODUCTION

CART (Computer Aided Reticulation of Townships) is a computer package that is being developed by the Electrical Engineering Department of the University of the Witwatersrand. CART is an integrated set of software tools which assist in the design of township reticulation schemes.

The ability to efficiently design township reticulation schemes is of major importance to the electrification programmes that are currently being implemented in South Africa. If the numerous electrification schemes that are under discussion at present are to be implemented, the need for effective and efficient design processes increases even further. There is a need to aid the designers of such schemes in producing an optimum solution so that cost effectiveness is maintained and more consumers may be connected[1]. Thus CART represents an attempt to provide a set of software tools that can both enhance the efficiency of the design process as well as to ensure that a cost effective cable layout is achieved.

At present, CART is mainly used to design new schemes - in its present form, no provision has been made to incorporate any existing networks that may already be in place in the area concerned. However, as CART becomes more widely used, it is envisaged that a need will arise to incorporate existing schemes into the design, to allow further additions to be made to the schemes, and also to allow the network that is in place to be analysed. At present this means that the designer would have to manually place all the existing components into the system.

The aim of the project described in this paper is to bring about the automation of a large portion of this process. It is intended that the designer will be able to use the software system to analyse a map and create entries for the various components of the existing reticulation network in the appropriate CART database. The object of this work is to investigate the applicability of Neural Network Techniques with respect to achieving this aim.

This paper is intended to present a concept, rather than a finished product.

## 2. THE USE OF NEURAL NETWORK TECHNOLOGY

It is important to realise that this project represents an *investigation* into the feasibility of adopting a Neurocomputing approach towards the solution of the problem. In order to better understand the reasons why this particular path was chosen, a brief overview of the relevant areas pertaining to Neural Network technology and their use in the field of Pattern Recognition, is provided in the two sections that follow.

### 2.1 NEURAL NETWORKS IN GENERAL

According to [2], a Neural Network is a computing system made up of simple, highly interconnected processing elements, which processes information by its dynamic state response to external inputs. Each processing element makes its computation based upon a weighted sum of its inputs. A subgroup of processing elements is called a *layer* in the network. The processing elements are seen as units that are similar to the neurons in a human brain, and hence, they are referred to as *artificial neurons* (or simply neurons).

Neurocomputing adopts a novel approach to information processing that does not require algorithm or rule development and that often significantly reduces the quantity of software that must be developed. For some type of problems, typically in areas such as sensor processing, pattern recognition, data analysis and control, this approach allows for the development of information processing

capabilities for which the algorithms or rules are not known. Furthermore, if they are known, often the software needed to implement them would be too expensive, time consuming, or inconvenient to develop. [3]

It is this property of flexibility inherent in Neural Network based applications which is highly desirable in the project at hand. The goal is to allow a *variety* of symbols be "taught" to the software system, without requiring a significant programming effort each time the symbol set is changed.

## 2.2 PATTERN RECOGNITION

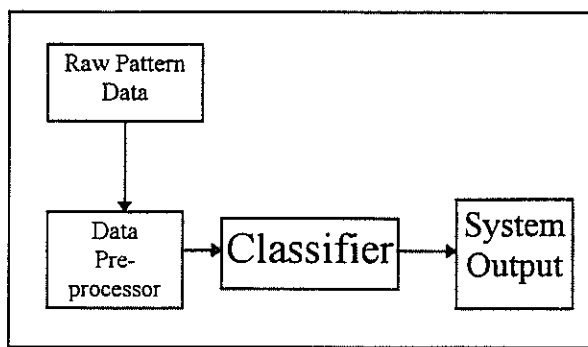


**Figure1:** A Basic Pattern Recognition System

A basic Pattern Recognition system consists of 4 fundamental elements. The *Raw Pattern Data* is the pattern that is being analysed, represented in its most basic form. The *Data Pre-Processor* manipulates this data into a form that can be used as meaningful input for the classifier, which is the next stage. For the case presented, the *Classifier* would be implemented by the Neural Network. Finally, the Classifier transmits its decision to the output module, which interprets the decision and conveys it in a meaningful way.[4]

It can therefore be seen that while the classifier plays a central role in the task of Pattern Recognition, there are other vital components that also need to be taken into account. These are discussed in further detail in the next section.

According to [4], the three most common approaches to Pattern Recognition are : Statistical Pattern Recognition, Syntactical Pattern Recognition and finally, Neural Networks. The Statistical approach is based upon the generation of probabilistic models, and uses estimation or decision theory to implement its classifier. As the name implies, this approach is usually adopted when there is a solid underlying statistical component to the problem. Syntactical

Pattern Recognition is based upon the development of formal grammars to store patterns and uses parsing to implement the classifier. Generally Syntactical Pattern Recognition is employed in cases where the *structure* of the pattern is of importance.

The Neural Network approach to Pattern Recognition combines elements of both the Statistical and Syntactical approach [4]. The classifier is implemented as a conceptual "black-box", based upon a stable state or weight array which is derived during training of the network. The one disadvantage of the Neural Network approach is that there is often a lack of semantic information from the network; it is not often possible to establish *why* the network made the decision that it did. However, this is not critical to the particular application being discussed.

## 3. THE TECHNIQUE

At present, the project is in the prototyping phase, and several different methods are being investigated. This section describes some of the possible avenues that are being explored and discusses the relevant issues that need to be considered.

### 3.1 DEVELOPMENT PHASES

Since the project presented may still be viewed as work in progress, a brief overview of the path that will be followed towards a final conclusion, is presented.

The first task that is to be completed is that of the development of the pattern recognition system itself. This includes the classifier, as well as the pre-processor. Initially, the Pattern Recognition system will be a stand-alone unit, which will be given a "window" of data as input, and will generate a decision as to whether there is a recognisable symbol within the window. This phase will allow different techniques to be explored both in terms of Neural Network topologies, as well as pre-processing strategies.

At present a prototype has been developed which allows a network to be trained, and then tested. A shape is entered graphically and presented to the network which produces a graphical output representing the choice that it has made. This prototype provides a useful framework within which the various aspects of the Pattern Recognition system can be tested.

Once the Pattern Recognition system is accepted, the next task will be to apply it to a map containing the

symbols. A moving "window" will be implemented, which will provide the input for the Pattern Recognition system. The "window" will only look at a small section of the map at a time. The Pattern Recognition system will examine this window and determine if any recognisable symbol is contained within. In this stage, the emphasis will be on developing a successful algorithm to move the window in order to achieve an acceptable success rate on "real-world" maps.

### 3.2 PRE-PROCESSOR

The pre-processor is a key element in terms of enhancing the robustness of the system. By passing the raw data through the pre-processor, properties such as Rotation-Scale-Translation (RST) invariance are introduced, which is necessary for the "real-world" environment in which the software is ultimately to be employed.

At present no pre-processor has been implemented, but several methods are being explored. Numerous techniques exist for extracting key features from images, thereby reducing the effects of noise as well as RST distortion. These includes methods such as taking central moments, as well as performing transforms (for example Fourier Transforms) on the raw image data.

### 3.3 NEURAL NETWORK CLASSIFIER

The Neural Network classifier is the central component of the Pattern Recognition system. There are three main aspects to consider in any Neural Network Pattern Recognition system: the network topology (or interconnection of the neurons); the characteristics of the individual units (neurons); the strategy used for learning or training. Each of these aspects is carefully considered in order to produce the most effective system.

As mentioned in Section 3.1, a simple prototype has already been developed. While the prototype is mainly aimed at developing a framework for further refinement and experimentation, a simple shape classifier has already been implemented, and this is described briefly below.

The prototype uses a two layer feed-forward log-sigmoid/log-sigmoid network to classify shape bit maps. The network has 64 inputs (and 8x8 image), 10 neurons in the first layer, and 3 in the 2nd layer. There are 3 outputs.

The network is trained to output a 1 in the correct position of the output vector and to fill the rest of the output vector with zeroes. However, noisy input vectors may result in the network not creating perfect ones and zeroes. Therefore, the output of the network is passed through a competitive layer which makes sure that the output corresponding to the shape most like the noisy input vector takes on a value of 1 and all others have a value of 0. The result of this post processing (i.e the competitive layer) is the output that is actually used.

The network is trained as follows: the weights and biases are initialised with Nguyen-Widrow initial conditions; the training method used is backpropagation and combines both an adaptive learning rate as well as momentum; both ideal and "noisy" picture matrices are used in the training set. The provision of both input as well as ideal output vectors means that the method of learning would be classified as *supervised*.

It is expected that the basic topology of the current network will not be altered significantly. Factors such as the size and resolution of the input window and the effect of the pre-processor, will however influence factors such as the number of layers and the number of neurons in each layer. Furthermore, alternate learning rules and training strategies will also be explored in order to find the most effective solution.

## 4. THE SOFTWARE IMPLEMENTATION

### 4.1 INTEGRATION INTO CART PACKAGE

The software that is being developed for this project forms part of a larger software project, which is a collaborative research effort being undertaken at WITS on the electrification of rural areas. Within the scope of this research project, a general framework, into which all present and future tools will seamlessly integrate, has been developed. (see [5]). It is into this framework that the Neural Network pattern recognition software will be incorporated.

### 4.2 ENVISAGED USAGE

It is often necessary for the designer of a reticulation network to be able to make use of the existing reticulation infrastructure at a particular site. In most cases, the existing network would not have been designed using the CART system, and thus the map of the existing network would not be in a form readable to the CART software package. It is proposed that through the implementation of the system described

the designer would no longer have to manually place all the existing elements of the network into the CART database. Instead, the intention is for the designer to be able to scan in a map of the relevant area, which will contain symbols depicting the various components of the existing network. The designer will classify the various symbols (such as transformers, junctions, stands) and the software system will recognise these symbols on the map and create entries for them in the appropriate CART data base.

In practical terms, the user would not be able to simply load a map, run the software, and return later to find a completed CART database. Instead, the user would work interactively with the program. When the system encounters a symbol it recognises, it will confirm with the user and allow the user to enter in the information that could not be inferred from the map. The only data that can be automatically entered into the database by the system would be positional information and the description of which type of object the symbol represents. Data such as transformer capacity and object names would either be set by the user for each individual object, or set as a global default. Furthermore, the system proposed would not be aware of any connections between objects - this would need to be specified by the user.

#### 4.3 IMPLEMENTATION ISSUES

With regard to the actual implementation of the ideas put forward, there are certain practical issues that need to be considered. Firstly, it is necessary to establish a method whereby the user can define the relevant symbols. In the initial stages of development, a standard set of common symbols will be used, and the network will be pretrained on these symbols. As the system progresses, however, a tool will be developed to facilitate user training of the network, on customised symbol sets.

The second issue that needs to be considered is the resolution of the map that is to be analysed. It is unreasonable to expect a Neural Network application to be able to recognise symbols that a human being cannot distinguish between (albeit possible), and therefore the assumption is made that any map presented to the system will be of a resolution that can be analysed by a human.

It is important to note that even in applications where neurocomputing is successful, it typically only solves the core of the problem. That is, the capturing of data and the initial processing is usually carried out via conventional programming techniques. Neurocomputing is therefore best thought of as an

*adjunct* to conventional computing. Neural Networks are thus usually treated as software subroutines called by conventional software programs, which allows them to be embedded into software wherever their capabilities are needed. [3]

The software system that is being developed is written in C++ in a Windows environment. The Neural Network will be implemented as a set of classes which will interface with the rest of the program. The actual interface of the final product will be dependent on which particular area of the reticulation software development project it is incorporated into.

#### 5. CONCLUSION

Neural Networks are a key technology in the area of Pattern Recognition. This paper has shown that there is much potential for making use of Neural Network technology in order to recognise electrical symbols on a township map. The work presented has not progressed to stage where it can be said with certainty that Neural Networks are the best technology to use for the application discussed; however, it is expected that Neural Networks will be applied successfully and that a useful, time-saving software tool will be developed.

#### 6. REFERENCES

- [1] Meyer, A.S., Dwolatzky B, "The effective computer generation of designs for township electrical distribution", Proceedings of the 1991 IEEE Power Engineering Society, pp. 659-663, September, 1991
- [2] Nelson, M., Illingworth, W.T, A practical guide to Neural Nets, Addison-Wesley, pp. 1-24, 1990
- [3] Hecht-Nielson, R., Neurocomputing., Addison-Wesley, pp. 1-42, 1989
- [4] Schalkoff, R., Pattern Recognition - Statistical, Structural and Neural Approaches
- [5] Dwolatzky, B., Meyer A.S, et al. "The software design of an integrated set of tools for planning electrical reticulation networks", SAUPEC, 1995

#### 7. ADDRESS OF AUTHOR

Mr J.C Shapiro,  
Department of Electrical Engineering,  
University of the Witwatersrand,  
Private Bag 3, P.O Wits, 2050

# Assessment of the failure of equalisers in a lap wound d.c. generator

A. Pagel, A.S. Meyer and C.F. Landy  
University of the Witwatersrand, South Africa

**Abstract** The design of equaliser windings for large lap wound d.c. machines is generally of an empirical nature. This paper presents an analytical technique, using finite element analysis, for the calculation of equaliser currents in lap windings. Each path in a simplex lap winding is influenced by a different pair of poles. It is practically impossible to make the fluxes of all poles identical in large d.c. machines. The result of uneven pole strength is that the voltages induced in the parallel paths are unequal. Since the paths are in parallel, circulating currents flow in the winding; when the machine is loaded the tendency will be to overload certain of the brushes. To mitigate this effect, permanent equaliser connections are usually made to the back of the winding to join points whose e.m.f. should at every instant be the same. The circulating currents then superimpose a partially correcting magnetic field. Since equaliser currents cannot be easily measured during operation, this investigation was undertaken to see how finite element analysis could be used to determine the equaliser current sensitivity to changes in the structure. The analytical technique was used to determine the equaliser currents in a large lap wound d.c. generator. The machine modelled had been rebuilt after a major breakdown when problems occurred with equaliser windings burning out.

this effect, permanent equaliser connections are usually made to the back of the armature winding, to join points whose e.m.f. should at every instant be the same. The circulating currents then superimpose a partially correcting magnetic field, that tends to wipe out the component flux producing the unbalance.

The minimum number and size of equalisers used are determined by the degree of imperfection; since this cannot be predicted, equalisers are usually designed from experience. This paper presents an analytical technique, using finite element analysis, for the calculation of equaliser currents in lap windings. Since equaliser currents cannot be easily measured during operation, this investigation was undertaken to see how finite element analysis could be used to determine the equaliser current sensitivity to changes in the structure. The iterative technique was used to determine the equaliser currents in a large lap wound d.c. generator. The machine modelled had been rebuilt after a major breakdown and problems occurred with equaliser windings burning out.

## 1 Introduction

In direct-current generators and motors, variations in the air-gaps due to manufacturing variations, or to bearing wear and other factors causes inequalities in the main pole fluxes. In lap windings, the number of parallel paths is always equal to the number of poles and also to the number of brushes. Each path, therefore, has its voltage generated by the flux of only two adjacent poles, and not all the poles. Thus if pole strengths are unequal, path voltages become unequal. This leads to the circulation of currents between paths. These currents must pass through the brushes, and when the machine is loaded the tendency will be to overload certain of the brushes; their temperature rise will become much too high and they will probably spark badly. To mitigate

## 2 Theory

The various imperfections in multipolar d.c. machines cause inequalities in the fluxes through both the main-poles and interpoles. The resulting non-uniformly distributed air-gap flux density pattern,  $\vec{B}_{Total}$ , can be considered to contain two superposed flux densities, a normal flux density,  $\vec{B}_{Normal}$ , uniformly distributed under all the poles, and a distorted flux density,  $\Delta\vec{B}$ , due to the imperfections.

$$\vec{B}_{Total} = \vec{B}_{Normal} + \Delta\vec{B} \quad (1)$$

Each flux density induces an e.m.f. in the armature winding. The e.m.f. induced by

the normal flux density is of the conventional nature for a d.c. machine; the distortion flux density induces the equaliser circuit e.m.f., and hence the equaliser currents. Equalisers are alternating-current taps, and whatever current flows presents an alternating-current phenomenon which primarily acts to correct the flux unbalance. This is essentially a case of damping, and as resistances in the equaliser circuits are low, the annulment of the original flux unbalance will be nearly perfect. That is, only enough flux will remain to set up the voltage necessary to maintain the equaliser circuit current through the resistance of the circuit. The equaliser currents are a function of the distortion, repeating once for every complete armature revolution.

Assuming that the machine imperfections can be either measured or predicted, the distorted flux density can be calculated using a modern numerical technique called finite element analysis. With finite element analysis we can model the entire distorted and undistorted machines, including the steel non-linearity;  $\Delta \vec{B}$  is then just the difference between the airgap flux densities. Given  $\Delta \vec{B}$ , a few techniques exist to calculate the equaliser currents, the most apparent being an iterative technique using the full non-linear finite element model; here equaliser currents are superimposed onto the armature currents until the distortion flux is nearly balanced, i.e. only enough flux must remain to set up the voltage necessary to maintain the equaliser circuit current through the resistance of the circuit. The advantage of this method is that it accounts for the demagnetising effect of the equaliser currents; the disadvantage is the difficulty in working backwards to calculate the actual current flowing in each of the equaliser connections. Section 3 explains how this approach was modified to do the required investigation.

### 3 Modelling

A 2D Field Simulator software package that uses the Finite Element Method (FEM) to solve electromagnetic problems, was used to model a d.c. Generator with the following rating:

$$\begin{array}{lll} P = 4100 \text{ Kw} & V = 1000 \text{ V} & I_f = 30 \text{ A} \\ I_a = 4100 \text{ A} & 500 \text{ rpm} & 14 \text{ pole} \end{array}$$

A 2D radial cross-section of the entire 14 pole generator was modelled. One pole of the d.c. generator geometry is shown in Fig. 1.

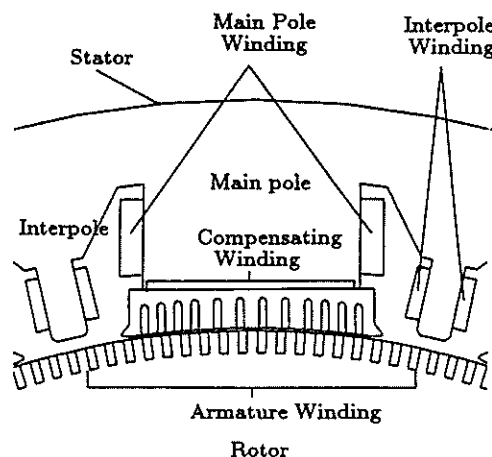


Figure 1: One pole of the machine geometry

A flux plot is shown in Fig. 2, for the d.c. generator under full-load, with the main pole, interpoles, armature and compensating windings excited. The model was verified in two ways. Firstly, the predicted airgap flux density at full-load, as calculated by the FEM, was compared to typical design values. Secondly, by comparing the torque calculated using the FEM software, with that calculated using standard d.c. Machine Theory, under full-load conditions. Very good agreement was achieved in both cases. End effects are ignored.

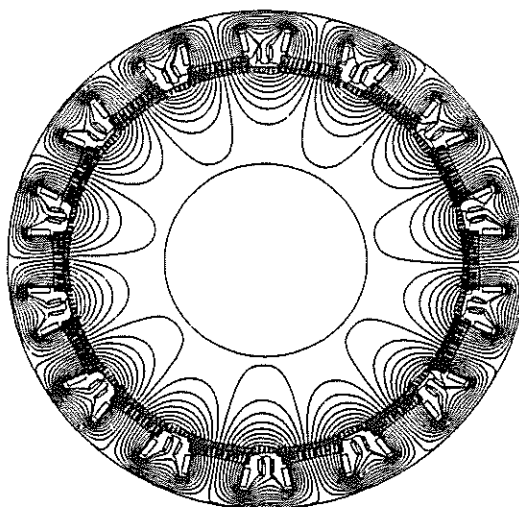


Figure 2: Flux plot for the d.c. generator at full-load

## 4 Method of calculation

The proposed method for calculating equaliser currents is possible only if the machine imperfections are known and can be quantified. For this investigation the air-gap distortions, usually due to manufacturing tolerances and bearing wear, were measured after some equaliser connections had burnt-out. The aim of the investigation was therefore, to check whether the measured distortions were large enough to cause failure, and also to determine the equaliser current sensitivity to airgap distortion.

The finite element geometry, once verified, can easily be changed to model the measured airgap variations. To simplify the problem it was decided to distort only one main-pole by the average measured amount, and to assume that this distortion is repeated regularly around the entire machine. The distorted flux density,  $\Delta \vec{B}$ , is shown in Fig. 3. Integrating, we obtained the maximum instantaneous flux that must be equalised. The finite element model was then used to calculate the additional main-pole m.m.f. required to superpose this flux on the undistorted machine. This was done iteratively by estimating the additional m.m.f., re-solving, and integrating. Equating this additional m.m.f. to the m.m.f. produced by one equaliser circuit, we obtain the peak equaliser current.

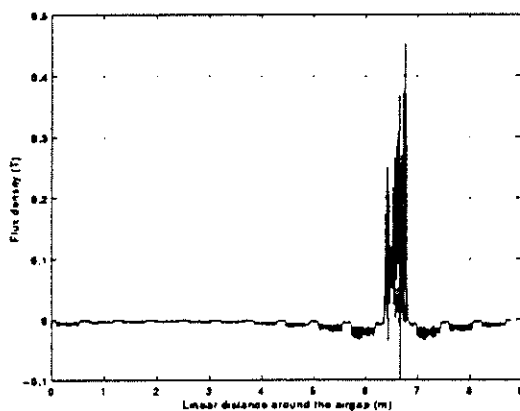


Figure 3: Distorted flux density

## 5 Results

The results are given in Table 1. For an average measured distortion of 10%, 110 A(peak) was required to equalise the distortion. The RMS current is  $110/\sqrt{2} = 77.7$  A.

Average radial airgap distortion (%)	10	5
RMS equaliser current (A)	77.7	34.9
Equaliser current density (A/mm <sup>2</sup> )	8.6	3.9

Table 1: Results

A good indicator of failure is the equaliser current density. For the average measured main-pole airgap distortion of 10% an equaliser current density of 8.6 A/mm<sup>2</sup> was calculated, which would easily destroy the winding. An average airgap distortion of 5%, causes an equaliser current density of 3.9 A/mm<sup>2</sup>, which would be acceptable.

## 6 Conclusions

A technique has been developed for calculating the equaliser currents in lap windings using finite element analysis. This technique can be used to determine the sensitivity of equaliser currents to changes in the structure of a large d.c. generator. Based on the equaliser current magnitude the possibility of equaliser burn-out can be assessed.

In this particular model an average distortion of 5% would most likely be acceptable but that of 10% would burn-out the equaliser. This investigation shows the use of modern analytical tools in the solution of problems previously solved empirically. This method could also be used to optimise the design of equaliser windings.

## 7 References

1. Clayton A.E., 1956, "Performance and design of direct-current machines", Second Edition, Sir Isaac Pitman & Sons, Ltd

2. Say M.G., Taylor E.O., 1980, "Direct current machines", First Edition, Pitman
3. Langsdorf A.S., 1959, "Principles of direct-current machines", Sixth Edition, McGraw- Hill Book Company
4. McPherson G., Laramore D.L., 1990, "An introduction to electrical machines and transformers", Second Edition, John Wiley & Sons
5. Moore A.D., 1926, "Theory of the action of equaliser connections in lap windings", Electric Journal, vol 23, pp. 624-627
6. Linville T.M., Strang D. P., 1950, "Current in equalisers connections of d.c. machine armature windings", Trans. AIEE, vol 69, 1219-1227

**Acknowledgement** The authors wish to thank Mr T. Uys of Anglo-Vaal for his assistance and support in this research.

## 8 Address of author

Mr A. Pagel, Department of Electrical Engineering, University of the Witwatersrand, P.O. Wits, 2050, South Africa.

Fax No : (011) 4031929

e-mail : pagel@odie.ee.wits.ac.za

# FLEXIBLE THREE PHASE CONVERTER FOR MICRO-PROCESSOR POWER CONTROL

J.A. du Toit

H.J. Beukes

P. Petzer

J.H.R. Enslin

R. Spée<sup>†</sup>

Stellenbosch University

<sup>†</sup>Oregon State University/ Stellenbosch University

## ABSTRACT

This paper presents a low cost flexible three-phase converter, developed for a variety of applications. Some of the practical features are discussed, as well as the controller hardware and control techniques.

## 1. INTRODUCTION

There is a continuous drive to improve the quality of power devices, i.e. higher switching frequency, higher blocking voltage, larger current handling capability and lower conduction losses.

In recent years the IGBT has shown that it has a major impact on new converter circuit designs [10]. Third generation devices already exists that can hard-switch 1000 A at a blocking voltage of 1800 V with switching frequencies of 20 kHz.

The availability of fast and cheap microcontrollers and DSP processors allows improved PWM methods to be implemented. These include cost function and current regulated delta modulation that optimise harmonic content or reference tracking errors. This is important for drives and utility applications.

It is important to select the right PWM technique for the specific application, therefore the controller has to be flexible to allow a comparison of results.

## 2. FLEXIBLE THREE PHASE PWM CONVERTER

The need has arisen for a reliable, flexible three phase converter for research, development and teaching in power electronics. This resulted in the development of a three phase 10 kVA converter with the following features:

- Complete protection against over voltage, over current, short-circuit current and over temperature;
- Status report to the micro-processor control,
- Phase current and voltage measurements;
- Optic and galvanic isolation to at least 1.5 kV;
- Energy dumping for machine braking.

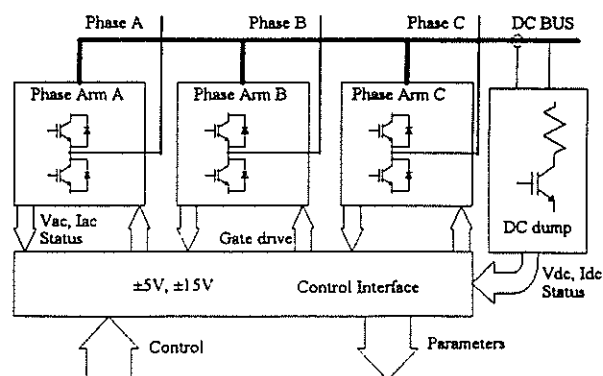


Figure 1: Block diagram of three phase converter

Figure 1 shows a block diagram of the converter where each block represents a pc-board in the converter. The phase arm block diagram is shown in Figure 2. Note that the phase current and voltage are measured onboard the phase arms, and it is isolated from the power circuit. The control circuit indicates the status of the converter by reading the status signals from the different boards. Information regarding a system shut-down would therefore be known.

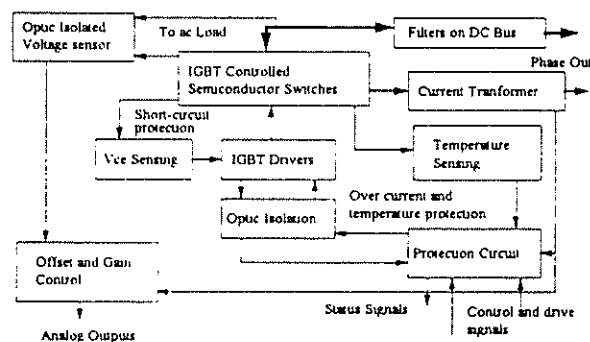


Figure 2: Block diagram of phase arm

The best choice for semiconductor switches is the IGBT, because of its fast switching ability. This results in high converter bandwidth and good load-current waveform quality in terms of harmonic content.

The converter has a dc-link voltage of nominally 400 V and a peak current rating of 30 A.

The performance of IGBT hard switching inverters is severely limited by two factors: the switching loss in the devices and the high dv/dt on the output of the

inverter. The first limitation causes excessive derating of device current rating. The  $dv/dt$  for IGBT's can be as high as 10 000 V/ $\mu$ s and can cause severe conducted and radiated EMI, as well as damage to motor insulation in drive applications. The EMI problem is partly solved by adding small RC snubbers across the IGBT's.

### 3. PWM METHODS

The following paragraphs will give a brief summary of the more popular PWM switching schemes.

*Sigma Delta Modulation ( $\Sigma\Delta M$ )* [2],[3]: This is the simplest method of voltage regulation for voltage fed inverters. The inverter output is fed back and the error determined ( $V_{ref}-V_{out}$ ). The error is fed to an integrator and comparator, thus a switching state is selected at every sampling instant. The structure is similar to hysteresis controllers, but with improved acoustic characteristics (white noise compared to individual tones).

*Current Regulated Delta Modulation (CRAM)* [1][2][3]: This is the simplest form of current regulator. CRAM is a zero hysteresis discrete time controller with only line-current feedback. The structure is similar to  $\Sigma\Delta M$  without the integration. Zero hysteresis provide infinite gain to decouple load parameters. The choice of inverter state is such that the error is always reduced as fast as possible. however the zero states are not used. This can cause higher  $dI/dt$  stresses leading to poorer harmonic performance.

*Space Vector Modulation (SVM)* [2][3]: This is a PWM control strategy used for 3-phase inverters. Instead of determining the switching state for each phase-arm separately, two inverter states are selected and the time that the inverter is in a particular state is determined. There are eight possible inverter states with states 0 and 7 referred to as the zero states

First, the three phase quantity is converted to a two phase (dq or stationary reference frame) vector and the time in each state determined. The reference voltage is assumed to be constant over the switching period and the average switching frequency is  $1/(2T_s)$ .

*Cost Function Modulation (CFM)* [3]: This can be called a truly optimal controller. An example of a cost function is as follows .

$$J = (I_A^* - I_A)^2 + (I_B^* - I_B)^2 + (I_C^* - I_C)^2 \quad (6)$$

The cost associated with each of the 7 inverter states are calculated and the state with the minimum cost is chosen. The performance of the above mentioned choice of J causes the system to degrade at lower switching frequencies. This is caused by a mismatch

of the measured and actual current values. The choice of J is therefore application dependent.

### 4. MICRO-PROCESSOR CONTROL

For most power converter system, two loops of control are used. The inner loop is usually a PWM controller, while the outer loop controller generates a reference for the inner loop (Torque/Flux control for induction motor, current/voltage for harmonic isolation etc.).

For the experimental inverter system to be as flexible as possible, a microprocessor or DSP is used as the inner loop controller, as compared to dedicated ASIC's or analogue hardware. This allows for easy comparison of PWM schemes as well as sampling rate selection. The outer loop controller is also based on a microprocessor, DSP or Transputer, available in the laboratory.

The choice of processor for the inner-loop controller is based on cost, control algorithm and switching frequency. These controllers are usually 16 bit microcontrollers or fixed point DSP processors. The microcontrollers allow for higher integration of components, by integrating high speed outputs and analog to digital converters on the processor itself. The performance of these components are acceptable if lower switching frequencies and simple control algorithms are used.

The DSP processors allow for higher switching frequencies and more complex control algorithms. Additional A/D converters and latches for control signals are needed, resulting in slightly more complex hardware.

Outer loop controllers can implement neural nets, fuzzy logic or other complex and computationally intensive control algorithms. These can be done with a standard PC, DSP processor or transputer. Transputers hardware is easy to implement and the concurrent process ability of the transputer make software easy to implement. The currently available transputers are relatively slow compared to DSP's.

A PC can also be used for outer loop control. The faster PC's will allow for medium to high switching frequencies. although voltage isolation becomes a bigger problem. Standard evaluation modules are available for the transputer, as well as the DSP's. These are available as stand-alone or PC based cards.

### 5. APPLICATIONS

#### *Utility Applications:*

Utility devices include solid state phase shifters, thyristor-controlled series capacitors and static VAR devices. While high power (> 5 MVA) transmission applications still require thyristor phase control or low

frequency GTO technology, on the distribution and reticulation levels ( $< 2$  MVA) modern IGBT power transistors can already effectively be utilised in low power devices ([7], [6], [9]), for the control of harmonics entering the network and flicker and dip in voltage. This results in high performance, yet low cost systems.

The converter is used to do proof of concept experiments on power devices, such as the unified power controller and the harmonic isolator.

These concepts will later be applied to high power (100 kVA) laboratory converters; eventually the goal is to implement a 1-2 MVA device to be used on a 88 kV network.

*Experimental Evaluation of Resonant Topologies:* AC-AC converter topologies can be broadly classified into three categories, depending upon the type of the intermediate power transfer link, i.e. dc link, ac link, or direct link. In the paper of Bhowmik [5] a theoretical study of major converter topologies and their performance, device requirements, cost/benefit and application opportunity is performed.

Attention has recently been focused on the use of soft-switching techniques for high-power inverters. The resonant dc link (RDCL) and the resonant pole inverter (RPI) have been shown to be viable topologies for high-power applications.

The converter is used also to evaluate the different resonant converter topologies experimentally. This is done by adding the resonant passive components as well as the active clamping components to the existing converter.

#### *Motor drives:*

The inverter can be used as a motor drive for a variety of ac machines for industrial applications.

#### *Teaching:*

The converter is used in the teaching of power electronic converter theory, electric machines and control systems. The reliability and robustness of the converter make it especially useful for the students to get familiar with a variety of converter concepts practically.

## 6. PRACTICAL SETUP

### 6.1 GENERAL SETUP

The following results were obtained using an Intel 80C196KC controller with the 10 kVA 3 phase converter. Figure 3 shows the general layout of the inverter with controller. The system was used as an inverter to run an induction machine with a DC-machine as a load.

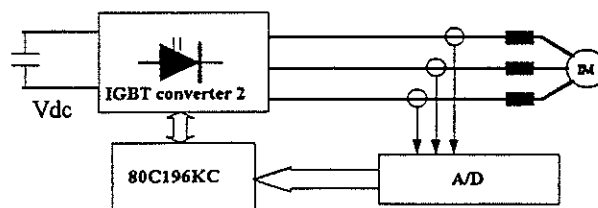


Figure 3 : Inverter setup

### 6.2 INDUCTION MACHINE DRIVE

The controller is a fixed frequency hysteresis controller. A switching frequency of 6 kHz can be maintained with the 80C196KC processor while maintaining the sinusoidal reference at a constant frequency.

For variable speed control of the induction motor, additional code had to be inserted and the switching frequency dropped to 4.5 kHz. The following results were obtained with the modified code.

Figure 4 shows the phase current drawn with the machine running at low speed. The current drawn by the machine is sinusoidal with minimal harmonic content.

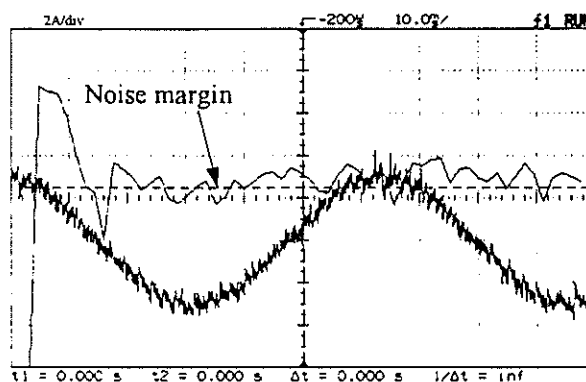


Figure 4 : Sinusoidal current waveform and frequency spectrum.

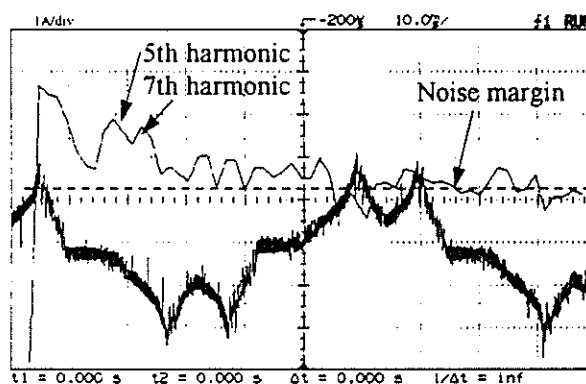


Figure 5 : Saturated current waveform and frequency spectrum.

Figure 5 shows the phase current with the machine running at higher speeds. The current deteriorates to six pulse and the presence of the 5th and 7th harmonics can be clearly seen from the graph.

This is caused by the back EMF of the induction machine becoming too large and insufficient voltage to induce the reference current. This problem can be alleviated by increasing the DC-bus voltage.

### 6.3 RESONANT TOPOLOGIES

The following figures show a comparison of soft and hard switched waveforms. Figure 7 show the measurements obtained with the resonant pole topology [8]. Note that the IGBT's switch at zero voltage, thus reduced switching losses. Unlike typical zero-voltage-switching topologies, which is characterised by high in-circuit voltage stresses, this circuit has voltage levels that are clamped at the supply voltage.

The same converter was also used without the resonating components as a hard switched inverter. The results obtained are shown in Figure 6.

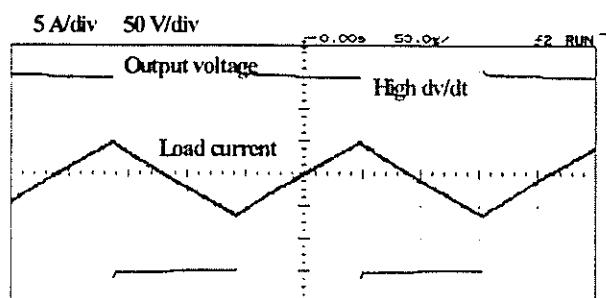


Figure 6: Hard switched waveforms

### 7. CONCLUSIONS

A low cost, flexible converter has been developed to be used as a tool for research and development work. The circuit is flexible and robust, allowing experimental topologies and control algorithms to be evaluated.

From the measured waveforms, it can be seen that the converter is already being used in different applications with great success. The 80C196KC industrial microcontroller is easy to use, but for higher switching frequencies, a DSP processor will have to be used.

Future work will include upgrading of the microcontroller to a more powerful TMS320C50 DSP processor from Texas Instruments.

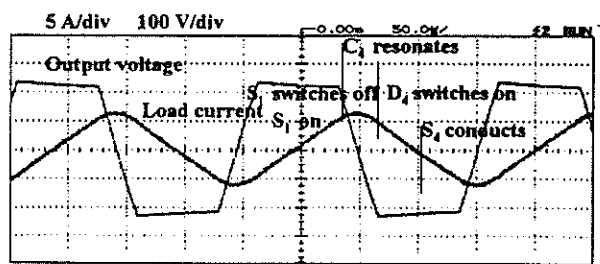


Figure 7: Inductor current and capacitor voltage of resonant pole inverter.

### 8. REFERENCES

- [1] T. Habetler, D.M. Divan, "Performance Characterisation of a New Discrete Pulse-Modulated Current Regulator", *IEEE Transactions on Industry Applications*, Vol.25, no.6, Nov/Dec 1989.
- [2] D.M. Divan, "Current regulators and Discrete Pulse Modulation.", Tutorial presented at Power Electronics Specialist Conference PESC'90.
- [3] J. Holtz, "Pulsewidth Modulation- A survey.", *IEEE Power Electronics Specialist Conference PESC'92 Rec.*, Vol. 1, pp.11-18, 1992.
- [4] D.M. Divan, G. Venkataramanan, "Com-paritive evaluation of soft switching inverter topologies", *IEEE-EPE Conf. Rec.*, 1991, pp. 2-013-2-018.
- [5] S. Bhowmik, R. Spée, "A guide to the application-oriented selection of ac/ac converter topologies", *IEEE Trans. on Power Electron*, Vol. 8, No. 2, 1993, pp. 156-163.
- [6] J.H.R. Enslin, J. Zhao, R. Spée, "Operation of the unified power controller as harmonic isolator", *IEEE-PESC Conf. Rec.*, 1994, pp. 167-176.
- [7] B. Acharya, D.M. Divan, R.W. Gascoigne, "Active power filters using resonant pole inverters", *IEEE Trans. Industry Applications*, Vol. 28, No. 6, 1992, pp. 1269-1276.
- [8] R.W. De Doncker, J.P. Lyons, "The auxiliary quasi-resonant dc-link inverter", *IEEE-PESC Conf. Rec.*, 1991, pp. 248-253.
- [9] H. Fujita, H. Akagi, "A practical approach to harmonic compensation in power systems - series connection of passive and active filters", *IEEE Trans. Industry Applications*, Vol. 27, No. 6, 1991, pp 1020-1025.
- [10] S.K. Sul, F. Profumo, G.H. Cho, T.A. Lipo, "MCT's and IGBT's: A Comparison of performance in power electronic circuits", *IEEE-PESC Conf. Rec.*, 1989, pp. 163-169.

## THE USE OF FINITE ELEMENT ANALYSIS TO DESIGN A LOW COST SYNCHRONOUS RELUCTANCE MOTOR FOR THE SOUTH AFRICAN MARKET

M.A. Rohde    A.S. Meyer    C.F. Landy  
University of the Witwatersrand  
South Africa

In South Africa the motor manufacturing industry is not large enough to effectively sustain a branch constructing only synchronous reluctance motors. The aim of this project is to allow an existing induction motor to be converted into a synchronous reluctance motor with minimal cost.

### Introduction

The project involves modifying the rotor of a squirrel cage induction machine so that it performs as a synchronous reluctance machine. The tool used for simulation purposes is a finite element package. The modified induction machine rotor was combined with the existing shell of the induction machine. This enables the utilisation of the bulk manufacturing process used to produce the induction machine, to obtain a comparatively cheap synchronous reluctance motor. The research is aimed at the smaller range of machines because here the bulk of the expense is the purchase price (not running cost) and the nature of the design demands certain concessions regarding efficiency and power factor[2]. The emphasis in the design is hence a low cost application. This also implies that the modifications to the rotor need to be simple.

### Significance for the South African Market

This is a great advantage for the local market because presently synchronous reluctance machines are not readily available in South Africa. In the past the synchronous reluctance machine has never been able to effectively compete with the induction motor. Recent developments, however do make the modern synchronous reluctance machine equivalent to the induction machine in efficiency and performance, but they are expensive and difficult to build.

Induction machines are readily accessible in South Africa. In comparison to the synchronous machine, they are available in various sizes and types. A process that converts induction machines into synchronous reluctance machines will make synchronous machines available at a comparatively low price. This is extremely practical for an application that demands a synchronous motor, as an existing induction machine

can be converted into a synchronous reluctance machine (eg. for precise speed control).

### Operation of a Synchronous Reluctance Motor

The synchronous reluctance machine operates on the principle that the rotor aligns itself with the path of least reluctance. After synchronisation, the rotor is effectively dragged around by the fundamental mmf wave in the airgap.

The primary concern when remodelling the induction machine rotor is to maximise the saliency ratio. This is the ratio of the inductance of the q-axis to the inductance of the d-axis. This is achieved by removing iron from the rotor in a specific way that roughly enforces the expected magnetic field distribution in the rotor. More specifically, the magnetic reluctance of the d-axis has to be maximised by introducing air gaps in its path without removing too much iron from the q-axis reluctance path.

The losses of the synchronous reluctance machine are distributed differently to those of the induction machine. Running at synchronous speed, the rotor losses fall away in the synchronous reluctance machine because the rotor is effectively operating with a constant flux. However, the flux density has increased due to the loss of iron in the rotor. This implies that the machine is now saturated and in order to compensate for this, the flux must be reduced, hence for the same output the current density in the stator increases. This increase in the current density now causes greater copper losses in the stator windings. This redistribution of losses also affects the heating of the machine, as the cooling circuit now needs to be different.

### Measurements on the Testbed

Modifications were made on an existing 5.5kW, 380V, 4-pole, 3 phase squirrel cage induction motor. The rotor has been remodelled into a simple salient pole structure as can be seen on the finite element plots (Figure 2 and 3). In order to determine the saliency ratio of this machine, the following equations are

used[1].

$$\cos(\phi) = (\alpha - 1) \sqrt{\frac{\sin(2\theta)}{2(\tan\theta + \alpha^2 \cot\theta)}}$$

$$T = \frac{3P}{2} (L_q - L_d) I_{ph}^2 \sin(2\theta)$$

where:  $\cos(\phi)$  = power factor  
 $\alpha$  = saliency ratio  
 $\theta$  = load angle  
 $L$  = inductance of relevant path  
 $p$  = no of poles  
 $I_{ph}$  = phase current  
 $T$  = torque

### Experimental Setup

The experimental setup is shown in the accompanying diagram.

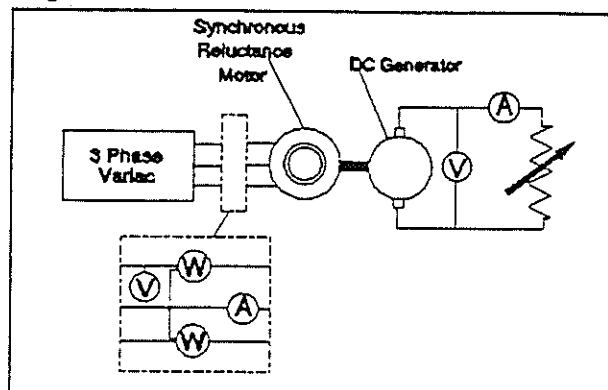


Figure 1 Experimental Setup

The instrumentation is laid out in such a fashion as to record the exact voltage, current and power measurements. The load angle is measured by placing a stroboscope set to the external line frequency onto the rotor (running at synchronous speed) and marking the deflections on a piece of paper fixed to the stator.

This machine was found to operate as a synchronous reluctance motor. The performance was not comparable to that of the original induction motor because the saliency ratio was only 1.77.

An interesting observation is that the synchronous reluctance motor effortlessly runs up to speed and synchronises. This is because the residue of the rotor cage is still present and effectively act as damper bars.

### Finite Element Analysis

The finite element is done on a computer package

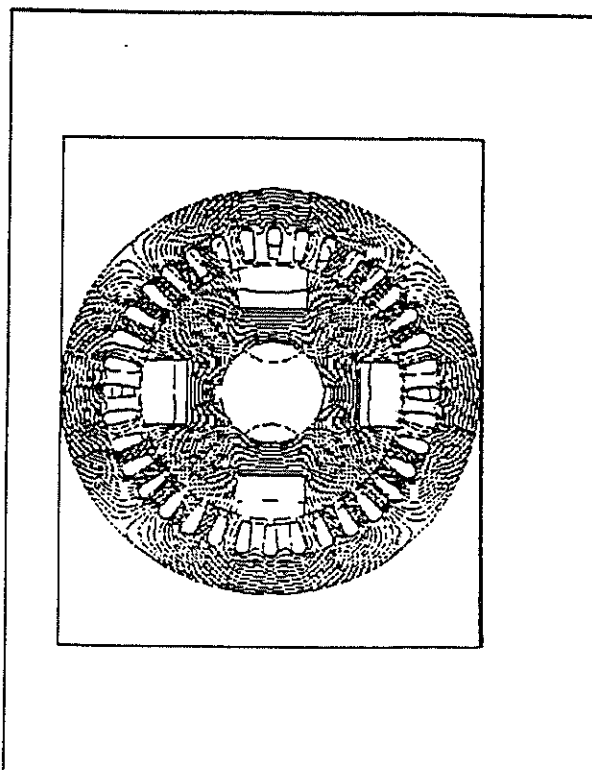


Figure 2 Finite Element Plot of the Q-Axis Flux Pattern

called Maxwell. The simulation depicts a single lamination of the synchronous reluctance motor on the testbed. In other words, the problem is modelled in only two dimensions. A magnetostatic approach is used in order to determine the saliency ratio. The lamination is excited with DC in such a configuration that depicts the AC supply frozen at one instant in time. The problem has hence been reduced into a static model that is easier to simulate.

The d-axis and the q-axis cases are considered separately. The rotor position varies between the two cases as the excitation is placed directly over the q-axis and then the d-axis. Effectively this means that the rotor needs to be modelled at frames that are 45 degrees mechanical (or 90 degrees electrical) apart from each other, as is depicted in the two finite element plots (figures 2 and 3).

It is clearly visible from the diagrams how the flux pattern differs as the excitation is placed directly over the d-axis and the q-axis respectively. The flux per pole may be calculated by integrating the normal component of flux density either in the rotor, the stator or the airgap. Consideration needs to be taken that all the flux contained in the pole crosses the specified line, except leakage flux. Placing the line in the airgap yields the most accurate results. It should be noted that

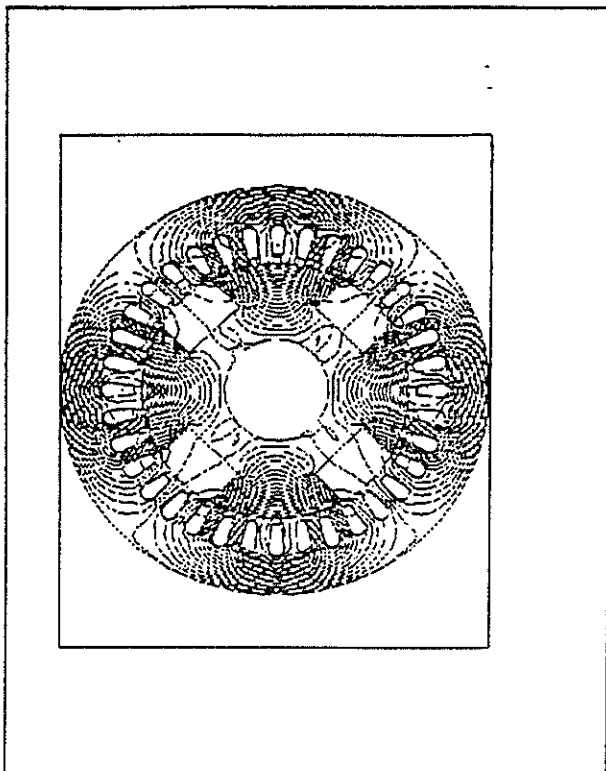


Figure 3 Finite Element Plot of the D-Axis Flux Pattern

for simplicity the rotor slots are omitted. In order for the synchronous reluctance machine to perform as well as the induction motor, a saliency ratio of 5.5 to 6 is required[1].

### Further Work

In order to arrive at a confidence test, the simulation needs to yield the same saliency ratio as the measured results on the actual machine. The objective of this confidence test is to ensure that further finite element simulations are accurate. It is difficult to correlate the excitation current of the simulation and the experimental machine as the simulation models the static case and the experiment the dynamic case. The current used in the simulation only represents the magnetisation current, whereas the experimental current includes other components.

The way to get around this problem is to consider the flux per pole. The finite element simulation directly produces the flux per pole when integrating the normal component of the flux density in one pole. In the experimental setup, the flux per pole may be calculated by first principles. For this purpose a motor design simulation program is used.

Once the confidence test is completed, the process of improving the rotor profile may begin. In order to achieve an optimum saliency ratio, the flux barriers need to trace the natural flux path as close as possible, limiting the d-axis as much as possible, while minimising interference with the q-axis flux.

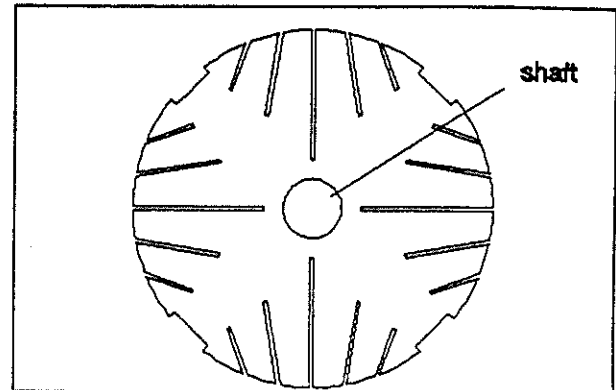


Figure 4 Improved Rotor Profile

The simulations for this task will be done exclusively on the finite element package. Once the optimisation is completed, the validity of the results need to be confirmed on the testbed. For this purpose an identical rotor to existing one (before modification) will be acquired and altered according to the optimised results. The envisaged improved rotor profile is shown in the accompanying figure (figure 4).

Another aspect that may be considered is to compare the performance of the final design with that of the induction machine. Due to the redistribution of losses it is possible that efficiency values comparable to those of the induction machine may be obtained. It needs to be evaluated exactly how competitive this type of synchronous reluctance motor is in comparison to the induction machine.

### Conclusions

The fact that the synchronous reluctance machine is capable of running up to speed and synchronising independently is a significant advantage over existing synchronous machines and will be useful in industrial applications. The tool used for simulation purposes was finite element analysis, which allows the reluctance paths of the rotor to be calculated. Hence finite element analysis is a powerful tool to iteratively optimise the saliency ratio of the synchronous reluctance machine.

Another aspect to consider is how competitive this synchronous reluctance machine is with the induction motor. It is expected that the saliency ratio will significantly be improved. In order to perform as effectively as the induction machine, the saliency ratio

needs to be increased to 5.5 or 6.

## References

1. D.A. Staton, T.J.E. Miller, S.E. Wood; Optimisation of the Synchronous Reluctance Motor Geometry; 5th International Conference on Electrical Machines and Drives; September 1991; London (IEEE)
2. N. Balbo, R. D'Andrea, L. Malesani, P. Tomasin; Synchronous Reluctance Motors for Low Cost, Medium Performance Drives

## Address of Author

M.A. Rohde, Department of Electrical Engineering,  
University of the Witwatersrand, Private Bag 3, 2050,  
South Africa, Fax Tel: 27-11-4031929, Pmail Address:  
ROHDE@ODIE.EE.WITS.AC.ZA

# SIMULATION AND IMPLEMENTATION OF SENSORLESS SPEED CONTROL APPLIED TO A CSI-FED FIELD ORIENTED CONTROLLED INDUCTION MOTOR

KJ Talbot CE Kleinhans RG Harley G Diana  
Department of Electrical Engineering, University of Natal, Durban, SA

## ABSTRACT

This paper presents a method of speed estimation for a CSI-fed induction motor under FOC (Field Oriented Control) which is based on the principle that as the machine is current fed, the rotor speed is proportional to the terminal voltage and the rotor flux. Results of simulations performed using *CASED* (Computer Analysis and Simulation of Electrical Drives) where the speed estimate is used in the speed feedback loop are presented. Results of the practical work implemented on a transputer based controller are also presented showing the practicality of applying Speed Sensorless Field Oriented Control to a CSI-fed induction motor.

## INTRODUCTION

CSI fed induction motor drives (not to be confused with current regulated VSI fed drives) have certain advantages over VSI drives. CSI drives become economically attractive at high power levels. Traditionally, the dynamic performance of the constant V/f controlled CSI drive has not compared favourably to the VSI drive, and most certainly not to that of the Field Oriented Controlled (FOC) VSI drive. In many applications the CSI drive operates adequately without a tacho if good dynamic performance is not important. More recently, FOC has been applied to CSI drives as well, although the tacho again becomes an essential component thereby detracting from the robustness of the CSI-fed motor.

In VSI drives much attention has been paid to applying FOC without a tacho (so-called speed sensorless drives) [1,2,3], but relatively little effort has been directed to developing a speed sensorless FOC controller for a CSI drive.

This paper proposes a simple yet reliable method of estimating the rotor speed from measurements of stator voltages and currents. The simulation environment *CASED* [4] is used to simulate the entire rectifier, inverter, the FOC control circuits, the motor and its load, as well as the speed estimation algorithm. The estimated speed is supplied to the speed controller, in other words, the SPEED ESTIMATOR is fast enough to use on line as the actual feedback signal which controls the motor. Many existing speed estimation methods require complex signal processing and might

be too slow for insertion into the feedback loop.

## THEORY

Since the machine is current fed, the voltage can be regarded as an output of the machine. This voltage is dependent on the speed of the machine and the rotor flux. Under FOC, the induction machine can be equated to a separately excited DC machine, which has the following voltage equation

$$E = K\Phi\omega \quad (1)$$

where  $E$  is the magnitude of the voltage,  
 $\Phi$  is the flux of the machine,  
 $\omega$  is the rotational speed and  
 $K$  is a machine constant.

For the induction motor,

$$\begin{bmatrix} v_{ds} \\ v_{qs} \end{bmatrix} = R_1 \begin{bmatrix} i_{ds} \\ i_{qs} \end{bmatrix} + \sigma L_1 p \begin{bmatrix} i_{ds} \\ i_{qs} \end{bmatrix} + \omega_e \begin{bmatrix} -\lambda_{qs} \\ \lambda_{ds} \end{bmatrix} \quad (2)$$

On rearranging eqn 2, the induction machine equations in the d-q reference frame are as shown in eqn 3, where the numerator is the induced emf providing the similarity with eqn 1.

$$\omega_e = \left[ \frac{v_s}{\lambda_s} - R_1 \frac{i_s}{\lambda_s} - \sigma L_1 p \frac{i_s}{\lambda_s} \right] / \left| \frac{\lambda_s}{\lambda_s} \right| \quad (3)$$

where  $\omega_e$  is the electrical speed,  
 $|v_s|$  is the magnitude of the stator voltage vector,  
 $R_1$  is the stator resistance  
 $|i_s|$  is the magnitude of the stator current vector,  
 $p$  is the differential operator,  
 $|\lambda_s|$  is the magnitude of the stator flux vector and

$$\sigma = 1 - \frac{L_m^2}{L_{11}L_{22}} \quad (4)$$

The slip, under FOC, is as follows

$$s\omega_e = \frac{R_2 L_m i_{qs}}{L_{22} \lambda_{dr}} \quad (5)$$

Instantaneous rotor speed is then calculated at every sampling instant from calculating  $\omega_e$  in eqn. 3 and slip in eqn. 5. The rotor flux is positioned on the d-axis, resulting in zero q-axis rotor flux as defined by the conditions of FOC, and is calculated as in eqn (6).

$$\lambda_{dr} = \frac{1}{\tau_r} \int (L_m i_{ds} - \lambda_{drOld}) \quad (6)$$

As a measure of whether or not the controller is holding FOC, the q-axis rotor flux can be calculated from the stator quantities as follows

$$\lambda_{qr} = \frac{L_{22}}{L_m} ((R_1 i_{ds} + p\lambda_{dr} - s\omega_e - \alpha L_{11} i_{qs}) \quad (7)$$

This flux should be zero, but due to parameter variation and an incorrect speed estimate, a build up in the q-axis rotor flux is possible. With the use of eqn (7), this build up of flux can be taken into account and incorporated into the calculation of the d-axis rotor flux.

In a further effort to divorce the speed estimate from the operation of the FOC controller, the calculation of the electrical angle is done independently of the speed estimate. This is done via the use of the alpha-beta reference frame where the relationship between the alpha-beta voltages is calculated and used to calculate the electrical angle as follows

$$\theta_e = \arctan \left( \frac{v_\alpha}{v_\beta} \right) \quad (8)$$

With eqn (8) providing the electrical angle, the speed estimate is only required for the speed control making the controller more stable.

## SIMULATION

The software package *CASED* was used to simulate the entire CSI drive under FOC with the speed estimate used in the speed feedback loop. A block diagram of the hardware system used is shown in Fig. 8, and is similar to the block diagram of the *CASED* implementation. In this system, the voltages and currents are used to calculate the electrical angle which is used in the Parks transform. The results of a simulation where a step speed reference of 100 rad/s is applied to the drive, with the estimated speed in the feedback loop, can be seen in Figs. 1 through to Fig 3. Figure 1 shows the estimated speed against the

simulated tacho speed with the tacho being the smoother curve. Figure 2 presents the d-axis rotor flux that is present in the machine. The lower of the two curves during runup is the d-axis flux when the q-axis flux is assumed to be zero. When the q-axis flux is taken into account for the d-axis flux calculations, which is the case for the upper curve in Fig. 2, this provides an improvement in the speed estimation in the regions of large slip. The q-axis rotor flux, calculated as per eqn. 7, is shown in Fig. 3 (smooth curve due to filtering) and is plotted against the q-axis flux that is calculated in the simulation of the machine. The relatively small nature of these q-axis fluxes indicates that the machine is in FOC. The FOC controller and speed estimator is written in C in the *CASED* simulation and is compiled using the INMOS C toolset for the transputer controller; this eliminates the need to write new code when going from the simulation to the implementation.

## HARDWARE AND PRACTICAL RESULTS

Two T800 transputers were used in order to execute the control algorithm and to output the control signals to the thyristors of a 7.5 kW drive. The currents were sampled at 4 kHz, the voltages at 2 kHz and the entire control algorithm ran at 1 kHz, corresponding to 40 calculations per shaft revolution at rated speed. Code scheduling and execution times are thus of importance and are implemented well within the hard real-time constraints. Two sets of results are presented, with Fig. 4 showing the estimated and actual speed of the induction motor with a 100 rad/s step in the speed reference confirming the accuracy of the estimation technique. In Fig. 5, the rotor fluxes are shown indicating the presence of FOC as the q-axis flux is nearly zero. The deviation of this flux from zero is primarily due to parameter variation and the lack of online parameter identification while the different runup times are due to different current limits imposed on the system. Figs 6 and 7 are produced when a step of 30 rad/s in the speed reference is applied to the drive showing the ability of the speed estimate in controlling the drive at low speeds.

## CONCLUSION

This paper describes the development and implementation of an all-digital CSI FOC controller for an induction machine drive, using a relatively simple speed estimator. The control algorithm is shown to provide accurate speed estimation and control, with practical results being presented showing the drive to be under FOC at all times.

## REFERENCES

- [1] Rubin N.P., Harley R.G. and Diana G. : "Evaluation of Various Slip Estimation Techniques for an Induction Motor Operating Under Field Orientation Control Conditions", IEEE Transactions on Industry Applications, Vol. 28, No. 6, November / December 1992.

- [2] Schauder C. : "Adaptive Speed Identification For Vector Control Of Induction Motors Without Rotational Transducers", IEEE Transactions, 1989, pp. 493-499.
- [3] Hurst K D, Habetler T G, "Sensorless Speed Measurement Using Current Harmonic Spectral Estimation in Induction Machine Drives", PESC'94, Taiwan, 20-25 June, 1994, pp. 10-15.
- [4] CE Kleinhans, G.Diana, RG Harley, MD McCulloch, M Randelhoff, DR Woodward, "Analysing a CSI-Fed Field Oriented Controlled Induction Motor using a New Simulation Package *CASED*", Conference Proceedings of the IEEE Industrial Electronics Society, IECON, 1994, Bologna, Italy, paper ref. No. EP237P102.

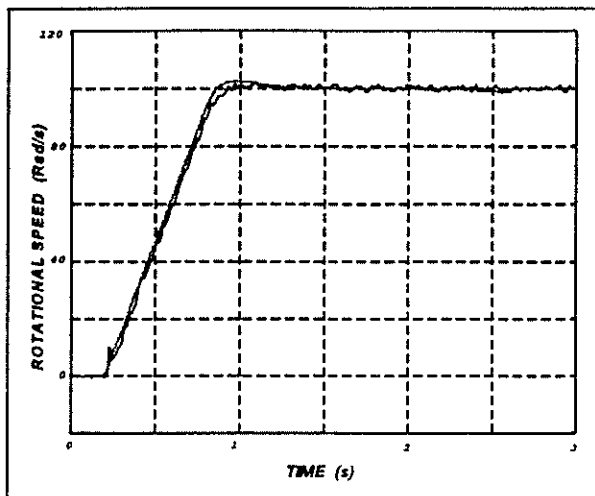


**Figure 1** Simulated Tacho and Estimated Speed Response with the Estimated Speed in the Feedback Loop.

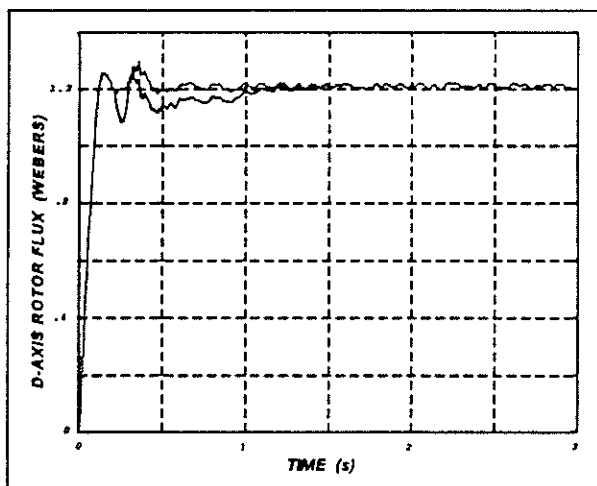


**Figure 2** d-axis Rotor Flux With and Without q-axis Flux Compensation.

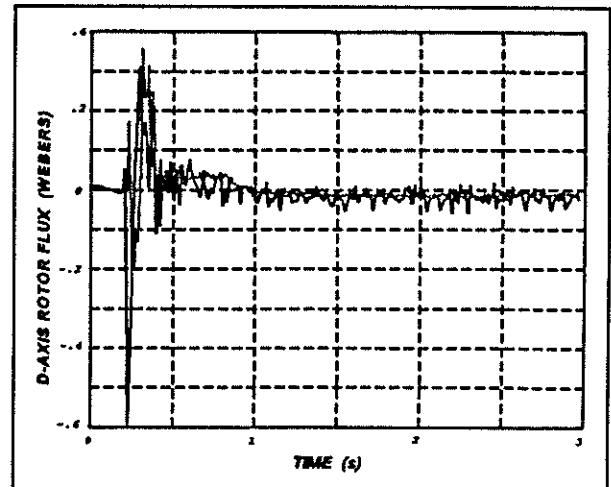


**Figure 3** Calculated and Actual q-axis Rotor Flux.

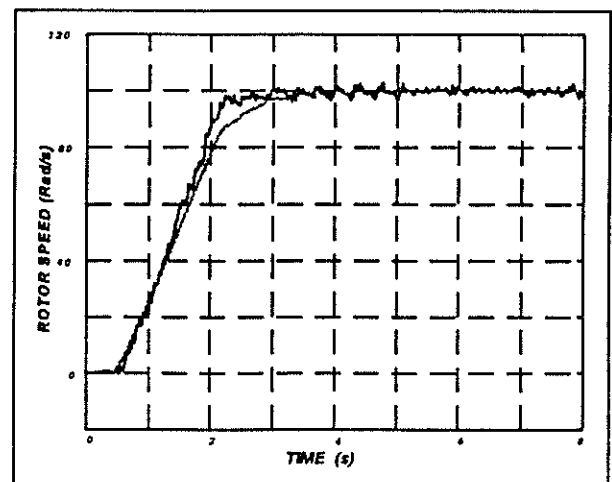


**Figure 4** Practical Tacho and Speed Estimate With Estimate in the Feedback Loop.

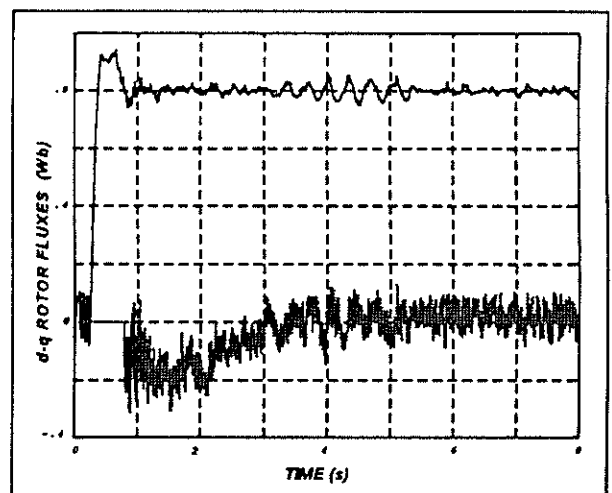


**Figure 5** d-q Rotor Fluxes for a 100 rad/s Step in Reference Speed.

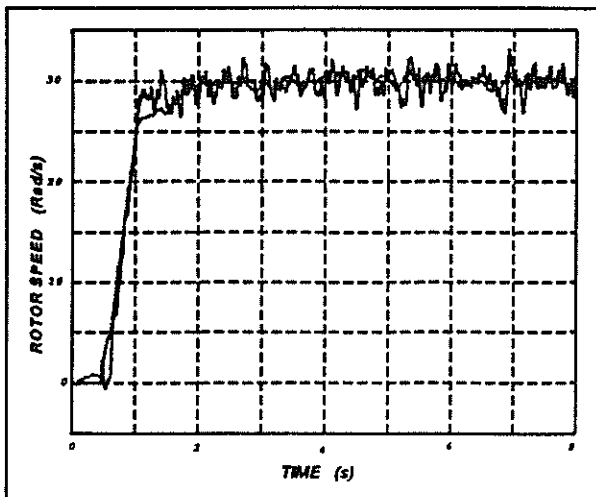


**Figure 6** Practical Tacho and Estimated Speed for a 30 rad/s Step in Speed Reference.

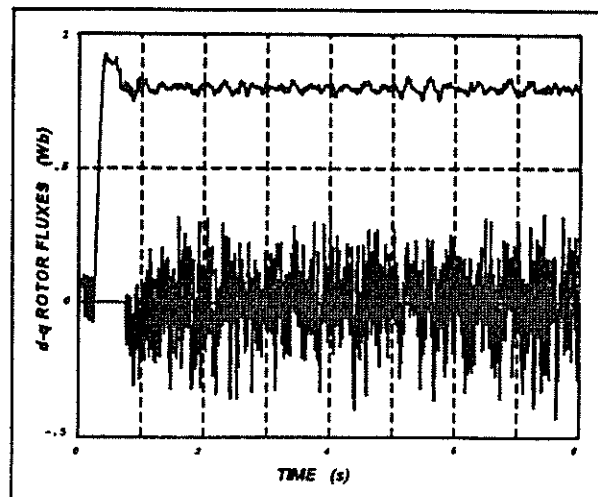


**Figure 7** d-q Axis Rotor Fluxes for a 30 rad/s Step in Speed Reference.

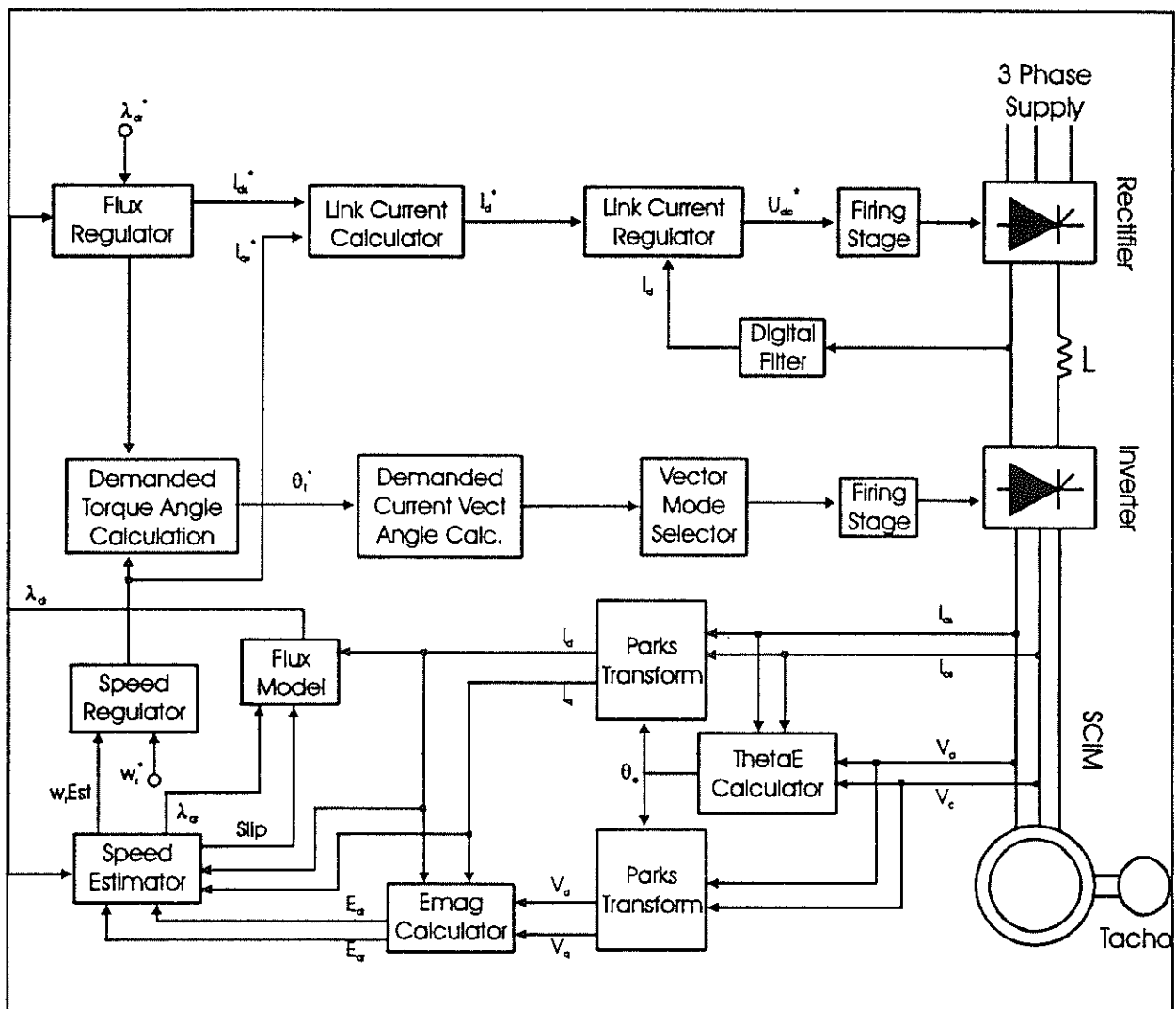


**Figure 8** Block Diagram of the CSI Drive with the Control Algorithm

## A NEW ROTATING UPS

E D Smith and JunYong Yang  
University of Pretoria, Pretoria, RSA

### SUMMARY

A class of UPS, containing a rotating machine as its central feature, are briefly reviewed and the various elements comprising the machine discussed. A new device, which combines many, previously separate elements, into one single machine is proposed.

### INTRODUCTION

Recent UPS research and development has been confined to small electronic devices for personal usage. A large market has also developed in these devices thereby suggesting that a latent demand also exists for large devices capable of providing an entire building, factory or mine with an uninterruptible supply of electrical power (UPS).

The small UPS finds application in association with computer activities. The large UPS is expected to provide service where emergency lighting, security systems, elevators, hoists and mine ventilation are typically involved.

Large scaled up versions of the small UPS have been used in the kilowatt to megawatt range but the batteries of wet cells that accompany them are costly and require large amounts of floorspace.

### EXISTING FORMS OF ROTATING UPS

The number of wet cells can be reduced by using a diesel generating set to supply the long term load while the wet cells only deliver power during the intermediary period while the diesel engine starts up [1 2]. It is possible to replace the battery of wet cells by a flywheel [1] as is found in a common

form of rotary UPS shown in fig 1 a comprising motor, alternator, flywheel, clutch, flexible coupling and diesel engine.

The electric machine in a rotating UPS sometimes used for the dual purpose of preventing harmonics, generated by the user, from propagating back into the reticulation system [3]. In these systems it is common to find two machines usually a synchronous machine or low-slip induction motor driving an alternator which supplies the harmonic rich load. Various devices such as inverters, flywheels or batteries supply power immediately after a break and prior to the diesel electric generator taking up load.

A system comprising a 30 000 rpm flywheel in a vacuum has been described [4] and various combinations and permutations of the above mentioned elements exist [5 6].

An unusual combination of these elements as illustrated in fig 1 b has been described [7].

### NEW MACHINE

The machine proposed here, fig 1 c combines many of the elements shown in fig 1 a into one machine which resembles a doubly wound induction machine with normal three phase windings on both the inner and outer members as shown in fig 2a. Both inner and outer members of the machine are free to rotate with their three phase connections being brought out through slip rings. The inner member, however, also carries a dc winding for excitation as a synchronous machine as illustrated in fig 2b. The inner member is rigidly fixed to the shaft of a diesel engine and the outer member to the incoming supply and load via the slip rings.

## OPERATION

Fig 3 shows the system within which the rotating UPS operates. Incoming three phase power enters the system through a *direction of power flow sensor*, circuit breaker or contactor to the load. Also attached to the supply line are power factor correction capacitors and the rotating UPS. The circuit breaker or contactor serves the function of disconnecting the UPS from the supply line in order to avoid sending reverse power into the rest of the reticulation system. The *direction of power flow sensor* senses the flow direction and controls the circuit breaker or contactor through the PLC. Up till the moment of the power failure the rotating UPS was connected to the three phase supply and the outer member rotated as a three phase synchronous motor [8] at synchronous speed (there being dc supplied to the electromagnet on the inner member). Immediately after the moment of power failure, however, the outer member of the rotating UPS continues to supply power to the load but now as an asynchronous generator or induction generator [8] deriving its energy from that stored in the flywheel and deriving the necessary excitation from the *power-factor correction and self-excitation capacitors* connected to the line, according to the normal manner of self-excitation of asynchronous generators. The rotating UPS is then supplying power,  $P$  in Watts, to the load from the stored rotational energy in the UPS outer member which rotates at radial velocity of  $\omega$  radians per second, and rapidly reducing as it gives up energy to the load. On fundamental grounds this must produce a reactionary torque of  $T$  Newton metres on the shaft and given by the equation  $T = P/\omega$ . The shaft of the rotating UPS is, however, connected rigidly to the shaft of the diesel engine which it starts up in a manner similar to reaction starting of an internal combustion machine. (The rotating UPS must be designed in order to supply the required torque for this purpose.) As the diesel engine speeds up and starts to take

load the electromagnetic brake shown in fig 3 is applied by the PLC so that the system then runs as a conventional diesel-alternator set with the outer member being held stationary.

## CONTROL

It is clear that the tempo with which the electromagnetic brake is applied will have a bearing on the frequency and voltage fluctuations occurring during the change over to diesel-alternator power. Suitable limits for these variations have been proposed [8] as 1 % and 5 % respectively.

The above expression for the diesel engine starting torque shows that this will be inadequate if the delivered power  $P$  is too low. In order to ensure sufficient torque under conditions of insufficient load it is necessary for extra load to be added artificially. This is the purpose of the *artificial load* shown in fig 3. The correct value is switched in by the PLC and is available for connection to the UPS when the latter is disconnected from the incoming reticulation network.

The PLC, similarly, also controls the correct value of capacitor for self-excitation of the asynchronous generation phase of the UPS. When these are not required for this purpose, during normal power supply from the reticulation network, the capacitors serve the function of power factor correction of the load. Information about the state of the load power factor can be derived from the *direction-of-power-flow sensors* the latter can conveniently be constructed around modified power measurement devices which incorporate the measurement of power factor [9].

## ECONOMIC ASPECTS AND CONCLUSIONS

In applications where security of supply is important the use of large UPS devices require consideration. The rotating UPS described above promises to be an economical alternative to the present designs as its main item, the rotary device, is merely a doubly wound machine for which manufacturing facilities already exist.

## REFERENCES

- 1 American National Standards Institute (1986) IEEE Recommended Practice for Emergency and Standby Power Systems for Industrial and Commercial Applications. ANSI/IEEE Std. 446-1987
- 2 Comeau, G E (1974) Mechanical and Battery-Stored Energy Systems for Meeting Uninterruptible and Buffer Electric Power Needs. IEEE Trans. on Industry Applications Vol. IA-10 No. 2 March/April 1974
- 3 Sachs, K (1986) New Developments in Low Impedance rotary UPS Design. INTELEC 86, Conference Proceedings, IEEE Service Centre, Piscataway NJ 08845-4150, USA pp S 637-645
- 4 Takahashi I & I Andoh (1992) The Development of Uninterruptible Power Supply Using Flywheel Energy Storage Techniques. Trans. Inst. Elect. Engngs. Japan Part D Vol. 112-D Iss. 9 pp 877-82.
- 5 Barba, V G & E E Shube (1989) Authority Limiter. US Patent 4 823 063
- 6 Gottfried C F (1984) Uninterruptible Power Supply. US Patent 4 460 834
- 7 Coburn K (1993) The Dynamic UPS System. Electron Vol 10 No 9 pp 59-61
- 8 Say M G (1983) Alternating Current Machines, Fifth Edition. Pitman Publishing Limited, London. ISBN 0-273-01968-6 pp 1-632
- 9 Sames (1994) SA105A Three Phase Power / Energy Metering IC Pulse Output. South African Micro-Electronic System (Pty) Ltd. PO Box 15 888 Lynn East, 0039 pp 1-10

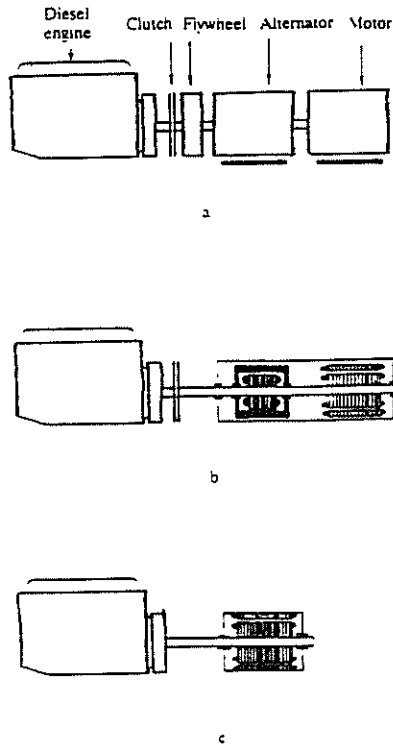


Fig 1 A diagrammatic representation showing various rotating UPS machines.  
 a A diesel engine, clutch, flywheel, alternator and motor in line.  
 b A UPS with flywheel incorporated into the outer member of the machine which is allowed to rotate.  
 c The UPS incorporated into one machine of which the outer member is allowed to rotate forming the flywheel. The airgap replaces the clutch.

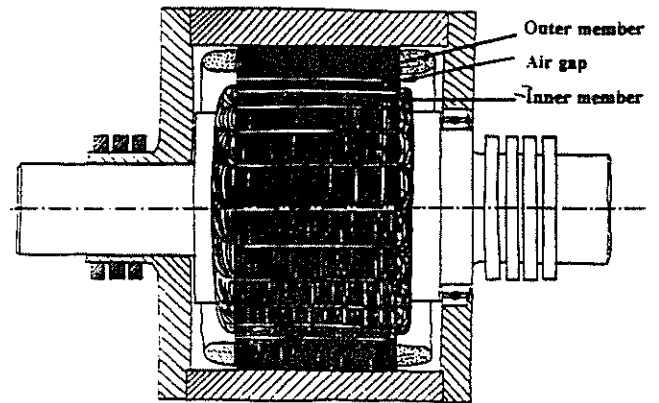


Fig 2a Sketch cross sectional drawing showing the construction of the electromagnetic unit.

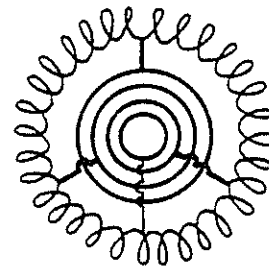


Fig 2b Diagrammatic representation of the connection between the four slip-rings and the three phase winding of the inner member of the electromagnetic unit.

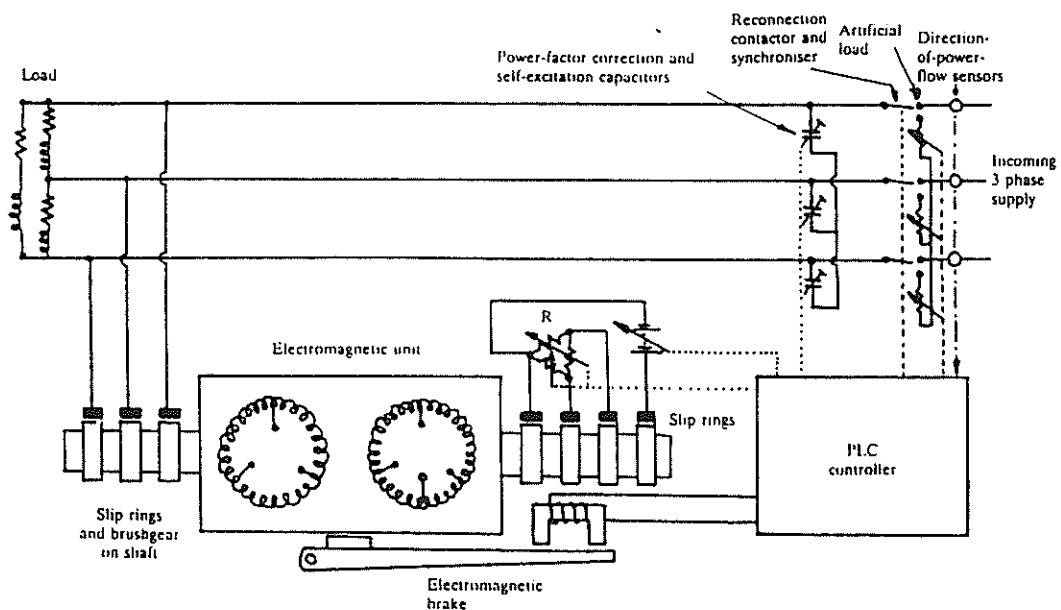


Fig 3. A schematic diagram showing the connection and relation between the electromagnetic unit and the supply, load, controller and other units.

# A FORMAL LINK BETWEEN THE POWER, MASS, SPEED AND EFFICIENCY OF ELECTRICAL MACHINES

H R van Niekerk,

University of Pretoria

**Abstract** - A new approach to the classical analysis of the performance of electrical machines is presented. A unique relationship is established between the power-to-mass ratio, speed, air gap flux density, efficiency and conductor material constants of an elementary machine model, by formal analysis. The formulae lay down absolute performance limits for machines with distributed windings. Allowance is made for non-active (overhang) conductor material and the remainder of the structural mass of the machine. Comparison of theoretical and practical specific power values for a few machines proved the validity of the analysis.

## I. INTRODUCTION

The efficiency of electrical machines is important, because of the economic importance of the minimisation of energy losses, and because the resulting heat needs to be removed to limit temperature rise. The mass of machines, on the other hand, is equally important where a high power-to-mass ratio is desirable.

Knowledge about the power, mass, efficiency and speed, particularly how these relate to one another, therefore is necessary to understand the capabilities of electrical machines and limitations in their potential applications.

The classical theoretical analysis of the steady-state performance of electrical machines allows the losses, efficiency, power and specific power output of a machine to be readily calculated for a chosen operating condition, provided that the machine parameters and the relevant constants particular to each loss mechanism are known [1, 2, 3, 4].

This procedure is indirect, and gives no indication of fundamental limits of performance. There has so far not been a direct, formal mathematical link between the power-to-mass ratio, the efficiency and the speed of electrical machines.

The analysis presented in this paper leads to a single formula, relating the ultimate theoretical limit of the power-to-mass ratio, to the efficiency and the operating speed.

Only the conduction losses in the main winding (stator of conventional ac machines and the rotor of

conventional DC machines) are taken into account, hence absolute limits of performance are established.

## II. THEORETICAL ANALYSIS

A typical textbook representation of an elementary electrical machine is shown in figure 1. The typical textbook equations, derived and simplified from Maxwell's equations, are the following:

$$\text{Induced voltage: } e = BLv \quad \text{V} \quad (1)$$

$$\text{Resulting force: } F = BLi \quad \text{N} \quad (2)$$

The mechanical power generated is given by:

$$P_m = Fv = BLiv \quad \text{W} \quad (3)$$

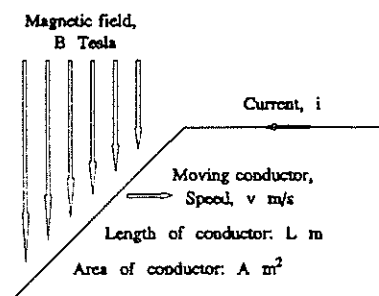


Fig. 1. Element of a fundamental electromagnetic machine

Referring to the equivalent circuit of Fig. 2 which represents the machine as a motor, the following further relations are identified:

The efficiency of the motor is given by:

$$\eta = BLvi/(Ui) = BLv/U \quad (4)$$

The current is given by:

$$i = (U - BLv)/R \quad \text{A} \quad (5)$$

The typical textbook model, however, does not assign physical features like mass and cross section area to the conductor of figure 1. If this is done, the analysis proceeds as follows:

$$\text{Mass of the conductor: } M = \sigma LA \quad \text{kg} \quad (6)$$

Resistance of the conductor:  $R = \rho L/A$  ohm (7)

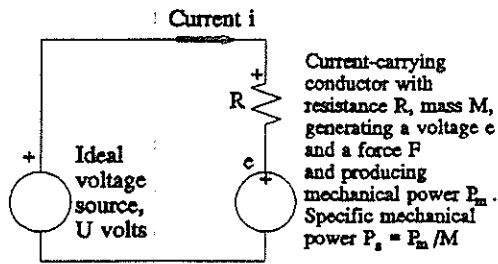


Fig. 2. Equivalent circuit of the fundamental electric motor powered from a voltage source

The specific power is obtained from equations 3 and 6:

$$P_s = BLiv/(\sigma LA) \text{ W/kg} \quad (8)$$

At a conductor speed value  $v_o$ , the ideal no-load speed, the induced voltage equals the supply voltage and the current is zero. The no-load speed  $v_o$  is given by:

$$v_o = U/(BL) \text{ m/s} \quad (9)$$

From equations 2, 7, 8 and 9 follows:

$$P_s = B^2 v(v_o - v)/(\rho \sigma) \text{ W/kg} \\ = B^2 v_o^2 (v/v_o - v^2/v_o^2)/(\rho \sigma) \text{ W/kg} \quad (10)$$

From equations 4 and 9 follows:

$$\eta = \frac{BLv}{BLv_o} = \frac{v}{v_o} = \frac{N}{N_o} \quad (11)$$

Combining equations 10 and 11:

$$P_s = B^2 v_o^2 (\eta - \eta^2)/(\rho \sigma) \text{ W/kg} \quad (12)$$

Efficiency may appear to be an independent variable in the above equation, but that is not the case - it is actually a result of the voltage loss over the resistor, caused by the chosen current.

Equation 12 is the formal link between specific power, efficiency and speed for a linear machine, according to the above model.

For a rotating machine, consider the conductor to be mounted on a rotor with diameter  $D$  m, rotating at  $N$  r/min (with  $N_o$  representing the no-load r/min).

Equation 12 then becomes:

$$P_s = \frac{\pi^2 B^2 N_o^2 D^2}{60^2 \sigma \rho} (\eta - \eta^2) \text{ W/kg} \quad (13)$$

Specific torque is readily derived:

$$T_s = \frac{\pi B^2 D^2 N_o}{120 \sigma \rho} (1 - \eta) \text{ Nm/kg} \quad (14)$$

Note that:

- Equation 13 gives a parabolic  $P_s$  curve with varying  $\eta$ .  $P_s$  is a maximum when  $\eta = 50\%$  (and then  $N = 0,5 N_o$ , equation 11). This is the well-known maximum power transfer relation, shown in Fig. 3.

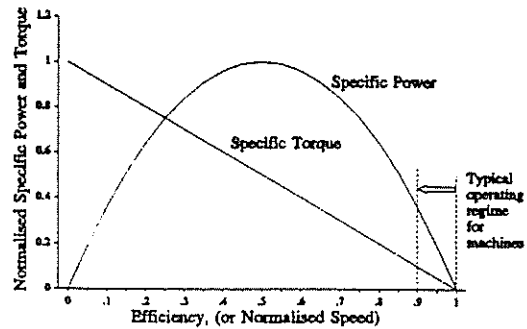


Fig. 3. Normalised specific power and specific torque curves, as a function of efficiency

- Equation 13 shows that for the same value of  $\eta$ ,  $P_s$  is proportional to  $(BN_o D)^2$ . Therefore, in the design of motors where low mass is important, the objective should be to use the highest practical values for these parameters.
- Specific torque can be seen from equation 14 to increase linearly from zero (at  $\eta = 100\%$  and  $N = N_o$ ) to a maximum value at standstill, when  $\eta = 0$ . As the specific torque is proportional to  $D^2$ , and mass is proportional to the length  $L$  in this fundamental machine model, it is clear that absolute torque is proportional to  $D^2 L$ , i.e. the well-known torque-volume relation.
- Only the dc losses in the conductors are considered, while all the other losses are ignored. Such losses occur in all practical machines, hence practical values of specific power and torque will be lower than the values obtained from the formulae.

5. Only the mass of the electromagnetically active part of a conductor was considered in the analysis, while the overhang was ignored. The effect of the overhang conductors is twofold, namely to increase the mass as well as the resistance, both effects lowering the specific values calculated. A constant  $(k_c)^2$ , with  $k_c$  equal to the ratio of mean conductor length to active conductor length, is included below the line in each equation.
6. Only the conductor mass was considered, while the rest of the structural mass, was not taken into account. Nett values of specific power and specific torque can be obtained by introducing into the equations a second factor  $(k_m)$  below the line to represent the ratio of conductor mass to the total mass of the machine.
7. A steady state (dc) situation is assumed in the derivation of these formulae, while it should be possible to apply them to all practical machines. By including the power factor of the ac machine and the form factor for a sine wave (1,1), allowance can be made respectively for the fact that the current and voltage are not in phase and the fact that the power developed is a function of the average value of current while the losses are related to the effective value of the current. The factor  $(\cos \phi / 1,1)$ , applicable to ac machines only, is therefore included in the formulae.

Assuming copper conductors are used, constants  $\rho$  and  $\sigma$  are given numerical values, namely  $22.10^{-9} \Omega \cdot m$  (to account for operation at  $70^\circ C$ ) and  $8800 \text{ kg/m}^3$  respectively. Equations 13 and 14 then respectively change to:

$$P_{sp} = \frac{14,16 B^2 D^2 N_c^2}{k_c^2 k_m} \left( \frac{\cos \phi}{1,1} \right) (\eta - \eta^2) \text{ W/} \quad (15)$$

$$T_{sp} = \frac{135 B^2 D^2 N_o}{k_c^2 k_m} \left( \frac{\cos \phi}{1,1} \right) (1 - \eta) \text{ Nm/} \quad (16)$$

### III. TESTING THE THEORY

The validity of the theory was tested firstly by comparing calculated and actual specific power values of four low speed machines, namely two slipring induction motors, a dc generator and a dc motor. Operation at rated load, and efficiency based only on the main winding conduction losses, were considered.

Numerical values of the parameters of the four machines were obtained from detailed design schedules [1, 2, 5].

Since the total mass of none of these machines was given, only the gross power-to-mass ratios (i.e. based on conductor mass only) were calculated. However, since equations 15 and 16 represent the active part of a practical machine, it is quite legitimate to test the validity of the theory at this level. The constant  $k_m$  in the expressions above was therefore taken as 1. In the case of the induction motors only the stator conductor mass was taken into account, because the rotor conductors may in this analysis be considered to be only part of the excitation circuit of the machine.

The difference between actual and calculated values of specific power was found to vary from 6 to 13 percent for the four motors.

A high speed, high performance traction motor [5, 6] was similarly investigated.

Fig. 4 shows for each machine the calculated and actual gross specific power values as a function of the product of the machine constants contained in equation 15, and with efficiency as a parameter. The two values are linked by a vertical line.

It is noted that the calculated and actual values are in close agreement in all five cases, although  $P_g$  varies over almost 2 decades. Furthermore, in all cases the actual efficiency value is close to the theoretical value.

### IV. DISCUSSION

Although the model used in this theory is idealised, in that only the dc losses and the armature conductor mass are considered, it has been shown to be accurate and useful, as can be seen in figure 4. If the remainder of the losses and the ratio of total mass to armature conductor mass in an actual machine is included in the calculation, the scales of figure 4 will change, but it will reflect the same trend.

No consideration was given in the analysis to the aspects of cooling and thermal dissipation. In stead, this factor was treated indirectly, by choosing in the analysis high values of efficiency, implying acceptable low losses. In practice, though, thermal constraints are to be taken into account in the usual way.

### V. CONCLUSION

Formulae for the absolute theoretical limits of specific power and specific torque of conventional electric

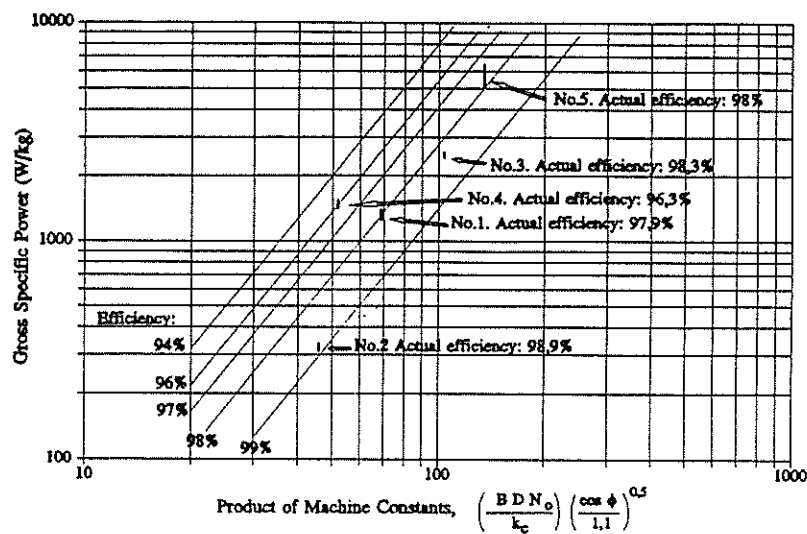


Fig.4. Absolute limiting values of gross specific power as a function of machine constants, and with efficiency as a parameter.

machines have been derived and it has been shown how these values depend on the flux density, rotational speed, rotor diameter, efficiency and conductor material constants.

Although the analysis was done for a DC model, the conclusions can be applied to AC machines as well, provided that allowance is made for the phase angle difference between the current and the flux, and the form factor of the current.

The accuracy of the resulting formulae has been tested by comparing theoretical and actual results for five machines, and close agreement of the results has been obtained.

## VI. NOMENCLATURE

A	Cross section area of a conductor ( $m^2$ )
B	Magnetic flux density (T)
D	Diameter of machine rotor (m)
e	Induced voltage (V)
F	Electromagnetic force on a conductor (N)
i	Current in a conductor (A)
$k_c$	Ratio of mean to active conductor length
$k_m$	Ratio of total mass to conductor mass for a machine
L	Length of a conductor (m)
M	Mass of a conductor (kg)
N	Rotational speed of a machine (r/min)
$N_o$	No-load rotational speed (r/min)
$P_m$	Mechanical power (W)
$P_s$	Specific power (W/kg)
$P_{sp}$	Specific power of practical machine (W/kg)
$P_{sa}$	Specific power of actual machine (W/kg)
R	Resistance of a conductor (ohm)
$T_{sp}$	Specific torque of a machine (Nm/kg)
U	Source voltage (V)
$\eta$	Efficiency

v	Speed of a conductor (m/s)
$v_o$	No-load speed of a conductor (m/s)
$\rho$	Specific resistance of conductor metal (ohm-m)
$\sigma$	Specific mass of conductor metal ( $kg/m^3$ )
$\phi$	Phase angle between voltage and current, i.e. flux

## VII. REFERENCES

- [1] M G Say. "The Performance and Design of Alternating Current Machines". Pitman, London, 1956.
- [2] A E Clayton. "The Performance and Design of Direct Current Machines". Pitman, London, 1956.
- [3] E Levi. "Polyphase Motors. A Direct Approach to their Design". Wiley Interscience, N.Y. 1983.
- [4] M G Say & E O Taylor. "Direct Current Machines". Pitman, London, 1890.
- [5] H R van Niekirk & J D van Wyk. "Electric Machines: A New Formulation for the Power-Mass-Efficiency-Speed Relationship". 1992 IEEE IAS Conference, Houston, USA, 4-9 October 1992.
- [6] R D King. "ETX-II 70 Hp Electric Drive System Performance - Component Tests". The 10th International Electric Vehicle Symposium, EVS-10, Hong Kong, December 1990, pp 878-887.

Author's address:

H R van Niekirk, Department of Electrical and Electronic Engineering, University of Pretoria, 0002 Pretoria.

# POSITION CONTROL OF A LINEAR INDUCTION MOTOR FOR CONVEYANCE APPLICATIONS

RJ Cruise    JF Pritchard    CF Landy  
University of the Witwatersrand

**Abstract:** A small scale single-sided linear induction motor is designed and constructed to determine the feasibility of using linear machines to access ultra-deep ore-bearing reefs. A horizontal conveyance system in the form of a vehicle running on a track is implemented and position control of the system is obtained using Quantitative Feedback Theory (QFT) techniques. The paper illustrates how the system was modelled and highlights the principles involved in designing the controller. The method used for the control design could also be easily applied to a linear induction motor propelled vertical hoisting scheme.

## 1. INTRODUCTION

There are many gold-bearing reefs in this country that still need to be mined, however most of these ore bodies occur at depths in excess of 4000 metres and cannot be economically exploited[1].

At present the deepest single-wind hoist operates only to 2500 metres[2]. The major limiting factor is the weight of the hoisting cable as by the time the cage reaches the bottom of the shaft, the cable alone weighs over 45 tonnes. Apart from restricting the maximum operating depth, a large amount of energy is unnecessarily wasted lifting this extra weight.

If the cable could be eliminated altogether, many restrictions imposed on present hoisting systems could be eradicated. One proposed hoisting system, that does not require the use of a cable, is a linear induction motor propelled lift.

## 2. BACKGROUND THEORY

Figure 1 illustrates that a linear induction motor can be thought of as an ordinary rotary induction motor cut by a radial plane and unrolled with the rotor replaced by a conducting sheet of aluminium and a magnetic back-iron[3]. To avoid confusion, when referring to a linear induction motor the terms stator and rotor are replaced by the words "primary" and "secondary".

One advantage of a linear induction motor is that it develops a tremendous thrust force without any mechanical contact between the primary and the

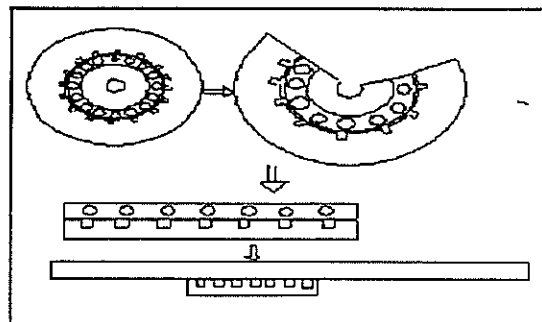


Figure 1: Relating a linear machine with its rotary counter-part

secondary. However, the non-continuous magnetic circuit gives rise to standing wave patterns or edge effects[4]. This phenomenon ensures that linear induction motors have an inherently poor power factor and efficiency when compared to their rotary counter-parts.

## 3. THE LABORATORY SET-UP

### 3.1 THE TEST TRACK

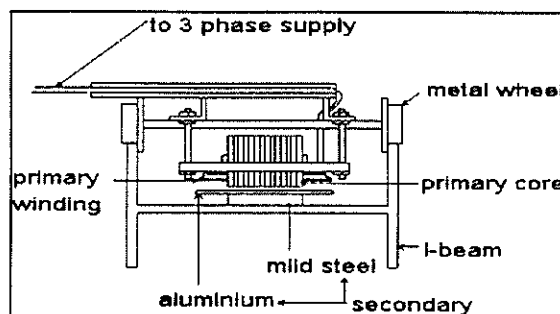


Figure 2: Cross-section of the laboratory test vehicle and its track

Since the main focus of this project is the control of the vehicle and not the design of a linear machine, an existing design proposed by E.R. Laithewaite[5] was used for the construction of the primary. The design of the secondary, that is the aluminium sheet and back-iron, was obtained using existing design equations derived from electromagnetic field theory[4].

A short primary, long secondary motor was found to be the most economical. Thus the secondary consisted of a strip of mild steel welded along the

centre of a 6 metre long I-beam with a sheet of aluminium 3 mm thick completing the arrangement. The test vehicle consisted of a set of steel flanged wheels with an under-carriage on which the linear induction motor was supported. The under-carriage could be adjusted to vary the air-gap, but it was found that an air-gap of 3 mm allowed for sufficient mechanical clearance while still providing adequate acceleration and deceleration of the vehicle for control purposes.

### 3.2 THE CONTROL SYSTEM

The first step in deciding on the control system was determining whether an analogue or digital controller should be used. Naturally a digital system is preferable since it is much more flexible than an analogue system. However, the sampling interval is usually the major limiting factor here. In this case, since a relatively slow physical system is being dealt with, it was decided that a digital control system would be fast enough to achieve adequate control.

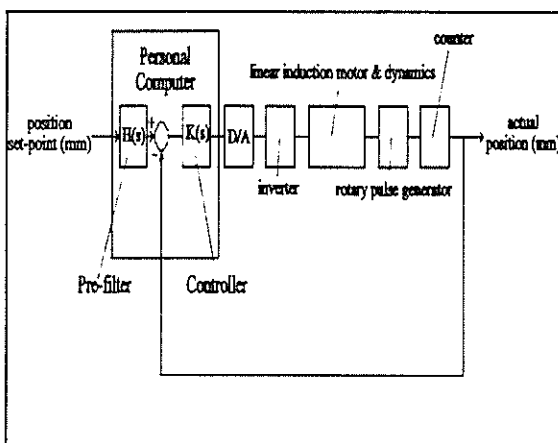


Figure 3: Block diagram showing the final logical set-up of the control system

The final logical set-up of the hardware is shown in Figure 3. The desired position is entered by the user on the computer keyboard. The controller and pre-filter are implemented on the computer using software. The control signal leaves the computer as a binary number and enters a digital-to-analogue converter. This signal then goes to a constant flux power electronic inverter which drives the machine. The position is monitored by using a rotary pulse generator attached to a wheel of the vehicle and a counting circuit. This is fed back into the computer which completes the control loop as shown.

Before any controller can be designed, a mathematical description of the plant has to be determined. The "plant" is everything off the

computer apart from the digital-to-analogue converter. In effect, one expects the plant to be quantified by a differential equation relating the output (position) to the input (the frequency reference of the inverter).

### 4. MODELLING THE PLANT

From the linear machine theory[6], it was expected that a non-linear model would be obtained for the plant. Thus a control design method that can cope with system non-linearities had to be employed. For this reason, it was decided to use the quantitative feedback control design philosophy (otherwise known as QFT). This technique treats the non-linear system as a series of linear systems and then treats the variations in the models as variations in the parameters of a nominal plant.

For this plant model, input-output relationships for every half metre combination on the 6 metre track were obtained. This was done using a manual control system with automatic measuring and logging of data done on the computer. Input/output data sets were obtained for the machine not carrying any load, as well as a 40 kg load. Second order models were then fitted to the input/output data and this information was transformed into the frequency domain since the entire control design was to be done there.

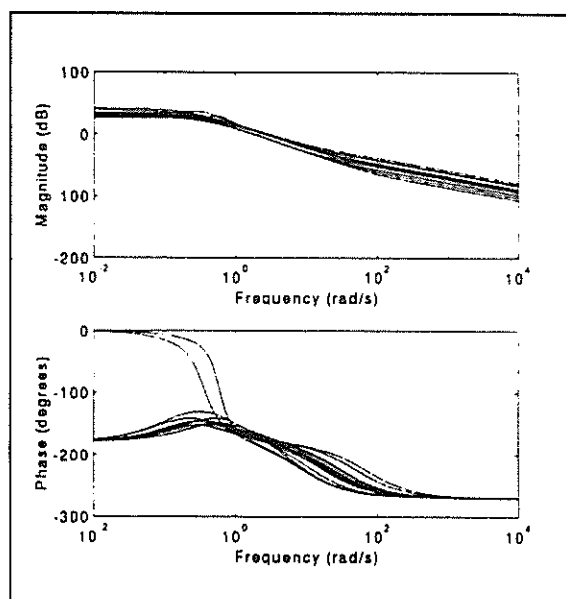


Figure 4: Plant models in Bode magnitude and phase format

Figure 4 shows all the plant models in Bode magnitude and phase format plotted on top of each other. One can see clearly that the models could be thought of as having a set amount of variation between two boundaries

## 5. CONTROL DESIGN

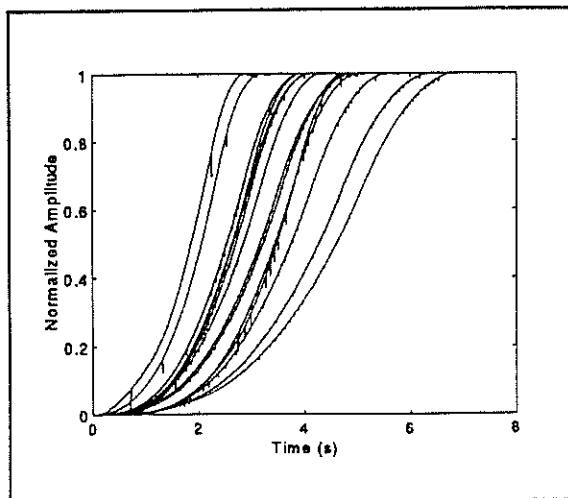


Figure 5: Normalised experimental step response specifications for the closed loop system

Once the plant had been modelled, it was necessary to determine the desired closed loop performance specifications. These specifications were in fact determined by manually driving the system in the way in which one would expect the closed loop controller to do it. Effectively, the inputs to the manual control system (the human operator) were step inputs of varying amplitudes and the outputs were the position responses associated with the inputs. Figure 5 shows the shape of the experimental responses normalised with respect to their step inputs. By fitting models to these sets of input/output data, the frequency domain specifications of the closed loop system were determined.

Figure 3 shows that the controller  $K(s)$  lies inside the loop, while the pre-filter  $H(s)$  lies outside and acts as an open loop controller. The QFT philosophy dictates that the purpose of the controller  $K(s)$  and feedback is to reduce the amount of variation in the system at a particular frequency to lie within the uncertainty bounds as dictated by the closed loop specifications. Once the plant uncertainty has been contained in this manner, the pre-filter  $H(s)$  is employed to meet the performance specifications.

There are standard ways of designing a controller using the QFT approach with the aid of a Nichols chart and Bode plots [7,8] and the controller  $K$  was designed using this technique. The pre-filter was designed after this to meet the performance specifications.

The controller and pre-filter are simply two differential equations. Once these had been

obtained, they were transformed into difference equations using the  $z$  transform and then implemented as software.

## 6. DISCUSSION OF RESULTS

The closed loop specifications on the system magnitude are shown in Figure 6 in the frequency domain as the dotted lines. The solid lines show how the final closed loop system with controller and pre-filter actually met the specifications.

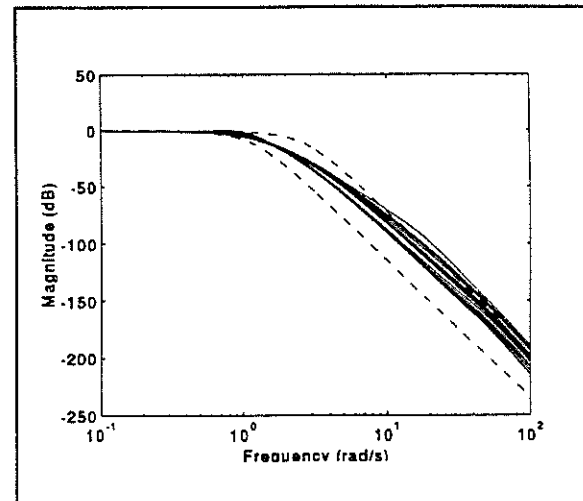


Figure 6: Showing how the closed loop system met the frequency domain specifications

One can see that the specifications were violated at high frequencies, but this is of little consequence since the gain is at most -65 dB at this point, which will have almost no effect on the system. There was also a small violation at 1 rad/s which could have been eliminated if more time was spent on the design of the loop controller  $K(s)$ .

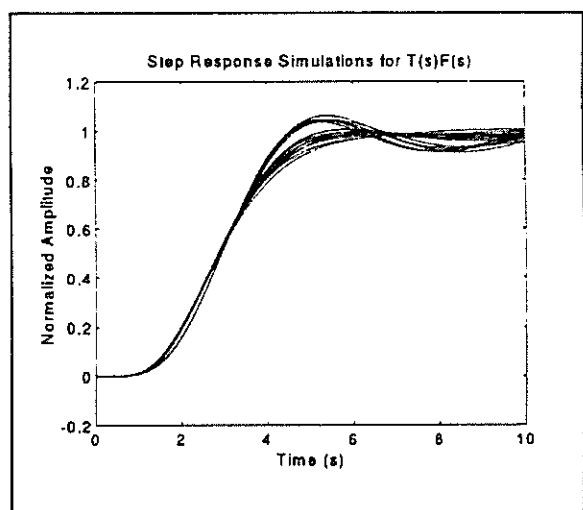


Figure 7: Normalised closed step responses of the system with the pre-filter and controller

Figure 7 shows the normalised closed loop step responses for the system that were obtained with the controller and pre-filter present. If one compares these to the time domain specifications in Figure 5, one can see that the rise times are all fairly similar and there is minimal overshoot. The overshoot is in fact due to the low frequency violation that was elaborated on earlier and could possibly have been eliminated with more careful design.

## 7. FUTURE TRENDS

Position control of linear induction motors is a relatively new subject. Very few papers on linear induction motors have discussed position control in any great detail and to date no papers have been found that have dealt with position control of linear machines in a quantitative manner.

Even though a linear induction motor lift has not physically been built, the results obtained showed that accurate position control of a linear induction motor can be achieved using Quantitative Feedback Theory. A similar control design approach could easily be employed for a vertical system.

Thus, if the proposed mine hoist scheme is implemented, the need for the cable would be eliminated altogether. Even with the poorer power factor and efficiency associated with linear induction motors, the overall energy utilisation of the hoisting system will be dramatically improved. More importantly, there is no limitation placed on the operating depth of the hoist.

These findings are particularly significant to the South African mining industry in that the mining houses are now one step closer to accessing the wealth of the ore-bodies lying below 4000 metres.

## REFERENCES

- [1] Stewart, A.T. Hoisting systems for ultra-deep vertical shafts, *Proceedings of the XVth Congress of Mining and Metallurgical Institutions*, Sun City, September 1994.
- [2] Girodo, A.M. and Sparg, A.N. Comparison of hoisting scenarios with a view to future trends, *Proceedings of the South African Institute of Mechanical Engineering Conference on Mine Transport Systems for Men, Minerals and Ore*, Johannesburg, September 1994.
- [3] Nasar, S.A. and Boldea, I. *Linear Motion Electric Machines*, New York: John Wiley & Sons, 1976.
- [4] Boldea, I. and Nasar, S.A. *Linear Motion Electromagnetic Systems*, New York: Wiley-Interscience, 1985.
- [5] Laithwaite, E.R. *Propulsion without Wheels*, 2nd ed., Aylesbury, Hazel Watson & Viney Ltd, 1970.
- [6] Pai, R.M., Boldea, I. and Nasar, S.A. A complete equivalent circuit of a linear induction motor with sheet secondary, *IEEE Transactions on Magnetics*, vol. 24, no. 1, January 1988, p639-654.
- [7] Horowitz, I. *Quantitative Feedback Theory*, vol. 1, Boulder: QFT Publications, 1992.
- [8] D'Azzo, J.J. and Huppis, C.A. *Linear Control System Analysis and Design - Conventional and Modern*, 3rd ed., New York: McGraw-Hill Publishers, 1988.

## ADDRESSES OF AUTHORS

Mr RJ Cruise, Department of Electrical Engineering, University of the Witwatersrand, PO Wits, 2050.

Mr JF Pritchard, Department of Electrical Engineering, University of the Witwatersrand, PO Wits, 2050.

Professor CF Landy, Department of Electrical Engineering, University of the Witwatersrand, PO Wits, 2050.

# SOLID STATE TORQUE CONTROL OF SLIP-RING INDUCTION MACHINES

Werner Deyzel

Anglo American Research Laboratories (PTY)LTD.  
Pretoria Technikon

## ABSTRACT

The purpose of this study is to, with the aid of experimentation and research, formulate a method of controlling and increasing the low speed torque of slip-ring induction motors by switching an external resistance in the rotor circuit and to synchronise this switching with the rotor frequency.

## INTRODUCTION

Three phase induction motors are used on a number of gold mining shafts as winders. The typical operation of a winder, i.e. that it starts with full load, requires that the motor generate a high starting torque. This is accomplished by inserting a resistance in the rotor circuit at start-up and removing this resistance to allow full speed to be achieved. In practice, a caustic soda bath is used as the resistance and this is varied by moving a dipper in the bath. The dipper is moved by a servo motor which uses as its set point the position of the drivers control lever. This is an extremely expensive system and requires constant maintenance and the system needs to be replaced at regular intervals.

Anglo American Research Laboratories was commissioned to undertake a feasibility study of an alternative method of torque control which uses no moving parts. The scope of this study encompasses examination of the present technique employed, a literature survey of alternative methods and the proposal of an acceptable alternative, if any exists.

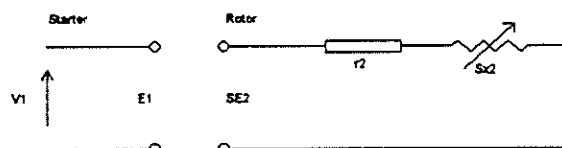


Figure 1: A representation of an ideal induction motor

Where:

- $V_1$  - applied voltage to stator winding
- $E_1$  - emf  $E_1$  induced by magnetic flux
- $SE_2$  - emf induced in rotor winding at slip  $S$
- $S$  - slip (0 - 1)
- $I_2$  - rotor current

$r_2$  - rotor resistance  
 $x_2$  - rotor inductance

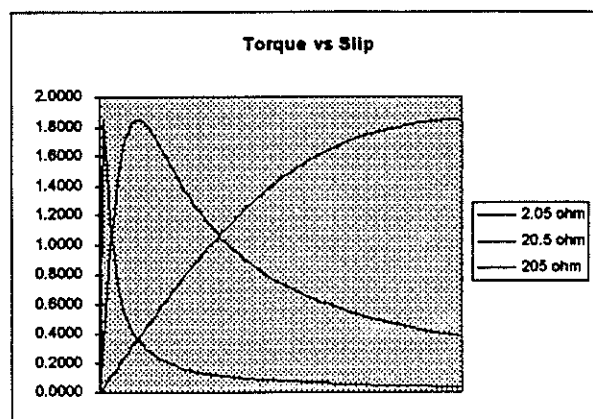


Figure 2: Rotor slip versus torque with different external resistance.

The graph shown above is typical of a slip-ring induction machine with different resistance switched in the rotor circuit. Slip of 1 indicates start-up and a slip of 0 indicates maximum rotor speed. It can clearly be seen that if the external resistance is gradually reduced the induction machine will have maximum torque at any value of slip. The smaller the change in resistance the closer the torque curve will be to a straight line at maximum torque. By using a solid state switching device to change the resistance value in each phase of the rotor circuit it will be possible to keep the machine as close as possible to it's maximum torque point, at all times.

## AVAILABLE SYSTEMS

One system which is currently available uses a number of external resistors in series in each phase of the rotor circuit. The speed of the rotor is constantly monitored and mechanical contacts are used to cut out one or a number of the resistors in each phase, depending on the speed of the machine at that instant. This reduces the external resistance and the rotor speed increases. The switching of resistors continues until the rotor circuit is short circuited (no external resistance) and the rotor can then turn at full speed, or the pre-selected operation speed is reached.

For mining winder applications this method is not suitable due to a shock induced into the winder ropes every time the resistance value is changed. This drastically shortens the lifetime of a rope, which can have a great cost implication for the mine. If an infinite number of resistors can be used the fluctuations in torque can be minimal, but this is not possible in practice.

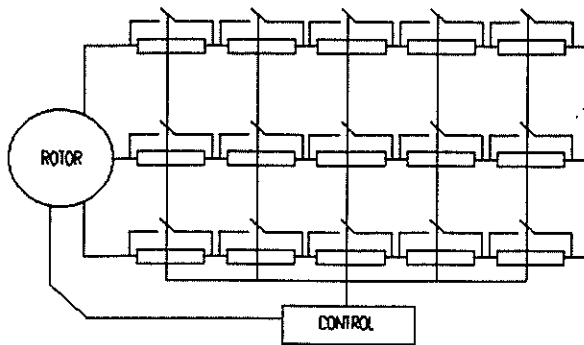


Figure 3: Typical system with number of series external resistors.

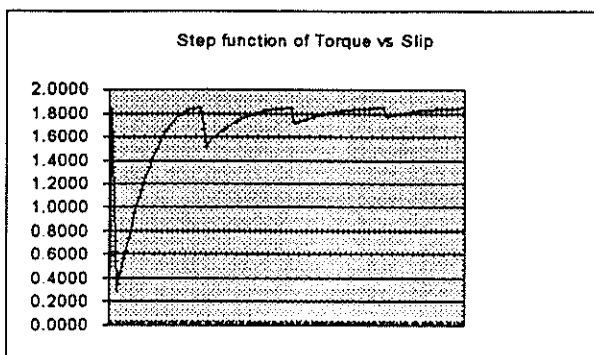


Figure 4: Torque curve of above system.

In the torque curve shown above a system with 5 resistors in each phase of the rotor circuit was used. It can be seen that the maximum torque varies and a step function is obtained. It is this step function which causes the shocks in the system. Although this specific torque step function is enlarged if compared to practice, it is merely to illustrate the effect of the increasing torque during resistance increase or decrease.

#### Scope of this study

In this study two different methods of switching the external rotor resistance was looked at.

#### METHOD 1: Single resistance in DC circuit

This method which will be the ideal system was only looked at in theory and it was then decided not to experiment any further with this specific configuration.

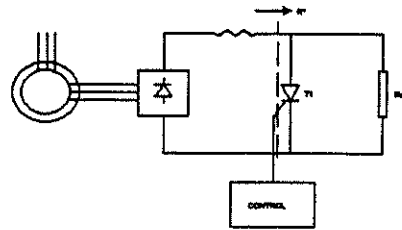


Figure 5: System with single resistance in DC circuit.

#### METHOD OF OPERATION

The rotor voltage is rectified and a single external resistor is placed in the DC circuit.

By switching T1 the effective external resistance  $R^*$  may be varied in a continuous and contact less manner. When the rotor reaches full speed the external resistance will be shunted, allowing the condition of low rotor resistance at high speeds to be met. This system does not require synchronisation with the rotor frequency and only need the speed of the rotor as an input to calculate the switching period of the switching device.

The type of device to use as the switching mechanism would typically be an Insulated Gate Bi-polar Transistor, commonly known as an IGBT. These devices can be controlled with a CMOS level signal which makes the design of the control circuitry uncomplicated. A number of these devices can be used in parallel which makes the current capabilities of these devices virtually unlimited.

One great shortcoming of these devices is the maximum potential difference which can be handled between cathode and emitter. The maximum voltage these devices (which is currently available locally) can handle is in the region of 400V. This maximum voltage includes the transients that can be generated during switching at high currents and if this maximum voltage is exceeded the device destroys itself.

For small induction machines with rotor voltages in the region of 110VAC this type of system would be perfect, but the purpose of this study is to find a method of switching the external rotor resistance in motors used on winders in the mines and the rotor voltage for these machines is in excess of 1000 volt.

#### METHOD 2: Three separate resistors, one in each phase of the rotor circuit.

This method was used for the experiments and control circuitry was developed to control the induction machine with this system.

In this configuration three single resistors are used, one in each phase of the rotor circuit. Each resistor has as its

switching device two thyristors places over the resistor, back to front. (see descriptive figure below)

This method of switching requires synchronisation with the frequency of the rotor, as the rotor voltage zero points are used to switch off the thyristors.

The rotor frequency is picked up using a transformer between two phases of the rotor. Two isolating resistors is used to isolate the transformer from the rotor and prevent short circuiting of the transformer at near full speed of the rotor when the theoretical frequency of the rotor voltage is zero hertz.

The frequency of only one phase of the rotor is measured and this is done by measuring the length of the positive half of that phase voltage. The assumption is made that the rotor speed will not change until the next positive cycle for this specific phase of the rotor. The frequency of the other two phases are therefor taken as the same as that of the first phase.

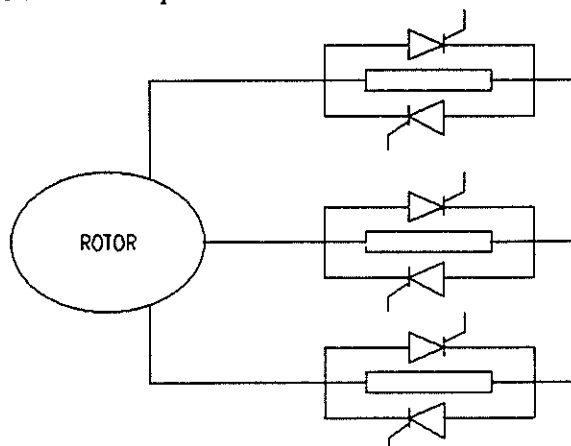


Figure 6: Setup of resistors and thyristors in rotor circuit

The figure above illustrates the method of switching which will be used. Each thyristor acts as a valve to let the rotor "see" a percentage of the resistor during each cycle. By changing the firing angle of the thyristors the amount of resistance switched into the rotor circuit can be increased or decreased depending on the speed of the rotor and the speed selection made by the machine operator.

The firing of the thyristors is symmetrical i.e. the top and bottom thyristor of each resistor have the exact same on and off time. The same applies for the thyristors in the second and third phases.

### CALCULATION OF EFFECTIVE EXTERNAL RESISTANCE

The effective resistance induced into the rotor circuit at specific firing angles can be calculated using the following diagram and equation.

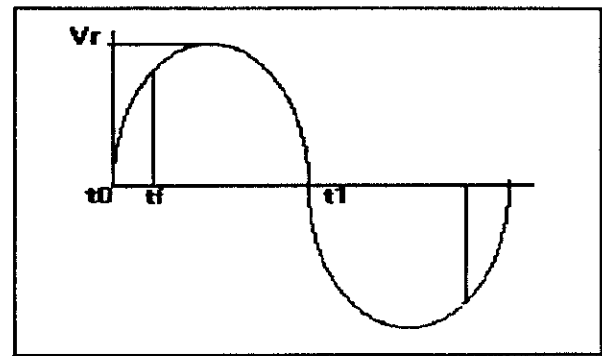


Figure 7: Firing angle on rotor voltage

Where:

$V_r$  = rotor voltage

$t_1 - t_0$  = rotor frequency (period)

$t_f$  = time of firing thyristor

The equation to calculate the effective resistance is as follows:

$$R_{eff} = R_{tot} \frac{\int_{t_f}^{t_1} \sin x dx}{\int_{t_0}^{t_1} \sin x dx}$$

Equation 1: Resistance calculation

Where:

$R_{eff}$  = Resistance induced in rotor circuit

$R_{tot}$  = Total external resistance

$t_f$  = firing angle

For the purposes of my experiments the percentage resistance change due to the holding voltage of the thyristors was ignored.

### SWITCHING CONTROL CIRCUIT

The thyristors will be switched by signals obtained from a Digital Signal Processor (DSP) controlled circuit which will use the rotor frequency as a synchronisation signal.

The processor used is a Texas Instruments DSP with a 14-bit analogue to digital converter, multiplexed to eight channels, as one of its inputs. An 8-bit digital input and output port and three 12-bit digital to analogue converters complete the I/O on this system.

The rotor frequency and a speed selection are read as analogue values and used by the DSP to calculate the firing angles of the six thyristors. The digital output port on the DSP card is used to output the pulses triggering the firing circuit of each individual thyristor.

The software running on the DSP was written in Assembly Language.

The firing order of the thyristors is equivalent to that of a thyristor controlled three phase full wave controllers.

### MODIFICATION OF SYSTEM

When the system was first tested there were constant interference between the different thyristor groups. The motor would start to run uneven and the speed would increase even if a high resistor value were selected.

The voltages across each thyristor were monitored and it could be seen that the firing of one bank of thyristors would distort the voltage across the next phase.

To solve this a small (only small in resistor value, not wattage) was placed in series with each external resistor to isolate the one bank from the other.

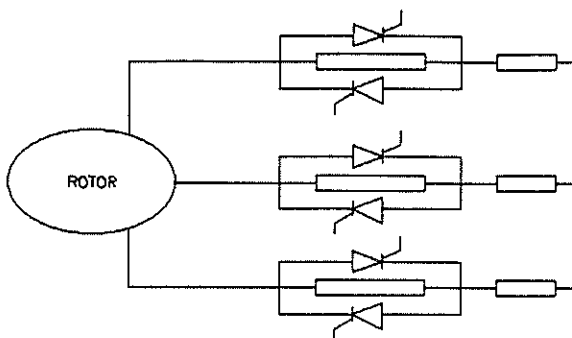


Figure 8: Extra resistors for isolation

The insertion of these resistors completely solved the problem of interference between the different rotor phases.

### GENERATION OF HARMONICS

One part of the project which is incomplete is the measurement on the motor and the mains power to determine the side effects caused by this method of switching.

Due to the gradual change in the external resistance which will cause the current in the rotor to stay constant I do not expect any heat build up in the rotor which has been side effects of other methods of resistance control.

One other side effect which will be measured for is the induction of harmonics in the mains power. If this is the case then different options in the firing angles of the thyristors can be looked at for instance non-symmetrical firing of the thyristor banks.

### CONCLUSION

With the results already obtained from these experiments, this method of switching the external resistance in the

rotor circuit of a slip-ring induction machine seems to be successful. The results however still needs to be extrapolated for induction machines in the mega watt range.

### REFERENCES

- [1] M.G. Say, "Alternating current machines", Pitman Publishing Limited 1977
- [2] T.A. Lipo, "Control by symmetrically triggered thyristors", IEEE Transactions on Power Apparatus and Systems, vol. PAS-90, No 2, pp. 515-525, March/April 1971.
- [3] C.Sen Pareesh, K.H.J. Ma, "Rotor chopper control for induction motor drive. TRC strategy", IEEE Transactions on Industry Applications, vol. 1A-11, No 1, pp. 43-49, January/February 1975.
- [4] P.R. Basu, "A variable speed induction motor using thyristors in the secondary circuit", IEEE Transactions on Power Apparatus and Systems, vol. PAS-90, No 2, pp. 509-514, March/April 1971.
- [5] M. Ramamoorthy, M. Arunachalam, "A solid state controller for slipring induction motors", pp. 88-93, IAS 1977 Annual.

### ADDRESS OF AUTHOR

Werner Deyzel, Anglo American Research Laboratories, Electronics Department, P.O. Box 106, Crown Mines, Johannesburg, 2025.

The inputs of the programmable controller are connected to devices such as control switches and sensors. The outputs of the programmable controller

are used to drive indicator lamps, relays and contactors. A microcomputer is used to control the process. It writes the program, which is then in turn transferred to the memory module in the S5-100U. The P C 100U is the programmable controller that executes the program. References [2] shows its internal structure and exterior.

A SAMES three phase power/Energy meter module is chosen to measure power and energy. Average power is calculated according to the formula:

$$\text{Average power} = \sqrt{1/t} \int v i dt,$$

This method of calculation takes the power factor into account. The measured energy and control is accessed via a serial interface having a RS 232 protocol. [3]

### 3 PROGRAMMABLE CONTROLLER OPERATION

For the control of rotating UPS, it need for low-cost, versatile and easily commissioned controllers has resulted in the development of programmable control systems standard units based on a hardware CPU and memory. Originally designed as a replacement for the hard-wired relay and timer logic to be found in traditional control panels, PLCs provide ease and flexibility of control based on programming and executing simple logic instructions (often in ladder diagram form). PLC have internal functions such as timers, counters and shift registers, making sophisticated control possible using even the smallest PLC.

A programmable controller operates by examining the input signals from a process and carrying out logic instructions (which have been programmed into its memory) on these input signals, producing output signals to drive process equipment or machinery. Standard interfaces built in to PLCs allow them to be directly connected to process actuators and transducers (e.g., circuit breakers and contactors) without the need for intermediate circuitry or relays.

Using PLCs it became possible to modify a control system without having to disconnect or re-route a single wire; it was necessary to change only the control program using a keyboard. Programmable controllers also require shorter installation and commissioning times than do hardwired systems. Although PLCs are similar to 'conventional' computers in terms of hardware technology, they have specific features suited to industrial control:

1. rugged, noise immune equipment;
2. modular plug-in construction, allowing easy replacement/addition of units (e.g. input/output);

3. standard input /output connections and signal levels;
4. easily understood programming language (e.g. ladder diagram or function chart);
5. ease of programming and reprogramming in-plant.

These features make programmable controllers highly desirable in a wide variety of industrial-plant and process-control situations.

The programming panel translates or compiles these graphic symbols into machine (logic) instructions that are stored in the PLC memory, relieving the user of this task.

S5-100u may use a personal computer connected to the controller via a serial link (normally RS232). The high speed operation and screen graphics facilities of machines like the IBM PC are ideal for graphics programming of ladder circuits, and allowing real-time observation of switches, gates and functions during program execution, this can be valuable for troubleshooting, especially when the target process is remote or inaccessible.etc. [4]

Ladder diagrams have been the most common method of describing relay logic circuits, so it was only natural to base PLC programming on them in order to create a familiar environment for the user and designer of small logic control systems.

The most common technique used for programming small PLCs is to draw a ladder diagram of the logic to be used, then convert this into mnemonic instructions which will be keyed into a programming panel attached to the programmable controller. These instructions are similar in appearance to assembly type codes, but refer to physical inputs, outputs and functions within the PLC itself.

These instructions are used to program logic control circuits that have been designed in ladder diagram form, by assigning all physical inputs and outputs with an operand (address) suitable to the PLC being used.

### -4 -PROGRAM DEVELOPMENT

Once a PLC with the necessary facilities has been selected for a particular application, the tasks of software design and development have to be considered. In rotating UPS control system (see Fig 1), the control functions can be implemented using combinational networks.

In rotating UPS control system, PLC control switches (k1,k2,.....k5) operate through program according to appropriate operate mode. Consider the following operate mode:

\* When rotating UPS operates as a three phase synchronous motor, sensor A is activated, main switch k11 on, load switch k2 on, measuring switch k3 on (k5 off), k4 electromagnetic brake switch off.

\* When rotating UPS operates as a asynchronous generator, sensor B is activated, main switch k13 on, load switch k2 on, k4 electromagnetic brake switch on, measuring switch k5 on (k3 off).

\* When rotating UPS operates as an extra load added artificially. Sensor B is activated, main switch k12 on, load switch k2 off, k4 switch on, k5 switch on, switches k2,k3 off.

It clearly illustrates the concept of the outputs determined purely by a combination of inputs. Logic circuits can be described using Boolean algebra, which provides a framework of standard rules and relationships concerning binary logic. Any logic circuit or program may be converted into a Boolean equation, which shows how the inputs are related to derive the output for that circuit.

Programmable controller operates with the following addresses for inputs and outputs listed in the left-hand column: (see table 5.1)

Table 5.1 PLC inputs and outputs variables.

Address	Variable
I 8.0	sensor A
I 8.1	sensor B
I 8.2	main switch
I 8.3	load switch
I 8.4	measuring switch
I 8.5	electromagnetic brake switch
Q 12.0	main switch
Q 12.1	load switch
Q 12.2	measuring switch
Q 12.3	electromagnetic brake switch
Q 12.4	load switch
Q 12.5	measuring switch

\* I : input variable

\* Q : output variable

Similar expressions would be produced for every output device in the system, based on the operate conditions and actions of the rotating UPS. At this level of ladder design, it is easily to sketch out the circuit operations and then produce the ladder logic version. This would then be encoded and programmed

into the target PLC. As can be seen from Fig 2, it can easily express the overall design of system ladder diagram.

Once ladder diagram and logic function have obtained for each output, they have to be translated into a form that can be entered into a PLC.

## 5 POWER MEASUREMENT

Power measurement is achieved by means of sensors, also called *direction of power flow sensor*, and involves the gathering of data and its display. (see Fig 1). Measurement is also concerned with providing information about the state of rotating UPS system. Here the objective of the measurement is to assist exercise control over the rotating UPS system and the measurement are made repeatedly, continually, and automatically.

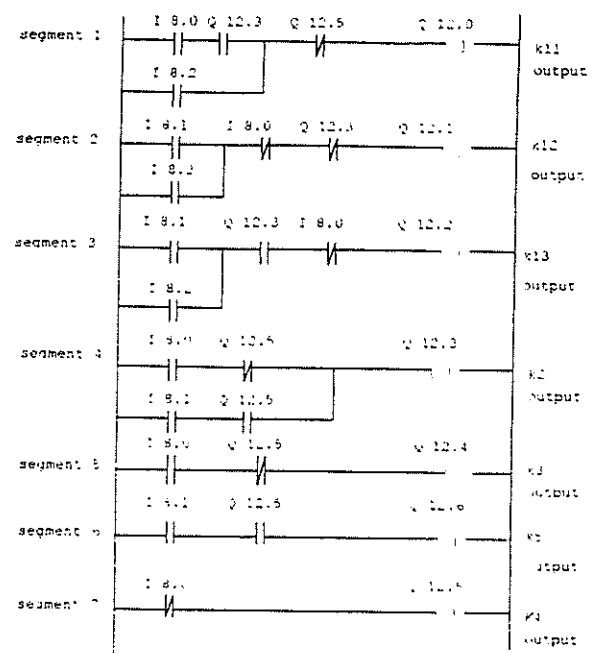


Fig 2 : System ladder diagram

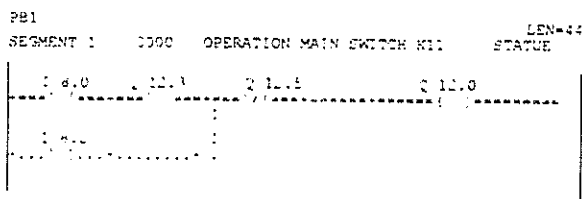
A SAMES three phase power/energy metering integrated circuit (IC) was employed to the measurement unit. [3] It designed to function in conjunction with a  $\mu$ -controller, performs the multiplication of the line current and voltage, over a dynamic range of greater than 60dB, to an accuracy of better than 1%. The measured energy as well as control of these measurements is accessed via a serial interface having a RS232 protocol, and transmitted to the personal computer. The current sensor use a shunt resistor for current sensing, power supply offer +5V, DC for integrated oversampling A/D converters.

## 6 TESTS AND MEASUREMENTS OF THE CONTROL SYSTEM

The inputs of the programmable controller are connected to the simulation control switches, and the outputs of the programmable controller are used to drive signal lamps. All of the control switches and signal lamps be used to simulate control switches of rotating UPS control system, and laidout on a simulation circuit-board.

Fig 3 illustrates a monitoring display with status information shown on the bottom of the screen. It is important to realize that the display on the programmer does not update as rapidly as the control program is executing, due to the delays in transmitting the data across to the terminal. To display all changes, the PLC should be run in single-step mode.

The monitor display shows a selected portion of the ladder program, using standard symbols to depict contacts, outputs and present functions. All elements within the display are dynamically monitored, indicating their status processing active (energized, de-energized, open or closed). [5]



\* ===+=== : circuit closed

\* ...+... : circuit open

Fig 3: Status processing active

Measurement unit's testing and simulation use a application software package, which supplied by SAMES [3].

## 7 CONCLUSIONS AND RECOMMENDATION

A rotating UPS control system using a programmable controller is proposed for the purpose of realizing high quality of power supply (for a large UPS), low voltage fluctuation, compact structure, low price and high reliability. A complete control scheme is proposed. PLC software is developed and verified by simulation and experiment.

The following conclusions can be obtained from the discussion presented in this thesis:

1. The proposed control system is very simple and reliable because of the use of a programmable

controller. The PLC is simplified with depend on user program and I/O points.

2. The program development and process control is monitored on-line. Indication of the status of input/output channels is provided by light-emitting diodes (LEDs) on I/O unit, making it simple to check the operation of process inputs and outputs from the PLC itself.

3. The mode of operation or control can easily be changed.

4. The control system program and installation is simple and flexible because of the use of standard program language.

5. Due to accurately measured power values, the low voltage fluctuation of the load is available when the rotating UPS changes its operation mode.

The power factor is measured on-line and automatically compensated for using the PLC.

## 8 ACKNOWLEDGEMENTS

I would like to thank the following people for their contribution to this article: My study leader professor E.D. Smith for his leadership, encouragement and support. Professor W J Taute for his support and assistance in his laboratory.

University of Pretoria for supplying me with a Research assistantship.

## 9 REFERENCES

1. Smith E D & J Yang, "A New Rotating UPS", SAUPEC 1995.
2. Siemens, Simatic S5 "Training course S10 part one of three", RSA, 1991. pp.6-29.
3. Sames. SA 9104 Three Phase Power/Energy Metering IC Serial interface, South African Micro-Electronic System (Pty) Ltd. PO Box 15888 Lynn East. 0039. pp.63-73, 1994.
4. Davie, I. D., "The PC user's workstation", PC '85 Conference Proceedings, Peter Peregrinus Ltd, No. 25.
5. Siemens. Simatic S5 "STEP 5 Basic package manual". Federerel Republic of Germany, No. 6ES5998-0sc21 Release 01. Siemens AG 1991. pp.6.1-48.

Mr J Yang and Prof E D Smith, Dept of Electrical and Electronic Engineering, University of Pretoria, PRETORIA, 0002.

# FINITE ELEMENT ASSESSMENT OF EDDY-CURRENT STARTERS

R Melaia, A S Meyer, C F Landy

University of the Witwatersrand, Johannesburg, South Africa

The electromagnetic properties of lossy inductor-based eddy-current starters for slip-ring induction motors were assessed with the aid of finite element methods. The results of the analyses were used to predict the frequency dependence and current dependence of the starter's magnetising inductance and core loss. Several designs were studied but since one of the main objectives of the research was to produce an improved application-and-design procedure for a particular design, most of the results apply specifically to this design. The paper includes descriptions of existing methods of determining eddy-current starter parameters and compares them with the method initiated for this research.

## 1. INTRODUCTION

Although power electronic drives are making slip-ring induction motors less and less common, there are still many applications in which this type of motor is more cost-effective or practical than a conventional motor with a variable speed drive, particularly where a large output is required. The only significant problem with the slip-ring induction motor is the starting device, which usually takes the form of an added resistance in the rotor circuit. The main types are switched resistors, liquid or vapour starters, and eddy-current starters.

When compared to other starting devices [1], the eddy-current starter has a smooth torque characteristic and is relatively maintenance-free, but it fails to produce as much motor torque as the other devices. The reason for the limited torque is the nature of the eddy-current starter designs themselves [2], most of which were developed before finite element methods (FEM) could be effectively utilised to optimise the design of the starter core. For this reason, the design and analysis of existing designs has been based partly on empirical approximations and equations [3,4,5,6,7,8] based on the real part of the

Poynting Vector, i.e. power transferred by an electromagnetic wave is given by the equation  $P = E \times H$  where  $E$  and  $H$  are the electric and magnetic field vectors respectively.

Although many FEM techniques for non-linear eddy-current problems have been documented [9-19], the implementation of these methods is time-consuming and difficult to apply to a variety of geometries. Despite their limitations, it was therefore considered practical to make use of commercially available FEM packages. Consequently, the analysis described in this paper illustrates many of the advantages and disadvantages of using existing finite element analysis packages for practical problem solving, as well as the importance of producing an accurate model which is as simple as possible in order to minimise computation time.

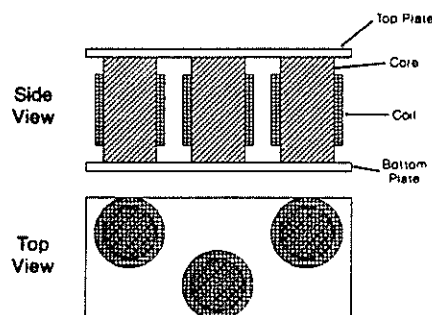


Figure 1: The basic geometry

## 2. THE BASIC FINITE ELEMENT MODEL

The requirements of the FEM study were to predict the two most important parameters of the starter: the core loss and the magnetising inductance. The available software [20] contained an eddy-current solver but this was limited to two-dimensional geometry and linear magnetic materials.

The model had to include compensation for the linear magnetic

material limitation but, by careful modelling of specific cross-sections of the starter, the two-dimensional solver was adequate.

Figure 1 illustrates the basic structure of a three-phase eddy-current starter. As indicated, the cores are solid cylinders while the top and bottom limbs are solid plates; both are made of mild steel which has suitable magnetic and electric properties. Since the core is designed to be heavily saturated in normal operating conditions, the magnetising flux is limited by the minimum effective cross-sectional area at any stage of the flux path, this parameter has to be determined by taking the whole geometry into account and then considering only that section of the flux path which presents the smallest effective cross-sectional area to the flux.

As far as the magnetising inductance is concerned, the general objective of the FEM modelling would be to determine this parameter with the aid of a two-dimensional model of the cross-section of two complete cores and the top and bottom plates between them. This provides an approximation of the three-dimensional effects of the starter's geometry on the flux path, effectively permitting leakage effects to be quantified.

It is very important to determine the magnitude of the leakage flux because the core remains heavily saturated during normal operation, and the magnetising inductance should be maintained as high as possible in order for the starter to have an acceptable power factor. A separate two-dimensional model of the cross-section of the core is used to determine the current density at all points in the core. The core loss is then equal to the product of the resistivity of the core material and the integral of the current density over the complete cross-sectional area [21].

The two models thereby enable the determination of the two most important parameters of the starter, approximating three-dimensional effects by using two separate two-dimensional models, both of which allow eddy-current effects to be included in the simulation.

### 3. FREQUENCY VARIATION AND SATURATION EFFECTS

Skin-depth and saturation are important parameters in the determination of the

equivalent circuit of the starter. Frequency effects are taken into account directly by the FEM solver, but since non-linear magnetic materials are not permitted by the solver, a technique of dividing the core cross-section into several thin concentric circles or segments of predetermined (constant) permeability is used to account for this limitation.

A numerical integral was developed to calculate the permeability of each segment as a function of frequency and excitation, making use of approximations [22,24] to take the magnetisation curve into account. Initial simulations and observations [23,25] verified that hysteresis loss was small enough to neglect in the core-loss calculations.

## 4. SIMULATION RESULTS

With the aid of the FEM simulation results and the approximate equations described, the performance of the eddy-current starter could be predicted by plotting the variation of the most important parameters with frequency and excitation. The most important of these graphs are as follows:

### 4.1 VARYING EXCITATION

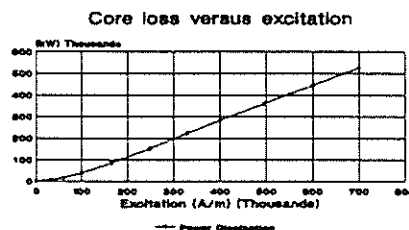


Figure 2: Core loss versus Excitation

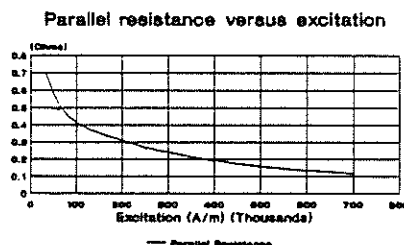
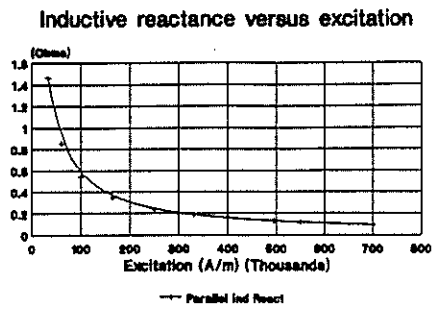
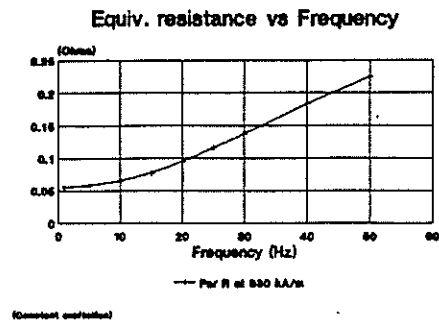


Figure 3: Resistance versus excitation



**Figure 4:** Inductive reactance versus excitation



**Figure 7:** Equivalent parallel resistance versus frequency for constant excitation

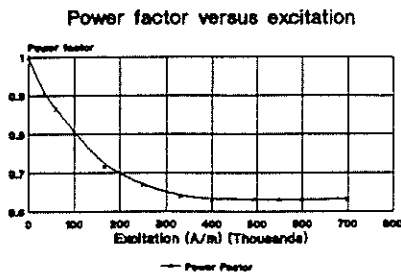


**Figure 5:** Power factor versus excitation

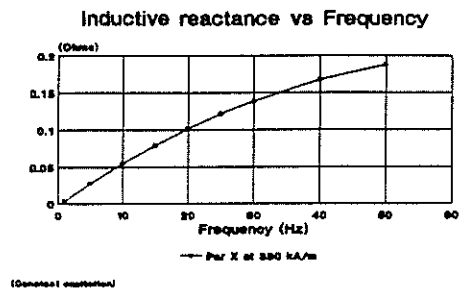


**Figure 8:** Equivalent parallel inductive reactance versus frequency for constant excitation

## 4.2 VARYING FREQUENCY

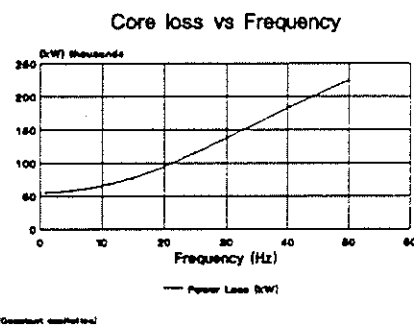


**Figure 6:** Core loss versus frequency with constant excitation

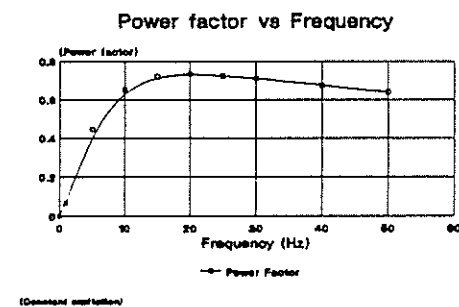


**Figure 9:** Power factor versus frequency for constant excitation

## 4.3 DISCUSSION OF RESULTS

With the exception of the graph of core loss against excitation, the parameters vary according to theoretical predictions. The magnetising inductance drops as the core is saturated, and the resistance is inversely

proportional to the square of the current; the graphs show the same trend being predicted by the FEM simulation results. The interesting parameter is power factor which shows a peak at an intermediate frequency and a steady decrease as excitation is increased.

## 5. IMPLEMENTATION OF RESULTS

The results of the analysis were implemented by approximating the resulting functions by polynomials, and including these in a computer program which calculates the torque-speed and current-speed curves for a motor and eddy-current starter system. Since the parameter variations are mostly non-linear, the main algorithm of the program is an iterative procedure based on Euler's method.

## 6. CASE STUDIES AND MEASUREMENTS

In order to illustrate the effectiveness of a correctly designed eddy-current starter system, the following two figures represent the torque-speed and current-speed curves for a 460 kilowatt slip-ring induction motor without any added rotor resistance (Figure 10) and with a commercially available eddy-current starter system installed in the rotor circuit (Figure 11).

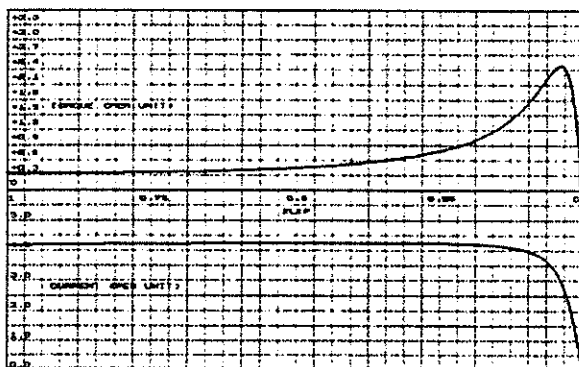
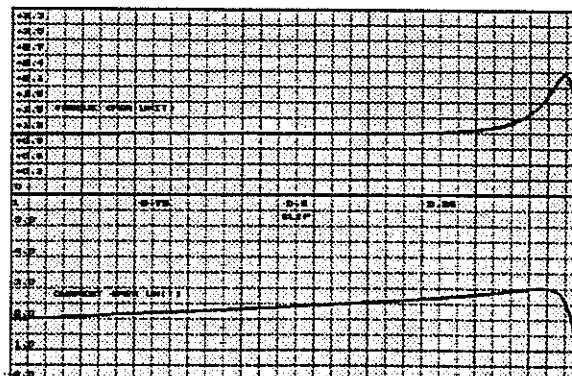


**Figure 10:** 460 kW motor performance without added rotor resistance

The example shows that an eddy-current starter can produce a considerable increase in torque and a corresponding decrease in current. Although these are simulation results, the method used has been applied to existing systems with good correlation.



## 7. CONCLUSION

This paper demonstrates the effective application of finite element analysis to a problem that shows no obvious evidence of previously being approached in such a way. It also shows the effectiveness of a correctly designed eddy-current starter and the problems associated with an incorrectly designed starter or incorrectly specified starter system, as well as the possibility of producing an improved design with the aid of FEM techniques.

## 8. ACKNOWLEDGEMENTS

The authors wish to extend their gratitude and appreciation to Mr Eric Stratford of Stratford Engineering (Pty) Ltd, and Mr John Stratford of Safronics (Pty) Ltd for assistance rendered throughout this research.

## 9. REFERENCES

- [1] Say, M.G.: "Alternating Current Machines" Fourth Edition, Pitman, pp. 282-285, 1976.
- [2] Holzhausen, H.F.: "Theory and design of eddy-current starters", Phd Thesis,, University of the Witwatersrand, 1957.
- [3] Mayergoyz, I.D., Abdel-Kader, F.M., Emad, F.P.: "On penetration of electromagnetic fields into nonlinear conducting ferromagnetic media" J. Appl. Phys. 55 (3), pp. 618-629, 1 February 1984.
- [4] Konrad, A.: "Eddy currents and modelling", IEEE Trans on Mag, Vol. MAG-21, No.5, pp.1805, Sept 1985.

- [5] Ramadan, A.M., Fawzi, T.H., Burke P.E.: "Calculation of the fields and power in a short magnetic cylinder in a transverse time-harmonic magnetic field", IEEE Trans on Magnetics, Vol. MAG-22, No.5, pp. 1254-1256, Sept. 1986.
- [6] Lavers, J.D. et al: "An evaluation of loss models for nonlinear eddy current problems", IEEE Trans on Magnetics, Vol. MAG-21, No.5, pp. 1850-1852, Sept. 1985.
- [7] Lammeraner, J., Stafl, M.: "Eddy Currents", Iliffe Books Ltd., pp. 165-214, 1966.
- [8] Chalmers, B.J.: "Electromagnetic problems of A.C. Machines", Chapman & Hall, pp. 65-77, 1965.
- [9] Ida, N.: "Modelling of velocity effects in eddy current applications", J. Appl. Phys., 63 (8), 3007-3010, 15 April 1988.
- [10] Chari, M.V.K., Bedrosian, G.: "A hybrid method for eddy current open-boundary field computation", J. Appl. Phys., 63 (8), pp. 3019-3021, 15 April 1988.
- [11] Chari, M.V.K.: "Nonlinear and hysteresis modelling of soft magnetic materials for electrical devices", J. Appl. Phys., 57 (1), pp. 3841-3843, 15 April 1985.
- [12] Lean, H.M.: "Dual simple-layer source formulation for two-dimensional eddy current and skin effect problems", J. Appl. Phys., 57 (1), pp. 3844-3846, 15 April 1985.
- [13] Fawzi, T.H., Ahmed, M.T., Burke P.E.: "Computation of high-frequency TM eddy-current losses in magnetic materials", J. Appl. Phys., 57 (1), pp. 3863-3865, 15 April 1985.
- [14] Ali, K.F., Ahmed, M.T., Burke, P.E.: "Surface impedance- BEM technique for nonlinear TM-eddy current problems", J. Appl. Phys., 61 (8), pp. 3925-3927, 15 April 1987.
- [15] Ratnajeevan, S., Hoole, H., Shin, J.K.: "Solution of cyclic magnetic fields in three dimensions", J. Appl. Phys., 61 (8), pp. 3928-3930, 15 April 1987.
- [16] Rodger, D., Eastham, J.P.: "A formulation for low frequency eddy current solutions", IEEE Trans on Magnetics, Vol. MAG-19, No. 6, pp. 2443-2446, November 1983.
- [17] Simkin, J.: "Eddy current modelling in three dimensions", IEEE Trans on Magnetics, Vol. MAG-22, No. 5, pp. 609-613, September 1986.
- [18] Fawzi, T.H., Ahmed, T.H., Burke, P.E.: "On the use of the impedance boundary conditions in eddy current problems", IEEE Trans on Magnetics, Vol. MAG-21, No. 5, pp. 1835-1840, September 1985.
- [19] Hussein, A.M., Biringer, P.P.: "Current distribution in conductors in the vicinity of magnetic bodies", IEEE Trans on Magnetics, Vol. MAG-21, No. 5, pp. 1844-1846, September 1985.
- [20] MAXWELL, Axial eddy-current FEM solver, Ansoft corp., 1994.
- [21] Balanis, C.A.: "Advanced Engineering Electromagnetics", Wiley, pp. 28-30, 1989.
- [22] Weeber, K. et al.: "Linear-exponential functions for eddy current analysis", J. Appl. Phys., 63 (8), pp. 3010-3012, 15 April 1988.
- [23] Mayergoyz, I.D.: "Mathematical models of hysteresis", IEEE Trans on Magnetics, Vol. MAG-22, No. 5, pp. 603-608, September 1986.
- [24] Brauer, J.R.: "Simple equations for the magnetisation and reluctivity of steel", Letters, IEEE Trans on Magnetics, Vol. MAG-21, No. 5, pp. 81, September 1985.
- [25] Doong, T., Mayergoyz, I.D.: "On numerical implementation of hysteresis models", IEEE Trans on Magnetics, Vol. MAG-21, No. 5, pp. 1853-1855, September 1985.

# MODELLING THE EFFICIENCY OF DOMESTIC HOT WATER PIPE SYSTEMS TO ASSESS THE POTENTIAL OF DSM OPTIONS

JC van Tonder & IE Lane

Centre for New Electricity Studies  
Department of Electrical and Electronic Engineering

LJ Grobler

Centre for Experimental and Numerical Thermoflow  
Department of Mechanical Engineering

University of Pretoria  
South Africa

## Abstract

*A numerical heat transfer analysis technique was used to estimate the effect of various parameters of a hot water pipe system on its efficiency. Simulation scenarios include different pipe materials, lengths of pipe and flow rates. These parameters represent various demand-side management options for hot water pipe systems. Efficiency profiles which were created by simulation are used to calculate the relative kilowatt hour losses under conservative assumptions. Results have shown that the use of polypropylene pipes should provide an excellent opportunity to improve energy efficiency of hot water pipe systems. Pipe lengths also influence the efficiency considerably. It is therefore advisable to keep locations of hot water supply points close together inside the home.*

## 1. Introduction

Demand-side management (DSM) plays an increasingly important part in the strategic planning process of electric utilities. As it does so, accurate forecasting of DSM program impacts becomes essential to incorporate the impact of these programs into utilities' resource plans with confidence [1]. One of the utility programs falling under the umbrella of DSM is strategic conservation [2]. This paper will focus on modelling DSM options that affect the efficiency of domestic water heating systems.

Most domestic water heating systems can be divided into two distinctly different components: the water heater and the pipes that carry the water to the location where it is consumed by the customer. Analysis of the energy performance of water heating systems [3] have had a tendency to emphasise the behaviour and losses of the storage vessel. The pipe losses have been shown to be of similar significance [4].

The efficiency of pipe systems in domestic homes is mainly influenced by the pipe material used, the length of pipes and the amount of water drawn at a time. To determine the efficiency of pipe installation one can resort to one of two main methods: Experimental investigation or theoretical calculation. Experimental investigation often involves high costs, therefore it was

decided to make use of mathematical modelling.

For the physical processes of interest here the mathematical model mainly consists of a set of differential equations. Since analytical solutions of very few problems of this type are possible, it is necessary to turn to numerical solving techniques. The resulting thermodynamic characteristic of different types of pipe installations will lead us to important conclusions of possible demand-side management options. These topics will now be discussed in more detail.

## 2. Pipe Losses in a Domestic Water Heating System

Pipe losses in a domestic water heating system take place under two distinguishable conditions. In the first instance the water in the pipes is stationary and part of the pipe connected to the geyser is heated because of conduction of heat from the geyser. Heat exchange with the surrounding air takes place through the mechanism of natural convection and results in loss of energy. When hot water flows the pipes can be heated to the temperature of the water. The heating mechanisms involved here are forced convection and conduction. Once the temperature of the pipe rises above ambient temperature heat energy is again lost through natural convection.

## 3. Mathematical Formulation of Heat Transfer Phenomena

The heat transfer phenomena involved in our investigation can be described by the following differential equation [5]:

$$\frac{\partial}{\partial t}(\rho c \phi) + \frac{\partial}{\partial x_j}(\rho c u_j \phi) - \frac{\partial}{\partial x_j} \left( k \frac{\partial \phi}{\partial x_j} \right) = S \quad (1)$$

The equation is represented in the Cartesian-tensor form where the subscript  $j$  can take the values 1, 2, 3 denoting the three space coordinates. The four terms in the differential equation are the unsteady term, the convection term, the diffusion term and the source term. Further the flow field should satisfy an additional

constraint, namely, the mass conservation or the continuity equation which is:

$$\frac{\partial}{\partial t}(\rho c) + \frac{\partial}{\partial x_j}(\rho c u_j) = 0 \quad (2)$$

The symbols are as follows:

$\phi$	=	temperature ( $^{\circ}\text{C}$ )
$t$	=	time (s)
$\rho$	=	density ( $\text{kg} / \text{m}^3$ )
$c$	=	specific heat ( $\text{J} / \text{kg} \cdot ^{\circ}\text{C}$ )
$u_i$	=	velocity ( $\text{m} / \text{s}$ )
$k$	=	thermal conductivity ( $\text{W} / \text{m} \cdot ^{\circ}\text{C}$ )
$S$	=	heat source ( $\text{W} / \text{m}^3$ )
$x_i$	=	displacement (m)

With the constraint expressed in equation (2) the differential equation of (1) can be written as:

$$\rho c \frac{\partial \phi}{\partial t} + \rho c u_j \frac{\partial \phi}{\partial x_j} + \frac{\partial}{\partial x_j} \left( k \frac{\partial \phi}{\partial x_j} \right) = S \quad (3)$$

A numerical solution of the differential equation consists of a set of numbers from which the distribution of the dependent variable  $\phi$  can be constructed. Thus the values of  $\phi$  will be treated as the unknowns at a finite number of locations (called the grid points) in the calculation domain. In focusing attention on the values at the grid points, we have replaced the continuous information contained in the exact solution of the differential equation with discrete values. We have thus discretized the distribution of  $\phi$ , and it is appropriate to refer to this class of numerical methods as discretization methods. The discretization of space and the dependent variables make it possible to replace the governing differential equation with simple algebraic equations, which can be solved with relative ease [5].

#### 4. Efficiency Analysis

The goal of the efficiency analysis is to compare different types of pipe that are found in houses. The three types of pipes in question are: Galvanized steel, copper and plastic (polypropylene) pipes. A certain length of pipe exposed to air is analysed for various flow rates and volumes of water drawn at different ambient temperatures. The different configurations that are considered is summarised in table 1.

Table 1

	Material	Length	Volume	Flow rate	Ambient temp.
1	Galvanized	5 m	60 l	0.3 l/s	25 $^{\circ}\text{C}$
2	Galvanized	5 m	60 l	0.3 l/s	6 $^{\circ}\text{C}$
3	Galvanized	5 m	30	0.1	25 $^{\circ}\text{C}$
4	Galvanized	5 m	3 l	0.05 l/s	25 $^{\circ}\text{C}$
5	Galvanized	3 m	60 l	0.3 l/s	25 $^{\circ}\text{C}$
6	Galvanized	7 m	60 l	0.3 l/s	25 $^{\circ}\text{C}$
7	Copper	5 m	60 l	0.3 l/s	25 $^{\circ}\text{C}$
8	Polypropylene	5 m	60 l	0.3 l/s	25 $^{\circ}\text{C}$

The volumes of water and flow rates were chosen to represent actual water use events. 60 l hot water at 0.3 l/s represents a bath being filled. A typical shower is 30 litre at 0.1 l/s and washing hands 3 litre at 0.05 l/s. These values were compiled from information obtained in [4, 6 & 7].

The obvious choice for initial conditions are steady state, i.e. the conditions that will prevail if no water was used for a long period of time. Under such conditions the pipe temperature at the storage vessel will equal the thermostat setting and it will exponentially decrease along the pipe. There is a slight temperature gradient from the centre of the pipe to the surface. Average profile for the different types of pipes are shown in figure 1.

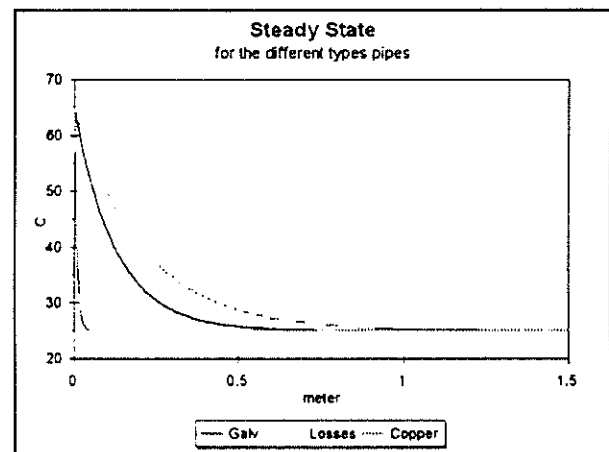


Figure 1: Initial temperature profiles for the different pipe materials

Before we can continue to compare results of the various scenario's, we have to define a way to calculate the efficiency and the related loss of energy.

#### 4.1. Definition of Efficiency

Since the pipes are heated once hot water starts to flow the rate of heat transfer will diminish once water flow is in progress. Consequently the efficiency will be a function of the volume of water that has flown. For this reason we shall define the instantaneous efficiency of the pipe system as follows:

$$\eta(v) = \frac{m \cdot C \{T_{out}(v) - T_{air}\}}{m \cdot C \{T_{in} - T_{air}\}} \quad (4)$$

where:

$T_{in}$  = water temperature at geyser outlet (assumed constant and equal to the thermostat set point)

$T_{out}(v)$  = water temperature at pipe outlet (this is a function of litres of water that is released from the geyser)

$v$  = The volume of water that has flowed (litre)

The input and output temperatures need to be normalised by subtracting the ambient temperature. The reason for this is that water delivered at ambient temperature implies no transfer of energy from the storage vessel to the outlet. To be able to calculate energy losses we need to know the cumulative efficiency which is:

$$\eta_c(L) = \frac{\int_0^L (T_{out}(v) - T_{air}) dv}{(T_{in} - T_{air}) \cdot L} \quad (5)$$

#### 4.2. Calculation of Energy Losses

There are two types of losses we are interested in. The first is the steady state losses which prevail under the initial steady state conditions. The other type of losses will be referred to as the dynamic losses. These losses occur as a result of water that is flowing and it includes losses which occur while the pipe is returning to steady state.

##### 4.2.1. Steady State Losses

The steady state losses can be calculated directly from the steady state temperature profile at the surface of the pipe. The losses are proportional to the surface area and the temperature difference between the pipe and the air. The proportionality constant  $h$  is the heat

transfer coefficient for air during free convection. Equation (6) shows the relationship.

$$P_{SL} = \int_0^M 2 \pi r_o h (T(z) - T_{air}) dz \quad \text{Watt} \quad (6)$$

where  $z$  is the distance from the heat source along the length of the pipe,  $M$  is the total length and  $d_o$  the pipe diameter.

##### 4.2.2. Dynamic Losses

The dynamic energy losses are defined by equation (7). It is a function of the cumulative efficiency and the input energy. The input energy in turn is defined as the energy that was added to the water inside the geyser, i.e. the energy needed to increase the water's temperature from ambient temperature to that of the thermostat setting.

$$Q_{loss}(L) = [1 - \eta_c(L)] Q_{in}(L) \quad (7)$$

where  $Q_{in}$  is represents the input energy.

#### 5. Results

Although temperatures for all coordinates in the calculation domain have to be calculated to obtain a solution we are only interested in the water temperature at the outlet. This information will enable us to calculate the cumulative efficiency and energy losses. The result of the first simulation listed in table 1 is shown in figure 2.

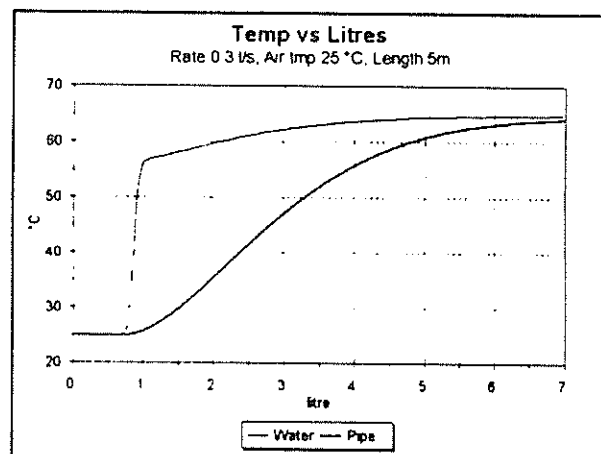


Figure 2: Average water and pipe temperatures at pipe outlet vs litres drawn

It can be seen that the average water and pipe temperatures reach steady state conditions after approximately seven litres of water has flown. The

efficiency plot of this simulation scenario is shown in figure 3.

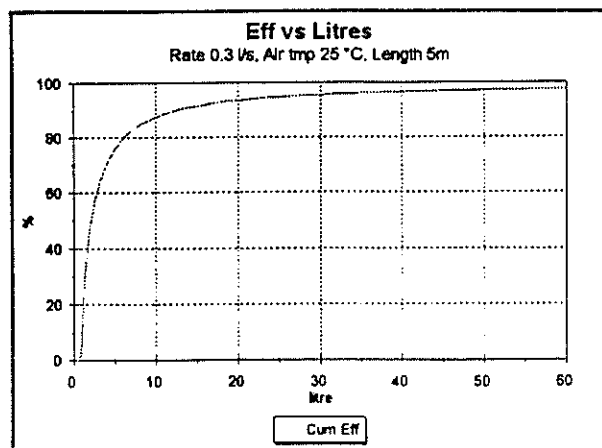


Figure 3: Efficiency of five metres of galvanized pipe for a flow rate of 0.3 l/s and ambient temperature 25 °C

We shall now continue to compare results of other simulations with this case.

### 5.1. The Effect of Ambient Temperature

Although the temperature profile for this case is different from figure 2 the efficiency profile looks exactly the same as the one in figure 3. The reason for this is obvious: none of the physical parameters of the pipe system were altered therefore the system efficiency will remain constant.

### 5.2. The Effect of Different Flow Rates

Flow restrictors is one DSM option that may be applied. The goal of this is to save energy by reducing the amount of water used for some applications like washing hands or showering. To estimate the impact of

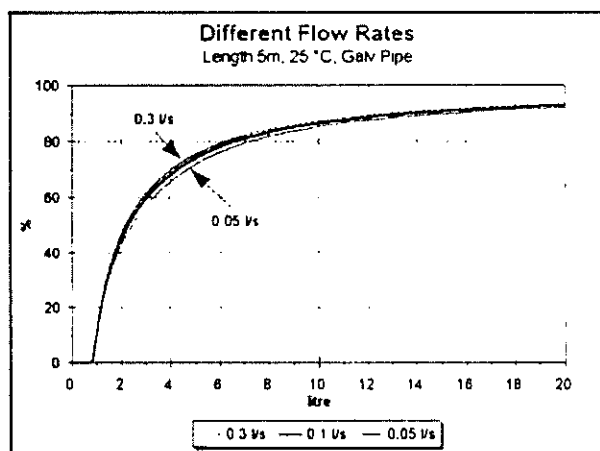


Figure 4: Efficiency for 5m of galvanized pipe at 25°C for different flow rates

this DSM option on the efficiency of the hot water pipe system simulations with varying flow rates were done. Efficiency curves for these simulations are shown in figure 4.

### 5.3. Efficiency for Variable Lengths of Pipe

Another DSM option concerning domestic water heating that may be applied is to create aqua cells inside the residents. The idea of this is to place all the hot water supply points inside the house like bathrooms and the kitchen close together. By doing so pipe losses may be minimised. Simulations for variable pipe lengths were executed to determine the effect this will have on the pipe efficiency. Results of these simulations is shown in figure 5.

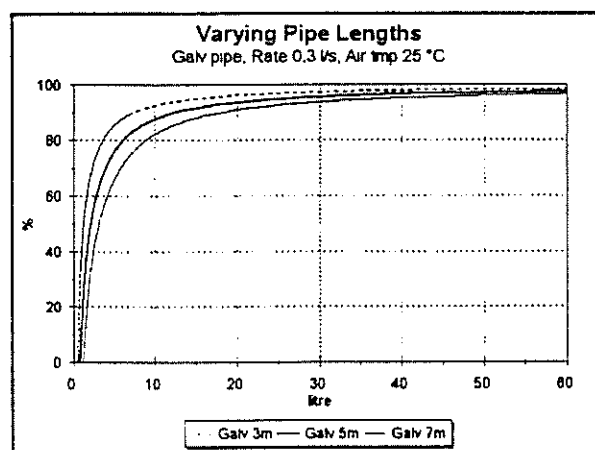


Figure 5: Efficiency profiles for varying lengths of galvanised pipe.

### 5.4. Efficiency for Different Pipe Materials

Traditionally galvanised pipes are used most frequently inside domestic homes in the interior while copper pipes are most popular along the coast. Recently plastic pipe also came on the scene. The thermodynamic properties

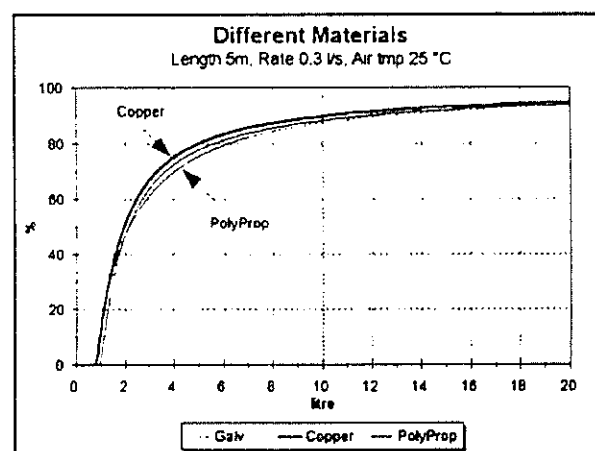


Figure 6: Comparative efficiency curves for different pipe materials

of these pipes keeps some promise for energy conservation as a DSM option. Comparative simulations were done for these types of pipes and the results are shown in figure 6.

## 6. Discussion

When a person fills her bath she desires to fill it to a certain level and wants the water to be at a comfortable temperature. Therefore a variation in pipe losses implies that she will need a different mixture of hot and cold water to fill the bath to personal preference. This variation will have an impact on the daily use of electricity for a typical house.

It is not possible to determine the exact energy savings for any of the options we considered. Even if the number and sizes of typical water use events for an average home were known calculations will be inaccurate since initial pipe conditions for every water use event will be different. Initial pipe conditions will depend on temperature variations on different times of the day as well as the time duration between water use events. For this reason we will compare steady state losses for the whole day at an average ambient temperature of 15 °C and dynamic losses for the first hot water use event of the day.

In both cases the pipe configuration and flow rates of table 1 will be considered with the following changes: An ambient temperature of 5°C and water usage of 60 ℓ will be use. Equation (6) is used to calculate steady state losses and equation (7) for the dynamic losses.

Table 2: Relative pipe losses per geysers per month

Pipe Losses for Base Scenario (kWh)		
	Steady State	Dynamic
2	2.35	2.84
Relative Losses of Other Scenario's (%)		
3	0	114 %
4	0	141 %
5	0	60 %
6	0	141 %
7	147 %	77 %
8	11 %	94 %

## 7. Conclusion

From the table above it is obvious that polypropylene pipes {8} stand out far beyond the rest, the reason for this being its extremely low losses under steady state

conditions. Although copper's {7} dynamic losses is less, polypropylene's low thermal conductivity together with its relative high specific heat, will cause it to remain at a higher temperature for a longer time after water was used, suggesting that during usage later in the day it may well outperform the copper pipes which has the highest thermal conductivity and the lowest specific heat.

A drawback of polypropylene pipes that also need to be considered is their mechanical properties. Creeping of the plastic together with the effect of abrupt temperature changes may cause problems in the long term.

The fact that lower flow rates {3, 4} influence the dynamic losses negatively doesn't imply that flow restricters is a bad DSM option. The difference in the efficiency is so little (see figure 4) that it is totally outweighed by the energy saved due to a reduction in water usage.

Variable pipe lengths have a definite influence on the energy losses of hot water pipe systems therefore the principle of keeping hot water supply locations as close as possible to the geysers inside the house will lead to considerable saving in the long term.

It is important that this study must only be considered as a starting point for further research since important factors such as the effect of flow patterns and pipes running inside brick walls were not taken into consideration. The losses listed in table 2 should therefore be viewed from this perspective and is only useful for qualitative comparison of the different scenarios.

## 8. References

- [1] B A Smith, M R McRae & E L Tabakin, "Issues in Forecasting Demand-Side Management Program Impacts", Proceedings of the IEEE, Vol. 73, No. 10, October 1985
- [2] C W Gellings, "The Concept of Demand-Side Management for Electric Utilities", Proceedings of the IEEE, Vol. 73, No. 10, October 1985
- [3] W W Shultz & V W Goldschmidt, "Energy Performance of a Residential Electric Water Heater"
- [4] N Beule, "Domestic Utilisation of Electrical Grid Energy in South Africa", Ph.D Thesis, Potchefstroom University for Christian Higher Education, 1993
- [5] S V Patankar, "Numerical Heat Transfer and Fluid Flow", Hemisphere Publishing Corporation, 1980
- [6] W Kempton, "Residential Hot Water: A Behavior-Driven System", Energy Vol. 13, No. 1, 1988
- [7] G. J. Parker & A. S. Tucker, "Dynamic Simulation of a Domestic Hot-Water System.", Applied Energy 40, 1991

# DOMESTIC STOCHASTIC PROCESS EVALUATION FOR NETWORKS OF DECENTRALISED LOAD CONTROLLERS

GL VAN HARMELEN

IE LANE

Centre for New Electricity Studies, Department of Electrical and Electronic Engineering, University of Pretoria, Pretoria, South Africa, 0002

## ABSTRACT

The stochastic process which describes the electrical usage patterns of a domestic dwelling has very strong periodic trends (notably daily and weekly variations), with determinable probability distribution parameters. This paper shows how a non-homogeneous Poisson process, as well as a vector exponential smoothing forecaster can be employed by a decentralised intelligent load controller algorithm to predict customer usage of a particular device. The paper concentrates on describing and modelling the times at which domestic events occur. This is of great importance if a domestic load controller is striving to optimise bill reductions under time-differentiated tariff conditions.

## INTRODUCTION

In the observation of domestic usage patterns, it is relatively evident that in general, domestic activity is high directly before and after working hours, medium during the afternoon luncheon period, and considerably lower at other times. In general it is therefore true that the average number of events per period displays a periodic nature with a 24 hour cyclic period. In those cases where expected usage is high, and the device is capable of storing energy, preventative control can be exercised (e.g. preheating water). If no storage capability exists, rescheduling could be an alternative and may be suggested to the occupants of the house. It is obvious therefore that being able to predict the load beforehand is an invaluable load controller input.

This paper presents an investigation into the modelling, simulation and estimation of domestic stochastic processes. This is done so as to gain a better understanding of them, and in order to use their predictability as inputs to intelligent load control algorithms.

## BACKGROUND

In order to model and understand domestic processes, it is necessary to model the periodic behaviour of the domestic environment. Probability distributions for the size of an event, once it has occurred, may be

found from the theory of random variables. In order to describe the change in distribution parameters as they progress in time, use must however be made of the theory of stochastic processes [3].

Stationary processes are special cases of stochastic processes where their statistical properties are invariant to a shift in the origin. This means that the process  $x(t)$  and  $x(t+c)$  have the same statistics for any  $c$ . However, this is not true for the domestic environment as the processes involved have a 24 hour (as well as weekly) cyclic nature. This 24 hour periodicity for the smallest element which makes up a totalized domestic load profile, namely a single house, may easily be shown from an autocorrelation analysis of the unprocessed totalized load current. Fig. 1. shows the autocorrelation function for data sampled during one week from a house in Brooklyn in Pretoria (only analysed during weekdays). Similar results were obtained from several other homes measured.

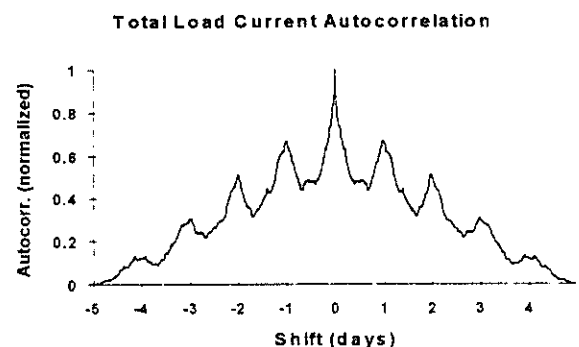


Fig. 1: Normalised autocorrelation of totalized load current for a single home.

Because the same things happen at the same times every day, the statistics of a domestic process for the same times should be deterministic. It has also been found that when large groups of data are averaged, the load values converge to a specific value. These factors indicate a cyclostationary process which means that the statistics of the process are invariant to a shift of time origin by integral multiples of a constant  $T$  (period) [3]. This means that at the same time every day, the statistical properties of the stochastic process are similar to that of the same time during the previous period, and are determined from the distribution function at that time such that,

$F(x_1 \dots x_n, t_1 + mT \dots t_n + mT) = F(x_1 \dots x_n, t_1 \dots t_n)$  (1)  
where  $F$  is a probability distribution function.

## SIZE OF EVENTS

Probability density functions depicting the magnitude (duration) of specific events for domestic activities may be found by measurement, utilising a questionnaire, or even by observing the electrical labelling on the equipment in use. Size of events relate to the their total energy consumption (amount of kWh used), and as most appliances have fixed ratings, this relates directly to the duration of their use. (e.g. if it takes 500 kJ to boil a small kettle, at a power rating of 2 kW, this would take 250 seconds). Once one is able to model when events will occur, their sizes (or duration) may be determined from size probability density functions, which are in general functions of time as in eq. 1. The next section deals with the modelling of when events occur, so that time dependant size distributions can be employed to estimate domestic energy usage functions.

## MODELLING EVENT OCCURRENCES

An intuitive way to describe the usage of a kettle would be to relate it's use to the number of times a person uses it in the morning, during the afternoon and during the evening. The same is true for the number of baths in the morning, or the number of rooms lit in the evening. In all these cases, the number of events per time interval is specified. This can also be stated in it's reciprocal form which would mean the average time between events.

Let  $\lambda$  stand for the average number of events per unit time in such a case. Depending on the time of day, this value will change and therefore in general  $\lambda = \lambda(t)$ . Suppose further that the events occurring in a household conform to the following postulates:

1) The duration of non-overlapping intervals between events are independent and obey the events per unit time criterion. It is therefore assumed that there is no reason why a short interval between two events would exert an influence on the duration between any two other events.

2) For a small interval  $\Delta t$ , the chance of an event occurring in that interval, is approximately proportional to the duration of that interval.

$$\frac{P(\text{exactly 1 event in } (t, t + \Delta t))}{\Delta t} \rightarrow \lambda(t) \text{ as } \Delta t \rightarrow 0 \quad (2)$$

This means that for small time intervals, doubling the length of the interval will double the probability that an event occurs in that interval.

3) The chance of more than 1 event in an interval of length  $\Delta t$  is negligible for  $\Delta t \approx 0$

If these postulates can be satisfied, then this process is called a non-homogeneous Poisson process, or a Poisson process in a varying environment. We know that if  $\lambda$  were constant and these postulates were satisfied, then  $N_t$ , the number of events in the period  $[0, t]$ , is Poisson distributed with parameter  $\lambda t$  [1].

In order to determine  $N_t$  if  $\lambda$  is a function of time, split the interval  $[0, t]$  into several smaller intervals so that  $\lambda(t) \approx \lambda(t_i)$  is approximately constant on the  $i$ 'th subinterval. The total number of events in  $[0, t]$  is then  $N_t = N_1 + \dots + N_n$  which is the sum of  $n$  independent Poisson random variables. Consequently,  $N_t$  is also a Poisson variable, distributed with parameter equal to the sum of the parameters

$$\lambda(t_1)\Delta t + \lambda(t_2)\Delta t + \dots + \lambda(t_n)\Delta t = \sum_{j=1}^n \lambda(t_j)\Delta t \quad (3)$$

When this sum is taken in the limit, it becomes an integral such that

$$\Lambda(t) = \int_0^t \lambda(u) du \quad (4)$$

This means that for  $j \geq 0$

$$P(N_t = j) = \frac{\Lambda(t)^j}{j!} e^{-\Lambda(t)} \quad (5)$$

with  $\Lambda(t)$  called the intensity function. From this, the probability may be found that the number of events are equal to some specific value  $j$ . This is however not very useful for determining when those events occurred and consequently the formulation for inter-event times is required instead [1,2].

## MODELLING INTER-EVENT TIMES

If we let  $T_1$  be the time until the first event occurs, then

$$\begin{aligned} P(T_1 > t) &= P(\text{no arrivals in } [0, t]) \\ &= P(N_t = 0) \\ &= \frac{\Lambda(t)^0}{0!} e^{-\Lambda(t)} \\ &= e^{-\Lambda(t)} \end{aligned} \quad (6)$$

which implies that  $T_1$  is exponentially distributed with parameter  $\Lambda(t)$ . Because non-overlapping intervals are independent, the same holds for  $T_2$ , because the process could be considered to have started at  $T_1$  (independence) and therefore the same argument can be used for the time between  $T_2$  and  $T_1$ .

From the definition of the probability distribution function

$$F(t) = P(T_1 \leq t) \quad (7)$$

so that

$$1 - F(t) = P(T_1 > t) = e^{-\Lambda(t)} \quad (8)$$

and

$$F(t) = \begin{cases} 0 & t \leq 0 \\ 1 - e^{-\Lambda(t)} & t \geq 0 \end{cases} \quad (9)$$

Since the probability density function is the derivative of the probability distribution function

$$f(t) = \begin{cases} 0 & t < 0 \\ e^{-\Lambda(t)} \frac{d\Lambda(t)}{dt} & t > 0 \end{cases} \quad (10)$$

We have thus found a way to determine the inter-event times for a non-homogeneous Poisson process if we know the intensity function. This result may now be used in a decentralised load controller to produce a forecast of when events occur (i.e. from inter-event times).

## IMPLEMENTATION

If information concerning the rates of domestic device usage is not available directly it is proposed here to derive this from an averaged load profile for that device. If the number of devices which are on at any time are known, then the time derivative of that function will produce a function depicting the change in the number of devices which are on per unit time. It is precisely this information which is required by equations 4-10.

The example which is shown here is for the lighting load in a domestic dwelling where it was assumed that the average light-bulb size was 100 Watt. Knowing the total lighting load, and subdividing this by the load for a single light-bulb, we therefore produce a function showing the number of light-bulbs ON at any time.

The average load curve for lighting measured over several houses for several months in Brooklyn is shown in Fig.2. From this, the average number of lights ON at any time may be determined if the assumption about average light-bulb size holds.

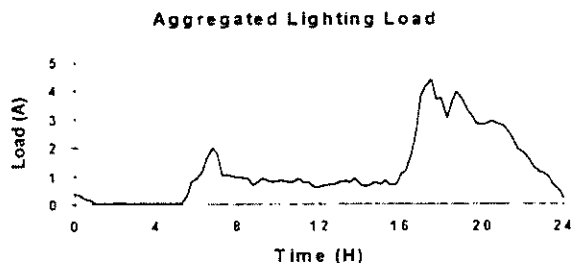


Fig. 2: Aggregated daily lighting load pattern.

The derivative of this function was taken, thus producing the ON and OFF switching rates as a function of time. Only being interested in those times at which lights are switched ON (the duration or size

of the lighting event must be determined by probability density functions), only those times where the derivative function was positive were considered. The average number of ON-switchings per time interval (i.e.  $\lambda(t)$ ) could therefore be found directly. The number of ON-switching events per unit time interval for the lighting load of Fig. 2 is shown in Fig. 3.

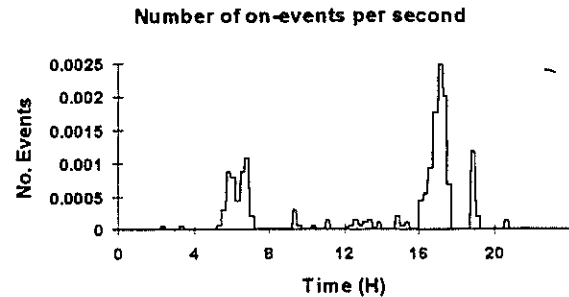


Fig.3: The switch-on events per unit time function  $\lambda(t)$ .

A simulation of 60 days' worth of lighting events was performed and the times that events occurred according to the exponential model were recorded. Assuming that each event has a duration which was Gaussian distributed with average 3 hours, at a rating of 100W, a predicted load profile could be rebuilt. In general the magnitude distribution must be a function of time also but this was not modelled in this paper. A graphical description of the process of rebuilding the lighting load is given in Fig. 4, and this resulted in a 24-hour before-hand prediction of lighting load as shown in Fig. 5.

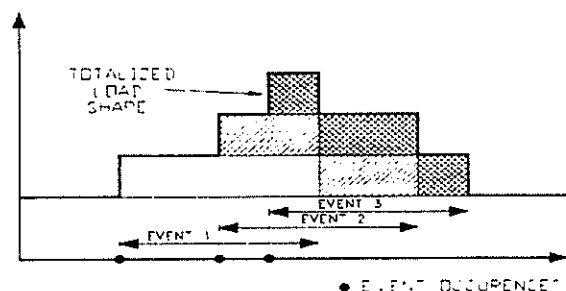


Fig. 4: Building a load profile from the occurrence of events, their duration and magnitudes.

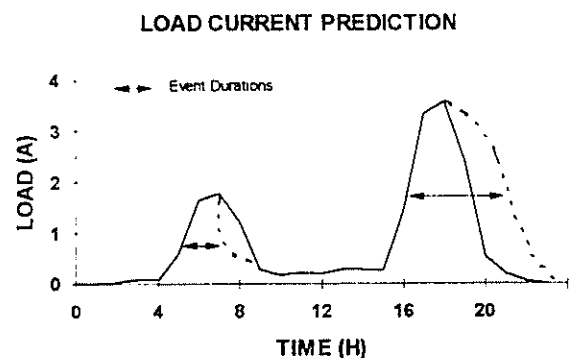


Fig. 5: Predicted load current from exponential model.

In an actual application, as the process continues, and measurements are added, a domestic load control algorithm could use a technique such as the exponential smoothing (to be discussed next) to modify  $\lambda(t)$  where such a system would indeed be "learning" the usage pattern.

If the size of event statistics were better known as a function of time, for example, instead of assuming a 3 hour average Gaussian distribution for all events (solid line), the morning events could well be shorter and the evening events longer (dotted line). This would obviously result in even greater accuracy when comparing predicted and actual loads (i.e. Fig.5 and Fig. 2.)

### VECTOR EXPONENTIAL SMOOTHING ESTIMATOR

In order therefore to continually adapt the estimate of the number of events per time interval, a vector exponential smoothing estimator is discussed next. This type of structure could be employed where the average usage for a time-slot (as in TOU tariff blocks) is required.

Due to the fact that the process of interest are not strictly stationary (i.e. the statistics of the process not independent of time), but cyclostationary, the process will in general have different statistics for different time intervals within a single period. If the total period  $T$  is therefore subdivided into  $n$  intervals, each of length  $dT$ , the statistics per period  $dT$  can be assumed to be constant if  $dT$  is small enough. A vector estimator can therefore be used, with one estimator for each of the  $n$  subintervals which make up  $T$ .

For each of the  $n$  estimators, the most well known forecasting by moving averages entails forecasting

$$\begin{aligned} F_{t+1} &= \frac{(X_t + X_{t-1} + \dots + X_{t-N+1})}{N} \\ &= \frac{1}{N} \sum_{i=t-N+1}^t X_i \end{aligned} \quad (11)$$

which is the same as writing

$$F_{t+1} = \frac{X_t}{N} + F_t - \frac{X_{t-N+1}}{N} \quad (12)$$

Supposing however that  $X_{t-N+1}$  is not available, it could be approximated by  $F_t$ , and substitution leads to

$$F_{t+1} = \left(\frac{1}{N}\right)X_t + \left(1 - \frac{1}{N}\right)F_t \quad (13)$$

Furthermore, substituting  $\alpha$  for  $1/N$ , the general form for forecasting by exponential smoothing is found as

$$F_{t+1} = \alpha X_t + (1 - \alpha)F_t \quad (14)$$

and this is also sometimes written as

$$F_{t+1} = F_t + \alpha e_t \quad (15)$$

where  $e_t = X_t - F_t$ . The forecaster thus corrects itself depending on it's previous prediction error [5].

For the vector estimator,  $n$  exponential smoothing forecasters are used in parallel, where each predictor operates on a specific period. For the results produced for lighting, the estimator for the period 16h00-20h00 is shown below, where for 30 days, the predicted and actual values are shown for the lighting load.

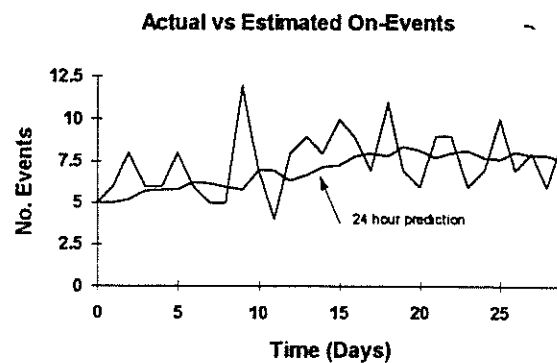


Fig. 6: Exponential smoothing prediction of number of events for the period 16h00-20h00.

In order to determine  $\alpha$ , the RMS error for this predictor was minimised by a gradient search algorithm. This found the optimum at  $\alpha = 0.200$  for this particular case. Because the process is considered stationary during the period during which the predictor is operational, and slowly varying with a long time constant (e.g. seasonal) it may be used successfully as forecaster for the following day's usage.

### CONCLUSION

In a domestic load controller environment, forecasting the customers usage is an important input parameter to load control algorithms, especially if the device in question has energy storage capabilities. In those cases, energy may be stored due to the expected usage which is forecast by a predictor.

The predictor which was shown here is easy to implement although the exponential smoothing requires optimisation of the alpha parameter which can be performed off-line. These methods may be used directly in domestic load controllers where the exponential distribution method has the advantage of being able to estimate when events occur so that the load controller can exercise appropriate control actions.

Future work entails implementing these algorithms and controllers in dedicated hardware, and evaluating them in the field on actual homes.

**NOMENCLATURE**

$F_t$	forecasted value at t
$X_t$	variable to be forecasted at time t
N	number of samples
T	period
$\alpha$	exponential smoothing adaptation gain
$\lambda(t)$	events per unit time, as a function of time
$\Lambda(t)$	intensity function, integral of $\lambda(t)$
F(t)	probability distribution function
f(t)	probability density function
TOU	Time of Use - tariff
P()	probability of ...
$N_t$	number of events at t
RMS	root mean square

**REFERENCES**

- 1 Solomon, F. : Probability and Stochastic Processes, Prentice Hall, Inc. 1987, pp. 116-246.
- 2 Leon-Garcia, A. : Probability and Random Processes for Electrical Engineering, University of Toronto, Addison-Wesley Publishing Company, 1989, pp. 194-258.
- 3 Papoulis, A. : Probability, Random Variables, and Stochastic Processes, 2nd Edition, Polytechnic Institute of New York, International Edition, McGraw-Hill Book Company, 1984, pp. 226-231.
- 4 Makridakis, S., Wheelright, S.C. : Forecasting : Methods and Applications, John Wiley & Sons, 1978, pp. 44-53.

# Domestic Lighting Load Shape Modelling Based on Survey Data

J.F. Peyper and I.E. Lane

Centre for New Electricity Studies (CNES)  
Department of Electrical and Electronic Engineering  
University of Pretoria

## Abstract

Three different functions which influence lighting consumption are defined. The concepts of an "availability" function, which statistically estimates the number of light fittings in a household that can be switched on, a "proclivity" function, which gives the probability that a light will be switched on at any given time of day, and the "usage" function, which gives the power rating of the light bulb, are developed for nine rooms. These functions are then used in an analytical method to generate a load profile for every room. The total load profile, for a winter season, is then compared to a measured profile and a simulated load profile.

## 1. NOMENCLATURE

$A_R$	-	availability of different numbers of light fittings
$D_R$	-	proclivity function
$K_R(xy)$	-	probability of getting X fittings with a category Y lights
$m$	-	number of types of light classified
$n$	-	maximum number of fittings in a specific type of room
$N$	-	total number of bulbs
$N_R$	-	total number of light switches surveyed specific to room type R
$N_{RO}(t)$	-	number of switches in room type R on at time t
$N_{RX}$	-	number of specific room light switches with X fittings
$N_Y$	-	number of bulbs with a rating of Y watts
$p(Y)$	-	the wattage of a light in category Y
$P_{CR}$	-	expected contribution, in watts, of the XY combination to the total expected installed power of lights in a specific room
$P_{IR}$	-	total expected installed power rating
$R$	-	denotes the specific type of room
$U(y)$	-	probability of having a bulb with a rating of Y watts
$X$	-	number of fittings on the same switch in a specific type of room
$Y$	-	category of light (type and wattage i)

## 2. INTRODUCTION

Load prediction in the electrical power industry has become increasingly important as regulatory constraints controlling the construction and siting of new generating plants become more restrictive. Load forecasting has also become more difficult as the factors determining load growth and change become

more complex.

A lighting load model is developed which includes "usage", "availability" and "proclivity" functions [1].

These functions are used to forecast the domestic lighting load.

## 3. THE USAGE FUNCTION:

This function places emphasis on the rating of the light inserted into the light fitting. This can also be seen as the "power rating" of the appliance. Survey data from the Lynnwood area was used to produce this function.

## 4. THE AVAILABILITY FUNCTION:

This function can also be seen as the appliance penetration function. It is usually indicated by the number of light fittings in every room that can be switched on. This function is also produced from questionnaires that were sent out by CNES in the Lynnwood area. For the purposes of correlating modeled load patterns with measurements it was decided not to include light fittings supplied from wall outlets.

## 5. THE PROCLIVITY FUNCTION:

This function can also be referred to as "the tendency function". Given the fact that an appliance and a person are available, that person will tend to do certain things at certain times with that appliance. Such tendencies determine, for example, when people eat, when they watch television, etc. Some of these tendencies are controlled by standard factors such as the work shift but others are controlled, to a large extent, by convention or habit.

The "proclivity" function for electric lights developed in this work is based on a survey performed by CNES. It resulted from the responses to questionnaires regarding the probable appliance usage during particular time frames. This was done for nine different rooms or groups of rooms regularly found in ordinary homes.

## 6. MATHEMATICAL MODEL

The usage function was determined with the help of probability functions [2] [3].

$$U(y) = \frac{\text{Number of Y watt lights}}{\text{Total number of fittings}} \quad (1)$$

Thus:

$$U(y) = \frac{N_Y}{N} \quad (2)$$

AND

$$N = \sum_{Y=1}^m N_Y \quad (3)$$

The "usage" function for a bedroom is shown in figure 1. Note that the legend gives incandescent bulbs according to wattage. Fluorescent lights are grouped together.

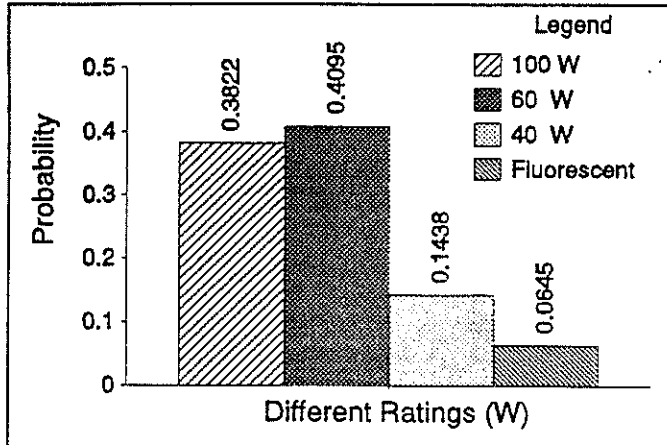


Figure 1 Bedroom lights usage function

A similar procedure was followed to determine the "availability" of different numbers of light fittings.

$$A_R(x) = \frac{N_{RX}}{N_R} \quad (4)$$

$$N_R = \sum_{X=1}^n N_{RX} \quad (5)$$

The "availability" function for a bedroom is shown in figure 2.

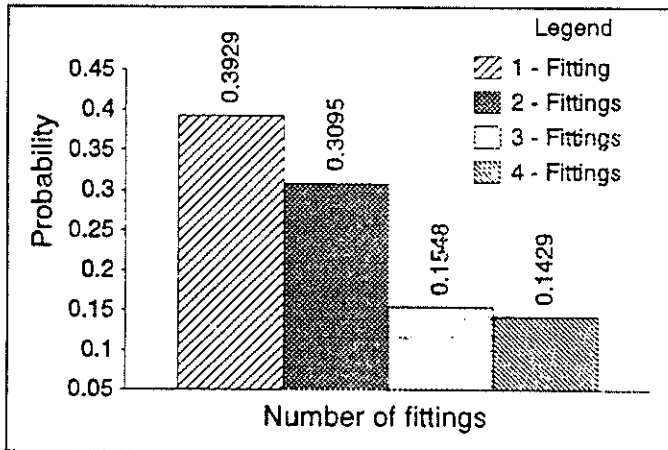


Figure 2 Bedroom lights availability

A light switching function was developed for the appliance, over one day, by dividing the given total of switches in the "on" position during each interval by the sum of the number of switches available to be switched on in a specific type of room.

$$D_R(t) = \frac{N_{RO}(t)}{N_R} \quad (6)$$

This function is the basic "proclivity" function for using the appliance. The "proclivity" function for bedrooms in the surveyed area is shown in figure 3.

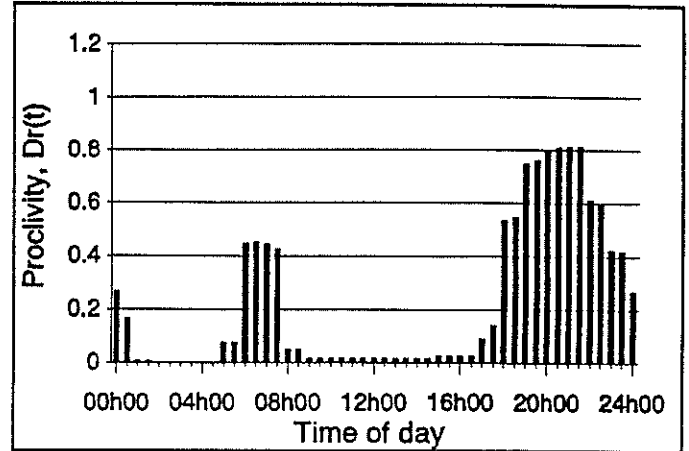


Figure 3 Bedroom lights proclivity for a typical weekday

In order to determine the probability,  $K$ , of getting  $X$  fittings with a category  $Y$  lights, the "usage" and "availability" functions were multiplied.

$$K_R(xy) = A_R(x) \cdot U(y) \quad (7)$$

The model in (7) assumes that the selection of light bulb ratings is statistically independent of the room type and the number of fittings per switch. This assumption may not necessarily be true, but the alternative of matching light bulb rating to room types and particular switches was not supportable with the available data. The error made by ignoring statistical dependence and using conditional probabilities is expected to be small. The size of this error should be tolerated for the sake of reducing the additional cost and effort required to conduct a more comprehensive survey.

The expected contribution,  $P_{CR}$  (in watts) of the combination of  $X$  fittings with category  $Y$  lights to the total expected installed power rating of lights in a specific room is given by

$$P_{CR}(XY) = K_R(XY) \cdot X \cdot p(Y) \text{ [W]} \quad (8)$$

The total expected installed power rating of lighting,  $P_{IR}$ , for a specific room then becomes

$$P_{IR} = \sum_{X=1}^n \sum_{Y=1}^m P_{CR}(XY) \text{ [W]} \quad (9)$$

The final step in determining the load profile for a single room is to multiply the "proclivity" function with the expected installed power rating.

$$P_R(t) = D_R(t) \cdot P_{IR} \text{ [W]} \quad (10)$$

The model used in (10) can also introduce errors due to the fact that statistical independence of all variables does not necessarily apply. The size of errors should be tolerated if they are small when compared to actual measurements. The reason for simplifying the models is to make "what-if" studies for demand-side

management strategy analysis compatible with regular computer spreadsheets. The model gives more practical value if it is kept simple for comparative analysis.

The expected load profile, from eq. 10, is shown in figure 4.

## 7. CALCULATION RESULTS

In order to evaluate the validity of the model the modelled load curves are compared to one obtained from simulation [4] and a recorded load curve for residences having similar stock of appliances. See figure 5.

From figure 5 one can see that the model

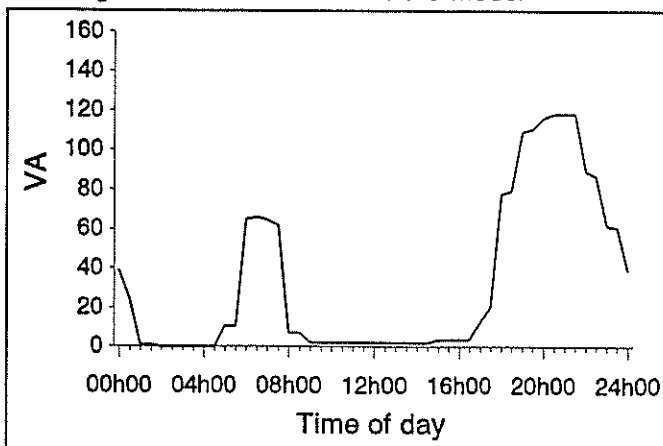


Figure 4 Expected bedroom load profile

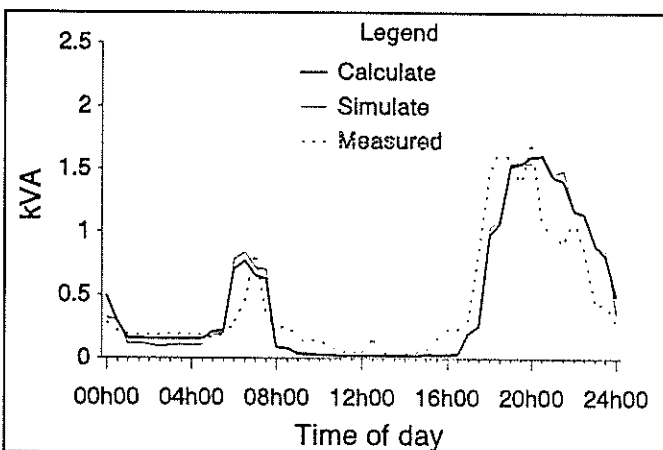


Figure 5 Load profile for one home

compares well with the measured data and with the results obtained by computer simulation. Since no measurement data on a room basis was available, the model is compared on the basis of whole-house measurements of lighting load profiles.

The load curve for an average three bedroom, two bathroom home was developed by adding the different calculated room load curves, as shown in figure 6.

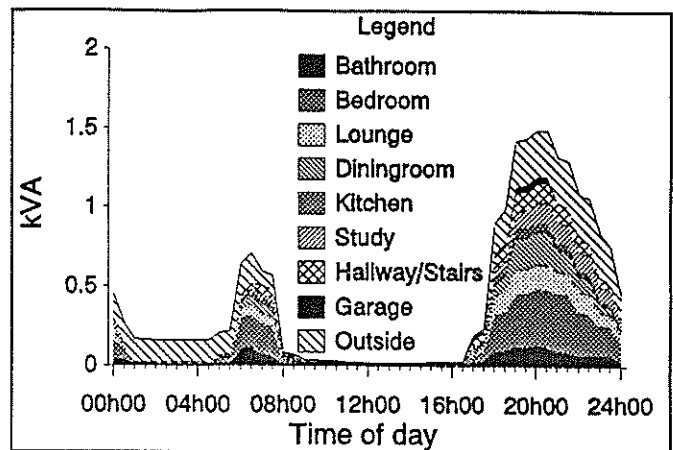


Figure 6 Stacked load curves for one home

An error function was constructed to compare the calculated load curve with the measured one.

$$ERR(f) = \frac{(\text{calculated value} - \text{measured value})^2}{(\text{measured value})^2}$$

The error function is shown in figure 7.

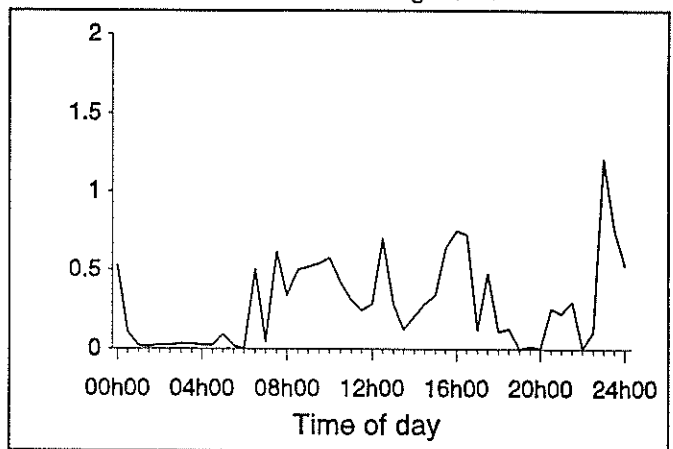


Figure 7 Error function

## 8. "WHAT IF" - STUDIES

The factors that influence the behaviour of a persons life style will be further looked at in this section. Some of the factors that have a major influence on human behaviour are as follows [5] [6] [7]:

- population density/income group;
- sunrise & sunset times (seasonal influences);
- consumer attitude (e.g. economy values, conservation values);
- power rating of light unit.

### 8.1 Case 1

The load curves of an average home and a large home are shown in figure 8. The two homes have the same rooms, but the smaller one has two bathrooms and three bedrooms whilst the larger one has five bedrooms and three bathrooms.

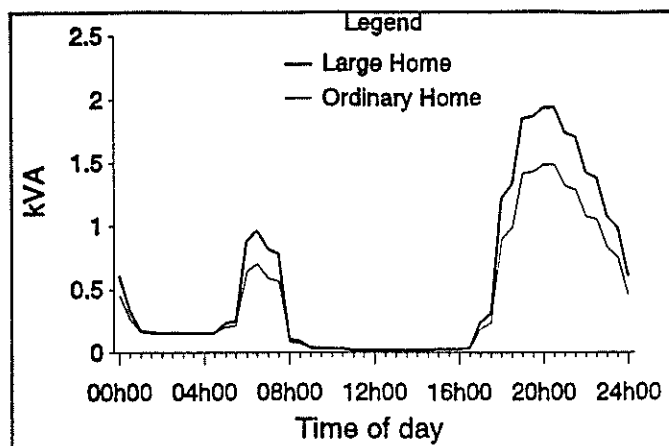


Figure 8 Ordinary and Large home load curves

### 8.2 Case 2

Here the smaller home lacks a study, hallway and stairs. The load curves are shown in figure 9.

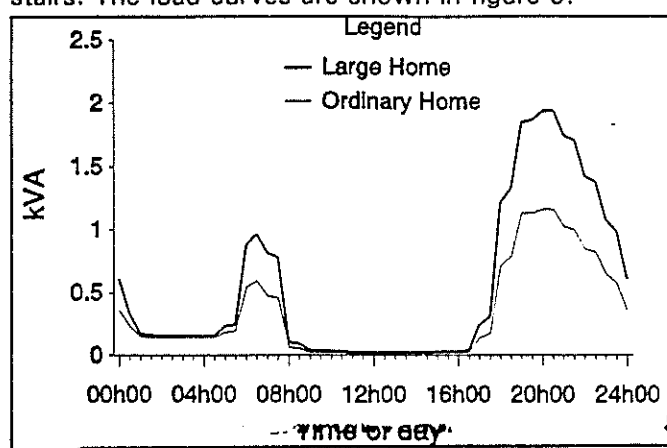


Figure 9 Ordinary and large home load curves

### 8.3 Case 3

If one replaces the incandescent bulbs in the kitchen, hallway, study, dining room and garage with fluorescent lights, the influence on the load curve is as in figure 10. ( 3 x 40W or 2 x 60W or 1 x 100W incandescent bulb  $\equiv$  1 x 40W fluorescent light).

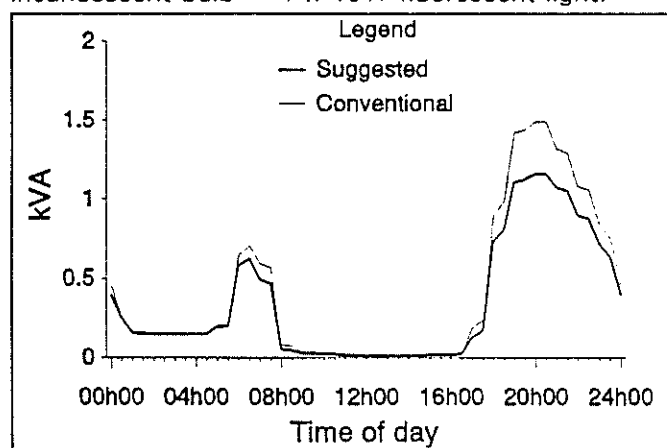


Figure 10 Load curve of ordinary and suggested home light set up

### 8.4 Case 4

Due to the fact that no summer survey data was

available, measured data is used to show the difference between winter and summer. See figure 11.

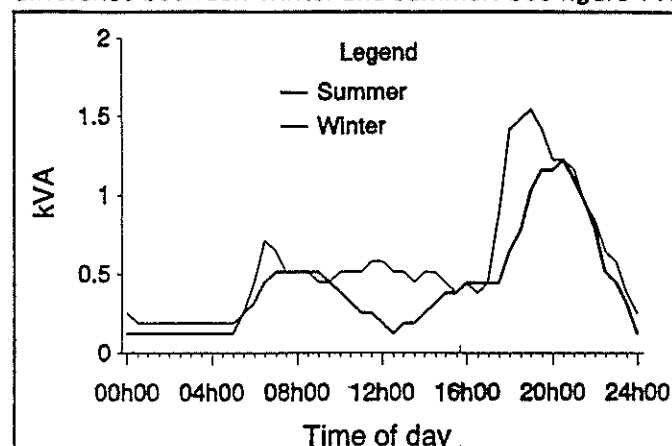


Figure 11 Measured load curves for Winter and Summer

## 8. SUMMARY AND CONCLUSIONS

The model used to simulate the electrical load includes user behaviour and selection considerations which affect people's use of electricity. These considerations are incorporated into the mathematical program primarily through "usage", "availability" and "proclivity" functions which have been developed primarily through various survey data.

From figure 6 one can see that bedrooms are the most prominent single factor in the load curve. This is due to the fact that every home has more than two bedrooms, whereas the number of dining rooms is normally one.

The second most prominent factor is that of the outside lighting. See figure 12.

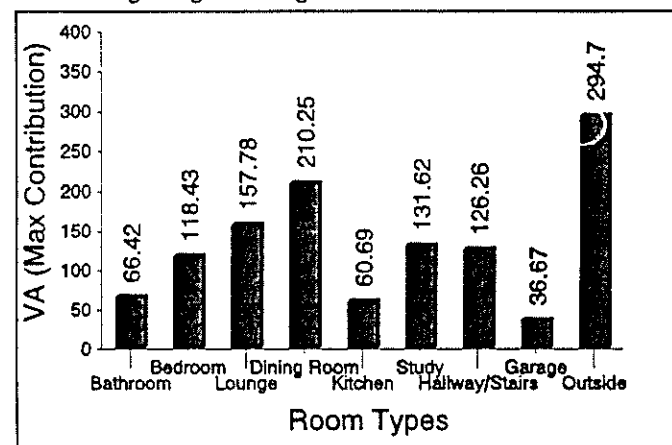


Figure 12 Maximum contribution of single location types

As the size of a home increases, so does the number of bedrooms and in a lesser manner that of the bathrooms. From figure 8 one can see that bedroom lights have a major influence on the load curve. If, however, the smaller home lacks a study, hallway and stairs, the difference in load curve between an ordinary and large home are even more drastic.

From case 3 the impact of the suggested change to fluorescent lights is shown. If bedroom lights are

changed to fluorescents, the system impact would be more dramatic. However, the consumer's preferences for fluorescent lights in specific home locations has yet to be tested.

The load researcher is faced with a great deal of work and occupation of costly measurement equipment if after diversity load profiles on domestic lighting are required from measurements on each location (or room) in the home. On the other hand whole-house measurements on lighting supplies in distribution boards are simpler and can be used to calibrate models based on survey data, as has been the approach described in this paper. More modern measurement techniques such as non-intrusive measurements would still not identify the locations of a light, even if it can register single light switchings from a central supply point. It appears that end-use surveys and load models is the most practical way to produce data for electrification, reticulation and demand-side planning with respect to domestic lighting at this time.

Generic after diversity lighting load profiles for various locations in the home have been shown to differ. "What-if" studies on a per-location basis are most useful because they add credibility to the whole-house after diversity load profile data to be used by reticulation designers and for demand management strategies. Subdivision of after diversity whole-house lighting load profiles on a per-location basis also brings the planner one step closer to analyzing the effects of user preferences and behaviour.

The assumptions made to simplify the load modelling task do not appear to create significant errors in after diversity load predictions based on survey data. Human inconsistencies of survey respondents or poorly designed survey questionnaires should be considered to be the most serious single source of error in predicting after diversity lighting loads when using the proposed load modelling method.

## 10. REFERENCES

1. C.F. Walker, J.L. Pokoski, "Residential Load Shape Modelling Based on Customer Behaviour", IEEE Transactions on Power Apparatus and Systems, Vol. PAS-104, No. 7, July 1985.
2. F.G. Stremler, "Introduction to Communication Systems", 3rd ed, University of Wisconsin, Madison, 1990, p 457 - 530.
3. R. Billinton and R.N. Allen, "Reliability Evaluation of Engineering Systems: Concepts and Techniques", Plenum, 1987, p 5 - 35.
4. J.C. van Tonder, "Windows Compatible Software", Department of Electrical and Electronic Engineering, University of Pretoria, Pretoria, August, 1994.
5. N. Beute, "Domestic Utilisation of Electrical Grid Energy in South Africa", Dissertation submitted in the Department of Electrical and Electronic Engineering of the Potchefstroom University for Christian Higher Education for the degree Philosophiae Doctor, Potchefstroom, 1993.
6. J.T. Grundy, "Our Lighting World - Our Environmental Lighting", Electricity + Control, August, 1991, p 29 - 33.
7. F.W. Leuschner, B. Baker, "Artificial and Natural Lighting Standards and Practices in South Africa", University of Pretoria and Lascon Lighting, Electricity + Control, August, 1992, p 21 - 25.

# SPECTRUM ANALYSIS TECHNOLOGY AS APPLIED TO POWER SYSTEMS

G. W. Louw, Prof M. J. Case

Randse Afrikaanse Universiteit, Johannesburg, South Africa

**Abstract** - This paper explores the theory relevant to spectrum analysis as applied to power systems and specifically power flow measurements. The Fourier transform, the Waterfall diagram and the Gabor transform will be investigated as possible techniques for obtaining the spectrum of a signal.

## 1. INTRODUCTION

The advances in power electronics and the increasing electrical demands of industry have forced the connection of more and bigger non-linear and time-variant loads to the ESCOM network. This in turn have caused great interest from both the supplier and consumer in power flow analysis and the detection of "network unfriendly" loads. The debate on tariff structures for non-sinusoidal loads rests on our ability to analyse the power flowing into or out of a branch in the power network.

## 2. POWER FLOW ANALYSIS

Consider the Norton equivalent circuit diagram of a balanced three phase power network as shown in Figure 2-1. The network consists of a point of common coupling (PCC) with branches 1 to k.

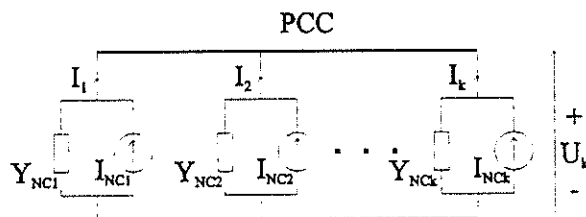


Figure 2-1: General PCC in a Power Network

Branches 1 to k-1 represent the loads and node k the Norton equivalent of all the supply lines connected to the PCC. Each load consists of a linear frequency dependant admittance  $Y_{NC}$  in parallel with a distortion current source  $I_{NC}$ . The supply branch k supplies power to the network through a current source  $I_{NCK}$  in parallel with a supply admittance  $Y_{NCK}$ . The distortion current sources 1 to k-1 represent the non-linear effects of the loads and at any frequency other than the fundamental frequency.

The complex apparent power delivered into the PCC by branch i will then be:

$$S_i(f) = U_k(f) I_{iNETT}(f)^* \quad (2.1)$$

where  $U_k(f)$  is the voltage at the PCC and  $I_{iNETT}(f)$  is the net current delivered to the PCC by branch i. This calculation can only be made if  $U_k$  and  $I_{iNETT}$  can be accurately measured and transformed to the frequency

domain which implies that  $U_k$  and  $I_i$  must be time-invariant.

The universally agreed upon definition of complex apparent power at a specific frequency can be used to define  $S_i(f)$ :

$$S_i(f) = P_i(f) + jQ_i(f) \quad (2.2)$$

It can be shown [1] by using the definition for complex apparent power and equation (2.1) that:

$$P_i(f) = \frac{|I_{iNETT}(f)|^2}{|Y_{NRi}(f)|^2} G_{NRi}(f) \quad (2.3)$$

and

$$Q_i(f) = \frac{|I_{iNETT}(f)|^2}{|Y_{NRi}(f)|^2} B_{NRi}(f) \quad (2.4)$$

where  $G_{NRi}(f)$  is the Norton equivalent residual-conductance of branch i and  $B_{NRi}(f)$  is the Norton equivalent residual-susceptance of branch i. The residual-conductance of branch i is defined as the sum of all the conductance in the network other than the one in branch i (see equation (2.5)). The residual-susceptance is defined in the same way (see equation (2.6)).

$$G_{NRi}(f) = \sum_{n=1, n \neq i}^k G_{Ni}(f) \quad (2.5)$$

and

$$B_{NRi}(f) = \sum_{n=1, n \neq i}^k B_{Ni}(f) \quad (2.6)$$

From equation (2.5) and (2.6) the rules for net power flow into or out of a branch in a network can now be defined:

1. The direction of net active power flow will always be out of the branch i into the PCC. It follows from the assumption that  $G_{NRi}(f)$  will always be positive therefore  $P_i(f)$  will always be positive.
2. The direction of reactive power flow will always be out of the branch i into the PCC for negative values of residual-susceptance (a predominantly inductive network) and into the branch i out of the PCC for positive values of residual-susceptance (a predominantly capacitive network).

It can be concluded that the sign of the active power (as calculated from equation ( 2.7)) at a given frequency measured at any point in a time-invariant balanced three phase power network will indicate the direction in which the power is flowing at that frequency. The reactive power can also be used to indicate the direction of power flow, but then some knowledge of the reactance seen from that point in the network will be needed.

$$P_i(f) = |U_k(f)| |I_{iNETT}(f)| \cos(\theta(f)) \quad (2.7)$$

where  $\theta(f)$  is the phase angle between  $U_k(f)$  and  $I_i(f)$ .

This result can be extended to unbalanced three phase networks [2] by using a special case of the Park transformation. It follows from the argument above that the active power calculated from the result of the Park transform can again be used to indicate the direction of power flow.

### 3. Characteristic Power System Wave Forms

In the foregoing paragraph it has been established that we need to measure the current and voltage and calculate the active power flowing through a point in the network in order to establish the direction of power flow. This result is only valid if all the calculations is carried out in the frequency domain.

The transformation of the current and voltage wave forms to the frequency domain is not as simple as it would seem and the accuracy of such transforms is largely dependant on the characteristics of the wave form.

The following list of current and voltage wave form characteristics commonly found in power systems will be referred to in later sections:

1. Wave forms can be extremely time-variant, for example the line current of a arc furnace
2. Switching transients can occur anywhere within a fundamental cycle.
3. Sub-fundamental frequencies can be present, again the example of a arc furnace applies.
4. Distortion at frequencies higher than the fundamental frequency does not necessarily have to be at harmonic frequencies.
5. The fundamental frequency is not fixed at exactly 50 Hz but can drift from 47 to 51 Hz.

The accuracy of the result obtained from spectral analysis is further complicated by the fact that the active component at non-fundamental frequencies is generally very small compared to the ambient level of reactive power. As can be seen from equation ( 2.7) the certainty with which the direction of the of power flow can be established is related to the accuracy with which the phase angle between the current and voltage spectral components can be calculated. If the active power is small compared to the reactive power, then  $\theta$  is close to 90 or -90 degrees which means that

a small change in  $\theta$  will result in a reversal of the direction in which the power is flowing. If a true frequency approach is to be use in power flow analysis, then the phase angle at a given frequency between the voltage and current has to be determined with great accuracy, typically within 1 degree or 0.27 percent.

### 4. Fast Fourier Transform

The fast Fourier transform (FFT) is a very quick and efficient algorithm for computing the discrete Fourier transform (DFT as defined in equation ( 4.3) and ( 4.4)) and was published in 1965 by J. W. Cooley and J. W. Tukey [3 and 4]. The DFT is a windowed version of the non-periodic discrete-time Fourier transform as defined for signals of infinite length by equation ( 4.1) and ( 4.2).

#### The Discrete-time Fourier Transform Pair

$$F(\omega) = \sum_{n=-\infty}^{\infty} f(n) e^{-i\omega n} \quad (4.1)$$

$$f(n) = \frac{1}{2\pi} \int_{-\pi}^{\pi} F(\omega) e^{i\omega n} d\omega \quad (4.2)$$

#### Discrete Fourier Transform Pair

$$F(k) = \sum_{n=0}^{N-1} f(n) e^{-i \frac{2\pi}{N} nk} \quad (4.3)$$

$$f(n) = \frac{1}{N} \sum_{k=0}^{N-1} F(k) e^{i \frac{2\pi}{N} kn} \quad (4.4)$$

It is important to note that the DFT or FFT\* is a only an approximation limited by the number of data point included in the calculations resulting in a discrete frequency representation. The accuracy of the FFT is also influenced by the border effects of the rectangular window.

#### 4.1 Some Result obtained from the FFT

A Mathcad program was used to generate simulated single phase power system wave forms that include the characteristics listed above. Another Mathcad program was then used to compute the FFT of these wave forms. Some of these results is included to highlight the restriction of the FFT mentioned above.

The first signal has a 50 Hz fundamental frequency with harmonic components added as seen Table 4-1. The total length of the signal is exactly 32 fundamental cycles sampled at 256 points per fundamental cycle, giving a total of 8192 data points or 640 ms. The signal starts of with the harmonic magnitudes and phase angles relative to the fundamental frequency as listed under Mag1 and Phase1 (column 3 and 4 of Table 4-1). At time  $t = 305ms$  a switching is simulated and the harmonic

\* The FFT is only a algorithm for computing the DFT and the properties and accuracy is the same for both.

content of the signal changes to the values listed under Mag2 and Phase2.

**Table 4-1: Harmonic content of Signal1**

H no.	Freq. in Hz	Mag1 in p.u.	Phase1 in dg.	Mag2 in p.u.	Phase2 in dg.
1	50	1	0	2	0
3	150	0.02	45	0.04	45
5	250	0.02	90	0.04	90
7	350	0.02	135	0.04	135
9	450	0.02	180	0.04	180
19	950	0	0	0.04	0
20	1000	0.02	90	0.02	90
50	2500	0.02	90	0.02	-90

Note that no sampling noise was added as the signal was sampled with an accuracy of 16 decimal points. Signal1 is an example of characteristic number 1 and 2 listed above. The result of a 8192 point FFT performed on Signal1 is shown in Table 4-2. Note that all the phase angles were measured with reference to the phase angle of the fundamental frequency.

#### Discussion of FFT results

The magnitudes of harmonics number 1, 3, 5, 7 and 9 doubles at time  $t = 305\text{ms}$  and the average value as would be expected from the FFT is 152.3 % of the value at the beginning of the signal. Although the fundamental frequency was analysed correctly the average of the 3rd harmonic is 135 % of the starting value, a error of 11.4 %.

**Table 4-2: Result of FFT for Signal1**

H no.	Freq. in Hz	Mag in p.u.	Phase in dg.
1	50	1.523	0
2	100	0.008	-118.991
3	150	0.027	37.969
5	250	0.029	90.457
7	350	0.029	137.705
9	450	0.031	178.153
19	950	0.021	-1.307
20	1000	0.019	90.998
50	2500	0.020	-96.086

The value of the 2nd harmonic is also included in the results to show the spreading of spectral energy caused by the transient in the signal.

None of the phase angles, except the 50th harmonic, was changed, but it is clear from Table 4-2 that the changes in magnitude have also influenced the phase angle.

The 20th harmonic was not changed in the transient, but was clearly influenced by the sudden introduction of a 19th harmonic.

The magnitude of the 50th harmonic was kept constant while it was swung through 180 degrees. It

can be argued that the average of the imaginary component should have been close to zero, instead a phase angle of -96.086 degrees was obtained.

From the discussion above it is clear that some form of time and frequency analysis is needed in order to analyse a time-invariant signal like the wave forms commonly found in power systems. Two possible solutions are the Waterfall diagram and the Gabor transform.

#### 5. Waterfall Diagram

One way to overcome the problem of time-invariant frequency analysis, is to shorten the length of the FFT to an integer multiple of fundamental periods. The signal is assumed to be time-invariant and periodic over this shortened interval. The surface plot obtained by placing the spectral curves of consecutive intervals next to each other is called a Waterfall diagram.

The fundamental problem with the Waterfall analysis is the shortened length of the FFT (the length of the FFT will be referred to as  $N$ ). If  $N$  is too large the effects of transients in the signal makes it no more accurate than normal Fourier analysis. The small number of fundamental periods included in one FFT results in an inability to analyse sub-fundamental and inter-harmonic frequencies (see characteristic 3 and 4 above).

The Waterfall diagram is also only valid if the fundamental frequency of the signal can be determined with great accuracy and if the signal can be sampled with the same accuracy. One of the characteristics of power system wave forms is the drifting of the fundamental frequency. Although the variation in the fundamental frequency is very small, the effect of incorrect sampling on a short FFT is enlarged at higher harmonic frequencies.

#### 6. Discrete Gabor Transform

The Gabor transform is a true two dimensional transform, it translates the time and frequency information of a wave form to a combined surface plot, with time on one axis and frequency on the other.

The transform takes the first  $N$  data points and multiplies this section with a Gaussian distribution of variance  $\sigma$ . A FFT is then performed on the resulting data. The rectangular window used to isolate the first  $N$  data points is now moved by a distance of  $\Delta M$  data points and the process is repeated to end of the signal, resulting in  $M$  spectral curves. Placed next to each other these curves form a time-frequency domain surface.

The parameters of the Gabor transform ( $N$ ,  $M$  and  $\sigma$ ) can be changed to fit the characteristics of the signal being analysed. For Signal1 a  $\sigma$  of 160 was chosen with a  $N$  of 2048. This means that the border effects of the 2048 point rectangular window is filtered out by the Gaussian distribution. By keeping  $\sigma$  smaller than the number of data points in a fundamental period the

effects of transients is limited to the immediate vicinity of the transient. By keeping  $N$  larger than one fundamental period a good phase representation is achieved at low frequencies and inter-harmonic frequencies can be analysed correctly. In order to get a flat time response from the consecutive Gaussian distributions a  $\Delta M$  of 32 data point or 2.5 ms was chosen resulting in 410 spectral curves ( $M=410$ ).

### Discussion of DGT results

A comparison of the results of the DGT to FFT will be presented in the same form as Table 4-2. The magnitude and phase spectral curves as taken at different time instances. The FFT was taken from the beginning of a fundamental cycle to the end of another, meaning that the border effects of the beginning and end of the signal did not influence the results. Likewise the border effects of the DGT will not be included and the first set of data that includes only signal data is were  $m=32$  (from 0 to 80 ms). The last set of time-invariant data before the transient is were  $m=90$  (from 225 to 305 ms) and the first set of time-invariant data after the transient. is were  $m=154$  (from 305 to 385 ms). Again the border effects at the end of the signal is ignored and the last set of data is taken at  $m=256$  (from 560 to 640 ms). The result of the DGT for  $m=32$  to  $m=90$  is constant for every  $m$  and listed under Mag1 and Phase1 in Table 6-3. Likewise the values obtained for  $m=154$  to  $m=256$  is constant for every  $m$  and listed under Mag2 and Phase2 in Table 6-3.

The largest error obtained from the results of the DGT in the time-invariant sections of the signal is the phase angle of the 20th harmonic which differs from the correct value by 0.042%. This level of accuracy is acceptable for power flow calculations.

The results not included in Table 6-3 is for  $m=91$  to  $m=153$ . In this region the time-frequency domain surface changes as it move through the transient. The best way to visualise this surface is by using cross sections along the time axes. As examples shows the magnitude of the fundamental component as it change from 1 per unit to 2 per unit.

Table 6-3: Result of DGT for Signal1

H no.	m=32..90		m=154..256	
	Mag1	Phase1	Mag2	Phase2
1	1.000	0.000	2.000	0.000
2	0.0003	0.115	0.0006	0.115
3	0.020	45.000	0.040	45.000
5	0.020	90.000	0.040	90.000
7	0.020	135.000	0.040	135.000
9	0.020	180.000	0.040	180.000
19	0.000	0	0.040	0.010
20	0.020	90.000	0.002	89.962
50	0.020	90.000	0.002	-90.000

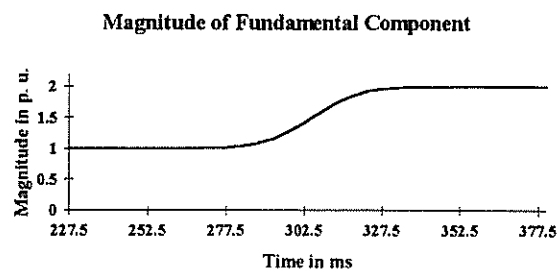


Figure 6-1: Magnitude of the fundamental component during transient

The effect of the Gaussian distribution can clearly be seen in Figure 6-1 and the time of the transient can be detected as 305 ms.

### 7. Conclusion

The Gabor transform extract more information from a signal than normal Fourier analysis resulting in a more accurate representation of the spectral content of a signal. If correctly set up the DGT can be used to determine the direction of power flow in a power system as a function of both time and frequency.

### References

- [1] Case, M. J., Swart P. H. and Van Wyk J. D.: "On Techniques for Localisation of Sources Producing Distortion in Electric Power Networks", *Proc. 2nd Int. Workshop on Power Definitions and Measurements under Non-sinusoidal Conditions*. Stresa, Sept. 8-10, 1993, pg. 187-190.
- [2] Cristaldi, L. and Ferrero, A.: "A Method and Related Digital Instrument for the Measurement of the Electric Power Quality", *Proc. of IEEE ICHIPS 17*. Bologna, Sept. 21-23, 1994, pg. 9-15
- [3] Cooley, J. W. and Tukey, J. W.: "An algorithm for Machine Calculation of Complex Fourier Series", *Math. of Computation*, vol. 19, 1965, pg. 297-301.
- [4] Cooley, J. W., Lewis, P. A. W. and Welch, P. D.: "Historical Notes on the Fast Fourier Transform" *Trans. IEEE*, AU-15, 1967, no. 2, pg. 76-84

### Address of Authors

Mr G W Louw, Laboratorium vir Energie, Ranse Afrikaanse Universitet, Posbus 524, Aucklandpark, 2006.

Pof M J Case, Laboratorium vir Energie, Ranse Afrikaanse Universitet, Posbus 524, Aucklandpark, 2006.

# COMFORT-COST ANALYSIS FOR THE OPTIMISATION OF DOMESTIC LOAD CONTROLLERS

GL VAN HARMELEN

IE LANE

Centre for New Electricity Studies, Department of Electrical and Electronic Engineering, University of Pretoria, Pretoria, South Africa

## ABSTRACT

A quantitative technique for benefit/cost level analysis is proposed as it is required in the design and evaluation of intelligent domestic load controllers. In this paper, a description of the concept of benefit (i.e. comfort) is derived and combined with the cost of electricity, to form a universal evaluation criterion. Benefit is calculated from  $n$  penalty functions which operate on  $n$  components of comfort, (e.g. temperature, total amount of end-use product produced, delay). Penalty functions quantify the loss of benefit as a result of the difference between requested and received comfort levels. The actual cost of that benefit (i.e. cost of electricity) on the other hand is calculated from a capital investment component, a variable energy charge component, and a losses component. This paper demonstrates a standard fuzzy logic controller optimising between benefit and cost.

## INTRODUCTION

The concept of benefit level analysis in the domestic sector relates directly to customer based perceptions of the value of different comfort levels and has thus far been a largely subjective matter. Experts in the load management field all exhibit an intuitive engineering feeling as to what actions will affect benefit/cost levels. A quantitative description of comfort is required to eliminate person/situation subjectiveness. Should such a benefit/cost analysis be available, domestic load controller strategies can be designed to optimise the trade-off between changes in electricity bills, and the inconvenience suffered from a modification of usage patterns[4].

A benefit-level function (BL) is therefore defined which quantifies the customer's perception of the value of the comfort he is receiving by employing penalty functions which operate on the errors between requested and received components of comfort. When the difference between the benefit level and the cost level (cost of electricity) is maximised (i.e. the most comfort for the least cost) the customer situation is optimal.

The function which describes the difference between the benefit level (BL) and cost level (CL) is called the service level (SL) function.

$$\text{service level} = \text{benefit level} - \text{cost level} \quad (1)$$

Domestic load controllers should strive to operate on the maximum service level point, as this will ensure maximum benefit for the least cost. In this paper, a conventional hysteresis controller will be evaluated against a fuzzy-logic controller (FLC) (for a hot water cylinder) using this method. It will be shown that the FLC easily out performs the conventional hysteresis controller under a time-of-use (TOU) tariff.

## THE CUSTOMER'S BENEFIT LEVEL

When a customer requests a specific amount of end use product, he expects specific conditions relating to the amount (usually measured in kilograms), the energy content level (i.e. temperature), the duration it takes to produce that comfort etc. These factors have been termed comfort components and the satisfaction of the customer depends on the errors associated with these comfort components. The comfort component error vector (CCE) is therefore the difference between requested comfort (RC) and actual received comfort (AC) components, with each component describing a specific aspect of comfort.

In general therefore, the benefit-level (BL), is quantified by

$$BL = C - \sum_{i=1}^n P_i(CCE_i) \quad (2)$$

where  $P_i$  is the  $i$ 'th penalty function, CCE is a column vector of comfort component errors, and  $C$  is a constant.

The benefit-level function quantifies the comfort errors in cents/unit and relates to that amount of money the customer is prepared to pay for the comfort per unit he has received. This function will necessarily change from product to product, and possibly from person to person.

The different comfort components also relate to the different types of control actions which are possible from domestic load controllers (e.g. modify the amount supplied, the average energy content of

supply, the time of supply, or modify the production duration) [5].

A proposed general form of the penalty functions (although not exhaustive) is shown in Fig.1 where negative penalties (i.e. rewards) are shown for negative errors (i.e. receiving more comfort than was actually requested).

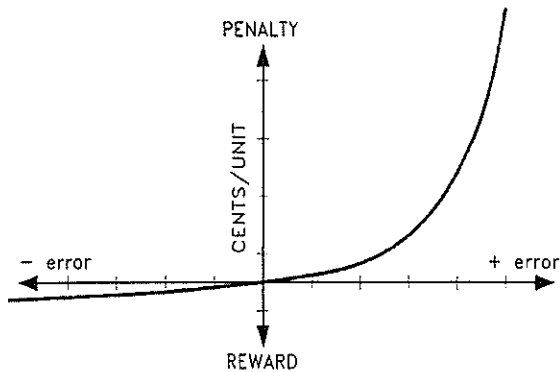


Fig. 1: Proposed form of the penalty functions.

In the hot-water cylinder case presented here, the only comfort component error is the temperature (average energy content) of the received water, as the requested amounts at the requested times are always supplied exactly.

Exponential functions are proposed as penalty functions so that in general

$$P_i(CCE_i) = A_i \cdot e^{\frac{CCE_i}{B_i}} \quad (3)$$

with  $A_i$  and  $B_i$  acting as appropriate scaling constants. As only a single comfort component error present in this case, the entire benefit-level function of eq. 2 reduces to

$$BL = C - A \cdot e^{\frac{CCE}{B}} \text{ c/unit} \quad (4)$$

where the scaling parameters  $C$ ,  $A$  and  $B$  have to be quantified and where

$$CCE = T_{REQUESTED} - T_{RECEIVED} \quad (5)$$

i.e., the comfort component error in this case is the difference between the requested and received water temperatures.

### THE COST OF COMFORT

Comfort (i.e. amount of end-use product) is usually produced via electricity, and therefore the cost of comfort relates directly to the cost of electricity used in producing that comfort. In order to calculate the cost of producing  $x$  kilograms of hot water for example, a cost level function (CL) is multiplied by the amount of usage per unit, resulting in a cost in cents.

$$CL [\text{c/unit}] \times \text{amount produced [units]} = \text{cost [c]} \quad (6)$$

The cost-level function for producing domestic comfort is modelled as having a fixed capital outlay component ( $F$ ), an energy consumption component ( $V$ ), and a loss component ( $L$ ) so that :

$$CL = F + V + L \quad (7)$$

As the benefit/cost theory of comfort is expanded, it is expected that more components may be added to this equation. The cost-level function therefore quantifies (in cents) the actual amount paid by the consumer to the electricity supply utility for the electricity used in the production of 1 unit of a particular type of end use product.

When this model for the cost of producing hot water is applied to the hot water cylinder problem, this results in :

$$F = \frac{C}{U_t} \quad (8)$$

$$V = (T - T_a) \cdot C_p \cdot R \quad (9)$$

$$L = (T - T_a) \frac{H \cdot t \cdot R}{U_t} \quad (10)$$

We see that the cost of comfort is proportional to the average energy content of the water (i.e. temperature) because there are no other comfort components errors to be considered.

A graphical representation of this cost level function is given in Fig. 2 below.

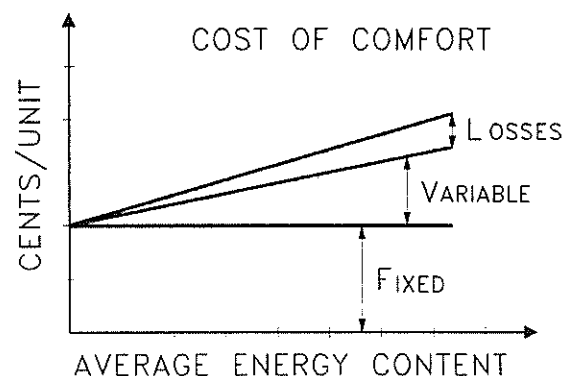


Fig. 2: Losses, variable and fixed components of the cost of producing comfort.

A general form for the cost of comfort in these situations may be specified as a straight line so that

$$CL(R, C, U_t, H, T_a, T, t) = m \times T + c \quad (11)$$

where the temperature  $T$  represents the average energy content of the end-use product.

### THE SERVICE LEVEL FUNCTION

In this paper it is assumed that the consumers benefit-level function (BL) always remains constant. In order to maximise the service-level from the consumer's

point of view, the cost-level minus the benefit-level must be minimised (see eq. 1). The control temperature set-point of the cylinder can be adjusted in order to effect this minimisation. A better controller will therefore exhibit a higher service level than a poorer counterpart.

The optimum system condition, from the consumer's point of view, would therefore be to maximise the benefit level minus cost level, or to minimise cost level minus benefit level.

The equation to be minimised is therefore, combining eq. 4 and 11

$$f(T) = m * T + c - C + Ae^{\left(\frac{T_R - T}{B}\right)} \quad (12)$$

and the root may be found by setting  $df(T)/dT=0$ .

### IMPLEMENTATION

A geyser example with numerical constants will be shown next as implementation of the theory presented here. The following constants were used :

Water usage for 30 days	= 5257 kg
Capital investment per month	= 4000 c
Energy charges	= 17c/kWh
Ambient Temperature	= 12°C
Size geyser	= 150 kg
Standing loss coefficient	= 3 J/K sec.

It was assumed for loss calculations that the water within the tank was always at the controller setpoint  $T_R$  (requested temperature) which means the loss rate was a constant. This is not strictly true and will lead to a small error as losses modelled analytically will be slightly higher than actual losses. The three components of the cost-level function are therefore found from equations 8-10 as being :

$$F = 0.762 \text{ c/kg} \quad (13)$$

$$V = 0.01983 * T - 0.238 \quad (14)$$

$$L = 0.007 * T - 0.0839 \quad (15)$$

and they are plotted separately and cumulatively in Fig. 3 where the unit value was chosen as being kilograms.

These graphs display the cost of producing 1 kg of water at different levels of average energy content (i.e. different temperatures). It should be immediately noted that the cost of losses is almost 40% of the cost of heating up the water (for this particular numerical case).

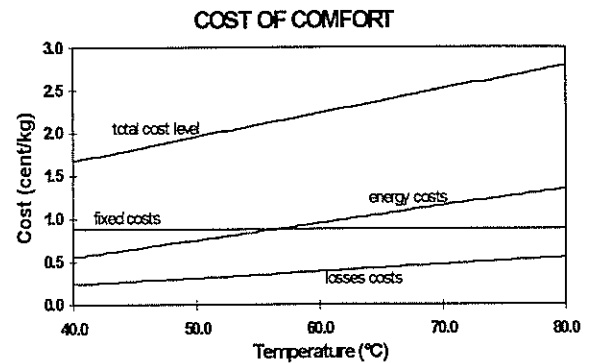


Fig. 3: Cost level functions for practical example.

Assuming the same amount of hot water is always used, the cost-level function is plotted for different rates of energy costs  $R$ , with the benefit-level function to be discussed next, in Fig. 4.

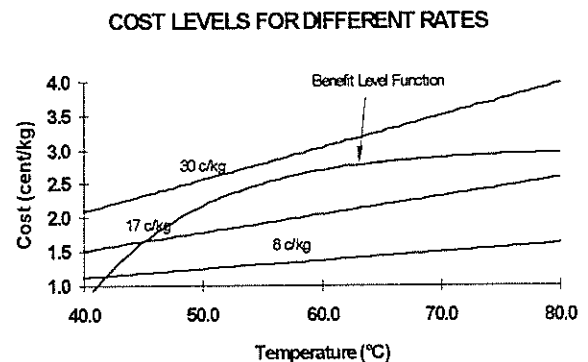


Fig. 4: Cost level functions for different energy rates.

For the case presented here, the benefit-level function was determined empirically as

$$BL(T) = 3.0 - 0.5 * \left(\frac{55 - T}{10}\right) \quad (16)$$

With all the constants required to solve the roots of eq. 12 now available, the roots were found for the three different rates as shown in Fig. 4, and the optimum operating temperatures were found as shown in Table 1.

Table. 1. Optimum operating temperatures

Energy Tariff [cents/kWh]	Operating Temperature
8	67.0
17	61.0
30	55.0

### FIRST ORDER GEYSER MODEL

The first order approximation of a hot water cylinder which is described by a linear first order differential equation is useful for describing energy conservation, standing losses and testing control algorithms. Higher order models can provide spatial temperature distribution information (e.g. stratification). However

the simulations required here do not need such information [7].

The first order differential equation employed as plant model was :

$$\frac{dT}{dt} = \frac{1}{MC_p} \left[ P - H * (T(t) - T_a) - \bar{m} * C_p * (T(t) - T_l) \right] \quad (17)$$

This equation was solved iteratively from a known initial condition  $T_o$ , using a fourth order Runge-Kutta:

$$T(k+1) = T(k) + \frac{h(f_1 + 2f_2 + 2f_3 + f_4)}{6} \quad (18)$$

and where  $f_1$ - $f_4$  are the Runge-Kutta function evaluations.

## NUMERICAL SIMULATIONS

Three numerical simulations representing the average service levels for 30 continuous days were run using this geyser model operating on water flow patterns which were generated via a probabilistic model [8].

### Generating water consumption patterns

The water consumption pattern was categorised into bathing, cooking, sink and household events. Each of these categories were assumed to be cyclostationary with individual statistics being used for each case [1,2].

The total consumption for 30 days was 5257 litres, with the daily usage being shown in Fig. 5. As was seen from the previous results, even with large daily variations in the amount of water consumed, the analytical and simulated results agreed within 3%. The daily average for simulations presented here was 175 kilograms per day.

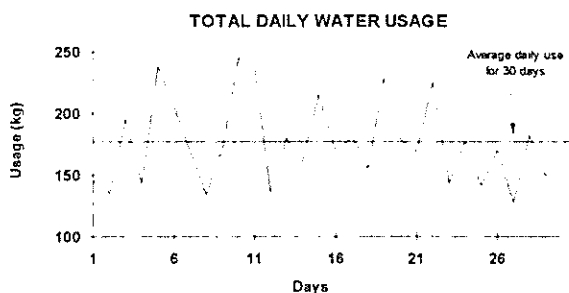


Fig. 5: Water usage for 30 continuous simulation days

### Service Level Simulations

Each time the element switches ON, a cost of comfort was computed and added to a cumulative sum representing the total service level. Each time a water draw event took place, a benefit level value was assigned to that event (depending on the temperature of the water received). The benefit level value was also

continuously subtracted from the cumulative service level value so that a totalized value was obtained for the service level after the simulation period.

The simulation results using this method agreed with the analytic solutions to within 3%, which is attributed to modelling losses as having a constant rate. The results for an energy rate of 30c/kWh are shown in Fig. 6. For these numerical simulations, a hysteresis controller with a hysteresis band of 1°C was used so that the set point temperatures could be controlled as accurately as possible. For the 30 day~ period simulated, the average tank temperature was verified to be within 0.5 °C of the hysteresis controller setpoint value.

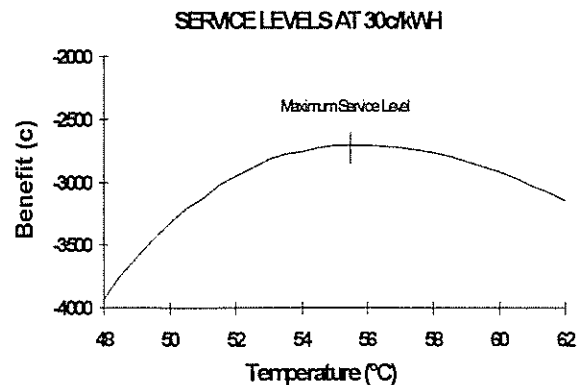


Fig. 6: Maximum service level found at 55.8°C.

## CONTROLLER EVALUATION

The purpose of modelling the cost- and benefit-level functions was to arrive at a universal service-level value to enable comparison and optimisation of different control algorithms. A hysteresis controller with a hysteresis band of 5°C, was accordingly compared under a TOU tariff, to a 11 rule fuzzy logic controller [3] to demonstrate this application area.

The TOU tariff which was employed is shown in Fig. 7. The temperature of the hysteresis controller was varied so that the optimum control temperature could be found using the totalised service level as evaluation parameter. The optimum control temperature for the hysteresis controller was found to be 60°C, with a accompanying service level of 1660 cents.

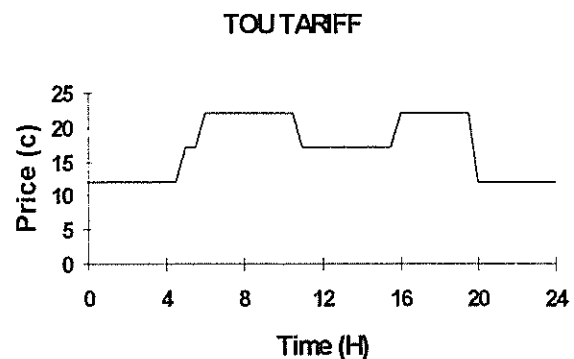


Fig. 7: TOU as used during numerical evaluations

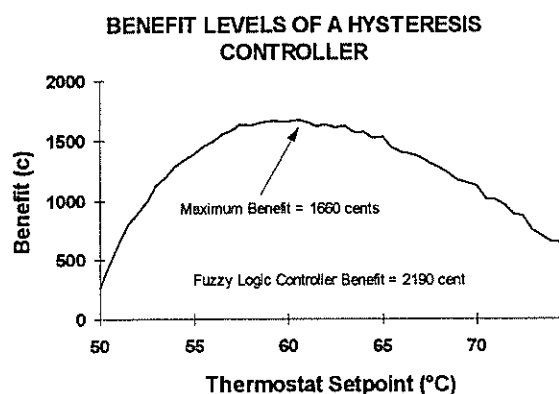


Fig. 8: Optimisation results of hysteresis controller.

The average daily tank temperature was calculated in 300 second intervals and averaged over the 30 days for the two controller cases presented. These results are presented in Fig. 9. It can be seen that the fuzzy logic controller pre-heats the water in the low price times, and runs at a lower average temperature during the expensive times.

The service level obtained from the fuzzy logic controller as described in Table 2 was 2190 cents which easily out-performed the optimised hysteresis controller case.

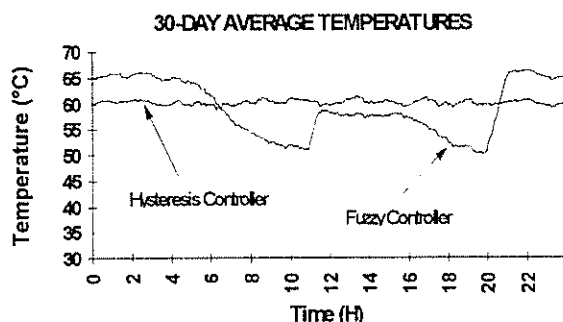


Fig. 9: Average temperature profiles for the two types of controllers

The fuzzy associative memory (FAM) for the hot water cylinder controller is shown in Table 2 where the horizontal axes represents fuzzy sets for price input, and the vertical axis represents fuzzy sets for the temperature input variable.

The controller therefore consists of rules of the form **IF PRICE=LL AND TEMP=LL THEN POWER=LH** and all values may be read off table 2.

Table 2. Fuzzy associative memory representation

	LL	SL	N	SH	LH
LL	LH	LH	LH	LH	LH
SL		LH	SH	N	
N		SH	N	SL	
SH		N	SL	LL	
LH	LL	LL	LL	LL	LL

The controller response surface which this FAM represents is presented in Fig. 10.

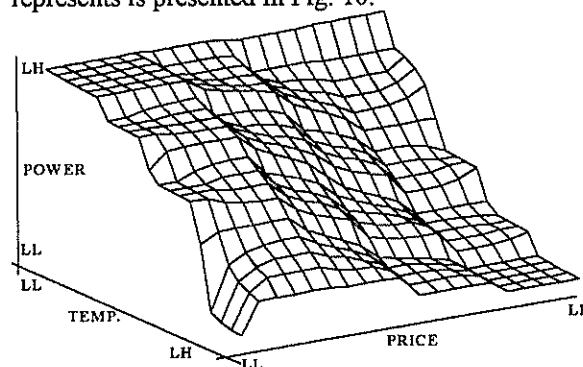


Fig. 10: Response surface of fuzzy-logic temperature controller.

## SUMMARY

A quantitative description of both the cost of electricity, and the benefit it produces (i.e. the value of the end-use product produced) was presented in this paper. A cost function minimisation approach based on the cost- and benefit-level functions was subsequently employed for controller evaluation and this function was termed the service-level function.

The service level function was employed to compare different control algorithms with each other, and to make a quantitative evaluation of their performance. In the geyser control case study presented, an 11 rule fuzzy logic controller easily out-performed an optimised hysteresis controller.

The service level approach which has been introduced in this paper may be applied to all forms of devices and control strategies, and future work entails expanding the theory and testing it in different situations.

## NOMENCLATURE

T(t)	temperature as a function of time	[°C]
II	standing loss coefficient	[J/sK]
P	element rating in cylinder	[J/s]
C <sub>p</sub>	specific heat capacity	[J/Kkg]
$\dot{m}$	mass flow rate	[kg/s]
T <sub>a</sub>	Ambient temperature	[°C]
T <sub>i</sub>	Incoming water temperature	[°C]
U <sub>t</sub>	total amount used over the period t	[kg]
t	duration period	[s]
R	energy cost of electricity	[c/J]
C	capital component	[c]
LL	Large Low	
SL	Small Low	
N	Normal	
SH	Small High	
LH	Large High	
f()	function of	

## REFERENCES

1. Kempton, W. : "Residential hot water: A Behaviourally-driven system", in *Energy*, Vol. 13, No. 1, pp. 107-114, 1988.
2. Probability, Random Variables, and Stochastic Processes, Athanasios Papoulis, 2nd Edition, McGraw-Hill Book Company, pp. 226-231, 1984.
3. Sutton, R., Towill, D.R., "An introduction to the use of fuzzy sets in the implementation of control algorithms", in *J. IERE*, vol. 55, no. 10, pp. 357-367, Oct. 1985.
4. Schweppe, F.C., Daryanian, B., Tabors, R.D. : "Algorithms for a spot price responding residential load controller", in *IEEE Trans. on Power Systems*, Vol. 4, No. 2, pp. 507-516, May 1989.
5. Daryanian, B., Bohn, R.E., Tabors, R.D. : "Optimal demand-side response to electricity spot prices for storage type customers", in *IEEE Trans. on Power Systems*, Vol. 4, No. 3, pp. 897-903, August 1989.
6. Introduction to Probability Models, S.M. Ross, Fourth Edition, Academic Press, pp. 473-504, 1989
7. Van Harnelen, G.L., Lane, I.E. : "A Physically based model for water heater controller design", in *Proc. of 1st Conference on Domestic Use of Electrical Energy (DUOEE-93)*, Cape Technikon, Cape Town, pp. 68-74, 18-19 October 1993.
8. Van Harnelen, G.L. Lane, I.E. : "Domestic Stochastic Process Evaluation for Networks of Decentralized Load Controllers", to be published in *Proceedings of 5th South African Universities Power Engineering Conference (SAUPEC-95)*, Pretoria, 19-20 January 1995.

# FACTS FRONT END FOR EMTP

N.H. Ramage  
Wits University

J.M. van Coller  
Wits University

R. Koch  
Eskom TRi

## ABSTRACT

This paper discusses the development of a Microsoft Windows based preprocessor for EMTP which will facilitate experimentation with FACTS devices. The paper discusses the issues of Software Quality and Maintenance and the implications they have on the development of the preprocessor. Also included is an overview of the specification of the preprocessor. The paper concludes with a short description of the main implementation points of the preprocessor.

## 1. INTRODUCTION

At present the main supply authority in South Africa (Eskom) is investigating the use of Flexible AC Transmission Systems (FACTS) devices to solve stability problems at the higher voltage levels, flicker problems associated with arc furnaces and voltage control at the lower voltage levels.

The Electromagnetic Transient Program (EMTP) is a transient analysis package used in many fields within the industry as well as in the power transmission industry. Unfortunately EMTP suffers from a major disadvantage in that it does not have a user-friendly interface. Even experienced users encounter problems with EMTP when attempting to model complex devices and systems. This problem combined with the actuality that FACTS devices are inherently complex and thus difficult to model makes experimentation with FACTS devices a non-trivial exercise. This is especially the case with users who are unfamiliar with EMTP and/or FACTS devices.

With the above point in mind a preprocessor for EMTP is being developed to make experimentation with FACTS devices easier. The final product will be able to guide users, who are unfamiliar with FACTS devices, through the design of a FACTS device as well as automatically including the FACTS model in the users own EMTP network file.

This paper describes the stages in the development of the preprocessor as well as a few details of the functional implementation of the preprocessor.

## 2. SOFTWARE QUALITY

### (a) Ease of use

The user's ability to learn an interface is crucial to its acceptance[1]. This is one of the reasons that applications developed for GUI's are becoming more

and more popular. Other factors include a consistent, easy-to-use interface and easier integration with other applications[2].

One of the prerequisites for the preprocessor is that it should be as easy to use as possible. With this in mind, it was decided to develop the preprocessor for the Microsoft Windows platform.

Programming for a GUI using a traditional language (structural language) can, however, be exceedingly difficult because of the sheer complexity of the Application Programming Interface (API). For example, Microsoft Windows has over 400 function calls, about 10 times as many as in MS-DOS. A simple program displaying a window with the text "Hello World" in it will take about 300 lines of code[2].

Fortunately Object-Oriented Programming (OOP) reduces the complexity of GUI programming because graphical environments have an inherent complexity that makes them good candidates for the benefits of OOP. OOP offers a way of building a higher layer on a GUI so that you don't have to know all the details of the API[2].

### (b) Documentation

User expectations of modern software has made development of serious software (eg. GUI applications with extensive online help etc.) much more complex. When developing software of this nature, one can no longer just sit down behind the computer with a general idea of what you want to do and start programming.

In line with recent Software Engineering quality principles, it was decided to develop the documentation for the program before starting to code the program. The documents listed below will be developed before coding and testing of the product will begin.

- User Requirement Specification (URS). The URS specifies the functionality that is required of the final product. When the final product has been developed, each of the specified items in the URS should be met before the software developer can claim that the software is complete.
- User Reference Manual (URM). The URM is written chiefly as a reference into the functionality of the program. The URM should

track the URS in terms of meeting the requirements specified in the URS. The URM is also written for the user so that he/she may consult it to determine how to perform a specific operation. The URM should also state the limitations of the product.

- Technical Reference Manual (TRM). The TRM contains information pertaining to the technical functionality of the product as well as details of the entire software design (in this case Object Oriented Design). The TRM is the main source of information on how the program works and is most useful when making changes to the program.
- Product Test Specification (PTS). The PTS is a specification of all the tests that should be performed on the program. The PTS should be comprehensive and attempt to test all possibilities that may occur in the program. The program should pass all tests set out in the PTS before it can be assumed that it is working according to specifications.

### (c) Software Maintainability

As mentioned before, structured programming languages make programming for GUI's prohibitively difficult. Inherent to structured programming is code that is difficult to maintain. One of the reasons is due to the fact that changes to a particular data structure will cause changes in all functions that use the data structure. In structured programming it is also common to see global data that is specific to the application. This global data makes it difficult to reuse code since many of the functions merely access the global data. OOP does not suffer from these limitations.

A goal of object orientation has always been to make changes easier[3]. OOP involves the encapsulation of both data and functions. Therefore, in a properly designed class structure, a change to a data structure will only affect the class in which the data was changed.

The major advantage of an object-oriented approach to interface design is the clear decomposition of structure and functionality, which makes it easier for a developer to design, maintain and reuse components. Since object-oriented systems support inheritance, new components can be specialized or extended from existing ones[2].

A good recommendation for maintainable software is that the code for the interface must be separated as much as possible from the code for the underlying

functionality of the system[4]. This ensures that the same functional code can be used when it is decided to modify the user interface. For example, in the case of the preprocessor data will be entered mostly as text. If the functionality of the preprocessor and the method of data entry is separated, it will be relatively painless to add a graphical data entry interface.

## 3. PRODUCT SPECIFICATION

Listed below is a short summary of a few of the specifications for the preprocessor.

### (a) Common work area

The preprocessor should provide a common working area for developing, editing and executing EMTP data files as well as providing the ability to view EMTP plots. These functions can be implemented by:

- providing a built-in text editor.
- acting as a "shell" from which EMTP may be called to execute a data file.
- acting as a "shell" from which an external plot program (e.g. PCPLOT) may be called to display the plot files.

### (b) Library management

The preprocessor should provide library functions to create a library of models, consisting of devices as well as their controllers. This library interface should form a lower level interface for the FACTS device modelling.

- Generally, the user should be able to Add, Edit and Delete devices and controllers from the model libraries. The user may also create his own libraries containing his most often used models, for example.

Specifically the following library functionality should be provided in order to set up a library i.e. when a new device or controller is added to the library, the product should be able to:

- extract input parameters by reading EMTP model files (the \$INCLUDE file generated by EMTP's *DATA CASE MODULE* directive).
- read EMTP \$INCLUDE files containing EMTP MODELS sections in order to extract input parameters.
- allow the user to build his own dialogue box for his model. This dialogue box will then be used when the user wishes to use a particular model. The following specifications are relevant while the user is creating the dialogue box.
  - i) The user should be able to specify descriptive names for the input parameters

- (read in as mentioned above). This will allow the user to create a model which has descriptive parameter names (as opposed to those used in the \$INCLUDE file).
- ii) In order to make a model easier to use the library interface should also allow *help text* to be entered for each parameter name that has been read from the \$INCLUDE file. The possibility of supplying default values as well as limits for numeric parameters should also exist.
- allow the user to set up a library model consisting of a number of existing library models. This feature will allow larger models to be built using sub-models.
- attach controllers to devices (ie. set a link between controllers and devices) so that controllers may only be used on devices they were designed for. Once a controller has been linked to a device common nodes and data should be specified. This allows the user to select a device and controller and not worry what the internal connections are.
- Models for specific FACTS devices should be provided as a standard feature of the programme.
- Code should be provided for each FACTS device to help the user with parameter selection. If necessary code should be provided to perform essential calculations for the user e.g. component selection given a devices power rating.
- Extensive help should be provided for each FACTS device catered for. Help text should include uses, selection criteria and a list of references for each FACTS device included with the preprocessor.

### (c) Integration of models with data files

The preprocessor should make the inclusion of library models into existing EMTP data files as easy and as seamless as possible.

- Inclusion of a model into a EMTP data file should consist of selecting a device model, selecting a controller for the device, if necessary, and then entering the required parameters for the device and controller. The parameters will be entered via the custom dialogue boxes designed for the device and controller respectively. The preprocessor should then update the users data file (the file to which he wants to add the model) automatically.
- The preprocessor should keep track of which data files and controller & device models are being used together. This may be done in the form of a project file which links all the files together. All parameters and other necessary information are stored in the project file. This will allow easy management of groups of data files and models.

### (d) FACTS support

FACTS device support should be provided by using the above specifications as a base from which to work. This means that the preprocessor should be able to work purely as a model library management program. The preprocessor should provide the following in terms of FACTS support:

## 4. IMPLEMENTATION

To keep this paper as short as possible, only a short description of each of the menus included in the main application menu bar will be included. The menu options include FILE, EDIT, MODEL, PROJECT, EXECUTE, OPTIONS, WINDOW and HELP.

### (a) File

The FILE menu provides commands for the opening, saving and printing of EMTP data files (or any other text files). The user uses this menu to load, save and print his EMTP data files.

### (b) Edit

The EDIT menu provides commands to manipulate text data within the built-in text editor. These include functions like cut, paste, text searches and moving the cursor to a specific line. The user uses this menu to edit text in his EMTP data files.

### (c) Model

The MODEL menu provides commands to Add, Modify and Delete models from the libraries maintained by the program. The user may also create his own libraries containing, say, only his most commonly used models. The user uses this menu mainly to create new devices and controllers.

### (d) Project

The PROJECT menu provides commands to open, close and edit project files. The project file keeps an entire EMTP simulation together. A project typically contains two things: the user's main EMTP data file and a list of models that are to be included in the data file. The data file is the user's main simulation file and contains all the necessary EMTP data cards to perform the simulation. When the user chooses to update the main file, the preprocessor writes the necessary data cards, for each of the models in the project file, to the main file.

Editing a project file allows the user to add or delete models to or from the project. It is from this Edit dialogue that the user may choose to include a FACTS device. (Note: FACTS devices are not explicitly handled in any of the menus listed here. This is because of the way the program was specified).

#### (e) Execute

This menu provides commands to run EMTP, view EMTP's output and execute a plot program to plot EMTP's plot file. The user uses this menu to run simulations, view output plots and check EMTP output errors.

#### (f) Options

This menu provides commands to specify default directories, for example EMTP data files. It also contains options to allow the user to otherwise customize the program.

#### (g) Window

This menu provides commands for managing multiple open windows. This menu also contains a list of all open windows. The user may tile, cascade, close or select windows from this menu.

#### (h) Help

This menu contains commands to help the user access the online Help. Included are categorized table of contents, an index and the ability to do a topic search.

## 5. CONCLUSIONS

The preprocessor discussed in this paper will make the use of predefined EMTP models easy to include into another specified EMTP data file. This will result in a substantial time saving because it takes the problem of interfacing the model with the data file away from the user.

FACTS devices are supported by adding an extra layer of functionality onto the "model library" specification specified in this paper. This is made easier with the use of OOP. The functionality of the model can be split from the functionality of how the data for the model is entered. This means that custom utilities can be developed for FACTS devices which will help the user to determine device parameters. The parameters are then passed to the normal model object in the model library. The model object has the functionality of writing the model to the main file and it is therefore not necessary to include this in the FACTS device object.

To date the User Requirement Specification has been completed and the first draft of the User Reference

Manual has been drawn up. Models for a Static Var Compensator (SVC) have also been completed. Once the URM has been finalized, the preprocessor design will be performed and documented in the Technical Reference Manual.

## 6. REFERENCES

- [1] Ege R., Stary C.: "Designing Maintainable, Reusable Interfaces", IEEE Software, November 1992, p24.
- [2] Urlocker Z.: "Object-Oriented programming for Windows", Byte. p287-294, May 1990.
- [3] Booch, G.: "Object-Oriented Development", IEEE Trans. Software Eng., February 1986, p211-221.
- [4] Schlumberger, M: "Definition and validation of user interfaces", Designing and Using Human-Computer Interfaces and Knowledge Based Systems, Proc. of the Third International Conference on Human-Computer Interaction, Boston, Massachusetts, p518-525, September 1989.

## 7. ADDRESS OF AUTHOR

Mr NH Ramage  
University of the Witwatersrand  
Private Bag 3  
Wits 2050  
South Africa

## DEVELOPMENT OF COST-EFFECTIVE ENERGY MANAGEMENT STRATEGIES

N.M. Ijumba

Department of Electrical and Electronic Engineering  
University of Nairobi, P.O.Box 30197, NAIROBI-KENYA

### ABSTRACT

*The escalating electrical energy costs have made it imperative for many institutions to closely examine their energy consumption practices, so as to reduce consumption and cut down costs. This paper discusses short and long term energy management strategies developed for the University of Nairobi, after conducting an energy audit and equipment survey. By operating at optimum power factors, savings of between 7% and 35% are possible, depending on the initial power factor, with pay back periods varying between 1 month and 6 months. Effective reduction in energy consumption is also possible through improvement in motor load factors, implementation of equipment maintenance schedules, and adoption of simple energy conservation measures.*

### INTRODUCTION

In many institutions, electricity is one of the main sources of energy, and so energy bills form a large proportion of the operating budgets. Variations in tariff rates lead to distortions in budgets and re-adjustment of expenditures. In Kenya, for example, there has been an upward review of unit costs almost annually, between 1990 and 1994. Within that

period, the University's energy bill increased by 145%), whereas the corresponding total electrical energy consumption increased only by about 12% (see Table 1).

Reduction in energy costs can be achieved by either reducing the cost, for the same level of Kwh consumption, through power factor correction, or by reducing the actual energy consumed through energy conservation and efficient electrical equipment operation. Energy conservation measures can either be short or long term, and the choice depends on technical and economic considerations. Technically feasible and financially viable measures are identified after obtaining and analysing data on energy consumption.

In this study, an energy audit programme and an equipment survey were carried out to obtain data on the energy consumption pattern, as well as establish an equipment data base. The data obtained was used to develop strategies for effective energy consumption and minimisation of energy costs.

## DATA ACQUISITION AND ANALYSIS

The study involved monitoring of active and reactive power consumption, and power factor measurements, at regular intervals, and on a daily basis, for about two weeks, at selected metering points. A total of 20 metering points were monitored. Previous electricity bills of the monitored points were also examined to establish the trend in consumption and energy costs. An equipment survey was also conducted to obtain name plate data, establish operation patterns and procedures, assess equipment physical conditions, and measure the instantaneous power consumption of the main loads.

From the energy monitoring, it was possible to obtain the average and peak values of active and reactive power, energy (Kwh), maximum KVA demand and power factor, as well as the daily load cycles. The equipment survey provided information on the operating cycles of the major loads, and motor load factors. This information was stored in a data base together with the assessed physical conditions of the equipment.

**Table 1:** Annual energy consumption and cost

YEAR	KWH $\times 10^{-6}$	KSHS.
1990/91	7.94	9,607,897.35
1991/92	6.71	9,396,354.25
1992/93	8.13	12,199,378.15
1993/94	8.96	23,564,805.55

The energy data was analysed using an interactive PASCAL Programme, and it was possible to obtain on optimum power factors, possible energy savings and the pay back periods, at different rates of interest on capital.

## RESULTS AND OBSERVATIONS

The results obtained showed that the average operating power factor at 90% of the metering points was below the statutory minimum of 0.9. The power factor differential (i.e. the difference between the operating and statutory minimum power factors) varied between 3% and 25%. Each metering point had an optimum power factor at which the possible savings in energy costs were maximum (Figure 1).

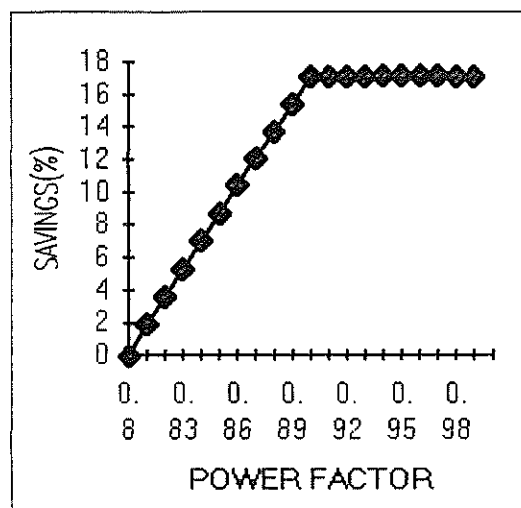


**Figure 1:** Variation of savings with power factor

The maximum savings and the pay back period for capital on power factor correction equipment were dependent on rate of interest on the capital.

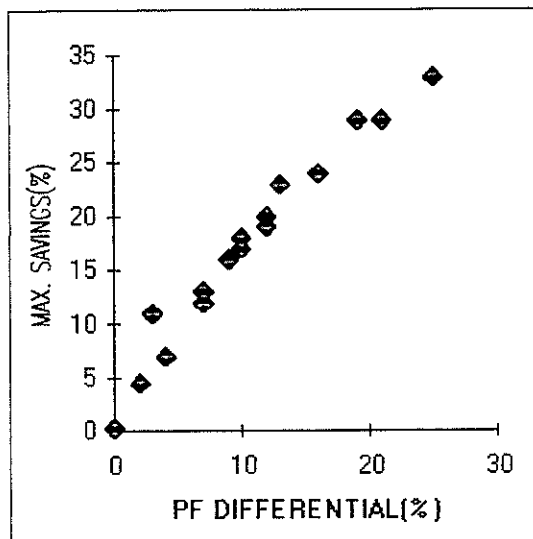


**Figure 2:** Correlation between power factor differential and maximum savings

Also, there was a positive correlation between the power factor differential and savings in energy costs, i.e. savings were higher at points with high power factor differentials (Figure 2). The calculated energy costs agreed quite well with actual monthly bills for the monitored points. This confirmed the accuracy of analysis in which data obtained over two weeks was used to calculate the monthly energy costs (Table 2).

Some of the surveyed equipment were poorly maintained. For example, thermostats of water heaters and the cold storage rooms were faulty, some motors had worn out bearings, luminaires were dirty and a number of fluorescent fittings had faulty ballasts. The instantaneous power measurements showed that a number of motors were operating at low load factors (i.e. between 25% and 40%).

## DISCUSSION

From the results of the energy and equipment survey, it was possible to come up with strategies for efficient energy utilisation and minimisation of costs. The strategies have been divided into two categories, i.e. short term measures for immediate implementation, and the long term ones for gradual implementation, as funds become available.

The short term strategies were:

- (i) Reduction of energy costs through power factor correction. The potential savings (i.e. 10% - 33%) when operating at optimum power factors, and the relatively short pay back periods (1 month to 6 months), made the proposal attractive for immediate installation of capacitor banks was recommended, starting with loads that are currently operating at very low power factors. If all the metering points were to operate at optimum power factor, the overall saving will be about 20%, within the pay back period. The accrued savings can be used to finance the implementation of the longer term strategies.
- (ii) Reduction of actual energy consumed by improving system operating efficiency. This can be achieved by:
  - Repairing the faulty equipment (e.g. replacement of thermostats for water heaters and cold storage rooms, and changing of faulty motor bearings).
  - Improvement of motor load factors.
  - Regularly cleaning luminaires and replacing faulty ballasts of fluorescent light fittings.

The long term strategies include:

- (i) Sizing of motor loads to improve load and power factors.
- (ii) Replacement of electric cookers in the catering units with gas cookers.
- (iii) Development of a maintenance schedule for all the major electrical equipment.
- (iv) Initiation of programmes to create awareness on energy conservation among University staff and students.
- (v) Appointment of an energy manager, who will see to the development and implementation of an energy audit and management programme.

## CONCLUSION

This presentation has discussed energy management strategies developed using data obtained from energy consumption and equipment surveys. The developed strategies include operating at optimum power factors, improvement load motor load factors through effective load matching, as well as regular and proper equipment maintenance to raise the overall system efficiency. The projected savings at optimum power factors are varying between 10% and 35%, depending on the initial power factor, and the pay back period for the majority of the power factor correction equipment is less than six months.

Continuous energy monitoring will be undertaken to assess the effectiveness of strategies being implemented.

**Table 2: Comparison of calculated monthly energy costs and actual bills**

LOCATION	CALC'TD COST(KSH)	ACTUAL BILL(KSH)
CCU	770,290.92	725,284.00
GANDHI	207,122.83	192,733.10
W/HALL	133,485.57	134,970.35
MAMLAKA	479,609.34	457,810.00
HALL 13	203,969.08	180,476.90
ADD	364,417.20	372,461.05
KIKUYU	193,390.43	180,705.15

## ACKNOWLEDGEMENT

The author wishes to thank the University Deans' Committee for financing this study.

## AUTHOR'S ADDRESS

*Professor N.M.Ijumba, Department of Electrical & Electronic Engineering, University of Nairobi, P.O.Box 30197, Nairobi - KENYA.*

# THE MODELLING OF ARC FURNACE FLICKER AND SYNCHRONOUS CONDENSER COMPENSATION

H.M. Petersen  
RAU

R.G. Koch  
ESKOM T-R-I

R. van Heerden\* P.H. Swart  
RAU

\*Eskom Transmission Operations and Maintenance South Africa

## ABSTRACT

The flicker phenomenon is reviewed. A method of simulating an arc furnace using a stochastic three phase arc resistance model is presented. A 33MVA arc furnace installation is simulated as a case study. A digital implementation of the flickermeter developed by UIE is included in the model to assess the flicker severity at the PCC and compare it with the measured values. Flicker compensation, using a synchronous condenser, with constant field excitation, has been investigated.

## 1. INTRODUCTION

The generation of electricity has to be perceived as a commercial process subject to quality control and assessment. Aspects of voltage quality, namely harmonics, unbalance and flicker currently enjoy growing attention world wide. With commerce and industry embarking on a new road of deregulation, previous state controlled industries, are now open to competition. Energy generation and distribution is one such industry, and therefore it is not surprising that the quality of supply has become an important consideration.

Arc furnaces are the largest end-users of electrical energy in industrial power supply networks [1,2]. They are non-linear and time-variant loads that adversely affect voltage quality in the forms of:

- \* voltage fluctuations
- \* harmonic distortion
- \* unbalance.

Flicker is the physiological perception of variations in light intensity as a result of voltage fluctuations. Flicker perceptibility threshold curves (fig. 1) show that fluctuations in voltage-amplitude of 0,3 % at frequencies between 8 - 10 Hz result in perceptible variations of luminosity with incandescent lamps [10].

The prediction of flicker has become an important consideration in the design procedure of new industrial power systems. The prediction techniques may be classified as [8]:

- \* Classical
- \* Empirical
- \* Simulation techniques.

Once a flicker severity value has been reasonably well predicted, it is possible to decide whether

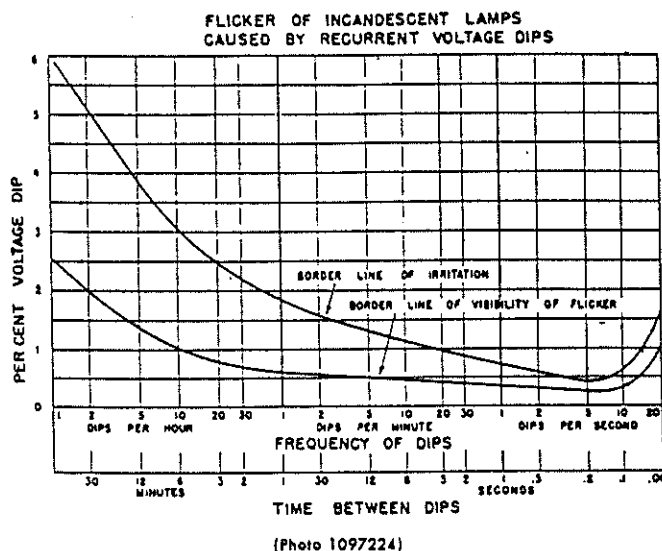


Figure 1. Flicker perceptibility threshold curves.

compensation will be necessary, and if so, what type of compensation should be used and where it should be employed. These techniques provide a means by which the selection of the most suitable network and compensation options can be achieved. Simulation techniques, in particular, allow for experimentation with flicker compensation options (e.g. SVC, synchronous machines). All available mitigation options can be investigated within a reasonable time frame and without great cost. Figure 2 shows a diagram of the modelled system.

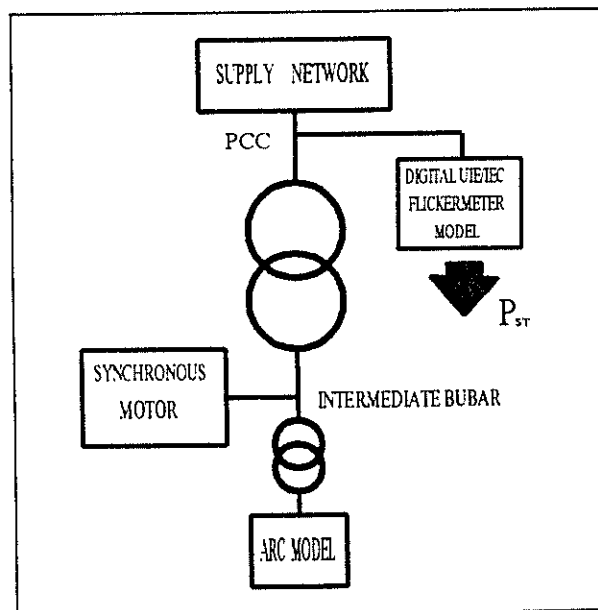


Figure 2. Simulation model.

## 2. AC ARC FURNACES.

An AC arc furnace generally consists of a refractory lined shell that holds the scrap metal. Three graphite electrodes, positioned in movable clamps, can provide arc length regulation and can be swung aside for scrap metal charging [4].

After being charged with scrap metal the electrodes are swung back into position and lowered into the scrap metal to strike an arc. When the arc has been initiated, the electrode control system regulates the vertical movement of the electrodes to provide an optimum arc length and hence a stable arc. The voltage across an arc, is relatively independent of the arc current and consists of 3 components [3,4]:

- \* the anode drop, typically 30V
- \* the cathodes drop, typically 10V
- \* the voltage across the arc column, typically 12V/cm.

Therefore the arc voltage may be:

$$V_{rms} = 40 + 12V/cm \quad (1)$$

The arc furnace has two natural limits of operation, an arc stability limit and a short circuit limit. To ensure stable operation of the arc, especially during bore-down, the arc is operated at arc lengths that will ensure that the arc reignites after every current zero crossing. This implies a relatively low power factor, as a result of:

- \* short arc lengths
- \* low arc voltages
- \* high arc currents.

The short circuit limit is reached when all three electrodes are in physical contact with the scrap metal.

Steel making from arc furnaces is a batch operation, where each heat is followed by another without many interruptions. Bore-down is the harshest of the furnace modes, where the arc is most unstable and the resulting flicker worst. The random motion of the electric arc, swirling of the molten bath, and changes in arc length cause random fluctuations in arc current. These fluctuations in arc current translate as voltage fluctuations higher up in the network.

## 3. IMPLEMENTATION OF A SIMPLE ARC-RESISTANCE MODEL

The 3 basic operating states of an electric arc furnace [4] are shown in figure 3. They produce significant voltage fluctuations and ultimately cause flicker. In the extreme, the furnace state can change from a complete 3 phase short circuit to an open circuit condition when the arc is extinguished. During normal operating conditions, the furnace

currents fluctuate randomly, causing flicker.

Statistical studies [9] have revealed that the variation of furnace parameters (resistance, reactance) in general is a quasi-stationary process. The probability density functions of these variations over a particular period, are not always truly Gaussian. In general, the distributions are more concentrated around the mean value than expected for a normal distribution. The approximation of these variations with a Gaussian distribution, is a simplification of the actual variations, but provides an acceptable model.

Random fluctuations in arc resistance are simulated by defining a mean furnace resistance  $\bar{R}$  and a variance  $\delta$  [6].

$$R_{arc} = \bar{R} \pm \delta \sqrt{-2\ln RAND1} \cos(2\pi RAND2) \quad (2)$$

The variance  $\delta$  can be chosen iteratively by making use of the voltage depression ratio, empirically determined as being 40 for  $P_{st}=1$ .

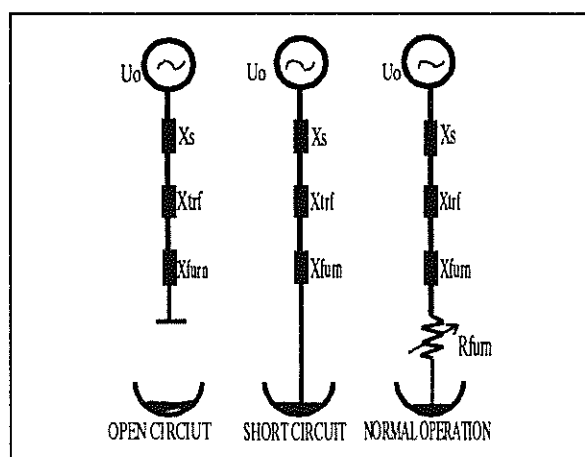


Figure 3. Operating state of an electric arc furnace [4].

## 4. DIGITAL MODELLING OF THE UIE FLICKER METER

The IEC specification on flicker evaluation prescribes the use of the flickermeter developed by the Disturbances Working Group of the International Union for Electro-heat (UIE) [10]. The instrument simulates the lamp-eye-brain response to voltage fluctuations on the supply voltage.

Simulation of the UIE-flickermeter was achieved in the model by digital processing of the voltage output. The results of the modelled flickermeter were compared with those of the Eskom analogue UIE-flickermeter for a square-wave modulated 110V 50Hz calibration signal (Table 1)

**Table 1.** Measured and simulated flickermeter outputs for a square-wave modulated 110V signal.

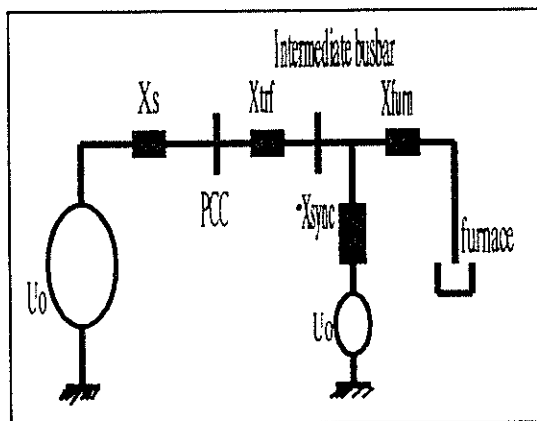
$\Delta V$ in (mV)	UIE Flickermeter $P_{st}$	Simulated $P_{st}$
134	0.48	0.41
327	1.06	1.06
474	1.52	1.51

## 5. SYNCHRONOUS CONDENSER COMPENSATION [8]

A synchronous condenser effectively raises the fault level at the intermediate busbar. Equation 3 shows an approximation of the expected voltage depression ratio [8]:

$$\frac{\Delta U}{U} = \frac{X_s}{X_s + X_{trf} + \left(1 + \frac{X_{furn}}{X_{sync}}\right) + X_{furn}} \quad (3)$$

- \*  $X_{furn}$  is the total reactance of the furnace (cables, electrodes and transformer).
- \*  $X_s$  is the supply impedance (to the PCC).
- \*  $X_{trf}$  is the reactance of the supply transformer.
- \*  $X_{sync}$  is the subtransient reactance of the condenser.

**Figure 4.** Single line diagram with synchronous condenser.

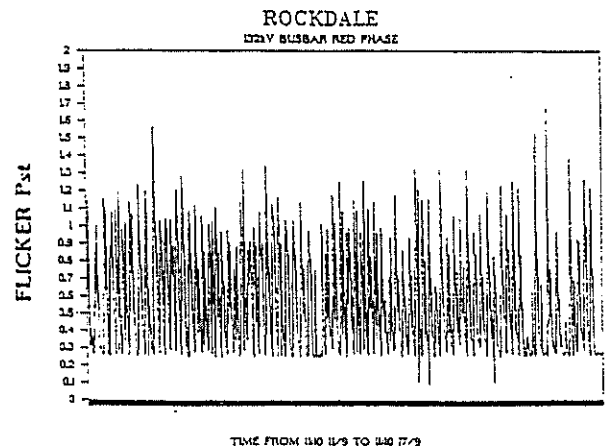
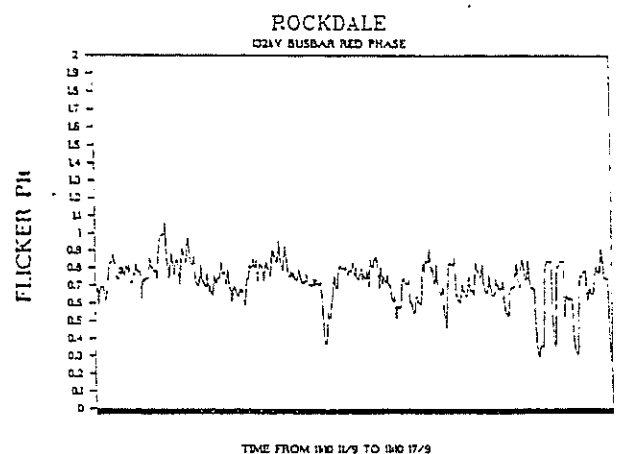
## 6. CASE STUDY: 33MVA FURNACE MODEL

A 33MVA furnace is supplied from the 132kV Eskom busbar (PCC) by a 40MVA transformer with an intermediate busbar voltage of 22kV. The delta-delta furnace transformer secondary voltages range from 229V (tap 1) to 426V (tap 13). Table 2 lists the relevant parameters.

**Table 2.** Network parameters for the modelled furnace installation. (Highest Tap - 990V).

PARAMETER	VALUE
Secondary resistance - R	0.415mΩ
Furnace cable & transf. -X	2.973mΩ
132/22 kV transformer	10.5%
Fault Level at 132 kV PCC	3546MVA

Flicker measurements were conducted at the 132kV busbar VT's over a 1 week period [9]. Figures 5 and 6 show the  $P_{st}$  and  $P_{lt}$  values over this period.

**Figure 5.** Short term flicker severity values.**Figure 6.** Long term flicker severity values.

The network with furnace and synchronous condenser models are implemented in EMTP on a 80486-DX2/66 micro-computer. The PCC voltage was written to an output file, for processing by the digital UIE-flickermeter model.

The modelled flicker values are compared with those measured. Assuming that the background flicker is negligible, the  $P_{st99\%}$  value over the measurement period was 1.3.

The modelled  $P_{st}$  values are presented in Table 3 for variances:  $4.20\text{m}\Omega \leq \delta \leq 4.28\text{m}\Omega$

**Table 3.** Predicted short term flicker severity values  $P_{st}$  of the simulation without compensation.

$P_{st}$ measured	$P_{st}$ modelled	$\delta$	$R$
1.30	1.28	4.20m $\Omega$	9.525m $\Omega$
1.30	1.31	4.22m $\Omega$	9.525m $\Omega$
1.30	1.33	4.24m $\Omega$	9.525m $\Omega$
1.30	1.36	4.28m $\Omega$	9.525m $\Omega$

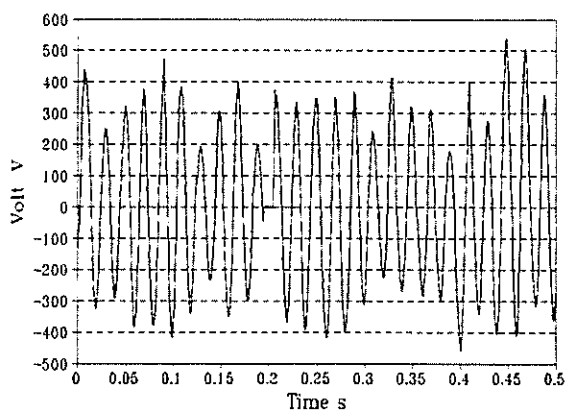
These values are statistically scattered around  $P_{st}=1.3$ , and are reasonable modelled value of the flicker severity, for a range of variances (44-45%).

Table 4 presents the predicted  $P_{st}$  value with synchronous compensation. Synchronous machine compensation was investigated, with constant field excitation, at flicker severity  $P_{st}=1.31$  and variance  $\delta=4.22\text{m}\Omega$  (row 2 table 3). Two machines were investigated at synchronous speed, without the application of excitation control.

Machine 1: 40MVA, 4 poles, 13.8kV, 50Hz, 250 A  
Machine 2: 25MVA, 4 poles, 13.8kV, 50Hz, 150 A

**Table 4.** Predicted flicker severity values of simulation with synchronous condenser compensation, with constant field excitation.

Device	$P_{st}$ Predicted	Reduction Factor
Machine 1	1.04	1.26
Machine 2	1.11	1.18



**Figure 7.** Simulated arc-voltage.

The predicted values above already provide significant reduction in flicker severity. The reduction factor is expected to considerably increase when field excitation is applied. A previous study [6], investigating SVC compensation on the same installation, projected a flicker reduction of 1.68. Synchronous condensers with high-speed excitation have shown flicker reduction values of 2 [8]. Figures 7, 8 and 9 show the arc voltage, current and resistance simulated waveforms, without synchronous compensation.

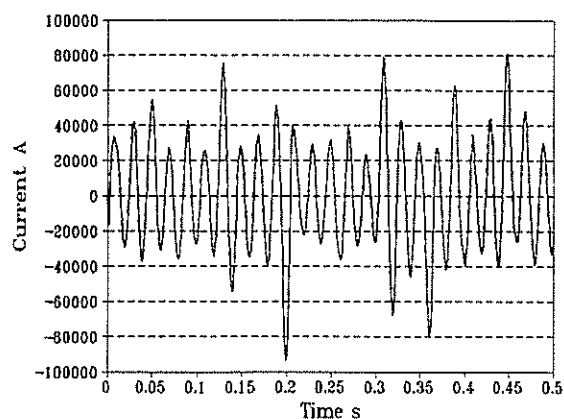


**Figure 8.** Simulated arc-current.

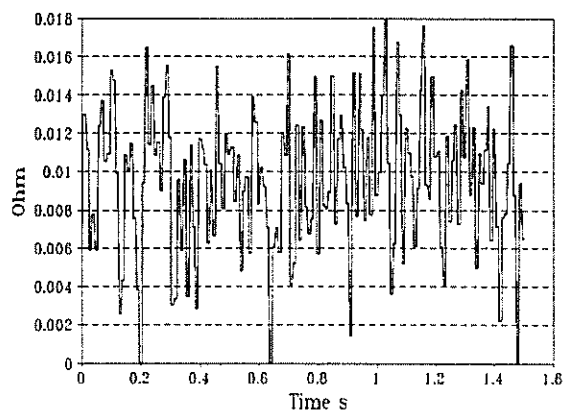


**Figure 9.** Simulated arc-resistance.

## 7. CONCLUSIONS

- 1) The arc-resistance model provides a simple simulation technique to assess flicker for a given installation. The effectiveness of various compensation techniques can be quickly and easily investigated. This has been illustrated with the modelling of a 33MVA furnace on the Eskom network.
- 2) The implemented synchronous machines, are experimentations with possible machine sizes. The final choice of a machine can be made, based on the simulation results,

- which include field excitation models.
- 3) Confidence in the simulated results will only be achieved by the application of this model to several other installations, and by comparison with experimental results.
  - 4) Simulated results, without compensation, are consistent with actual measurements.

#### ACKNOWLEDGEMENTS

To P.M. Roussow of Eskom T-R-I for measurements.

#### REFERENCES

- [1] Dan, A.M., et al.: 'Comparison of Different Ways to Simulate Arc Furnace Power Quality Impacts', Proceedings of IEEE ICHPS VI, September 1994.
- [2] Schau, H., Stade, D.: 'Mathematical Modelling of Three-Phase Arc Furnaces', Proceedings IEEE ICHPS VI, September 1994.
- [3] Bowman, B.: 'The Physics of High-Current Arcs', Journal of the Iron and Steel Institute, pp 798-805, June 1969.
- [4] Manchur, G., Erven, C.C.: 'Development of a Model for Predicting Flicker from Electrical Arc Furnaces', IEEE Transactions on Power Delivery, Vol. 7, No. 1, January 1992.
- [5] Lavers, D., Danai, B.: 'Computer Evaluation of Electrical Arc Furnace Disturbances', Paper No. 83143 IEEC, 1983.
- [6] Koch, R.G., et al.: 'The Modelling of Arc Furnace Flicker and SVC Compensation Requirements', South African Universities Power Engineering Conference, 1994.
- [7] Koch, R.G.: 'Power System Planning for Large Distribution Loads', Part 2 - Arc Furnace Simulation and SVC Compensation Requirements, T-R-I Report No. TRR/E/93/QS009, 1993.
- [8] Koch, R.G.: 'Power System Planning for Large Distribution Loads', Part 1 - Flicker Produced by Arc Furnaces, T-R-I Report No. TRR/E/93/QS008, 1993.
- [9] Robert, A.: 'Assessing Power Quality with Relation to Harmonics, Flicker and Unbalance', Working Group CC02, Cired 36-05/ Cired 2, 02-05-1991.
- [10] IEC Report, 'Flickermeter Functional and Design Specifications', Publication 868, 1986.

# BOFREKWENSIE DRYWINGSMETER EN BOFREKWENSIE DRYWING TARIEFSTELSEL

W J van der Merwe, P H Swart en M J Case

Randse Afrikaanse Universiteit

## SINOPSIS

*Een metode waarmee vervormingsbronne gelokaliseer kan word, is om die strome en spannings in die insetterminale van gebruikers te meet en die drywing in die bofrekwensies te bepaal. Die propagasie-richting van bofrekwensie aktiewe drywing gee 'n aanduiding aan watter kant van die meetpunt die vervormingsbron hom bevind. Deur die normale tariewe op die fundamentele aktiewe drywing en die maksimum MVA-aanvraag te hef, soos tans die geval is, maar ook daarby addisionele heffings op die "maksimum-bofrekwensie" opwekking deur 'n verbruiker te hef, kan verbruikers ontmoedig word om vervormingsbronne in hulle stelsels aan te wend, of om kompenserings van hierdie vervormingsdrywing te implementeer. 'n Relatief eenvoudige analoog meter wat aan hierdie vereistes voldoen, word hier bespreek.*

## 1. INLEIDING

Gedurende die afgelope dekade was daar 'n dramatiese toename in bofrekwensie besoedeling in elektriese kragverspreidingsnetwerke. Hierdie besoedeling, wat deur vervorming van die stroom- en spanningsgolfvorms gekarakteriseer word, word onder meer voortgebring deur die groeiende aantal en grootte van nie-lineêre drywing-elektroniese apparaat wat toenemend aan hierdie stelsels verbind word.

Dit is in die belang van energie-voorsiensers om gebruikers te ontmoedig om vervorming-strome uit hulle netwerke te trek. Elektriese apparaat moet in die eerste plek netvriendelik wees, of gebruikers moet aangespoor word om vervormingskompensering uit te voer en die stroomgolfvorms weer na hulle optimale sinusoidale vorms te restoureer. As gevolg van die netwerkimpedansies bring die nie-sinusoidale strome dan ook vervormde spanningsvalle mee, wat op hulle beurt weer vervormde spanningsgolfvorms op gebruikersterminale tot gevolg het.

Die vervormde spannings- en stroomgolfvorms in die verbruikers se insetterminale verteenwoordig bofrekwensie-drywing wat óf deur die gebruiker geabsorbeer óf deur hom opgewek word. Soms is daar vervormde

strome en spannings aanwesig wat nie noodwendig naby aan die meetpunt opgewek word nie, maar resonansie van die netwerk by daardie punt verteenwoordig. By hierdie metings lê die knoop, aangesien dit nie eenduidig deur afsonderlike metings van die spannings of die strome bepaal kan word aan watter kant van die meetpunt die vervormingsbron lê nie.

Daar is reeds getoon<sup>[1]</sup> dat die bofrekwensie aktiewe drywing in 'n lyn gebruik kan word om die ligging van die skuldige vervormingsbron, relatief tot die meetpunt, aan te toon. Bofrekwensie aktiewe drywing sal altyd uit die rigting van die oorsprong daarvan in die teenoorgestelde rigting gepropageer word. Indien die gebruiker 'n netto opwekker van bofrekwensie drywing is, sal bofrekwensie aktiewe drywing uit sy terminale in die rigting van die bron vloei en in die reële komponente van die netwerk-immitansies aan die netwerkkant van die gebruiker se terminale verkwis word.

Dit is moontlik om deur middel van relatief eenvoudige analoog-stroombane die fundamentele- en die bofrekwensie-komponente van die stroom- en van die spanningsgolfvorms in 'n gebruiker se terminale afsonderlik te bepaal. Die suiwer fundamentele strome en spannings kan dan deur konvensionele meetapparaat verwerk word en die bofrekwensie aktiewe drywing en die bofrekwensie skyndrywing kan dan afsonderlik ook deur hierdie apparaat geprosesseer word om op soortgelyke wyse as wat in die geval van die fundamentele drywing gebruik word, tariewe op die bofrekwensie "skade" te hef.

## 2. BOFREKWENSIEDRYWING

Die bofrekwensie komponente se stroom  $i_h(t)$  en spanning  $v_h(t)$  word onderskeidelik uit die Fourier analise gedefiniëer as :

$$v_h(t) = \sum_{n=2}^{\infty} V_n \cos(n\omega t + \phi_{vn}) \dots\dots\dots (1)$$

$$\text{en } i_h(t) = \sum_{n=2}^{\infty} I_n \cos(n\omega t + \phi_{in}) \dots\dots\dots (2)$$

$V_n$  en  $I_n$  verteenwoordig die onderskeie wgk-harmoniese skalaar-koeffisiënte en  $\phi_{vn}$  en  $\phi_{in}$  die onderskeie harmoniese fase-hoeke in die spanning en in die stroom by die gegewe harmoniese ordes  $n$ . Die wgk-waardes van hierdie harmoniese stroom en spanning kan gedefinieer word as :

$$V_h = \sqrt{\frac{1}{T} \int_0^T v_h(t)^2 dt} \quad \dots\dots\dots (3)$$

en 
$$I_h = \sqrt{\frac{1}{T} \int_0^T i_h(t)^2 dt} \quad \dots\dots\dots (4)$$

Die amplitudes van die bofrekwensie *aktiewe drywing* en van die *bofrekwensie skyndrywing* kan nou onderskeidelik gedefinieer word as:

$$P_h = \frac{1}{T} \int_0^T v_h(t) i_h(t) dt \quad \dots\dots\dots (5)$$

en 
$$S_h = V_h I_h \quad \dots\dots\dots (6)$$

### 3. BOFREKWENSIE DRYWINGSMETER

In die praktyk sal metings by groter gebruikers altyd drie-fase apparaat benodig, maar in die geval van kleiner stelsels (soos woonhuise of klein industrië) word enkel-fase meters gebruik. Op hierdie stadium word slegs na 'n enkel-fase meter gekyk.

Die werking van die apparaat, wat hierin beskyf word, benodig periodiese golfvorms met 'n vaste fundamentele frekwensie en bofrekwensies wat veelvoude van die grondfrekwensie is. Die werking van die analoogmeter word in fig. 1 in blokdiagrammatiese vorm voorgestel. Die enkel-fase spanning  $v_s(t)$  en stroom  $i_s(t)$  word op die normale wyse in die apparaat ingevoer. Die fasesluitlusse, blokke FSL in fig. 1, word in groter besonderhede in fig. 2 geïllustreer. Soos getoon, bestaan FSL uit 'n fase-detektor FD, 'n onderlaatfilter OLF en 'n spanningsbeheerde ossillator SBO. Hierdie drie komponente produseer 'n lae-distorsie sinusoidale sein van arbitrêre amplitude maar met nul-deurgange wat met die "gestadigde" fundamentele komponent s'n ooreenstem.

Die sinusoidale groothede  $v'_h(t)$  en  $i'_h(t)$  besit arbitrêre amplitude en word uit die gestadigde nul-deurgange van die insette  $v_s(t)$  en  $i_s(t)$  gesintiseer. Hierdie uitsette word in 'n amplitude-beheerder AB ingevoer, waarin die oorspronklike amplitude van die fundamentele komponente  $v_1(t)$  en  $i_1(t)$  weer aan hierdie komponente toegeken word deur die skema

wat in meer besonderhede in fig. 3 getoon word. AB bestaan op sy beurt weer uit twee analoog vermenigvuldigers, 'n winsbeheer-baan WB en 'n analoog integreerder baan met konstante vermenigvuldiging  $\sqrt{2}$ . Hierdie baan is daartoe in staat om beide die fundamentele komponente en die gesamentlike bofrekwensie komponente van spanning en stroom afsonderlik met die korrekte fases en amplitudes te lewer.

Die analoog-groothede  $v_1(t)$  en  $i_1(t)$  is beskikbaar vir verwerking deur konvensionele meetapparaat. Die groothede  $v_h(t)$  en  $i_h(t)$ , wat onderskeidelik die tydafhanklike funksies is van die gesamentlike bofrekwensies (met net die fundamentele komponente verwyder), is ook nou beskikbaar vir verdere verwerking. Die bofrekwensie skyndrywingsamplitude  $S_h$  word volgens verg. (6) bereken, deur  $v_h(t)$  en  $i_h(t)$  onderskeidelik eers na wgk waardes om te sit en dan te vermenigvuldig. Die gemiddelde aktiewe drywing  $P_h$  wat in  $v_h(t)$  en  $i_h(t)$  gesetel is, word uit verg. (5) verkry.

Die werking van elk van die bane in fig. 1 word nou in meer besonderhede bespreek:

#### (a) Die fasesluitlus (FSL)

Die FSL bestaan uit 'n fasesdetektor FD, 'n onderlaatfilter OLF en 'n sinusoidale spanningsbeheerde ossillator SBO. Vir die hergenerasie van die fundamentele frekwensie komponent word 'n lae totale harmoniese distorsie baan in SBO<sup>[2]</sup> gebruik (THD < 0.5%). Hierdie baan lewer 'n uitsetsein met vaste amplitude, naamlik  $v'_1(t)$  of  $i'_1(t)$ . Die FD vergelyk die fase van die insetsein met die SBO uitsetsein en lewer 'n foutsein wat deur die OLF die SBO beheer.

Beide die insetseine  $v_s(t)$  en  $i_s(t)$  en die opgewekte SBO uitsetseine  $v'_1(t)$  en  $i'_1(t)$  word deur vergelykers na die FD teruggevoer. Vergelyking van die seine word deur Analog Devices CMP-01 vlokkies bewerkstellig. 'n Positiefgaande randsneller FD (tipe II - 4046) word gebruik om die fasesluit lus mee te bedryf. Die OLF bepaal grootliks die stabiliteit van die FSL en word deur 'n passiewe tweede orde OLF geïmplementeer.

#### (b) Die amplitude-beheerder (AB)

Die vaste-amplitude sinusoidale seine  $v'_1(t)$  en  $i'_1(t)$ , wat deur die twee SBO stroombane gelewer word, word volgens die amplitude van die fundamentele frekwensie komponente van die insetseine  $v_1(t)$  en  $i_1(t)$  geskaleer. Indien die insetsein  $v_1(t)$  of  $i_1(t)$  voorgestel word deur:

$$x(t) = v(t) \text{ of } i(t) = A \cos(\omega t) + \sum_n C_n \cos(n\omega t) \quad \dots\dots\dots (7)$$

en die SBO uitset deur:

$$y(t) = v_1(t) \text{ of } i_1(t) = B \cos(\omega t) \quad \dots\dots\dots (8)$$

word die integraal van die produk gelewer as:

$$z(t) = \int_T x(t)y(t)dt = \frac{AB}{2} \quad \dots\dots\dots (9)$$

Die vermenigvuldiger uitset word dan verkry as:

$$\frac{AB}{2 \cdot 10} \quad \dots\dots\dots (10)$$

Indien die uitset amplitudes van die SBO-stroombane gelyk gestel word aan  $B=10V$  sal die uitsetamplitude dus  $A/2$  wees. Die wgk-waarde van die insette se fundamentele komponente word egter verlang om die amplitude van die gegenereerde fundamentele waardes  $v_1(t)$  en  $i_1(t)$  aan te pas. Die uitset moet dus met die faktor  $\sqrt{2}$  vermenigvuldig word.

'n Winsbeheerder (WB) word gebruik om die SBO-uitset te skaleer. Die wgk waarde van die SBO uitsette word in die WB-terugvoerlus met die verlangde wgk waarde en die SBO uitsetamplitude vergelyk en word dienooreenkomstig aangepas.

### (c) Drywingstroombane

Vanuit die FSL en AB stroombane word die fundamentele frekwensie komponente  $v_1(t)$  en  $i_1(t)$ , asook die bofrekwensie spannings en strome  $v_h(t)$  en  $i_h(t)$  direk verkry. Deur vergelykings (1) en (2) toe te pas, kan die bofrekwensie aktiewe drywing  $P_h$  en bofrekwensie skyndrywing  $S_h$  bereken word. Die wgk-waardes word met 'n wgk-na-gelykstroom vlokkie (Analog Devices AD536) verkry.

## 4 EKSPERIMENTELE RESULTATE

Hierdie faset van die werk maak nie voorsiening vir die byvoeging van die lopende gemiddelde fundamentele maksimum aanvraag of die bofrekwensie maksimum aanvraag berekening nie.

Die akkuraatheid van die bestaande stroombane is op die volgende wyse getoets. 'n Vervormde periodiese spanning  $v_s(t)$  en 'n vervormde periodiese stroom  $i_s(t)$ , met dieselfde fundamentele frekwensie en verstelbare fundamentele fase verskil tussen die twee, word onderskeidelik opgewek deur sommering van 'n reeks sinusoidale frekwensies, wat t.o.v. mekaar gesluit is.

Die analise bestaan uit twee komponente en is eenvoudig. Die tydafhanklike fundamentele komponent  $v_{s1}(t)$  of  $i_{s1}(t)$  wat gebruik word om die vervormde spanning of stroom mee te sintiseer, word vergelyk met die fundamentele komponent  $v_1(t)$  en  $i_1(t)$  wat uit die analoog-meter verkry word (verwys fig. 1) en die wgk-verskil daar tussen, word volgens die onderstaande vergelyking bereken:

$$\Delta V = \sqrt{\frac{1}{T} \int_T (v_{s1} - v_1)^2 dt} \quad \dots\dots\dots (11)$$

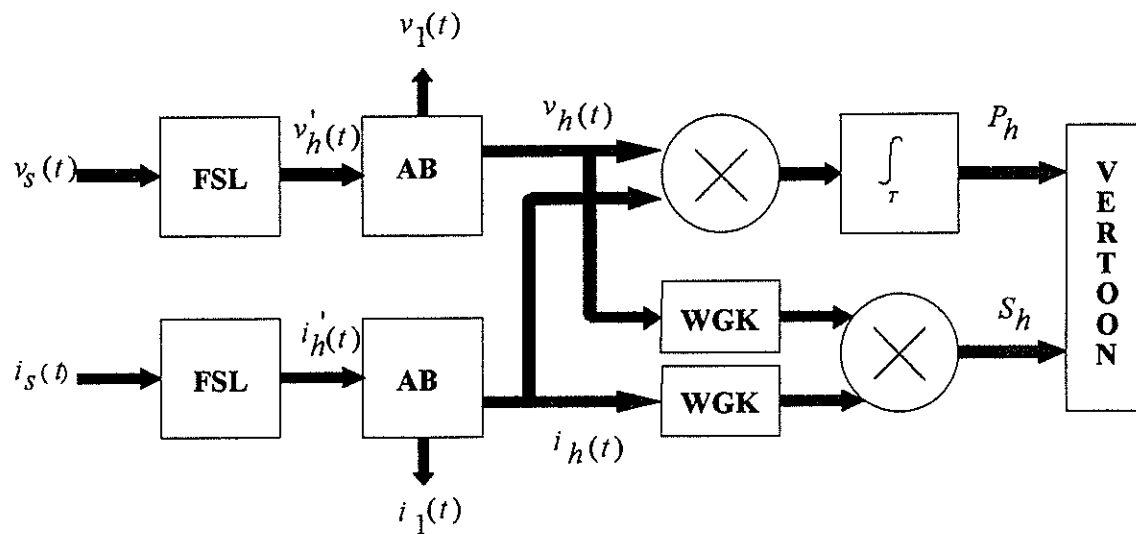
$$\text{en } \Delta I = \sqrt{\frac{1}{T} \int_T (i_{s1} - i_1)^2 dt} \quad \dots\dots\dots (12)$$

Bostaande wgk-verskille is verteenwoordigend van foute in amplitude sowel as in fase en dit volg dat  $\Delta V \rightarrow 0$  en  $\Delta I \rightarrow 0$  in die ideale geval. Een metode om die akkuraatheid van die "verwyderde" komponent uit te druk, is om dit as 'n persentasie van die wgk-waarde van die gesintiseerde sein,  $V_s$  of  $I_s$  uit te druk.

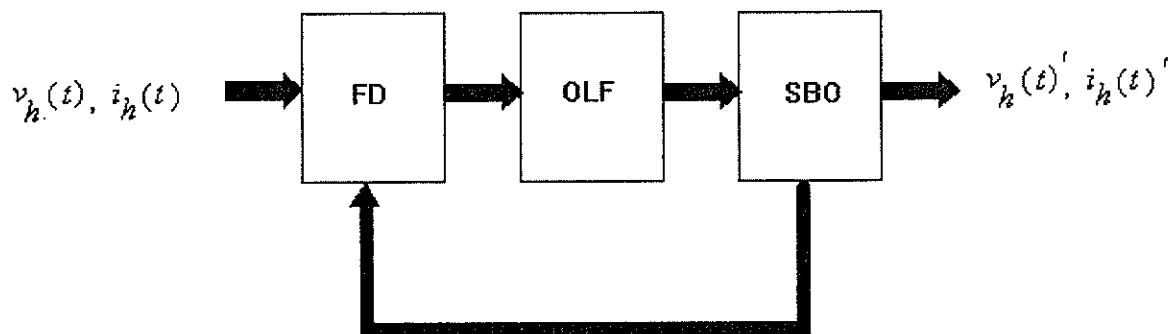
Op hierdie stadium word bestendige waardes van  $\Delta V/V_s$  en  $\Delta I/I_s$  van so laag as 0,75% verkry. Hierdie waardes is nog nie aanvaarbaar nie. Wat ongelukkig op hierdie stadium ook waar is, is dat die apparaat nog etlike sekondes neem om te stabiliseer na perturbasies in die inset stroom of spanning. Omdat die werking van die apparaat op relatief-groot tydkonstantes berus, juis om die fundamentele frekwensie in amplitude en fase uit die vervormde golfvorm te sintiseer, moet 'n optimale waarde van hierdie tydkonstantes gevind word, wat die akkuraatheid van die instrument teen die tyd-responsie daarvan afspeel.

## VERWYSINGS

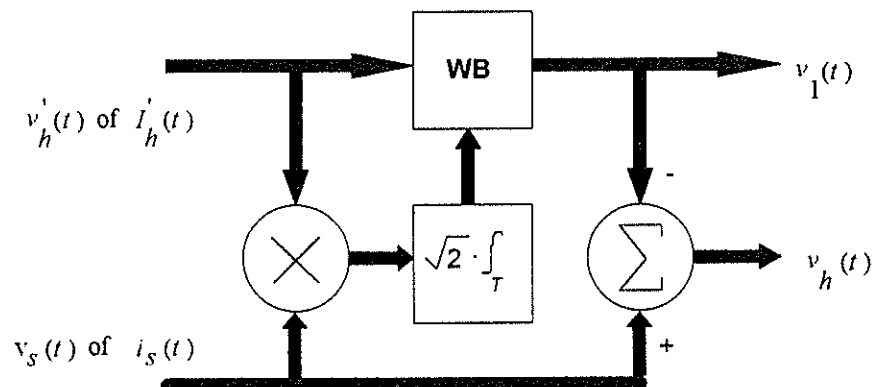
- [1] Swart, P.H., Case M.J., van Wyk J.D.: "On Techniques for Localization of Sources Producing Distortion in Electric Power Networks", Paper presented at the Second International Workshop on Power Definitions and Measurements under Non-sinusoidal Conditions, Stresa, Italy, September 8-10, 1993.
- [2] Filanovsky, I.M., Shui-sheng, Q., Kothapalli, G.: "Sinusoidal Oscillator with Voltage Controlled Frequency and Amplitude" International Journal of Electronics, Vol. 68, No. 1, pp. 95-112, Jan. 1990.



FIGUUR 1 : Blokdigrammatiese voorstelling van die analoog bofrekwensie drywingsmeter.



FIGUUR 2 : Diagrammatiese voorstelling van die fasesluitlusse (FSL).



FIGUUR 3 : Diagrammatiese voorstelling van die amplitude beheerders (AB).

## ELEKTRO-OSMOTIESE DROGING VAN STEENKOOL

W. Mulder en E. D. Smith

Departement Elektriese en Elektroniese Ingenieurswese  
Universiteit van Pretoria  
Suid-Afrika

### OPSOMMING

Gevestigde beginsels van elektro-osmose word beskryf. 'n Ondersoek na die toepassing daarvan op die droging van steenkool word gegee saam met die resultate van laboratorium proewe. 'n Berekening gebaseer op die voorafgaande proewe wys dat elektro-osmotiese, hittelose waterverwydering uit steenkool by kragstasies moontlik is met slegs 6% van die drywing wat andersins met termiese droging benodig sou word.

### 1.- Inleiding

Elektro-osmose is 'n redelik onbekende elektro-chemiese proses wat eers sedert die laat sewentigerjare in die kollig geplaas is deur die eksperi-mentele werk van veral H. Yukawa en H. Yoshida van Japan. Die belang van die proses van elektro-osmose lê in die feit dat ontwatering geskied onafhanklik van die grootte van die individuele porieë of gapings waardeur die water onttrek word. Dit maak die proses by uitstek geskik vir die ontwatering van stowwe wat tradisioneel moeilik ontwaterbaar is.

### 2.- Die elektriese dubbellaag

Meeste stowwe ontwikkel 'n oppervlakte lading wanneer dit in kontak kom met 'n polêre medium (soos water). Dit geskied deur die meganismes van ionisasie, ioonadsorpsie en ioondissolusie. Hierdie oppervlaktelading beïnvloed die ladings in die polêre medium. Ione met 'n lading teenoorgesteld aan die van die oppervlak (teen-ione) word aangetrek tot die oppervlak en ione met dieselfde lading word weer afgestoot. Dit lei tot die vorming van 'n elektriese dubbellaag bestaande uit 'n

gelaai oppervlakte en daaroor 'n neutraliserende laag teen-ione wat op 'n diffuse wyse versprei is in die polêre medium.

Die kwantitatiewe voorstelling van die elektriese dubbellaag is 'n moeilike en in baie gevalle onopgeloste probleem. Die model waarvolgens gewerk word kan soos volg vereenvoudig word (Gouy (1910) en Chapman (1913)):

- (1) Die oppervlakte word geneem as plat en eenvormig gelaai.
- (2) Die ione in die diffuse deel van die dubbellaag word beskou as puntladings met 'n verspreiding in ooreenstemming met die Boltzman-vergelyking.
- (3) Vir die doeleindes van berekeninge word 'n enkele simmetriese elektroliet met ladingsgetal  $z$  aanvaar.

Met die vereenvoudigde model kan die volgenede verhoudings afgelei word [1]:

- (1) Potensiaal in die dubbellaag is direk eweredig aan die eksponent van die wortel van die elektrolietkonsentrasie.
- (2) Die oppervlaktepotensiaal is direk eweredig aan die oppervlakte ladingsdigtheid en is omgekeerd eweredig aan die wortel van die elektroliet-konsentrasie.

Die aanname dat die ione in die diffuse deel van die dubbellaag puntladings is, is egter onakuraat. Die eindige groter van die ione plaas 'n fisiese perk op die binnegrens van die diffuse deel van die dubbellaag. Die rede is dat 'n ioonmiddelpunt die oppervlak slegs kan nader

tot op die afstand van sy gehidreerde radius voor dit geabsorbeer word. Stern (1924) het 'n model voorgestel waarvolgens die elektriese dubbellaag verdeel word deur 'n sogenaamde Stern-vlak op 'n afstand van een gehidreerde ionradius vanaf die oppervlak. Ione buite die Stern-vlak vorm die diffuse deel van die dubbellaag (die buite Helmholtz-vlak) en is mobiel, terwyl ione met hul middelpunte binne die Stern-vlak geadsorbeer is (dit wil sê hulle is deur elastrostatiese of Van der Waals-kragte styf aan die oppervlak verbind).

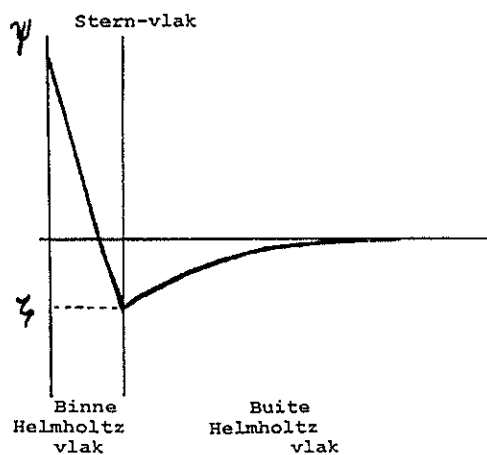


**Fig.1 Skematiese voorstelling van 'n elektriese dubbellaag**

Die grootte van die elektro-kinetiese beweging word bepaal deur die Zeta-potensiaal; die potensiaal by die vlak wat die geadsorbeerde ione (in die Stern-vlak) en die ione in die oplossing wat gebind is aan die gelaai oppervlak skei van die res van die diffuse laag ione. Buiten by baie hoë potensiale en elektroliet konsentrasies dien die Stern-vlakpotensiaal as goeie benadering van die Zeta-potensiaal. Die waarde van Zeta is intrinsiek aan 'n bepaalde stof in kontak met 'n bepaalde elektroliet.

### 3.- Elektro-osmose

Wanneer 'n elektriese veld oor 'n dubbellaag aangewend word, veroorsaak dit die beweging van ione na die elektrodes toe. Hierdie ione neem die watermolekules saam en ontwater sô die medium.

Uit die Smoluchowski-vergelyking blyk dit duidelik dat elektro-osmotiese vloeitempo

onafhanklik is van individuele openinge [1], [7]:

$$q = \frac{A \cdot E \cdot \epsilon \cdot Z}{\eta} \quad \dots\dots\dots(1)$$

...q: elektro-osmotiese vloeitempo [ $\text{m}^3/\text{s}$ ]

...A: totale deursnit area [ $\text{m}^2$ ]

...E: elektriese veldsterkte [ $\text{V/m}$ ]

...ε: elektriese permitiwiteit

...Z: Zeta-potensiaal [V]

...η : vloeistofviskosititeit

### 4.- Toepassing op steenkool

Figuur 2 toon 'n ideale toestand, vir berekening doeleindes, met 'n gaatjie, gevul met water, in 'n blok steenkool met 'n

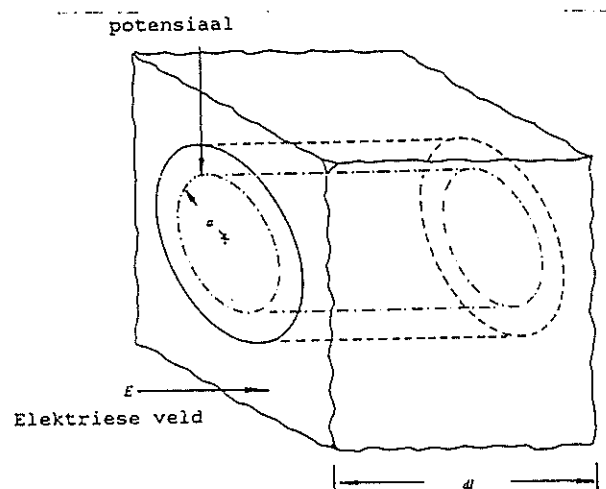


**Fig. 2 Steenkool met 'n gaatjie daarin.** elektriese veld daaroor aangelê. Die volume water ( $\pi a^2 dl$ ) kan in s sekondes deur elektro-osmose verpaas word en daardeur aanleiding gee tot 'n volumevloei van  $V \text{ m}^3 \text{ s}^{-1}$  met;

$$V = (N \pi a^3 \sigma E) / (4 \eta) \quad \dots\dots\dots(2)$$

Waar:

a = straal van een gaatjie

E = die elektrieseveldsterkte

S = die vrye-steenkool-oppervlakte regstandig met die vektore van E

N = die aantal gaatjies met straal oor die oppervlak S

σ = die ladingdigtheid wat aanleiding gee tot die elektro-

osmotiese krag

$\eta$  = viskositeit van die vloeistof.

Die porositeit  $\epsilon$  van die steenkool word gedefinieer as die verhouding van die vrye oppervlak  $S$  tot die totale area van gaatjies daarin, naamlik;

$$\epsilon = S / (N \pi a^2) \quad \dots\dots\dots(3)$$

Vervanging van 3 in 2 gee die volgende;

$$V = \beta S E \quad \dots\dots\dots(4)$$

Waar:

$$\beta = (a \sigma) / (4 \epsilon \eta)$$

Die konstante  $\beta$ , hierin genoem die konstante van elektro-osmose, berus op juiste gegewens oor die struktuur, tipe, porositeit ens. van die steenkool sowel as resistiwiteit,  $\rho$ , en pH van die water. Dit kan gerieflik deur middel van 'n eksperiment bepaal word. Hoë waardes van  $\beta$  verteenwoordig 'n hoë vloeitempo met minimale veldsterkte.

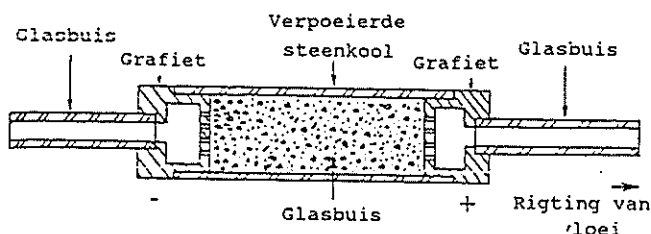


Fig.3 'n Snit van 'n sel vir bepaling van die konstante van elektro-osmose.

'n Sel vir die bepaling van  $\beta$  word in figuur 3 getoon. Gemete waardes van  $\beta$ , vir gepoeierde steenkool van die Grootgeluksteenkoolmyn word in tabel I gegee.

Dit blyk duidelik uit tabel I dat pH 'n beduidende invloed uitoefen oor  $\beta$  en dus oor die tempo van ontwatering en dat hoë stroomdigthede ook kontraproduktief is. Waardes van  $\beta$  so hoog as  $1,3 \times 10^{-6} \text{ m}^2 \text{ s}^{-1} \text{ V}^{-1}$  blyk haalbaar te wees by 'n pH van 6 en

'n ontwateringstempo van  $5 \times 10^{-9} \text{ m}^3 \text{ s}^{-1}$ .

TABEL I

Sel-metings van die Konstante van Elektro-osmose vir steenkool uit die Grootgeluksteenkoolmyn.

pH	V $\text{m}^3 \text{ s}^{-1}$	J $\text{A.m}^{-2}$	$\beta$ $\text{m}^2 \text{ s}^{-1} \text{ V}^{-1}$
8	$-0,6 \times 10^{-9}$	0,16	$-0,05 \times 10^{-6}$
6	$5 \times 10^{-9}$	0,16	$1,3 \times 10^{-6}$
6	$52 \times 10^{-9}$	272	$0,012 \times 10^{-6}$

### 5.- Vergelyking met termiese droging

Vergelyking 4 kan soos volg geskryf word;

$$E = V / (\beta S)$$

Die drywing wat benodig word om  $V$  kubieke meter water per sekonde te verwyder uit 1 meter steenkool ( $l$  regstandig op  $S$ ) word gegee deur;

$$P = (V^2 l) / (\beta^2 S \rho) \quad \dots\dots\dots(5)$$

Vergelyking 5 kan toegepas word om die drogingtempo van die elektro-osmotiese-vervoerband getoon in figuur 4 waar die gemiddelde hoogte  $l$  van die steenkool beskou

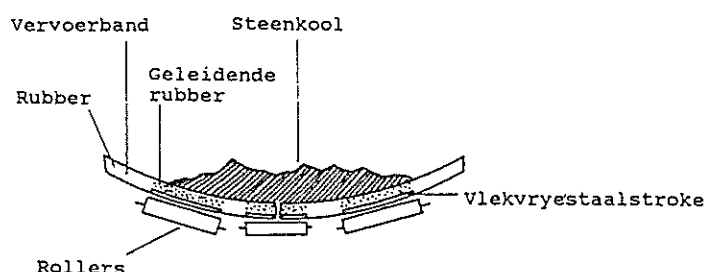


Fig. 4 Skets van 'n voorgestelde elektro-osmotiese vervoerbanddroër.

word as 0,05 m. Ander aannames is;

$$\begin{aligned}
 S &= 20 \text{ m}^2 \\
 V &= 1 \text{ m}^3 \text{ s}^{-1} \\
 \beta &= 0,4 \times 10^{-6} \text{ m}^2 \text{ s}^{-1} \text{ V}^{-1} \\
 \rho &= 100 \text{ } \Omega \text{ m}
 \end{aligned}$$

Vervanging in vergelyking 5 gee 'n drywing van 156 MW. Dit kan vergelyk word met termiese droging waar 2600 MW nodig sou word of 6 %.

### 6.- Gevolgtrekking

Uit teoretiese oorwegings nodig droging met elektro-osmose slegs 6 % van die drywing wat andersins met termiese droging verbruik sou word.

### 7.- Bronnelys

- [1] D.J. Shaw, "Introduction to Colloid and Surface Chemistry" Butterworth (pp. 148 - 182), 1980.
- [2] N.C. Lockhart en R.E. Stickland, "Dewatering Coal Washery Tailings Ponds by Electroosmosis," Powder Technology (Vol. 40 p. 215 - 221), 1984.
- [3] L.W. Heath en T. Demirel, "Pressurized Electroosmotic Dewatering of Fine Coal Suspensions," MS-verhandeling, Iowa State University, Ames, Iowa (p. 178 - 187), 1982.
- [4] S. Ju, M.E. Weber en A.S. Mujambar, "Electroosmotic dewatering of Bentonite Suspensions," Separating Technology (vol. 1 p.214 - 221),1991.
- [5] H. Yoshida en H. Yokawa, "Electroosmotic dewatering and Design Equations," Drying Technology (vol. 6 No.3 p.473 488 - 490), 1988.
- [6] M. Iwata, H. Igami, T. Murase en H. Yoshida, "Analysis of Electroosmotic Dewatering," Journal of Chemical Engineering of Japan (vol. 24, No. 1, p.45 - 50), 1991.
- [7] D. Ensminger, "Acoustic and Electro-acoustic methods of dewatering," Drying Technology (vol. 6, No.3, pp. 473, 488 - 490), 1988.
- [8] N. Berkowitz, "An introduction to Coal Technology," Academic Press (pp. 176 - 177), 1979.

## List of Authors

RM daP Adanjo	University of Pretoria . . . . .	53
R Ahlschlager	University of Cape Town . . . . .	175
S Ahmed	University of Cape Town . . . . .	61
C Badenhorst	University of Cape Town . . . . .	17
T Baker	University of Cape Town . . . . .	134
M Baret	University of Cape Town . . . . .	Supl
DC Barry	Pretoria Technikon . . . . .	42
HJ Beukes	University of Stellenbosch . . . . .	202,Supl
D Birtwhistle	Queensland University of Technology, Australia . . . . .	1
EC Botha	University of Pretoria . . . . .	105
J Bouwer	Pretoria Technikon . . . . .	65
AC Britten	Eskom TRI . . . . .	Supl
B Burton	University of Natal . . . . .	69
MJ Case	Rand Afrikaans University . . . . .	254,277
L Chen	University of Cape Town . . . . .	61
R Cruise	University of the Witwatersrand . . . . .	222
S Darie	University of CapeTown . . . . .	163
P Davel	University of Stellenbosch . . . . .	143
GJ Delport	University of Pretoria . . . . .	109
W Deyzel	Pretoria Technikon & Anglo American Research Laboratories . . . . .	226
G Diana	University of Natal . . . . .	77,210
AE Dickson	University of the Witwatersrand . . . . .	190
CE Dingley	University of Cape Town . . . . .	13,17,21,134,175
JA duToit	University of Stellenbosch . . . . .	202
B Dwolatzky	University of the Witwatersrand . . . . .	179,183,194
JPG Engelbrecht	University of Pretoria . . . . .	113
JHR Enslin	University of Stellenbosch . . . . .	121,Supl
I Ferguson	Eskom . . . . .	17
MM Ferreira	Potchefstroom University for CHE . . . . .	97
JA Ferreira	Rand Afrikaans University . . . . .	73
A Gaylard	University of the Witwatersrand . . . . .	45
JF Gieras	University of Cape Town . . . . .	81
LJ Grobler	University of Pretoria . . . . .	239
RG Harley	University of Natal . . . . .	69,77,85,89,167,210
R Herman	University of Stellenbosch . . . . .	5
M Hippner	University of Natal . . . . .	57
HV Hitzeroth	University of Cape Town . . . . .	9
A Hoch	University of Natal . . . . .	Supl
DA Hoch	University of the Witwatersrand . . . . .	186
JP Holtzhausen	University of Stellenbosch . . . . .	38,143
NM Ijumba	University of Nairobi . . . . .	268
IR Jandrell	University of the Witwatersrand . . . . .	151,171,179
GD Jennings	University of Natal . . . . .	167
MA Khan	University of Cape Town . . . . .	Supl
CE Kleinhans	University of Natal . . . . .	77,89,210
RG Koch	Eskom TRI . . . . .	121,264,272
G Kwasnik	Technikon Witwatersrand . . . . .	147

CF Landy	University of the Witwatersrand . . . . .	49,198,206,222,234
IE Lane	University of Pretoria . . . . .	93,97,101,105,109,113,117
		125,129,138,239,244,249,258
D Levy	Sydney University, Australia . . . . .	69,89
GW Louw	Rand Afrikaans University . . . . .	254
M Malengret	University of Cape Town . . . . .	Supl
MD McCulloch	Oxford University, UK . . . . .	77
L McKinnon	Queensland University of Technology, Australia . . . . .	1
R Melaia	University of the Witwatersrand . . . . .	234
AS Meyer	University of the Witwatersrand . . . . .	49,183,194,198,206,234
MSA Minhas	University of the Witwatersrand . . . . .	186
SD Michie	University of Cape Town . . . . .	21
W Mulder	University of Pretoria . . . . .	101,281
GH Muller	University of Stellenbosch . . . . .	25
L Mzamo	University of CapeTown . . . . .	163
G Naldrett	University of Cape Town . . . . .	Supl
SD Nielsen	University of the Witwatersrand . . . . .	151
T Orbach	University of the Witwatersrand . . . . .	179
A Pagel	University of the Witwatersrand . . . . .	198
E Palmer	Queensland University of Technology, Australia . . . . .	1
GMJ Parsley	University of Pretoria . . . . .	53
AR Perkin	University of Natal . . . . .	57
H Peterson	Rand Afrikaans University . . . . .	272
A Petroianu	University of Cape Town . . . . .	9,34,61,159
P Petzer	University of Stellenbosch . . . . .	202
JF Peyper	University of Pretoria . . . . .	249
J Pritchard	University of the Witwatersrand . . . . .	222
S Purmanund	University of Cape Town . . . . .	Supl
FGT Radloff	University of Pretoria . . . . .	93
TA Rae	University of Natal . . . . .	167
NH Ramage	University of the Witwatersrand . . . . .	264
MC Randelhoff	University of Natal . . . . .	77,89
PJ Randewijk	University of Stellenbosch . . . . .	Supl
P Rasekhi	WITS Technikon . . . . .	155
B Rautenbach	University of Pretoria . . . . .	129
MG Redelinghuys	University of the Witwatersrand . . . . .	171
D Reynders	University of the Witwatersrand . . . . .	151
JP Reynders	University of the Witwatersrand . . . . .	151,186,190
BS Rigby	University of Natal . . . . .	85
JL Rodgerson	University of Natal . . . . .	69,Supl
M Rohde	University of the Witwatersrand . . . . .	206
SD Roos	Rand Afrikaans University . . . . .	73
JG Roos	University of Pretoria . . . . .	105
JC Shapiro	University of the Witwatersrand . . . . .	194
C Slabbert	University of Stellenbosch . . . . .	45
JJ Smit	University of Pretoria . . . . .	138
ED Smith	University of Pretoria . . . . .	214,230,281
F Smith	University of Stellenbosch . . . . .	38
R Spée	Oregon State University, USA . . . . .	121,202
SR Stadler	University of Stellenbosch . . . . .	25
PH Swart	Rand Afrikaans University . . . . .	272,277
DA Swift	University of Natal . . . . .	Supl

J Talbot	University of Natal . . . . .	210
I Terblanche	University of Cape Town . . . . .	Supl
DR Theron	University of Stellenbosch . . . . .	5
R Traynor	University of the Witwatersrand . . . . .	151
JM van Coller	University of the Witwatersrand . . . . .	264
FS van der Merwe	University of Stellenbosch . . . . .	45
H van der Merwe	Eskom . . . . .	155
WC van der Merwe	University of the Witwatersrand . . . . .	171
WJ van der Merwe	Rand Afrikaans University . . . . .	277
J van Eyssen	Eskom . . . . .	34
GL van Harmelen	University of Pretoria . . . . .	117,244,258
R van Heerden	Eskom . . . . .	272
HR van Niekerk	University of Pretoria . . . . .	218
J van Rooijen	University of Stellenbosch . . . . .	25
JC van Tonder	University of Pretoria . . . . .	239
A van Zyl	University of Stellenbosch . . . . .	121
J Vermaak	University of Pretoria . . . . .	125
HJ Vermeulen	University of Stellenbosch . . . . .	25,45
O Von Abo	Eskom, Pretoria Technikon . . . . .	29
WL Vosloo	University of Stellenbosch . . . . .	143
PA Weyers	Pretoria Technikon . . . . .	42
MT Wishart	University of Natal . . . . .	167
G Wyatt	University of Cape Town . . . . .	13
J Yang	University of Pretoria . . . . .	214,230
R Zivanovic	Pretoria Technikon . . . . .	42,159

